DNAPL Remediation of Fractured Rock Evaluated via Numerical Simulation

by

Ti Wee Pang

A thesis submitted to the College of Science and Engineering in conformity with the requirements for the degree of Doctor of Philosophy.

The University of Edinburgh
Edinburgh, Scotland, United Kingdom March, 2010

DECLARATION

I hereby declare that all the material presented in this thesis is original, unless stated otherwise.

Author: Ti Wee Pang Date

ABSTRACT

Fractured rock formations represent a valuable source of groundwater and can be highly susceptible to contamination by dense, non-aqueous phase liquids (DNAPLs). The goal of this research is to evaluate the effectiveness of three accepted remediation technologies for addressing DNAPL contamination in fractured rock environments.

The technologies under investigation in this study are chemical oxidation, bioremediation, and surfactant flushing. Numerical simulations were employed to examine the performance of each of these technologies at the field scale. The numerical model DNAPL3D-RX, a finite difference multiphase flow-dissolution-aqueous transport code that incorporates RT3D for multiple species reactions, was modified to simulate fractured rock environments. A gridding routine was developed to allow the model to accurately capture DNAPL migration in fractures and aqueous phase diffusion gradients in the matrix while retaining overall model efficiency. Reaction kinetics code subroutines were developed for each technology so as to ensure the key processes were accounted for in the simulations. The three remedial approaches were systematically evaluated via simulations in two-dimensional domains characterized by heterogeneous orthogonal fracture networks parameterized to be representative of sandstone, granite, and shale.

Each simulation included a DNAPL release at the water table, redistribution to pools and residual, followed by 20 years of 'ageing' under ambient gradient conditions. Suites of simulations for each technology examined a variety of operational issues including the influence of DNAPL type and remedial fluid injection protocol. Performance metrics

included changes in mass flux exiting, mass destruction in the matrix versus the fractures, and percentage of injected remedial fluid interacting with the target contaminant.

The effectiveness of the three remediation technologies covered a wide range; the mass of contaminants destroyed were found to range from 15% to 99.5% of the initial mass present. Effectiveness of each technology was found to depend on a variety of critical factors particular to each approach. For example, in-situ chemical oxidation was found to be limited by the organic material present in the matrix of the rocks, while the efficiency of enhanced bioremediation was found to be related to factors such as the location of indigenous bacteria present in the domain and rate of bioremediation.

In the chemical oxidation study, the efficiency of oxidant consumption was observed to be poor across the suite of scenarios, with greater than 90% of the injected permanganate consumed by natural oxidant demand. This study further revealed that the same factors that contributed to forward diffusion of contaminants prior to treatment are critical to this remediation method as they can determine the extent of contaminant destruction during the injection period.

Bioremediation in fractured rock was demonstrated to produce relatively good results under robust first-order decay rates and active microorganisms throughout the fractures and matrix. It was demonstrated that under ideal conditions, of the total initial mass present, up to 3/4 could be reduced to ethene, indicating bioremediation may be a promising treatment approach due to the effective penetration of electron donor into the

matrix during the treatment period and the ongoing treatment that occurs after injection ceases. However, when indigenous bacteria was assumed to exist only within the fractured walls of sandstone, it was found that under the same conditions, the rate of dechlorination was 200 times less than the Base Case. Since the majority of the mass resided in the matrix, lack of bioremediation in the matrix significantly reduced the effectiveness of treatment.

Surfactant treatment with Tween-80 was proven to be a relatively effective technique in enhanced solubilisation of DNAPL from the fractures within the domain. However, by comparing the aqueous and sorbed mass at the start and end of the Treatment stage, it is revealed that surfactant treatment is not efficient in removing these masses that reside within the matrix. Furthermore, DNAPLs identified in dead end vertical fractures were found to remain in the domain by the end of the simulations across all scenarios studied; indicating that the injected surfactant experiences difficulty in accessing DNAPLs entrapped in dead end fractures.

Altogether, the results underscore the challenge of restoring fractured rock aquifers due to the field scale limitations on sufficient contact between remedial fluids and in situ contaminants in all but the most ideal circumstances.

DEDICATION

To my parents, Bernard, Christine and brother, Ti Yong.

To my partner Wenus.

ACKNOWLEDGEMENTS

The work contained in this thesis was funded by University of Edinburgh, University of Western Ontario, and by Queen's University through funding made available by the Environmental Security Technology Certification Program (ESTCP), project no. ER-0424. Technical support and resources were provided by Geosyntec Consultants, Queen's University, and University of Edinburgh.

I am deeply grateful to my supervisor Dr. Jason Gerhard for not only his financial support, guidance, interest and dedication to the research program from which I have benefited greatly, but also to his valuable resources, encouragement and invaluable feedbacks over the years. Thanks are expressed to Dr. Bernard Kueper for the time and expert advice he has provided during and since my stay at the Queen's University. I would also like to extend by appreciation to Mike West and Gavin Grant for their excellent technical input and their time in answering questions. Special thanks to Margaret Taylor and David Stewart who have provided valuable support over the years.

I would also like to thank my family and my partner Wenus. Words are insufficient to express my appreciation for the unconditional and unending support from them. This thesis would never have been completed without their words of support and encouragement.

FORWARD

Chapter 1 presents a general introduction to the research. Chapter 2 provides a review of the relevant literature. Chapter 3 describes the model development and model verification simulations conducted. Chapters 4, 5, and 6 – examining the effectiveness of chemical oxidation, bioremediation, and surfactant flooding in fractured rock, respectively - consist of manuscripts that are to be submitted to refereed journals within several weeks of completing this thesis. Chapter 7 provides a summary and general conclusion of the research. Appendices A through C provide additional information that was not included in the manuscripts (one for each manuscript chapter).

TABLE OF CONTENTS

DECLARATION.....**ii**
ABSTRACT..... **iii**
DEDICATION.....**vi**
ACKNOWLEDGEMENTS .....**vii**
FORWARD .....**viii**
LIST OF TABLES..... **xiv**
LIST OF FIGURES.....**xv**
NOTATION AND DEFINITION OF TERMS..... **xxviii**
CHAPTER 1 – INTRODUCTION.....**1**
CHAPTER 2 – LITERATURE REVIEW.....**9**
2.1 Key Processes 9
2.1.1 Single Phase Flow.....9
2.1.2 Multiphase Flow.....12
2.1.3 Dissolution 16
2.1.4 General Governing Equations.....23
2.1.5 Diffusion.....28
2.1.5.1 Introduction.....28
2.1.5.2 Stages of Diffusion.....30
2.1.5.3 Sorption ….....31
2.1.5.4 Fracture and Matrix Mass Storage Capacities.....33
2.1.5.5 Rates of DNAPL Loss from Single Fractures.....34
2.1.5.6 Rate of Diffusion in Fractured Network.....37
2.1.5.7 Limitation of Analytical Diffusion Models.....39
2.2 Numerical Modelling Methods for Multiphase Flow and Aqueous Phase Transport in Fractured Media…….....40
2.3 Chemical Oxidation…….....50
2.3.1 General…….....50
2.3.2 Chemical Oxidation in Fractured Environments…….....52
2.3.2.1 Permanganate.....52

2.4 Enhanced Bioremediation.....60
2.4.1 General 60
2.4.2 Hydrogen Release Compound.....67
2.4.3 Methane Enhanced Bioremediation 69
2.4.4 Electron Donors 71
2.4.5 Biobarriers 73
2.4.6 Numerical Modelling of Bioremediation.....74
2.4.7 Conclusion for Literature Review of Bioremediation.....75
2.5 Surfactant Flushing.....77
2.5.1 General 77
2.5.2 Processes that Reduce Surfactant Flood Efficiency.....79
2.5.3 Surfactants in Fractured Rock.....81
CHAPTER 3 – MODEL DEVELOPMENT.....83
3.1 Governing Equations 83
3.1.1 DNAPL3D Governing Equations..... 83
3.1.2 RT3D Governing Equations 86
3.1.3 Equations Relevant to Fractured Rock 87
3.2 Gridding Routine…….....89
3.2.1 Purpose of Gridding Routine 89
3.2.2 Method 90
3.3 Verification and Model Testing 95
3.3.1 Advection-dispersive Transport.....95
3.3.2 Two Phase Flow 95
3.3.3 Matrix Diffusion 97
3.3.4 Sorption …….....99
3.3.5 Testing on Multi-Fracture Scenarios 101
CHAPTER 4 – NUMERICAL SIMULATION OF DNAPL SOURCE ZONE REMEDIATION WITH IN SITU CHEMICAL OXIDATION IN FRACTURED ROCK ……113
4.1 Abstract…….....113
4.2 Introduction 115
4.3 Outline of Numerical Simulations 121

4.3.1 Model Description.....121
4.3.2 Chemical Oxidation Reactions 124
4.3.3 Model Verification 127
4.4 Numerical Simulations 129
4.4.1 Modelled Scenario 129
4.4.2 Base Case and Sensitivity Simulations 134
4.4.2.1 Injected Potassium Permanganate Concentration 137
4.4.2.2 Pulsed Injection of Permanganate 137
4.4.2.3 Rock Type.....138
4.4.2.4 DNAPL Type 138
4.5 Results and Discussions 141
4.5.1 Base Case Results 142
4.5.2 Sensitivity Simulations 155
4.5.2.1 Sensitivity to Potassium Permanganate Concentration 155
4.5.2.2 Sensitivity to Pulsed Injection 157
4.5.2.3 Sensitivity to Rock Type 160
4.5.2.4 Sensitivity to DNAPL Type 168
4.6 Conclusions 173
CHAPTER 5 – NUMERICAL SIMULATION OF DNAPL SOURCE ZONE REMEDIATION WITH ENHANCED IN SITU BIOREMEDIATION IN FRACTURED ROCK …….....177
5.1 Abstract…….....177
5.2 Introduction 179
5.3 Model Development …….....183
5.3.1 Bioremediation Equations 184
5.3.2 Model Verification 189
5.4 Numerical Simulations 194
5.4.1 Modelled Scenario 194
5.4.2 Base Case and Sensitivity Simulations 196
5.4.2.1 Microorganisms in Fractures/Matrix …….....200
5.4.2.2 Dechlorination Rate Parameters.....201
5.4.2.3 Pulsed Injection of Organic Substrate.....201

5.4.2.4 Organic Substrate Concentration.....202
5.4.2.5 Rock Type.....202
5.4.2.6 DNAPL Type.....203
5.5 Results and Discussions 203
5.5.1 Base Case Results 204
5.5.2 Sensitivity Simulations 219
5.5.2.1 Sensitivity to Microorganisms in Fractures/Matrix 219
5.5.2.2 Sensitivity to Dechlorination Rate Parameters ….....223
5.5.2.3 Sensitivity to Pulsed Injection of Organic Substrate 227
5.5.2.4 Sensitivity to Organic Substrate Concentration 229
5.5.2.5 Sensitivity to Rock Type 232
5.5.2.6 Sensitivity to DNAPL Type 239
5.6 Conclusions 245
CHAPTER 6 – NUMERICAL SIMULATION OF DNAPL SOURCE ZONE REMEDIATION WITH SURFACTANT FLUSHING IN FRACTURED ROCK ……249
6.1 Abstract…….....249
6.2 Introduction 251
6.3 Model Development …….....253
6.3.1 Surfactant Flushing Kinetics 253
6.3.1.1 Solubilisation …….....254
6.3.1.2 Micellar Partitioning Below DNAPL Solubility …….....255
6.3.1.3 Surfactant Reaction Module ……..…….….....258
6.3.1.4 Sorption ……..…….….....259
6.3.1.5 Mass Transfer …….....261
6.3.2 Model Verification …….....262
6.3.4.1 Surfactant Flushing Verification …….....263
6.4 Numerical Simulations 267
6.4.1 Modelled Scenario 267
6.4.2 Base Case and Sensitivity Simulations 271
6.4.2.1 Surfactant Concentration …….....275
6.4.2.2 DNAPL.....276

6.4.2.3 Rock Type.....276
6.4.2.4 Aging Time.....276
6.4.2.5 Mass Transfer Model.....277
6.5 Results and Discussions 277
6.5.1 Base Case Results 278
6.5.2 Sensitivity Simulations 293
6.5.2.1 Sensitivity to Surfactant Concentration …….....293
6.5.2.2 Sensitivity to DNAPL …….....298
6.5.2.3 Sensitivity to Rock Type …….....301
6.5.2.4 Sensitivity to Aging Time 310
6.5.2.5 Sensitivity to Mass Transfer Model 313
6.6 Conclusion 318
CHAPTER 7 – SUMMARY.....322
7.1 Overall Conclusions 322
CHAPTER 8 – REFERENCES.....328
APPENDIX A – ADDITIONAL INFORMATION FOR INSITU CHEMICAL OXIDATION STUDY IN FRACTURED ROCK……...357
APPENDIX B – ADDITIONAL INFORMATION FOR INSITU BIOREMEDIATION IN FRACTURED ROCK….....372
APPENDIX C - ADDITIONAL INFORMATION FOR SURFACTANT FLUSHING IN FRACTURED ROCK.....397

LIST OF TABLES

Table 3-1. Regridding Options for Near-Fracture Matrix Nodes and Associated Spacing Control Factors ……...…91
Table 4-1. Field Scale ISCO Fractured Rock Simulations ……..……...135
Table 4-2. Properties of Field Scale Fractured Rock Template Sites…….….135
Table 4-3. Fracture Density of Field Scale Fractured Rock Template Sites……..…..136
Table 4-4. Fluid Properties and Reaction Parameters ……..…..136
Table 4-5. Summary of Results for All ISCO Simulations…….……141
Table 5-1. Fluid Properties and Reaction Parameters for Verification Simulation …192
Table 5-2. Field Scale EISB Fractured Rock Simulations ……..……...197
Table 5-3. Properties of Field Scale Fractured Rock Template Sites…….….198
Table 5-4. Fluid Properties and Reaction Parameters ……..…..199
Table 5-5. Summary of Results for All EISB Simulations…….……204
Table 6-1. Fluid Properties and Reaction Parameters for Verification Simulation …264
Table 6-2. Field Scale Surfactant Flushing in Fractured Rock Simulations……272
Table 6-3. Properties of Field Scale Fractured Rock Template Sites…….….273
Table 6-4. Fluid Properties and Reaction Parameters ……..…..273
Table 6-5. Summary of Results for All Surfactant Flushing Simulation…….……278
Table A1. Summary of Different Rock Properties for Sandstone, Shale and Granite …357

LIST OF FIGURES

Figure 3.1: Example of grid refinement on a single coarse node occupied by a vertical fracture employing N=9 and (a) no refinement, (b) linear increasing refinement, (c) exponentially increasing refinement, and (d) equally spaced refinement……92

Figure 3.2: A fracture intersection 0.9m by 0.9m ……..……....93

Figure 3.3: A fracture intersection defined for a coarse finite difference domain with DX=DY=0.1; the domain after grid refinement using (a) equal spacing; (b) exponential spacing and (c) increasing spacing; with N = 9. The dots identify node centers ……..……..93

Figure 3.4: Verification of DNAPL3DRX-FRAC against Ogata and Banks (1961)…..96

Figure 3.5: Verification of DNAPL3DRX-FRAC against McWhorter and Sunada (1990)……96

Figure 3.6: Verification of DNAPL3DRX-FRAC for a solute diffusion in single half-fracture and adjacent matrix against Sudicky and Frind (1982)……...…98

Figure 3.7: Verification of linear sorption within the model for a single node …..……100

Figure 3.8: Verification of Langmuir sorption within the model for a single node…....101

Figure 3.9: A pair of identical 1m long fractures, one oriented vertically and the other oriented horizontally.……..……..…102

Figure 3.10: A 13m by 13m domain with the nodes that contain the two fractures variably discretized into seven exponentially spaced sub-nodes. The rest of the matrix is discretized using a 0.1m nodal spacing……..…….103

Figure 3.11: A 13m by 13m domain discretized uniformly using a 0.1m nodal spacing…….....104

Figure 3.12: Distribution of TCE after 1 year of DNAPL dissolution (Base Case)..….107

Figure 3.13: Distribution of TCE after 1 year of DNAPL dissolution (foc = 0.0005)…107

Figure 3.14: Cumulative aqueous and sorbed TCE from all sinks and sources after 1 year of dissolution (foc = 0.005)……..……108

Figure 3.15: Cumulative aqueous and sorbed TCE from all sinks and sources for lower foc simulation after 1 year of dissolution (foc = 0.0005)……..……..108

Figure 3.16: Various concentration profiles into the matrix over time.……...110

Figure 3.17: Model layout for chemical oxidation and enhanced bioremediation ……111

Figure 3.18: Model layout for surfactant flushing……...112

Figure 4.1: Verification of DNAPL3D-RX FRAC with model results from West et al. (2008) for various mass transfer expressions. Note: Results from West et al. (2008) are indicated with solid line while results from DNAPL3DRX-FRAC are indicated by symbols ……..…..……129

Figure 4.2: Distribution of permeability for the field scale fractured rock domains: (a) sandstone, (b) shale, and (c) granite. Colour corresponds to fracture permeability according to the scale bar provided; matrix permeability is uniform (black). Note that fracture apertures are exaggerated for visual purposes …….…….....140

Figure 4.3: DNAPL distribution for Base Case at (a) t_{TOTAL} = 0.5 years when DNAPL inflow and outflow are equal, and (b) t_{TOTAL} = 1 year when all DNAPL migration has ceased ……..…… 143

Figure 4.4: Distribution of aqueous and sorbed TCE after 20 years (t_{TOTAL} = 21 years) of DNAPL dissolution (i.e., Site Ageing stage)…….……..…..144

Figure 4.5: Distribution of aqueous species concentrations at t_{TOTAL} =23 years for Base Case after 2 years of chemical oxidation (i.e., Treatment stage): (a) TCE, (b) MnO_4, (c) MnO_2…….146

Figure 4.6: Distribution of aqueous TCE concentrations at t_{TOTAL} =28 years for Base Case, 5 years after chemical oxidation (i.e., Post-Treatment stage)……..…147

Figure 4.7: Concentration profile of aqueous TCE across a single fracture for the Base Case. Shown is a 1.0 m cross-section across a horizontal fracture (dotted line denotes location of the facture)……..…….…..……147

Figure 4.8: Cumulative aqueous and sorbed TCE from all sinks and sources for Base Case ……...…….…….....149

Figure 4.9: Cumulative mass of species involved in chemical oxidation for Base Case ……..…….……...…150

Figure 4.10: Comparison of total boundary mass discharge for base case with (a) a simulation where no ISCO was carried out and (b) since the start of the Treatment Stage only (timescale expanded for clarity) ……..……..…….153

Figure 4.11: Concentration of TCE at all three horizontal fractures in the Sandstone base case at the downgradient boundary over (a) the latter 18 years, and (b) since the start of the Treatment stage only (timescale expanded for clarity) …….....154

Figure 4.12: Cumulative mass of TCE destroyed for various MnO4 concentrations …156

Figure 4.13: Comparison of total boundary mass discharge for base case with (a) various MnO4 concentration injected and (b) since the start of the Treatment stage only (timescale expanded for clarity)……..…….…156

Figure 4.14: Cumulative mass of TCE destroyed for various pulsing periods ……..… 158

Figure 4.15: Comparison of total boundary mass discharge for base case with (a) various pulsing method and (b) since the start of the Treatment stage only (timescale expanded for clarity). …….……...……...…..159

Figure 4.16: Distribution of aqueous TCE after 20 years (t_{TOTAL} = 21 years) of DNAPL dissolution (i.e., Site Ageing stage) in (a) Sandstone, (b) Shale and (c) Granite ……...161

Figure 4.17: Comparison of total boundary mass discharge for different rock types; (a) from the beginning of the simulation to end of Site Ageing stage and (b) Treatment stage only (timescale expanded for clarity)…….164

Figure 4.18: Mass of aqueous and sorbed TCE in various rock domain at end of Site Ageing stage (i.e., t_{TOTAL} = 21 years) vs. Peclet number (log scale) for each individual domain……165

Figure 4.19: Cumulative mass of TCE destroyed for various rock types ……167

Figure 4.20: Cumulative aqueous and sorbed PCE from all sinks and sources for PCE Simulation…….……..169

Figure 4.21: Downgradient water volume discharge for (i) TCE and (ii) PCE Simulations……..……171

Figure 4.22: Cumulative mass of (i) contaminants mass destroyed (right axis) and (ii) MnO_4 injected……..……...…….172

Figure 4.23: Comparison of total boundary mass discharge for (a) various DNAPL (b) Treatment stage only (timescale expanded for clarity)……..…….172

Figure 5.1: Sketch of domain layout for verification simulation…….……193

Figure 5.2: Cumulative aqueous mass of TCE and various chlorinated by-products in the domain over time……193

Figure 5.3: Cumulative aqueous mass of TCE, various chlorinated by-products and lactate in the domain over time……194

Figure 5.4 Distribution of permeability for the field scale fractured rock domains: (a) sandstone, (b) shale, and (c) granite. Colour corresponds to fracture permeability according to the scale bar provided; matrix permeability is uniform (black). Note that fracture apertures are exaggerated for visual purposes……..205

Figure 5.5: DNAPL distribution for Base Case at (a) t_{TOTAL} = 0.5 years when DNAPL inflow and outflow are equal, and (b) t_{TOTAL} = 1 year when all DNAPL migration has ceased……..206

Figure 5.6: Distribution of aqueous and sorbed TCE after 20 years (t_{TOTAL} = 21 years) of DNAPL dissolution (i.e., Site Ageing stage)……207

Figure 5.7: Distribution of aqueous species concentrations at t_{TOTAL} =23 years for Base Case after 2 years of lactate injection (i.e., Treatment stage): (a) TCE; (b) 1,1, DCE; (c) VC; (d) Ethene; (e) Chloride; (f) Lactate……210

Figure 5.8: Distribution of aqueous species concentrations at t_{TOTAL} =28 years for Base Case (i.e., 5 years Post-Treatment stage): (a) TCE; (b) 1,1, DCE; (c) VC; (d) Ethene; (e) Chloride; (f) Lactate……212

Figure 5.9: Cumulative aqueous and sorbed TCE from all sinks and sources for base case……214

Figure 5.10: Cumulative mass of species involved in bioremediation for Base Case.....216

Figure 5.11: Cumulative mass of lactate involved in bioremediation for Base Case…217

Figure 5.12: Comparison of total boundary mass discharge (TCE) for base case with a simulation where no lactate was injected…….217

Figure 5.13: Concentration of TCE in various horizontal fractures at downgradient boundary……..218

Figure 5.14: Cumulative mass of species involved in bioremediation for the case when indigenous bacteria is only present in fractures……..220

Figure 5.15: Cumulative mass of chloride produced for microorganisms active in the matrix and fractures (base case) versus in fractures only (Run 2)……221

Figure 5.16: Comparison of total boundary mass discharge (TCE) for base case with (a) bioremediation within fractures only and (b) since the start of the Treatment Stage only (timescale expanded for clarity)…….221

Figure 5.17: Concentration of TCE in various horizontal fractures at downgradient boundary for bioremediation within fractures only…… 222

Figure 5.18: Cumulative mass of chloride being produced over time for different decay rate parameters…….224

Figure 5.19: Cumulative mass of various species within the domain involved in (a) high decay rate and (b) low decay rate parameters over time……225

Figure 5.20: Comparison of total boundary mass discharge (TCE) for base case with (a) various decay rate (b) since the start of the Treatment Stage only (timescale expanded for clarity)……226

Figure 5.21: Cumulative mass of ethene being produced over time for different pulsing method……227

Figure 5.22: Cumulative mass of ethene being produced over time for different pulsing method……228

Figure 5.23: Comparison of total boundary mass discharge (TCE) for base case with (a) various pulsing methods (b) since the start of the Treatment Stage only (timescale expanded for clarity)……228

Figure 5.24: Cumulative mass of chloride being produced over time for different injected concentration……230

Figure 5.25: Cumulative mass of lactate discharged over time for different injected concentration……231

Figure 5.26: Comparison of total boundary mass discharge (TCE) for base case with (a) various lactate concentration (b) since the start of the Treatment Stage only (timescale expanded for clarity)…….. 231

Figure 5.27: Distribution of aqueous TCE after 20 years (t_{TOTAL} = 21 years) of DNAPL dissolution (i.e., Site Ageing stage) in (a) Sandstone, (b) Shale and (c) Granite…….234

Figure 5.28: Comparison of total boundary mass discharge for different rock types; (a) from the beginning of the simulation to end of Site Ageing stage and (b) Treatment stage only (timescale expanded for clarity)……236

Figure 5.29: Mass of aqueous and sorbed TCE in various rock domain at end of Site Ageing stage (i.e., t_{TOTAL} = 21 years) vs. Peclet number (log scale) for each individual domain……..237

Figure 5.30: Cumulative mass of chloride and ethene produced over time for different rock types……238

Figure 5.31: Cumulative mass of lactate present in the domains over time……238

Figure 5.32: Downgradient water volume discharge for (i) TCE and (ii) PCE Simulations……241

Figure 5.33: Cumulative aqueous and sorbed PCE from all sinks and sources for PCE Simulation ……241

Figure 5.34: Cumulative mass of lactate over time for different DNAPL simulations.....243

Figure 5.35: Cumulative mass of chloride and ethene produced over time for different DNAPL simulations……244

Figure 5.36: Comparison of total boundary mass discharge for (a) different DNAPL and (b) since the start of the Treatment Stage only (timescale expanded for clarity)…… 244

Figure 6.1: Extramicellar concentration of (a) TCE and (b) PCE in Tween-80 solution (Data extracted from Kim et al., 2007)……257

Figure 6.2: Extramicellar best fit curves for TCE based on results extrapolated from Kim et al., 2007……258

Figure 6.3: Sketch of domain layout for test simulation…….....264

Figure 6.4: Cumulative aqueous mass of aqueous TCE, micelles, and surfactant species in a node over time for verification run……...265

Figure 6.5: TCE saturation along the length of fracture over time……266

Figure 6.6: Verification of rate-limited model and compared against results from Dickson and Thomson, 2003……..267

Figure 6.7 Distribution of permeability for the field scale fractured rock domains: (a) sandstone, (b) shale, and (c) granite. Colour corresponds to fracture permeability according to the scale bar provided; matrix permeability is uniform (black). Note that fracture apertures are exaggerated for visual purposes……274

Figure 6.8: DNAPL distribution for Base Case at (a) t_{TOTAL} = 0.5 years when DNAPL inflow and outflow are equal, and (b) t_{TOTAL} = 1 year when all DNAPL migration has ceased……...279

Figure 6.9: Distribution of aqueous and sorbed TCE after 20 years (t_{TOTAL} = 21 years) of DNAPL dissolution …… 280

Figure 6.10: Distribution of (a) Aqueous TCE; (b) Surfactant; (c) Micelles; (d) TCE Saturation, 2 years after surfactant injection……281

Figure 6.11: Distribution of (a) Aqueous TCE; (b) Aqueous Tween 80; (c) Micelles; (d) TCE saturation, 5 years after surfactant injection……283

Figure 6.12: Cumulative aqueous and sorbed TCE from all sinks and sources for Base Case Simulation……286

Figure 6.13: Cumulative aqueous and sorbed surfactant from all sinks and sources for Base Case Simulation…….286

Figure 6.14: Cumulative mass of TCE, surfactant and micelles for Base Case Simulation……287

Figure 6.15: Comparison of total boundary mass discharge (TCE) for (a) base case with a simulation where no surfactant was injected (b) since the start of the Treatment Stage for 1 year only (timescale expanded for clarity)……..…290

Figure 6.16: Comparison of total boundary mass discharge of TCE and micelles for base case simulation since the start of the Treatment Stage for 1 year only (timescale expanded for clarity)……....290

Figure 6.17: Cumulative TCE mass discharged at downgradient boundary……291

Figure 6.18: Concentration of TCE in various horizontal fractures at downgradient boundary……292

Figure 6.19: Total TCE DNAPL present in domain over time for (a) Base Case, (b) 20000mg/L and (c) 60000 mg/L of surfactant injected……294

Figure 6.20: Cumulative mass of TCE solubilised by micelles over time for different injected concentration Cumulative …….……295

Figure 6.21: Cumulative mass of surfactant discharged over time for different injected concentration…….296

Figure 6.22: Cumulative mass of surfactant used for solubilising DNAPL over time for different injected concentration……296

Figure 6.23: Cumulative TCE mass discharged at downgradient boundary for various concentrations…….297

Figure 6.24: Comparison of cumulative DNAPL mass solubilised by micelles and surfactant injected for period between 21 to 28 years……300

Figure 6.25: Comparison of total boundary mass discharge for different DNAPL with a simulation where no surfactant treatment (sandstone) was carried out for period between 21 to 28 years……...300

Figure 6.26: Cumulative mass discharged at downgradient boundary for various DNAPL simulations…….……301

Figure 6.27: Distribution of aqueous TCE after 20 years (t_{TOTAL} = 21 years) of DNAPL dissolution in (a) Sandstone, (b) Shale and (c) Granite……304

Figure 6.28: Mass of aqueous and sorbed TCE in various rock domain at end of Site Ageing stage (i.e., t_{TOTAL} = 21 years) vs. Peclet number (log scale) for each individual domain……305

Figure 6.29: Cumulative TCE mass solubilised by surfactant over time for various rock types…….306

Figure 6.30: Cumulative surfactant injected and used for TCE solubilisation for various rock types simulations……..307

Figure 6.31: Comparison of total boundary mass discharge for (a) different rock type with a simulation where No surfactant treatment (sandstone) was carried out for period between 21 to 28 years (b) since the start of the Treatment Stage for 1 year only (timescale expanded for clarity)…….....……309

Figure 6.32: Cumulative mass discharged at downgradient boundary for (a) sandstone; (b) shale and (c) granite……..310

Figure 6.33: Cumulative mass of TCE solubilised over time for different aging period……...311

Figure 6.34: Comparison of total boundary mass discharge for different aging period with a simulation where no surfactant treatment was carried out for period from 2 years of Treatment and 5 years of Post-Treatment…… 312

Figure 6.35: Cumulative mass discharged at downgradient boundary for (a) 0 years aging; (b) 5 years aging (c) 10 years aging and (d) 20 year aging……...313

Figure 6.36: Cumulative TCE captured and Tween-80 injected over time for rate-limited mass transfer simulation……314

Figure 6.37: Cumulative TCE mass in domain for (a) rate-limited mass transfer simulation (b) Base Case, over time……315

Figure 6.38: Distribution of TCE saturation, at the end of Treatment stage (i.e., t_{TOTAL} = 23 years) ……..315

Figure 6.39: Comparison of total boundary mass discharge for (a) different mass transfer model with a simulation where No surfactant treatment (equilibrium mass transfer) was carried out for period between 21 to 28 years (b) since the start of the Treatment Stage for 1 year only (timescale expanded for clarity)……317

Figure 6.40: Cumulative mass discharged at downgradient boundary for (a) equilibrium and (b) rate limited mass transfer model……..….318

Figure A1: Distribution of aqueous species concentrations at t_{TOTAL} =23 years for 5000 mg/L of MnO4 Simulation, after 2 years of chemical oxidation (i.e., Treatment stage): (a) TCE, (b) MnO_4, (c) MnO_2……358

Figure A2: Distribution of aqueous species concentrations at t_{TOTAL} =23 years for 1250 mg/L of MnO4 Simulation, after 2 years of chemical oxidation (i.e., Treatment stage): (a) TCE, (b) MnO_4, (c) MnO_2……359

Figure A3: Distribution of aqueous species concentrations at t_{TOTAL} =23 years for 3 Months Pulsing Simulation, after 2 years of chemical oxidation, aging period: (a) TCE, (b) MnO_4, (c) MnO_2……360

Figure A4: Distribution of aqueous species concentrations at t_{TOTAL} =23 years for 6 Months Pulsing Simulation, after 2 years of chemical oxidation, aging period: (a) TCE, (b) MnO_4, (c) MnO_2……361

Figure A5: Distribution of aqueous species concentrations at t_{TOTAL} =23 years for 1 Year Pulsing Simulation, after 2 years of chemical oxidation, aging period: (a) TCE, (b) MnO_4, (c) MnO_2……362

Figure A6: DNAPL distribution for (a) Shale and (b) Granite at t_{TOTAL} = 1 year when all DNAPL migration has ceased……363

Figure A7: Distribution of aqueous species concentrations at t_{TOTAL} =23 years for Shale, after 2 years of chemical oxidation, aging period: (a) TCE, (b) MnO_4, (c) MnO_2……364

Figure A8: Distribution of aqueous TCE concentrations at t_{TOTAL} =28 years for Shale, 5 years after chemical oxidation……365

Figure A9: Cumulative aqueous and sorbed TCE from all sinks and sources for (a) Shale Simulation and (b) Granite Simulation……365

Figure A10: Distribution of MnO4 concentrations at t_{TOTAL} =22 years for Shale, 1 years after chemical oxidation……...366

Figure A11: Concentration profile of (a) aqueous TCE; (b) MnO_4 and (c) MnO_2across a single fracture for the Base Case. Shown is a 1.0 m cross-section across a horizontal fracture (dotted line denotes location of the facture)……367

Figure A12: Distribution of aqueous species concentrations at t_{TOTAL} =23 years for Granite, after 2 years of chemical oxidation, aging period: (a) TCE, (b) MnO_4, (c) MnO_2……369

Figure A13: Distribution of aqueous TCE concentrations at t_{TOTAL} =28 years for Granite, 5 years after chemical oxidation……370

Figure A14: DNAPL distribution for PCE Simulation at t_{TOTAL} = 1 year when all DNAPL migration has ceased……370

Figure A15: Distribution of aqueous PCE after 20 years of site aging (i.e., t_{TOTAL} = 21 years) for PCE simulation……371

Figure B1: Distribution of (a) Aqueous TCE; (b) Aqueous DCE; (c) Aqueous VC; (d) Ethene; (e) Chloride; (f) Lactate, 5 years after lactate injection for indigenous bacteria present in facture only……..372

Figure B2: Distribution of (a) Aqueous TCE; (b) Aqueous DCE; (c) Aqueous VC; (d) Ethene; (e) Chloride; (f) Lactate, 5 years after lactate injection for low decay rate. ……..374

Figure B3: Distribution of (a) Aqueous TCE; (b) Aqueous DCE; (c) Aqueous VC; (d) Ethene; (e) Chloride; (f) Lactate, 5 years after lactate injection for high decay rate .....……..376

Figure B4: Total boundary mass discharge for various species in (a) Base Case; (b) High Decay Rate Parameter; (c) Low Decay Rate Parameter over time ….....…….378

Figure B5: Distribution of (a) Aqueous TCE; (b) Aqueous DCE; (c) Aqueous VC; (d) Ethene; (e) Chloride; (f) Lactate, 5 years after lactate injection for 3 Months pulse injection simulation. . ……..380

Figure B6: Distribution of (a) Aqueous TCE; (b) Aqueous DCE; (c) Aqueous VC; (d) Ethene; (e) Chloride; (f) Lactate, 5 years after lactate injection for 6 Months pulse injection simulation. . ……..382

Figure B7: Distribution of (a) Aqueous TCE; (b) Aqueous DCE; (c) Aqueous VC; (d) Ethene; (e) Chloride; (f) Lactate, 5 years after lactate injection for 12 Months pulse injection simulation. . ……..384

Figure B8: Distribution of (a) Aqueous TCE; (b) Aqueous DCE; (c) Aqueous VC; (d) Ethene; (e) Chloride; (f) Lactate, 5 years after lactate injection for 1000mg/L of lactate injection simulation. ……...386

Figure B9: Distribution of (a) Aqueous TCE; (b) Aqueous DCE; (c) Aqueous VC; (d) Ethene; (e) Chloride; (f) Lactate, 5 years after lactate injection for 4000mg/L of lactate injection simulation. . ……..388

Figure B10: Distribution of (a) Aqueous TCE; (b) Aqueous DCE; (c) Aqueous VC; (d) Ethene; (e) Chloride; (f) Lactate, 5 years after lactate injection for Shale simulation. . ……..390

Figure B11: Distribution of (a) Aqueous TCE; (b) Aqueous DCE; (c) Aqueous VC; (d) Ethene; (e) Chloride; (f) Lactate, 5 years after lactate injection for Granite simulation ..……..392

Figure B12: Distribution of (a) Aqueous PCE (b) Aqueous TCE; (c) Aqueous DCE; (d) Aqueous VC; (e) Ethene; (f) Chloride; (g) Lactate, 5 years after lactate injection for PCE simulation ……..394

Figure C1: Extramicellar best fit curves for PCE based on results interpolated from Kim et al., 2007 ...……..……..397

Figure C2: Cumulative aqueous and sorbed TCE from all sinks and sources for No Surfactant Simulation ……..…….....……..397

Figure C3: Comparison of total boundary mass discharge (TCE) for base case with (a) various Tween-80 concentration (b) zoom in of results……..398

Figure C4: Distribution of (a) Aqueous TCE; (b) Tween-80; (c) TCE occupied micelles, 5 years after injecting 20000mg/L of Tween-80……..399

Figure C5: Distribution of (a) Aqueous TCE; (b) Tween-80; (c) TCE occupied micelles, 5 years after injecting 60000mg/L of Tween-80……..400

Figure C6: Distribution of (a) Aqueous TCE; (b) Tween-80; (c) TCE occupied micelles, 5 years after surfactant injection for a domain inhibited with PCE ….……..401

Figure C7: Distribution of (a) Aqueous TCE; (b) Tween-80; (c) TCE occupied micelles, 5 years after surfactant injection for Shale ……..……..402

Figure C8: Distribution of (a) Aqueous TCE; (b) Tween-80; (c) TCE occupied micelles, 5 years after surfactant injection for Granite ……..403

Figure C9: Distribution of (a) Aqueous TCE; (b) Tween-80; (c) TCE occupied micelles, 5 years after Tween-80 injection for a 0-year ‘aged’ site ……..404

Figure C10: Distribution of (a) Aqueous TCE; (b) Tween-80; (c) TCE occupied micelles, 5 years after Tween-80 injection for a 5-years ‘aged’ site ……..405

Figure C11: Distribution of (a) Aqueous TCE; (b) Tween-80; (c) TCE occupied micelles, 5 years after Tween-80 injection for a 10-years ‘aged’ site …..……..406

Figure C12: Distribution of (a) Aqueous TCE; (b) Tween-80; (c) TCE occupied micelles, 5 years after surfactant injection for rate-limited mass transfer model …..……..407

NOTATION AND DEFINITION OF TERMS

Typical units are presented in brackets. [-] denotes a dimensionless parameter.

a^n specific interfacial area between DNAPL and groundwater for a REV [L^2L^{-3}]

a_0 specific contact area between the NAPL and the aqueous phase and is defined as the ratio of the NAPL/aqueous phase contact area per unit volume [L^{-1}]

α adsorption constant related to the binding energy in a Langmuir Isotherm (L^3M^{-1})

β maximum amount of solute that can be adsorbed by the solids (MM^{-1}) in a Langmuir Isotherm

B either the fracture spacing for slabs or the sphere radius [L]

C solute concentration in the bulk aqueous phase [M/L^3]

C_{eq} concentration at equilibrium (solubility) [M/L^3]

C_f average concentration in the fracture plane [M/L^3]

C_i concentration in the surrounding aqueous phase in the fracture [M/L^3]

C_M concentration in the matrix [M/L^3]

C_s concentration of sorbed aqueous phase [M/M]

C_{sw} concentration at the fracture surface boundary and is equal to the aqueous solubility of the chemical [M/L^3].

C_w concentration of solute in the aqueous phase [M/L^3]

C_{cmc}^{CE} concentration of chlorinated ethene DNAPL at CMC

C_{eq}^{CE} equilibrium chlorinated ethene solute concentration in the presence of a given surfactant concentration greater than the CMC

CMC critical micellar concentration

C^{Surf} surfactant concentration

C_{cmc}^{Surf} surfactant CMC

C_{TCE}^{EX} equilibrium extramicellular mass fraction of TCE at a given surfactant concentration

$\partial C_w / \partial x_i$ chemical concentration gradient defined in the opposite direction of the flux[M/L^3/L]

d_m mean particle diameter [L]

dh/dx magnitude of hydraulic gradient applied across the fracture plane [-]

D_e effective diffusion coefficient [L^2/T]

D^0, D^* free solution diffusion coefficient [L^2/T]

D^*_{im} matrix effective molecular diffusion coefficient [L^2/T]

D_{ij} hydrodynamic dispersion tensor [L^2/T]

D_m molecular diffusion coefficient for the soluble constituent [L^2 /T]

D_M effective diffusion coefficient in the matrix [L^2/T]

e fracture aperture [L]

e_h hydraulic aperture [L]

e_f frictional loss aperture [L]

e_{mb} mass balance aperture [L]

erfc complementary error function [-]

f_{oc} fraction of organic carbon [-]

g gravity [L/T^2]

J solute mass flux from the DNAPL to the aqueous phase [M/L^{3}T]

J_D diffusive flux [M/L^{3}T]

K mass transfer coefficient [L/T]

K_d distribution coefficient of the compound of interest [L^3/M].

Koc organic carbon partition coefficient [L^3/M]

k_e	effective mass transfer coefficient [L/T]
k_i	intrinsic mass transfer coefficient [L/T]
k_{la}	average mass transfer coefficient for the DNAPL-water interface [L/T]
k	permeability of the fracture [L^2]
kr_w	relative permeabilities to the wetting phases [-]
kr_{NW}	relative permeabilities to the non-wetting phases [-]
L_i	matrix block length in each of the principle directions [L]
M_m	maximum chemical mass storage capacity in the matrix
M_f	mass storage capacity in the fractures
M_t	total mass diffused into the matrix per unit area of fracture face
MSR	molar solubilization ratio [mol/mol]
nw	water-imbibition fitting exponent
P_e	entry pressure of the fracture [Pa]
P_w	wetting phase pressure [Pa]
P_{NW}	nonwetting phase pressure [Pa]
P_i	a function of the dimensionless time variable [$D_e t/RL_i^2$] [-]
Q	volumetric flow rate [L^3/T]
q_M	mass flux exchange between the matrix and the fracture [$M/L^2/T$]
q_d	aqueous phase source due to dissolution from the presence of NAPL in the fracture plane [$M/L^3/T$]
Re	Reynold's number
R	contaminant retardation factor [-]
Sh	Sherwood number [-]
Solub	solubility of DNAPL

Sn*(t)	normalized DNAPL saturation
Sn(t)	DNAPL saturation
$Sn_{8\%}$	DNAPL saturation when 8% of initial mass is removed
S_w	degree of water saturation [-]
S_{wb}	water breakthrough saturation [-]
T	tortuosity of the matrix [-]
T_f^r	aqueous-phase relative transmissivity [L^2/T]
Y_{H2}	Hydrogen yield coefficient [-]
t	time [T]
x	distance in the x-direction [L]
w	fracture width perpendicular to flow [L]
t_D	disappearance time [T]
υ	magnitude of the average aqueous phase velocity in the fracture [L/T]
υ_i	average aqueous phase velocity in the fracture plane [M/T]
α_L	longitudinal dispersivities [L]
α_T	transverse dispersivities [L]
δ	aperture ratio [-]
δ_{ij}	Kroneker delta function [-]
μ	fluid viscosity [P.T]
μ_w	viscosity of wetting phase [P.T]
μ_{NW}	viscosities of nonwetting phases [P.T]
ρ	density of the flowing fluid [M/L^3]
ρ_W	density of the wetting phases [M/L^3]

ρ_{NW} density of the nonwetting phases [M/L^3]

ρ_b dry bulk density [M/L^3]

σ interfacial tension between the fluids [M/L]

θ porosity of the porous medium [-]

λ first-order decay constant [T^{-1}]

$Ø_b$ bulk porosity [-]

$Ø_m$ matrix porosity [-]

$Ø_f$ fracture porosity [-]

CHAPTER 1 – INTRODUCTION

Groundwater pollution by hazardous industrial liquids is a serious environmental problem. Since the turn of the century, contamination has resulted from releases of chlorinated solvents such as trichloroethylene (TCE), tetrachloroethylene (PCE) and dichloromethane (DCM), presenting a challenge to subsurface investigation and remediation (Pankow and Cherry, 1996). These contaminants form part of a larger group of common industrial liquids known as non-aqueous phase liquids (NAPLs). NAPLs characteristically have very low solubilities in water and, as a result, are able to persist as a separate liquid phase in the subsurface. Upon contact with flowing groundwater, entrapped NAPL dissolves into the aqueous phase resulting in a plume that migrates in the direction of groundwater flow. However, despite their low solubilities, NAPLs typically produce dissolved phase concentrations that are in excess of the strict drinking water standards for these compounds (McCarty et al., 1998). In addition, apart from being toxic themselves, NAPLs can degrade to form other hazardous substances, such as vinyl chloride (VC), which can threaten human health and inhibit land reutilization (Gandhi et al., 2002).

The problem of groundwater clean-up is exacerbated by the desire to return aquifers to drinking-water quality, which for many important organic contaminants requires concentrations less than 100 parts per billion (ppb) and in some cases less than 5 ppb. However, the concentrations in groundwater drawn by wells are controlled in part by transfer of contaminant mass to the flowing water from other phases acting as contaminant reservoirs: contaminant sorbed by the aquifer solids, contaminant present in immobile pockets of contaminated groundwater in less permeable but porous strata or

lenses, vapour spreading from residual or pooled NAPL in the vadose zone, or dissolution of residual or pooled NAPL in the saturated zone. Such mass reservoirs can cause the extracted groundwater to exceed drinking-water standards for prolonged periods of time, in part due to the inherently rate-limited nature of these mass transfers process (Mackay and Cherry, 1989).

NAPLs include fluids that are less dense than water (LNAPLs), such as petroleum solvents or fuels, and those that are denser than water (DNAPLs), such as chlorinated solvents and creosote. Upon introduction to the subsurface, the high densities and typically low viscosities make DNAPLs extremely mobile in both saturated and unsaturated media (Kueper and Frind, 1991a). The subsurface migration of DNAPLs is not dictated by groundwater flow but by geological structures (e.g., fissures, faults and bedding planes), soil properties (e.g., porosity and permeability) and advective and diffusive gradients in the immiscible phase liquid itself. As a result, DNAPL migration patterns are often complex and exhibit sensitivity to the fluid properties of the immiscible organic liquid and to centimetre-scale variations in capillary properties surrounding the release location (Kueper and Frind, 1991b).

Many industrial sites where DNAPLs have been released to the subsurface are characterized by near-surface fractured rock or fractured clay deposits. Subsurface aquifers that exhibit groundwater presence in both a primary porosity and secondary fracture porosity are termed fractured permeable formations (Birkhölzer et al. 1993a). In such formations the fracture porosity typically amounts to no more than a few percent,

but can contribute substantially to the effective conductivity (Pettijohn et al. 1987) of the entire formation. Fractured rock can generally be classified into two main categories: (i) Fractured media with low matrix porosity and (ii) Fractured media with high matrix porosity. Fractured media with low matrix porosity are common in crystalline rock including granite, gneiss, and schist. Examples include bedrock in the Piedmont and Blue Ridge Mountain region of the southeastern United States and Dartmoor in the south of England. The primary transmissive feature in fractured media with low matrix porosity settings is secondary permeability caused by fractures, because little to no void space exists in the matrix. The permeability of the matrix is considered to be less than 10^{-17} m^2 ($K < 10^{-10}$ m/s). However, the bulk permeability of the media is dependent on the frequency, aperture size, and degree of interconnection of the fractures, such that the anticipated range of bulk permeability values is 10^{-15}–10^{-11} m^2 ($K = 10^{-8}$–10^{-4} m/s). It has also been noted that in such media, the porosity of both the matrix and the fractures is typically small (i.e., less than 1 percent). However, in regions where crystalline rock has been extensively weathered (e.g., at the top of bedrock), the bulk media can behave more like a porous medium than what would be expected from a fractured rock type setting (WSTB, 2004).

The second type of fractured rock – fractured media with high matrix porosity – includes systems where fractures are the primary transmissive feature and there is significant void space in the matrix. The permeability of the matrix is considered to be less than 10^{-17} m^2 ($K < 10^{-10}$ m/s) while the anticipated range of bulk permeability values, due to generally smaller fracture apertures, is 10^{-16}–10^{-13} m^2 ($K = 10^{-9}$–10^{-6} m/s). The porosity

of the fractures relative to the total unit volume is small (e.g., <1 percent). However, unlike fractured media with low matrix porosity, the porosity of the matrix in a fractured media with high matrix porosity is anticipated to fall in the range of 1-40 percent. Fractured media with high matrix porosity are commonly encountered in sedimentary rock (e.g., limestone, dolomite, shale, and sandstone) and fractured clays. Examples include the Niagara Escarpment in the vicinity of the Great Lakes and fractured lake-deposited clay in Sarnia, Ontario, Canada (WSTB, 2004).

Some of the scenarios in which fractured environments play a central role include contaminant transport in a rock aquifers, radionuclide migration from a nuclear waste repositories and the recovery of hydrocarbons from the subsurface. Some examples of DNAPL-impacted sites located in fractured geologic materials media are presented by Smith and Schwartz (1984), Villaume (1985), Cherry (1989), Mackay and Cherry (1989), and Feenstra (1991) among others. Numerous theoretical and experimental studies on the processes of NAPL migration and solute transport in fractured rock have been conducted over the years using both artificial and natural fractures in a variety of rock types (e.g., National Research Council, 1994; Cherry, 1989; Forsyth, 1991; Grisak and Pickens, 1981; Konzuk and Kueper, 2004; Lerner et al., 2002; Wealthall et al., 2001; Parker et al., 1994). These studies have shown that fractures in the host rock and the interaction of these fractures with the adjacent rock matrix play a critical role in determining a wide range of multiphase flow and contaminant transport processes.

If released in sufficient volume, DNAPL may penetrate to significant depth in the subsurface, primarily under the influence of gravity, until the source is depleted or the invading fluid is immobilized by capillary forces (Kueper and McWhorter, 1991). Predicting DNAPL migration requires accurate representations of the local scale constitutive relationships (Gerhard and Kueper, 2003c). Reitsma and Kueper (1994) presented an analysis of the hysteretic relationship between capillary pressure and fluid saturation for a single rough walled fracture. This study demonstrated that the form of the relationship between capillary pressure and saturation that is central to DNAPL migration, in unconsolidated porous media is also applicable to DNAPLs in fractures. In general, the principles governing DNAPL migration in unconsolidated porous media (e.g., entry pressure, relative permeability) are found to also apply to DNAPL migration in fractured porous media.

When a DNAPL spill occurs in the vicinity of surface or near-surface deposits of fractured clay or fractured sedimentary bedrock, it is normal for the free phase to completely penetrate the thin overburden, and subsequently accumulate above the fractured media. Fracture penetration occurs when the capillary pressure at the base of this DNAPL accumulation, or pool, exceeds the entry pressure of a fracture. Upon breaching this capillary barrier, the DNAPL will migrate downwards under the influence of both pressure and gravity forces (Mercer et al., 1990) and may flow laterally in the fracture network if fracture closure with depth prevents downward migration or if vertical pathways are unable to accept the total DNAPL flux (Kueper et al., 1992; Kueper and McWhorter, 1991). Kueper and McWhorter (1991) revealed that the time taken for a

DNAPL to migrate through a fractured sequence is inversely proportional to the aperture of the fractures, the fracture dip from horizontal, and the height of the DNAPL pool above the fractured unit. If sufficient pool heights are available, the DNAPL may penetrate extensive fracture sets and migrate to significant depth, forming networks of pools and interconnected pathways of DNAPL (Kueper et al., 2003).

In fractured bedrock aquifers where DNAPL migration is excluded from the matrix, fluid movement will be limited to the interconnected fracture porosity (Ross and Lu, 1999). For many bedrock aquifers, the fractures represent only 0.001-0.1% of the bulk volume of the rock mass (Mackay and Cherry, 1989). Such exclusion is possible since matrix permeabilities in rock are typically low while matrix entry pressures are correspondingly high (Kueper and McWhorter, 1991); thus DNAPL flow in a fracture network is often restricted to the open fractures, which therefore serve as the primary pathways for DNAPL movement in the subsurface (Pankow and Cherry, 1996). This migration scenario suggests that even a small amount of DNAPL can travel a long way in a fractured bedrock aquifer (Reitsma and Kueper, 1994).

As in unconsolidated porous media, in regions of the fracture network where imbibition has occurred, residual ‘blobs and ganglia’ of DNAPL will be formed. Once formed, the fate of residual DNAPL in a fractured rock mass may be governed by matrix diffusion for the case of high DNAPL solubility and high matrix porosity (Parker et al., 1994). In fractured porous media, dissolution can occur within the fracture plane as well as into the porous matrix surrounding the fracture (matrix diffusion). The amount of mass available

to diffuse into the matrix is dictated primarily by the amount of residual formed during the initial migration event (Logino and Kueper, 1999). A driving force for diffusion into the matrix is provided by the concentration gradients between the aqueous phase present at the fracture surface and the essentially immobile pore water in the matrix. As dissolution and diffusion proceeds, the amount of DNAPL in the fracture is diminished and, eventually, all the contaminant mass may be transferred to the matrix. The diffusing aqueous phase contaminant in the matrix can both continue to travel further into the matrix and can sorb to the matrix solid.

The restoration of fractured porous media contaminated by a DNAPL release is often more difficult than for more unconsolidated porous media. This is due to the difficulty in identifying the source zone, and also the fact that many traditional remedial technologies (e.g., pump and treat) are relatively ineffective in vastly heterogeneous situations such as fractured rock (Powers et al. 1991; National Research Council 1994). The reason is that little or no water flushes through dead-end fracture segments or through the porous but relatively impervious matrix, both of which are likely to retain the bulk of the contaminated mass (Mackay and Cherry, 1989). Clean water flushed through the fractures does reverse the concentration gradients and allows mass to be removed from the matrix. However, the relatively slow rate of release of contaminants from the clay/rock matrix by diffusion, coupled with the potentially appreciable contaminant mass contained in dissolved and sorbed form in the matrix, can cause a long-term bleed of contaminants into the aquifer during remediation (USEPA, 2001). Furthermore, if pumping is ceased before all of the contaminant is removed, the

contaminant concentrations in the groundwater will rebound (USEPA, 2001).

The investigation and application of remedial technologies to DNAPLs in fractured environments is lagging far behind their application to sandy, unconsolidated media (SERDP 2001). At this time, three in situ technologies with significant promise and supported by substantial research (in any type subsurface environment) are chemical oxidation, enhanced biodegradation, and surfactant flushing (Geosyntec 2004). These three are the leading candidates for consideration at sites dominated by fractured rock but very little is known about their relative effectiveness or the influence on their performance of site-specific or engineering application parameters (Geosyntec 2004).

CHAPTER 2 – LITERATURE REVIEW

This chapter presents a summary of research relevant to the modelling of fluid flow and transport in fractured porous media. Emphasis is placed on a few key areas, including multiphase flow, governing equations of flow, and dissolution and diffusion in fractured rock. Numerical modelling approaches employed for simulating multiphase flow and aqueous phase transport in fractured media is examined. The pertinent theory and available studies for the application of chemical oxidation, surfactant flushing and bioremediation to DNAPL source zones in a fractured media are also summarized.

2.1 KEY PROCESSES

2.1.1 Single Phase Flow

In order to have a better understanding of the mechanisms that govern fluid flow and to predict migration patterns and timescales, the study of phase interactions is essential. Although the study of phase interactions at the pore scale is important, it is generally considered to be impractical. The continuum concept considers the fluid phases and the solid phase as spatially continuous across a macroscopic (local scale) volume of the subsurface (Bear, 1972). This approach enables the theoretical framework to shift from the pore scale (microns) to the more practical local scale (centimetres). Although it is known that phase properties are spatially discontinuous at the pore scale, the continuum concept involves the averaging of pore scale phase properties over a minimum volume of subsurface to give macroscopic or local scale property values. The representative elementary volume (REV) is the minimum volume over which the macroscopic property

values are valid (i.e., the volume above which the average property values do not vary). Thus the local (REV) scale is that at which Darcy's law is considered valid (Bear, 1972).

Fluid flow through a fracture is typically conceptualized as laminar flow between two perfectly smooth parallel planes, (i.e., constant fracture aperture). However, in reality, fractures predominantly exhibit rough surfaces with irregular, spatially varying apertures which are often over parts of the planar fracture areas (Witherspoon et al., 1980). Although the parallel plate approximation is an oversimplification of the nature of fractures, it facilitates useful analyses of contaminant behaviour. At the macroscopic scale, a hydraulic aperture can be defined from single-phase flow test data using the cubic law for laminar flow between two parallel plates (Bear, 1972):

$$Q = -\frac{e_h^{\,3} w \rho g}{12\mu}\frac{dh}{dx} \qquad (2.1)$$

where Q is volumetric flow rate [L^3/T], w is fracture width perpendicular to flow [L], ρ is the density of the flowing fluid, μ is the fluid viscosity and dh/dx is the magnitude of hydraulic gradient applied across the fracture plane. The hydraulic aperture, e_h, represents the equivalent separation of two parallel plates required to produce the observed flow rate for a given hydraulic gradient.

Comparing Equation 2.1 to Darcy's Law indicates that the intrinsic permeability (k) of the parallel plate fracture equals $e^2/12$ (e.g., Konzuk and Kueper, 2004). The cubic law has been shown by others to be a valid approximation over a wide range of conditions

with aperture ranging down to a minimum of 0.2μm (e.g., Lomize, 1951; Louis, 1969). The cubic law was also found to be valid whether the fracture surfaces were open or being closed under stress, and it is not dependent on the type of rock but on the magnitude of the aperture (Witherspoon et al., 1980). Further supporting the usefulness of Equation 2.1, bulk fracture hydraulic conductivity was also demonstrated by Hoek and Bray (1981) to increase proportionally to the cube of the fracture aperture and to the number of fractures per unit length of rock.

Tracer tests are often used to investigate the flow characteristics of fractures and can provide an alternative means to determining its "equivalent aperture". However, such measurements were generally not in agreement with the "equivalent aperture" as determined by Equation 2.1 (Tsang, 1992). Tsang (1992) demonstrated that this apparent disagreement was due to a fundamental difference in the approaches taken to calculate the respective equivalent aperture. A comparison of the frictional loss (e_f), mass balance (e_{mb}) and hydraulic aperture in experimental fracture planes reveal the following ordering (Tsang, 1992):

$$e_{mb} \geq e_h \geq e_f \qquad (2.2)$$

The hydraulic and frictional loss apertures are essentially dependent on the hydraulic head difference across the fracture plane, and are therefore sensitive to the regions of high head loss, which correspond to the smaller aperture regions. These aperture measurements are hence sensitive to local heterogeneities, and are weighted towards the smaller apertures encountered along the flow path (Dickson and Thomson, 2002).

Conversely, the mass balance aperture is not sensitive to the head loss across the fracture plane, but to the storage of tracer in the void space, which occurs in the larger aperture regions. The mass balance aperture therefore represents an average aperture along the flow path of tracer transport, and is considered to provide the best estimate of the arithmetic mean aperture (Tsang, 1992) of the domain.

2.1.2 Multiphase Flow

A review of previous work done on NAPL was carried out by Mercer and Cohen (1990), who then provided an extensive overview of NAPL properties and behaviour in the subsurface. Over the years, much research has been carried out in relation to multiphase flow in fractured environments (e.g., Pankow and Cherry, 1996; Reynolds, 2001; Reitsma and Kueper, 1994; Kueper and McWhorter, 1991; Birkhölzer, 1993, Cherry, 1989; Longino and Kueper, 1999; Mendoza, 1992; Parker et al., 1994; Wealthall and Lerner, 2002). With respect to multiphase flow, the spatially variable distribution of apertures in the fracture plane makes it behave essentially like a two-dimensional porous media. Two of the main differences between unfractured and fractured deposits are that (i) the residual nonwetting phase saturations may be higher in a fracture due to the decreased possibility of by-passing, and (ii) as DNAPL comes into contact with the wetting phase in the fracture, the wetting phase is able to escape through the matrix (Reynolds, 2001). With respect to the first, it is generally acknowledged in unconsolidated deposits that residual DNAPL saturations are on the order of 5-15%. For experimentally measured fractures, Longino and Kueper (1999) determined a value of 3-21%. Overall, unlike unconsolidated porous media, wetting phase behaviour in fractured environments is not

purely a function of pore size distribution and trapping.

Multiphase flow at the REV scale is described by constitutive relationships that express the interdependence of capillary pressure, saturation, and relative permeability. The majority of work on constitutive relationships has been confined to (consolidated and unconsolidated) unfractured media (Gerhard and Kueper, 2003). However, a key study by Reitsma and Kueper (1994) measured constitutive relationships for a natural rock fracture. That study reported that the Brooks-Corey capillary pressure-saturation function was more appropriate for a fracture than the van Genuchten function due in part to the presence of a distinct displacement pressure; a conclusion that is mirrored by research in sandy porous media (Gerhard and Kueper, 2003a). Agreement was found by the percolation modelling study of Steele and Lerner (2001). Reitsma and Kueper (1994) further demonstrated hysteretic behaviour in the relationship between capillary pressure and fluid saturation in a single, rough-walled fracture as is typical in unfractured porous media. Similar findings were reported by Mendoza (1992). Overall, the evidence suggests that capillary pressure constitutive theory developed primarily for unconsolidated porous media environments is appropriate for multiphase flow through fractures as well.

With respect to relative permeability, Reitsma and Kueper (1994) suggest that the Brooks-Corey relationship used in porous media is adequate in describing relative permeability in fractures. Relative permeability functions were measured for two-phase flow in rough-walled fractures by Persoff and Pruess (1995). This study determined that

significant interference between the flowing phases due to viscous drag caused significant reductions in the relative permeability of each at intermediate saturations, similar to flow through unconsolidated media. That study concluded that significant simultaneous movement of both phases was favoured with increasing anisotropic aperture distributions and with increasing spatial correlation length in the direction of flow.

Mendoza (1992) developed the following volume-based relationship that relates the degree of water saturation in a fracture to the relative transmissivity of the wetting phase:

$$T_f^r = 1 - \left[erfc\left(\frac{S_w - S_{wb}}{1 - S_{wb}} \right)^{nw} \right]^2 \qquad (2.3)$$

where T_f^r is the aqueous-phase relative transmissivity [L^2/T]; *erfc* is the complementary error function; S_w is the degree of water saturation [-]; S_{wb} is the water breakthrough saturation [-]; and *nw* is a water-imbibition fitting exponent [-]. The water breakthrough saturation is defined by Mendoza (1992) as the degree of water saturation at which point groundwater flow can first occur in a fracture that is initially filled with non-aqueous-phase liquid. This is similar to the concept of emergence saturation for DNAPL flow in water-saturated unconsolidated porous media (Gerhard and Kueper, 2003b). The above relationship was based on the results of extensive Monte Carlo analyses of two-phase flow through a two-dimensional, rough-walled fracture plane. It is concluded from the limited work available, that relative permeability constitutive theory developed primarily for unconsolidated porous media may reasonably approximate behaviour in fractured media.

It is possible under certain circumstances for NAPL to penetrate the matrix from the fracture plane. In static systems, such an occurrence depending on the pore throat size of the matrix generally requires extremely large capillary pressures in the fracture so as to overcome the matrix displacement pressure. Haghighi et al. (1994) investigated this phenomenon for dynamic systems using a series of etched glass micromodel experiments. Through these experiments, it was found that matrix invasion only occurred above a certain flow rate in the fracture, which depended on the critical capillary number of the matrix pores (Note: capillary number expresses the ratio of viscous to capillary forces).

Another fundamental difference in a fractured environment from an unfractured porous medium is the presence of dead-end fractures. When DNAPL enters a fractured aquifer, it flows mainly through the interconnected fractures and comes to rest in discontinuous segments of the fracture system - a process that may result in pooling of contaminant in the dead-end fractures (Mackay and Cherry, 1989). Meanwhile, relatively small volumes of DNAPL can move far into the fractured medium due to the small retention capacity offered by the dead-end fractures as compared to the larger fractures. When attempts are made to clean fractured rock aquifers by pumping water through them, major improvements in water quality are exceedingly slow because little or no water flushes through these dead-end fracture segments (Mackay and Cherry, 1989). Yeo et al. (2003) demonstrated that surfactant-enhanced remediation has difficulty in removing DNAPL trapped from vertical downward dead-end fractures, due to the lack of water flow through them. In general, this study demonstrated that effective delivery of remedial fluids to dead-end fractures is very difficult to achieve. In these segments, it is only the process

of diffusion, both along the fractures and into the adjacent matrix, which will lead to the disappearance of the DNAPL (VanderKwaak and Sudicky, 1995).

2.1.3 Dissolution

When two immiscible phases, say DNAPL and water, come into contact, the molecules of the different compounds interact across an interfacial boundary that separates them. When the net flux of molecules across the boundary is zero, equilibrium is reached and the concentration of the DNAPL compound (assuming a single component DNAPL) in the wetting phase is equal to the compound's theoretical effective solubility (Geller and Hunt, 1993). At equilibrium, the mass transfer is at steady state and the dissolution rate equals to zero.

Much research effort has recently been focused on understanding the dissolution of pooled or residual DNAPL located above and below the water table in granular media (Fried et al., 1979; Abriola and Pinder, 1985a,b; Hunt et al., 1988a,b; Mackay et al., 1991; Anderson et al., 1992a,b; Johnson and Pankow, 1992; Geller and Hunt, 1993). These studies indicated that long contact times between the DNAPL and the groundwater produce aqueous-phase concentrations near or at their effective equilibrium solubility values, at least in the vicinity of the DNAPL source. Miller et al. (1998) and others have observed that near-equilibrium concentrations are achieved in the wetting phase within short travel distances through NAPL-occupied porous media. This is consistent with the findings of Frind et al. (1999), where near-equilibrium concentrations were observed immediately downgradient of an emplaced uniform DNAPL source at the

Borden field site. Numerical studies often assume equilibrium partitioning of the contaminant between the non-aqueous and aqueous phases in granular media including Baehr and Corapcioglu (1987), Kaluarachchi and Parker (1990), Forsyth (1991) and Unger et al. (1995).

However, the equilibrium assumption is known to have restricted applicability. Miller et al. (1990), studying mass transfer between a NAPL phase and an aqueous phase in a porous media using an experimental approach, reported that dissolution is mainly made up of three distinct stages: an initial pseudo-steady stage, a transient stage, and a tailing stage. The initial pseudo-steady stage was characterized by initially high effluent concentrations, which gradually decreased as greater volumes of water passed through the system, distinguishing the transient stage of the profile. Eventually the effluent concentrations established another steady condition, this time at a much lower concentration, indicative of the tailing stage of the profile. The majority of the mass removal occurred during the initial pseudo-steady stage which persists as long as no more than 10% of the initial mass trapped is dissolved (Miller et al., 1990).

Over the years, numerous researchers (e.g. Miller et al., 1990, Powers et al., 1992; Gellar and Hunt, 1993, Imhoff et al., 1993; Saba and Illangasekare, 2000; Nambi and Powers, 2003) have attempted to measure and describe the rate-limited transfer of mass from the NAPL to the aqueous phase. These studies traditionally employ one-dimensional columns packed with homogeneous, unconsolidated porous media, and focus on the influence of flow dimensionality and the dissolution of residual non wetting phase blobs and ganglia.

All of these expressions reveal that the rate of mass transfer is a function of the driving force (concentration gradient) and an interfacial area between the two phases of concern (Miller *et al.*, 1990):

$$J = k_{la} a^n \left(C_s - C\right) \qquad (2.4)$$

where J [$ML^{-3}T^{-1}$] is the solute mass flux from the DNAPL to the aqueous phase, k_{la} [LT^{-1}] is the average mass transfer coefficient for the DNAPL-water interface, a^n is the specific interfacial area [L^2L^{-3}] between DNAPL and groundwater for a REV, C_s [ML^{-3}] is the aqueous phase concentration that corresponds to the condition of thermodynamic equilibrium with the non-aqueous phase (i.e., effective solubility), and C [ML^{-3}] is the solute concentration in the bulk aqueous phase. By combining the mass transfer coefficient and the specific interface area in Equation 2.4 into a lumped mass transfer term, K_l [T^{-1}], the following equation is derived:

$$J = K_l \left(C_s - C\right) \qquad (2.5)$$

K_l, is typically determined from laboratory measurements that employ a modified Sherwood number:

$$Sh = K_l d_m^2 D_m^{-1} \qquad (2.6)$$

where *Sh* is the Sherwood number, d_m [L] is the mean particle diameter, and D_m [L^2T^{-1}] is the molecular diffusion coefficient for the soluble constituent (Miller *et al.*, 1990). Empirical models (referred to as correlation expressions) of *Sh* have been developed by numerous researchers (e.g. Miller *et al.*, 1990; Parker *et al.*,1991; Powers *et al.*, 1992; Gellar and Hunt, 1993; Imhoff *et al.*, 1993; Powers *et al.*, 1994; Saba and Illangasekare,

2000; Nambi and Powers, 2003). Comparison of the different empirical models revealed that the expressions for each model are only valid under the very specific and narrow conditions under which they were derived and that predictions of mass transfer are very sensitive to the empirical model chosen (Grant and Gerhard, 2004).

Dissolution of DNAPLs located in fractures is governed by the same principles as in unfractured porous media. However, the interaction between flow and mass transfer is modified by the different geometry of fluids in the fractured pore space and also by the presence of the mass sink of the matrix. The following discussion will focus on mass transfer from DNAPL to aqueous phase in the fractures.

Parker et al. (1994) were one of the first to investigate DNAPL dissolution in fractured porous media. It was demonstrated, using a revised conceptual model, in fractured materials such as sandstone and granite, the dissolution rate was observed to increase with the groundwater flow rate in the fracture, but for different reasons in each rock type. In the granite, which has both a low porosity and a low hydraulic conductivity matrix, there occurs negligible flow and little diffusion in the matrix such that the DNAPL disappearance time is controlled by aqueous-phase advective-dispersive transport in the fractures. Depending on the flow rate of water through the fracture network, the DNAPL can persist in granite for many decades. On the other hand, the disappearance time from a fracture in the moderately porous and pervious sandstone was found to be affected by advective-dispersive transport in the aqueous phase both in the fracture and the matrix because of its effects on the concentration gradient at the fracture-matrix

interface in the vicinity of the DNAPL source. It was also reported that sorption will tend to reduce DNAPL disappearance times in all cases because the solid phase will act as an additional reservoir to store contaminant that previously existed in the aqueous phase (Parker et al., 1994).

Esposito and Thomson (1999), using a coupled multiphase flow and dissolution numerical model that employed a version of Equation 2.4 to describe rate-limited mass transfer, reported that the time frame for NAPL dissolution is clearly sensitive to the mass transfer coefficient. It was also found that increasing the hydraulic gradient across the fracture plane can aid in the removal of free-phase mass; however, diffusion-controlled mass transfer is necessary to dissolve NAPL that is trapped in regions of the fracture plane not accessible to aqueous phase flow.

Glass and Nicholl (1995) simulated a fracture plane using etched glass to study the dissolution of an entrapped air phase and were not able to explain their results using any existing conceptual dissolution models. Based on both experimental and simulation results, Detwiler et al. (2001) proposed a simple exponential relationship with a constant bulk mass transfer coefficient to model the temporal change in DNAPL saturation in a variable aperture fracture. Detwiler et al. (2001) noted that as dissolution pathways become hydraulically connected to the effluent end of the fracture, flow bypassing may cause the bulk mass transfer rate to decrease and their exponential relationship to break down.

Sudicky (1990) proposed a geometry-dependent mass transfer parameter (α) [L] to simulate the exchange between fracture and matrix:

$$\alpha = \frac{d\phi_m D^*_{im}}{B^2} \qquad (2.7)$$

where *d* is an integer equal to 3 for a slab approximation to the matrix and 15 for a sphere approximation, ϕ_m [-] is the matrix porosity, D^*_{im} is the matrix effective molecular diffusion coefficient [L^2/T] , and *B* is either the fracture spacing for slabs or the sphere radius [L].

To account for the mass transfer relationship in a two-dimensional multi-phase flow model in fractures, Reynolds (2001) employed the work carried out by Mason and Kueper (1996) which effectively demonstrated that mass transfer in a porous medium is dependent on both velocity and saturation by:

$$K = \left(aq^b + k_i\right)\left(S_w^3 - S_w^5\right) \qquad (2.8)$$

where, *K* is the mass transfer coefficient [L/T]; a and b are coefficients taken from the published literature or calibrated from laboratory experiments; k_i is the intrinsic mass transfer coefficient [L/T], which in turn is a function of the medium and the particular chemical being used in the simulation.

Through conducting eight long-term dissolution experiments in two laboratory-scales dolomitic limestone fractures, an empirical dissolution model was developed by Dickson and Thomson (2003). This study revealed that extreme aperture regions are responsible for controlling flow pathways and solute transport. This study also identified the three

distinct stages of dissolution previously reported by Miller et al. (1990) for unconsolidated porous media. Here, too, it was observed that the majority of the mass removal occurred during the initial pseudo-steady stage of the dissolution profile, which lasted until approximately 5–10 % (average 8%) of the initial mass trapped was dissolved. The major advantage of this model is that it is continuous over the transition between the pseudo-steady and transient stages of dissolution. However, the model was developed using laboratory-scale fracture planes with relatively low matrix porosities, with trichloroethene (TCE) and 1,1,1 TCA as the DNAPLs, under a specific range of experimental conditions. Therefore, the model is only valid in situations as specified by the experiments.

VanderKwaak and Sudicky (1996) demonstrated that in order to estimate the time required for a non-aqueous-phase contaminant source to disappear from a fractured geologic material, the intricate advective and diffusive interactions that occur during aqueous-phase contaminant migration in the vicinity of DNAPL sources must be taken into consideration, especially in cases where groundwater flow rates are enhanced through pump-and-treat remediation of a complex fracture system. This study involved numerical modelling assuming local equilibrium partitioning of the contaminant between the non-aqueous and aqueous phases. At the same time, it was also demonstrated that if the matrix is relatively porous but of low hydraulic conductivity, such as clay, then the DNAPL disappearance time is relatively rapid and is controlled by matrix diffusion, a result that is consistent with the analysis by Parker et al. (1994).

Reynolds and Kueper (2004) studied the migration of DNAPL and dissolved phase contamination through a fractured heterogeneous porous medium that contains fractures in the lowest permeability lenses, through the use of a multiphase compositional model. All simulations conducted in this work included equilibrium dissolution as well as advective/dispersive transport of the dissolved phase. The study demonstrated that the rate of transport of the dissolved phase compounds resulting from the DNAPL was approximately the same as the non-wetting phase. This is mainly due to the reduced relative permeability of lenses containing DNAPL, and due to diffusive losses of mass to the matrix of fractured clay and silty-clay lenses. Some exceptions to this were found when the DNAPL could not overcome the displacement pressure of a lens, and could not by-pass the lens due to the lack of available driving force after the source had been shut off. These findings indicate that in highly heterogeneous deposits, the existence of fractures is less important than in more homogeneous situations, and that the spatial variability of the porous media permeability is a more effective mitigant.

2.1.4 General Governing Equations

The governing equations, which are equivalent to those for multiphase flow and transport in porous media, are assumed to hold for either a discrete 2D fracture plane or a 3D porous matrix block. The governing equations as employed by Kueper and McWhorter (1991) to simulate simultaneous two-phase flow in a single vertical fracture using a mass conservation approach are:

$$\frac{\partial}{\partial x}\left[\frac{ekk_{rw}}{\mu_w}\left(\frac{\partial P_w}{\partial x}\right)\right]+\frac{\partial}{\partial x}\left[\frac{ekk_{rw}}{\mu_w}\left(\frac{\partial P_w}{\partial x}+\rho_w g\frac{\partial z}{\partial x}\right)\right]=\phi e\frac{\partial S_w}{\partial t} \qquad (2.9)$$

$$\frac{\partial}{\partial x}\left[\frac{ekk_{rnw}}{\mu_{nw}}\left(\frac{\partial P_{nw}}{\partial x}\right)\right]+\frac{\partial}{\partial x}\left[\frac{ekk_{nrw}}{\mu_{nw}}\left(\frac{\partial P_{nw}}{\partial x}+\rho_{nw} g\frac{\partial z}{\partial x}\right)\right]=\phi e\frac{\partial S_w}{\partial t} \qquad (2.10)$$

where, e is the fracture aperture [L]; k is the permeability of the fracture [m^2]; kr_w and kr_{NW} are the relative permeabilities to the wetting and non-wetting phases respectively; μ_w and μ_{NW} are the viscosities of the wetting and nonwetting phases respectively [Pa • s]; P_w and P_{NW} are the wetting and nonwetting phase pressure respectively [Pa]; ρ_W and ρ_{NW} are the densities of the wetting and nonwetting phases respectively, [M/L^3]; S_W is the wetting phase saturation; ϕ is the porosity; t is time [T] and g is gravity [L/T^2].

For DNAPL to enter a fracture, Kueper and McWhorter (1991) assumed that locally the fracture resembles a parallel plate opening and performed a force balance for entry into the fracture, resulting in:

$$P_e=\frac{2\sigma\cos\theta}{e} \qquad (2.11)$$

where, P_e is the entry pressure [Pa], pressure of the fracture, σ is the interfacial tension between the fluids [M/L], θ is the contact angle [°] measured through the wetting phase and e is the fracture aperture [L]. Kueper and McWhorter (1991) further demonstrated that at a finely discretized scale (2cm), the fracture is assumed to behave as a set of parallel plates and the nodal permeability can be calculated as follows:

$$k=\frac{e^2}{12} \qquad (2.12)$$

where *k* [L^2]is the permeability of the fracture.

The advection-dispersion equation governing aqueous-phase contaminant transport in porous media, including process of equilibrium sorption and first-order decay, is (Bear, 1972):

$$\phi R\frac{\partial c}{\partial t}+q_i\frac{\partial c}{\partial x_i}-\frac{\partial}{\partial x_i}\left[\phi D_{ij}\frac{\partial c}{\partial x_j}\right]+R\phi\lambda_c=0, \quad \text{i, j = 1,2} \qquad (2.13)$$

where c = c(x_i,t> [M L^{-3}] is the concentration; *R* is the contaminant retardation factor describing equilibrium contaminant partitioning onto the solid phase; and λ [T^{-1}] is a first-order decay constant. The hydrodynamic dispersion tensor, D_{ij} [L^2 T^{-1}], describing the spreading of the aqueous-phase contaminant due to mechanical dispersion and molecular diffusion, is (Bear, 1972):

$$\theta D_{ij}=(\alpha_L-\alpha_T)\frac{q_iq_j}{|q|}+\alpha_i|q|\delta_{ij}+\phi\tau D^*\delta_{ij} \qquad (2.14)$$

where α_L and α_T are the longitudinal and transverse dispersivities, respectively [L]; T is the tortuosity [-] of the porous medium; *D* * [$L^{2}T^{-1}$] is the free-solution diffusion coefficient of the contaminant; and δ_{ij} is the Kronecker delta. The product τD* represents an effective diffusion coefficient for the porous medium.

Esposito and Thomson (1999) adapted these equations to develop a numerical model to simulate non-equilibrium dissolution and aqueous phase transport in a variable aperture fracture and corresponding matrix and coupled it with an existing two-phase flow model from Murphy and Thomson (1993). In this study, the mass transport equation within the

fracture was developed to be:

$$b\frac{\partial C_f}{\partial t} = -b\frac{\partial}{\partial x_i}\left[\left(v_i C_f\right) - \left(D_{ij}\frac{\partial C_f}{\partial x_j}\right)\right] + q_M\big|_{z=b} + bq_d \qquad i, j = x, y \qquad (2.15)$$

with the hydrodynamic dispersion tensor defined as:

$$D_{ij} = \alpha_T|\upsilon|\delta_{ij} + (\alpha_L - \alpha_T)\frac{\upsilon_i\upsilon_j}{|\upsilon|} + D^*\delta_{ij} \qquad (2.16)$$

and

$$q_M\big|_{z=b} = q_M = \theta D_M\frac{\partial C_M}{\partial z}\big|_{z=b} \qquad (2.17)$$

where C_f is the average concentration in the fracture plane (M/L^3); υ_i is the average aqueous phase velocity in the fracture plane (M/T); q_M represents the mass flux exchange between the matrix and the fracture ($M/L^2/T$); q_d represents the aqueous phase source due to dissolution from the presence of NAPL in the fracture plane ($M/L^3/T$); α_L and α_T are the longitudinal and transverse dispersivities, respectively (L); υ denotes the magnitude of the average aqueous phase velocity in the fracture (L/T); δ_{ij} is the Kroneker delta function; D^* is the free solution diffusion coefficient (L^2/T); $D_M = \tau D^*$ is the effective diffusion coefficient in the matrix; τ is tortuosity in the matrix; θ is the porosity in the matrix; and C_M is the concentration in the matrix (M/L^3). By employing the hydrodynamic tensor in Equation 2.16, and assuming the effective diffusion coefficient D_M is uniform throughout the matrix; and matrix sorption is assumed to be instantaneous, reversible and dependent of the concentration of the contaminant, the source of mass transferred from the NAPL to the aqueous phase in Equation 2.15 by q_d can be represented by the stagnant single-film model (Nernst, 1904).which may be written as,

$$q_d = k_e a_0 \left(C_{eq} - C_i \right) \qquad (2.18)$$

where k_e is the effective mass transfer coefficient which is a function of the flow conditions and the diffusion coefficient, and in general is an experimentally determined quantity (L/T); a_0 is the specific contact area between the NAPL and the aqueous phase and is defined as the ratio of the NAPL/aqueous phase contact area per unit volume (L-^{1}); C_{eq} is the concentration at equilibrium (solubility), and C_i is the concentration in the surrounding aqueous phase in the fracture (i=F) or in the matrix (i=M).

Reynolds (2001) further extended the general flow equations by taking sorption of the dissolved non-aqueous phase to the aquifer material and the transient behaviour of flow due to the effects of storage in the porous medium and the fluids into consideration:

$$\frac{\partial}{\partial t}\left(c_{tb}\phi S_\beta x_{i\beta} + \rho_b K_d c_{t\beta} x_{i\beta} + c_{t\beta} x_{i\beta}(\alpha + \beta_w \phi) P_\beta\right) + \nabla \cdot \left(c_{t\beta} x_{i\beta} v_\beta\right) - \nabla \cdot \left[\phi S_\beta D_{i\beta} \nabla\left(c_{t\beta} x_{i\beta}\right)\right]$$

$$- q_{i\beta} - I_{i\beta} = 0 \qquad \beta = 1..n_p,\ I = 1..n_c \qquad (2.19)$$

where, β is the particular of interest; $c_{t\beta}$ is the molar density of phase β, S_β is the saturation of phase β; $x_{i\beta}$ is the mole fraction of component i in phase β; υ_β is the Darcy flux of phase β; $q_{i\beta}$ is the source/sink term for component i in phase β; $I_{i\beta}$ represents the inter-phase mass transfer of component i to or from phase β; ρ_b is the bulk density of the aquifer material; K_d is the distribution coefficient for the contaminant; α is the porous medium

compressibility; β_w is the compressibility of water; n_p is the number of phases; n_c is the number of components.

2.1.5 Diffusion

2.1.5.1 Introduction

A significant difference between mass transport in a relatively homogeneous unconsolidated porous medium and in a highly heterogeneous or fractured medium is the presence in the latter of the matrix material between the highly permeable pathways, which constitutes significant, relatively immobile zones. The loss of solute mass to the matrix is known as matrix diffusion, and can account for significant retardation of the solute plume when matrix porosities are large (Parker et al., 1994). In addition, relatively soluble DNAPL initially present in a fracture can rapidly disappear because of aqueous-phase diffusion into the adjacent porous matrix provided the matrix has at least a moderate porosity (Parker et al., 1994).

Molecular diffusion is the process by which chemical molecules migrate via random (i.e. Brownian) motion from an area of high concentration to an area of lower concentration. This process is defined by Fick's first law of diffusion, in which the diffusive flux ($J_{D,}$ defined here in the context of groundwater transport) is (Parker et al., 1994):

$$J_D = -\phi D_e \frac{\delta C_w}{\delta x} \qquad (2.20)$$

where J_D equals to the diffusive flux [M/L^{3}T]; $\emptyset$ is the matrix porosity [-]; D_e is the effective diffusion coefficient [L^2/T]; C_w is the dissolved aqueous-phase concentration

and x equals to the distance [L].

As contamination solute migrates through a fractured rock aquifer, it tends to diffuse from the flowing fracture aqueous phase into the rock's relatively stagnant matrix pore water. As discussed by Parker et al. (1994; 1997), chemical mass dissolving into the adjacent water film in a fracture establishes a chemical concentration gradient in the aqueous phase which causes the contaminant mass to move into the porous matrix by molecular diffusion. If a significant amount of the DNAPL dissolves, the remaining amount of DNAPL may disconnect and redistribute within the larger fracture aperture regions so as to achieve minimal interfacial energy between the two fluids. Depending on the chemical and porous medium properties, some DNAPLs (particularly the chlorinated solvents), are known to disappear from fractures in very short time periods, resulting in nearly all of the contaminant mass ultimately moving into the matrix as dissolved and sorbed contaminant. This process of matrix diffusion tends to retard a contamination plume's advance through a fractured rock aquifer and also substantially increase the difficulty of removing contamination from the aquifer. As reported by Lever and Bradbury (1985), matrix diffusion can lead to effective retardation factors in excess of 100 and reduce peak concentrations by three to four orders of magnitude, assuming that the groundwater velocity is relatively small.

Lowering the aqueous phase concentration in the fracture, perhaps as a result of flushing of the fractures with uncontaminated groundwater, may lead to a reversal of the concentration gradient, thus causing diffusion out of the matrix into the fracture (i.e.,

back-diffusion) (Mackay and Cherry, 1989). This process means that the cleaning up of fractured rock aquifer can be extremely difficult with contaminants diffused into the matrix acting as a persistent source of groundwater contamination producing an extensive plume in the direction of groundwater flow.

Parameters which most strongly govern the degree to which matrix diffusion prolongs the aquifer restoration process includes both fracture and matrix porosity, fracture spacing, matrix diffusivity, the type of contaminant being released and the length of time the aquifer has been contaminated (Parker 1996).

2.1.5.2 Stages of Diffusion

As presented by Mutch et al. (1993), the diffusive movement of contaminant can be mainly classified into three stages. The initial stage begins when DNAPL enters the fracture and diffuses from the high concentrations in the mobile contaminated zone to the uncontaminated pore water zone in the rock matrix. The intermediate stage begins when the contaminant source in the fracture is removed. Although no contaminant continues to diffuse into the matrix block during this stage, part of the contamination in the rock matrix continues to diffuse inwards to the centre of the block while a portion of the contaminant, in response to a lower concentration gradient now occurring in the fracture water, begins to diffuse outward. The final phase of diffusion begins when the concentration at the centre of the block reaches a maximum, and due to the higher concentration in the matrix block as compared to other parts of the fractured rock aquifer, the diffusive flux moves outwards to the fracture flow system.

However, if the matrix diffusivity is relatively high, the fracture spacing small, or the period of NAPL presence long, contaminant will be able to fully permeate the matrix block, achieving a steady-state concentration equal to that in the mobile fracture water. In such cases, the intermediate phase does not occur and the contamination phase moves from the initial phase to the final phase (Mutch et al., 1993). Since each stage of diffusion necessarily occurs consecutively, the time required to bring about a significant improvement in water quality of a contaminated fractured rock aquifer can be exceedingly long.

2.1.5.3 Sorption

Many organic chemicals are subject to sorption processes occurring both on the fracture surfaces and in the porous rock matrix. This, together with the diffusion of the organic chemical from the fractures into the matrix in the aqueous phase, retards migration rates along the fracture network. A single fracture in an infinite porous medium is assumed for the following discussion. One of the most important parameters in governing the rate of diffusion in the fractured matrix is the effective diffusion coefficient (D_e). However, since D_e is rarely available, it is normally defined as the product of the free-solution diffusion coefficient, D^*, and the tortuosity of the porous medium (Dullien, 1992; Lerman, 1979; Millington and Quirk, 1961):

$$D_e = D^* T \qquad (2.21)$$

where D_e is the effective diffusion coefficient [L^2/T]; D^* is the free solution diffusion coefficient [L^2/T] and T is the apparent tortuosity of the porous medium [-], which can

vary from 0 to 1. The free-solution diffusion coefficient is generally well-known for most solutes, or can be calculated using a correlation equation developed by Wilke and Chang (1955) for dilute solutions of single organic solutes in water.

Since the chemical mass in the matrix consists of the dissolved mass in the pore water and the mass sorbed to the matrix solids, the equilibrium partitioning of chemicals between the aqueous and solid phases is commonly described using the distribution coefficient K_d, which assumes sorption to be instantaneous, linear, and reversible. Using this approach, the retardation factor R could be predicted by (Parker et al., 1994):

$$R = 1 + \frac{\rho_b}{\phi_m} K_d \qquad (2.22)$$

where R [-] is the retardation factor; ρ_b refers to the dry bulk density [M/L^3]; ϕ_m [-] is the matrix porosity; and K_d [L^3/M] is the distribution coefficient of the compound of interest.

For non-ionic organic compounds, the equilibrium distribution coefficient K_d can be predicted using the equation (Schwarzenbach and Westhall, 1981; Karickhoff et al., 1979; Karickhoff, 1981, 1984):

$$K_d = K_{oc} f_{oc} \qquad (2.23)$$

where K_{oc} is the partition coefficient of the compound of interest [L3/M]; f_{oc} is the fraction organic carbon in the porous matrix [-].

While K_{oc} values can be predicted using a correlation equation (Karickhoff, 1984):

$$\text{Log } K_{oc} = -a \log C_{sw} + b \qquad (2.24)$$

where *a* and *b* are correlation coefficients and C_{sw} is the concentration at the fracture surface boundary and is equal to the aqueous solubility of the chemical [M/L^3]. The values of *a*, *b* and S_w can easily be obtained from literature (e.g. Schwille, 1988, Fetter, 1993), thus allowing the distribution coefficient to be predicted.

Johns and Roberts (1991) demonstrated that solute can be retarded considerably due to mass exchange between the channels, the small aperture regions of the fracture, and the rock matrix. The extent of solute retardation is insensitive to the solute capacity in the small-aperture regions and the area between channels in the fracture plane, but is very sensitive to the mass transfer rates between the channel and the small-aperture region.

2.1.5.4 Fracture and Matrix Mass Storage Capacities

The maximum chemical mass storage capacity in the matrix per unit volume of fractured porous medium is (Parker et al., 1997):

$$M_m = Ø_m C_{sw} R \qquad (2.25)$$

where M_m is the maximum chemical mass storage capacity in the matrix; $Ø_m$ is the matrix porosity [-]; C_{sw} is the concentration at the fracture surface boundary and is equal to the aqueous solubility of the chemical [M/L^3] and *R* is the retardation factor accounting for chemical partitioning from the aqueous phase to the matrix solids [-]. For an idealized fracture network with a specified fracture porosity, the initial DNAPL storage capacity

expressed as mass is (Parker et al., 1997):

$$M_f = Ø_f \rho \qquad (2.26)$$

where M_f is the mass storage capacity in the fractures; ρ is the density of the nonwetting phase [M/L^3] and $Ø_f$ is the fracture porosity [-].

If $M_m \geq M_f$, then there is a possibility that all the DNAPL present in the fracture can be dissolve and diffuse into the matrix, since the matrix has a higher storage capacity than the fracture (i.e., there is enough capacity in the matrix to accommodate the amount of DNAPL in the fracture) (Parker et al. 1994).

2.1.5.5 Rates of DNAPL Loss from Single Fractures

Analytical models are useful tools for investigating relatively simple behaviour in ideal systems. They can provide basic insight into the governing processes and provide a basis for verification of numerical models. The relative simplicity of the diffusion process has allowed a number of useful analytical solutions to be derived for contaminant migration from fractures into the surrounding matrix.

The aqueous-phase diffusive flux from a NAPL-occupied fracture to the matrix can be investigated using Fick's Second Law, derived by combining Fick's first law with the equation for conservation of mass and written in three-dimensional form (Parker, 1997):

$$\frac{D_e}{R}\left\{\frac{\partial^2 C_w}{\partial x_1^2}+\frac{\partial^2 C_w}{\partial x_2^2}+\frac{\partial^2 C_w}{\partial x_3^2}\right\}=\frac{\partial C_w}{\partial t} \qquad (2.27)$$

where R is the retardation factor; C_w is the concentration of solute in the aqueous phase [M/L^3]; $\partial C_w / \partial x_i$ is the chemical concentration gradient defined in the opposite direction of the flux[M/L^3/L]; and De is the effective diffusion coefficient [L^2/t].

The analytical solution for diffusive flux at the fracture surface (x=0) at any time t is as shown below:

$$J_D(0,t) = \phi C_{sw} \sqrt{\frac{RD_e}{\pi t}} \qquad (2.28)$$

where $\emptyset$ is the matrix porosity [-]; C_{sw} is the concentration at the fracture surface boundary and is equal to the aqueous solubility of the chemical [M/L^3]; and t is time.

Integrating Equation 2.28 over the time period of interest provides the total mass diffused into the matrix per unit area of fracture face. For the parallel plate fracture case, the solution is (Parker et al., 1994; VanderKwaak and Sudicky; 1996):

$$M_t = \phi C_{sw} \frac{4}{\sqrt{\pi}} \sqrt{R(D_e)t} \qquad (2.29)$$

where M_t is the total mass diffused into the matrix per unit area of fracture face; C_{sw} is the concentration at the fracture surface boundary and is equal to the aqueous solubility of the chemical [M/L^3].

Equation 2.29 above accounts for diffusion happening in both the positive and negative directions (diffusion from both fracture surfaces). The disappearance time, t_D, which refers to the time difference between when the DNAPL first arrives in the fracture and

when it completely disappears, can be obtained directly from Equation 2.29. By assuming $t = t_D$, M_t will correspond to the product of the void volume of the fracture with the density of the DNAPL, all divided by the surface area in the fracture. And by expressing M_t in terms of the parallel plate fracture aperture e, the disappearance time becomes (Pankow and Cherry, 1996):

$$t_D = \frac{\pi\rho^2}{16C_{sw}^{\ 2}\phi_m^{\ 2}D_eR}(e)^2 \qquad (2.30)$$

As demonstrated by Equation 2.29, M_t is directly proportional to the matrix porosity and the concentration at the fracture surface, while at the same time, proportional to the square root of retardation factor, effective diffusion coefficient and time. However, upon closer examination, it could be seen that some of the properties in this equation are inter-related. For example, the retardation factor (R) is affected by C_{sw}, and the porosity of the matrix affects both tortuosity and R. By letting R=1, Parker et al. (1994), demonstrated that diffusion into the matrix of a fractured rock aquifer can be a very important process leading to the disappearance of DNAPL from the fractures. It was also established that the rate of disappearance is strongly dependent on the concentration at the fracture surface and matrix porosity, as compared to the amount of time the DNAPL is in the fracture.

As mentioned earlier, the solubility of the DNAPL has a direct effect on the amount of mass loss from a fracture and an indirect effect on its mass loss through its influence on the partitioning to the matrix solids. Since the solubility of a DNAPL is inversely related to its K_{oc} value (and, therefore, to its K_d value), a DNAPL with a lower solubility

tends to have a higher preference for organic carbon. Therefore, a lower solubility DNAPL, after dissolving, tends to be retarded more in its aqueous phase transport relative to one of higher solubility (lower K_{oc} value). The effect of retardation due to sorption, is also observed to be more significant when there is a higher amount of organic carbon in the porous matrix.

2.1.5.6 Rate of Diffusion in Fractured Network

The rate of DNAPL diffusion into fractured network will be discussed by considering matrix volume as blocks. Similar to the one-dimensional fracture case, the effect of the diffusion time is assumed to be insignificant and is neglected here. As presented by Parker et al. (1997) the solution for calculating the total mass diffused at any selected time (Mt) is:

$$M_t = C_{sw} R \emptyset_m L_1 L_2 L_3 (1 - P_1 P_2 P_3) \qquad (2.31)$$

where,
$$P_i = \frac{8}{\pi^2} \sum_{n=1,3,5,..}^{\infty} \frac{1}{n^2} \exp\left(- n^2 \pi^2 \frac{D_e t}{R L_i^2} \right) \quad i = 1, 2, 3 \qquad (2.32)$$

P_i is a function of the dimensionless time variable $(D_e t/RL_i^2)$; L_i is the matrix block length in each of the principle directions.

By using Equations 2.31 and 2.32, Parker et al. (1997) demonstrated that, due to a much larger surface area for diffusion in the 3-dimensional case, the rate of diffusion is much

higher compared to a 1-dimensional situation. The work further concluded that smaller and more closely-spaced fractures - resulting in larger surface to volume ratios for the DNAPL, also enhances the diffusion rate. Thus, a shorter time is required for the DNAPL to diffuse into the matrix as compared to a case where fractures are widely spaced with larger apertures.

By employing a 2-dimensional numerical model, Vanderkwaak and Sudicky (1996) compared a plume of dissolved contaminants in a moderately porous fractured sandstone and a relatively non-porous fractured granite. Since the sandstone has an order of magnitude greater matrix porosity (0.2) than does the granite (0.02), the sandstone has a much higher effective diffusion coefficient, and hence the rate of solute mass transfer from the fracture to the matrix. Through this study, it was observed that if the matrix is relatively porous, the DNAPL disappearance time is relatively rapid and is controlled by matrix diffusion. It was also demonstrated that the plume in the fractured granite case travel distances far exceed the distances of migration for the sandstone case. This study further concluded that matrix diffusion into the porous matrix can have an effect on DNAPL flow rates and distribution if sufficient mass is lost leading to a measurable effect on the DNAPL driving forces and permeability in the fracture.

Esposito and Thomson (1999) extended the work of Murphy and Thomson (1993) to account for the processes of non-equilibrium dissolution, advective–dispersive transport in the fracture, and three-dimensional matrix diffusion. This extension allows for the development of a more realistic NAPL distribution in the fracture plane, and hence, will

provide a better understanding of the subsequent dissolution and aqueous phase transport that may be expected to occur in fractured-porous media environments. This study reported diffusion controlled mass removal from both the matrix and from the hydraulically inaccessible zones within the fracture itself, thus resulting in an extremely large time frames for significant mass removal from these systems. It was also observed that the success rate in aqueous phase mass removal from the matrix is very sensitive to the effective fracture spacing, porosity and effective matrix diffusion coefficient. However, the model of Esposito and Thomson (1999) is limited by the lack of the hysteretic behaviour in the functional relationships for capillary pressure and relative permeability.

2.1.5.7 Limitations of Analytical Diffusion Models

Much of this discussion has been based on analytical solutions that utilize a number of important assumptions, some of which are highly idealized. For example, they assume a single component DNAPL, smooth parallel-plates fractures either in isolation or arranged in an idealized array. In addition, the degree of fracture inter-connection, which determines the hydraulic communication in a system of independent fractures, is essential to the evaluation of the hydraulic and transport properties of a fractured rock mass. By overestimating the degree of fracture inter-connection, the rate of diffusion may also be overestimated since the amount of surface area available for diffusion to occur is overestimated at the same time.

By evaluating only single-component DNAPLs in this body of work, the evolving

chemical mole fractions in the DNAPL have been ignored. This is important in multiphase flow since individual components leave the main source of contaminant at different rates due to different aqueous solubilities (hence leading to different concentration gradients) and different diffusion coefficients. The effective solubilities of DNAPL compounds will thus change continuously with time as the composition of the DNAPL changes.

Analytical models of diffusion have clearly provided valuable insight into simple systems at a limited scale. However, by necessity, these fail to account for dynamic multiphase flow processes or realistic fracture networks. For more comprehensive and realistic investigations of the interactions between multiphase flow and advective-dispersive-diffusive process in fractured environments, robust numerical models are required.

2.2 NUMERICAL MODELING METHODS FOR MULTIPHASE FLOW AND AQUEOUS PHASE TRANSPORT IN FRACTURED MEDIA

Numerical modelling is an efficient and essential tool for predicting DNAPL migration fate patterns in the subsurface. Intentional release of hazardous immiscible liquids into the natural environment (e.g., for the purposes of experimentation) has been prohibited by law in many regulatory jurisdictions. Numerical simulations thus became one of the main ways to investigate field-scale behaviour of DNAPLs (Kueper and Frind 1991a). A discussion of the field of numerical simulation for multiphase flow can be found at Kueper and Frind (1992).

The simplest adaptation of a porous medium continuum model to account for the dual porosity nature of fractured rocks is represented by the dual domain model. A dual domain model assumes that the REV contains both a mobile domain and an immobile domain. The mobile domain refers to the domain made up of fractures with high hydraulic permeability, while the immobile domain refers to the matrix domain where the hydraulic permeability is very low as compared to that in the fractures. Each domain has a different porosity such that:

$$Ø_b = Ø_m + Ø_f \qquad (2.33)$$

where, $Ø_b$ is the bulk porosity; $Ø_m$ is the matrix porosity and $Ø_f$ equals to the fracture porosity.

The governing equations, without taking sorption into consideration are as shown:

$$\phi_f \frac{\delta C_f}{\delta t} + \phi_m \frac{\delta C_m}{\delta t} = \frac{\delta}{\delta x_i}(\phi_f D_{ij} \frac{\delta C_f}{\delta x_j}) - \frac{\delta}{\delta x_i}(\phi_f v_i C_f) + q_s C_s - q'_s C_f - \lambda_{1,f} \phi_f C_f - \lambda_{1,m} \phi_m C_m \qquad (2.34)$$

$$\phi_m \frac{\delta C_m}{\delta t} = \xi(C_f - C_m) - \lambda_{1,m} \phi_m C_m \qquad (2.35)$$

As the mass transfer rate (ζ) increases, i.e. the exchange between the mobile and immobile domains become increasingly fast, dual domain model will behave more like a single-domain model with the porosity approaches the total porosity of the porous medium. On the other hand, if the mass transfer rate (ζ) approaches zero, the dual domain also behaves more like a single domain, but with the porosity approaching that of the mobile domain. (MT3DMS manual, p. 2-14). Dual domain modelling allows for

both advective and diffusive processes to be accounted for in a general way, and is thus a useful advance for considering dissolved phase contaminant transport. However, as it does not allow for an explicit representation of a fracture network, it is not appropriate for modelling multiphase flow processes.

Numerical and experimental investigations (e.g., Pruess and Tsang, 1990; Reitsma and Kueper, 1994; Kueper and McWhorter, 1991) have shown that NAPL behaviour within a realistic single fracture can vary significantly from that predicted in a fracture conceptualized as parallel plates with an average aperture. This is due to the rough-walled nature of fractures, such that the aperture varies over the entire fracture plane. One reason for these differences is the impact of aperture on the spatial distribution of key porous media properties such as capillarity and permeability. However, Kueper and McWhorter (1991) demonstrated that at a fine scale of nodal discretization (0.02m), the fracture may be assumed to behave as a set of parallel plates. A number of models have been developed based on this assumption (e.g. Lunati and Kinzelbach, 2004; Pruess and Tsang, 1990; Maloszewski and Zuber, 1993; Parker et al., 1994; Esposito and. Thomson, 1999)

Significant work has been undertaken to investigate the scaling of hydraulic conductivity of porous and fractured media (e.g., Zhang et al., 1996; Zhang and Sanderson, 1999). Most attention to date has been given to the scaling of the intrinsic permeability tensor for single phase fracture flow (e.g. Zhang and Sanderson, 1999) and large scale averaging approaches in dual porosity systems (e.g. Chen, 1995).

Much less work has been performed on the scaling of the constitutive relationships for discretely fractured rock media. Using numerical modelling to investigate upscaling in fractured systems, Reynolds (2001) investigated the sensitivity of large-scale constitutive relationships (effective permeability and capillary pressure) to the statistics underlying the aperture distribution and also the importance of fracture terminations. This study found that the large-scale capillary pressure-saturation relationship was sensitive to the statistics governing the underlying aperture distribution, where the overall effects on the relationships were found to be analogous to porous media. It was reported that increasing or reducing of the variance of the aperture distribution would result in a corresponding steepening or shallowing of the capillary pressure-saturation curve respectively. On the other hand, it was found that the large-scale effective permeability curves representative of flow in the vertical direction followed the general form of the underling local-scale Brooks Corey constitutive relationship and were relatively invariant with changing variance of the aperture distribution; a finding which is significantly different when examining flow in the horizontal direction. At the same time, in the presence of dead-end vertical fractures in the network, large-scale relationships were biased towards higher nonwetting phase saturations and less hysteresis between the drainage and wetting limbs (Reynolds ,2001).

The behaviour of two immiscible liquids in a single fracture, although complex, is analogous to the movement of such liquids through a porous medium in that the distribution of apertures within the fracture parallels the distribution of pores and pore throats in a porous medium (Kueper and McWhorter, 1991). To accurately model this

behaviour, an explicit definition of flow within the fracture plane is required. Most investigations concerned with two-phase flow in a fractured environment have, by necessity, focused on how the phases behave in a single fracture with a stochastically-generated description of the aperture at discrete locations.

Percolation theory (e.g., Pyrak-Nolte, 1991; Kueper and McWhorter, 1992) and lattice modelling methods (e.g. Mendoza, 1992) have been used to simply assess fracture saturation of an invading fluid for a given applied pressure under static equilibrium conditions. Regions within a fracture can be inaccessible to the invading fluid because a critical neck cannot be penetrated until the entry pressure for that aperture is satisfied. Capillary pressure–saturation relationships can be obtained by these methods, and relative permeabilities can be determined by solving the flow problem for the two fluids separately, but these approaches lack a true time-dependent fluid invasion component.

Pruess and Tsang (1990) developed a model for two-phase flow in a variable aperture fracture using a local parallel-plate assumption. Phase presence was defined in accordance with capillary pressure and global accessibility criteria. This allowed any grid elements accessible directly by the invading fluid with apertures larger than a cut-off capillary pressure to be occupied by the non-wetting phase; however, this model again lacks a temporal component. A two-phase model with a true time-marching scheme was presented by Kueper and McWhorter (1991), in which variable apertures in a single fracture were represented by an effective hydraulic conductivity and coupled with the capillary pressure relationship. Analogous to a two-phase porous media model, it does

not define phase presence explicitly within the fracture but rather expresses the saturation level of the invading fluid. In addition, the hysteretic behaviour in a capillary pressure – saturation constitutive relationship was not taken into consideration in this model.

Another possible modelling approach is presented by the dynamic two-dimensional two-phase flow model by Murphy and Thomson (1993), which does not require an empirical capillary pressure-saturation relationship. A unique feature of this model is the use of an exact representation of the fluid phase distribution by an explicit definition of the phase presence at each location within the domain. In order to achieve this definition, a phase distribution was assigned to each fracture sub-region. Knowledge of the phase distribution then allows calculation of interface capillary pressure based on the fracture aperture. Simulation results showed that this model can account for the following flow processes: the simultaneous advance of the fluid–fluid interface at various locations; reversible penetration due to pressure field variations; pressure gradients due to fluid flow; the independent movement of isolated fluid globules; non-wetting phase refusal at the edges of tight regions; and down-slope migration of fluid counter-current to flow of a less dense fluid. However, the simulated results of a two-phase flow in two-dimensional variable apertures were not verified due to a lack of analytical solution for such a case.

Although many investigators have focused only on the consideration of flow regimes within a fracture, some of this work has involved the use of tracers in either laboratory or field situations. This has led to the desire to accurately model solute transport in a single

fracture; however, the physical complexity of a fracture, the difficulty in measuring its geometry, and the desire to have computationally simple models has rendered the task difficult (Esposito and Thomson, 1999). To date, there has been no general agreement on a model which correctly and efficiently accounts for all the processes that may be in play under a given set of circumstances. In fact, a good fit to tracer data is not a sufficient criterion for regarding a model to be valid (Maloszewski and Zuber, 1993).

Research into solute behaviour in discrete fractures grew out of apparent anomalies in tracer studies and in response, a host of models have been developed that allow for transport in the fracture as one-dimensional advection and one-dimensional diffusion into the matrix, normal to the fracture (e.g., Grisak and Pickens, 1981; Sudicky and Frind, 1982). In an attempt to overcome the limitations of these one-dimensional models, other forms of discrete fracture transport models have surfaced. For example, Maloszewski and Zuber (1993) developed the single fracture dispersion model that uses a parallel plate approximation and an 'intrinsic dispersivity' to account for dispersion due to either flow channelling or the presence of multiple fractures while Novakowski (1992) developed a model for radial solute transport between two wells which accounts for channelling by the use of a tortuosity term. Although both of these models account for matrix diffusion, neither uses an explicit definition of the velocity variations within the fracture. Conversely, Moreno et al. (1988) incorporated velocity variations using a particle tracking method in their flow model. Residence time for each particle within each variable-aperture element was determined in their model from the flow rate through the element and the volume involved. They hypothesize that the effects of the different

residence times along the various pathways within the single fracture is the chief source of overall dispersion in the fracture, and therefore, did not include the effects of molecular diffusion, matrix diffusion or local dispersion.

Matrix diffusion has, perhaps, the most dominant effect on solute arrival times and has been proven to be an important process even in short-term tracer tests (Maloszewski and Zuber, 1993). When a NAPL is present in the fracture, sharp concentration gradients contribute significantly to the removal of this pure-phase mass from the fracture into the matrix by aqueous phase diffusion.

Esposito and Thomson (1999) extended the two-phase flow model developed by Murphy and Thomson (1993) to account for the processes of non-equilibrium dissolution, advective–dispersive transport in a single fracture, and three-dimensional matrix diffusion. This extension allows for the development of a more realistic NAPL distribution in the fracture plane, and hence, will provide a better understanding of the subsequent dissolution and aqueous phase transport that may be expected to occur in fractured-porous media environments.

Fully compositional, three-dimensional simulation of multiphase flow and transport in fractured systems was presented by Slough et al. (1999a). In this model, both the matrix and fracture systems are treated explicitly, and no equilibrium assumptions are made. The effects of matrix diffusion upon the migration of a DNAPL through fractured clay were looked into in this study. However, the model of Slough et al. (1999a) is limited

by the lack of the hysteretic behaviour in the functional relationships for capillary pressure and relative permeability. The use of a constant nonwetting phase injection boundary condition prevents the system from performing in a natural manner and causes an overestimation of the effects of matrix porosity on the rate of DNAPL migration.

A study of the effects of grid discretization on the migration of DNAPL within a discrete-fracture network embedded in a porous rock matrix was presented by Slough et al. (1999b). A finite-volume discretization in which the rock matrix is represented by three-dimensional block elements, while the discrete-fracture elements are represented by two-dimensional planar, rectangular elements was employed in this study. Slough et al. (1999b) clearly demonstrated that if the nodal spacing at junctions where fractures intersect were not properly refined - especially near the intersection of a wide aperture horizontal fracture and narrow vertical fracture - an overestimation of vertical migration and an underestimation of lateral migration would be induced.

VanderKwaak and Sudicky (1996) carried out a study on the dissolution of NAPLs in discretely-fractured porous media networks, using a transient, two-dimensional groundwater flow and contaminant transport model. The model accounts for matrix diffusion, equilibrium sorption and non-linear relative transmissivity effects that influence groundwater flow within fractures as the DNAPL disappears. The standard Galerkin finite-element formulation is employed to discretize the equations governing groundwater flow and aqueous-phase contaminant transport. The finite-element or finite-difference matrix equations are solved using an iterative method employing

conjugate-gradient stabilized (CGSTAB) acceleration (van der Horst, 1992; Chin and Forsyth, 1993) with level-one incomplete factorization of the coefficient matrix used for preconditioning (VanderKwaak et al., 1995). However, the single-component dissolution algorithm in the model cannot be readily extended to handle multiple contaminant components, due to the possibility of contaminants of different solubilities back-diffusing into fractures from the matrix. The model of VanderKwaak and Sudicky (1996) is further limited by the lack of differentiation between drainage and imbibition in the functional relationships for capillary pressure and relative permeability.

As understanding of NAPL behaviour in a fractured media improves, the desire to accurately model it in combination with solute transport in fractures intensified. However, the physical complexity of a fracture, the difficulty in measuring its geometry, and the desire to have computationally feasible models has rendered the task difficult. The use of numerical simulators to investigate multiphase flow and aqueous phase transport in fractured geologic media has been demonstrated to be a powerful tool, allowing insights into the controlling physics at both the local and macro scales. In order to obtain insight into the performance of different remediation methods in fractured environments, a numerical model that is able to account for the processes of non-equilibrium dissolution, advective–dispersive transport, matrix diffusion as well as multiphase flow in combination with the bio/geo/chemical reactions of the different remediation methods is essential.

2.3 CHEMICAL OXIDATION

2.3.1 General

Chemical oxidation, commonly referred to as in-situ chemical oxidation (ISCO) involves the injection of an oxidizing agent to chemically degrade chlorinated solvents into non-toxic by-products in the subsurface. An extensive review of the different chemical oxidization agents and their associated chemistry with respect to tetrachloroethene (PCE), trichloroethene (TCE), dichloroethene (DCE), and oxidizable aquifer materials (OAM) was conducted by Seol et al. (2003). Many laboratory and field studies have investigated in situ chemical oxidation of DNAPL in aquifers characterized by relatively uniform conditions and with limited heterogeneity (Vella and Veronda 1994, Yan and Schwartz 1996, Case 1997, Schnarr et al. 1998).

An adequate understanding of ISCO technologies exists for permeable groundwater aquifers with limited heterogeneity; however, understanding is not complete for more complex sites such as those with fractured bedrock (Siegrist, 2001). Moreover, technology development and demonstrations have previously focused on unconsolidated porous media, particularly using settings with relatively simple geology and shallow contamination. Because most practitioners have more familiarity with investigation and remediation in unconsolidated settings, the result is an industry that has been addressing remediation of fractured rock sites primarily by drawing on expertise and conceptual approaches developed in unconsolidated deposits (EPA, 2001).

Some of the most common chemical oxidants used today to remediate contaminated sites

include potassium permanganate, hydrogen peroxide and sodium persulfate. Potassium permanganate is a commonly used oxidant for chlorinated ethenes, but is generally not effective for chlorinated ethanes (ITRC, 2001; ERM, unpublished data). Hydrogen peroxide, when catalyzed with ferrous or chelated iron forms hydroxyl radicals (OH) (i.e., Fenton's chemistry) that react non-selectively with oxidizable inorganics and organics, including both chlorinated ethenes and ethanes. Sodium persulfate is a relatively new oxidant for ISCO. It generally requires activation by thermal enhancement or with iron (normally ferrous iron) as a catalyst. It is effective in treating both chlorinated ethenes and ethanes (ERM, unpublished data).

Cho et al. (2002) carried out a series of detailed laboratory studies to evaluate the efficiency of different remediation technologies on 1,1,1-trichloroethane (TCA) in a fractured bedrock source area. The different technologies tested included chemical oxidation, low-temperature thermal degradation, and bioremediation using a carbon amendment and an exogenous culture (these latter experiments are discussed in Chapter 6). Cho et al. (2002) studied three chemical oxidants in the bench-scale tests: potassium permanganate, hydrogen peroxide and sodium persulfate, using bedrock samples collected from a fractured bedrock sites. During the study of sodium persulfate, chelated iron was used as the activating agent as it allows the reaction to take place at more neutral pH conditions, minimizing any dissolution of metals from the rock matrix. Cho et al. (2002) demonstrated that both Iron-EDTA-catalyzed hydrogen peroxide and sodium persulfate show promise for in situ treatment, at fractured bedrock sites, of TCA-contaminated groundwater, where TCA concentration was drastically reduced,

accompanied by near complete destruction of DCA and DCE, daughter products of TCA.

In accordance with this literature review, only the potential of permanganate in a fractured environment is discussed here.

2.3.2 Chemical Oxidation in Fractured Environments

2.3.2.1 Permanganate

Permanganate has been shown to oxidize certain environmental contaminants such as trichloroethene (TCE), tetrachloroethene (PCE), methyl tert-butyl ether (MTBE), chlordane (C10H6Cl8), and styrene in the aqueous phase (Damm et al., 2002; Gates-Anderson et al., 2001; Hood et al., 2000; Yan and Schwartz, 1999). Permanganate (MnO_4^-) is a non-selective oxidization agent that reacts with chlorinated products to produce carbon dioxide (CO_2), chloride (Cl^-), manganese dioxide (MnO_2) and hydrogen ions (H^+). Two of the most common chemical agents used to deliver the permanganate ion to the subsurface are potassium permanganate and sodium permanganate.

An example of an overall generic permanganate reactions are as follows (Tunnicliffe and Thomson, 2004):

$$C_aCl_bH_c + dMnO_4^- \rightarrow aCO_2 + bCl^- + dMnO_2(s) + cH^+ \qquad (2.37)$$

In a series of proof-of-concept experiments, Gonullu and Farquhar (1989) and Schnarr et al. (1998) emplaced a free phase DNAPL source within sand packed columns and were

able to demonstrate that the removal of the free phase zone was accelerated under permanganate flushing conditions. Schnarr et al. (1998) reported the continuous flushing of well-defined residual source zones placed in unconsolidated media showed >99% mass removal. Encouraged by these research findings and others, accelerated use of permanganate in larger pilot-scale field trials have led to a host of full-scale applications (e.g., ITCR, 2001; Battelle, 2001; USEPA, 2003b). In spite of the widespread use of permanganate, several research studies have identified some potential issues hindering the ability of continual permanganate flush to sustain enhanced mass removal rates (e.g., Schnarr et al., 1998; Schroth et al., 2001; MacKinnon et al., 2002; Conrad et al., 2002). These issues are mostly related to the in-situ production of carbon dioxide and manganese dioxide.

For example, MacKinnon and Thomson (2002) performed a permanganate flush of a PCE pool in a two-dimensional laboratory model aquifer and showed that the decrease in the oxidation rate as the flush progressed was related to the formation of MnO_2 deposits at the pool interface. Although these deposits affect the ability of the oxidant to remove or access free phase mass, they may also serve to provide a potential long-term barrier that could effectively contain the free phase and reduce mass transfer once the oxidant flush has terminated. A 56% reduction in the overall mass transfer rate relative to pre-oxidation conditions was observed. This potential long-term decrease in mass transfer may inhibit the ability of the remaining DNAPL to generate an aqueous phase plume. However, due to the significant difference in structure between unconsolidated media and fractured geologic media, the results achieved in the former may not be directly relevant

in the latter.

Williams and Spiers (2002) carried out two phases of pilot studies to evaluate the effectiveness of ISCO for remediation of impacted groundwater in a fractured bedrock aquifer using sodium permanganate. In the first phase, laboratory tests were conducted in order to assess the required oxidant dose concentration, natural oxidant demand and reaction kinetics using soil and groundwater samples obtained from the site. At the same time, these tests also aimed to conduct a pilot test of ISCO with sodium permanganate using an existing pumping recovery well and a nearby monitoring well screened in a partially weathered bedrock aquifer. The primary objectives of the second phase pilot tests were to (i) evaluate the feasibility of using permanganate to treat the groundwater plume in off-facility areas, and (ii) evaluate the ability of the permanganate to degrade TCE in a fractured bedrock aquifer under non-pumping or natural flow conditions. These studies demonstrated that fractured rock environments, despite their inherent complexity and heterogeneity, can be quite suitable for successful sodium permanganate applications. In particular, fractured rock provides an environment often low in natural organic matter resulting in naturally low demand for oxidant material. Williams and Spiers (2002) further reported on the importance of characterizing the geology and hydrogeology of the site when carrying out an ISCO technology scheme in a fractured rock environment, an observation similarly made in studies employing Fenton's Reagent in a fractured environment (e.g. Bill et al., 2002).

As previously mentioned, Werner (2002) demonstrated the incapability of Fenton's

Reagent to completely remove the contamination from a fractured environment. That study then replaced the Fenton's Reagent with sodium permanganate (NaMnO4) and subsequently flushed the fractures with the new oxidizer. The advantage of sodium permanganate over hydrogen peroxide is that it is able to persist in the aquifer for longer than the OH radicals, and its advantages over potassium permanganate is that it could be delivered to the aquifer at a higher dosage concentration and contained fewer impurities (Amarante, 2000). The second, more successful ISCO application was performed by injecting 11,000 lbs. of NaMnO4 as a 20 percent concentration solution into the fractured aquifer, which resulted in a reduction of the original PCE mass by greater than 95 percent. Werner (2002) further concluded that some fracture rock sites maybe be treated successfully by first flooding the primary and secondary porosity with high concentration solutions of $NaMnO_4$ followed by supplemental, high volume but low concentration treatments that specifically address the residual contaminant mass remaining in the saturated portion of the aquifer matrix.

MacKinnon et al. (2002) conducted a series of treatability studies under laboratory simulated site conditions, using materials from two fractured bedrock sites to examine the influence of performance factors on the oxidative reduction of TCE and PCE in fractured rock. These studies were completed using core material representing three rock types (shale, siltstone, and crystalline bedrock) collected from the two field sites. The performance factors being studied included (i) the oxidant demand of the groundwater and geologic materials, (ii) the potential impacts of oxidation on the inorganic chemistry of groundwater, including mobilization of metals from the geologic materials, (iii) the

potential for precipitate formation which may decrease the transmissivity of the fractured bedrock, (iv) losses of permanganate through diffusion into the bedrock matrix that would represent an additional oxidant demand of the matrix, but that may also oxidize DNAPL mass in the rock matrix; and (v) the impact of the oxidant treatment on both fracture face and bulk bedrock matrix geochemistry.

The results of MacKinnon et al. (2002) indicated that the groundwater and the rock matrix did not exert a significant oxidant demand, and that minimal precipitate was formed. Groundwater quality with respect to metals and anions was largely unaffected by the addition of potassium permanganate. The study observed that concentrations of metals decreased, with the exceptions of potassium and manganese; suggesting that ISCO will not adversely impact the groundwater chemistry in a field application, with the exception of transient increases in the concentration of these metals. It was further noted by the authors that the low demand for oxidant in the test may be a result of pulverization of the bedrock samples prior to testing, a process which significantly increased the surface area available for reaction relative to that expected during field application.

With respect to oxidant diffusion, MacKinnon et al. (2002) found minimal penetration of the oxidant into the rock matrix. This could probably be due to the low porosity of the bedrock materials. The authors concluded that the oxidant demand resulting from diffusive loss of $KMnO_4$ into the bedrock matrix is unlikely to have a significant impact on oxidant delivery in the field during an extended treatment using permanganate. They

conclude from these treatability studies that ISCO may be effective for aggressive remediation of TCE and PCE in fractured contaminated sites, with the potential to reduce the duration of groundwater remediation activities relative to conventional pump-and-treat options. Specifically, permanganate demonstrated the ability to degrade high concentrations of TCE and PCE within very short time frames (days to weeks).

Despite the encouraging results shown by various researchers, it is widely accepted that the majority of groundwater and DNAPL flow that occurs through a fracture is highly influenced by the aperture distribution (Tsang and Tsang, 1987; Anderson and Thomson, 1999). Thus, changes in the (effective) aperture distribution due to the formation of reaction by-products during ISCO could potentially influence aqueous transport pathways and DNAPL mass transfer rates.

Tunnicliffe and Thomson (2004) demonstrated the incapability of permanganate flush to increase the bulk mass removal rate for two single vertical fractures in a laboratory environment. Each fracture was characterized by hydraulic and tracer tests and the aperture field for one of the fractures were mapped using a co-ordinate measurement machine. Permanganate solution was then flushed through the fractures to remove emplaced DNAPL. The rapid reduction of flow observed in this study for the initial stage of the oxidant flush suggests that physical changes (i.e., the development of flow obstructions) occurred within the fractures that altered the aperture distribution. During the batch tests, MnO_2(s) was observed to precipitate in large quantities (>1 mm thick) at the DNAPL/aqueous phase interface as a result of the interaction between the

permanganate solution, oxidation end products, and the DNAPL. Tunnicliffe and Thomson (2004) suggest that the resulting development of MnO_2(s) in and around existing diffusion controlled regions plugs the pore structure of the fractures. This plugging is expected to limit both permanganate diffusion into existing and newly formed stagnant zones and, simultaneously, the diffusion of the organic compound towards any remaining flow pathways.

However, while no enhanced mass removal was observed in the two fracture experiments performed by Tunnicliffe and Thomson (2004), the post-treatment mass flux was reduced as a result of the oxidant flush. The physical changes to the aperture field and the locations and magnitude of the flow rate reductions observed during this work suggested that permanganate flushing of DNAPL source zones in fractured rock may offer some beneficial results. In addition to plugging diffusion pathways in the matrix, the development of an insoluble product adjacent to DNAPL within a fracture could effectively encapsulate portions of the free phase. As in porous media work, this study suggests that reduction or complete elimination of advective regions near fracture-based DNAPL source zones would limit mass transfer rates, and therefore limit the ability of the remaining DNAPL to generate an aqueous phase plume.

Various numerical models have been developed to look into both single (e.g., Tsang and Tsang, 1987; Reitsma, 1992) and multiphase flow in fractures (e.g., Parker and Park 2004; Mundle et al., 2007; Pruess and Tsang, 1990; Eikemo et al., 2009). A conceptual model developed by Kueper and McWhorter (1991) found that in both clay and rock, DNAPL

will preferentially enter the larger apertures due to their lower displacement pressures. A numerical model developed by Harrison et al. (1992) found that fractures as small as 10 μm in a clayey aquitard can greatly increase the transport of dissolved contaminants into underlying aquifers.

Numerical models for the ISCO of chlorinated solvents with permanganate have been previously developed for unconsolidated porous media (Hood and Thomson, 2000; Zhang and Schwartz, 2000; West et al, 2008). West (2009) conducted a series of numerical simulations to evaluate the efficacy of in situ chemical oxidation with permanganate for TCE and PCE in heterogeneous unconsolidated porous media at the field scale. It was found that source zone remediation can be effective during, or shortly following, the period of active treatment. However, over the long-term, depending on the dissolution kinetics and the characteristics of the aquifer, the benefit of partial treatment can be greatly reduced due to dissolution tailing. This work suggested that a large fraction of injected permanganate may be competitively consumed by the natural oxidant demand (NOD) at field sites. In addition, the performance of permanganate was also found to be highly variable due to MnO_2 (i.e., rind) formation, DNAPL architecture, and geologic characteristics. That work emphasized the difference between the simplicity of batch studies and the complexity of field scenarios and how, for the latter, heterogeneity and fluid access issues may dominate overall performance.

Only one study has been published modelling the effectiveness of ISCO in fractured porous media. Mundle et al. (2007) developed a pseudo-two-dimensional, transient

flow and transport numerical model to simulate ISCO of TCE and PCE by potassium permanganate in clay containing a single fracture. This work suggested that the NOD of the organic material may significantly reduce the efficiency of ISCO remediation in fractured rock. To the author's knowledge, no systematic studies exist of ISCO in fractured bedrock at the field scale.

Apart from the challenge associated with optimizing the in-situ reactions, these studies illustrate some common fracture properties such as the degree of interconnection between the overburden and bedrock units, the lateral continuity, hydraulic properties and overall importance attached to the uppermost weathered bedrock layer, and the heterogeneity of the fracture system are all issues that impact the hydraulic behaviour of the system. They are critical components of an overall conceptual understanding of the problem and will impact delivery of the oxidant to the region(s) containing DNAPL and dissolved phase contamination.

2.4 ENHANCED BIOREMEDIATION

2.4.1 General

Laboratory and field research conducted over the last decade has shown that micro-organisms that are naturally present in subsurface environments possess the capability to biodegrade chlorinated ethenes (e.g., PCE, TCE, DCE, and VC) to non-chlorinated, environmentally acceptable end-products such as ethene, carbon dioxide and chloride (Suthersan and Payne 2005). The biodegradation reactions occur under a wide range of environmental conditions and are mediated by a variety of different

microorganisms. Furthermore, the natural degrading ability of indigenous microorganisms can be enhanced through amending the groundwater with a supply of inorganic nutrients and a supplemental carbon source (e.g., phenol, propane, or methane). A number of different groups of anaerobic bacteria including methanogens (methane-producers), acetogens (acetate-producers), sulfate-reducers, and fermenting microorganisms can promote partial dechlorination of PCE and TCE to cis-1,2-DCE (Castellanos et al., 2002). In general, chlorinated ethenes can be degraded by either dehalorespiration or cometabolism. The dehalorespiration process is an oxidation-reduction reaction depending on the presence of elemental hydrogen. This thesis will focus on dehalorespiration and will use the terms 'dehalorespiration' and 'dechlorination' interchangeably.

During dehalorespiration, the chlorinated compound is used by the bacteria as the terminal electron acceptor and hydrogen as the electron donor. Specific dehalo-respiring microorganisms, that use chlorinated solvents as their terminal electron acceptors, can derive energy from this reaction. To date, a number of distinct types of dehalo-respiring bacteria have been identified, including Dehalospirillium multivorans (Scholz-Muramatsu et al., 1995), Dehalobacter restrictus (Schumacher and Holliger, 1996) and Dehalococcoides ethenogenes (Maymò-Gatell et al., 1997). Of these dehalo-respiring microorganisms only Dehalococcoides ethenogenes has been documented to dechlorinate TCE past cis-1,2-DCE to ethene. Unfortunately, these dehalo-respiring microorganisms do not appear to be ubiquitous (Geosyntec 2004). Alternatively, these microorganisms are present but are not active. As a result,

dechlorination of PCE and TCE generally stalls at cis-1,2-DCE at many sites, resulting in accumulation of cis-1,2-DCE in groundwater.

Biodegradation is characterized by the consumption of electron acceptors and the production of metabolic byproducts and daughter products. When these byproducts are produced, the subsurface in the vicinity could be affected by transient ion exchange, adsorption, mineral precipitation and dissolution (Hunter et al., 1998). Some of the common reactions that can occur in the subsurface include aerobic respiration, anaerobic respiration and fermentation. However, in order for these reactions to be carried out, chemical substances (substrates) for interacting with the enzymes of the microbe have to be present. After a substrate is introduced to an organism, a period of metabolic acclimation is required before the microbe can utilize the compound. This lag is commonly referred to as the metabolic lag (Wood et al., 1995). In many aerobic and anaerobic reactions, the organic contaminant serves as the electron donor primary substrate. However, the capability of the microbes to use the electron donor can be limited by either the minimum concentrations required for acclimation/enzymatic induction or the maximum sustainable concentration in the media (toxicity).

The bulk of bioremediation research has explored the dehalogenation of aqueous phase chlorinated ethenes at relatively low concentrations (e.g., Nyer et al., 1998; Lee et al., 1998; Dayan et al., 1999). However, recent research is exploring the effectiveness of enhanced bioremediation of DNAPL source zones, which are characterized by aqueous concentrations typically thought to be toxic to microorganisms (Yang and McCarty, 1998).

This emerging research has shown that in addition to degrading these high chlorinated ethane concentrations, enhanced in situ bioremediation (EISB) can also significantly enhance DNAPL solubilisation which would further reduce the time for source remediation.

Under anaerobic conditions, chlorinated aliphatic hydrocarbons (CAHs) such as PCE may be metabolized by indigenous microorganisms. The reductive dechlorination process results in the sequential transformation of PCE into TCE, 1,2-DCE, VC, ethene, and finally carbon dioxide and chloride. With each step, a chlorine atom is removed from the compound resulting in a less oxidized molecule. For this natural process to occur, hydrogen (the electron donor) takes the place of chlorine in the CAH (electron acceptor) during reduction. When the process is documented to proceed without interference this is referred to as natural attenuation. Based on site-specific conditions, including the specific microorganisms present and the availability of hydrogen and nutrients (e.g., phosphorus) required by the microorganisms, the rates and degree of completeness of biodegradation varies between sites (Kozar et al., 2002). Typically, the process can be accelerated via addition of a carbon substrate and/or nutrients (enhanced biostimulation) and even further by injecting a microbial consortium of known degraders (bioaugmentation) (Major et al., 2002).

While hydrogen can be injected directly (e.g., Adamson et al., 2003), more typical is to provide a carbon substrate (e.g., lactate, ethanol, pentanol, glucose) that is converted to hydrogen via fermentative microorganisms (Ellis et al., 2000; Major et al., 2002; Fennell

et al., 1997; Carr and Hughes, 1998; Wu et al., 1998; Yang and McCarty, 1998; Yang and McCarty, 2000a)). Engineering design of these technologies is rapidly evolving, although to date there is considerable uncertainty in determining the quantities of carbon substrate required and the impacts of dosing requirements on field performance (Hood et al., 2007). Lactate is one of the most common carbon substrates used in the industry and research studies (Sung et al., 2003; Christ and Abriola, 2007; Hood et al., 2007; Sorenson, 2002). Due to its high solubility, maintaining sufficient concentrations of hydrogen to support EISB typically requires continuous dosing with lactate throughout the treatment period (Major et al., 2002). Emulsified Vegetable Oil (EVOs) on the other hand has been recognized as a promising remediation technique that does not require continue dosing (Long and Border, 2006). Dechlorination may be slowed or inefficient in the presence of competing electron accepting processes that consume the available hydrogen, including sulphate reduction, iron reduction, and methoanogenesis (Chapelle, 1996).

While the majority of laboratory and field work has focused on EISB for relatively dilute CAH plumes, it has been demonstrated that the approach has potential for treating dense non-aqueous phase liquid (DNAPL) source zones (e.g., Seagren et al., 1994; Yang and McCarty, 2000a; Yang and McCarty, 2002). Not only are the fermentors and dehalogenataors able to metabolize CAHs at concentrations previously assumed toxic, the suppression of methanogensis in these environments favours efficient dechlorination (Yang and McCarty, 2000a). Furthermore, EISB within the source zone has additional benefits of reducing DNAPL longevity by increasing the driving force for mass transfer

to the aqueous phase (Seagren et al., 1994; Yang and McCarty, 2000a; Yang and McCarty, 2002; Christ et al., 2005; Amos et al., 2007).

Due to the variety of ways that bioremediation can be accomplished, several strategies exist in the industry for remediation/containing contaminated sites. The focus here is on enhanced bioremediation methods employed for contaminated fractured environments.

In a wide variety of subsurface environments, bioremediation has been demonstrated to effectively remediate/contain the spread of contaminants (including many chlorinated solvents) while converting a significant fraction of their mass to harmless byproducts (National Research Council, 1994). However, the nature and extent of these processes in the vadose zone and/or fractured rock are not well-understood. There is some field evidence that biodegradation of chlorinated solvents can occur in the vadose zone of fractured rock settings (e.g., Conrad et al., 1997b), but major questions remain as to how to characterize the extent of naturally occurring biological activity and how to stimulate and monitor it for the remediation of contaminated aquifers. While the numbers of indigenous bacteria in the vadose zone of fractured rocks in arid regions are low, experiments have indicated that their activity may be stimulated with the addition of water, nutrients and organic carbon (Palumbo et al., 1994).

Geller et al. (2000) presented an experimental approach for investigating the potential for bioremediation of DNAPLs in fractured rock vadose zones. The specific geology, liquid seepage patterns and the indigenous microorganisms of the site was incorporated into the

approach. A key aspect of this study was to consider the close coupling between fluid flow dynamics and biotransformation processes. Fluid flow and distribution of the microorganisms within fracture networks may be a significant factor in the ability of microorganisms to degrade DNAPLs, as they affect the availability of substrate, moisture and nutrients. Biological activity can change liquid surface tension and generate biofilms that may change the wettability of solid surfaces, locally alter fracture permeability and redirect infiltrating liquids. This study reported that a mixed culture of viable bacteria exists on fracture surfaces. Geller et al. (2000) hypothesized that the activity of these bacteria can be stimulated by contact with liquid water and organic contaminants, and this activity will not only be localized along active seepage pathways, but will also occur in the presence of vapor-phase organic contaminants and water-saturated air – an observation previously made by Palumbo et al. (1994). It was further concluded that the NAPL will pond at vertical discontinuities of the fractured rock and the presence of residual water may redirect the NAPL to areas not contacted by the flowing water. Thus, much of the rock mass may be exposed to contamination due to the transfer of volatile and soluble organic compounds from the NAPL to the aqueous, vapour and solid phases, whereupon biological degradation of the organic contaminant may be a significant process in controlling its further migration.

Although the nature and extent of these processes in fractured rock are not well-understood. There is some field evidence that biodegradation of chlorinated solvents can occur in the vadose zone of fractured rock settings (e.g., Conrad et al., 1997b), but major questions remain as to how to characterize the extent of naturally

occurring biological activity and how to stimulate and monitor it for the remediation of contaminated aquifers. Newell et al. (2006) reported downgradient source concentration half-life values to range from as low as 0.7 years for PCE to constant (or even increasing) concentrations for TCE while Tang et al. (1981) proposed that matrix degradation rates were similar to the fracture for radioactive species.

Previously, deep fractured rock vadose zones in arid regions have been thought of as biologically inactive due to dry conditions and minimal organic matter (Palumbo et al., 1994). Although the numbers of indigenous bacteria are ubiquitous and have been found in such environments, albeit in low numbers, experiments have indicated that their activity may be stimulated with the addition of water, nutrients and organic carbon (Palumbo et al., 1994; Colwell et al., 1992). Additionally, studies of microbial activity in deep fractured granite rock have shown a diverse microbial population to be attached to the fracture walls (Pedersen and Ekendahl, 1990), and evidence has been presented for natural biodegradation (intrinsic bioremediation) of chlorinated ethenes in a fractured dolomite aquifer (Yager et al. 1997).

Some of the strategies in enhanced bioremediation methods investigated for fractured environments are presented below.

2.4.2 Hydrogen Release Compound

Hydrogen Releasing Compound (HRC) is a proprietary polylactate ester that is food grade and, upon being deposited into the aquifer, is slowly hydrolyzed to release lactic

acid and other organic acid derivatives for about one to two years (Nakashima et al., 2002). The lactic acid is fermented by acetogens to pyruvic acid and finally to acetic acid due to the generation of ATP during glycolysis; for every mole of lactic acid fermented, two moles of hydrogen gas are created (Koenigsberg and Farone, 1999). The hydrogen produced supports reductive dechlorination, which can dechlorinate contaminants such as tetrachloroethylene (PCE), trichloroethylene (TCE), dichloroethylene (DCE), and vinyl chloride (VC) (Cornuet et al., 2000). Lactic acid degrading bacteria are extremely common and are generally not expected to be a limiting factor for the reaction (e.g., Kean et al., 2002). The injected HRC not only serves as a hydrogen source, but also as an essential nutrient when it changes into a series of organic acids that support microbial growth.

Kozar (2002) carried out a pilot test to field implement the HRC technology, via subsurface injection into a shallow fractured sedimentary bedrock site. This test aimed to evaluate, through performance monitoring, the ability of HRC to affect ground water chemistry and reduce the concentration of the aqueous phase of PCE and its daughter products in the shallow fractured bedrock zone. An increase in TCE, cis-1,2-DCE and vinyl chloride concentrations was observed following the injection of HRC, consistent with degradation of PCE by reductive dechlorination. This study demonstrated that by creating anaerobic conditions via HRC in a fractured environment, PCE and its daughter products (e.g. 1,1-DCE, TCE and cis-1,2 DCE) could be metabolized by indigenous micro-organisms.

Tony et al. (2002) conducted two separate pilot-scale test plots by injecting HRC into a saprolite and a fractured crystalline bedrock aquifer. Following the treatment, the increased biologic activity was observed to create favourable geochemical changes in both aquifers. Biologically-based reductive dechlorination was evidenced by discernable changes from TCE to cis-1,2-dichloroethylene (cDCE) in both aquifers. It was also noted that the degree of TCE transformation is significantly affected by distance/residence time of a unit volume of ground water within an appropriately reduced section of the aquifer. The bedrock aquifer also generally maintained metabolic acid concentrations approximately 3-4 times greater than in the saprolite, leading to a greater degree of TCE degradation achieved in bedrock. This observation was further supported by the evidence that ethene and ethane were detected in the bedrock aquifer, indicating a more accelerated and complete conversion of TCE. Tony et al. (2002) concluded that major factors that may be affecting this difference are geochemical settings, aquifer flow dynamics, and existing microbial populations associated with the two different aquifer systems.

2.4.3 Methane Enhanced Bioremediation

Andrews et al. (2002) aimed to examine the effectiveness of enhanced aerobic biological injection processes utilizing hydrofracturing to address the low transport rates in a fractured claystone environment combined with the injection of methane to stimulate the production of the mono-oxygenase enzyme to remediate groundwater impacted with 1-1 DCE, 1,1,1 TCA and TCE in a fractured bedrock environment. Prior to the full-scale field application, a series of microcosm studies were conducted. Microcosm studies

demonstrated that enhancement of the indigenous aerobic biodegradation activity may be achieved by amending the groundwater with a supply of inorganic nutrients and a supplemental carbon source such as phenol, propane and methane. Due to the wide distribution of methanotrophic populations throughout the plume, likely resultant from the natural presence of methane as well as hydrogen and other light hydrocarbon gases in the formation, methane was selected as the primary carbon substrate to stimulate the production of the mono-oxygenase enzyme to remediate groundwater impacted with 1-1 DCE, 1,1,1 TCA and TCE. The microcosm results showed an average of 35 % decline of the concentrations of TCA, TCE, DCM and 1,1 DCE in replicate microcosm samples amended with methane and inorganic nutrients over an 8-week period as compared to the unamended control samples.

Andrews et al. (2002) additionally employed a further technique of modulating additions of primary growth substrates. In this way, a more spatially dispersed microbial population was achieved (Kitanidis et al., 2002) since co-oxidative processes were demonstrated to be inherently more efficient under alternating cycles between growth and starvation of the primary substrate. By periodically removing the primary substrate, competitive inhibition for the substrate undergoing co-oxidation is relieved. Results from this field application of the process after the initial six months of full scale application of the system, revealed that the 1,1-DCE concentrations significantly declined across 90% of the contaminated plume, with a greater decay rate in the central portion of the plume.

In addition, the study by Andrews and Mahaffey (2002) demonstrated an enhanced aerobic biological injection processes utilizing hydrofracturing to address the low transport rates in a fractured claystone environment. Hydrofracturing is a common process utilized in fractured environments during installation of the injection wells as a delivery mechanism to establish favourable in situ bioremediation conditions (USEPA, 1994). Hydrofracturing creates/enhances the storage capacity of the subsurface, thereby increasing the effective porosity and yield of the formation, which provides the means for injected nutrients to be more effectively distributed in the subsurface.

2.4.4 Electron Donors

MacKinnon et al. (2002) conducted a series of treatability studies under laboratory simulated site conditions, using materials from two fractured bedrock sites to review the possibility of whether indigenous microorganisms can be stimulated to dechlorinate the site DNAPL through the addition of electron donors in an anaerobic environment. These studies were completed using core material representing three rock types (shale, siltstone, and crystalline bedrock) collected from the two field sites. The controls and treatments constructed for each of the sites included anaerobic sterile and intrinsic controls, microcosms amended with either soluble electron donors (MEAL) a mixture of methanol, ethanol, acetate and lactate or molasses [Site 1 only]), or a slow release electron donor (canola oil). Each electron donor treatment was replicated with a set of microcosms bioaugmented with KB-1 (a naturally occurring, non-pathogenic dehalorespiring bacterial culture developed by the University of Toronto and GeoSyntec).

MacKinnon et al. (2002) demonstrated that bioaugmented microcosms indicate that the process may be very effective for remediation of DNAPL source areas, with the potential to reduce the duration of groundwater remediation activities relative to conventional pump-and-treat options. In the bioaugmented MEAL microcosms for Site 1, TCE was completely dechlorinated to ethene within 13 days following bioaugmentation. TCE was also completely dechlorinated to ethene for both the bioaugmented canola oil and molasses treatments, but the time for complete TCE dechlorination was longer (30 and 26 days, respectively). In contrast to the Site 1 microcosms, the amendment of MEAL electron donors into the Site 2 groundwater resulted in PCE dechlorination via TCE to cis-1,2-DCE at both source zone and core plume concentrations. PCE dechlorination in the canola oil microcosms was also observed, but at a significantly slower rate than the MEAL microcosms. Further dechlorination of cis-1,2-DCE via VC to ethene was not observed in either the MEAL or canola oil microcosms, indicating that the indigenous bacteria in the fractured rock at the site were incapable of completely dechlorinating PCE to ethene. Bioaugmentation of groundwater from either site with dehalorespiring bacteria was reported to have significantly accelerated the rate and extent of DNAPL dechlorination to ethene with complete dechlorination observed within weeks of bioaugmentation. The results of these treatability studies have demonstrated the ability of enhanced bioremediation to destroy high dissolved phase concentrations within very short time frames, which will increase the rate of dissolution of remaining DNAPL, and in turn reduce the duration of remedial activities.

2.4.5 Biobarriers

Biological barriers, generated by stimulating groundwater bacteria, aim to effectively contain (as opposed to treat) polluted groundwater in fractured media (Ross and Bickerton, 2002). Biobarriers are formed following attachment of bacteria and excretion of exopolymeric substances (EPS), which clog the geological material and thus, decrease the hydraulic conductivity (Baveye et al., 1998). In fractured bedrock, biobarriers would have the advantage of needing low maintenance, requiring relatively low investment, and having the potential to be dismountable (James and Hiebert, 2001). Ross et al. (2002) employed a large-scale planar fracture apparatus to carry out a biostimulation experiment to assess the persistence and resistance of the biobarriers, and to validate monitoring tools. Groundwater bacteria were stimulated via the injection of a simple carbon source in a large-scale planar fracture. By doing this, a biofilm having 1.7 times the width of the initial nutrient plume was developed. After developing the biobarrier, the resistance and persistence of the biofilm were being tested simultaneously. The resistance of the biobarrier was tested by stopping nutrient injection for a period of 45 days, while the persistence of the biobarrier was being tested by increasing the ground water velocity by 6 times. After the nutrient injection was stopped, a significant increase in the density of planktonic cells for the first 5 days was observed followed by decrease in the planktonic cells density. While the assessment for the biobarrier led to a significant decrease in the density of planktonic cells and planktonic EPS, suggesting biofilm sloughing. Ross et al. (2002) concluded by using tracer tests to demonstrate the development of the biofilm was effective to partially clogged the fracture plane, and in turn caused retardation and dispersion of the flow. Note that this suggests that,

regardless of the intended purpose of stimulating bacterial growth, biofilms will be expected to reduce the hydraulic conductivity of fractures as they multiply and occupy the pore space.

Kalish et al. (1964) observed permeability reductions due to bacterial clogging via injection experiments with sandstone cores. It was found that depending on the permeability of the cores, bacterial clogging can vary from less to 2 inches to 5 or 6 inches. It was also noted that depending on the bacteria size, the depth of penetration into the cores can similarly varies. Charbonneau et al. (2006) on the other hand found that biofilm formed within dolostone cores reduces the effective porosity via radial diffusion experiments with a conservative tracer. In other works, Yu and Pinder (1994) and de Beer et al. (1997) observed significant reductions in effective diffusivity for various solutes due to biofilm formation.

2.4.6 Numerical Modelling of Bioremediation

Numerous numerical models have been developed for simulating chlorinated ethene transport and degradation. Dechlorination kinetics have been approximated by first-order (Carr et al., 2000; Sleep and Sykes, 1993), Michaelis-Menten (Haston and McCarty, 1999) and Monod-type expressions (Chu et al., 2004; Cupples et al., 2004a,b; Christ and Abriola, 2007). The latter two forms often include limitations on the rate of dechlorination due to the availability of hydrogen (e.g., Fennell and Gossett, 1998; Amos et al., 2007) and competition between CAHs (Cupples et al., 2004a,b; Yu and Semprini, 2004). Depending on the quantities of alternate electron acceptors are not present,

competition for hydrogen can be neglected (Cupples et al., 2004a; Amos et al., 2007) or included (Fennel and Gossett, 1998; Lee et al., 2004; Christ and Abriola, 2007). A few models consider excessive acid formation limiting the rate of dechlorination (Zhuang and Pavlostathis, 1995; Cope and Hughes, 2001; Lee et al., 2002; Adamson et al., 2004). In general, models that employ first-order decay expressions incorporate all of the sources of limitation implicitly in the rate constant. A few models explicitly include DNAPL dissolution (Carr et al., 2000; Chu et al., 2003; Widdowson, 2004; Amos et al., 2007; Christ and Abriola, 2007). To the author's knowledge, no models have been developed or employed to investigate EISB in fractured rock.

2.4.7 Conclusion for Literature Review of Bioremediation

These studies have indicated that indigenous bacteria activity in the fractured rock may be stimulated with the addition of water, nutrients and organic carbon and have underscored the close coupling between fluid flow dynamics and biotransformation processes. In addition, bioaugmented microorganisms have been demonstrated in microcosm experiments as potentially effective for aggressive remediation of DNAPL source areas in fractured rock environments, with the potential to reduce the duration of remediation activities. Experiments have also indicated that major factors that may affect the efficiency of bioremediation in fractured environments include geochemical settings, flow dynamics and existing microbial populations associated with the different aquifer systems.

Most published work focuses on microcosm studies. Like those conducted to support

bioremediation efforts in unconsolidated media, these studies have demonstrated the ability of enhanced bioremediation to destroy high concentrations within short time frames, as compared to the unamended control samples. Such studies indicated the potential for an increased rate of DNAPL dissolution which, in turn, could reduce the duration of remedial activities.

Of the few available bioremediation studies in fractured environments, the most well investigated method creates anaerobic conditions through injecting HRC. This method has been observed to metabolize PCE and its daughter products by indigenous micro-organisms at the fractured rock sites investigated. Due to the low permeability of a fractured environment, hydrofracturing is often used in combination with bioremediation in order to more effectively distribute injected nutrients.

Research into biobarriers has suggested that they may be a useful tool in causing retardation of contaminated groundwater in fractured bedrock. This research underscores the ability of enhanced biofilm growth to clog the pore space in fractures, altering the hydrodynamic behaviour of the environment's dominant flow paths.

There appears to be essentially no available information on the interaction of biofilms with the matrix of fractured porous materials, or on the ability of bioremediation to address diffused contamination in the matrix. Moreover, as with all remediation technologies in fractured porous media, delivery of the fluids to the contaminated area and monitoring of remediation progress are significant hurdles not easily remedied.

2.5 SURFACTANT FLUSHING

2.5.1 General

Surfactants are surface acting agents that concentrate at interfacial regions between two fluid phases (e.g., oil and water). They are amphiphilic agents that exhibit dual behaviour (i.e., affinity for both water and oil). This behaviour is possible due to their molecular structure which is made up of one soluble and one insoluble moiety. Surfactants are classified according to the nature of the hydrophilic portion of the molecule. The head can be positively charged (cationic), negatively charged (anionic), both negatively and positively charged (zwitterionic) or not charged (nonionic) (West and Harwell, 1992). Individual surfactant molecules are single monomers. However, when the aqueous concentration of monomers exceeds a critical value - the critical micelle concentration (CMC) - and the solution is above the limiting Krafft temperature, T_k, the monomers form into micelles. Micelles are capable of encapsulating NAPL and forming microemulsions.

Due to these properties, surfactants can decrease the interfacial tension (IFT) between water and NAPL and can increase the effective aqueous solubility of NAPL components. The former allows NAPLs contacted with surfactants to be mobilized towards recovery wells due to a reduction in capillary resistance to flow, while the latter allows NAPL mass to be removed by enhanced dissolution. The use of surfactants for remediation of subsurface sites contaminated by DNAPL has been investigated by numerous research groups (e.g., Ellis et al., 1986; Abdul et al., 1990; Gannon et al., 1992; Pennell et al., 1994; Pope and Wade, 1995; Shiau et al., 1995; Fountain et al., 1996; Martel and Gelinas,

1996; Hirasaki et al., 1997).

However, mobilization of DNAPL in particular may cause it to move deeper into former uncontaminated zones (Pankow and Cherry, 1996). For this reason, some researchers recommend using solubilisation rather than mobilization as the primary surfactant flushing mechanism in DNAPL systems. However, solubilisation of contaminant by the surfactant creates a microemulsion phase that is denser than the surrounding groundwater and can travel downward before being captured by an extraction well (Ramsburg and Pennell, 2002).

In addition, for pooled DNAPL, the risk of downward remobilization is difficult to avoid as it can be initiated by only small reductions in IFT (Lunn and Kueper, 1999). Methods have been proposed to prevent downward mobilization of DNAPL during chemical flooding such as a preconditioning step that uses aqueous alcohol solutions that partition into the DNAPL and thereby reduce its density prior to miscible displacement (Lunn and Kueper, 1997; 1999), or the use of neutrally-buoyant microemulsions instead of surfactants (Kostarelos et al., 1998). Alternatively, brine solutions have been employed to increase the resident aqueous phase density effectively reversing the density difference between the organic and aqueous phases (Miller et al., 2000). The Density-Modified Displacement (DMD) method was developed to eliminate the risk of downward DNAPL migration during immiscible displacement using traditional horizontal flushing techniques (Ramsburg and Pennell, 2002).

For a NAPL-water system, the addition of a surfactant can yield one of three potential types of microemulsion systems, distinguished for the design of the surfactant systems to produce ultralow IFTs: Windsor Type I, Type II and Type III. In a Type I system, the surfactant is preferentially water soluble and is in the form of oil-swollen micelles in the aqueous phase. In a Type II system, the surfactant is preferentially oil soluble and virtually all the surfactant is found in the form of water-swollen reverse micelles in the oil phase. In a Type III system, the surfactant has nearly equal affinity for both phases and creates a new middle phase microemulsion that contains almost all of the surfactant and large quantities of the organic chemical and water. The volume of organic chemical per unit weight of surfactant in the middle phase is known as the solubilisation parameter, an increase in which corresponds to a decrease in IFT (West and Harwell, 1992).

2.5.2 Processes that Reduce Surfactant Flood Efficiency

Successful surfactant use to enhance remediation goes beyond selection of a surfactant (or surfactant system) that will efficiently solubilise or mobilize NAPLs. The surfactant must also be matched to the subsurface conditions so that it remains active, since surfactants that coalesce on organic liquid-water interfaces can also be expected to coalesce on solid-liquid interfaces (Rosen, 1989; Harwell, 1984). Surfactant adsorption is therefore a threat to the success of surfactant-enhanced remediation because it reduces the active concentration of surfactant. Although research has found that anionic surfactant can be expected to sorb less than nonionics to most mineral surfaces, they are subject to losses by precipitation (Stellner, 1988; 1989).

At low concentrations, surfactant monomers gather near to the surface of the solid-fluid interface to form micelle-like structures, which are known as admicelles or hemimicelles. Once these structures start to form, more sorption of the surfactant monomers will take place until a complete bilayer of surfactant covers the solid-fluid interface. The tendency of the surfactant to form admicelles or hemimicelles is dependent on interactions between the hydrophilic moiety of the surfactant, the solid interface and temperature (West and Harwell, 1992). Other factors that affect the amount of surfactant being sorbed include pH, contaminant chemistry, ionic strength and cation exchange capacity. A thorough review of the fundamental mechanisms driving anionic and nonionic surfactant sorption is provided by Sardin et al. (1998).

Due to their ability to form micelles, the precipitation behaviour of ionic surfactants is very different from that of simple inorganic salts. Scamehorn (1986) found that any factor that lowers the CMC of a surfactant system will decrease the susceptibility of the surfactant to precipitation, hence indicating that by mixing several surfactants together, the probability of the surfactant to precipitate, sorb and form coacercate phases (i.e. two separate phases, a surfactant-rich aqueous phase and an aqueous phase) can be reduced (West and Harwell, 1992).

One concern with using surfactant to remediate contaminated aquifers is the recalcitrance and toxicity of surfactants in the subsurface environment. In general, both cationic and anionic surfactants are toxic to soil bacterial (Lewis, 1991; Lawrence 1970), while nonionic surfactants tend to have low toxicity. By introducing surfactants into the

environment, the rate of biodegradation has been reported to have either diminished or stopped entirely (Oberbremer et al., 1990; Srivastava et al., 1990). Therefore, surfactant flushing at a site may preclude subsequent bioremediation in some cases.

2.5.3 Surfactants in Fractured Rock

Laboratory-scale experiments have demonstrated that DNAPLs can be efficiently recovered in unconsolidated porous media using two-phase (immiscible) displacement technologies (e.g., Lunn and Kueper, 1999; Ramsburg and Pennell, 2002; Miller et al., 2000; Kostarelos et al., 1998).

In a wide variety of subsurface environments, surfactant enhanced aquifer remediation (SEAR) has been extensively studied and demonstrated to effectively remediate/flush the spread of contaminants (including many chlorinated solvents) (Taylor et al., 2004; Zhong et al., 2003, Abriola et al., 2005; Suchomel et al., 2007).

The possibility and efficiency of using surfactant as a remediation methodology for DNAPL trapped in fractures was studied by Yeo et al. (2003). In this work, three experiments were carried out to test existing method and develop an effective methodology for removing DNAPL trapped in vertical downward dead-end fractures. A water-flushing method failed to remove DNAPL TCE from fractures in which no fluid flow occurred, failing to overcome the capillary and gravity forces that trapped the DNAPL. Subsequently, a fluid denser than TCE (made up of a mixture of 50% water and 50% calcium bromide) was injected into the fracture network, but this too did not

displace TCE. More calcium bromide was then added to water to further increase the density of the injected fluid plus approximately 0.8% SDS (sodium doceyl sulfate) surfactant was also added to generate a decrease in IFT. Through this experiment, Yeo et al., (2003) demonstrated that by decreasing the interfacial tension between the dense fluid and TCE, while at the same time increasing the density of the invading phase, DNAPL trapped in dead end fractures could be effectively displaced.

No additional literature beyond this one study was found on surfactant flushing to remediate DNAPLs in fractured environments. Considerably more research has been carried out focusing on employing this technology for LNAPLs in fractured environments (e.g., Babadagli, 2002; Zekri and Almehaideb, 2003). This research has proved surfactant to be a promising method to remove LNAPL from fractured environments by changing the IFT of the non-wetting phase.

CHAPTER 3 – MODEL DEVELOPMENT

The model developed for this work (DNAPL3DRX-FRAC) involves the coupling of the three-dimensional two-phase flow model (DNAPL3D) (Gerhard et al., 1998, 2001; Gerhard and Kueper, 2003a,b,c; Gerhard et al., 2007) and RT3D, a three-dimensional multi-species contaminant transport model with non-linear kinetic reactions (Clement, 1997; Clement et al., 1998). This coupling was executed with DNAPL3D-RX (West et al., 2008) using a split-operator approach following Grant and Gerhard (2004). Within a time step, DNAPL migration is initially simulated using DNAPL3D. The contaminant solute is then added to the aqueous phase at nodes with DNAPL present via equilibrium or non-equilibrium mass transfer routines (Grant and Gerhard, 2004; Grant and Gerhard, 2007b). RT3D is then employed within the same time step to simulate advection, dispersion and reactions of the solute. Finally, the phase saturations are updated at the end of the time step in accordance with the amount of mass transferred from the DNAPL to the aqueous phase. Although DNAPL3D-RX is three-dimensional, all fractured rock simulations presented in this thesis are two-dimensional. A brief summary of the model's relevant characteristics and governing equations are presented here.

3.1 GOVERNING EQUATIONS

3.1.1 DNAPL3D Governing Equations

The fluid fluxes can be mathematically described by extending Darcy's law to multiphase flow:

$$q_W = -\frac{k_{ij}k_{r,W}}{\mu_W}\left(\frac{\partial P_W}{\partial X_j} + \rho_W g \frac{\partial Z}{\partial X_j}\right) \qquad \text{i, j = x, y, z} \qquad (3.1)$$

$$q_{NW} = -\frac{k_{ij}k_{r,NW}}{\mu_{NW}}\left(\frac{\partial P_{NW}}{\partial X_j} + \rho_{NW} g \frac{\partial Z}{\partial X_j}\right) \qquad \text{i, j = x, y, z} \qquad (3.2)$$

where q_W and q_{NW} are the wetting phase and non-wetting phase fluxes respectively [L/T], k_{ij} are the medium permeability [L^2], $k_{r,W}$ and $k_{r,NW}$ are the relative permeabilities to the wetting and non-wetting phases respectively [-], μ_W and μ_{NW} are the wetting and non-wetting phase viscosities respectively [M/LT], P_W and P_{NW} are the wetting and non-wetting phase pressures, respectively [M/LT^2], ρ_W and ρ_{NW} are the wetting and non-wetting fluid densities respectively [M/L^3]; g is the gravitational constant [L/T^2].

Equations 3.1 and 3.2 are then substituted into the continuity equations for mass balance of the wetting and non-wetting fluid phases giving the following simultaneous equations:

$$\frac{\partial}{\partial X_i}\left[\frac{k_{ij}k_{r,W}}{\mu_W}\left(\frac{\partial P_W}{\partial X_j} + \rho_W g \frac{\partial Z}{\partial X_j}\right)\right] = \theta \frac{\partial S_W}{\partial t} \qquad \text{i, j = x, y, z} \qquad (3.3)$$

$$\frac{\partial}{\partial X_i}\left[\frac{k_{ij}k_{r,NW}}{\mu_{NW}}\left(\frac{\partial P_{NW}}{\partial X_j} + \rho_{NW} g \frac{\partial Z}{\partial X_j}\right)\right] = \theta \frac{\partial S_{NW}}{\partial t} \qquad \text{i, j = x, y, z} \qquad (3.4)$$

where S_W and S_{NW} are the wetting and non-wetting saturations respectively [-], θ is the porosity of the porous medium [-].

Although equations 3.3 and 3.4 contain four unknowns: P_W, P_N, S_W and S_N, the two pressures unknowns are related to the capillary pressure, where:

$$P_C = P_{NW} - P_W \qquad (3.5)$$

while the saturations are related by:

$$S_W + S_{NW} = 1 \qquad (3.6)$$

By substituting equations 3.5 and 3.6 to replace P_{NW} and S_{NW} in equations 3.3 and 3.4, the final two partial differential equations (Kueper and Frind, 1991) in terms of two unknowns P_W and S_W are:

$$\frac{\partial}{\partial X_i}\left[\frac{k_{ij}k_{r,W}}{\mu_W}\left(\frac{\partial P_W}{\partial X_j}+\rho_W g\frac{\partial Z}{\partial X_j}\right)\right]=\theta\frac{\partial S_W}{\partial t} \qquad \text{i, j = x, y, z} \qquad (3.7)$$

$$\frac{\partial}{\partial X_i}\left[\frac{k_{ij}k_{r,NW}}{\mu_{NW}}\left(\frac{\partial (P_C+P_W)}{\partial X_j}+\rho_{NW} g\frac{\partial Z}{\partial X_j}\right)\right]=-\theta\frac{\partial S_W}{\partial t} \qquad \text{i, j = x, y, z} \qquad (3.8)$$

Equations 3.7 and 3.8 are solved simultaneously to predict the movement of wetting and non-wetting phases with respect to both space and time. Their solution further requires definition of constitutive relationships for capillary pressure $P_C\ (S_W)$ and relative permeability $kr(S_W)$, which introduces nonlinearity via *Sw*. The equations are solved in a node-centered finite difference domain via discretized equations that are second order accurate in space and first order accurate in time and are solved fully implicitly via Newton Raphson iteration as discussed in Gerhard and Kueper, 2003.

3.1.2 RT3D Governing Equations

In RT3D, the governing equations of contaminant transport of the mobile and immobile species are (Clement, 1997; and Clement et al., 1998):

$$\frac{\partial(\theta C_m^n)}{\partial t} = \frac{\partial}{\partial x_i}\left(\theta D_{ij}^n \frac{\partial C_m^n}{\partial x_j}\right) - \frac{\partial}{\partial x_i}\left(\theta v_i C_m^n\right) + q_s C_s^n + \sum R_m \quad \text{i, j = x, y, z} \qquad (3.9)$$

$$\frac{\partial(\theta C_{im}^n)}{\partial t} = \sum R_{im} \qquad (3.10)$$

where D_{ij} is the hydrodynamic dispersion tensor [L^2/T], v_i is the average linear groundwater velocity [L/T], q_s is a volumetric flux representing sources and/or sinks [T^{-1}], R is the rate of all reactions [M/L^3T], and *t* is time [T].

The superscript *n* denotes the species number, while the subscripts *m* and *im* denote the mobile and immobile species respectively; the subscript *s* denotes a source or a sink. Sorption of the contaminant (assuming a linear sorption isotherm) is represented through a retardation factor (R_s) defined as:

$$R_s = 1 + \frac{\rho_b}{\theta} K_{oc} f_{oc} \qquad (3.11)$$

where ρ_b is the soil dry bulk density [M/L^3], K_{oc} is the organic carbon partition coefficient [L^3/M], and f_{oc} is the fraction organic carbon [-].

The advection and dispersion of individual solute species was solved using the standard explicit finite-difference method (Clement, 1997; Clement et al., 1998); while there are

several solver options available to the user in RT3D, testing with the template sites revealed that the former technique was a good balance between memory usage and computational run-time. All solute reactions were solved using the automatic switching Gear-stiff/non-stiff solver option in RT3D.

3.1.3 Equations Relevant to Fractured Rock

DNAPL3D, RT3D, and DNAPL3D-RX were developed and previously only employed for simulating scenarios involving unconsolidated porous media. Modifications to handle fractured porous media were developed for this thesis and are presented below.

The fracture hydraulic conductivity used in the model was calculated according to (Kueper and McWhorter, 1991; Witherspoon et al., 1980):

$$K = -\frac{e^2 k_{rw} \rho_w g}{12 \mu_\omega} \qquad (3.12)$$

where e is the hydraulic aperture of the fracture [L] and, k_{rw} is the relative permeability [-]. The relative permeability (k_{rw}) term was calculated using the Brooks – Corey constitutive model (Brooks and Corey, 1966). The Brooks – Corey constitutive model was demonstrated to be a valid for representing capillary pressure functions in fractures by Reitsma and Kueper (1994). The harmonic mean of the nodal hydraulic conductivities was calculated and multiplied by the hydraulic gradient across the fracture to obtain the wetting phase flux in the fracture. The average linear ground water velocity (v) for each individual node was calculated by dividing the flux by the local wetting phase saturation.

DNAPL to water mass transfer is treated as an equilibrium process in the simulations presented in this work. Although researchers have reported both equilibrium (e.g., Miller et al. 1998; Frind et al. 1999) and non-equilibrium (e.g., Glass and Nicholl, 1995; Dickson and Thomson, 2003) mass transfer in experimental fractured systems, the focus in the majority of this work is on behaviour of remediation systems after substantial aging periods for the DNAPL source zone (e.g., 20 years). Additionally, sensitivity tests revealed that in most cases all DNAPL dissolves in the first few years of aging irregardless of the mass transfer routine chosen. In an attempt to acquire a more in-depth understanding of the effects of mass transfer models on fractured rocks, a rate-limited model adopted from Dickson and Thomson (2003) was incorporated into the model. This rate-limited model was then employed in a single comparison simulation for the surfactant flushing study.

The entry pressure of each fracture was calculated according to (Kueper and McWhorter, 1991):

$$Pe = \frac{(2 \times IFT)}{e} \qquad (3.13)$$

where, P_e is the fracture entry pressure [M/LT^2], *IFT* is the interfacial tension between DNAPL and water [M/L], and *e* is the hydraulic aperture of the fracture [L] (assumed to be representative of the hydraulic aperture giving rise to the first connected non-wetting phase pathway through the computational cell of interest along main drainage). In this equation, DNAPL is assumed to be perfectly nonwetting, hence the contact angle in this equation (as compared to equation 2.11) is assumed to be 0°. In all the simulations

presented in this work, the entry pressure of the matrix is assumed to be sufficient to prevent the penetration of DNAPL; this assumption provides the technologies considered the best opportunity for success by restricting the DNAPL mass to the connected fracture network which is accessible by injected treatment fluids.

3.2 GRIDDING ROUTINE

3.2.1 Purpose of Gridding Routine

As demonstrated by Slough et al., (1999), if fracture elements in a domain are not sufficiently discretized, an over-prediction of the volume of DNAPL that continues to migrate vertically at the intersection of a vertical and horizontal fracture can occur. In addition, correctly capturing the diffusion of aqueous compounds into and out of the matrix requires sufficiently fine grid resolution (Slough et al., 1999). By finely discretizing the fracture and adjacent matrix nodes in a rock domain (e.g., at the scale of one centimetre or less), this problem can be accurately resolved. However, such fine resolution implies that traditional (i.e., equal grid spacing) methods of discretization will lead to a large computational expense.

A gridding routine was therefore developed specifically for this work to refine the nodal spacing of a two-dimensional finite difference domain such that appropriate node size reduction occurs only in those nodes that represent fractures and in the adjacent matrix nodes. This permits DNAPL migration and aqueous species diffusion to be captured accurately while minimizing the overall number of nodes. The routine takes a

coarsely-discretized finite difference domain and refines it so that the width of fracture nodes are equal exactly to the user-specified aperture and grid spacing in the matrix progressively increases with perpendicular distance outwards from the fracture; beyond a specified distance from all fractures, the coarse grid is retained. It applies to 2D finite difference domains consisting of any number of vertical and horizontal fractures of varying length and intersections. It assumes no variability of aperture along the length of a particular fracture, but permits a distribution of apertures across the domain. The degree of grid refinement and the distribution of spacing between the new (refined) nodes are left flexible, controlled by user-defined variables.

3.2.2 Method

The procedure used to refine nodal spacing is presented here, using an example of a single (original, coarse) node with width *DX* containing a vertical fracture with an aperture of 'e', as presented in a cross-sectional view of Figure 3.1(a), The user specifies how many refined nodes (*N*) will be contained in a fracture-containing coarse node after regridding. The coarse node is then divided into '*N*' regridded nodes; Figure 3.1(b) illustrates the example of *N*=9. Since the distributions to the left and the right side of the fracture are symmetrical, and identical calculations are employed for the right of the fracture, the following discussion refers only to the left half of the fracture node.

A new node (*i*=0) is defined in the centre of the coarse node, such that:

$$\Delta x_0 = e \qquad (3.14)$$

The number of matrix nodes to be generated in one half of the coarse node, NNSC, is:

$$NNSC = \frac{(N-1)}{2} \qquad (3.15)$$

FRACD equals the distance from the fracture wall to the edge of the coarse node, representing half of the total distance to be refined into matrix nodes:

$$FRACD = \frac{(DX - e)}{2} \qquad (3.16)$$

Finally, the width of each sub-node is determined through:

$$\Delta x_i = FRACD \left[\frac{\left(e^i\right)^{CF1}}{\left(\sum_{i=1}^{NNSC} e^i\right)^{CF2}} \right] \qquad i = 1, \text{NNSC} \qquad (3.17)$$

where, *CF1* and *CF2* are user defined spacing control factors. As shown in Table 3.1, by choosing different combinations of the control factors, the regridded matrix nodes can be subdivided equally, or with linearly or exponentially increasing nodal widths with distance from the fracture. These are illustrated for a one-dimensional case in Figure 3.1(b), (c) and (d).

Table 3.1. Regridding Options for Near-Fracture Matrix Nodes and Associated Spacing Control Factors for Equation 3.17

	Exponentially Increasing Spacing	Linearly Increasing Spacing	Equal Spacing
CF1	1	1	0
CF2	1	0	1

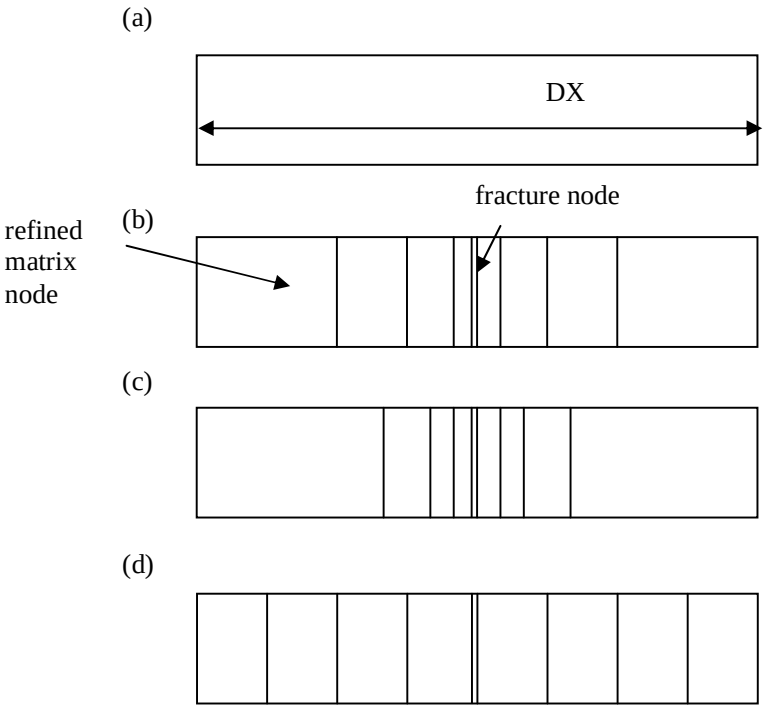

Figure 3.1: Example of grid refinement on a single coarse node occupied by a vertical fracture employing N=9 and (a) no refinement, (b) linear increasing refinement, (c) exponentially increasing refinement, and (d) equally spaced refinement.

Equations 3.14 – 3.17 are applied iteratively across the entire original domain in both horizontal and vertical directions to achieve refinement in and around all fractures and fracture intersections. Figure 3.2 presents the cross sectional view of a two-dimensional single fracture intersection, while Figures 3.3 (a) – (c) provide examples of GR being applied to a two-dimensional singe fracture intersection. In these examples, the original coarse grid contains 81 nodes while the refined domain after GR contains 144 nodes.

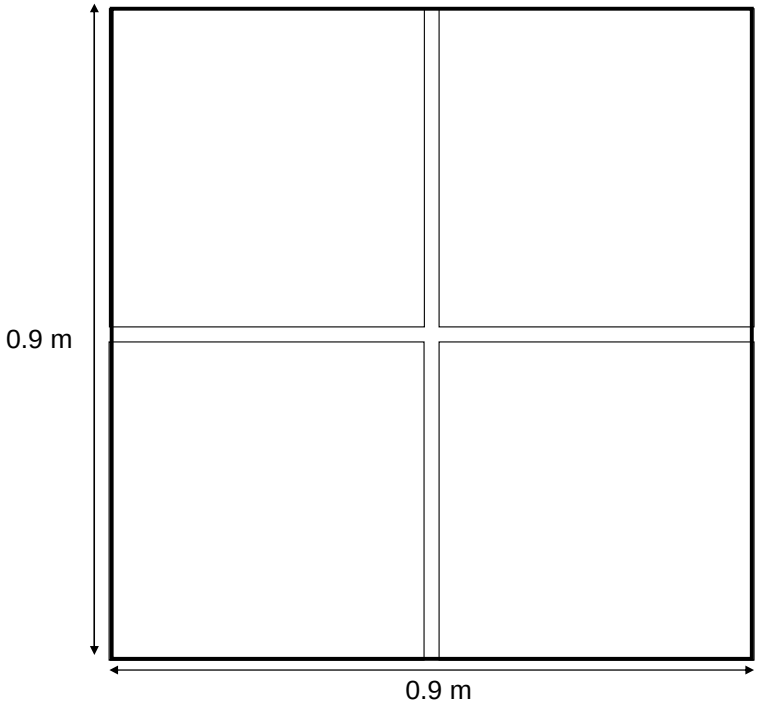

Figure 3.2: A fracture intersection 0.9m by 0.9m

(a)

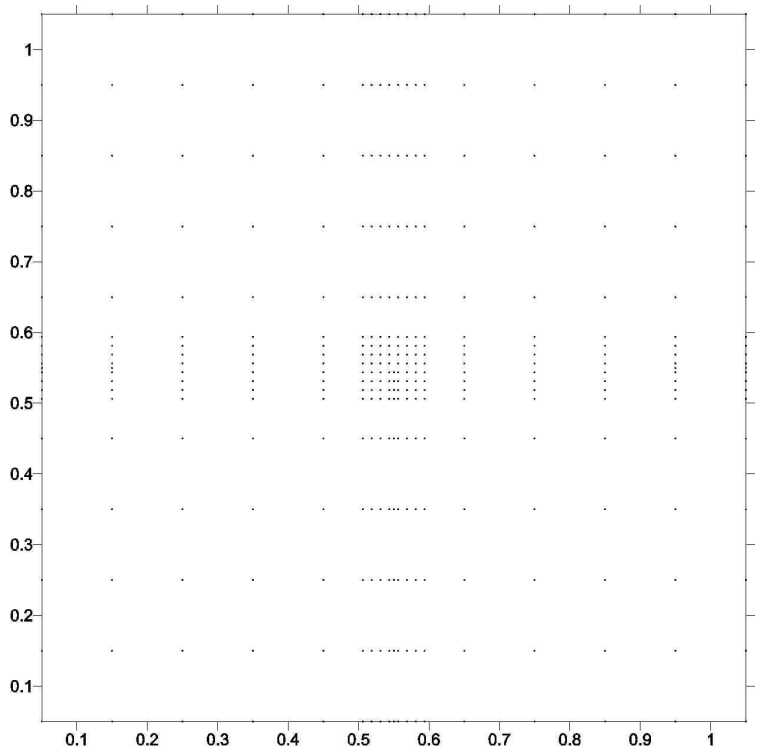

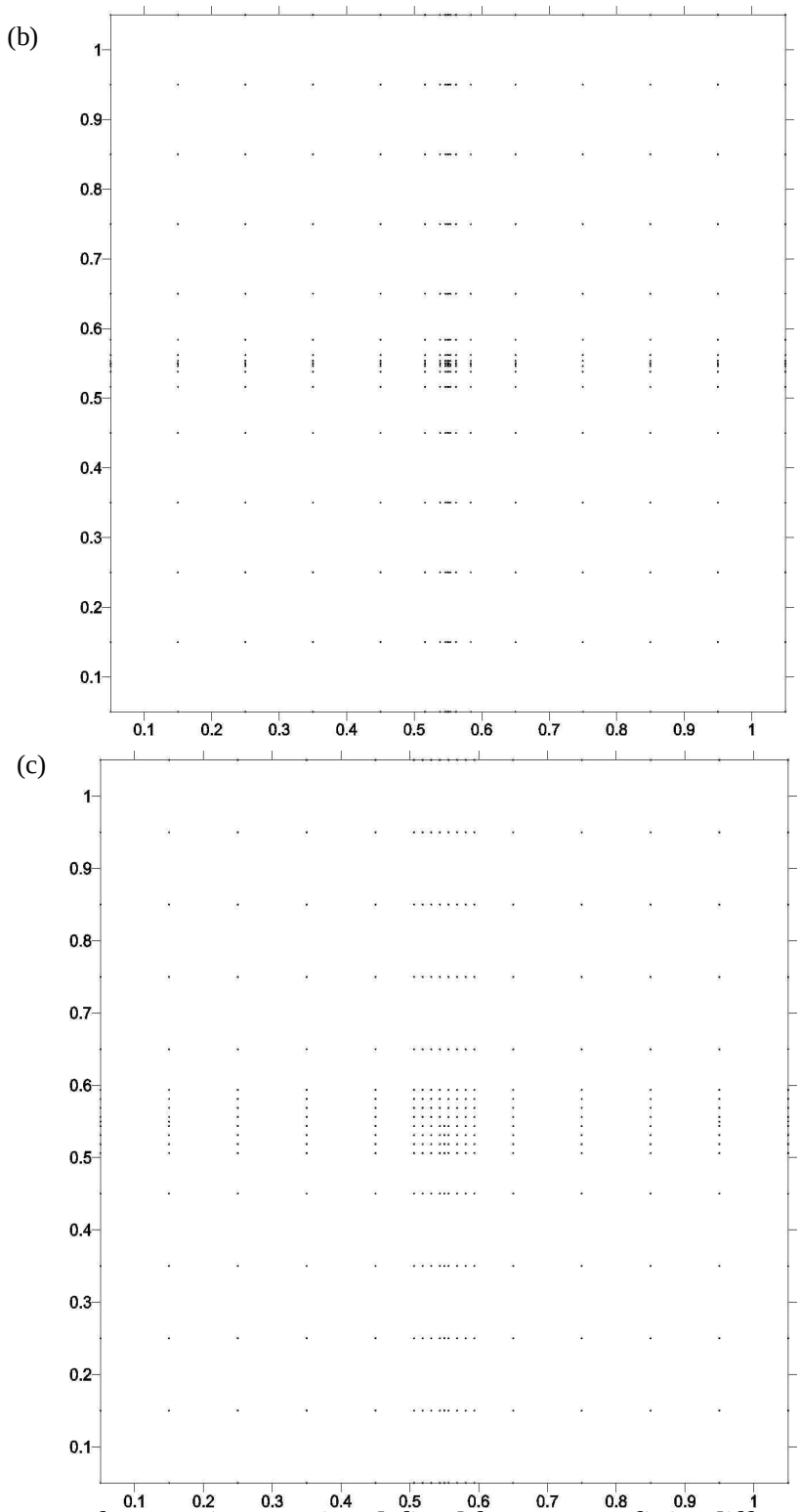

Figure 3.3: A fracture intersection defined for a coarse finite difference domain with DX=DY=0.1; the domain after grid refinement using (a) equal spacing; (b) exponential spacing and (c) increasing spacing; with N = 9. The dots identify node centers.

3.3 VERIFICATION AND MODEL TESTING

3.3.1 Advection-dispersive Transport

After DNAPL3DRX-FRAC was developed, various steps were carried out to build confidence in the new model. These steps included comparing advective-dispersive transport in the matrix against the Ogata and Banks (1961) one-dimensional analytical solution. The aim of this verification process is to ensure the advection –dispersion package of the model is running properly.

In this simulation, the physical setting of a one-dimensional horizontal column was used. The nodes in this column were coarsely discretized with a 0.05m discretization. Steady-state flow of groundwater is assumed with the lefthand boundary node assigned a constant concentration of 1000mg/L of TCE solute. A constant hydraulic gradient of 0.004 flowing from left to right was employed. The matrix medium in the column was assigned a porosity of 0.077 (i.e., similar to a sandstone domain) (Lipson et al., 2005) and a longitudinal dispersivity of 0.01 in the x-direction. Figure 3.4 presents both the analytical and numerical solution over the entire column.

3.3.2 Two Phase Flow

The second check carried out for the model was done by comparing the model with McWhorter and Sunada (1990). This check was done to ensure the two-phase flow equations are solved correctly. The analytical solution consisted of a one-dimensional horizontal column initially saturated with wetting phase throughout. The material in the column was assigned a permeability of $5 \times 10^{-11} m^2$, a porosity of 0.35, a residual wetting

phase saturation of 0.05, a pore size distribution index of 2.0, and a displacement pressure of 2000Pa. Figure 3.5 presents both the analytical and numerical solution along the column for four separate time of 0.6, 2.9, 5.8 and 9.3 days respectively.

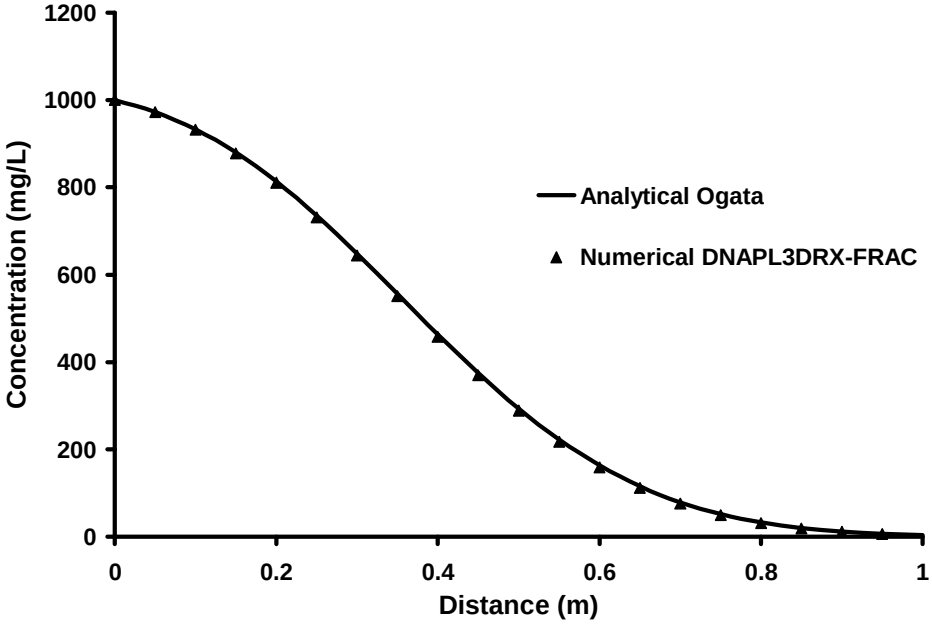

Figure 3.4: Verification of DNAPL3DRX-FRAC against Ogata and Banks (1961)

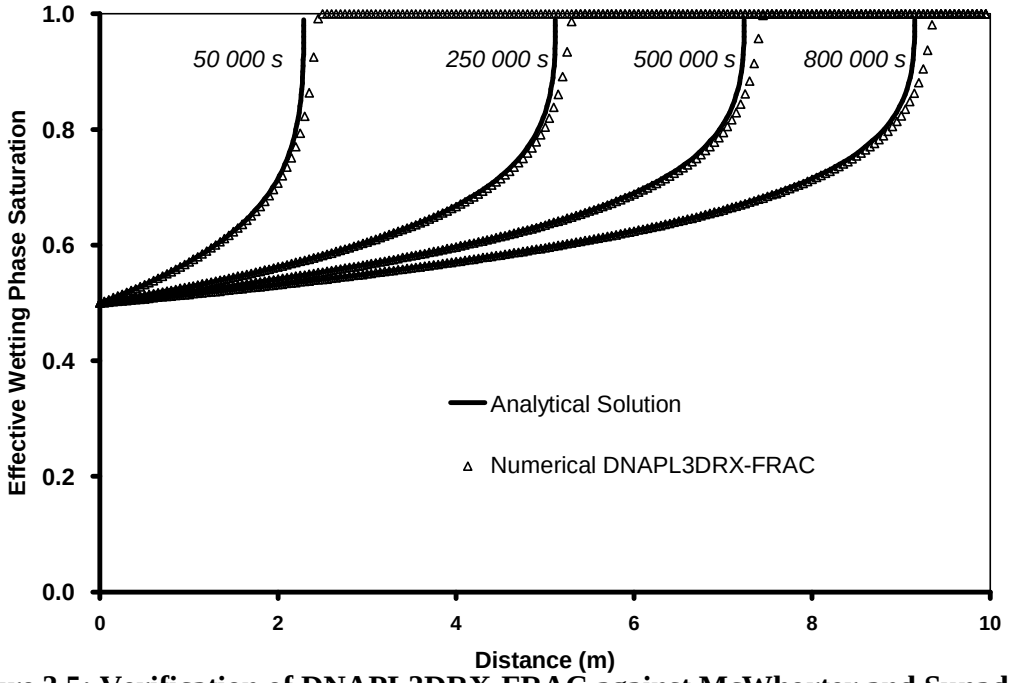

Figure 3.5: Verification of DNAPL3DRX-FRAC against McWhorter and Sunada (1990)

3.3.3. Matrix Diffusion

In order to gain a proper insight of the required degree of discretization to adequately capture diffusion gradients in the matrix, DNAPL3DRX-FRAC was verified with the analytical solution developed by Sudicky and Frind (1982). This analytical solution solves for transient contaminant transport in a set of discrete, parallel fractures situated in a diffusion-dominated porous matrix. For verification, a two-dimensional domain 10.0 m x 1.05 m with a single vertical fracture running through the entire domain was used.

The domain exhibited a coarse gridding of 0.05 m and the nodes containing the fracture were discretized using the 'exponentially increasing spacing' gridding method as described in the previous section with increasingly refinement (N = 3, 5, 15). The matrix medium in the domain was assigned a porosity of 0.3 and a permeability of $1x10^{-17}m^2$. A constant concentration of 1400mg/L of solute was injected from the top of the fracture and allowed to flow through the entire fracture. A diffusion coefficient of $1x10^{-9}$ m^2/s was assumed for the solute in this simulation. Since the analytical model of Sudicky and Frind (1982) (CRAFLUSH) only provides the solution for half the domain, in order to compare the results from both models, Figure 3.6 presents the numerical and analytical solution starting from the centre of the fracture to 0.4m of the right side of the matrix. From this figure, it is observed that as, as expected, increased matrix discretization results in more accurate simulation of the analytical solution. However, as discretization increases, more memory is required and the speed of the simulation decreases. For example, as the near-fracture discretization of 0.05 m increased from 3 to 5 to 15 nodes, the total root-mean-squared error between the numerical and analytical

solutions decreased from 22.9 mg/L to 12.5 mg/L to 7.76 mg/L but the speed of the simulation decreased approximately 5 folds with each increase. It was determined that, for field scale simulations in this work, a reasonable compromise between speed and accuracy was reached at N=5 for the GR routine throughout the domain.

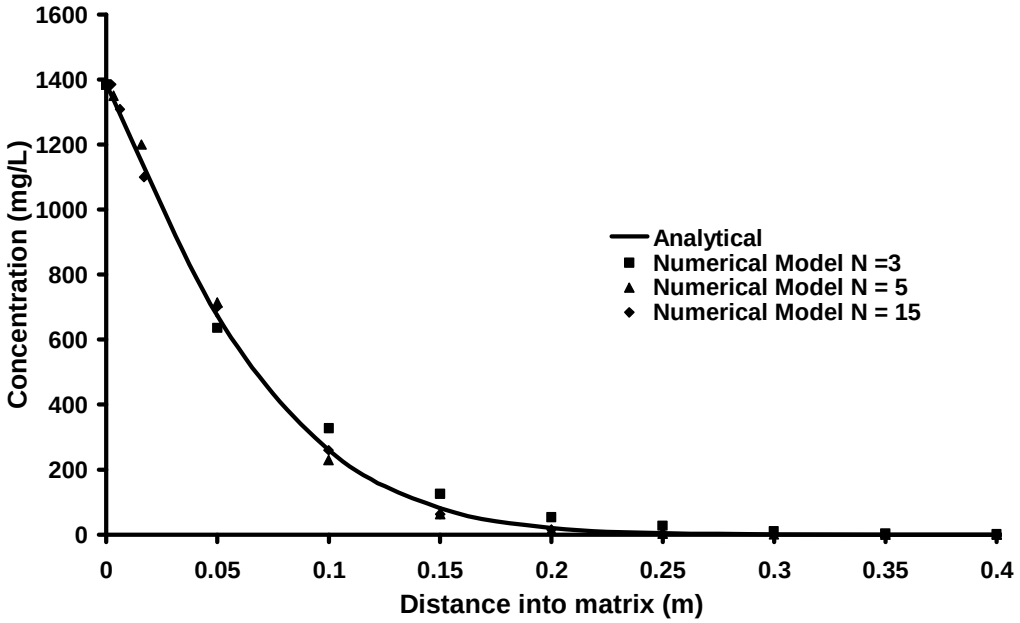

Figure 3.6: Verification of DNAPL3DRX-FRAC for a solute diffusion in single half-fracture and adjacent matrix against Sudicky and Frind (1982).

3.3.4 Sorption

RT3D typically calculates the change in concentration of a mobile species due to various sorption isotherms, but does not track the mass of sorbed contaminant. For this project, tracking the amount of chlorinated solvent sorbed to soil particles was important as permanganate will destroy the sorbed mass as well as the aqueous phase mass. Code was written to explicitly treat sorbed contaminant as an immobile species and the local (nodal) amount was calculated following the approach of Mundle et al. (2007) in which the concentration of sorbed TCE (*Cs*) was back calculated based upon the solved concentration of dissolved TCE (*Cw*):

$$C_s = C_w Kd \frac{\rho}{\theta} \qquad (3.18)$$

where $Kd = K_{oc} \times f_{oc}$ (Karickhff et al., 1979), K_{oc} is the organic carbon partition coefficient (L^3M^{-1}), and *foc* is the local (i.e., nodal) fraction of organic carbon (-), ρ is the dry bulk density (ML^{-3}), and θ is the porosity (-). To verify that this approach was being correctly implemented, the concentration of chlorinated solvent was graphed against the concentration of soluble chlorinated solvent in one node. As shown in Figure 3.7, the employed linear isotherm is confirmed.

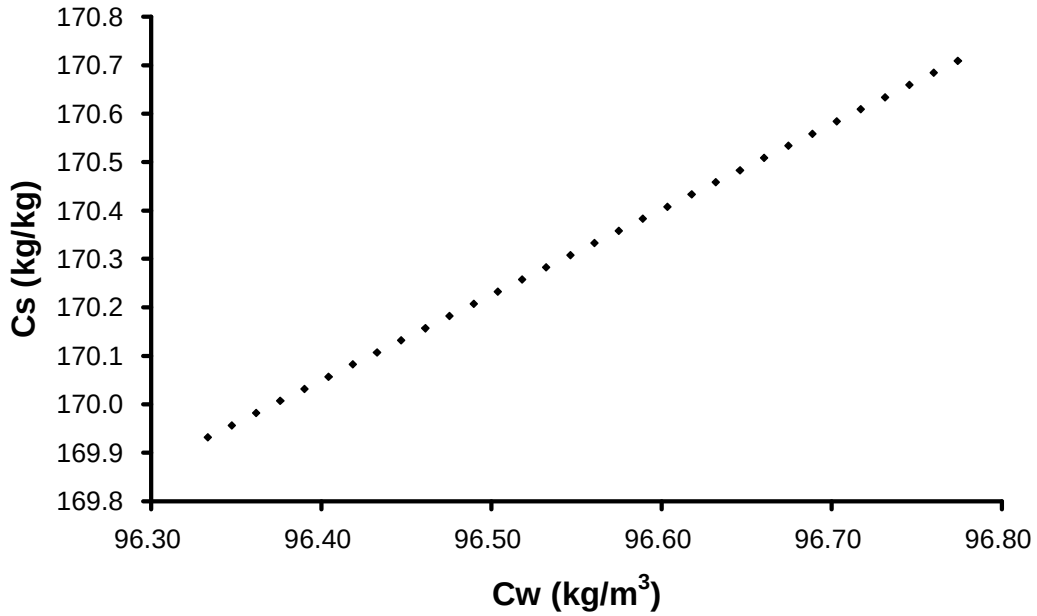

Figure 3.7: Verification of linear sorption within the model for a single node.

Abriola et al. (2005) found that sorption of Tween-80 to sand conformed to a Langmuir isotherm. The Langmuir sorption isotherm is described as (Fetter, 1993):

$$\frac{C_w}{C_s} = \frac{1}{\alpha\beta} + \frac{C_w}{\beta} \qquad (3.19)$$

where α is an adsorption constant related to the binding energy (L^3M^{-1}) and β is the maximum amount of solute that can be adsorbed by the solids (MM^{-1}).

To verify that this approach was being correctly implemented, data from Abriola et al. (2005) was employed and the concentration of solvent was graphed against the concentration of sorbed solvent in one node. By employing a maximum sorption capacity of 0.17 mg/g and an adsorption constant of 0.12 L/mg, the Langmuir sorption isotherm is demonstrated in Figure 3.8.

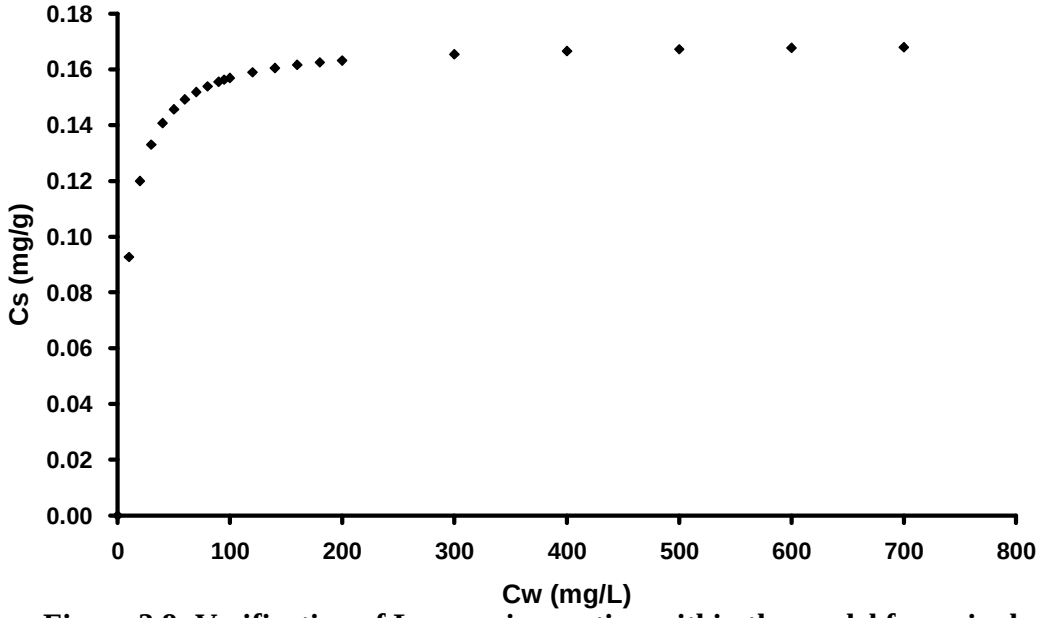

Figure 3.8: Verification of Langmuir sorption within the model for a single node.

3.3.5 Testing on Multi-Fracture Scenarios

The first study examined multi-phase flow (only) in fractures using a 13m by 13m domain with two orthogonal fractures cross-cutting the centre of the domain (Figure 3.9). The domain was first discretized using a coarse nodal spacing of 0.1m while the nodes that contain the two fractures were refined using N=7, and by employing 'exponentially increasing spacing'; this resulted in a total of 18495 nodes in the domain. The DNAPL distribution at t=100,000 s is plotted in Figure 3.10. An identical simulation, in which the fracture nodes were not refined, was conducted (N=1; total of 16900 nodes in domain).

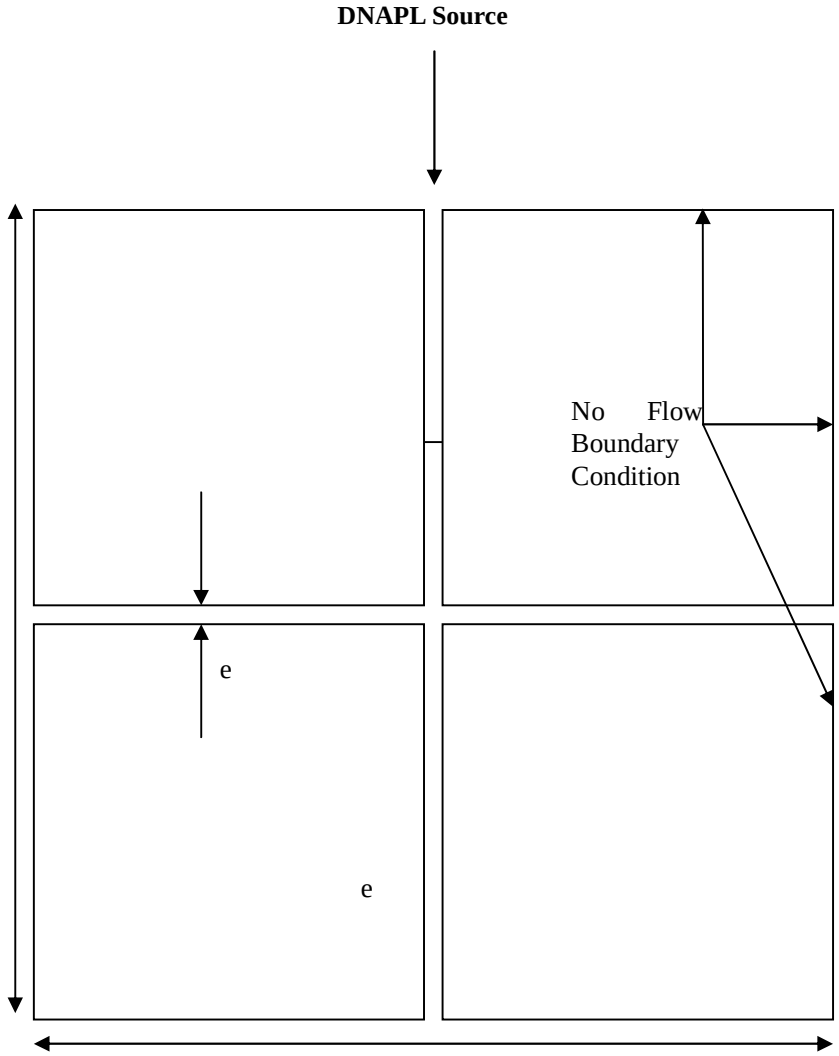

Figure 3.9 A pair of identical 1m long fractures, one oriented vertically and the other oriented horizontally.

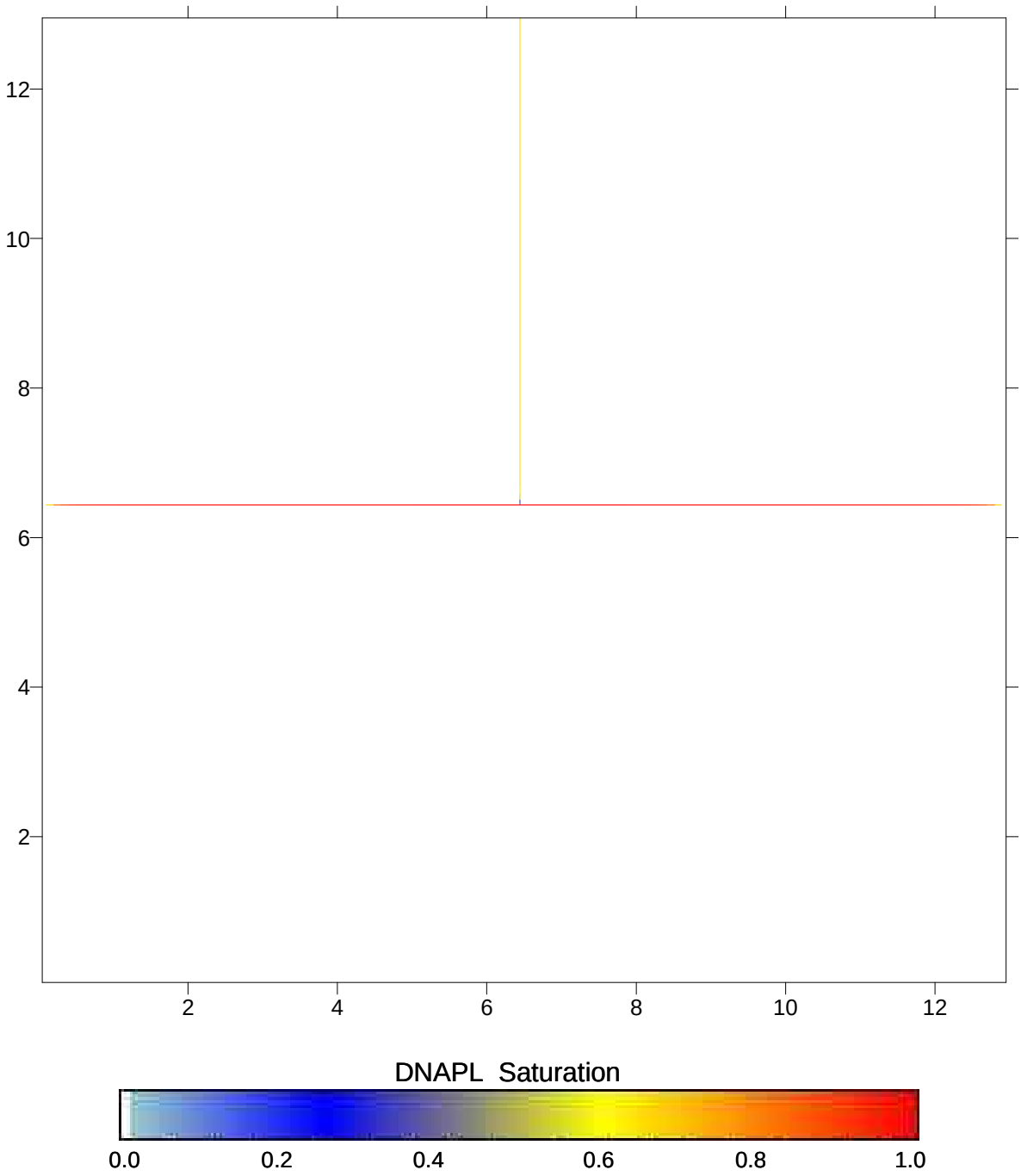

Figure 3.10: A 13m by 13m domain with the nodes that contain the two fractures variably discretized into seven exponentially spaced sub-nodes. The rest of the matrix is discretized using a 0.1m nodal spacing.

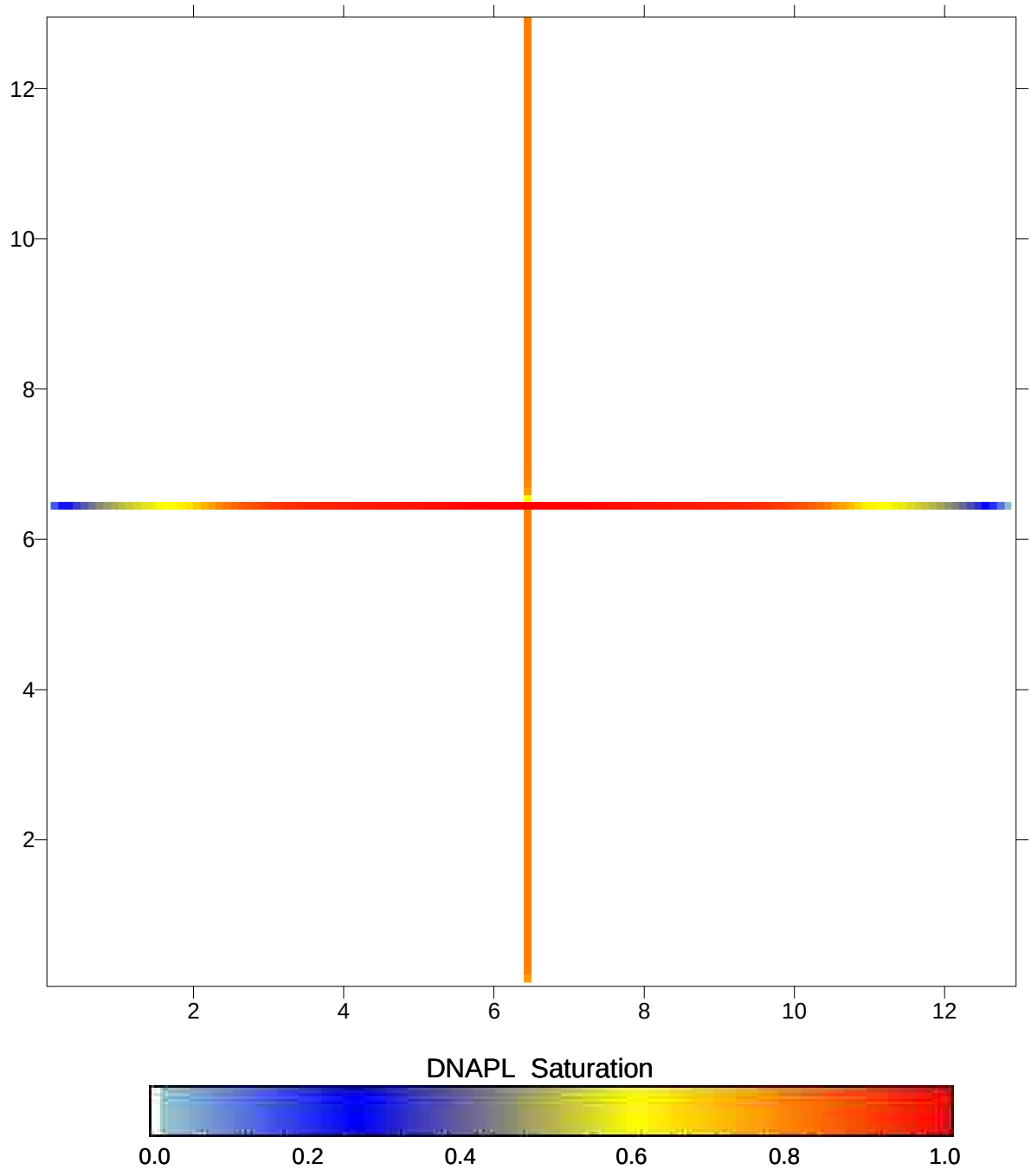

Figure 3.11: A 13m by 13m domain discretized uniformly using a 0.1m nodal spacing.

The DNAPL distributions at t=100,000 s for the two simulations are presented in Figures 3.10 and 3.11 respectively. The results indicate that the uniformly discretized domain results in a higher degree of vertical migration predicted and a lower degree of lateral migration predicted; in fact, it predicts penetration of the vertical fracture beyond the fracture intersection that the more accurate (refined) simulation suggests should not occur. This underscores the importance of sufficient nodal refinement in the vicinity of fracture intersections for properly simulating DNAPL migration. This finding agrees generally with the observations of Slough et al. (1999); where if fracture elements in a domain are not sufficiently discretized, an over-prediction of the volume of DNAPL that continues to migrate vertically at the intersection of a vertical and horizontal fracture can occur. As demonstrated by Slough et al., (1999), by finely discretizing the fracture and adjacent matrix nodes in a rock domain (e.g., at the scale of one centimetre or less), this problem can be accurately resolved.

The second study was a more comprehensive test, employing a larger scale domain with multiple vertical and horizontal fractures, multiphase flow, mass transfer and advective-dispersive-diffusive transport. Two simulations were conducted in which only the fraction of organic carbon (f_{oc}) was varied (0.005 vs 0.0005).

For both simulations, a domain of 20m by 5m with 3 horizontal and 4 vertical fractures was adopted for this study. The porosity of the matrix and fractures were assigned 0.077 and unity respectively. The coarse, uniformly discretized domains employed DX = 0.25 m and DY=0.25 m, for an original domain of 1600 nodes. Grid refinement was conducted using N = 5, and exponential increasing node spacing was employed resulting

in a final domain with 3072 nodes.

At t = 0, TCE DNAPL was released into the domain across the entire top boundary by specifying a non-wetting phase saturation of 0.3 and wetting phase pressure of zero. Constant head specified at the side boundaries during DNAPL migration established a zero hydraulic gradient across the domain. The water table was set to be coincident with the top boundary. The bottom boundary was set so as to permit the free exit of both water and DNAPL, while the side boundaries permitted only the flow of water. DNAPL was permitted to flow into the domain for 0.5 years, at which time saturations had achieved steady state values. The DNAPL source was then terminated, and DNAPL redistribution was simulated for 6 months, at which time DNAPL movement had ceased. DNAPL dissolution was not simulated during the DNAPL migration period.

At t = 1 year, the side boundary conditions were changed to provide a hydraulic gradient of 0.005 from left to right across the domain that was maintained throughout the remainder of the simulation. DNAPL dissolution, aqueous phase transport, diffusion, and sorption of TCE was enabled for 1 year (t=1 yr – 2 yr). During this period, a constant concentration of 550 mg/L TCE was specified at the left boundary, representing upgradient contamination entering the domain. The solubility of TCE was specified to be 1100 mg/L with a TCE free solution diffusion coefficient of 1.01 $x10^{-9}$ m^2/s (Pankow and Cherry, 1996).

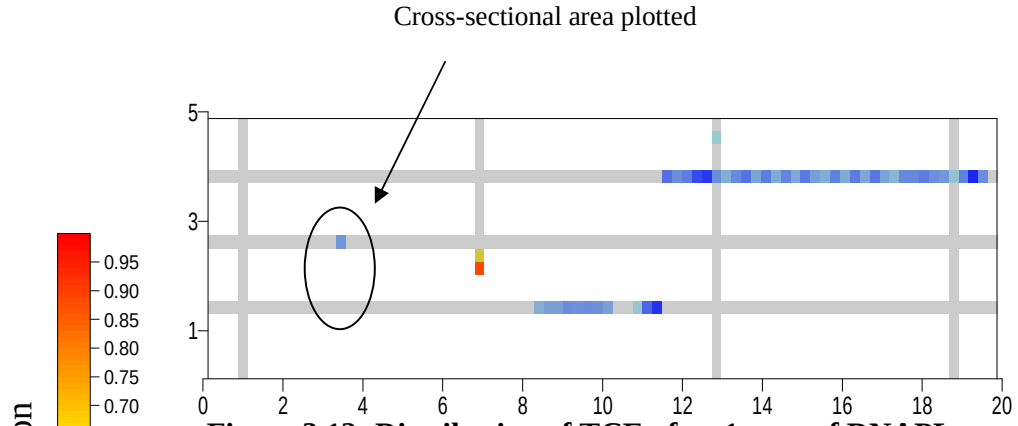

Figure 3.12: Distribution of TCE after 1 year of DNAPL dissolution (Base Case) (foc = 0.005)

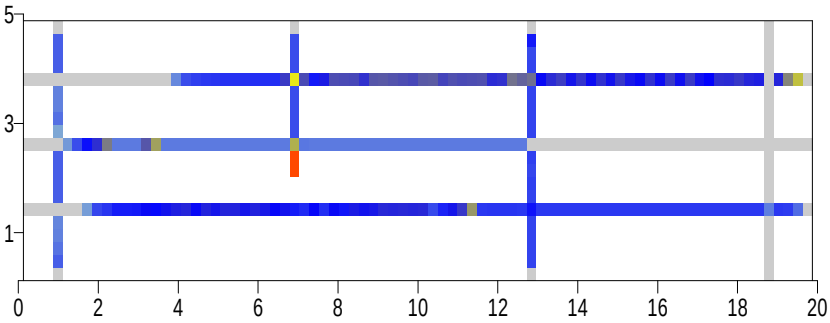

Figure 3.13: Distribution of TCE after 1 year of DNAPL dissolution (foc = 0.0005).

Note: Fractures are exaggerated in the above figures for visual purpose.

As demonstrated by Figures 3.12 and 3.13, the amount of DNAPL that remained in the domain increases, after one year of dissolution, with a lower f_{oc}. In addition, as demonstrated via Figures 3.14 and 3.15, with a lower f_{oc}, the amount of solute sorbed decreases dramatically, while the amount of solute that remained in the domain as aqueous phase increases. This inverse relationship between the persistence of DNAPL and f_{oc} is consistent with expectations (e.g., Pankow and Cherry, 1996).

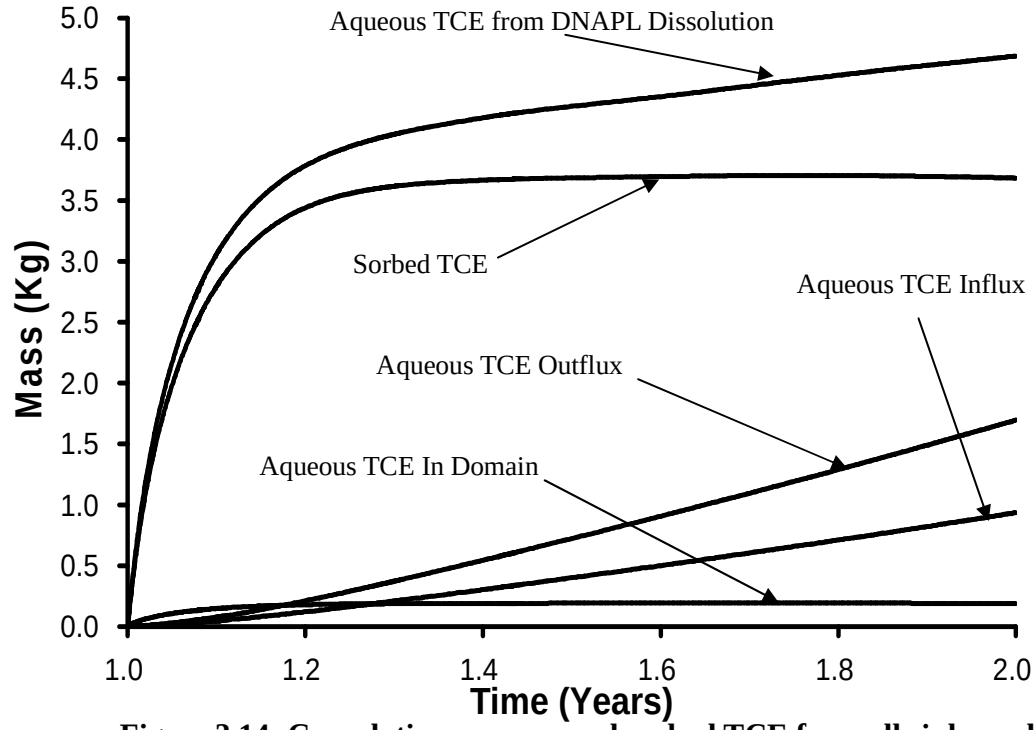

Figure 3.14: Cumulative aqueous and sorbed TCE from all sinks and sources after 1 year of dissolution (foc = 0.005).

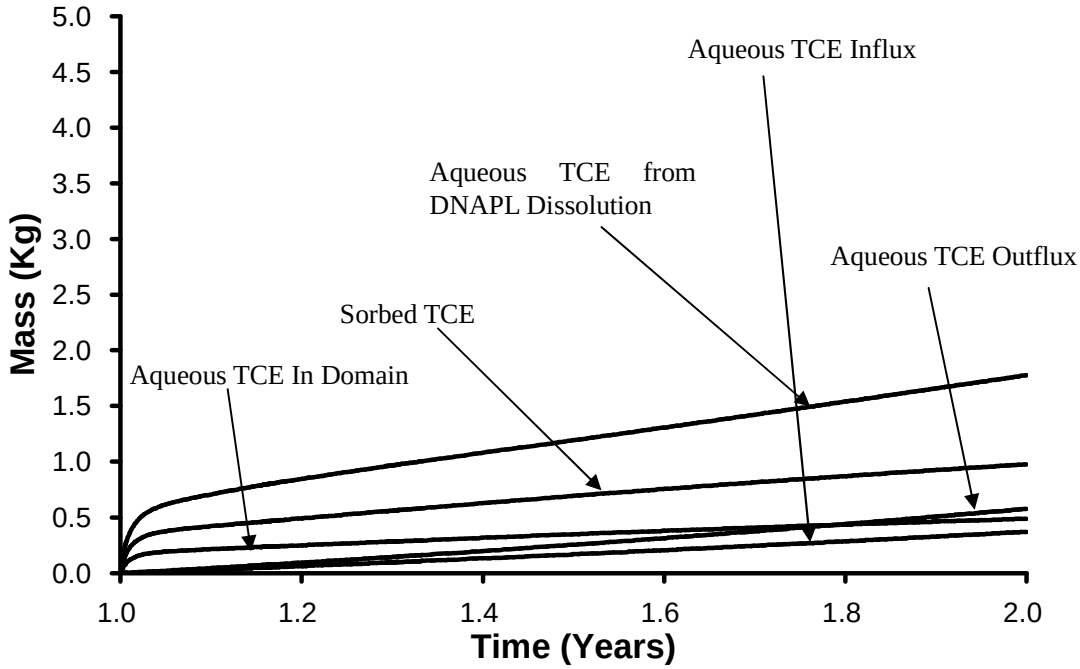

Figure 3.15: Cumulative aqueous and sorbed TCE from all sinks and sources for lower foc simulation after 1 year of dissolution (foc = 0.0005).

Figure 3.14 and 3.15 presents the cumulative mass of all TCE species inside the field scale sandstone domain for the period 1 yr $\leq$ t $\leq$ 2yrs (i.e., for the first year of dissolution) for the f_{oc} = 0.005 and the f_{oc} = 0.0005 cases, respectively. Figure 3.14 illustrates that the majority of aqueous TCE arising from DNAPL dissolution diffuses into the matrix and then sorbs at early time. The amount of sorbed TCE peaks after approximately 0.5 yrs of dissolution, after which the majority of dissolving TCE flows out of the domain through the fractures, as evidenced by the difference between the aqueous TCE influx and outflux plots (and the steady mass of aqueous TCE in the domain).

Figure 3.15 illustrates that a 10-fold reduction in the f_{oc} results in approximately a two-thirds reduction in the amount of aqueous TCE arising from dissolution after 1 year. It further demonstrates that sorption accounts for a smaller, although still significant, percentage of the aqueous TCE arising from dissolution and the cumulative mass sorbed has not yet peaked after 1 year. In addition, the figure shows that despite the reduced total mass of TCE dissolved, a higher cumulative TCE mass is present in the aqueous phase in the low f_{oc} case. Finally, it is noted that the cumulative TCE influx (from the left hand side boundary condition) is reduced in the low f_{oc} case as a result of reduced aqueous phase velocity through the source zone: the high DNAPL saturations that persist result in reduced wetting phase relative permeability in the fractures. These results provide confidence that diffusion and sorption are being properly simulated by the model.

Figure 3.16 provides a sequence of aqueous TCE concentration profiles across a horizontal fracture and the adjacent matrix on either side (the specific cross-section

chosen is indicated in Figure 3.12) after the simulation was continued for a further of 19 years. Figure 3.16 presents the data during the site aging period (i.e., $t \leq 21$ yrs). As demonstrated in this figure, the concentration is equal to solubility within the fracture at t=4 yrs since DNAPL is still present (see Figure 3.12). Once DNAPL in the fracture dissolves away (approx. t=3 yrs) the concentration in the fracture drops significantly, and from t=6 yrs until t=21 yrs it steadily increases due to the upgradient aqueous TCE source. Note that, despite its proximity to the upgradient boundary, the fracture never reaches the 550 mg/L influent concentration due to diffusion and sorption in the 3 m interval.

Overall, these series of figures provide confidence that the key processes of multiphase flow, mass transfer, advective-dispersive transport, matrix diffusion (forward and backwards) are all simulated in agreement with expectations. The reactions specific to the various treatment technologies examined are tested in the respective studies to follow.

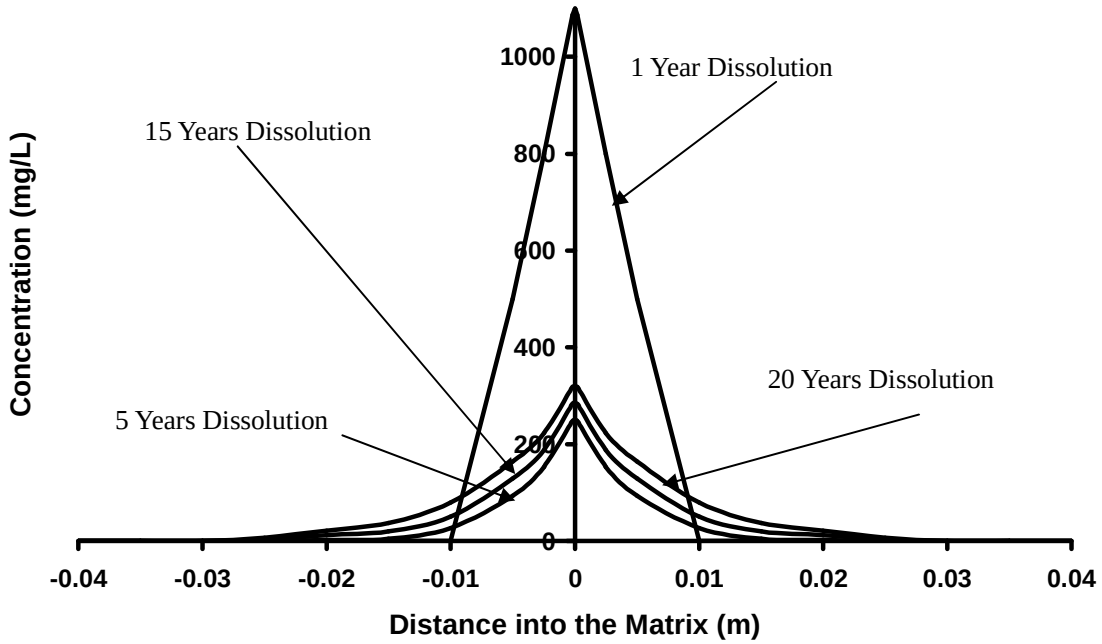

Figure 3.16: Various concentration profiles into the matrix over time.

A layout of the model for chemical-oxidation and enhanced bioremediation is displayed in Figure 3.17. Figure 3.18 demonstrates the model layout for surfactant flushing.

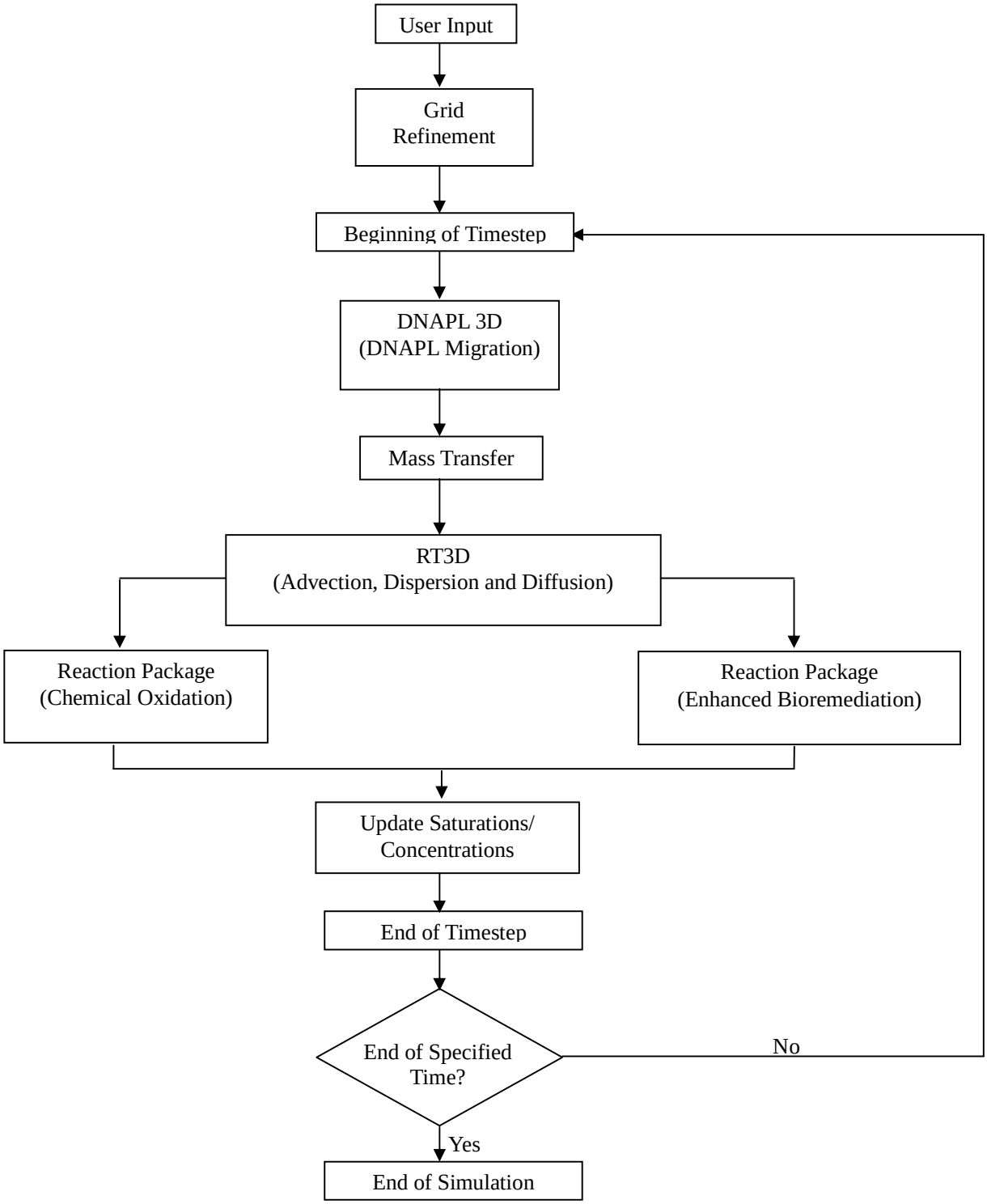

Figure 3.17: Model layout for chemical oxidation and enhanced bioremediation.

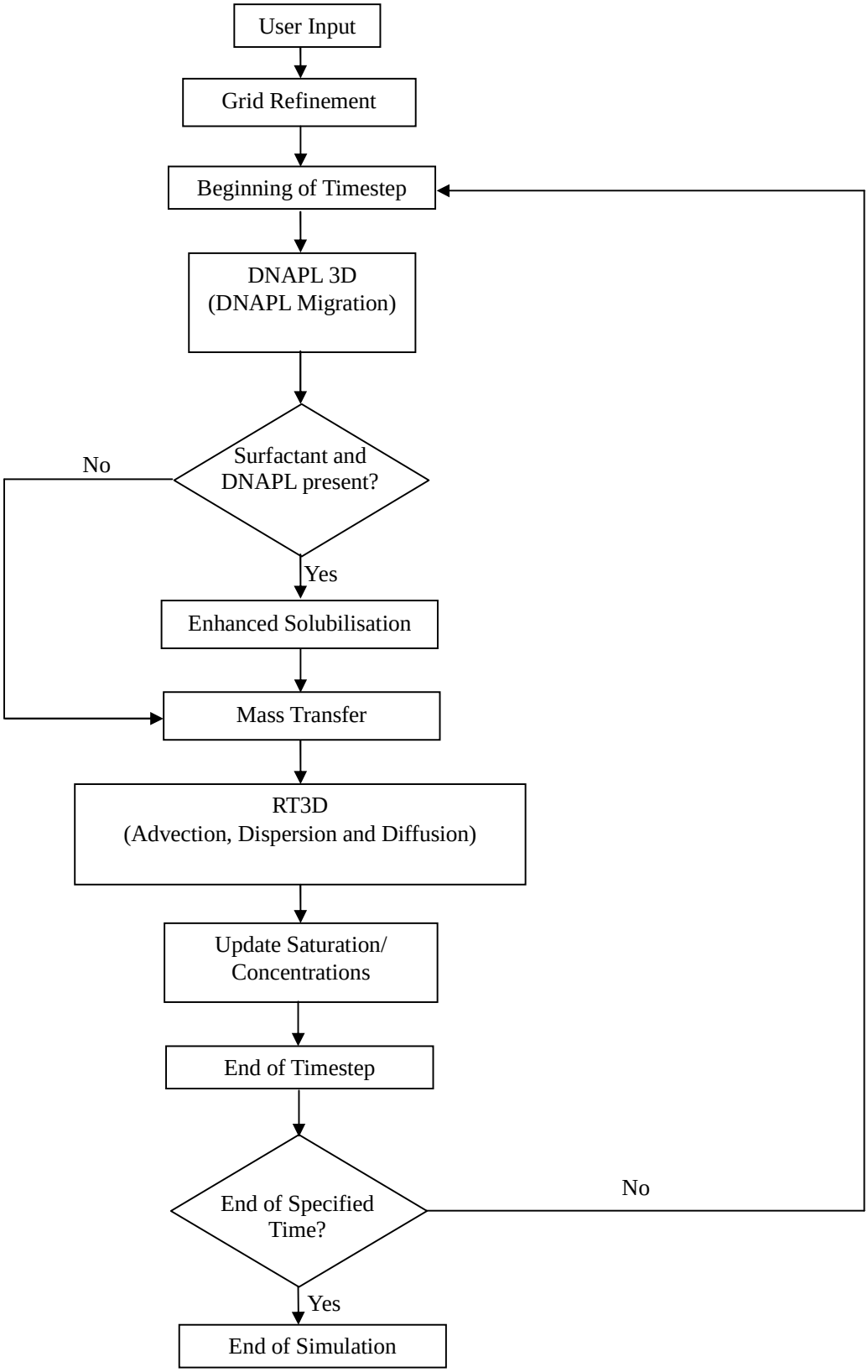

Figure 3.18: Model layout for surfactant flushing.

CHAPTER 4 – NUMERICAL SIMULATION OF DNAPL SOURCE ZONE REMEDIATION WITH IN SITU CHEMICAL OXIDATION (ISCO) IN FRACTURED ROCK

4.1 ABSTRACT

Fractured rock formations represent a valuable source of groundwater aquifers and can be highly susceptible to contamination by dense, non-aqueous phase liquids (DNAPLs). Numerical simulations were conducted to investigate the benefits and challenges of *in situ* chemical oxidation (with permanganate) for chlorinated solvent DNAPL in fractured rock aquifers at the field scale. An established finite difference multiphase flow-transport-reaction simulator was employed after modification with a gridding routine (GR); the GR was designed to permit sufficient grid refinement within and near fractures to adequately capture DNAPL migration and aqueous species diffusion while maximizing computationally efficiency. Simulations were conducted in two-dimensional cross-section with fracture apertures constant within fractures but varying across the source zone. In each of the 9 simulations conducted, a DNAPL release stage was followed by a 20-year site ageing stage prior to simulating a chemical oxidation treatment stage followed by a 5-year post-treatment stage. The suite of simulations examined (i) permanganate injection concentration, (ii) pulsed-injection strategy, (iii) bedrock type (sandstone, shale, and granite), and (iv) DNAPL type (TCE and tetrachloroethylene, PCE). Results confirm that matrix diffusion and sorption to matrix organic carbon dominates the fate of chlorinated solvent in the source zone during site ageing, although the depth of matrix contamination is reduced in those scenarios characterized by

increased peclet number (e.g., granite). In all of the cases considered, the efficiency of oxidant utilization was observed to be poor, with greater than 90% of the injected permanganate consumed by the natural oxidant demand. In sandstone (7 simulations), the contaminant mass destroyed was never greater than 11% of the total mass present in the system despite injecting more than 3 times the theoretical oxidant demand for the chlorinated solvent. Oxidant destruction exceeded supply in all sandstone cases, causing virtually no treatment to occur when injection was not active. In all cases, the narrow spatial and temporal extent of the ISCO treatment relative to the extent of diffusive matrix contamination limited any effective influence on the long term mass discharge from the source zone.

4.2 INTRODUCTION

Dense nonaqueous phase liquid (DNAPL) contamination of fractured geologic media is a long-standing and challenging environmental issue. In fractured bedrock aquifers where DNAPL is excluded from the matrix, fluid movement will be limited to the interconnected fracture porosity (Ross and Lu, 1999; Wealthall, 2002). Such exclusion is possible since matrix permeabilities in rock are typically low while matrix entry pressures are correspondingly high (Kueper and McWhorter, 1991). Thus, DNAPL flow in a fracture network is often restricted to the open fractures, which therefore serve as the primary pathways for DNAPL movement in the subsurface (Pankow and Cherry, 1996). For many bedrock aquifers, the fractures represent only 0.001-0.1% of the bulk volume of the rock mass (Mackay and Cherry, 1989), allowing even a small amount of DNAPL to migrate a significant distance (Reitsma and Kueper, 1994).

In fractured porous media, dissolution can occur within the fracture plane as well as into the porous matrix surrounding the fracture (matrix diffusion). The fate of DNAPL residing in a fractured rock mass may be governed by matrix diffusion for the case of high DNAPL solubility and high matrix porosity (Parker and Gillham, 1994). The amount of DNAPL mass available to dissolve and diffuse into the matrix is dictated primarily by the amount of residual formed during the initial migration event (Longino and Kueper, 1999). The driving force for diffusion into the matrix is provided by the concentration gradient between the aqueous phase present at the fracture surface and the essentially immobile pore water in the matrix. As dissolution and diffusion proceeds, the amount of DNAPL in the fracture is diminished and, eventually, a substantial fraction

of the contaminant mass may be transferred to the matrix. The diffusing aqueous phase contaminant in the matrix can both further penetrate the matrix and can sorb to the matrix solid (Parker et al., 1994).

The restoration of fractured porous media contaminated by DNAPL is often more difficult than for unconsolidated porous media. This is due to the difficulty in identifying the source zone, and also the fact that many traditional remedial technologies (e.g., pump and treat) are relatively ineffective in highly heterogeneous environments such as fractured rock (Powers et al. 1992; National Research Council 1994). The reason is that little or no water flushes through dead-end fracture segments or through the porous but relatively impervious matrix, both of which are likely to retain the bulk of the contaminated mass (Mackay and Cherry, 1989). Clean water flushed through the fractures can reverse the concentration gradients thereby permitting mass to be removed from the matrix. However, the relatively slow rate of release of contaminants from the clay/rock matrix by backwards diffusion, coupled with the potentially appreciable contaminant mass contained in dissolved and sorbed form in the matrix, can cause a long-term bleed of contaminants into the aquifer during remediation (USEPA, 2003b). Furthermore, if pumping is ceased before all of the contaminant is removed, the contaminant concentrations in the groundwater will typically rebound (USEPA, 2003b).

Previous studies of groundwater and DNAPL flow in fracture rock have illustrated that the degree of interconnection between the overburden, uppermost weathered bedrock layer, and bedrock units, as well as the lateral continuity, hydraulic properties and the

heterogeneity of the fracture system are all issues that impact the hydraulic behaviour of the system (Lerner et al., 2002; Wealthall et al., 2001; Kueper and McWhorter, 1991).

Chemical oxidation, commonly referred to as in-situ chemical oxidation (ISCO) involves the injection of an oxidizing agent to chemically degrade chlorinated solvents into non-toxic by-products in the subsurface. An extensive review of the different chemical oxidization agents and their associated chemistry with respect to tetrachloroethene (PCE), trichloroethene (TCE), dichloroethene (DCE), and organic aquifer materials (OAM) was presented by Seol et al. (2003). Many laboratory and field studies have investigated ISCO of DNAPL in aquifers characterized by relatively uniform conditions and with limited heterogeneity (e.g., Vella and Veronda 1992; Yan and Schwartz 1999; Schnarr et al. 1998; Yan and Schwartz, 1999; Zhang and Schwartz 2000; Hood and Thomson 2000; MacKinnon et al., 2002; Schroth et al. 2001; Conrad et al. 2002). However, only a limited number of studies are available for more complex sites and, in particular, those with fractured bedrock (Siegrist, 2001).

Williams and Spiers (2002) carried out two phases of laboratory studies to evaluate the effectiveness of ISCO for remediation of impacted groundwater in a fractured bedrock aquifer using sodium permanganate. These studies demonstrated that fractured rock environments, despite their inherent complexity and heterogeneity, can be quite suitable for successful sodium permanganate applications. In particular, that work argued that fractured rock provides an environment often low in natural organic matter resulting in naturally low demand for oxidant material.

MacKinnon et al. (2002) conducted a series of laboratory treatability studies under simulated site conditions, using materials from two fractured bedrock sites, to examine the influence of performance factors on the oxidative reduction of TCE and PCE by potassium permanganate ($KMnO_4$) in fractured rock. They found minimal penetration of the oxidant into the rock matrix, likely due to the low porosity of the shale and siltstone employed. The study concluded that the oxidant demand resulting from diffusive loss of $KMnO_4$ into the bedrock matrix is unlikely to have a significant impact on oxidant delivery in the field during an extended treatment using permanganate. Specifically, it was concluded that permanganate exhibited the ability to degrade high concentrations of TCE and PCE within very short time frames (days to weeks). However, the study acknowledged that the positive results may have been biased due to pulverization of the bedrock samples prior to testing, a process which significantly increased the surface area available for reaction relative to that expected during field application.

While microcosm studies with crushed bedrock material are valuable, they may overestimate the benefits of chemical oxidation by oversimplifying the system. For example, it is widely accepted that the majority of groundwater and DNAPL flow that occurs through a fracture is highly influenced by the aperture distribution (Tsang and Tsang, 1987; Anderson and Thomson, 1999). Thus, the influence of the fracture network distribution at real sites is expected to dominate the spatial and temporal distribution of DNAPL and of oxidant, as well as on their contact time. In addition, changes in the (effective) aperture distribution due to the formation of reaction by-products during ISCO could potentially influence aqueous transport pathways and

DNAPL mass transfer rates. Laboratory research has demonstrated that the precipitation of manganese dioxide (MnO_2(s)) decreases the hydraulic conductivity between 50 and 90% (Schroth et al., 2001) in sand-packed columns, and resulted in pore plugging and the formation of a distinct manganese oxide layer in the vicinity of the NAPL that reduced the post-treatment mass transfer (Mackinnon et al., 2002; Conrad et al., 2002; Urynowicz and Siegrist, 2005).

Tunnicliffe and Thomson (2004) demonstrated the incapability of a $KMnO_4$ flush to increase the bulk mass removal rate for two single vertical fractures in a laboratory environment. Permanganate solution was flushed through each of the well characterized fractures to remove emplaced DNAPL. The rapid reduction of flow observed in this study for the initial stage of the oxidant flush suggests that flow obstructions developed within the fractures altering the aperture distribution. Tunnicliffe and Thomson (2004) suggested that the resulting development of MnO_2(s) in and around existing diffusion controlled regions plugs the pore structure of the fractures. This had the effect of limiting permanganate diffusion into both existing and newly formed stagnant zones and, simultaneously, the diffusion of the organic compound towards remaining flow pathways.

Various numerical models have been developed to look into both single (e.g., Tsang and Tsang, 1987; Reitsma, 1992) and multiphase flow in fractures (e.g., Parker and Park 2004; Mundle et al., 2007; Pruess and Tsang, 1990; Eikemo et al., 2009). A conceptual model developed by Kueper and McWhorter (1991) found that in both clay and rock, DNAPL will preferentially enter the larger apertures due to their lower displacement pressures. A

numerical model developed by Harrison et al. (1992) found that fractures as small as 10 μm in a clayey aquitard can greatly increase the transport of dissolved contaminants into underlying aquifers.

Numerical models for the ISCO of chlorinated solvents with permanganate have been previously developed for unconsolidated porous media (Hood and Thomson, 2000; Zhang and Schwartz, 2000; West et al, 2008). West et al. (2008) conducted a series of numerical simulations to evaluate the efficacy of in situ chemical oxidation with permanganate for TCE and PCE in heterogeneous unconsolidated porous media at the field scale. It was found that source zone remediation can be effective during, or shortly following, the period of active treatment. However, over the long-term, depending on the dissolution kinetics and the characteristics of the aquifer, the benefit of partial treatment can be greatly reduced due to dissolution tailing. This work suggested that a large fraction of injected permanganate may be competitively consumed by the natural oxidant demand (NOD) at field sites. In addition, the performance of permanganate was also found to be highly variable due to MnO_2 (i.e., rind) formation, DNAPL architecture, and geologic characteristics. That work emphasized the difference between the simplicity of batch studies and the complexity of field scenarios and how, for the latter, heterogeneity and fluid access issues may dominate overall performance.

Only one study has been published modelling the effectiveness of ISCO in fractured porous media. Mundle et al. (2007) developed a pseudo-two-dimensional, transient flow and transport numerical model to simulate ISCO of TCE and PCE by potassium

permanganate in clay containing a single fracture. This work suggested that the NOD of the organic material may significantly reduce the efficiency of ISCO remediation in fractured rock. To the author's knowledge, no systematic studies exist of ISCO in fractured bedrock at the field scale.

The objective of this work is to examine the benefits and challenges of DNAPL source zone remediation by ISCO in fractured aquifers at the field scale. This paper employs numerical simulation to investigate the sensitivity of DNAPL source zone treatment with $KMnO_4$ to a variety of site and engineering design parameters. In so doing, the research aims to cast light on the fractured rock scenarios under which ISCO may be expected to provide cost-effective benefit.

4.3 OUTLINE OF NUMERICAL SIMULATIONS

4.3.1 Model Description

The model developed for fractured rock simulations (DNAPL3DRX-FRAC) involves the coupling of the three-dimensional two-phase flow model (DNAPL3D) (Gerhard et al., 1998, 2001; Gerhard and Kueper, 2003 a,b,c; Gerhard et al., 2007) and RT3D, a three-dimensional multi-species contaminant transport model with non-linear kinetic reactions (Clement,1997; Clement et al.,1998). This coupling was first developed for simulations involving unconsolidated porous media as DNAPL3D-RX (West et al., 2008) using a split-operator approach following Grant and Gerhard (2004). Within a time step, DNAPL migration is initially simulated using DNAPL3D. The equations solved are identical to those of the porous media model (Gerhard and Kueper, 2003c):

$$\frac{\partial}{\partial x_i}\left[\frac{k_{ij}k_{r_w}}{\mu_W}\left(\frac{\partial P_W}{\partial x_j}+\rho_W g\frac{\partial z}{\partial x_j}\right)\right]+S_W(\alpha+\theta\beta)\frac{\partial P_W}{\partial t}-\theta\frac{\partial S_W}{\partial t}=0,\qquad i,j=x,y,z \qquad (4.1)$$

$$\frac{\partial}{\partial x_i}\left[\frac{k_{ij}k_{r_{NW}}}{\mu_{NW}}\left(\frac{\partial(P_W+P_c)}{\partial x_j}+\rho_{NW} g\frac{\partial z}{\partial x_j}\right)\right]+(1-S_W)(\alpha)\frac{\partial P_W}{\partial t}+\theta\frac{\partial S_W}{\partial t}=0,\ i,j=x,y,z \qquad (4.2)$$

where P is pressure {M L^{-1} T^{-2}}, P_C is capillary pressure {M L^{-1} T^{-2}}, k_{ij} is the intrinsic permeability tensor {L^2}, k_r is relative permeability {-}, μ is dynamic viscosity {M L^{-1} T^{-1}}, ρ is fluid density {M L^{-3}}, θ is porosity {-}, S is phase saturation {-}, g is gravitational acceleration {L T^{-2}}, α is porous medium compressibility {M^{-1} L T^2}, β is wetting phase compressibility {M^{-1} L T^2}, t is time {T}, and x, y, z denote spatial coordinates. The subscripts W and NW specify the wetting and non-wetting phase, respectively. DNAPL3DRX-FRAC employs a finite difference formulation in which the primary variables, P_W and S_W, are solved fully implicitly using Newton Raphson iteration.

The contaminant solute is then added to the aqueous phase at nodes with DNAPL present via equilibrium or non-equilibrium mass transfer routines (Grant and Gerhard, 2004). RT3D is then employed within the same time step to simulate advection, dispersion, diffusion, and reactions for the solute (Clement, 1997; and Clement et al., 1998):

$$\frac{\partial(\theta C_m^n)}{\partial t}=\frac{\partial}{\partial x_i}\left(\theta D_{ij}^n\frac{\partial C_m^n}{\partial x_j}\right)-\frac{\partial}{\partial x_i}\left(\theta v_i C_m^n\right)+q_s C_s^n+\sum R_m,\quad i,j=x,y,z \qquad (4.3)$$

$$\frac{\partial(\theta C_{im}^n)}{\partial t}=\sum R_{im} \qquad (4.4)$$

where D_{ij} is the hydrodynamic dispersion tensor {L^2 T^{-1}}, v_i is average linear

groundwater velocity {L T^{-1}} obtained from the multiphase flow model, q_s is volumetric flux representing sources and/or sinks {T^{-1}}, R is the rate of a single reaction {M L^{-3} T^{-1}}, and t is time {T}. The superscript n denotes the species number, the subscripts m and im designate mobile and immobile species, respectively, and the subscript s denotes a source or a sink. Finally, the phase saturations are updated at the end of the time step in accordance with the amount of mass transferred from the DNAPL to the aqueous phase.

For this work, the model was further modified for simulating DNAPL migration, mass transfer, and advective-dispersive-diffusive-reactive transport in fractured porous media environments. The model is capable of simulating the sustained release of DNAPL across one or multiple fractures as well as the redistribution of DNAPL to residual and stable pools after the termination of the source. Further details are provided in Chapter 3.

The detailed submodels of $P_C(S_W)$ and $k_r(S_W)$ of Gerhard and Kueper (2003a,b) employed, which incorporate key hysteresis and other characteristics of DNAPL invasion and trapping, have been validated against physical experiments in homogeneous and heterogeneous unconsolidated porous media (Gerhard and Kueper, 2003a,b; Grant et al., 2007). The underlying form of the constitutive relationships has been demonstrated, however, to also well represent multiphase flow in natural, rough walled fractures (Reitsma and Kueper, 1994). In this work, it is therefore assumed that the constitutive model of Gerhard and Kueper (2003a,b) is a reasonable basis for simulating DNAPL migration and redistribution in fractured porous media. It is noted that the DNAPL

migration simulations in this work are only employed to provide reasonable initial conditions for ISCO treatment scenarios and thus the conclusions on remediation performance are not expected to be sensitive to the constitutive model employed.

Accuracy in simulating matrix diffusion by multiple aqueous phase constituents was achieved by developing and implementing a grid refinement (GR) technique described in Section 3.2

4.3.2 Chemical Oxidation Reactions

For the purpose of this study, the subsequent discussion is limited to chemical oxidation of PCE and TCE DNAPL by $KMnO_4$. The stoichiometry of chemical oxidation of PCE and TCE, respectively, by $KMnO_4$ can be described as (Seol et al., 2003; Yan and Schwartz, 1999):

$$C_2Cl_4 + 2MnO_4^- \rightarrow 4Cl^- + 2CO_2 + 2MnO_2(s) \qquad (4.5)$$

$$C_2Cl_3H + 2MnO_4^- \rightarrow 3Cl^- + 2CO_2 + 2MnO_2(s) + H^+ \qquad (4.6)$$

The relevant reaction kinetics are (West et al., 2008):

$$\frac{\partial[TCE]}{\partial t} = \frac{-K_{rxns}[TCE][MnO_4^-]}{R_{TCE}} \qquad (4.7)$$

$$\frac{\partial[TCE_s]}{\partial t} = -K_{rxns}[TCE][MnO_4^-] \qquad (4.8)$$

$$\frac{\partial[MnO_4^-]}{\partial t} = -2K_{rxns}[TCE][MnO_4^-] \qquad (4.9)$$

$$\frac{\partial[MnO_2]}{\partial t} = 2K_{rxns}[TCE][MnO_4^-] \qquad (4.10)$$

where the square brackets [ ] denote molar concentration, *Krxns* is the second-order reaction constant between aqueous TCE and MnO_4^- $\{M^{-1}\ L^3\ T^{-1}\}$ and $[TCE_s]$ is the concentration of sorbed TCE.

During ISCO, permanganate reacts with organic aquifer material (OAM). For the purposes of this study, it was presumed that OAM was homogeneous throughout the rock matrix and not present in the fractures. The reaction between OAM and permanganate was represented (Mumford et al., 2005):

$$3CH_2O + 4MnO_4^- \rightarrow 3CO_2 + 4MnO_2(s) + H_2O + 4OH^- \qquad (4.11)$$

The reaction rate was modelled (Mundle et al., 2007):

$$\frac{\partial[OAM]}{\partial t} = -M_{MnO_4^-/OAM} K_{OAM}[OAM][MnO_4^-] \qquad (4.12)$$

where K_{OAM} is the second-order kinetic reaction rate constant. The OAM is assumed to comprise solely of organic carbon (*foc*) with an associated K_{OAM} of $1x10^{-6}$ $m^3/kg\ s$ (Hood and Thomson, 2002).

The model simulates OAM, sorbed contaminant mass and MnO_2 as immobile species, while the contaminant solute and MnO_4 are simulated as mobile aqueous species. To simulate the reaction of $KMnO_4$ with both sorbed and aqueous chlorinated solvents, it

was necessary to modify RT3D so that sorbed compounds were treated as an explicit species. A linear sorption isotherm (Mundle et al., 2007) was employed, in which the concentration of sorbed TCE (*Cs*) was back calculated based upon the solved concentration of dissolved TCE (*Cw*) :

$$C_s = C_w Kd \frac{\rho}{\theta} \qquad (4.13)$$

where $Kd = K_{oc} \times f_{oc}$ (Karickhff et al., 1979), K_{oc} is the organic carbon partition coefficient (L^3M^{-1}), and *foc* is the local (i.e., nodal) fraction of organic carbon (-), ρ is the dry bulk density (ML^{-3}), and θ is the porosity (-).

The proper functioning of this sorption isotherm for TCE was subsequently verified at both the scales of a single node and field scale simulation (see Chapter 3.3.4 for details). The model also accounts for species-dependent diffusion coefficients (West et al., 2008).

The retardation factor is computed locally from the nodal *foc* concentration (e.g., Fetter, 1993):

$$R_i = 1 + Koc \times foc_i \frac{\rho}{\theta} \qquad (4.14)$$

where ρ is the dry bulk density (ML^{-3}), θ is the porosity of the matrix (-), and *Koc* is the organic carbon partition coefficient (L^3M^{-1}). While *R* is commonly defined as the ratio of the velocity of groundwater to that of the sorbing contaminant, when incorporated into the governing advection-dispersion equation (Equation 4.3) it has the effect of reducing not only advective velocity but also hydrodynamic dispersion (in the case of rock matrix,

this is pure diffusion) by this factor (e.g., Fetter, 1993). Sorption is known to reduce the rates of both advection and diffusion (Lyman et al., 1992), but it is acknowledged that a linear reduction in diffusion with respect to *R* is a widely held and almost universally applied assumption (Pankow and Cherry, 1996). The role of *R* in sorption with respect to matrix diffusion is acknowledged in Lyman et al (1992) in presentation of an equation for 'rock capacity factor' α, which measures a rock's capacity to store organic contaminants, that is identical to (4.15) where $\alpha = R/\theta$ (Equation 10.2, pg 265). In this work, as OAM is consumed by permanganate, the decreasing foc is reflected in decreasing R and decreasing α which corresponds to a reduction in the sorptive capacity of the matrix.

While the model simulates the production of MnO_2(s) via (4.5, 4.6 and 4.11), permeability reduction associated with MnO_2 accumulation is not considered in this work. Since all the simulations presented are in two dimensions, it is expected that including pore-clogging would significantly restrict the flow field in a manner that may not be representative of three-dimensional behaviour (e.g., bypassing in the third dimension). For this reason, the presented results should be considered as a 'most promising' envelope of results for the elimination of DNAPL by $KMnO_4$ in fractured rock, since rind formation is known to inhibit achievement of this objective (e.g., Tunnicliffe and Thomson, 2004; West et al., 2008).

4.3.3 Model Verification

Advective-dispersive transport was verified against the Ogata and Banks (1961)

one-dimensional analytical solution (see Section 3.3.1 for details). DNAPL migration in a horizontal fracture was verified against the one-dimensional analytical solution of McWhorter and Sunada (1990) (see Section 3.3.2 for details). Simulations of transient contaminant transport in a set of discrete, parallel fractures situated in a diffusion-dominated rock matrix were verified against the analytical solution of Sudicky and Frind (1982) (see Chapter 3.3.3 for details). Additional simulations were conducted to provide confidence in the developed model for scenarios/processes for which analytical solutions do not exist, including (i) one-dimensional simulations of DNAPL dissolution and lateral diffusion from a DNAPL occupied vertical fracture, and (ii) DNAPL migration, dissolution, and aqueous phase diffusion in a domain characterized by a single, orthogonal fracture intersection (see Chapter 3 for details). This body of work established that the governing equations were being solved correctly and provided confidence in the modelling approach and developed GR. Furthermore, these simulations provided insight into the minimum degree of discretization required in order to adequately capture diffusion gradients in the matrix (see Chapter 3 for details).

The chemical oxidation reaction kinetics (Equations 4.7 – 4.10) were verified in DNAPL3D-RX-FRAC by successfully reproducing the published simulations of a one-dimensional DNAPL dissolution and $KMnO_4$ treatment scenario in an unconsolidated porous medium (West et al., 2008). West et al. (2008), in turn, demonstrated successful reproduction of column ISCO experiments by Schroth et al. (2001) that employed residual TCE DNAPL treated by potassium permanganate. Results with three different DNAPL dissolution routines, and their simulated impact on

TCE degradation by $KMnO_4$, are shown in Figure 4.1. The plot demonstrates that DNAPL3DRX-FRAC has accurately implemented both the mass transfer and chemical oxidation reaction kinetics.

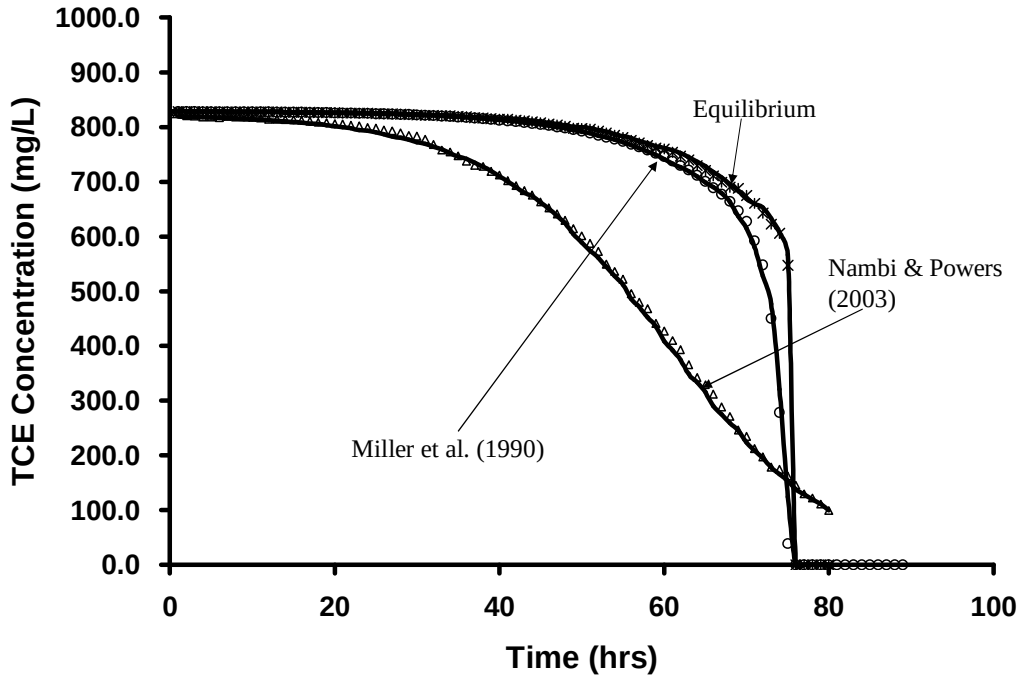

Figure 4.1: Verification of DNAPL3D-RX FRAC with model results from West et al. (2008) for various mass transfer expressions. Note: Results from West et al. (2008) are indicated with solid lines while results from DNAPL3DRX-FRAC are indicated by symbols.

4.4 NUMERICAL SIMULATIONS

4.4.1 Modelled Scenario

This section describes characteristics common to all of the simulations conducted in this thesis, while the next details the characteristics of the individual runs. All simulations consider a portion of a fractured rock formation within a field scale DNAPL source zone via a two-dimensional, vertical cross-section domain 20 m wide × 5 m high with unit depth. This domain exhibits an underlying, coarse, uniformly discretized grid with

nodes that are $\Delta x = 0.25$m and $\Delta y = 0.25$m (total of 1600 coarse nodes). A network of horizontal and vertical fractures, with an aperture distribution and fracture density appropriate for the rock type considered (refer to Table 4.2 for the three different rock type properties), was then defined as an overlay. Grid refinement was then conducted using the GR parameters determined as optimal from preliminary analyses (5 refined nodes per coarse node, exponentially increasing spacing with distance from fracture; see Chapter 3 for details). This resulted in an approximate doubling of the number of nodes; for example, for the base case with 7 fractures, the final domain exhibited 3072 nodes with the fracture nodes dimensioned in width equal to the fracture aperture and with matrix nodes as small as $\Delta x = 2.5 \times 10^{-4}$ m and $\Delta y = 7.6 \times 10^{-4}$ m in the matrix immediately adjacent to fracture intersections.

The matrix was assigned a uniform distribution of initial OAM at a representative concentration for each rock type (Table 4.2). The assigned porosity of fractures was unity and fractures were not assigned any OAM (and thus do not exhibit sorption). Lipson et al. (2005) studied a system of equally spaced fractures from the field and determined that when matrix diffusion effects are dominant, fracture retardation can be assumed equal to unity.

Each simulation evolved according to five distinct stages: (i) DNAPL Release, (ii) DNAPL Redistribution, (iii) Site Ageing, (iv) Treatment Application, and (v) Post-Treatment Ageing. For all stages, the water table was set to be coincident with the top boundary. During the DNAPL Release and DNAPL Redistribution stages, constant

head specified at the side boundaries during DNAPL migration established a zero hydraulic gradient across the domain. The bottom boundary permitted the free exit of both water and DNAPL. At t = 0, the 'DNAPL Release' stage began by specifying a constant nonwetting phase saturation of 30% across the entire top boundary. Note that in this work, DNAPL is considered the nonwetting fluid. DNAPL was permitted to flow into the domain for 6 months, by which time it was established that saturations had achieved steady state values (i.e., DNAPL inflow at the top equalled DNAPL outflow at the bottom). The DNAPL source was then terminated, and DNAPL redistribution was simulated for 6 months, at which time it was established that DNAPL movement had effectively ceased. Thus, at the end of the 'DNAPL Redistribution' stage, at t_{TOTAL} = 1 yr, the fracture network exhibited a complex distribution of DNAPL pools and residual characteristic of the fracture network of the rock type under investigation. DNAPL dissolution was not simulated during the DNAPL emplacement stages in order to better distinguish the fate of TCE during the Site Ageing stage; while a simplification, it is not expected that this assumption significantly impacts the conclusions of this work.

For the 'Site Ageing' stage, the side boundaries were modified such that a groundwater hydraulic gradient of 0.005 from left to right across the domain was established. DNAPL dissolution, aqueous phase transport, diffusion, and sorption of aqueous phase chlorinated solvent were simulated for 20 years during this stage (i.e., 1 yr $\leq t_{TOTAL} \leq$ 21 yrs). During this stage, a constant aqueous phase concentration of 550 mg/L TCE was specified along the entire left boundary, representing the impact of additional upgradient DNAPL upon the domain. This recognized that only a subsection of a typical source

zone was simulated and resulted in (i) increased longevity of the DNAPL by reducing the concentration gradient driving dissolution and (ii) additional mass loading to the matrix within the domain.

In the 'Treatment Application' stage, chemical oxidation was initiated by injecting a constant aqueous phase concentration of 2.5g/L MnO_4 for 2 years (i.e., 21 yrs $\leq t_{TOTAL} \leq$ 23 yrs) at the horizontal fractures along the left boundary (i.e., analogous to a fully screened well). During permanganate application, the hydraulic gradient across the domain was increased to 0.025 to represent active amendment conditions. As well, the upgradient TCE boundary condition was terminated (assuming complete and instantaneous treatment of the upgradient source zone); while this is highly idealized, it provides the best opportunity for success within the domain and thus supports viewing these results as approximating a best case for the technology. In all cases, stoichiometric calculations confirm that the total mass of MnO_4 injected is greater than the theoretical MnO_4 mass required to destroy all the TCE in the domain at the start of the Treatment stage; for example, in the base case 45.5 kg (382 moles) of MnO_4 was injected which, compared to the 7.3kg (55.6 moles) of TCE mass in the domain, represents an excess of 300% (considering that 1 mole of TCE is destroyed by 2 moles of MnO_4, Equation 4.6).

Following the Treatment stage, an additional five years were simulated (i.e., 23 yrs $\leq t_{TOTAL} \leq$ 28 yrs). During this Post-Treatment stage, the ambient hydraulic gradient of 0.005 was again employed, but no upgradient concentration of any species (i.e.,

permanganate or TCE) was applied.

Several assumptions were employed in this work to facilitate reasonable simulation times:

1. All fractured rock simulations presented are two-dimensional; this assumption likely benefits the technology since the reduced dimensionality is expected to reduce bypassing of the treatment fluid around DNAPL-occupied fractures;
2. The matrix is presumed to have a sufficient displacement pressure so as to exclude DNAPL entry; this assumption likely benefits the technology because the highest fraction of DNAPL is retained in the fractures which are most accessible to the treatment fluid;
3. Advection of groundwater through the matrix is assumed to be negligible; this is reasonable given that the high permeability contrast between the fractures and matrix. For example, for the sandstone Base Case, the matrix permeability is approximately 6 orders of magnitude less than the average fracture permeability. The Peclet number for the matrix ($Pe = vx/D$ where v is horizontal velocity in matrix) if advection were not neglected is 0.166; since $Pe<1$ it is reasonable to assume that the matrix is diffusion dominated and advection is negligible (Trivedi et al., 2008).
4. Equilibrium mass transfer from DNAPL to aqueous phase was assumed; this assumption also favours improved performance of the technology by maximizing aqueous phase solvent concentrations.

4.4.2 Base Case and Sensitivity Simulations

Table 4.1 presents the suite of 10 simulations conducted in this study. The base case considered a fractured sandstone template site. Table 4.2 presents the parameters employed to characterize the sandstone as well as the other two rock types (shale and granite). The sandstone domain, employed in all simulations except Run 7 and Run 8, is presented in Figure 4.2a. The sandstone parameters were chosen to be broadly representative of North American sandstone aquifers (e.g., Lipson et al., 2005). Table A1 (Appendix A) provides, for each rock type, the observed ranges for each parameter synthesized from the literature. Table 4.3 reveals that this sandstone exhibits - relative to the other template rock types - low fracture density, low mean aperture (125μm), high matrix porosity (7.7%), and intermediate foc (0.005).

The sandstone base case employed TCE as the DNAPL released and as the aqueous phase and sorbed chlorinated compound subsequently targeted by ISCO. Fluid properties and reaction parameters are listed in Table 4.4. The base case also employed a continuous injection of $KMnO_4$ at 2.5 g/L for 2 years during the Treatment stage (Table 4.1).

Table 4.1 Field Scale ISCO Fractured Rock Simulations

Run No.	DNAPL Type	Material	KMnO4 Concentration (mg/L)	Pulsing	Pulsing Strategy
1 (Base Case)	TCE	Sandstone	2500	No	Continuous KMnO4 Injection for 2 Years
2	TCE	Sandstone	5000	No	Continuous KMnO4 Injection for 1 Year
3	TCE	Sandstone	1250	No	Continuous KMnO4 Injection for 4 Years
4	TCE	Sandstone	2500	Yes	3 Months On 3 Months Off for 4 Years
5	TCE	Sandstone	2500	Yes	6 Months On 3 Months Off for 4 Years
6	TCE	Sandstone	2500	Yes	12 Months On 12 Months Off for 4 Years
7	TCE	Shale	2500	No	Continuous KMnO4 Injection for 2 Years
8	TCE	Granite	2500	No	Continuous KMnO4 Injection for 2 Years
9	PCE	Sandstone	2500	No	Continuous KMnO4 Injection for 2 Years

Table 4.2 Properties of Field Scale Fractured Rock Template Sites

Rock Type	Fracture Spacing (m)	Matrix Permeability (m^2)	Matrix Porosity	Foc	Bulk Density (g/cm^3)	Matrix Tortuosity	Fracture Aperture Range (μm)	Mean Aperture (μm)
Sandstone	6.0 (Ver) [*] [a] 1.0 (Hor) [a]	1.05×10^{-15}	7.7% [a]	0.005 [a]	2.49 [a]	0.2 [a]	25 - 230 [a]	125
Shale	4.0 (Ver) [*] 1.0 (Hor) [*]	1.05×10^{-15}	3.0% [b]	0.009 [*]	2.619 [**]	0.1 [*]	50 - 250 [c]	150
Granite	2.0 (Ver) [d] 2.0 (Hor) [d]	1.05×10^{-15}	0.1% [*]	0.0005 [*]	2.697 [**]	0.05 [*]	100 - 500 [e]	300

[a] *Lipson et al., 2005*
[b] *Morris and Johnson, 1967*
[c] *Jardine et al., 1999*
[d] *Sousa 2007*
[e] *Sausse 2002*
**Data supplied by B.H Kueper (personal communication) based upon consulting experience on sites of all three rock types.*
*** Calculated using Bulk Density = Grain Density x (1-porosity), assuming a grain density of 2.7 for Shale and Granite.*
Ver – Vertical Fractures
Hor – Horizontal Fractures

Table 4.3 Fracture Density of Field Scale Fractured Rock Template Sites

	Sandstone	Shale	Granite
Fracture Length (m)	77.0	82.0	84.0
Density (m-1)*	0.77	0.82	0.84

**Fracture Length / Total Domain Area*

Table 4.4 Fluid Properties and Reaction Parameters

Parameter	Notation	Value
TCE Density [a]	ρ_{NWtce}	1460 kg/m^3
TCE Viscosity [a]	μ_{NWtce}	0.0005 Pa s
TCE Solubility [a]	$Solub_{TCE}$	1100 mg/L
TCE Koc [a]	KOC_{TCE}	126 L/kg
PCE Density [a]	ρ_{NWpce}	1630 kg/m^3
PCE Viscosity [a]	μ_{NWpce}	0.0009 Pa s
PCE Solubility [a]	$Solub_{PCE}$	200 mg/L
PCE Koc [a]	KOC_{PCE}	364 L/kg
TCE Free Solute Diffusion Coefficient [b]	D^O_{TCE}	1.01 x10^{-9} m^2/s
PCE Free Solute Diffusion Coefficient [b]	D^O_{PCE}	9.40 x10^{-10} m^2/s
MnO_4^- Free Solute Diffusion Coefficient [c]	D^O_{MnO4}	1.63 x 10^{-9} m^2/s
Kinetic Reaction Rate for TCE [d]	K_{TCE}	4.11 x 10^{-3} m^3/kg s
Kinetic Reaction Rate for PCE [d]	K_{TCE}	2.85 x 10^{-4} m^3/kg s
Kinetic Reaction Rate for OAM [e]	K_{OAM}	1.0 x 10^{-6} m^3/kg s

a – Pankow and Cherry (1996)
b –Wilke and Chang (1955) at 25^{o}C
c - Lide (2004)
d – Yan and Schwartz (2000)
e –Hood and Thomson (2002)

As illustrated in Table 4.1, Runs 1 - 6 examine variations in treatment strategy, while Runs 7-8 and 9 explore the influence of site conditions and different DNAPLs respectively. All parameters, boundary conditions, and source conditions were established identically to the base case for all simulations, except for changing the parameter(s) whose influence was being examined in each study. It is noted that for all simulations except Runs 7 and 8, the results during the DNAPL Release, DNAPL Redistribution, and Site Ageing stages are identical with the differences occurring from the start of the Treatment stage.

It is noted that a 'No ISCO' case (Run 10) was simulated for comparison purposes. This simulation was identical to the base case in all respects but one: the 2-year Treatment stage employed identical boundary conditions as the base case except no upgradient concentration of permanganate was applied.

4.4.2.1. Injected Potassium Permanganate Concentration

In Runs 1-3, the concentration of $KMnO_4$ injected was increased by 100% and reduced by 50% relative to the base case (Table 4.1). All of these values are within the range of those employed in field studies (Geosyntec, 2007). In order to ensure the total volume of $KMnO_4$ injected was kept constant, the injection period was changed accordingly (Table 4.1). This sensitivity study comprised three simulations.

4.4.2.2. Pulsed Injection of Permanganate

The effects of pulsing are examined in Runs 1 and 4-6 by subdividing the base case

injection period (2 years) into equal length $KMnO_4$ injection on and off intervals. Pulsed injection intervals of 3 months, 6 months and 12 months were examined. Pulsed treatment has been demonstrated to be valuable in other remediation options (e.g., Gerhard et al., 2001) and has been considered for permanganate in unconsolidated porous media as a means to reduce rind formation and increase destructive capacity for a given mass of treatment fluid injected (e.g., Thomson et al., 2008). This sensitivity study comprised four simulations.

4.4.2.3. Rock Type

Runs 1, 7, and 8 compare ISCO performance in three different types of fractured rock at the field scale, each exhibiting a characteristic set or range of hydrogeological parameters (Table 4.2). Figure 4.2 presents the distribution of intrinsic permeability for the three domains, illustrating the distribution of fractures. In each case, the mean aperture is at the midpoint of the range specified in the table. It is noted that, characteristic of these rock types in natural environments, the shale template site exhibits (relative to the other two) intermediate fracture density, low mean aperture (150μm), intermediate matrix porosity (3%), and high *foc* (0.009) while the granite exhibits high fracture density, high mean aperture (300μm), low matrix porosity (0.1%), and low *foc* (0.0009).

4.4.2.4. DNAPL Type

Runs 1 and 9 compare performance for TCE and PCE in the sandstone domain. The full set of PCE fluid parameters employed for Run 9 are presented in Table 4.4. Note that, while the boundary conditions in each run were identical, the distribution of DNAPL

resulting from infiltration and redistribution were not identical due to contrasting fluid properties. As well, different solubilities and sorptive capacities resulted in different distributions of aqueous phase and sorbed phase concentrations after the Site Ageing stage. This sensitivity study comprised of two simulations.

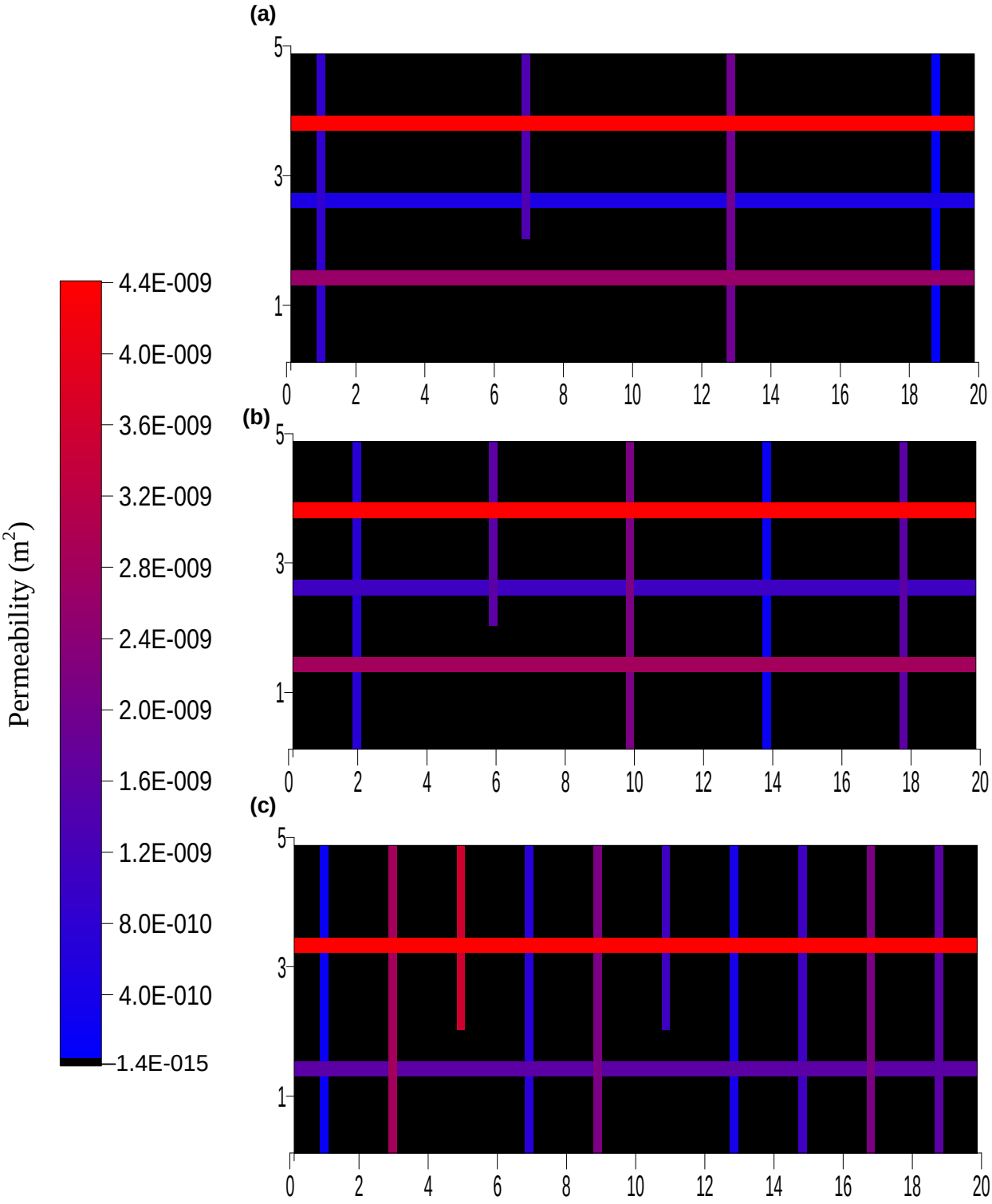

Figure 4.2: Distribution of permeability for the field scale fractured rock domains: (a) sandstone, (b) shale, and (c) granite. Colour corresponds to fracture permeability according to the scale bar provided; matrix permeability is uniform (black). Note that distance is in metres, domain is vertically exaggerated, and fracture apertures are exaggerated for visual purposes.

4.5 RESULTS AND DISCUSSION

Table 4.5 summaries a selection of key numerical results for all 10 simulations conducted in this study. These data will be discussed as each set of simulations is presented.

Table 4.5: Summary of Results for All ISCO Simulations

Run No.	DNAPL St 2 (kg)	DNAPL St 3 (kg)	Aq + Sorb St 3 (kg)	MnO_4 Inject (kg)	DNAPL St 5 (kg)	Aq + Sorb St 5 (kg)	Mass Discharge St 5 (10^{-3} mg/s)	MnO_4 React (kg)	CS React (kg)
1	5.26	0.00	7.3	45.5	0.00	5.10	3.97	44.9	0.78
2	5.26	0.00	7.3	44.8	0.00	5.25	4.21	44.3	0.82
3	5.26	0.00	7.3	45.0	0.00	4.85	3.56	44.4	0.80
4	5.26	0.00	7.3	44.7	0.00	4.86	3.56	44.2	0.81
5	5.26	0.00	7.3	45.1	0.00	4.86	3.56	44.6	0.80
6	5.26	0.00	7.3	45.4	0.00	4.86	3.56	44.9	0.78
7	6.86	0.01	6.8	59.6	0.00	3.05	0.36	41.9	2.33
8	11.53	4.23	0.68	538.8	4.17	0.37	0.02	23.2	0.30
9	6.03	0.11	3.3	46.7	0.08	2.59	0.67	46.1	0.22
10	5.26	0.00	7.3	0.0	0.00	5.18	4.06	0.00	0.00

St 2 = mass present at the end of Stage 2 (DNAPL redistribution)
St 3 = mass present at the end of Stage 3 (Site Ageing)
St 5 = mass present at end of Stage 5 (Post-Treatment)
DNAPL = mass of DNAPL present
Aq + Sorb = combined mass of aqueous and sorbed chlorinated solvent present
MnO_4 Inject = mass of MnO4 injected during the treatment period
Mass Discharge = mass per time of chlorinated solvent leaving the domain at the end of Post-Treatment stage
MnO_4 React = total mass of MnO_4 that reacted (with OAM + chlorinated solvent in all phases)
CS React = total mass of chlorinated solvent (in all phases) destroyed by MnO_4

4.5.1 Base Case Results

Figures 4.3(a) and 4.3(b) illustrate the distribution of the TCE DNAPL at the end of the infiltration and redistribution phases, respectively (relevant to all simulations except Runs 7 - 9). Figures 4.3(a) and 4.3(b) reveal a heterogeneous distribution of DNAPL pools (i.e., connected phase) and residual (i.e., trapped blobs and ganglia) due to the influence of capillary forces (and, specifically, fracture entry pressures), the order of encounter of fractures, and the permeability contrasts between fractures. At the end of the DNAPL infiltration stage, the average local DNAPL saturation (i.e. average saturation of all nodes containing DNAPL) was 0.75, the mass of DNAPL in the domain equaled 11.68 kg, the DNAPL volume was 0.008 m^3 (compared to a total fracture volume of 0.012 m^3) with 100% of the nodes on drainage (i.e., DNAPL displacing water). At the end of DNAPL redistribution stage, the average DNAPL saturation was 0.3, the DNAPL volume was 0.0036 m^3 (equal to a mass of 5.26 kg) and the pool to residual ratio was 71:29%. Note in Figure 4.3(b) that, as expected, the lone remaining pool exhibiting a high DNAPL saturation resides in a vertical dead-end fracture, and other pools of various lengths occur in horizontal fractures, separated by areas of residual DNAPL.

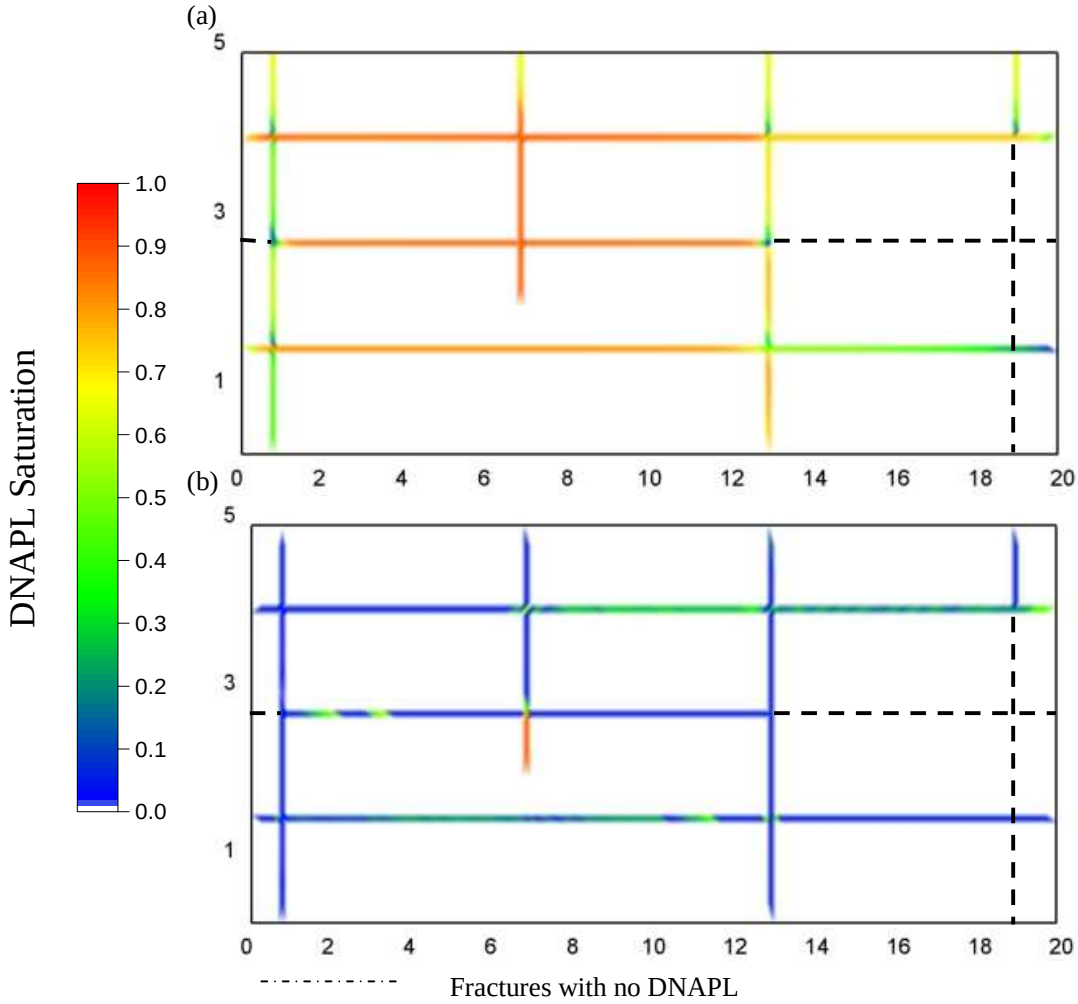

Figure 4.3: DNAPL distribution for Base Case at (a) t_{TOTAL} = 0.5 years when DNAPL inflow and outflow are equal, and (b) t_{TOTAL} = 1 year when all DNAPL migration has ceased.

Figure 4.4 illustrates the distribution of aqueous phase TCE at the end of the 20 year Site Ageing stage (t_{TOTAL} = 21 years). Evident are the expected diffusion halos in the sandstone matrix blocks adjacent to fractures containing DNAPL as well as those horizontal fractures without DNAPL but subject to significant aqueous mass flux (Figure 4.3b). However, it is noted that due to the lack of DNAPL in the rightmost vertical fracture (i.e., x=19.0 m) and continuous injection of aqueous TCE in the horizontal

upgradient, no aqueous phase TCE surrounding the immediate vicinity of this fracture is noted. At this time, no DNAPL remained in the domain. This occurred despite the constant influent concentration equal to 50% of TCE solubility. The reason is the substantial TCE sink provided by matrix diffusion and sorption. At this time, the total mass of TCE in the domain was 7.3 kg, of which 99% resided in the matrix; of the mass in the matrix, 98% was sorbed and only 2% remained in the aqueous phase. The significant porosity and foc of the sandstone matrix combine so that it acts as a substantial sink for TCE, rapidly promoting DNAPL dissolution. The complete disappearance of DNAPL from fractures in sandstones and similar scenarios is not unexpected (Parker et al., 1994).

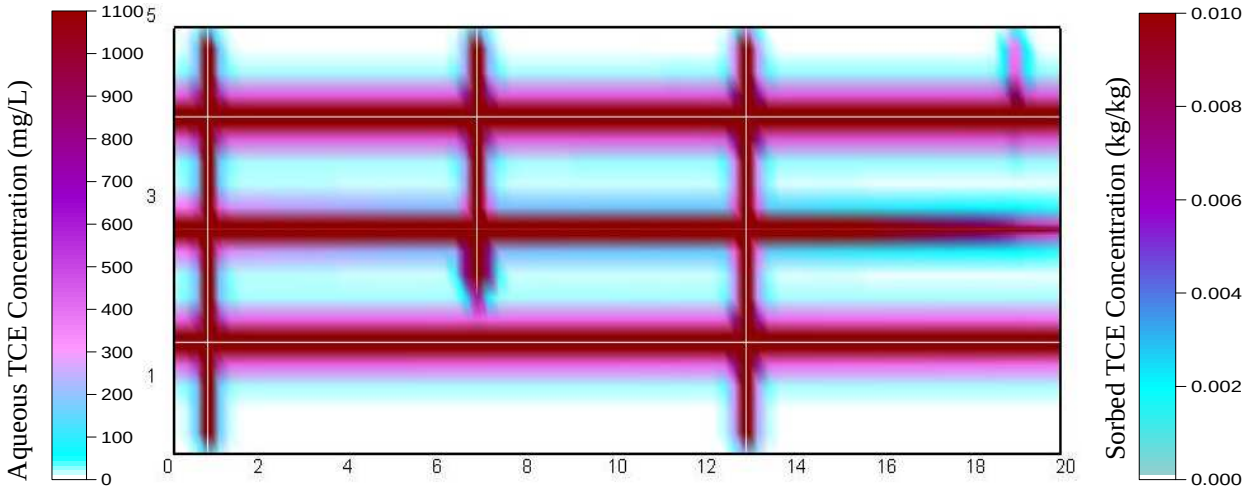

Figure 4.4: Distribution of aqueous and sorbed TCE after 20 years (t_{TOTAL} = 21 years) of DNAPL dissolution (i.e., Site Ageing stage).

Figure 4.5 provides the concentration of aqueous and precipitated species throughout the domain after the Treatment stage (i.e., 2 years of MnO_4 injection, t_{TOTAL} = 23 years). It reveals the limited penetration of MnO_4 at this time, due to its reaction with TCE in the

fractures and its diffusion and subsequent destruction by OAM, aqueous TCE, and sorbed TCE in the matrix. As expected, that absence of TCE is most prominent in the fractures near the injection boundary, although it should be noted that TCE concentrations also decrease due to an ongoing mass flux of TCE flux out of the downgradient boundary. Horizontal penetration is noted to be least in the middle fracture, which exhibits the smallest aperture (see Figure 4.2a). It is further noted that the horizontal extent of MnO_2(s) penetration closely corresponds to the extent of TCE disappearance.

Figure 4.6 provides the concentration of aqueous TCE throughout the domain after the Post-Treatment stage (i.e., 5 years after the completion of MnO_4 injection, t_{TOTAL} = 28 years). Back diffusion of TCE solute into the fractures is observed while all of the MnO_4 has been consumed.

Figure 4.7 plots the evolution of the aqueous TCE concentration profile along a cross-section perpendicular to the fracture (in this case for the top horizontal fracture with the cross-section located 3.0 m from the left side boundary). In this figure, back diffusion of TCE into the fracture after the MnO_4 injection is demonstrated. At t_{TOTAL} = 21 years, the maximum aqueous TCE concentration was observed. Over the 2 year injection period, the concentration of aqueous TCE in the fracture decreased from approximately 325mg/L to 20mg/L as a result of the treatment and the eliminated upgradient boundary condition. However, the concentration profile within the fracture is observed to rebound as back diffusion begins during the Post-Treatment stage. Figure 4.7 further illustrates that the concentration profile in the matrix is little affected by the

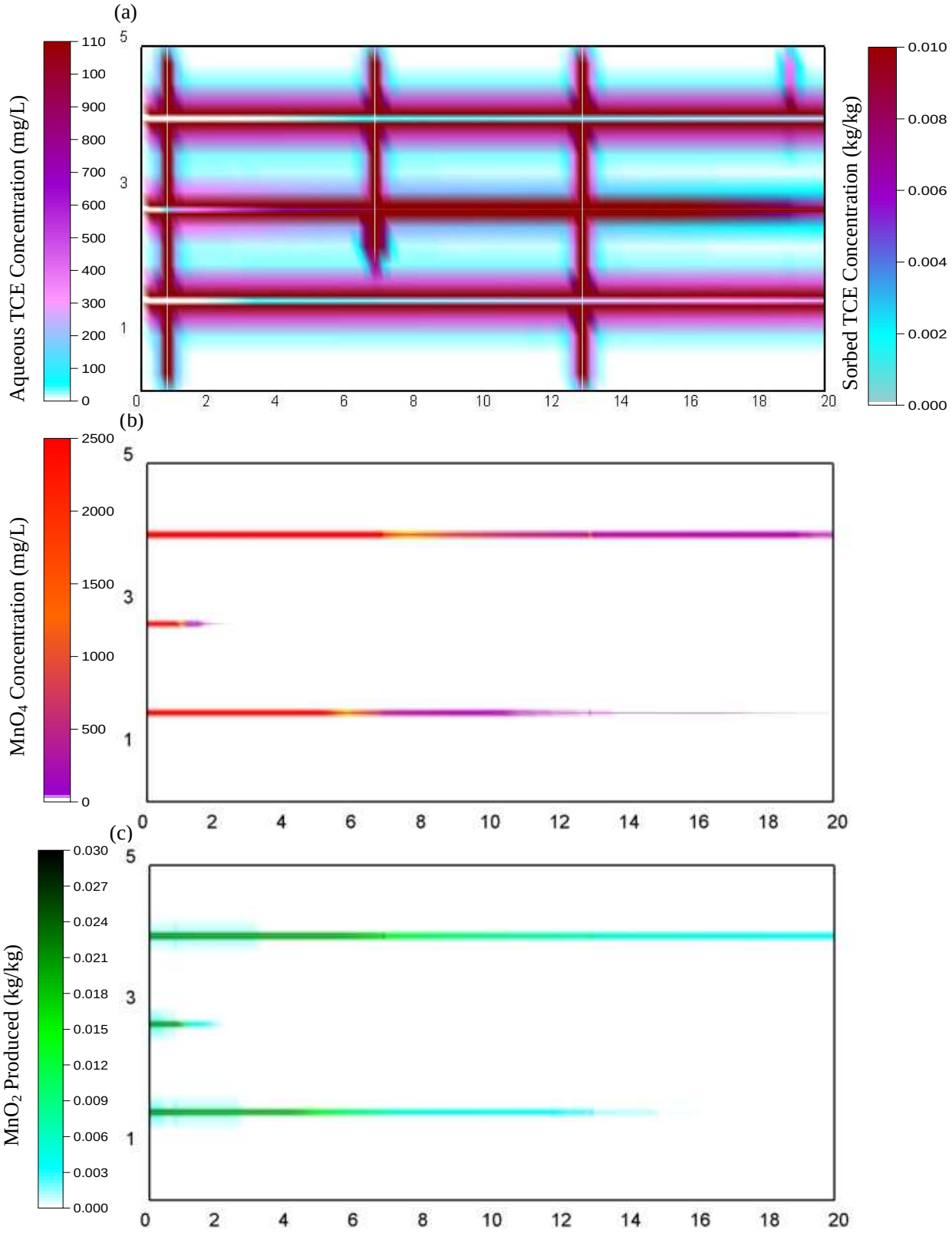

Figure 4.5: Distribution of aqueous species concentrations at t_{TOTAL} =23 years for Base Case after 2 years of chemical oxidation (i.e., Treatment stage): (a) TCE, (b) MnO_4, (c) MnO_2.

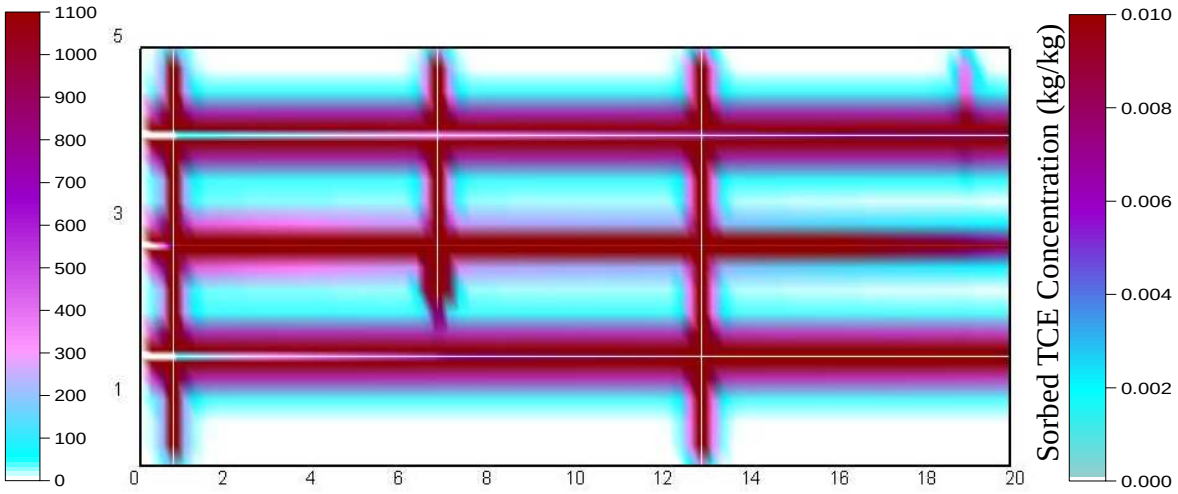

Figure 4.6: Distribution of aqueous TCE concentrations at t_{TOTAL} =28 years for Base Case, 5 years after chemical oxidation (i.e., Post-Treatment stage).

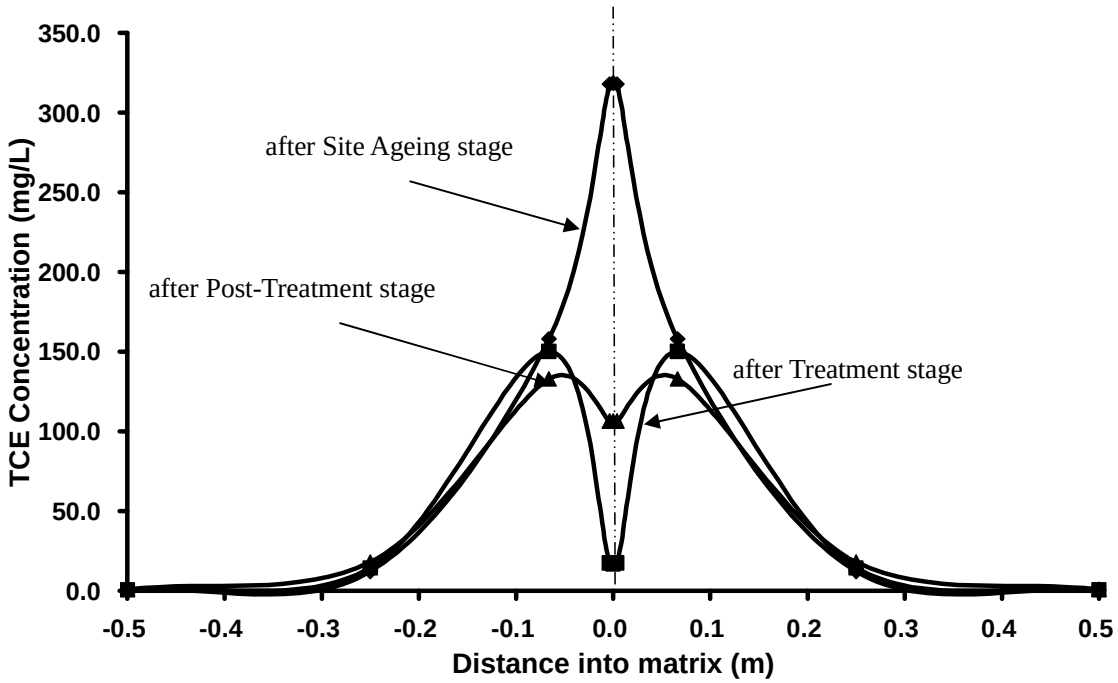

Figure 4.7: Concentration profile of aqueous TCE across a single fracture for the Base Case. Shown is a 1.0 m cross-section across a horizontal fracture (dotted line denotes location of the facture).

chemical oxidation treatment, indicating that (as observed in Figure 4.5) the permanganate had minimal interaction with the TCE in the matrix.

Figure 4.8 presents cumulative mass plots of all sinks and sources of TCE during the base case simulation. Summed totals of the sinks and sources in this plot, where:

Mass Dissolved + Mass Influx =

Mass Destroyed + Mass Outflux + Mass Sorbed + Mass In Domain (4.16)

reveal that the model has excellent mass balance for TCE (plots not shown to improve clarity of the figure); this was further confirmed by excellent computed mass balance on all modelled species. The figure reveals that the majority of DNAPL dissolution occurred rapidly at the beginning of the simulation due to partitioning to groundwater in the fractures, diffusion into the matrix, and simultaneously a rapid increase in sorbed TCE in the matrix. Until t_{TOTAL} = 3 years, TCE flux out of the domain was greater than flux into the domain due to a proportion of the dissolved TCE exiting via fracture flow. However, beyond this time, with dissolution virtually complete, TCE influx exceeded outflux as the incoming background TCE contributed to a steady rise in mass retained via sorption. It is also noted the cumulative mass of aqueous TCE in the domain (sum of that in the fractures and matrix) is a small fraction of the amount sorbed.

Figure 4.8 further illustrates that when MnO_4 was injected, at t_{TOTAL} = 21 years, the amount of TCE solute destroyed began to rise. However, the magnitude of this rise was less than the magnitude of the reduction in sorbed TCE. The additional desorption occurred for two reasons: (i) as a result of back-diffusion induced by the flushing of aqueous TCE out of the domain via fracture flow, and (ii) the reduction in sorptive

capacity caused by the destruction of OAM. During the Post-Treatment stage, as illustrated by Figure 4.8, the amount of aqueous TCE destroyed increases at a rate that is minor (i.e. 0.0024 kg over 5 years of post-treatment dissolution) relative to that achieved during the Treatment stage (i.e., 0.78 kg over 2 years of MnO_4 injection).

Figure 4.9 presents the cumulative mass in the domain of the species involved in the oxidation reactions; note that the time axis originates at the beginning of the Treatment stage. This figure reveals that the rate of MnO_4 consumption was essentially constant during the injection period. Of the total mass of 382 moles of MnO_4 injected (i.e., 45.5 kg MnO_4), at the end of the Treatment stage 95.7% had been consumed by OAM while 4.3% had been consumed by TCE. Of the 7.3 kg of aqueous TCE solute present in the domain at the end of the 20 year Site Ageing stage, only 0.78 kg (i.e., 10.7% of the initial mass) was destroyed by the injected MnO_4 at the end of the 5-year Post-Treatment stage.

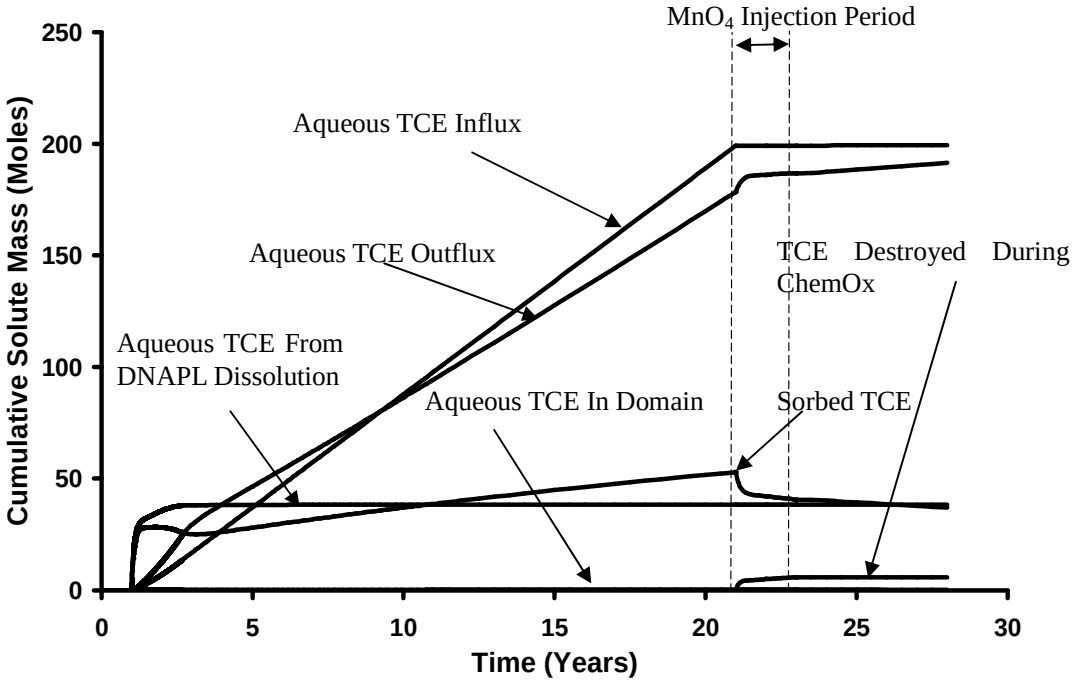

Figure 4.8: Cumulative aqueous and sorbed TCE from all sinks and sources for Base Case.

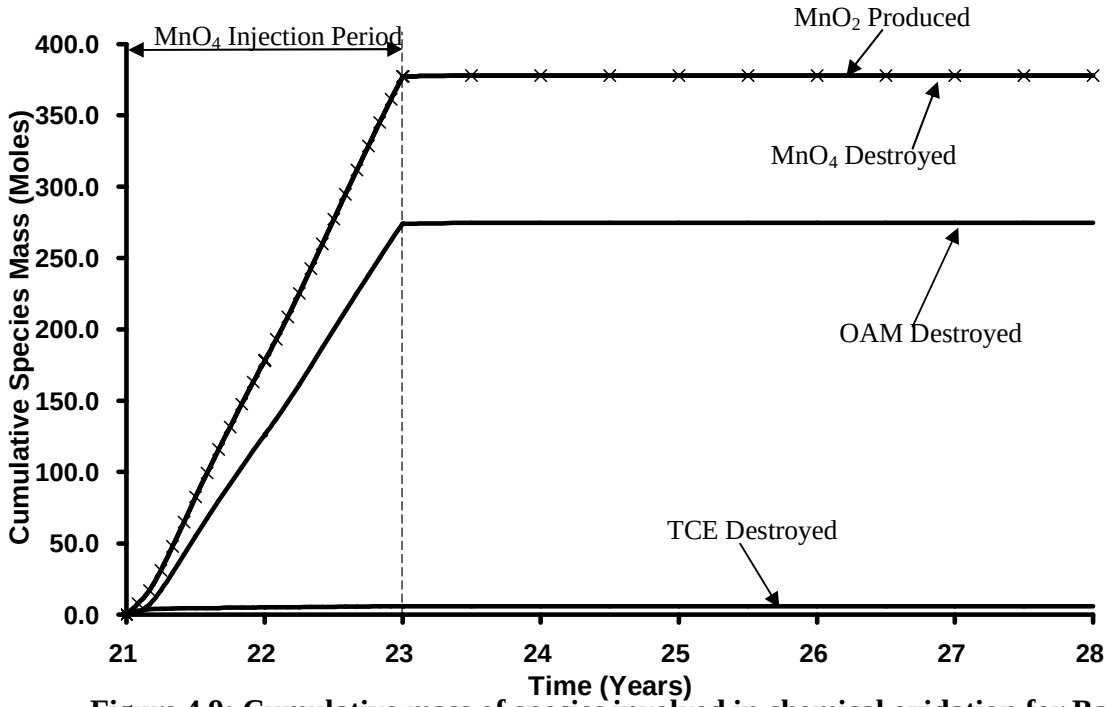

Figure 4.9: Cumulative mass of species involved in chemical oxidation for Base Case.

Figure 4.10 presents the TCE mass discharge at the downgradient boundary of the domain for the base case and No ISCO simulations. The figure illustrates that mass discharge initially increased during the Ageing stage as the DNAPL dissolved, peaked when all DNAPL has disappeared, then decreased to a constant level. The very slowly increasing mass discharge at the exit reflects the mass influx at the inlet modified by a significant amount of forward diffusion from the matrix that decreases slowly with time. The mass flux then spiked at the start of the Treatment stage due to the increase in hydraulic gradient (from 0.005 to 0.025) that flushed out the fractures. The mass discharged after treatment is substantially lower than before treatment, but this is largely a function of removing the constant influx of TCE solute. Comparison with the No ISCO simulation in Figure 4.10 reveals the small but not insignificant effect of treatment to further reduce the mass flux during the Treatment stage. However, it also reveals

that the Post-Treatment mass discharge is essentially identical for the two cases (see also Table 4.5). This illustrates that, for the base case scenario modelled, ISCO effectively targeted TCE in the hydraulically active fractures during treatment but had a relatively insignificant influence on the TCE in the matrix that was responsible for long term mass flux. Total TCE mass in the domain at the end of the simulations were 5.103 kg and 5.179 kg (1.5% difference) for the base and No ISCO cases, respectively.

Figure 4.11 presents the average TCE solute concentration in each of the three horizontal fractures at the downgradient boundary. The figure first demonstrates that concentrations in none of the three fractures were in equilibrium with the matrix after 20 years of Site Ageing, as evidenced by exit concentrations less than the 550 mg/L specified at the upgradient boundary. This agrees with Figure 4.4 in that large concentration gradients span only 0.5 m into the matrix even after 20 years. Figures 4.4 and 4.11 also reveal that higher exit concentrations correlate to higher degrees of mass loading to the matrix, which in turn result from higher initial DNAPL saturation present in these fractures. The gradual increase in exit concentrations observed for all three fractures during the Site Ageing period reflects the gradual loading of the matrix such that forward diffusion gradients are reduced.

During the Treatment stage, Figure 4.11 reveals that the two larger fractures (i.e., 178μm and 230μm) experienced concentrations that decreased significantly; this was primarily due to dilution by injected water rather than chemical oxidation (as evidenced by the similarity to the No ISCO case). Flow rates in these fractures were so large that reverse

diffusion from the matrix could not occur fast enough to significantly elevate concentrations. However, soon after the commencement of the Treatment stage, a small concentration rebound is observed in the No ISCO case while the base case observed no such rebound (Figure 4.11b); this difference accounts for the mass flux difference observed (Figure 4.10) and illustrates the relative benefit of MnO_4 penetration and treatment in the larger fractures (Figure 4.5b). Later in the Post-Treatment stage, steady concentrations attained only 20-25% of the pre-treatment amounts and no difference was observed between the ISCO and No ISCO cases; this reflects the long term bleed from matrix-bound TCE and the inability of the 2-year treatment to significantly affect this stored mass (see also Table 4.5).

In contrast, Figure 4.11 reveals that TCE concentrations in the smallest horizontal facture (i.e., 76 μm, the central fracture in Figure 4.5) increased during the Treatment stage. This occurred because the rate of groundwater flow, although elevated, was still low relative to the rate of reverse diffusion (occurring downgradient from the limited zone of MnO_4 penetration, Figure 4.5b) so that mass entering the fracture impacted the exit concentrations. The fact that no significant difference is observed in solute concentrations before and after treatment in this fracture reveals further that both the upgradient TCE boundary condition and the small MnO_4 treated zone have no impact on the exit boundary after 5 years. And the lack of significant difference from the No ISCO case reveals the negligible influence of treatment on such low-flow fractures (given a constant head boundary condition, which results in the majority of injected water flowing through the larger aperture fractures).

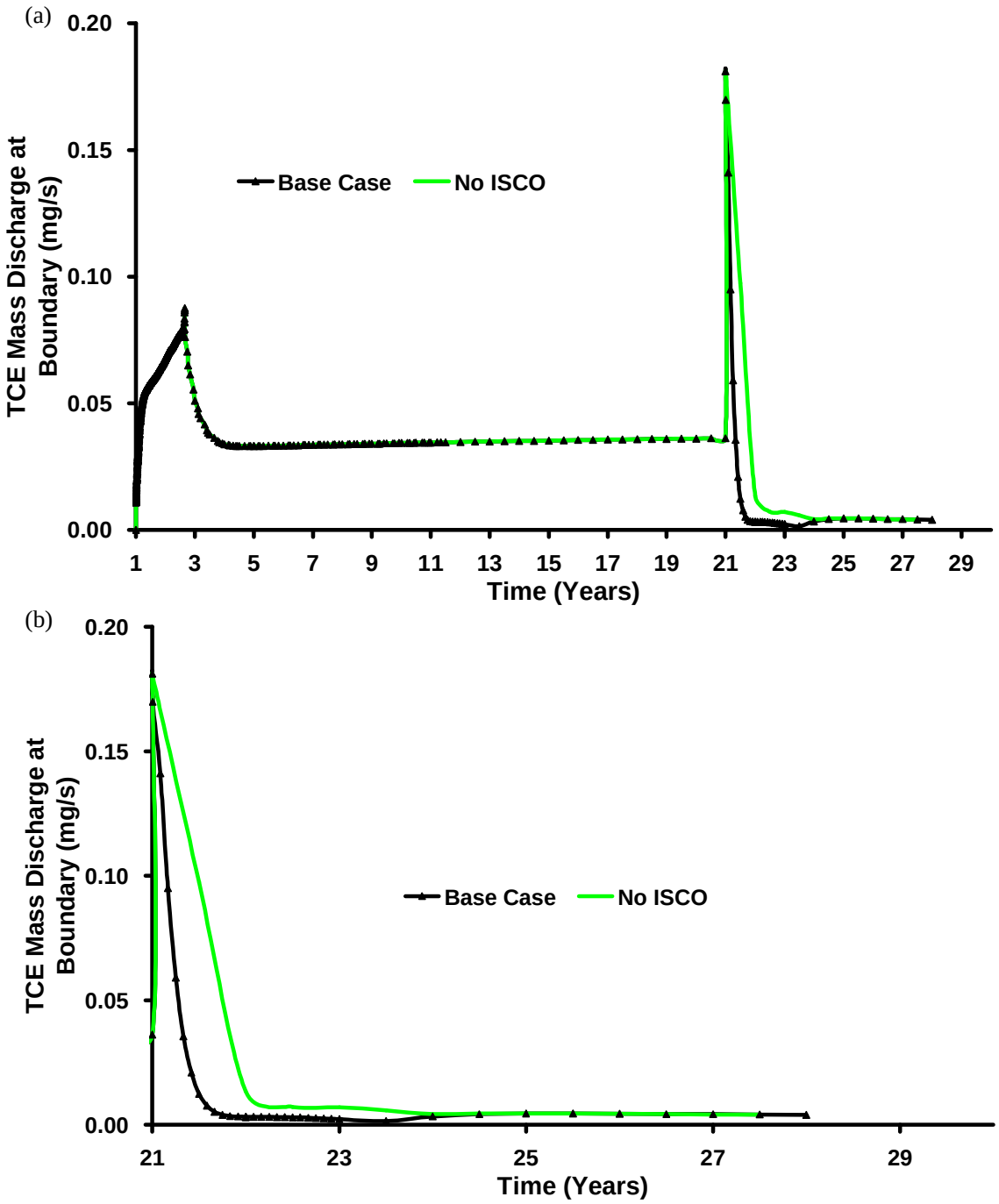

Figure 4.10: Comparison of total boundary mass discharge for base case with (a) a simulation where no ISCO was carried out and (b) since the start of the Treatment Stage only (timescale expanded for clarity).

(a)

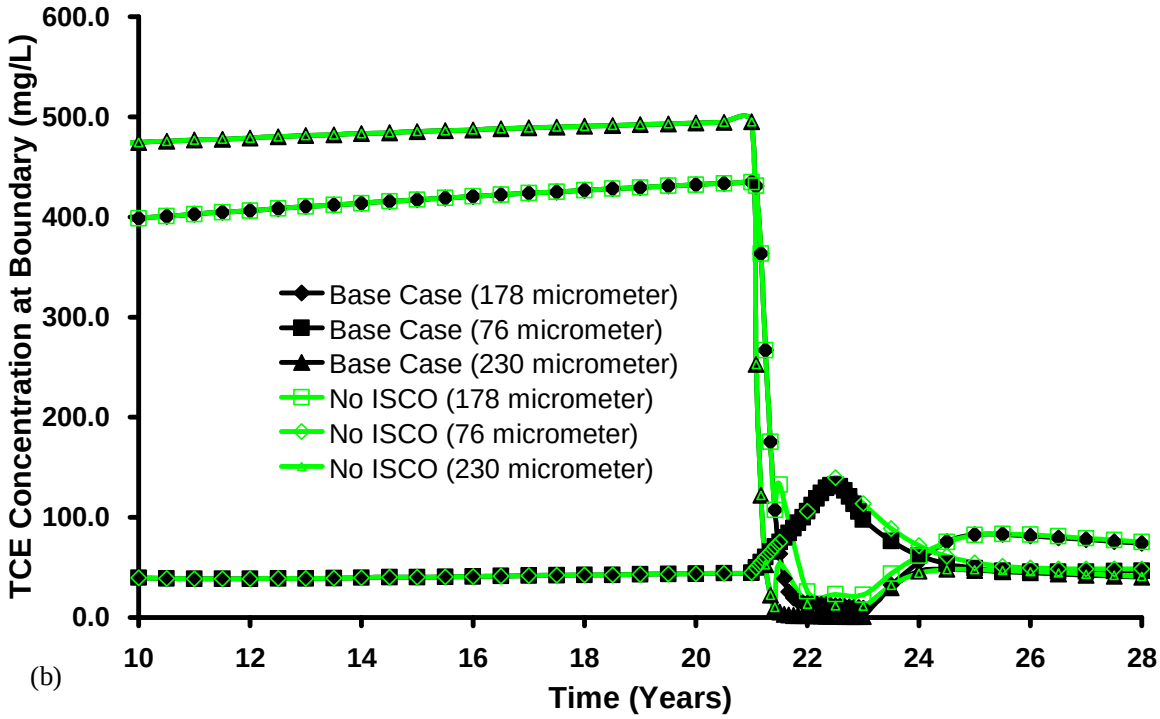

(b)

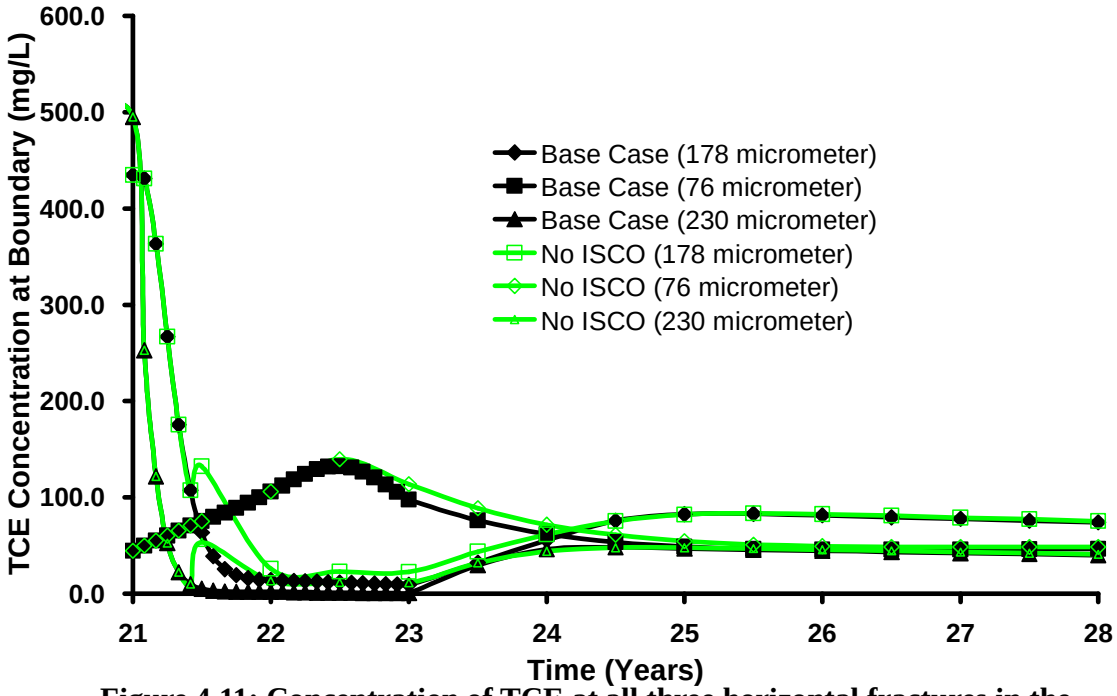

Figure 4.11: Concentration of TCE at all three horizontal fractures in the Sandstone base case at the downgradient boundary over (a) the latter 18 years, and (b) since the start of the Treatment stage only (timescale expanded for clarity).

4.5.2 SENSITIVITY SIMULATIONS

4.5.2.1 Sensitivity to Potassium Permanganate Concentration

Figure 4.12 plots the cumulative mass of TCE destroyed for Runs 1, 2, and 3, in which the injected concentration of MnO_4 was varied but the total mass injected was kept constant (by varying the length of the Treatment stage). Note that the plot shows data from the start of the Treatment stage only. It reveals that, for the scenario considered, the rate of TCE mass destruction is a function of the injected MnO_4 concentration, but the total TCE mass destroyed is only a function of the total mass of oxidant injected.

Furthermore, once the injection process ceased, additional TCE destruction was negligible in all three cases. This occurs because of the limited pathways available for permanganate transport, and the fact that oxidant demand (from OAM + TCE) significantly exceeds oxidant supply in all three simulations. In addition, the Post-Treatment period is dominated by reverse diffusion of TCE mass and all three simulations have similar, negligible effect on the matrix-stored mass. No significant difference between the 3 cases is observed during the Post-Treatment stage with respect to mass flux (Figure 4.13) or exit concentrations of MnO_4 (figure not shown). Moreover, the distribution of TCE, MnO_4, and MnO_2 are observed to be essentially identical after the Treatment stage (compare Figure 4.5 and Figures A1 and A2 in Appendix A).

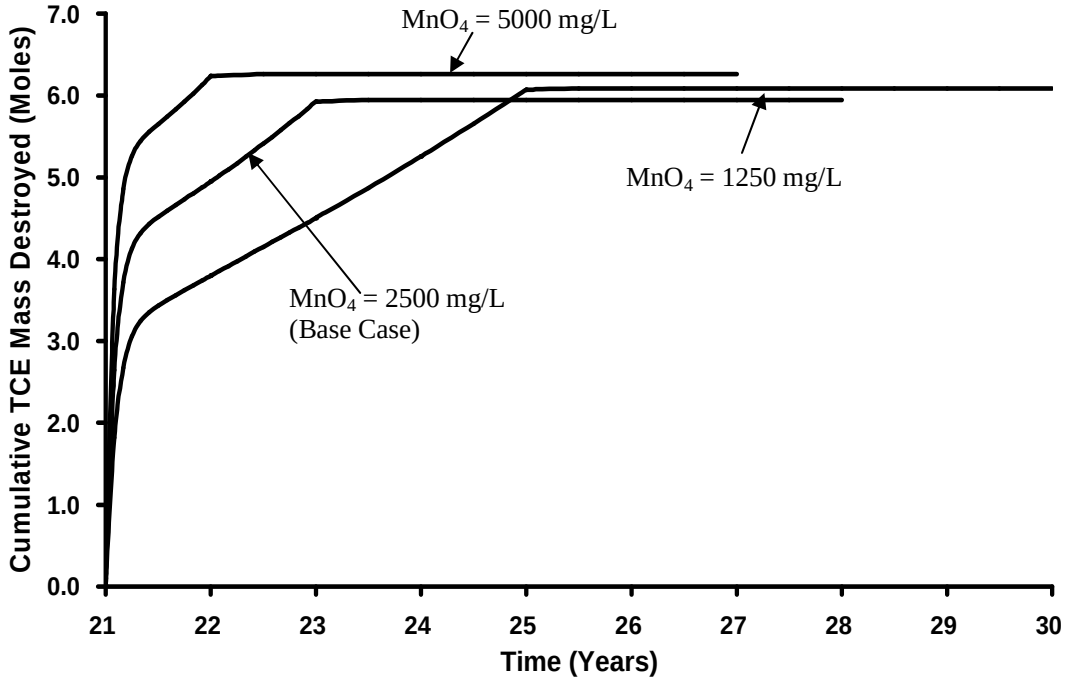

Figure 4.12: Cumulative mass of TCE destroyed for various MnO4 concentrations.

(a)

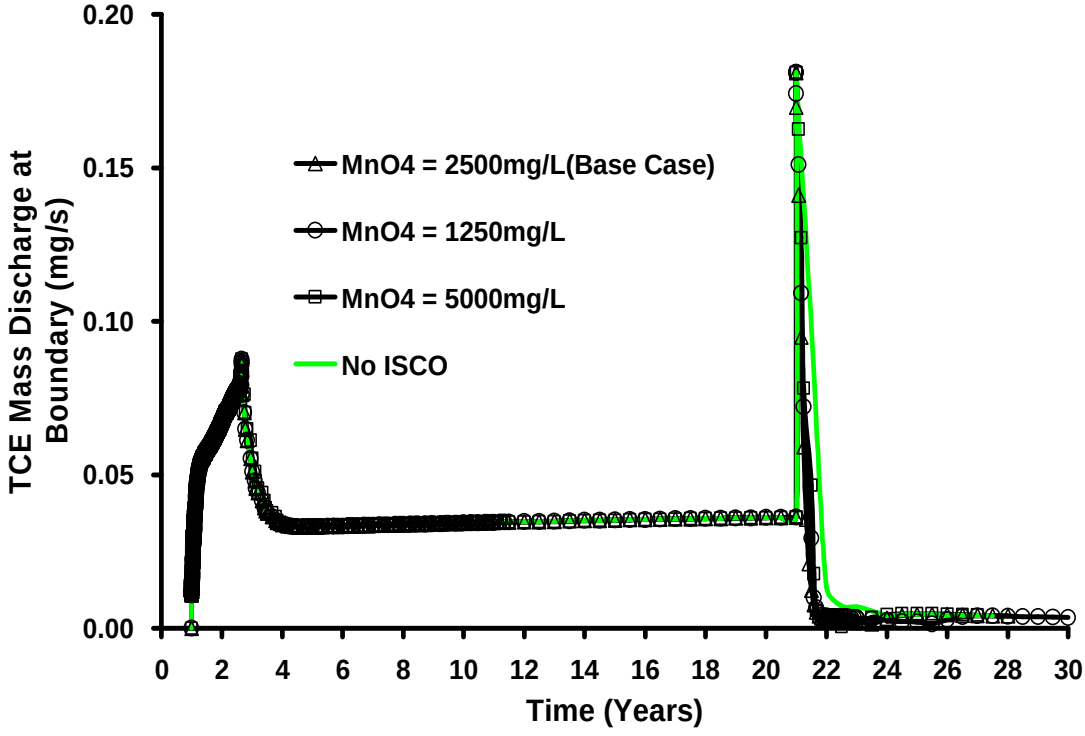

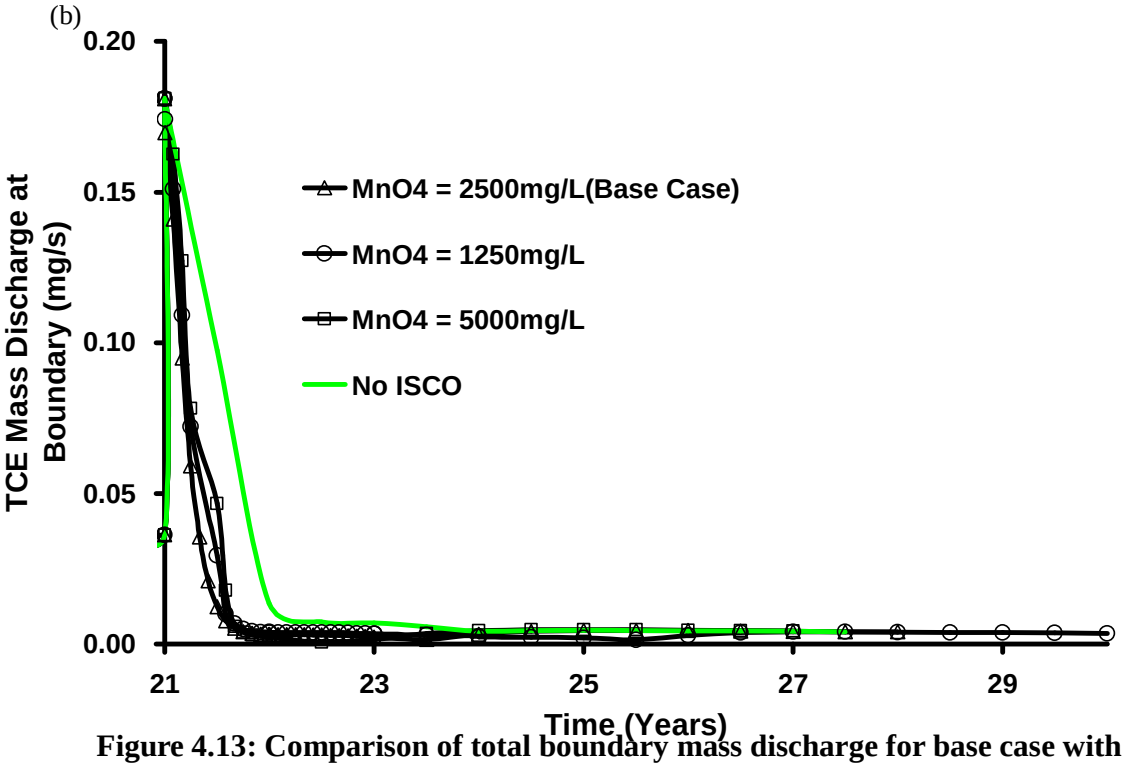

Figure 4.13: Comparison of total boundary mass discharge for base case with (a) various MnO4 concentration injected and (b) since the start of the Treatment stage only (timescale expanded for clarity).

4.5.2.2 Sensitivity to Pulsed Injection

Figure 4.14 plots the cumulative mass of TCE destroyed for Runs 1, 4, 5 and 6, in which the MnO_4 was added via pulsed injection periods of varying length, including no pulsing, ensuring that the total mass injected was constant (by varying the length of the Treatment stage). As demonstrated in Figure 4.14, the total mass of TCE destroyed at the end of the Treatment stage (and thereafter) is nearly identical in all cases due to the fact that the cumulative injected MnO_4 mass is constant. No significant difference between the 4 cases is observed during the Post-Treatment stage with respect to mass flux (Figure 4.15) or exit concentrations of MnO_4 (figure not shown). Moreover, the distribution of TCE, MnO_4, and MnO_2 are observed to be essentially identical after the Treatment stage

(compare Figure 4.6 and Figures A3, A4 and A5 in Appendix A). Figure 4.15(b) reveals that for each interlude between a MnO_4 pulse, TCE mass flux begins to rise immediately due to reverse diffusion delivering mass to the hydraulically active fractures and then decreases at the start of the next pulse as MnO_4 reacts with TCE in the fractures. This reconfirms that the injected permanganate was quickly consumed by the high oxidant demand in the matrix of the fractured rock. and that no residual permanganate remained to provide ongoing treatment of TCE mass bleeding into the fractures during the pump-off periods.

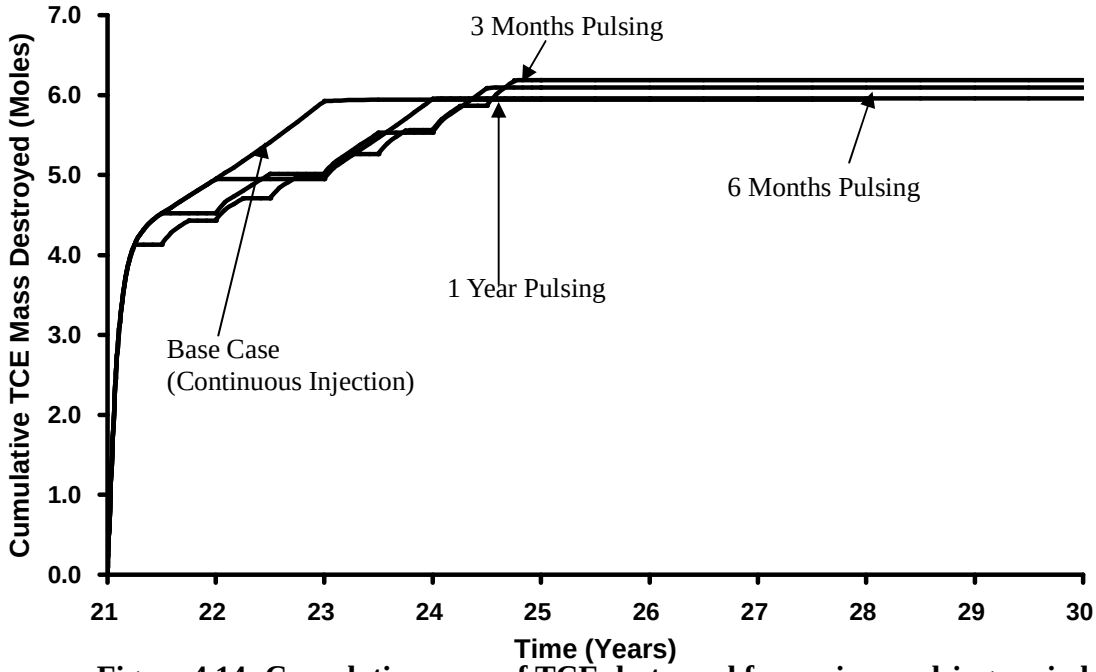

Figure 4.14: Cumulative mass of TCE destroyed for various pulsing periods.

(a)

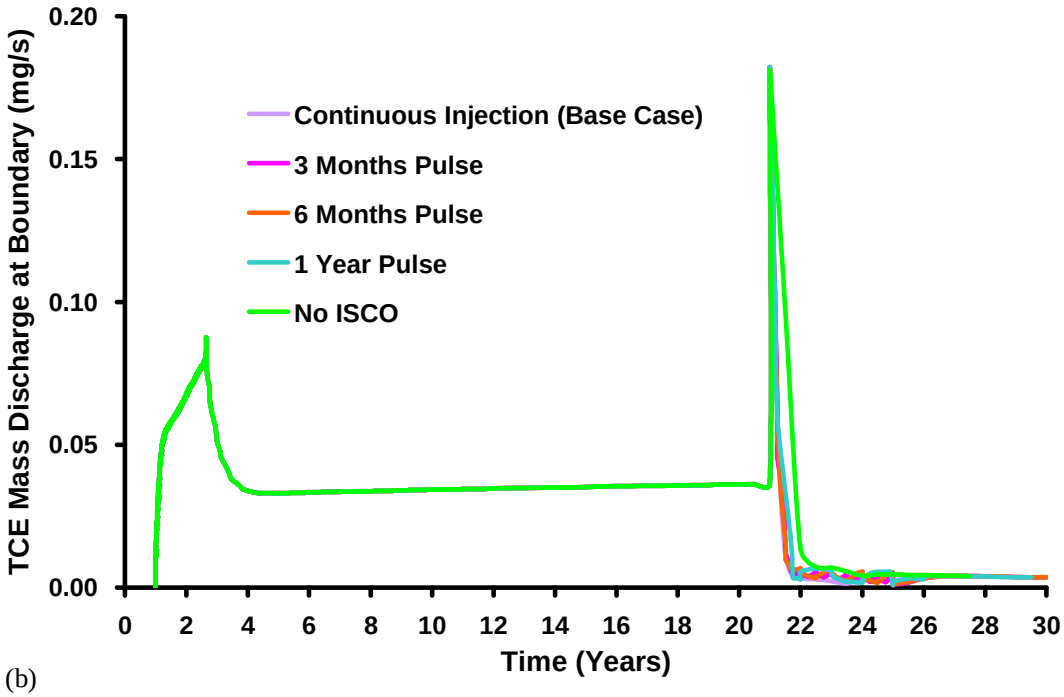

(b)

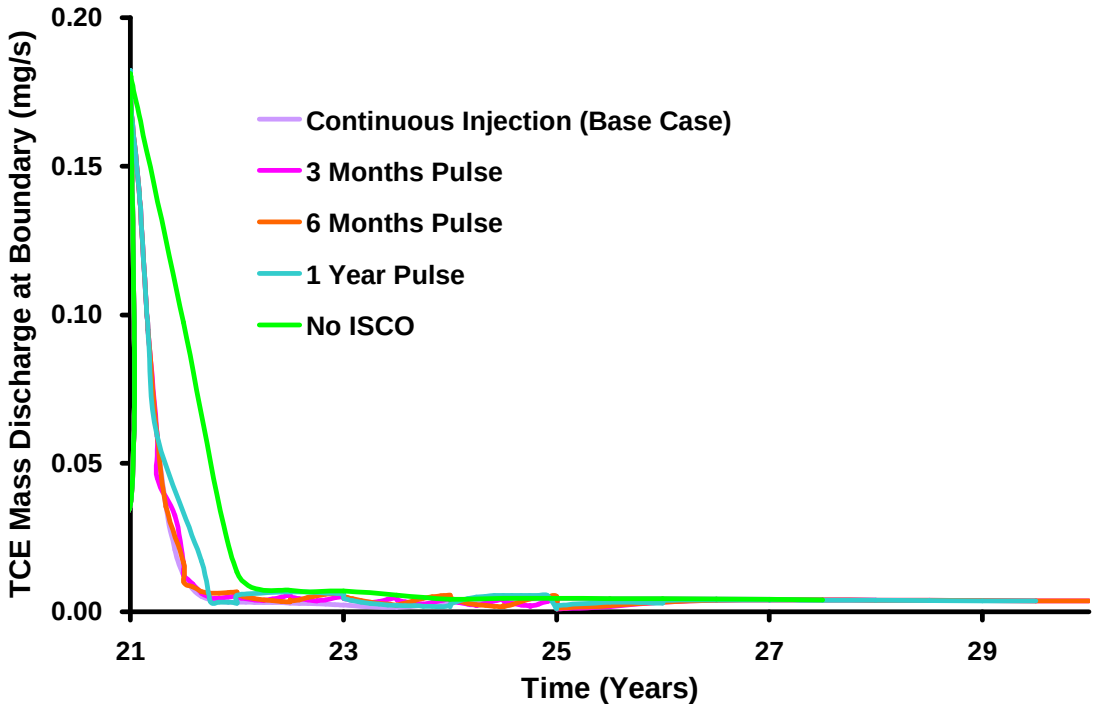

Figure 4.15: Comparison of total boundary mass discharge for base case with (a) various pulsing method and (b) since the start of the Treatment stage only (timescale expanded for clarity).

4.5.2.3 Sensitivity to Rock Type

At the end of the DNAPL Infiltration stage, the average DNAPL saturation was 0.75, the volume of DNAPL in the domain was 0.008 m^3, 0.01 m^3 and 0.018 m^3 for sandstone, shale and granite with 100% of the invaded nodes on drainage for all 3 rock types. At the end of the DNAPL redistribution stage, the average DNAPL saturation was 0.3 for all 3 rock types, the volume of DNAPL was 0.0036 m^3, 0.0047 m^3 and 0.0079 m^3 while the pool to residual ratio was 71:29%, 72:28% and 90:10% for sandstone, shale and granite respectively. The distributions of TCE DNAPL at the end of the redistribution stage for each rock type are illustrated in Figure 4.3 and Figure A6, Appendix A.

At the end of the 20 years Site Ageing stage (t_{TOTAL} = 21 years) the total mass of aqueous and sorbed TCE in the domain was 7.3 kg (55.6 moles), 6.8kg (50.8 moles) and 0.68 kg (5.08 moles) for sandstone, shale and granite respectively. In each case, 97-99% of the total mass resided in the matrix, of which 97-98% was sorbed and only 1-2% remained in the aqueous phase. Although no DNAPL was left in the sandstone and shale domain at this time, 4.23 kg of DNAPL was found present in the granite domain. This observation is consistent with the findings in Parker et al. (1994) where it was suggested that due to the low porosity in granite, DNAPL could remain present in the fractures for decades. Figure 4.16 illustrates the distribution of aqueous phase TCE in the sandstone, shale and granite simulations at the end of the 20 year Site Ageing stage. In each case, the matrix immediately surrounding the fractures exhibits diffusion halos of TCE. However, the depth and extent of TCE penetration of the matrix is observed to be highly dependent on properties of both the fractures and the matrix for each rock type. The combination of

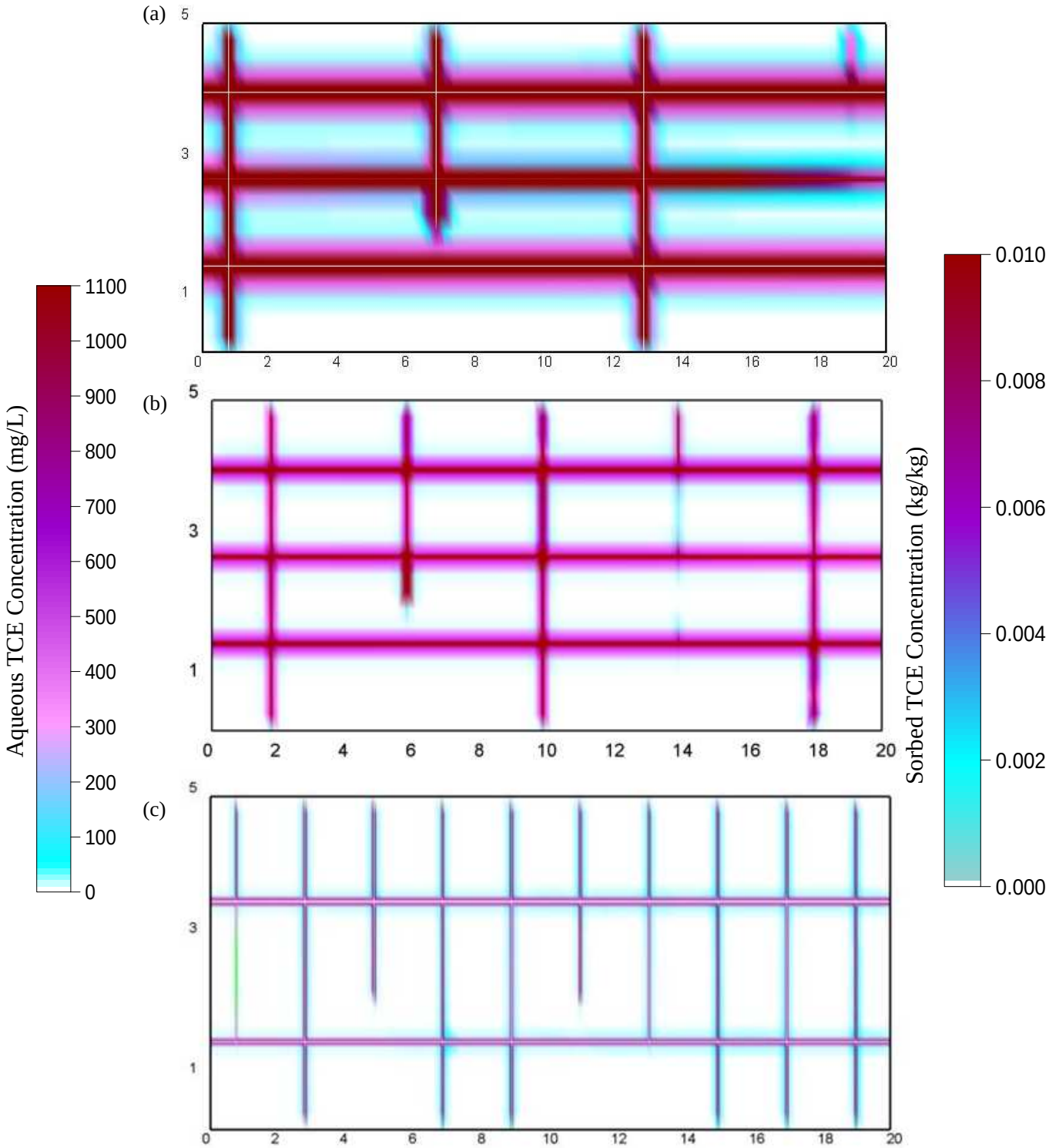

Figure 4.16: Distribution of aqueous TCE after 20 years (t_{TOTAL} = 21 years) of DNAPL dissolution (i.e., Site Ageing stage) in (a) Sandstone, (b) Shale and (c) Granite.

these impacts residence time of TCE in the source zone and it is the relative rates of TCE transport through fractures versus diffusion to the matrix that affects the final distribution of mass.

The effective diffusion rate is proportional to matrix tortuosity multiplied by the free solute diffusion coefficient (Bear, 1972; Pankow and Cherry, 1996); referring to Table 4.2 for the three rock types, the product of these two values is 2.02 $x10^{-10}$ m^2/s for the sandstone, 1.01x 10^{-10} m^2/s for the shale, and 5.05 x 10^{-11} m^2/s for the granite. Countering this is the sorptive capacity of the matrix, which is proportional to foc and inversely proportional to porosity (Equation 4.13). The (pre-treatment) matrix retardation coefficient *R* (Equation 4.14) is 21, 100 and 170 for sandstone, shale and granite, respectively. This corresponds to rock capacity factors, α, values of 270, 3300, and 170,000 for sandstone, shale, and granite, respectively. Overall the depth of penetration of TCE into the matrix in a direction perpendicular to the fractures is expected to be proportional to the effective diffusion rate divided by the rock capacity factor; this is calculated for sandstone, shale, and granite as 7.4 x 10^{-13}, 3.0 x 10^{-14}, and 3.0 x 10^{-16}, respectively. Figure 4.16 confirms that the ability of TCE to penetrate to depth in the matrix follows the order of this calculation, namely sandstone > shale > granite.

With respect to the impact of rock fractures on mass storage and mass flux, the dominant properties are fracture density, mean aperture, and distribution of apertures. In particular, the residence time of TCE in the horizontal fractures is key. The mean aperture of the horizontal fractures only for sandstone, shale, and granite are 161 μm, 192

μm, and 400 μm, respectively. The mean horizontal groundwater velocities across the domain (in the absence of DNAPL) for sandstone, shale, and granite were found to be 1.06 x 10^{-4} m/s, 1.50 x10^{-4} m/s, and 6.54 x 10^{-4} m/s, respectively. These correspond to mean residence times across the 20 m domain for sandstone, shale, and granite of 2.21 days, 1.56 days, and 0.36 days, respectively.

Figure 4.17 demonstrates that the mass discharge of TCE out of the right boundary of the domain during the Site Ageing stage follows the order granite > shale > sandstone. The vertical axis of Figure 4.18 demonstrates that the percentage of initial TCE mass retained in the domain at the end of Site Ageing follows the order sandstone > shale > granite (see also Table 4.5 for the mass retained in domain). These two results, mass lost to advection versus mass retained via sorption, reflect the overall balance of residence time versus matrix diffusion. Peclet number (Pe) for fractured rock is defined as the ratio of advection to diffusion rates, Pe = ve/($D^o\tau$), where v is the advective velocity in the fracture, e is the mean aperture, D^o is the free solute diffusion coefficient and τ is the matrix tortuosity (e.g., Fetter, 1993). Here v is taken as the mean horizontal advective velocity across each domain and e is the mean aperture of all horizontal fractures for each rock type. Figure 4.18 reveals that the percentage of TCE retained (in aqueous and sorbed forms) exhibits a linear dependence on the log(Pe) for the three rock types (R^2 = 0.9923) at the end of the Site Ageing stage (i.e., t_{TOTAL} = 21 years). This confirms expectations that lower Pe (i.e., lower advective velocity, smaller apertures, higher effective diffusion) corresponds to increased matrix diffusion (e.g., sandstone) while higher Pe corresponds to increased mass loss via advection (e.g., granite). Note that this

relationship is specified to the 3 domains tested; it is expected that if more simulations were conducted with a wider property of each rock type more scatter will be observed.

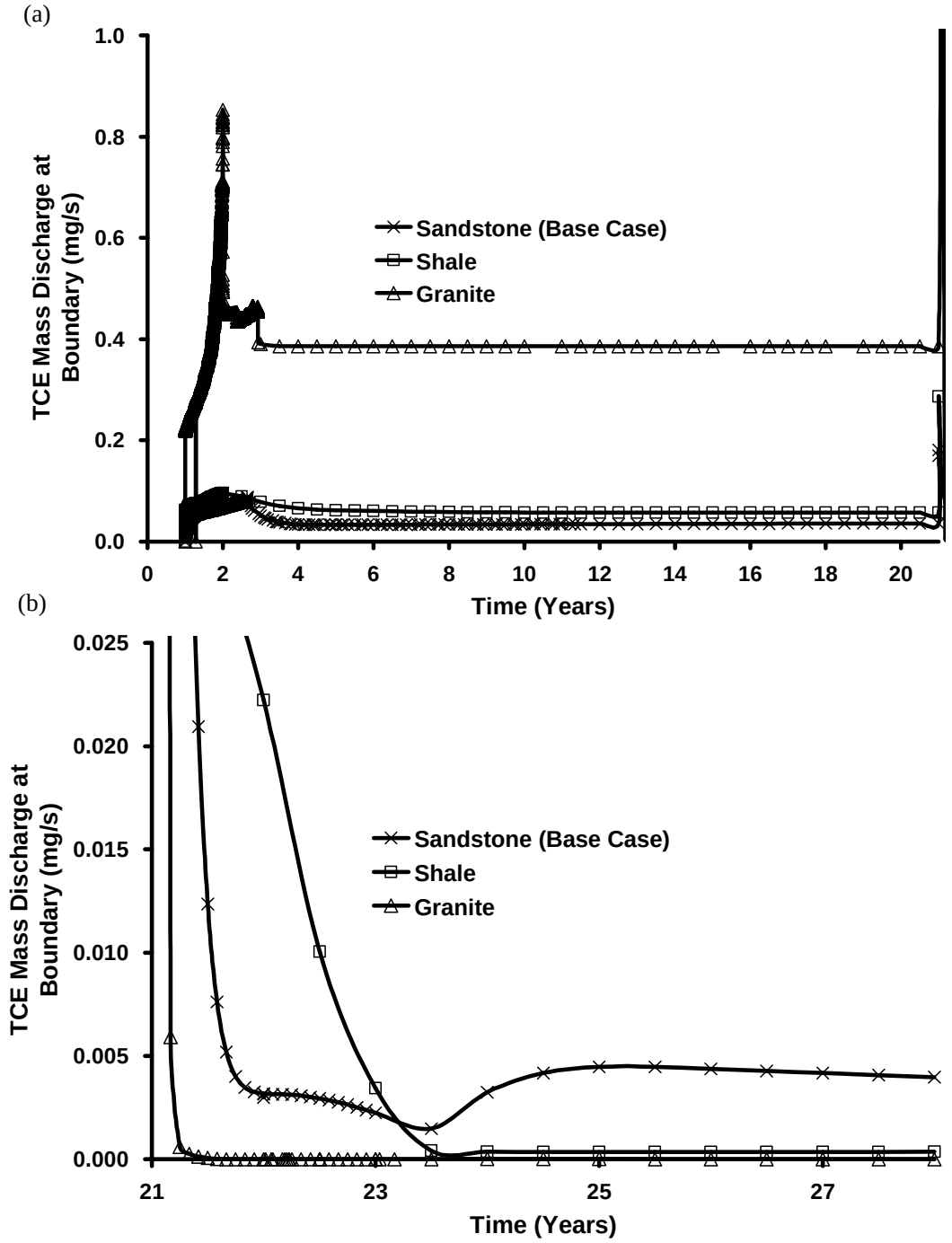

Figure 4.17: Comparison of total boundary mass discharge for different rock types; (a) from the beginning of the simulation to end of Site Ageing stage and (b) Treatment stage only (timescale expanded for clarity).

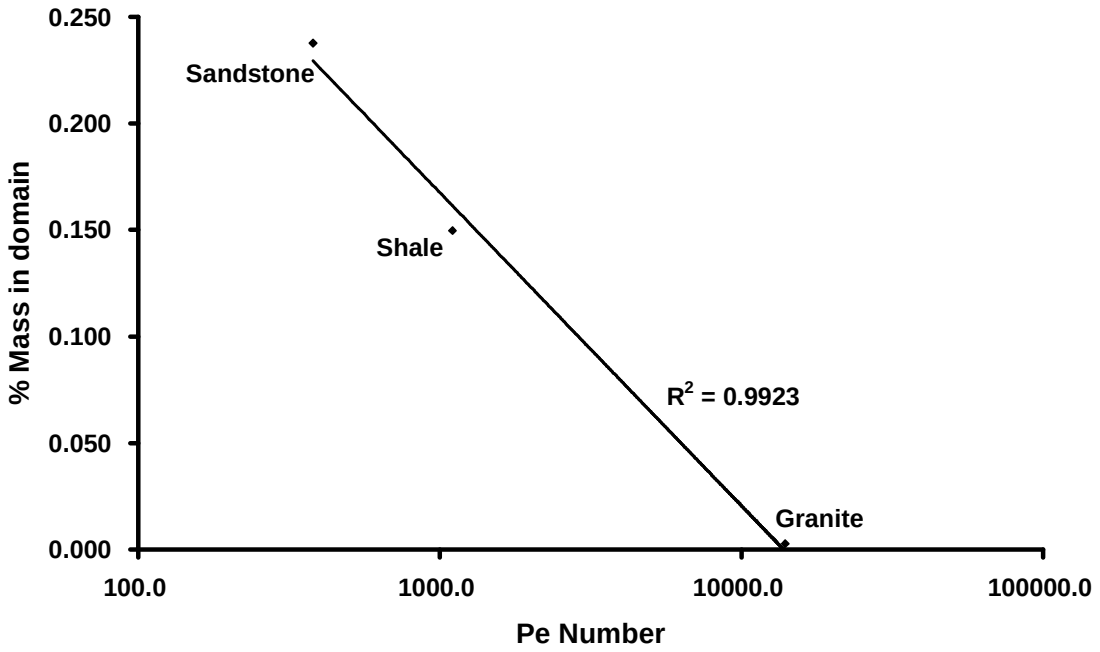

Figure 4.18: Mass of aqueous and sorbed TCE in various rock domains at end of Site Ageing stage (i.e., t_{TOTAL} = 21 years) vs. Peclet number (log scale) for each individual domain.

During the Treatment stage, 45.5 kg (382 moles), 59.6 kg (501 moles) and 538.8 kg (4531 moles) of MnO_4 were injected into the domain for sandstone, shale and granite respectively. The amount of MnO_4 injected is equivalent to 3.4 times, 4.5 times and 40.8 times greater than the theoretical MnO_4 mass required to destroy all the TCE in the domain at the start of the Treatment stage. The differences in MnO_4 mass injected are due the differences in bulk effective horizontal hydraulic conductivity while treatment period, injection concentration and hydraulic gradient were all held constant.

As demonstrated in Figure 4.19, the total moles of aqueous TCE destroyed is 5.94 moles, 17.7 moles and 2.26 moles for sandstone, shale and granite respectively. This mass destroyed is equivalent to 10.7%, 34.8% and 44.5%, respectively, of the initial mass

present in the respective domains prior to the Treatment stage. It is not surprising that the percentage of TCE mass destroyed increases as the depth of penetration of TCE into the matrix decreases, since the TCE is more available for reaction in the fractures than the matrix. In terms of efficiency, measured as the moles of TCE destroyed per moles of MnO_4 injected, the values for the sandstone, shale, and granite are 0.016, 0.035, and 0.0005, respectively. In all 3 rock types, the majority (specifically 69% – 91%) of the total mass destroyed was accomplished in the first 4 months of the two-year Treatment period. The change in slope (i.e., rate of mass destruction) indicates that the injected MnO_4 destroys the contaminant mass easily accessed, in the fracture and stored in the matrix immediately adjacent to the fractures, at early time but is less able to access the TCE mass deeper in the matrix in all rock types. It is noted that MnO_4 has a diffusion coefficient of the same order of magnitude as TCE and, since it is not subject to sorption (i.e., R=1), its diffusive flux into the matrix is approximately one (sandstone) to two (shale and granite) orders of magnitude greater than TCE.

Recall that diffusive flux is highest for the sandstone, decreased one order of magnitude for shale, and decreased two orders of magnitude for granite. This, in part, explains the poor loading of TCE into the matrix for granite (discussed above, Figures 4.16 and Figure A9, Appendix A) and the limited extent of TCE destruction (Figure 4.19). This also helps account for the observed differences between sandstone and shale in the Figure 4.19 despite the similar initial mass of TCE present in the domain (7.3 kg for sandstone and 6.8kg for shale) at the beginning of the Treatment period. It is noted that, in the case of shale, the end of TCE destruction after 1 year in Figure 4.19 suggests that this is

the length of time required for the MnO_4 to reach the limit of the TCE diffusion halo in the matrix, at least within the small portion of the domain that MnO_4 actually penetrated (this is confirmed by Figure A10 in Appendix A). Figure A11 (a) and (b) in Appendix A further demonstrates that after 1 year of MnO_4 injection, aqueous TCE concentration both within the matrix and fracture of the shale domain remained relatively constant over time. On the other hand, Figure A11 (c) (Appendix A) revealed MnO_2 continued to increase over time until the end of the Treatment stage (i.e., t_{TOTAL} = 23 years); this indicates that a majority of injected MnO_4 after the first year of Treatment was consumed by the organic carbon within the matrix. However, the same figures for sandstone (Figures 4.5 and 4.19) indicate that additional TCE would have been destroyed if the treatment period had been extended since the rate of mass destruction was still increasing and matrix contamination persisted.

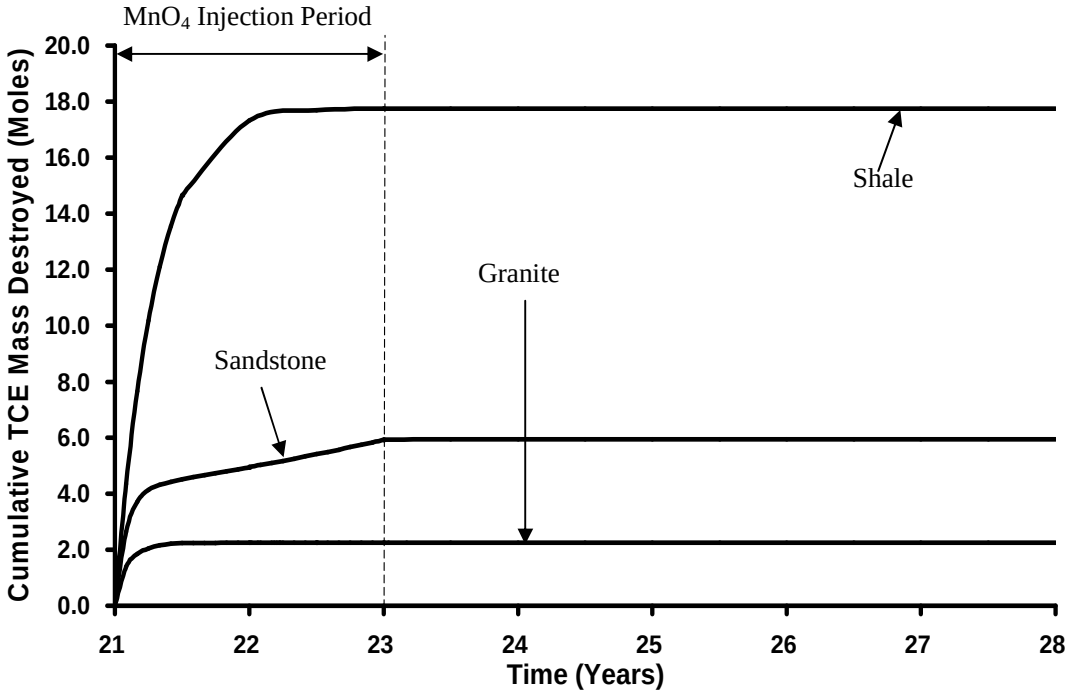

Figure 4.19: Cumulative mass of TCE destroyed for various rock types.

4.5.2.4 Sensitivity to DNAPL Type

In this study, results were compared between PCE and TCE; in contrast to the previous simulations, the distribution of DNAPL at the start of the Site Ageing stage was not identical. At the end of the DNAPL Infiltration stage, the average DNAPL saturation was 0.75 while the volume of DNAPL in the domain was 0.008 m^3 (compared to a total fracture volume of 0.012 m^3) with 100% of the nodes in drainage in both simulations. At the end of the DNAPL redistribution stage, the average DNAPL saturation was 0.3 for both TCE and PCE , the volume of DNAPL present was 0.0036 m^3 (5.26 kg) and 0.0037 m^3 (6.03 kg), and the pool to residual ratio was 71:29% and 51:49% for TCE and PCE, respectively (Figures 4.3 and A14 respectively). The higher density of PCE, leading to higher mobility and more DNAPL migration out of the bottom of the domain, is most likely the cause of the reduced pool-to-residual ratio in that case.

At the end of the Site Ageing stage (t_{TOTAL} = 21 years) the total mass of TCE and PCE in the domain was 7.3 kg (55.6 moles) and 3.3kg (20.2 moles) respectively (Table 4.5). As demonstrated by Figure 4.20, the PCE DNAPL was almost completely dissolved after 16 years of Site Ageing (t_{TOTAL} = 17 years), as compared to only 2.5 years for TCE (base case, Figure 4.8). One reason for this is the lower solubility of PCE (Table 4.4). Another reason is that the PCE DNAPL in the fractures caused reduced relative permeability to water; in conjunction with a fixed gradient, this caused reduced water flux through the source zone. Figure 4.21 confirms that identical boundary conditions resulted in considerably different time series of water discharge (m^3/s) at the exit boundary. Both simulations experience increasing water discharge as DNAPL dissolves

until the maximum is achieved when no DNAPL remains, but the rate of increase varies due to the difference in DNAPL dissolution rates. The reduced aqueous phase relative permeability in the fractures in the presence of PCE DNAPL resulted in reduced water velocities and, in turn, even further reduced aqueous PCE mass flux. Grant and Gerhard (2007b) comment upon this dynamic link between DNAPL saturation and water velocity and its impact on the evolution of source zones in unconsolidated porous media. Of the 3.3 kg (20.2 moles) PCE mass in the domain at the end of Site Ageing, more than 99.9% resided in the sandstone matrix, of which 98.7% was sorbed and only 1.3% remained in the aqueous phase.

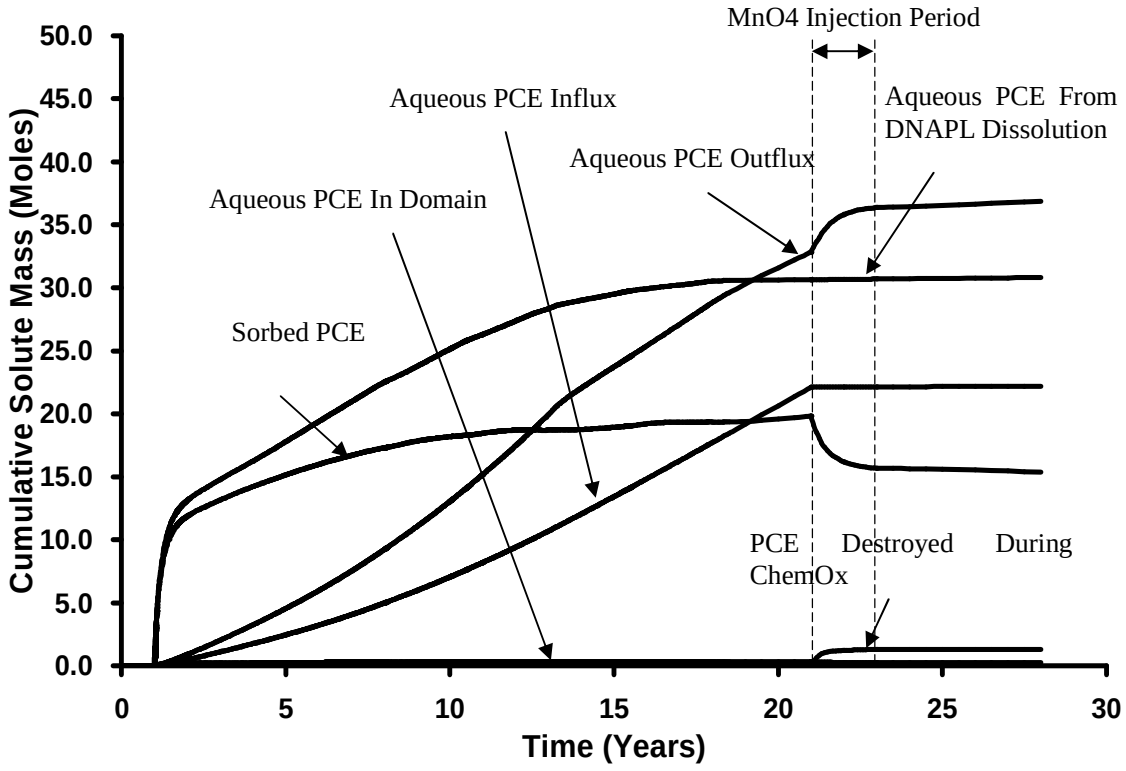

Figure 4.20: Cumulative aqueous and sorbed PCE from all sinks and sources for PCE Simulation.

The distribution of aqueous and sorbed PCE at the end of Site Ageing is shown in Figure A15, Appendix A, as compared to that for TCE at the same time (Figure 4.4). There are a number of reasons why the depth of matrix penetration for PCE is considerably less than TCE. First, the constant concentration of aqueous solvent provided at the upgradient boundary throughout the Site Ageing stage (50% solubility) was much lower for PCE (100mg/L) than TCE (550mg/L). In addition, the R and alpha value for PCE is 60 and 780, while for TCE is 21 and 270, this is because the Koc for PCE is approximately 3 times greater than TCE (Table 4.4). The effective diffusion rate for PCE is 1.88×10^{-10} m^2/s while for TCE it is 2.02×10^{-10} m^2/s. Therefore, the diffusion rate divided by the rock capacity factor for PCE is 2.4×10^{-13}, while for TCE it is 7.4×10^{-13}. For these reasons, although the initial volume of DNAPL was similar in both simulations, the mass present in the PCE domain at the end of the Site Ageing stage (3.3 kg) is much lower than the TCE domain (7.3 kg).

As demonstrated in Figure 4.22, although the total permanganate injected into the domain is similar in both simulations, the total mass destroyed by the injected permanganate is much lower for PCE (1.32 moles) than TCE (5.94 moles). As a fraction of the mass present, this represents 6.5% and 10.7% of the total mass destroyed for PCE and TCE, respectively. The changing rate of chlorinated solvent destruction (i.e., the decreasing slopes in Figure 4.22) is likely due to differences in the distribution of the contaminants in the matrix and the one order of magnitude lower reaction rate between MnO_4 and PCE versus MnO_4 and TCE (Table 4.4).

While it appears for the TCE case that it would have benefited from continued oxidant injection, the PCE case is clearly approaching an asymptotic limit within the two-year treatment period.

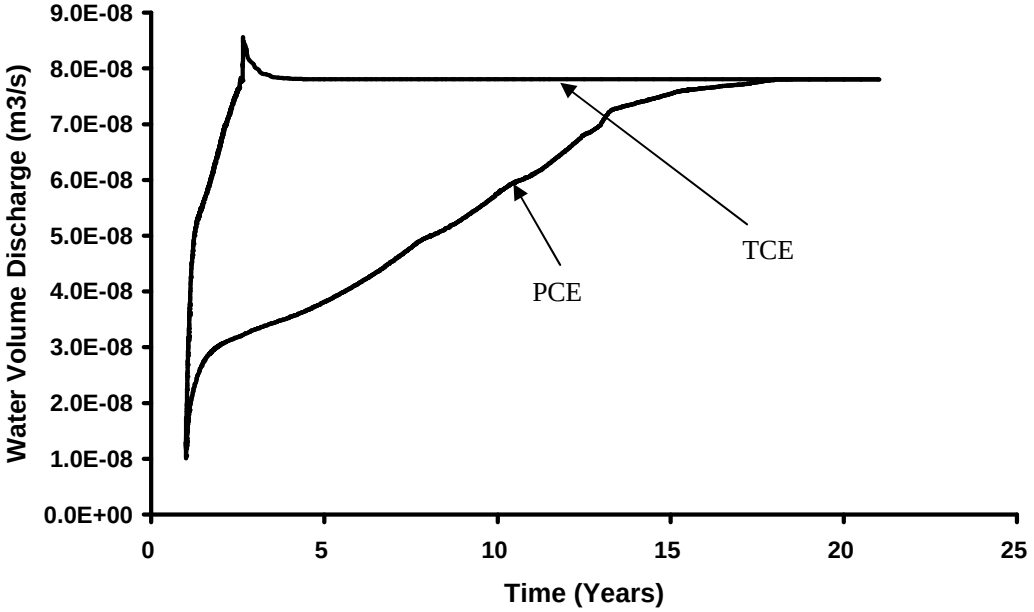

Figure 4.21: Downgradient water volume discharge for (i) TCE and (ii) PCE Simulations.

Figure 4.23 indicates the mass outflux at the boundary rebounds after the Treatment stage as a result of reverse diffusion. This rebound was observed to be much higher in the TCE than the PCE simulation (Table 4.5). This reflects that the same factors that promote increased forward diffusion in the TCE case (lower R, higher concentration gradients due to higher solubility) also result in increased reverse diffusion.

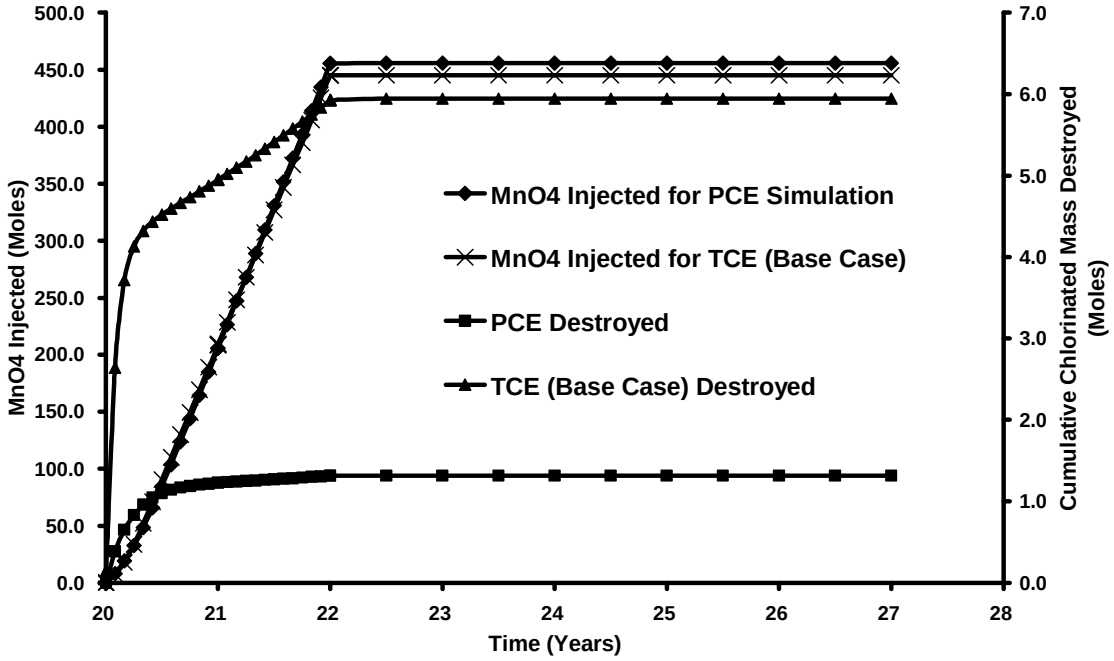

Figure 4.22: Cumulative mass of (i) contaminants mass destroyed (right axis) and (ii) MnO_4 injected.

(a)

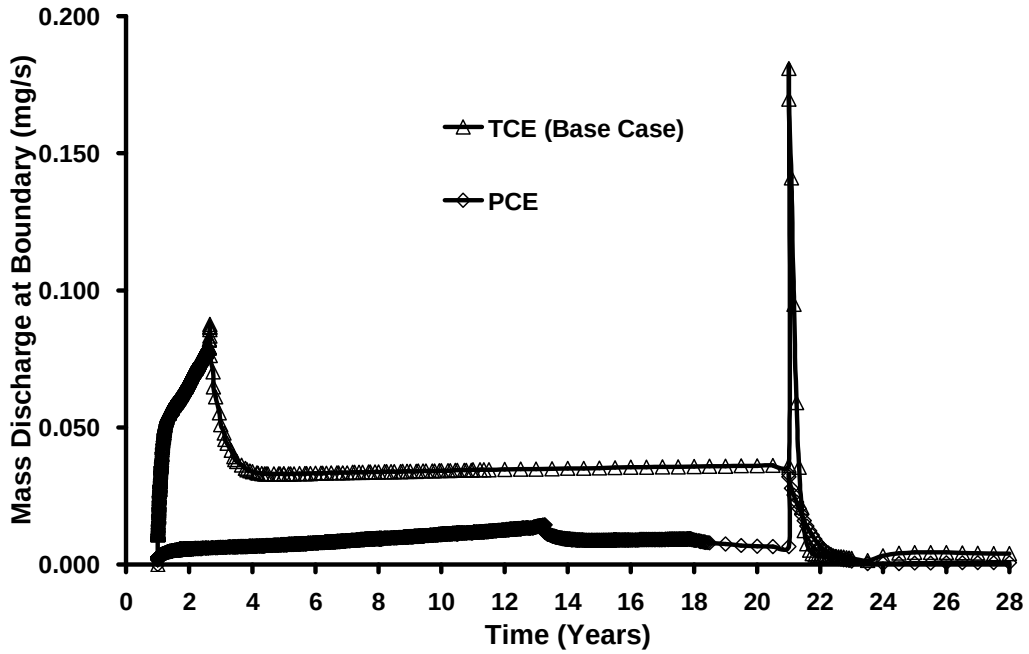

(b)

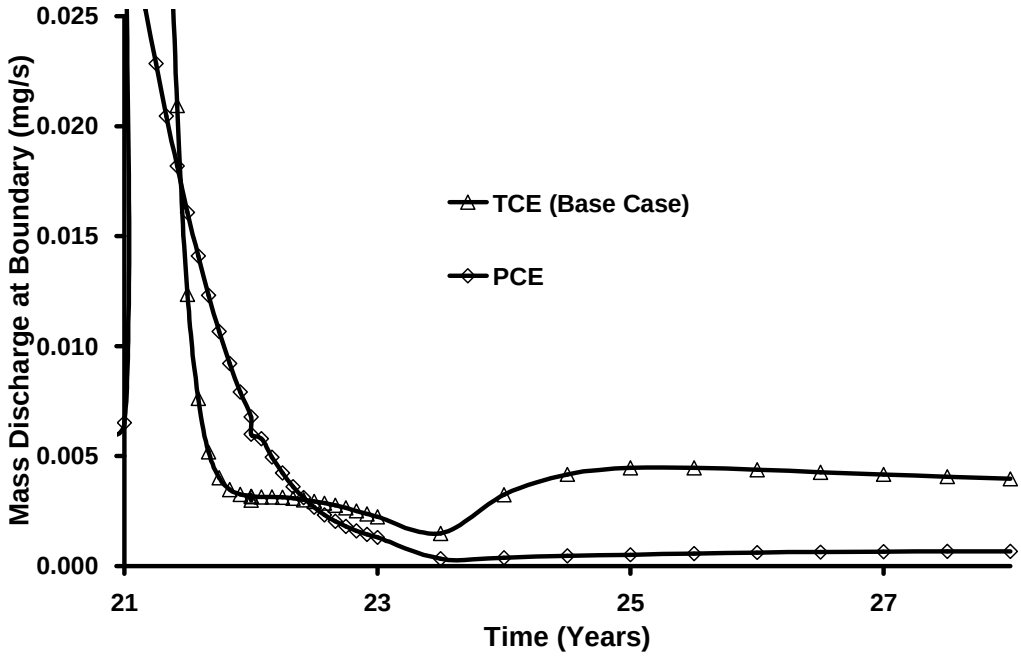

Figure 4.23: Comparison of total boundary mass discharge for (a) various DNAPL (b) Treatment stage only (timescale expanded for clarity).

4.6 CONCLUSIONS

In all of the cases considered here, after 20 years of Site Ageing, the majority (>97%) of the mass in the domain was sorbed to the matrix. The efficiency of oxidant consumption was observed to be poor across the suite of scenarios, with greater than 90% of the injected MnO_4^- consumed by natural oxidant demand.

For scenarios in which diffusive flux is significant (e.g., sandstone/TCE simulations) substantial mass becomes stored in the matrix via forward diffusion. High diffusive flux is promoted by high matrix porosity, high diffusion coefficient, high aqueous solvent concentrations (i.e., high solubility), and low sorptive capacity (i.e., low Koc and/or low foc). The extent to which source zone mass is retained in the matrix was observed to be

inversely proportional to the logarithm of the mean peclet number of the horizontal fractures. Vertical fractures, contaminated by the downward vertical movement of DNAPL and its subsequent dissolution and diffusion, appear to be relatively unaffected by horizontally driven chemical oxidation.

In the high diffusive flux scenarios, permanganate injection appears to be relatively inefficient. Across all the sandstone simulations, the contaminant mass destroyed was never greater than 11% of the total mass present in the domain after injecting never less than 3 times the theoretical demand from TCE. Mass destruction, while highest at early time for the most accessible TCE, did continue at a significant rate throughout the injection period. The same factors that resulted in significant forward diffusion of TCE prior to treatment were observed to result in significant destruction (i.e., forward penetration of MnO_4 and TCE reverse diffusion during treatment, resulting in ongoing treatment of the matrix). Oxidant demand and rate of destruction exceeded supply in all sandstone cases, causing virtually no treatment to occur when injection was not active.

Additionally, in these high diffusive flux scenarios, and for the same reasons, reverse diffusion was significant after treatment ceased. It is not possible in this work to quantify the reduction in mass discharge or concentration rebound associated directly with treatment in the domain due to the upgradient mass flux of contaminant coincidentally terminated at the end of the Site Ageing stage. Chemical oxidation clearly suppressed mass discharge and exit concentrations during active treatment in sandstone. However, following treatment the mass discharge and downgradient

concentrations quickly rebounded to reveal no significant difference relative to a No ISCO case.

Higher mass destruction ratios were observed in the shale and granite scenarios, with TCE mass reduced during treatment 35% and 45%, respectively. However, these scenarios did not exhibit more efficient use of the injected oxidant. Rather, high large scale peclet numbers associated with these rock types were found to correspond to significantly reduced TCE forward diffusion, thereby concentrating the TCE near the fractures and increasing access of the oxidant.

The total mass of PCE destroyed via the injected permanganate was found to be 6.5% of the total mass present in the domain at the start of the Treatment stage. This difference in mass destroyed from the base case (i.e., 10.7%), is mainly due to differences in the distribution of the contaminants in the matrix and the one order of magnitude lower reaction rate between MnO_4 and PCE versus MnO_4 and TCE. The rebound of mass discharge at the boundary after the Treatment stage was observed to be higher in the TCE than in the PCE simulation. The same factors that limit forward diffusion for PCE relative to TCE (increased sorption, reduced concentration gradients) also result in reduced reverse diffusion, resulting in much lower PCE concentration rebound and long term mass discharge at the boundary.

For the sandstone base case investigated, all of the metrics examined proved insensitive to the injection strategy (varied concentration or pulsed injection). Because oxidant

demand and destruction rate always exceeded supply, the only relevant parameter was the total mass of MnO_4 injected. Extrapolating forward, it is estimated that approximately 678 total kg of MnO_4 (15 times the current mass injected) would have been required to destroy the 7.3 kg of TCE present in the domain. In the PCE, shale, and granite cases, no such 'complete treatment' calculation is possible since all observed sharp declines in the rate of destruction after the first 4 months of treatment, indicating that the diffusive flux limitations in these cases were a significant barrier to further clean-up. In all cases, the short duration of the treatment relative to the long duration of site ageing was an impediment to effectively changing the mass discharge in the long term.

It is acknowledged that numerous assumptions and simplifications were employed in this work. In the majority of circumstances, the assumptions were chosen to present a 'best case' scenario that favours effective treatment (e.g., no rind formation, constant injection concentration with elevated gradient, two-dimensional flow with little opportunity for bypassing, etc.). This approach underscores the challenges associated with effectively treating aged source zones in fractured rock with ISCO. The limited number of simulations conducted using specific site templates on a small field scale implies that these results cannot be directly extended to a wide variety of complex real sites. Nevertheless, it is expected that the diffusive flux limitations and OAM demand inefficiencies impeding effective treatment observed here are likely widely applicable to chlorinated solvent-impacted fractured rock scenarios.

CHAPTER 5 – NUMERICAL SIMULATION OF DNAPL SOURCE ZONE REMEDIATION WITH ENHANCED IN SITU BIOREMEDIATION (EISB) IN FRACTURED ROCK

5.1 ABSTRACT

Numerical simulations were conducted to investigate the benefits and challenges of enhanced *in situ* bioremediation (EISB) (with lactate) for trichloroethylene (TCE) and tetrachloroethylene (PCE) DNAPL in fractured rock aquifers at the field scale. An established finite difference multiphase flow-transport-reaction simulator was employed with a gridding routine. Simulations were conducted in two-dimensional cross-section with fracture apertures constant within fractures but varying across the source zone. In each of the 13 simulations conducted, a DNAPL release stage was followed by a 20-year site ageing stage prior to simulating an EISB treatment stage followed by a 5-year post-treatment stage. The suite of simulations examined (i) lactate injection concentration, (ii) pulsed-injection strategy, (iii) bedrock type (sandstone, shale, and granite), and (iv) DNAPL type (TCE and PCE).

The effectiveness of EISB was observed to vary widely across the suite of scenarios. A critical factor was the assumed spatial distribution of the microbial consortium; the TCE mass fraction reduced to ethene decreasing from 74% (microbes assumed to be in the fractures and matrix) to 0.006% (microbes assumed in the fractures only). EISB effectiveness during and after the treatment process was found to be sensitive to total mass of lactate injected but not the rate of lactate injection, pulsed injection, or lactate

concentration. In addition, the results are highly sensitive to the first-order decay rates assigned to the microbes in the matrix, indicating that EISB effectiveness is expected to decrease dramatically with factors such as increased inhibition and competition for hydrogen. Furthermore, it was revealed that DNAPL type and rock type significantly affect EISB performance in the case of matrix bioremediation, with increased performance associated with increased diffusive flux of lactate to the matrix-bound contaminant mass (i.e., source zones characterized by lower peclet numbers). Overall, the results indicate that relatively ideal conditions (i.e., low inhibition, high microbial concentrations throughout the matrix, and low peclet number) are required for EISB to be effective. In contrast with in situ chemical oxidation, the simulations suggest that ongoing EISB treatment of the matrix after lactate injection ceases is possible under these ideal conditions. However, if bioremediation activity is restricted to the fractures, ongoing treatment of back-diffusing contaminant mass is relatively insignificant and no difference in post-treatment downgradient mass discharge is observed from the identical scenario with no EISB applied.

5.2 INTRODUCTION

Enhanced In Situ Bioremediation (EISB) is increasingly being used as a remediation approach for contaminated aquifers. EISB has been demonstrated to effectively remediate/contain the spread of contaminants (including many chlorinated solvents) while converting a significant fraction of their mass to harmless byproducts (National Research Council, 1994). Laboratory and field research conducted over the last decade has shown that micro-organisms that are naturally present in subsurface environments possess the capability to degrade chlorinated ethenes (e.g., tetrachloroethylene (PCE), trichloroethene (TCE), dichloroethylene (DCE) and vinyl chloride (VC)) to non-toxic end-products such as ethene, carbon dioxide, and chloride (Suthersan and Payne, 2005).

Under anaerobic conditions, chlorinated aliphatic hydrocarbons (CAHs) such as PCE may be metabolized by indigenous microorganisms. The reductive dechlorination process results in the sequential transformation of PCE into TCE, DCE, VC, ethene, and finally carbon dioxide and chloride. With each step, a chlorine atom is removed from the compound resulting in a less oxidized molecule. For this natural process to occur, hydrogen (the electron donor) takes the place of chlorine in the CAH (the electron acceptor) during reduction. When the process is documented to proceed without interference this is referred to as natural attenuation. Based on site-specific conditions, including the specific microorganisms present and the availability of hydrogen and nutrients (e.g., phosphorus) required by the microorganisms, the rates and degree of completeness of biodegradation varies between sites (Kozar et al., 2002). Typically, the process can be accelerated via addition of a carbon substrate and/or nutrients

(biostimulation) and even further by injecting a microbial consortium of known degraders (bioaugmentation) (Major et al., 2002).

While hydrogen can be injected directly (e.g., Adamson et al., 2003), more typical is to provide a carbon substrate (e.g., lactate, ethanol, pentanol, glucose) that is converted to hydrogen via fermentative microorganisms (Ellis et al., 2000; Major et al., 2002; Fennell et al., 1997; Carr and Hughes, 1998; Wu et al., 1998; Yang and McCarty, 1998; Yang and McCarty, 2000a)). Engineering design of these technologies is rapidly evolving, although to date there is considerable uncertainty in determining the quantities of carbon substrate required and the impacts of dosing requirements on field performance (Hood et al., 2007). Lactate is one of the most common carbon substrates used in the industry and research studies (Sung et al., 2003; Christ and Abriola, 2007; Hood et al., 2007; Sorenson, 2002). Due to its high solubility, maintaining sufficient concentrations of hydrogen to support EISB typically requires continuous dosing with lactate throughout the treatment period (Major et al., 2002). Emulsified Vegetable Oil (EVOs) on the other hand has been recognized as a promising remediation technique that does not require continue dosing (Long and Borden, 2006). Dechlorination may be slowed or inefficient in the presence of competing electron accepting processes that consume the available hydrogen, including sulphate reduction, iron reduction, and methanogenesis (Chapelle, 1996).

While the majority of laboratory and field work has focused on EISB for relatively dilute CAH plumes, it has been demonstrated that the approach has potential for treating dense

non-aqueous phase liquid (DNAPL) source zones (e.g., Seagren et al., 1994; Yang and McCarty, 2000; Yang and McCarty, 2002). Not only are the fermentors and dehalogenataors able to metabolize CAHs at concentrations previously assumed toxic, the suppression of methanogensis in these environments favours efficient dechlorination (Yang and McCarty, 2000). Furthermore, EISB within the source zone has additional benefits of reducing DNAPL longevity by increasing the driving force for mass transfer to the aqueous phase (Seagren et al., 1994; Yang and McCarty, 2000; Yang and McCarty, 2002; Christ et al., 2005; Amos et al., 2007).

The majority of laboratory work, field trials, and field applications of EISB have been conducted in unconsolidated porous media aquifers (e.g., sands and gravels). However, the nature and extent of these processes in fractured rock are not well-understood. There is some field evidence that biodegradation of chlorinated solvents can occur in the vadose zone of fractured rock settings (e.g., Conrad et al., 1997b), but major questions remain as to how to characterize the extent of naturally occurring biological activity and how to stimulate and monitor it for the remediation of contaminated aquifers. Newell et al. (2006) reported downgradient source concentration decay rates to range from as low as 0.34/year for TCA to 0.11/year for TCE.

Kalish et al. (1964) observed permeability reductions due to bacterial clogging via injection experiments with sandstone cores. It was found that in high permeability, bacterial clogging is limited to 5 to 6 inches, while in low permeability cores clogging zones were noted to be less than 2 inches. It was also found that depending on the

bacteria size, the depth of penetration into the cores can similarly varies. Charbonneau et al. (2006) found that biofilm formed within dolostone cores reduces the effective porosity via radial diffusion experiments with a conservative tracer. In other works, Yu and Pinder (1994) and de Beer et al. (1997) observed significant reductions in effective diffusivity for various solutes due to biofilm formation.

Previously, deep fractured rock vadose zones in arid regions have been thought of as biologically inactive, due to dry conditions and minimal organic matter (Palumbo et al., 1994). Although the numbers of indigenous bacteria are ubiquitous and have been found in such environments, albeit in low numbers, experiments have indicated that their activity may be stimulated with the addition of water, nutrients and organic carbon (Palumbo et al., 1994; Colwell et al., 1992). Additionally, studies of microbial activity in deep fractured granite rock have shown a diverse microbial population to be attached to the fracture walls (Pedersen 1990), and evidence has been presented for natural biodegradation (intrinsic bioremediation) of chlorinated ethenes in a fractured dolomite aquifer (Yager et al. 1997). In general, there is a significant knowledge gap regarding the effectiveness of EISB in fractured rock at the field scale.

Numerous numerical models have been developed for simulating chlorinated ethene transport and degradation. Dechlorination kinetics have been approximated by first-order (Carr et al., 2000; Sleep and Sykes, 1993), Michaelis-Menten (Haston and McCarty, 1999) and Monod-type expressions (Chu et al., 2004; Cupples et al., 2004a,b; Christ and Abriola, 2007). The latter two forms often include limitations on the rate of

dechlorination due to the availability of hydrogen (e.g., Fennell and Gossett, 1998; Amos et al., 2007) and competition between CAHs (Cupples et al., 2004a,b; Yu and Semprini, 2004). Depending on the quantities of alternate electron acceptors present, competition for hydrogen can be neglected (Cupples et al., 2004a; Amos et al., 2007) or included (Fennel and Gossett, 1998; Lee et al., 2004; Christ and Abriola, 2007). A few models consider excessive acid formation limiting the rate of dechlorination (Zhuang and Pavlostathis, 1995; Cope and Hughes, 2001; Lee et al., 2002; Adamson et al., 2004). In general, models that employ first-order decay expressions incorporate all of the sources of limitation implicitly in the rate constant. A few models explicitly include DNAPL dissolution (Carr et al., 2000; Chu et al., 2003; Widdowson, 2004; Amos et al., 2007; Christ and Abriola, 2007). To the author's knowledge, no models have been developed or employed to investigate EISB in fractured rock.

The objective of this work is to examine the benefits and challenges of DNAPL source zone remediation by EISB in fractured rock aquifers. This paper employs numerical simulation to investigate the sensitivity of DNAPL source zone treatment with lactate to a variety of site history and engineering design parameters. In so doing, the research casts light on the fractured rock scenarios under which EISB may be expected to provide cost-effective benefit.

5.3 Model Development

A more detail description on the model development of DNAPL3DRX-FRAC is provided in Chapter 3. The processes described here are aimed to provide the reader with an

understanding of the approach being adopted to develop the bioremediation package of the model.

5.3.1. Bioremediation Equations

For the purpose of this study the subsequent discussion is limited to anaerobic bioremediation of chlorinated solvent DNAPLs employing lactate as the organic substrate.

H_2, the direct electron donor, is obtained via the in situ fermentation of injected lactate and employed by reductive dehalogenating microorganisms to dechlorinate contaminants such as PCE, TCE, DCE, and VC (Cornuet et al., 2000). The fermentation of lactate and of its byproduct acetate may be represented as follows (Macbeth et al., 2004):

$$\underset{\text{Lactate}}{C_3H_5O_3} + 2H_2O \rightarrow \underset{\text{Acetate}}{C_2H_3O_2} + CO_2 + H_2O + 2H_2 \qquad (5.1)$$

$$\underset{\text{Acetate}}{C_2H_3O_2} + 4H_2O \rightarrow 2CO_2 + 2H_2O + 4H_2 \qquad (5.2)$$

Equations 5.1 and 5.2 indicate that each mole of lactate is theoretically capable of producing 6 moles of hydrogen. In reality, a number of factors will reduce the amount of H_2 available to dechlorinating bacteria, such as incomplete fermentation and the presence of competing terminal electron accepting processes (e.g., Yang and McCarty, 1998). Fermentation processes are not explicitly simulated in this work; instead a hydrogen yield coefficient, Y_{H2}, is employed to describe the fraction of the theoretical maximum H_2 available to dechlorinating microorganisms:

$$\text{Lactate} \rightarrow Y_{H2}\ 6[H_2] \qquad (5.3)$$

The microbial mediated sequential reductive dechlorination of PCE and its daughter products are modelled as follows (Clement, 1997):

$$\underset{\text{PCE}}{C_2Cl_4} + H_2 \rightarrow \underset{\text{TCE}}{C_2HCl_3} + HCl \qquad (5.4)$$

$$\underset{\text{TCE}}{C_2HCl_3} + H_2 \rightarrow \underset{\text{DCE}}{C_2H_2Cl_2} + HCl \qquad (5.5)$$

$$\underset{\text{DCE}}{C_2H_2Cl_2} + H_2 \rightarrow \underset{\text{VC}}{C_2H_3Cl} + HCl \qquad (5.6)$$

$$\underset{\text{VC}}{C_2H_3Cl} + H_2 \rightarrow \underset{\text{Ethene}}{C_2H_4} + HCl \qquad (5.7)$$

In 5.9 – 5.12, H_2 is not explicitly modelled as an independent chemical species. Rather, 5.8 is inserted into 5.9 – 5.12, such that $[H_2]$ is replaced by $(1/6)Y_{H2}$ [lactate]. In this way, fermentation is assumed to occur in respond to local (i.e., nodal) demand for H_2 and dechlorination can only proceed in nodes where lactate and chlorinated ethenes are co-located. Moreover, tracking of lactate mass in space and time ensures that the extent of dechlorination at a given node cannot exceed the potential supply of H_2 in a given timestep. In this way, the physical distribution of lactate in the fractures and matrix, relative to the distribution of chlorinated ethenes, is a dominant factor in determining bioremediation success in these simulations.

Hydrogen yield coefficients in the range 0.20 – 1.0 are reasonable depending on the efficiency of the fermentors, fate of acetate, and availability of competing electron accepting processes (Robinson et al., 2009). It is reasonable not to permit H_2 to

build-up and transport in the subsurface since H_2 is typically scavenged by an electron accepting process as soon as it becomes available (Fennell et al., 1997; Yang and McCarty, 1998) and therefore H_2 concentrations in these systems tend to remain very low. Moreover, it is reasonable to simulate that H_2 is generated in response to the presence of H_2 sinks (i.e., electron accepting processes) (Robinson et al., 2009). However, the adopted methodology does imply that all electron accepting processes (dechlorination + others) occur only in tandem when in fact they occur independently.

By using a split-operator approach for transport processes (Clement, 1997; Clement et al., 1998), the relevant kinetic equations treated as first-order processes are as follows (Clement 1997):

$$\frac{d[PCE]}{dt} = -\frac{K_P[PCE]}{R_P} \tag{5.8}$$

$$\frac{d[TCE]}{dt} = \frac{Y_{T/P}K_P[PCE] - K_{T1}[TCE]}{R_T} \tag{5.9}$$

$$\frac{d[DCE]}{dt} = \frac{Y_{D/T}K_T[TCE] - K_{D1}[DCE]}{R_D} \tag{5.10}$$

$$\frac{d[VC]}{dt} = \frac{Y_{V/D}K_{D1}[DCE] - K_{V1}[VC]}{R_V} \tag{5.11}$$

$$\frac{d[ETH]}{dt} = \frac{Y_{E/V}K_{V1}[VC] - K_{E1}[ETH]}{R_E} \tag{5.12}$$

$$\frac{dy[Cl]}{dt} = \frac{Y1_{C/P}K_{P1}[PCE] + Y1_{C/T}K_{T1}[TCE] + Y1_{C/D}K_{D1}[DCE] + Y1_{C/V}K_{V1}[VC]}{R_C} \tag{5.13}$$

where the square brackets [ ] denote molar concentration, *KP, KT1, KD1, KV1,* and KE1 are first-order anaerobic degradation rates{M^{-1} L^3 T^{-1}} for PCE, TCE, DCE, VC, and ETH, respectively; RP, RT, RD, RV, RE, and RC are retardation factors for the

chlorinated ethenes, respective; YT/P, YD/T, YV/D, and YE/V are chlorinated compound yield coefficients for the respective chlorinated ethenes (their values, computed from 5.9 – 5.12, are: 0.79, 0.74, 0.64 and 0.45, respectively); Y1C/P, Y1C/T, Y1C/D, and Y1C/V are yield values for chloride (their values, computed from 5.8 – 5.11, are: 0.21,0.27, 0.37, and 0.57, respectively).

The retardation factor is computed locally from the nodal *foc* concentration (e.g., Fetter, 1993):

$$R_i = 1 + Koc \times foc_i \frac{\rho}{\theta} \quad (5.14)$$

where ρ is the dry bulk density (ML^{-3}), θ is the porosity of the matrix (-), and *Koc* is the organic carbon partition coefficient (L^3M^{-1}) (see Section 4.3.2 for details). Reductive dechlorination is assumed to occur only in the aqueous phase of the chlorinated products (Domenico 1987).

First-order kinetics for dechlorination represents the assumption that there are no rate-limiting factors (e.g., nutrients are in excess, microbial populations not inhibited by, for example, non-neutral pH or high concentrations of chlorinated ethenes). In this study, the microbial populations are not simulated explicitly, but rather are implicitly assumed to be mature populations of constant concentration that are relatively immobile. The model permits the microbial consortium (i.e., fermentors and dechlorinators) to be present on the fracture surface only or in both the fracture and the matrix (as defined by the user). This flexibility is permitted since the depth of penetration of the microorganisms into the matrix; which was found to be dependent on the size of the

microbial involved (Cumbie and MacKay, 1999; Becker et al., 2003; Driese and MacKay, 2004), and the extent of dechlorination occurring in rock matrices remains an open research question.

Equations 5.8 – 5.13 are implemented in the model by employing the inbuilt RT3D sequential dechlorination reaction module. The reaction module was, however, modified to allow for transport and in situ fermentation of lactate to (implicitly) generate H_2. The model explicitly simulates all chlorinated ethenes (PCE, TCE, DCE, VC) as well as their end-products (Cl, ETH) and lactate as mobile aqueous species. RT3D was modified to account for species-dependent diffusion coefficients (West et al., 2008) and to permit the retardation factor of each species to be computed locally from the fraction of organic carbon (f_{oc}) at each node. The adsorption of lactate, however, is assumed to be negligible (Wu et al., 2007).

Using equations 5.4 – 5.13, the simplification 5.3, and robust first-order rate constants for dechlorination results in predictions of bioremediation proceeding to the maximum extent possible at a node for a given timestep limited only by the local availability of lactate at that time. While this is a gross oversimplification of reality, it is appropriate for the simulations in this work that focus on the field scale feasibility of bioremediation in fractured rock from an engineering perspective. This approach ensures that fermentation is not the limiting factor for success in these simulations. Moreover, employing the first-order kinetic approach and rate constants representing healthy dechlorinating populations, there are no geochemical or microbiological limits on the rate

of dechlorination. These generous assumptions create a 'best case' scenario for bioremediation in which the success of the EISB application depends most significantly on the physical flow and transport processes in fractured rock (i.e., the spatial and temporal distribution of lactate and chlorinated ethenes in both fractures and matrix).

5.3.2 Model Verification

A more detail description on the model verification process of DNAPL3DRX-FRAC is provided in Chapter 3. For the purpose of this study the subsequent discussion is limited to the verification of the bioremediation package of the model.

The bioremediation reaction kinetics equations 5.8 – 5.13 were verified by reproducing and comparing the results of a single horizontal fracture simulation using DNAPL3DRX-FRAC and the original inbuilt RT3D sequential dechlorination reaction module in RT3D. Fluid properties and reaction parameters are listed in Table 5.1. Note that in order to effectively compare the results with the original inbuilt RT3D sequential reaction module, the effects of lactate fermentation was neglected in this verification test.

The verification simulation considers a representative sandstone formation at the scale of a localized DNAPL source zone via a two-dimensional domain 20 m wide × 2.25 m high with unit depth. The coarse, uniformly discretized domain employed DX = 0.25m and DY = 0.25m. A single horizontal fracture was defined with an aperture of 128μm. Grid refinement was then conducted using N = 5 together with the 'exponentially increasing' spacing option.

A 5.0m pool of TCE, 1.0m from the left hand boundary, characterized by an effective wetting phase saturation of 0.3 was placed within the fracture at the start of the simulation (Figure 5.1). The watertable was set to be coincident with the top boundary while the bottom boundary permitted the free exit of both water and DNAPL. Side boundaries were modified such that a hydraulic gradient of 0.005 from left to right across the domain was established throughout the entire simulation. DNAPL was then allowed to redistribute for 1 year with no DNAPL dissolution or reactions permitted. Following the cessation of NAPL movement, DNAPL dissolution, aqueous phase transport and EISB were simulated for 1 year. The microbial consortium was assumed to be present in the matrix and fractures equally and the first-order rate constants were applied in the presence of chlorinated compounds since fermentation was ignored. As demonstrated by Figure 5.2 the results generated by DNAPL3DRX-FRAC were an exact match to the results produced by the original inbuilt RT3D sequential dechlorination reaction module.

In order to provide confidence in the in-situ organic substrate fermentation process added to the model, an expanded version of this verification exercise was conducted. All conditions were identical, except that following the end of the first year, the hydraulic gradient was increased to 0.025 for 2 years during which lactate was injected at a constant concentration of 2.0 g/L from the left-hand boundary. At the end of 2 years of lactate injection (i.e., t_{TOTAL} = 3 years), lactate injection was terminated and the hydraulic gradient was reduced back to 0.005. Following the EISB stage, an additional five years were simulated. In this case, dechlorination is only permitted to occur in the presence of sufficient lactate (i.e., H_2) in both the fracture and the matrix.

As demonstrated by Figure 5.3, and in contrast to Figure 5.2, the various TCE daughter products only begin to form when lactate was injected into the domain at t_{TOTAL} = 2 years. Mass balance of chloride, lactate and chlorinated compounds was found to be excellent for both the global domain and for single nodes (figure not shown). These simulations provide confidence in the model to calculate both the bioremediation reaction stoichiomtery (equations 5.3 – 5.7), reaction kinetics (equations 5.8 – 5.13), and the dependence of dechlorination on lactate fermentation as intended.

Table 5.1 Fluid Properties and Reaction Parameters for Verification Simulation

Parameter	Notation	Value
TCE Density [a]	ρ_{NWtce}	1460 kg/m^3
TCE Viscosity [a]	μ_{NWtce}	0.0005 Pa s
TCE Solubility [a]	$Solub_{TCE}$	1100 mg/L
TCE Free Solute Diffusion Coefficient [b]	D^O_{TCE}	1.01 x10^{-9} m^2/s
PCE Free Solute Diffusion Coefficient [b]	D^O_{PCE}	9.40 x10^{-10} m^2/s
DCE Free Solute Diffusion Coefficient [b]	D^O_{DCE}	9.03 x10^{-10} m^2/s
VC Free Solute Diffusion Coefficient [b]	D^O_{VC}	1.06 x10^{-10} m^2/s
Ethene Free Solute Diffusion Coefficient [b]	D^O_{Eth}	1.34 x10^{-9} m^2/s
Chloride Free Solute Diffusion Coefficient [b]	D^O_{Cl}	2.03 x10^{-9} m^2/s
First-Order PCE Degradation Rate [c]	K_{PCE}	0.0413 / Day
First-Order TCE Degradation Rate [c]	K_{TCE}	0.0481 / Day
First-Order DCE Degradation Rate [c]	K_{DCE}	0.0326 / Day
First-Order VC Degradation Rate [c]	K_{VC}	0.0300 / Day
Hydrogen Yield Coefficient	Y_{H2}	0.50

a – Pankow and Cherry (1996)
b –Wilke and Chang (1955) at 25^{o}C
c –Suarez and Rifai (1999)

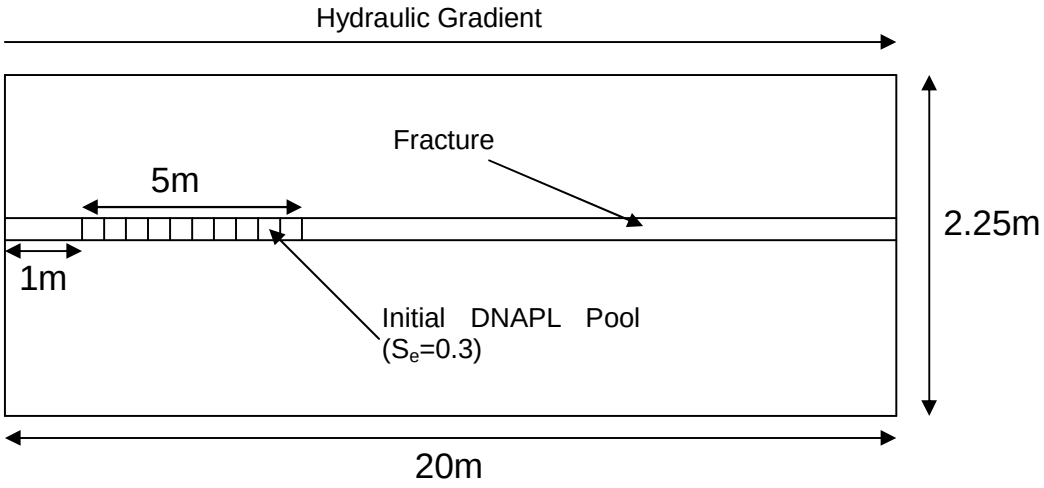

Figure 5.1: Sketch of domain layout for verification simulation.

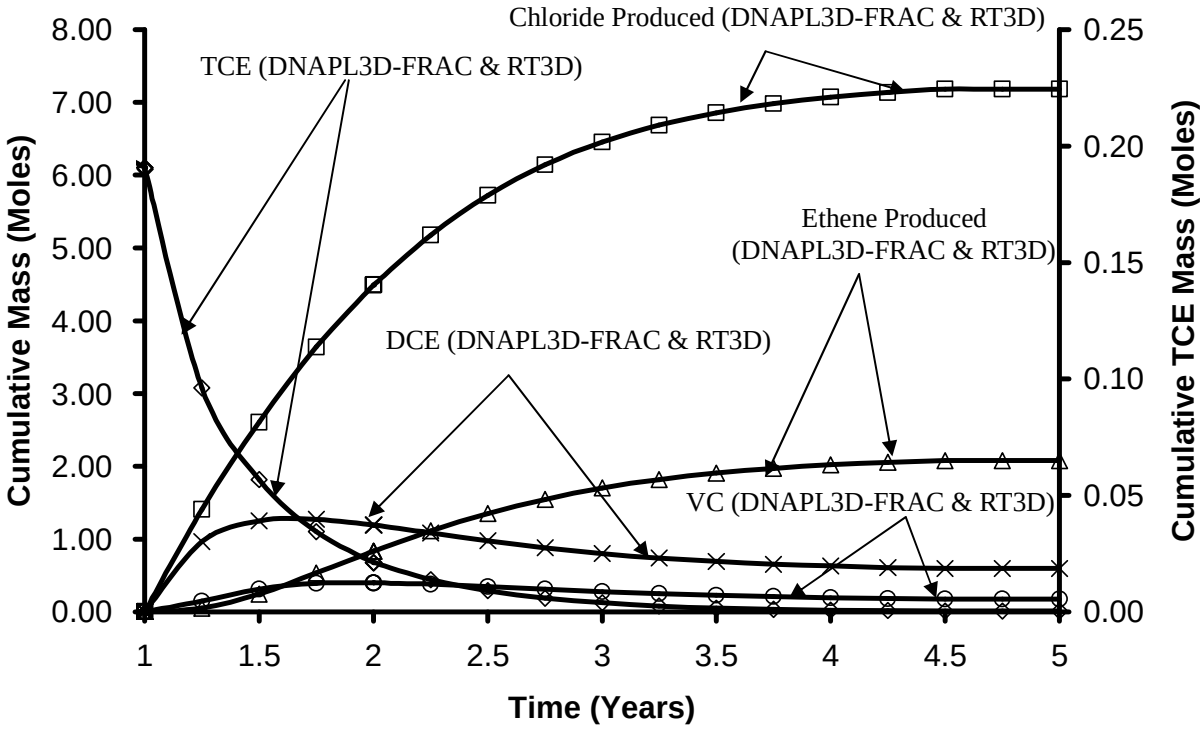

Figure 5.2: Cumulative aqueous mass of TCE and various chlorinated by-products in the domain over time.

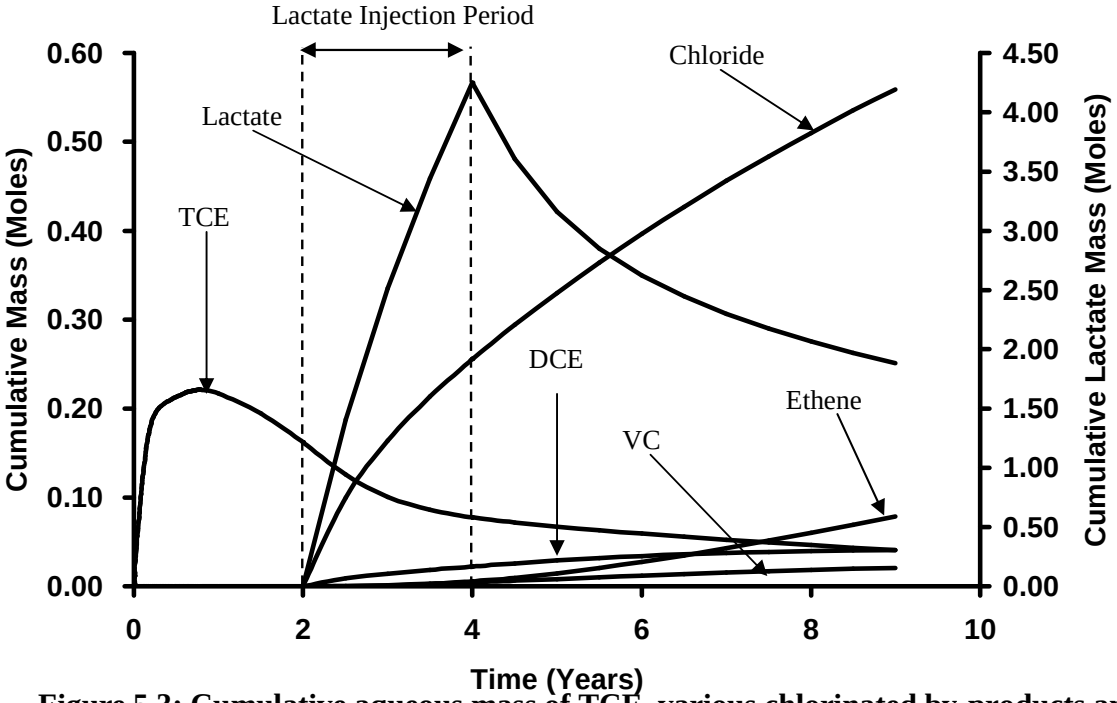

Figure 5.3: Cumulative aqueous mass of TCE, various chlorinated by-products and lactate in the domain over time.

5.4 NUMERICAL SIMULATIONS

5.4.1 Modelled Scenario

This section describes characteristics common to all of the simulations conducted for the bioremediation study (See Section 4.4.1 for the layout of the domain, boundary conditions and the five distinct stages applicable to each simulation), while the next details the characteristics of the individual runs. Note that stages one to three (i.e., i) DNAPL Release, (ii) DNAPL Redistribution, (iii) Site Ageing) are similar for both ISCO and EISB simulations.

During the 'Treatment Application' stage, EISB was initiated by injecting a constant aqueous phase concentration of 2.0g/L lactate (Geosyntec) for 2 years (i.e., 21 yrs $\leq t_{TOTAL} \leq$ 23 yrs) along a fully screened well at the left boundary (with penetration of the

formation assumed only at the horizontal fractures intersecting the well). During lactate application, the hydraulic gradient across the domain was increased to 0.025 to represent active amendment conditions. As well, the upgradient chlorinated solvent injection was terminated (assuming complete and instantaneous treatment of upgradient source zone); while this is unrealistic, it provides the best opportunity for success within the domain and thus supports viewing these results as approximating a best case for the technology. In all cases, stoichiometric calculations confirm that the total mass of lactate injected is greater than the theoretical lactate mass (accounting for the hydrogen yield coefficient assumed, 0.50) to theoretically dechlorinate all TCE and its daughter-products in the domain at the start of the Treatment stage. For example, for the Base Case, 48.5 kg or 545 moles of lactate was injected, compared to the 7.3kg or 55.6 moles of TCE mass in the domain, representing an excess of 980% (given that 1 mole of TCE is reduced to ethene by 1 mole of lactate (via 3 moles of hydrogen, when $Y_{H2} = 0.50$ in Equation 5.3).

Following the Treatment stage, an additional five years were simulated (i.e., 23 yrs $\leq t_{TOTAL} \leq$ 28 yrs). During this Post-Treatment stage, the ambient hydraulic gradient of 0.005 was again employed, but no upgradient concentration of any species (i.e., lactate or chlorinated solvent) was applied.

Several assumptions were employed in this work to facilitate reasonable simulation times:

1. All fractured rock simulations presented are two-dimensional; this assumption likely benefits the technology since the reduced dimensionality is expected to

reduce bypassing of the treatment fluid around DNAPL-occupied fractures;

2. The matrix is presumed to have a sufficient displacement pressure so as to exclude DNAPL entry; this assumption likely benefits the technology because the highest fraction of DNAPL is retained in the fractures which are most accessible to the treatment fluid;
3. Advection of groundwater through the matrix is assumed to be negligible; this is reasonable given that the high permeability contrast between the fractures and matrix. For example, for the sandstone Base Case, the matrix permeability is approximately 6 orders of magnitude less than the average fracture permeability. The Peclet number for the matrix (Pe = vx/D where v is horizontal velocity in matrix) if advection were not neglected is 0.166; since Pe<1 it is reasonable to assume that the matrix is diffusion dominated and advection is negligible (Trivedi et al., 2008).
4. Equilibrium mass transfer from DNAPL to aqueous phase was assumed; this assumption also favours improved performance of the technology by maximizing aqueous phase solvent concentrations.
5. Lactate is assumed not to sorb (Wu et al., 2007) and reductive dechlorination is assumed to occur only in the aqueous phase of the chlorinated products (Domenico 1987).

5.4.2 Base Case and Sensitivity Simulations

Table 5.2 presents the suite of 13 simulations conducted in this study. The Base Case considered a fractured sandstone template site. Table 5.3 presents the parameters

employed to characterize the sandstone as well as the other two rock types (shale and granite). The sandstone domain, employed in all simulations except Run 10 and Run 11, is presented in Figure 5.4a. The sandstone parameters were chosen to be broadly representative of North American sandstone aquifers (e.g., Lipson et al., 2005). Table A1 (Appendix A) provides, for each rock type, the observed ranges for each parameter synthesized from the literature. Table 4.3 reveals that this sandstone exhibits - relative to the other template rock types - low fracture density, low mean aperture (125µm), high matrix porosity (7.7%), and intermediate foc (0.005).

The Base Case employed TCE as the DNAPL released and as the aqueous phase and sorbed chlorinated compound subsequently targeted by EISB. Fluid properties and reaction parameters are listed in Table 5.4. The Base Case also employed a continuous injection of lactate at 2.0 g/L for 2 years during the Treatment stage (Table 5.2).

Table 5.2 Field Scale EISB Fractured Rock Simulations

Run No.	DNAPL Type	Material	Lactate Concentration (mg/L)	Rate	Pulsing Strategy	Bioremediation Location
1 (Base Case)	TCE	Sandstone	2000	Mean	Continuous Lactate Injection for 2 Years	Fracture + Matrix
2	TCE	Sandstone	2000	Mean	Continuous Lactate Injection for 2 Years	Fracture
3	TCE	Sandstone	2000	High	Continuous Lactate Injection for 2 Years	Fracture + Matrix
4	TCE	Sandstone	2000	Low	Continuous Lactate Injection for 2 Years	Fracture + Matrix
5	TCE	Sandstone	2000	Mean	3 Months on 3 Months Off for 4 Years	Fracture + Matrix
6	TCE	Sandstone	2000	Mean	6 Months on 6 Months Off for 4 Years	Fracture + Matrix
7	TCE	Sandstone	2000	Mean	1 Year on 1 Year Off for 4 Years	Fracture + Matrix
8	TCE	Sandstone	1000	Mean	Continuous Lactate Injection for 4 Years	Fracture + Matrix
9	TCE	Sandstone	4000	Mean	Continuous Lactate Injection for 1 Year	Fracture + Matrix
10	TCE	Shale	2000	Mean	Continuous Lactate Injection for 2 Years	Fracture + Matrix
11	TCE	Granite	2000	Mean	Continuous Lactate Injection for 2 Years	Fracture + Matrix
12	PCE	Sandstone	2000	Mean	Continuous Lactate Injection for 2 Years	Fracture + Matrix
13	TCE	Sandstone	0	Mean	No Treatment	Fracture + Matrix

Table 5.3 Properties of Field Scale Fractured Rock Template Sites

Rock Type	Fracture Spacing (m)	Matrix Permeability (m^2)	Matrix Porosity	Foc	Bulk Density (g/cm^3)	Matrix Tortuosity	Fracture Aperture Range (μm)	Mean Aperture (μm)
Sandstone	6.0 (Ver) [*] 1.0 (Hor) [a]	1.05×10^{-15}	7.7% [a]	0.005 [a]	2.49 [a]	0.2 [a]	25 - 230 [a]	125
Shale	4.0 (Ver) [*] 1.0 (Hor) [*]	1.05×10^{-15}	3.0% [b]	0.009 [*]	2.619 [**]	0.1 [*]	50 - 250 [c]	150
Granite	2.0 (Ver) [d] 2.0 (Hor) [d]	1.05×10^{-15}	0.1% [*]	0.0005 [*]	2.697 [**]	0.05 [*]	100 - 500 [e]	300

[a] *Lipson et al., 2005*
[b] *Morris and Johnson, 1967*
[c] *Jardine et al., 1999*
[d] *Sousa 2007*
[e] *Sausse 2002*
**Data supplied by B.H Kueper (personal communication) based upon consulting experience on sites of all three rock types.*
*** Calculated using Bulk Density = Grain Density x (1-porosity), assuming a grain density of 2.7 for Shale and Granite.*
Ver – Vertical Fractures
Hor – Horizontal Fractures

Table 5.4 Fluid Properties and Reaction Parameters

Parameter	Notation	Value
TCE Density [a]	ρ_{NWtce}	1460 kg/m^3
TCE Viscosity [a]	μ_{NWtce}	0.0005 Pa s
TCE Solubility [a]	$Solub_{TCE}$	1100 mg/L
PCE Density [a]	ρ_{NWpce}	1630 kg/m^3
PCE Viscosity [a]	μ_{NWpce}	0.0009 Pa s
PCE Solubility [a]	$Solub_{PCE}$	200 mg/L
TCE Free Solute Diffusion Coefficient [b]	D^O_{TCE}	1.01 x10^{-9} m^2/s
PCE Free Solute Diffusion Coefficient [b]	D^O_{PCE}	9.40 x10^{-10} m^2/s
DCE Free Solute Diffusion Coefficient [b]	D^O_{DCE}	9.03 x10^{-10} m^2/s
VC Free Solute Diffusion Coefficient [b]	D^O_{VC}	1.06 x10^{-10} m^2/s
Ethene Free Solute Diffusion Coefficient [b]	D^O_{Eth}	1.34 x10^{-9} m^2/s
Chloride Free Solute Diffusion Coefficient [b]	D^O_{Cl}	2.03 x10^{-9} m^2/s
Lactate Free Solute Diffusion Coefficient [c]	D^O_{Lac}	2.57 x 10^{-9} m^2/s
First-Order PCE Degradation Rate [d]	K_{PCE}	0.0413 / Day
First-Order TCE Degradation Rate [d]	K_{TCE}	0.0481 / Day
First-Order DCE Degradation Rate [d]	K_{DCE}	0.0326 / Day
First-Order VC Degradation Rate [d]	K_{VC}	0.0300 / Day
Hydrogen Yield Coefficient	Y_{H2}	0.50

a – Pankow and Cherry (1996)
b –Wilke and Chang (1955) at 25^{o}C
c – Lide (2004)
d – Suarez and Rifai (1999)

As illustrated in Table 5.2, Runs 5 - 9 examine variations in treatment strategy, while Runs 2 - 4 and 10 - 12 explore the influence of site conditions. All parameters, boundary conditions, and source conditions were established identically to the Base Case for all simulations, except for changing the parameter(s) whose influence was being examined in each study. It is noted that for all simulations except Runs 10, 11 and 12. the results during the DNAPL Release, DNAPL Redistribution, and Site Ageing stages are identical with the differences occurring from the start of the Treatment stage.

It is noted that a 'No EISB' case was simulated for comparison purposes. This simulation was identical to the Base Case in all respects but one: no lactate was injected during the Treatment stage. As a result, no fermentation or reductive dechlorination processes were simulated in this simulation.

5.4.2.1 Microorganisms in Fractures/Matrix

Although bacteria has been known to reside within both fractures and matrix (Crow, 1968; National Research Council, 1984), in order to examine the influence of the spatial distribution of microorganisms in fractured rock aquifers, the Base Case (Run 1) assumed significant biological activity in both the fractures and in the matrix (homogeneously distributed) while Run 2 assumed the microbiological consortium being present only in the fractures. This sensitivity study comprised two simulations, representing the endpoints of a spectrum of possible configurations.

5.4.2.2 Dechlorination Rate Parameters

The overall influence of the rate at which the chlorinated ethenes are being dechlorinated was examined. It is known that the dechlorination rate parameters can vary significantly depending on many factors including the scale and format of the study (e.g., microcosm, column, or field) (Suarez and Rifai, 1999), the type of microbial community present (Yu and Semprini, 2004), microbial concentration (Fennell et al., 1997), and a wide variety of inhibiting factors such as pH (Lowe et al.,1993), H_2S concentrations (Kalyuzhnyi et al., 1997), PCE/TCE toxicity (Bailey 1986), etc. In this study, a first-order approach is employed that lumps all of these effects together, allowing an investigation of the impact of modified dechlorination rates without reference to the specific cause of the modification. The first-order rate parameters used in this study were obtained from Suarez and Rifai (1999). The first-order rate parameters for all chlorinated ethenes in Run 3 are increased by one order of magnitude while the rate parameters used in Run 4 are decreased by one order of magnitude relative to the Base Case. These values are representative of rates recorded from previous laboratory experiments and previous sites respectively. This sensitivity study comprised three simulations.

5.4.2.3 Pulsed Injection of Organic Substrate

The effects of pulsing were examined by subdividing the Base Case injection period (2 years) into periodic, equal length lactate injection on and off intervals. Pulsed injection intervals of 3 months (Run 5), 6 months (Run 6) and 12 months (Run 7) were examined. Pulsed treatment has been demonstrated to be valuable in other DNAPL remediation options, such as waterflooding (Gerhard et al., 2001) and is often considered for other

treatment options involving injected fluids to reduce operation and maintenance costs while maintaining performance (e.g., reducing biofouling of wells during enhanced bioremediation). In all cases, the application period was adjusted so that the total mass of lactate injected was identical. This sensitivity study comprised four simulations.

5.4.2.4 Organic Substrate Concentration

To examine the influence of lactate concentration, the concentration at the injection well was halved (1 g/L, Run 8) and doubled (4 g/L, Run 9) relatively to the Base Case. In order to ensure that the total mass of lactate injected was kept constant, the injection period was changed accordingly (4 years and 1 year, respectively). This sensitivity study comprised three simulations.

It is noted that these simulations also represent a sensitivity study to Y_{H2} (i.e., hydrogen yield for dechlorination per mole of lactate). Run 8 represents a Y_{H2} of 0.25 (i.e., decreased efficiency, for example due to high sulphate concentrations in the groundwater) and Run 9 represents a Y_{H2} of 1.0 (i.e., perfect efficiency, complete fermentation of lactate and acetate to H_2 and no competition or losses) for a 2g/L lactate injection concentration. The study can be viewed from either perspective, since the model is formulated (equation 5.3) such that the extent of dechlorination is dependent upon the product of the molar concentration of lactate and the yield coefficient.

5.4.2.5 Rock Type

Runs 1, 10, and 11 compare EISB performance in three different types of fractured rock

at the field scale, each exhibiting a characteristic set or range of hydrogeological parameters (Table 5.3). Figure 5.4 presents the distribution of intrinsic permeability for the three domains, illustrating the distribution of fractures. In each case, the mean aperture is at the midpoint of the range specified in the table. It is noted that, characteristic of these rock types in natural environments, the shale template site exhibits (relatively) intermediate fracture density, low mean aperture (150μm), intermediate matrix porosity (3%), and high *foc* (0.009) while the granite exhibits high fracture density, high mean aperture (300μm), low matrix porosity (0.1%), and low *foc* (0.0009).

5.4.2.6 DNAPL Type

Runs 1 and 12 compare performance for both TCE and PCE in the sandstone domain. The full set of PCE fluid parameters employed for Run 12 is presented in Table 5.4. Note that while the boundary conditions in each run were identical, the distribution of DNAPL resulting from infiltration and redistribution were different due to the contrasting fluid properties. As well, different solubilities and sorptive capacities resulted in different distributions of aqueous phase and sorbed phase concentrations after the Site Ageing stage. This sensitivity study comprised two simulations.

5.5 RESULTS AND DISCUSSION

Table 5.5 summaries a selection of key numerical results for all 13 simulations conducted in this study. These data will be discussed as each set of simulations is presented.

Table 5.5: Summary of Results for All ISCO Simulations

Run No.	DNAPL St 2 (kg)	DNAPL St 3 (kg)	Aq + Sorb St 3 (kg)	Lactate Inject (kg)	DNAPL St 5 (kg)	Aq + Sorb St 5 (kg)	Mass Discharge St 5 (10^{-3} mg/s)	Lact React (kg)	CS React (kg)
1	5.26	0.00	7.3	48.5	0.00	0.018	0.017	3.180	7.77
2	5.26	0.00	7.3	48.5	0.00	5.140	3.885	0.017	0.07
3	5.26	0.00	7.3	48.5	0.00	0.000	0.000	2.200	8.97
4	5.26	0.00	7.3	48.5	0.00	2.940	2.340	0.724	2.45
5	5.26	0.00	7.3	48.5	0.00	0.003	0.003	3.530	7.83
6	5.26	0.00	7.3	48.5	0.00	0.003	0.003	3.450	7.83
7	5.26	0.00	7.3	48.5	0.00	0.003	0.003	3.181	7.83
8	5.26	0.00	7.3	48.5	0.00	0.003	0.003	3.521	7.83
9	5.26	0.00	7.3	48.5	0.00	0.041	0.040	2.895	7.70
10	6.86	0.01	6.8	35.1	0.00	0.971	0.293	2.902	0.61
11	11.53	4.23	0.68	436.3	4.10	0.378	0.017	0.001	0.01
12	6.03	0.11	3.3	48.5	0.04	0.474	0.116	1.181	2.61
13	5.26	0.00	7.3	0.0	0.00	5.180	3.956	0.000	0.00

St 2 = mass present at the end of Stage 2 (DNAPL redistribution)
St 3 = mass present at the end of Stage 3 (Site Ageing)
St 5 = mass present at end of Stage 5 (Post-Treatment)
DNAPL = mass of DNAPL present
Aq + Sorb = combined mass of aqueous and sorbed chlorinated solvent present
Lactate Inject = mass of lactate injected during the treatment period
Mass Discharge = mass per time of chlorinated solvent leaving the domain at the end of Post-Treatment stage
Lact React = total mass of lactate that reacted with chlorinated solvent in all phases
CS React = total mass of chlorinated solvent (in all phases) dechlorinated

5.5.1. Base Case Results

Figures 5.5a and 5.5b illustrate the distribution of the TCE DNAPL at the end of the infiltration and redistribution phases, respectively (relevant to all simulations except Runs 10, 11, and 12). Figures 5.5a and 5.5b reveal a heterogeneous distribution of DNAPL pools (i.e., connected phase) and residual (i.e., trapped blobs and ganglia) due to the influence of capillary forces (and, specifically, fracture entry pressures), the order of encounter of fractures, and the permeability contrasts between fractures. At the end of the DNAPL infiltration stage, the average DNAPL saturation was 0.75, the mass of

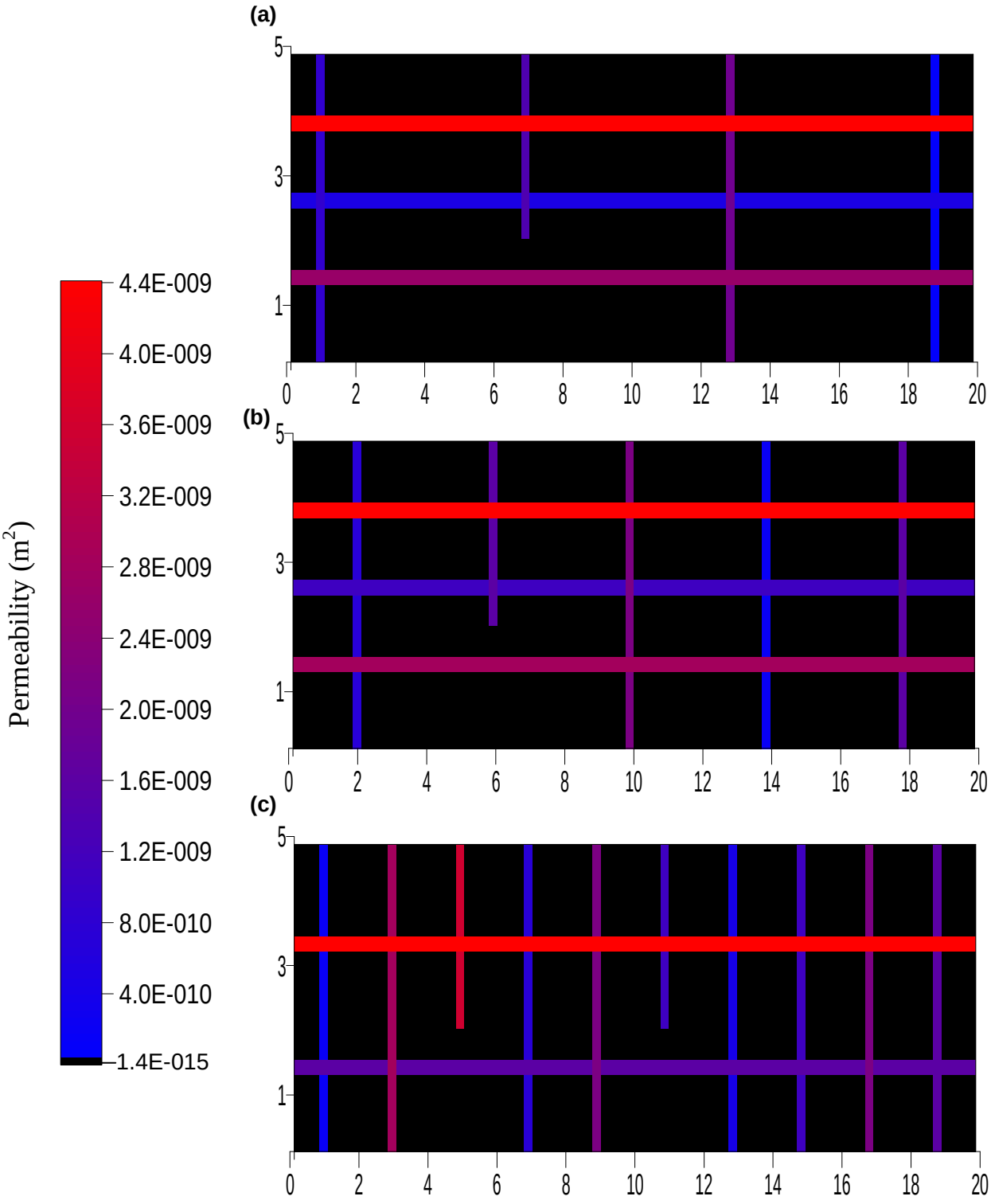

Figure 5.4 Distribution of permeability for the field scale fractured rock domains: (a) sandstone, (b) shale, and (c) granite. Colour corresponds to fracture permeability according to the scale bar provided; matrix permeability is uniform (black). Note that fracture apertures are exaggerated for visual purposes.

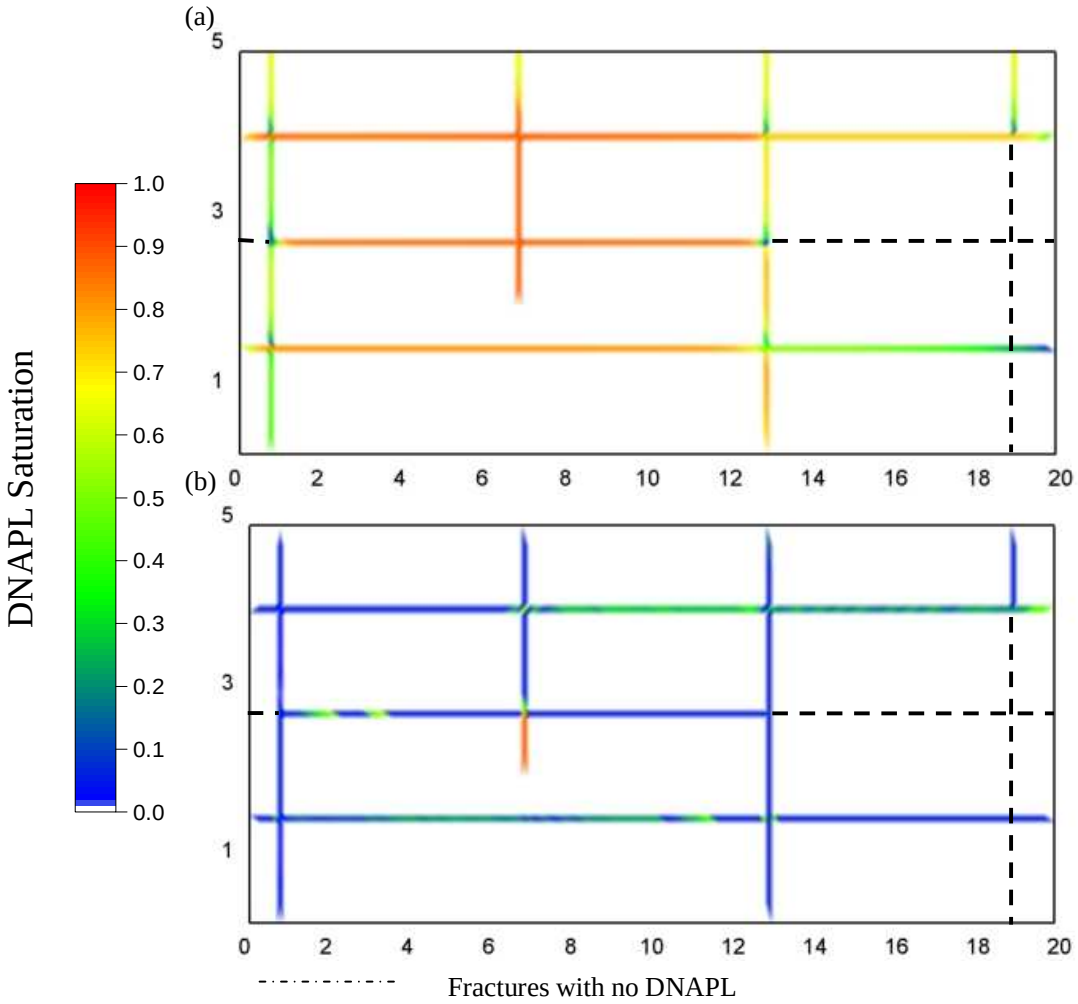

Figure 5.5: DNAPL distribution for Base Case at (a) t_{TOTAL} = 0.5 years when DNAPL inflow and outflow are equal, and (b) t_{TOTAL} = 1 year when all DNAPL migration has ceased.

DNAPL in the domain equaled 11.68 kg, the DNAPL volume was 0.008 m^3 (compared to a total fracture volume of 0.012 m^3) with 100% of the nodes on drainage (i.e., DNAPL displacing water). At the end of DNAPL redistribution stage, the average DNAPL saturation was 0.3, the DNAPL volume was 0.0036 m^3 (equal to a mass of 5.26 kg) and the pool to residual ratio was 71:29%. Note in Figure 5.5b that, as expected, the lone remaining pool exhibiting a high DNAPL saturation resides in a vertical dead-end fracture, and other pools of various lengths occur in horizontal fractures, separated by

areas of residual DNAPL.

Figure 5.6 illustrates the distribution of aqueous phase TCE at the end of the 20 year Site Ageing stage (t_{TOTAL} = 21 years). Evident are the expected diffusion halos in the sandstone matrix blocks adjacent to fractures containing DNAPL as well as those horizontal fractures without DNAPL but subject to significant aqueous mass flux (Figure 5.5b). At this time, no DNAPL remained in the domain. This occurred despite the constant influent concentration equal to 50% of TCE solubility. The reason is the substantial TCE sink provided by matrix diffusion and sorption. At this time, the total mass of TCE in the domain was 7.3 kg, of which 99% resided in the matrix; of the mass in the matrix, 98% was sorbed and only 2% remained in the aqueous phase. It appears that the matrix acts as a substantial sink for TCE, rapidly promoting DNAPL dissolution and solvent diffusion.

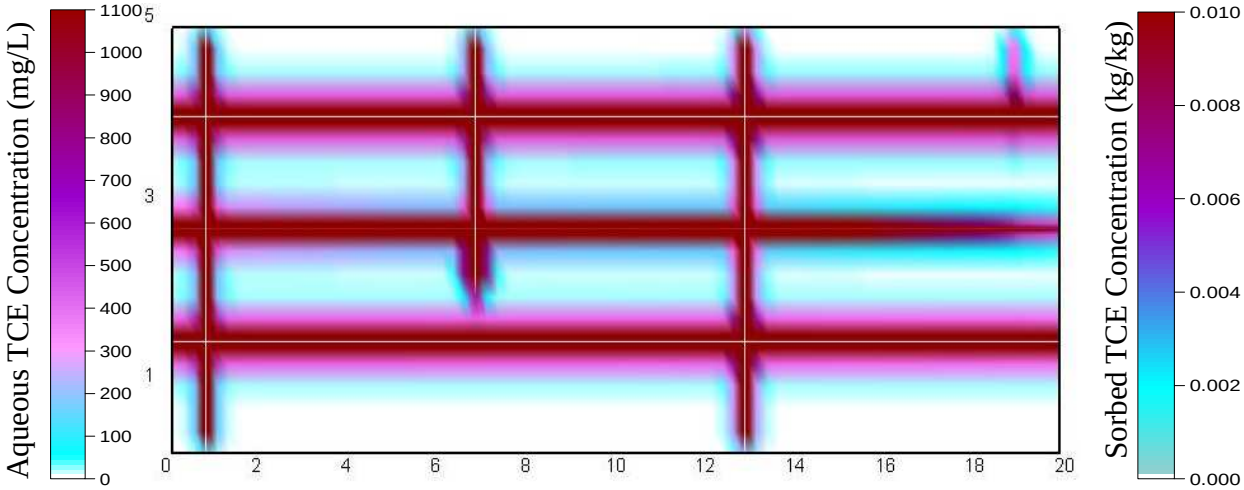

Figure 5.6: Distribution of aqueous and sorbed TCE after 20 years (t_{TOTAL} = 21 years) of DNAPL dissolution (i.e., Site Ageing stage).

Figure 5.7 provides the concentration of aqueous TCE and its various daughter-products throughout the domain after the Treatment stage (i.e., 2 years of lactate injection, t_{TOTAL} = 23 years). It reveals that the majority of the initial aqueous TCE mass present in the domain has been converted to daughter-products. It is noted that, by this time, the injected lactate has successfully penetrated the full extent of all the three horizontal factures present in the domain as well as a significant distance into the matrix. Figure 5.7e further demonstrates that chloride, a commonly used measure of the extent of reductive dechlorination, was present to some degree in most of the domain.

Figure 5.8 presents the concentration of aqueous TCE and its daughter-products throughout the domain at the end of the Post-Treatment stage (i.e. 5 years after lactate injection, t_{TOTAL} = 28 years). During this stage, further dechlorination of all chlorinated ethenes was observed; the lactate remaining (Figure 5.7f) clearly provided a continuing source of electron donor. This is confirmed by further decreases in the spatial distribution of TCE, DCE and VC (Figures 5.8a, b, and c, respectively) and the simultaneous increase in ethene and chloride concentration (Figures 5.8d and e). Figure 5.8f reveals that lactate has widely penetrated the domain and is nearing depletion within and near both horizontal and vertical fractures. Moreover, there is a strong correlation between the areas of lactate depletion and high concentrations of the non-toxic products ethane and chloride. Thus, while reverse diffusion and fracture flushing no doubt is occurring in the Post-Treatment phase, the figures suggest that significant dechlorination continues to occur within fractures and within the adjacent matrix.

(a)

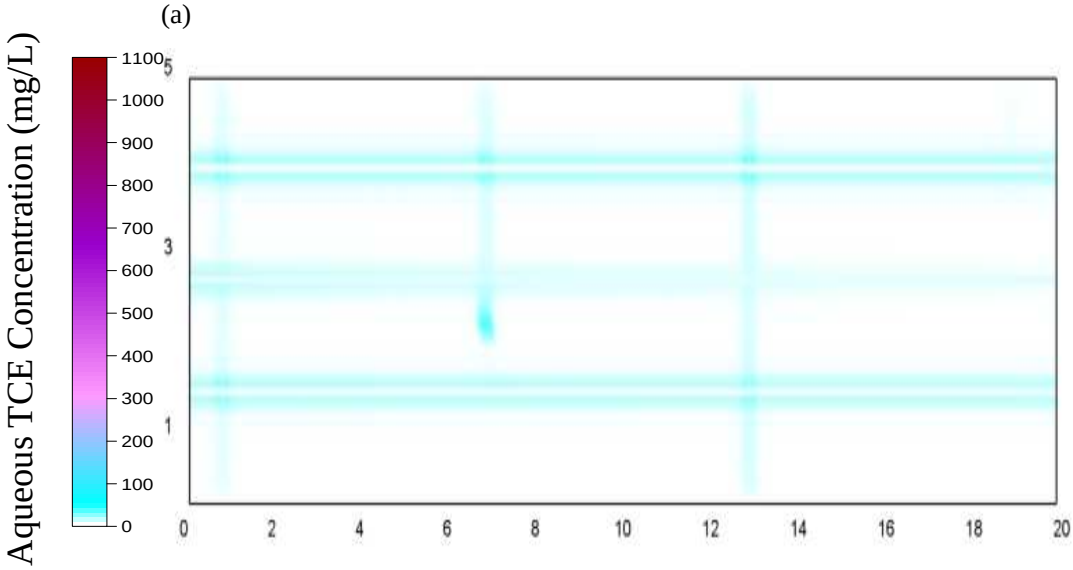
Aqueous TCE Concentration (mg/L)
1100
1000
900
800
700
600
500
400
300
200
100
0
5
3
1
0
2
4
6
8
10
12
14
16
18
20

(b)

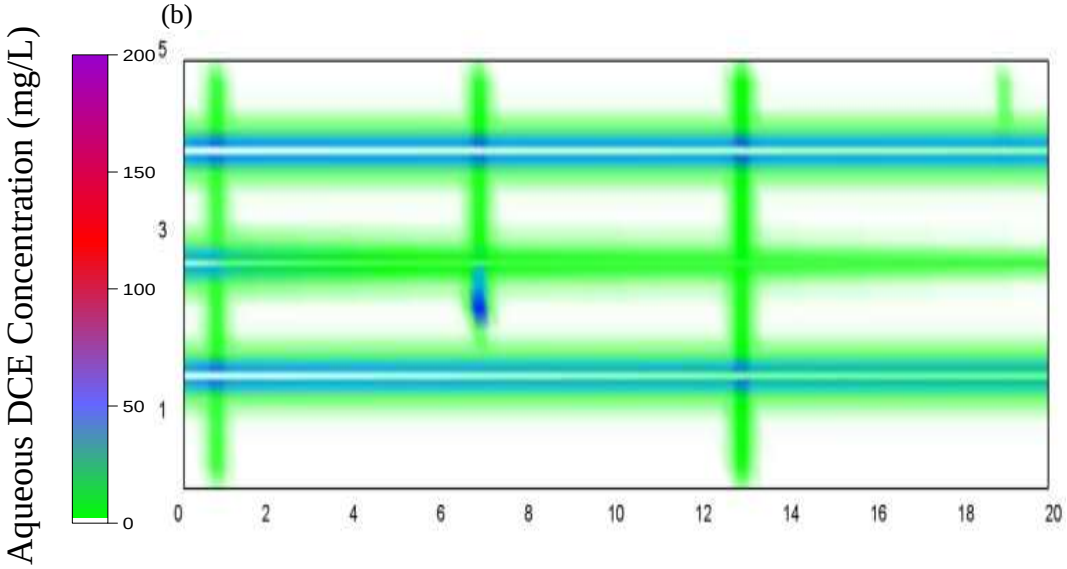
Aqueous DCE Concentration (mg/L)
200
150
100
50
0
5
3
1
0
2
4
6
8
10
12
14
16
18
20

(c)

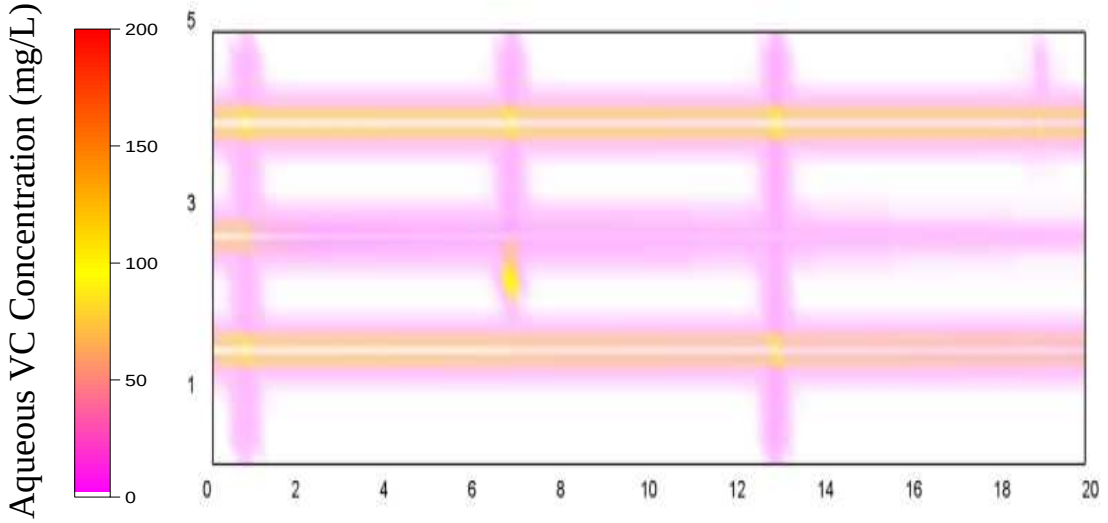
Aqueous VC Concentration (mg/L)
200
150
100
50
0
5
3
1
0
2
4
6
8
10
12
14
16
18
20

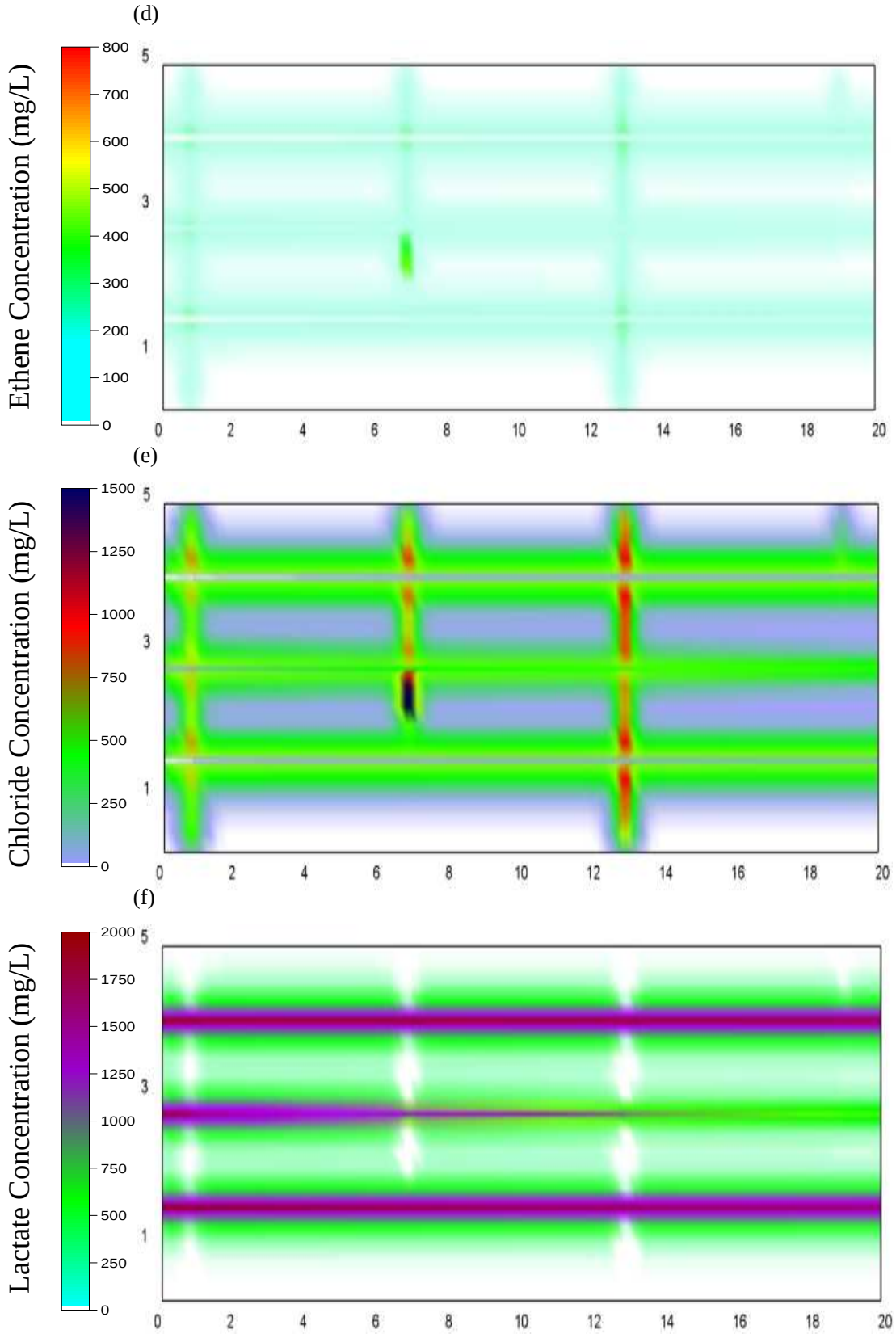

Figure 5.7: Distribution of aqueous species concentrations at t_{TOTAL} =23 years for Base Case after 2 years of lactate injection (i.e., Treatment stage): (a) TCE; (b) 1,1, DCE; (c) VC; (d) Ethene; (e) Chloride; (f) Lactate.

Figure 5.9 presents cumulative mass plots of all sinks and sources of TCE during the Base Case simulation. Summed totals of these plots, in which:

Mass Dissolved from DNAPL + Mass Inflow - Mass Destroyed - Mass Discharged = Mass Sorbed + Mass Aqueous in Domain (5.15)

revealed that the model has excellent mass balance (plots not shown to improve clarity of the figure) and this was confirmed by excellent computed mass balance on all species. The figure reveals that the majority of DNAPL dissolution occurred rapidly at the beginning of the simulation due to DNAPL dissolution and diffusion, corresponding to a rapid increase in sorbed TCE in the matrix. Until t_{TOTAL} = 3 years, TCE flux out of the domain was greater than flux into the domain due to a proportion of the dissolved TCE exiting via fracture flow. However, beyond this time, with dissolution virtually completed, TCE flux into the domain exceeded the flux out as the incoming background TCE contributed to a steady rise in mass retained via sorption. It also reveals that the cumulative mass of aqueous TCE in the domain (sum of that in the fractures and matrix) was a small fraction of the amount sorbed.

Figure 5.9 further illustrates that when lactate was injected, at t_{TOTAL} = 21 years, the amount of 'TCE Reduced During EISB' began to rise. Over the 2-year treatment period the total amount of 'TCE Reduced During EISB' was approximately 13% less than the magnitude of the reduction in sorbed TCE. The additional desorption occurred mainly as a result of back-diffusion induced by the low concentrations of TCE in the flowing

horizontal fractures.

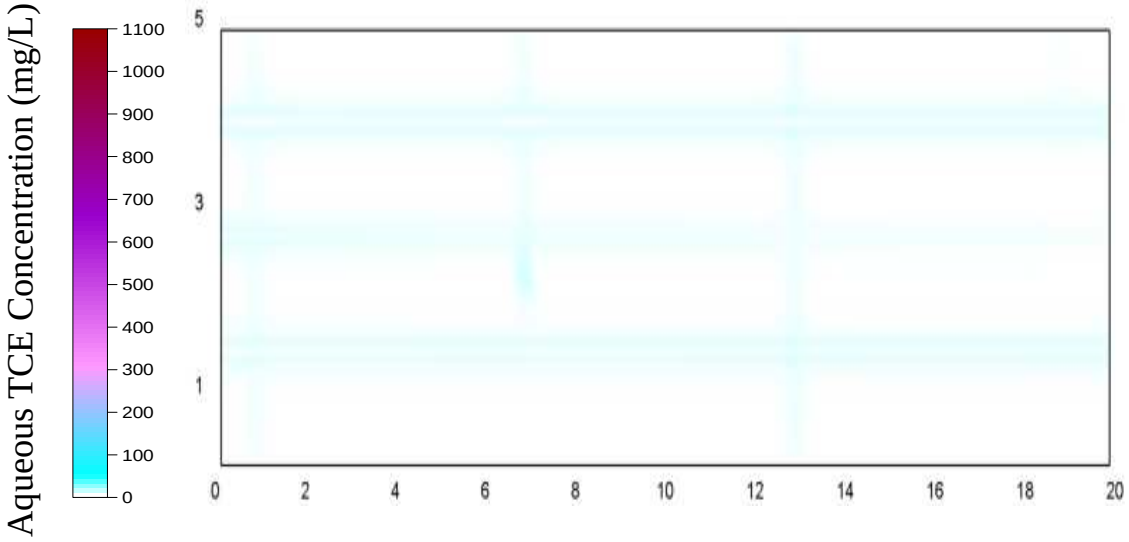

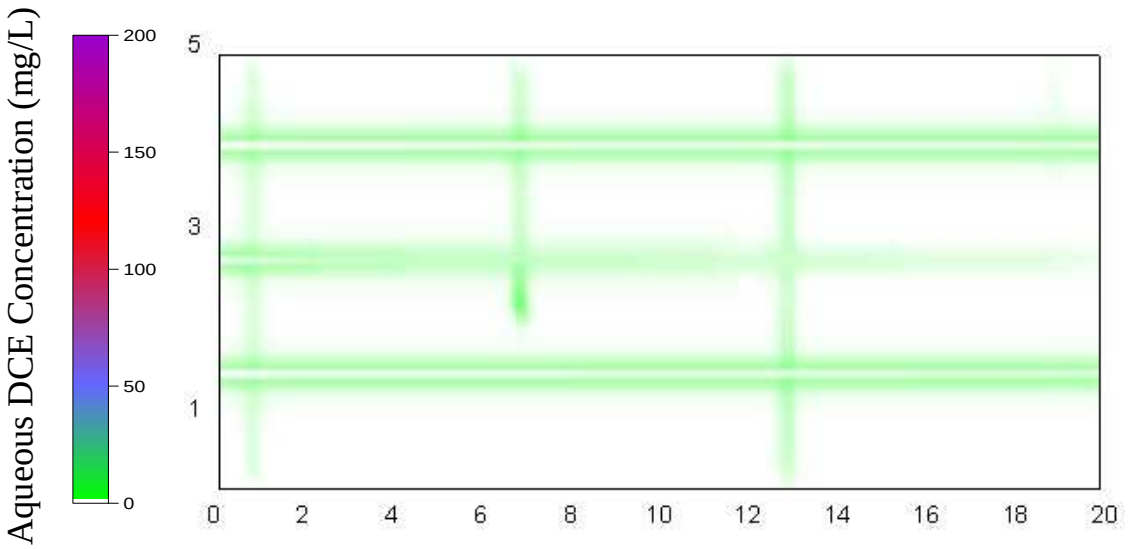

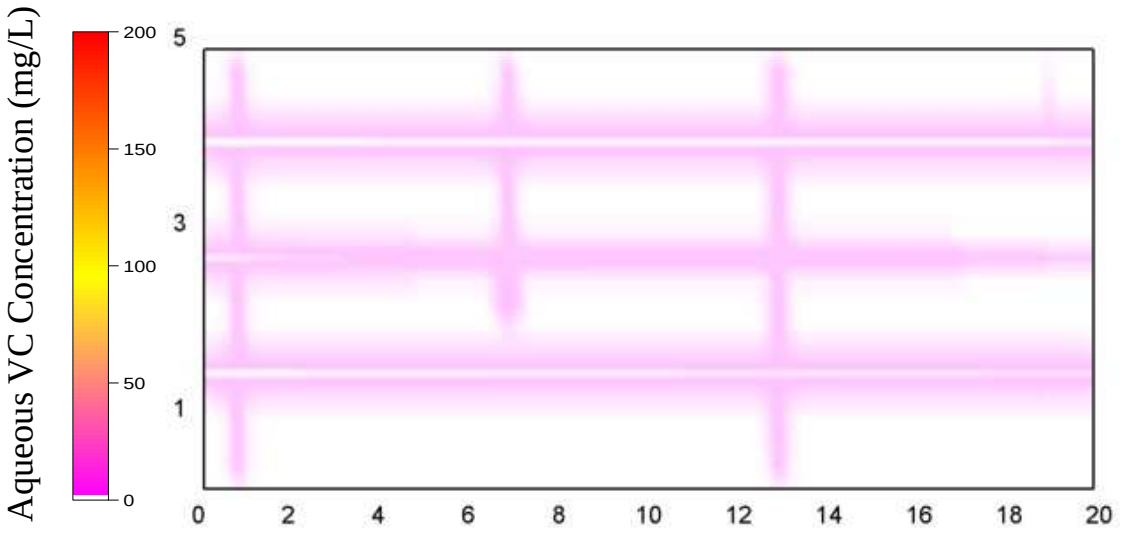

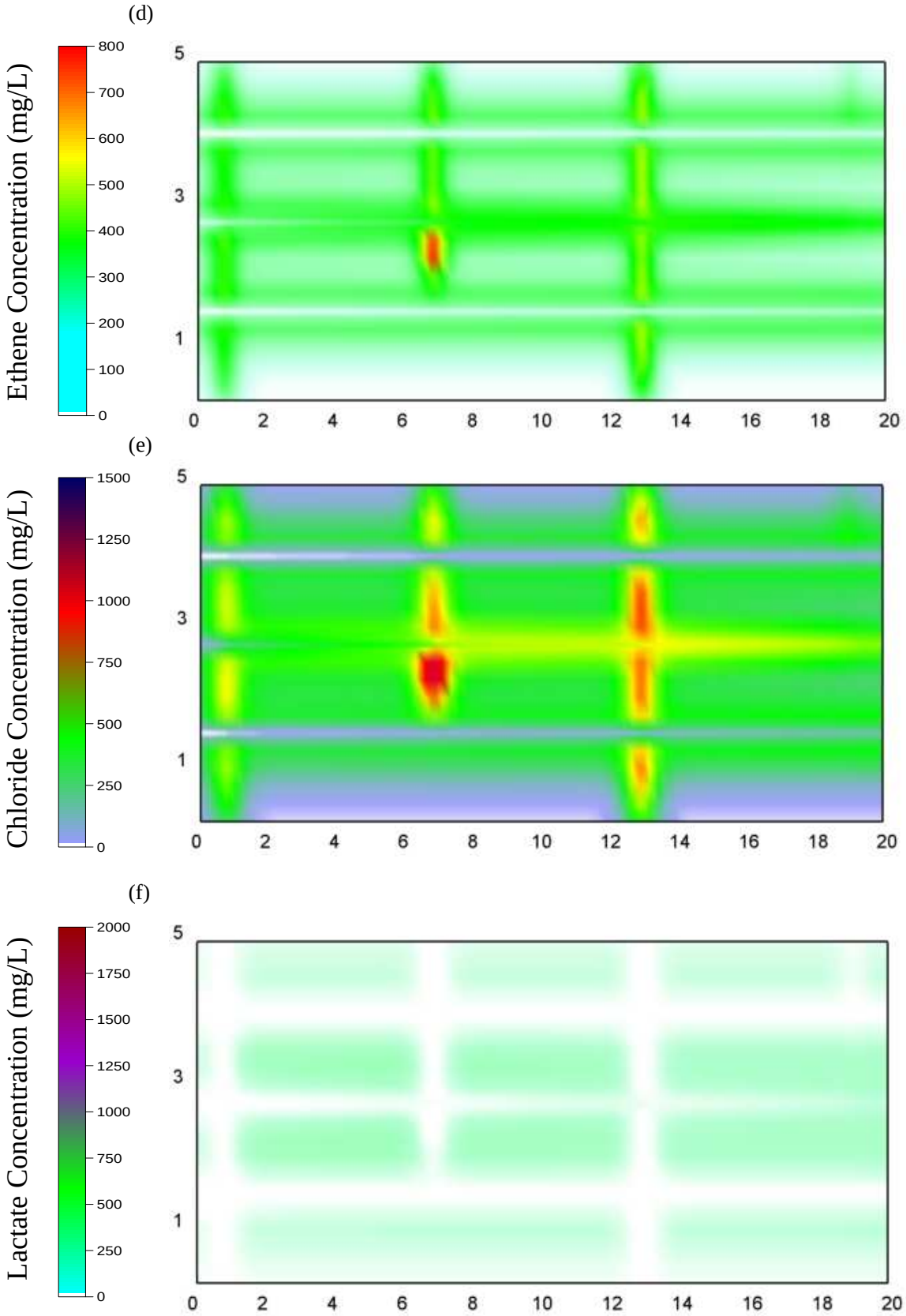

Figure 5.8: Distribution of aqueous species concentrations at t_{TOTAL} =28 years for Base Case (i.e., 5 years Post-Treatment stage): (a) TCE; (b) 1,1, DCE; (c) VC; (d) Ethene; (e) Chloride; (f) Lactate.

Figure 5.9 further reveals that the rate of TCE destruction rapidly declines with time: from rapid destruction due to early-time remediation of the fractures to successively lower rates associated with the comingling of organic substrate with chlorinated solvents at successive depths into the matrix. Interestingly, Figure 5.9 reveals that the rate of TCE destruction appears to be unaffected by termination of the treatment application at the injection well; this underscores that sufficient lactate was present in the matrix during the Post-Treatment stage to continue dechlorination.

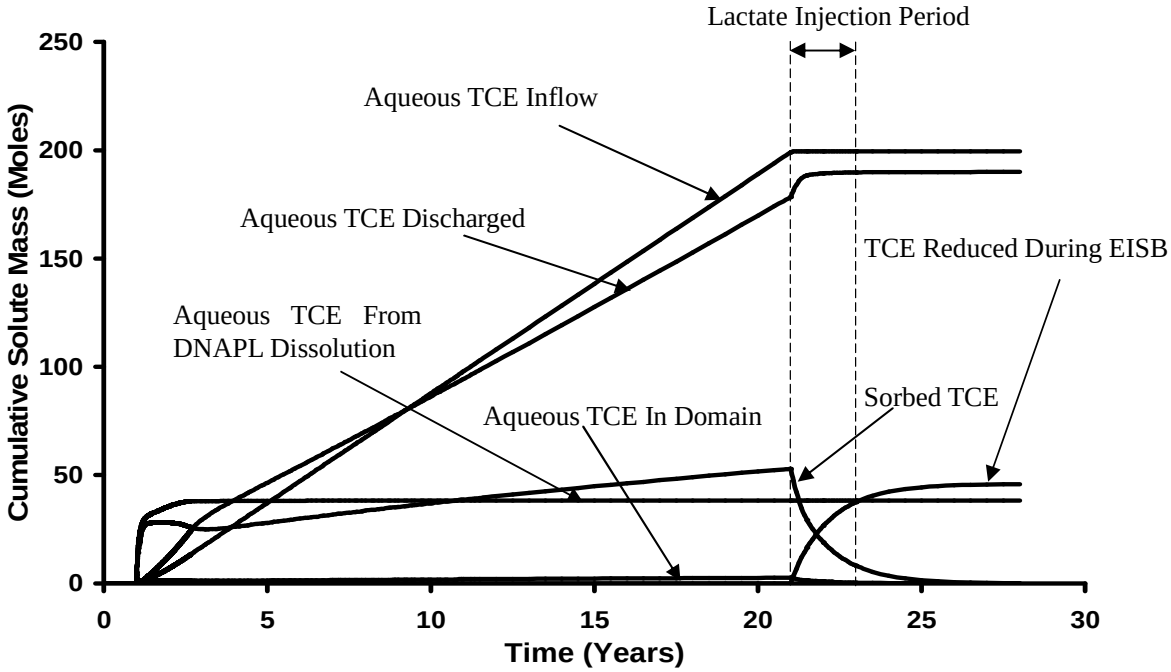

Figure 5.9: Cumulative aqueous and sorbed TCE from all sinks and sources for base case.

Figure 5.10 presents the cumulative mass in the domain of the species involved in EISB; note that the time axis originates at the beginning of the Treatment stage. This figure reveals that the rate of chloride being produced during lactate injection period was constant, indicating a steady rate of chlorinated products being reduced. It confirms that this rate was relatively unaffected by the termination of the lactate injection. Analysis

of Figure 5.10 reveals that of the 7.3 kg of TCE (aqueous plus sorbed) present in the domain at the end of the 20 years Site Ageing stage (t_{TOTAL} = 21 years), approximately 67.6% was successfully converted to daughter products (DCE + VC + ETH) by the end of the treatment period, and 6.03 kg (i.e., 82.6%) was converted by the end of Post-treatment period (t_{TOTAL} = 28 years). Of the TCE mass dechlorinated, 89.0% was converted to ethene.

Figure 5.10 reveals that reductive dechlorination continues at ever diminishing rates throughout the Post-Treatment period. At t_{TOTAL} = 25.5 years, the chloride and ethene curves reveal that the amount of chloride production was less than the amount being flushed out of the domain. This occurred despite 5.2 moles of lactate and a total of 7.5 moles of chlorinated ethenes still present in the domain at this time. As demonstrated by Figure 5.8a through c and Figure 5.8f, the remaining 5.2 moles of lactate in the domain were embedded deep within the matrix while the remaining chlorinated ethenes were present nearer to the fractures. This suggests that while an excess of lactate was injected, matrix diffusion (both forward and reverse) caused a deficiency in electron donor in the matrix near the fractures at late time. It is noted that the lactate, with no sorption or retardation, exhibits a diffusive rate approximately 20 times greater than the chlorinated compounds in sandstone. Thus, it is likely that relatively rapid reverse diffusion of the lactate will result in eventual comingling with the chlorinated ethenes and therefore more complete clean-up in time is theoretically possible.

Figure 5.11 reveals that of the 545 moles of lactate injected, 91.3% was flushed out of the

domain via advection in the fractures, while only 6.5% was consumed by the TCE, DCE and VC in the domain; the difference (2.2%) remains unreacted, embedded within in the matrix 5-years post-treatment.

Figure 5.12 presents the total mass discharged at the right-hand boundary of the domain for the Base Case and 'No EISB' simulations. The figure illustrates that the TCE mass discharge decreased dramatically in the 'No EISB' case because (i) the upgradient TCE source was removed, and (ii) the gradient was increased from 0.005 to 0.025. Nevertheless, during the Treatment stage (i.e., t_{TOTAL} = 21 to 23 years), the Base Case exhibited a lower mass discharged than the 'No EISB' at all times by 59% to 71%. Moreover, during the Post-Treatment stage, the 'No EISB' simulation exhibited a low but relatively constant mass discharge associated with reverse diffusion. Meanwhile, the mass discharged in the Base Case during this period was not detectable (i.e., <0.0001 mg/s).

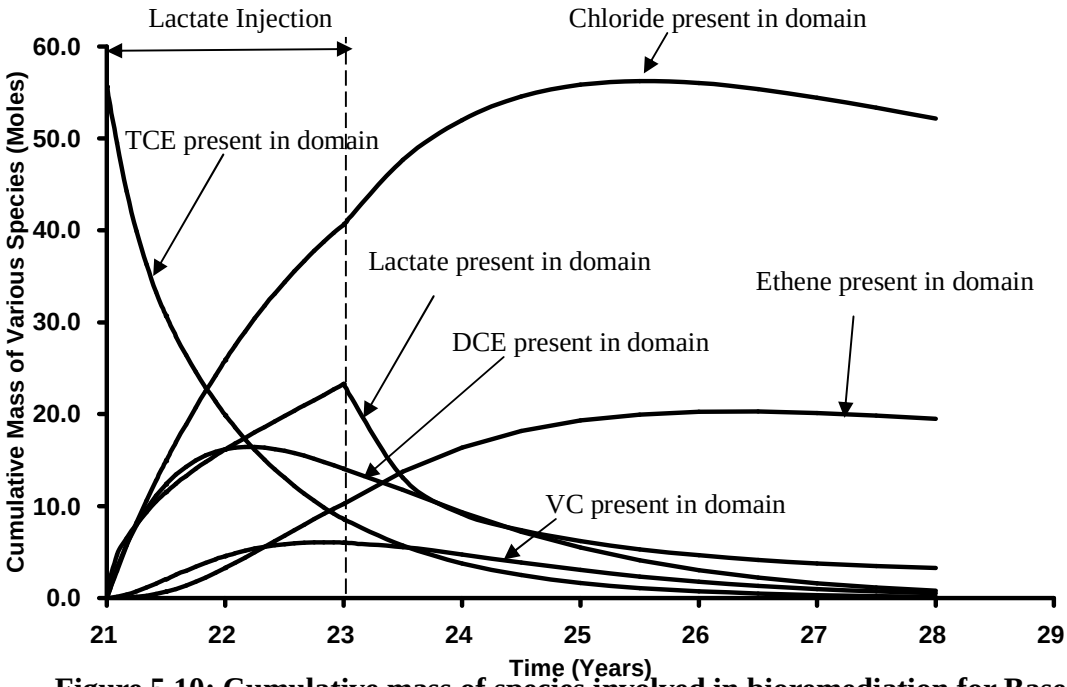

Figure 5.10: Cumulative mass of species involved in bioremediation for Base Case.

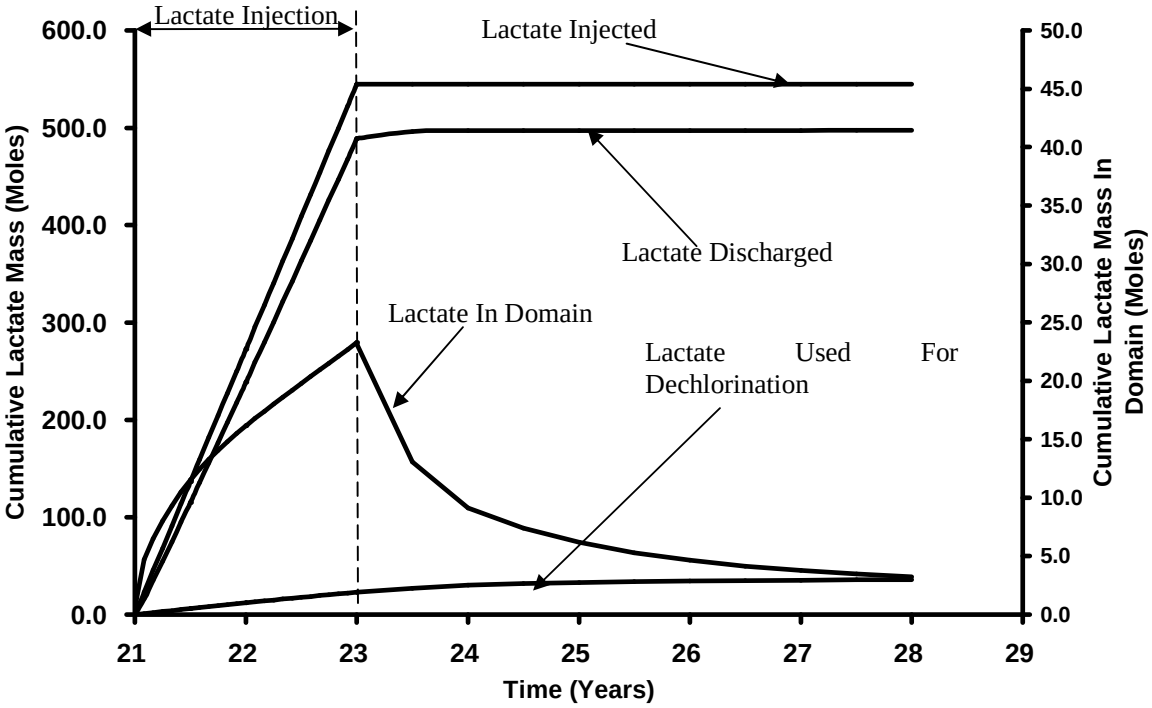

Figure 5.11: Cumulative mass of lactate involved in bioremediation for Base Case. Note: The plot 'lactate in domain' uses the right axis.

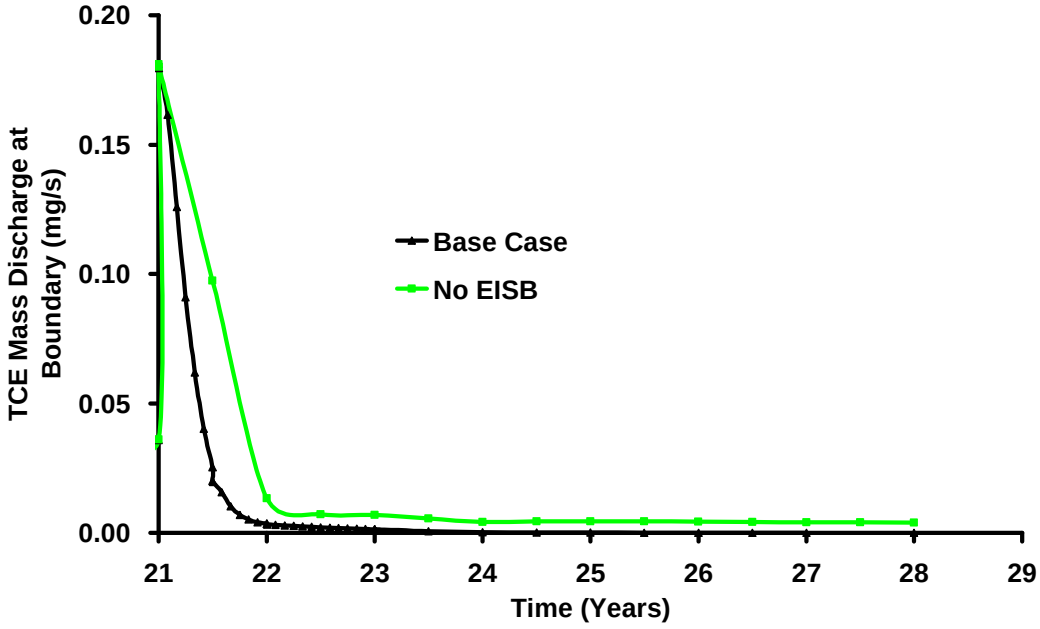

Figure 5.12: Comparison of total boundary mass discharge (TCE) for base case with a simulation where no lactate was injected.

Figure 5.13 plots the TCE solute concentration for each of the three horizontal fractures at the downgradient boundary. This figure demonstrates, during the Treatment Stage, that the rapid concentration decrease observed in the larger aperture fractures (e.g., 178μm and 230μm) in the Base Case is indistinguishable from that of the 'No EISB' case. However, for the smallest facture aperture (i.e., 76 μm), considerably lower concentrations are observed in the Base Case since the significant concentrations of TCE emerging from back-diffusion and flushing (in particular, associated with the TCE-loaded dead-end fracture, see Figure 5.7a) observed in the 'No EISB' case are treated by reductive dechlorination. The difference in downgradient concentrations in the Post-Treatment period is dramatic, with ongoing treatment of back-diffusing TCE (via primarily destruction in the matrix) in the EISB Base Case.

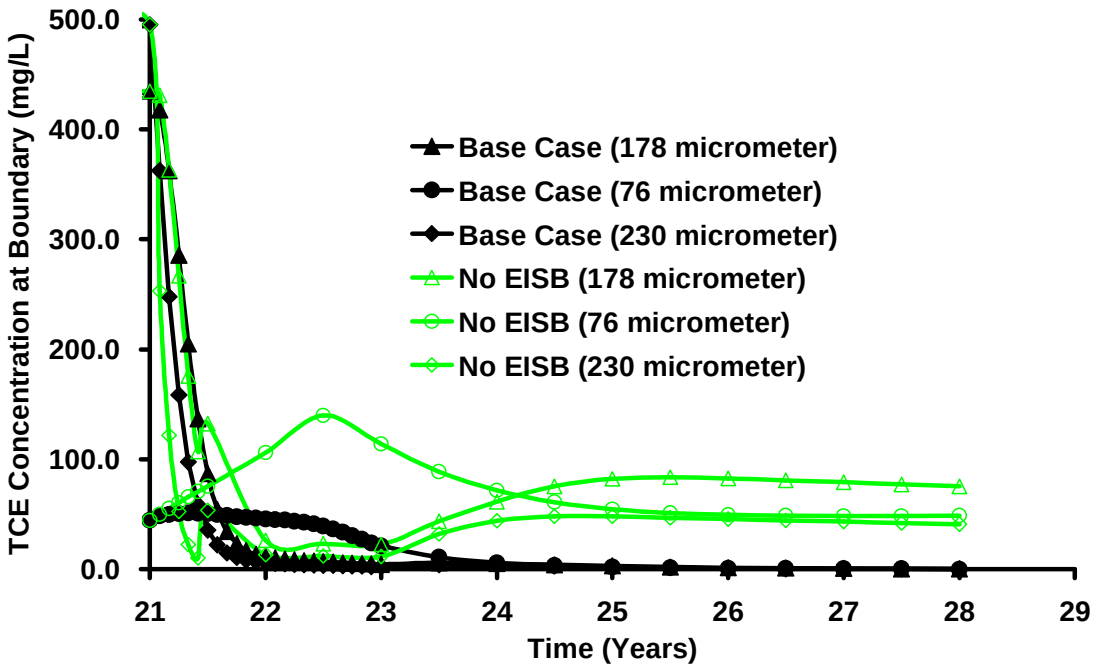

Figure 5.13: Concentration of TCE in various horizontal fractures at downgradient boundary.

5.5.2 Sensitivity Simulations

In order to compare the impact various parameters have on the effectiveness of bioremediation in fractured rock at the field scale, two metrics were chosen: (i) the total mass of chloride generated, and (ii) total mass of VC dechlorinated to ETH (since accumulation of toxic VC is a significant concern for bioremediation applications).

5.5.2.1 Sensitivity to Microorganisms in Fractures/Matrix

Figure 5.14 demonstrates that, despite a similar amount of lactate delivered, the mass of total TCE dechlorinated for microorganisms active in the fractures only (Run 2) is 98.8% less than the Base Case (compare to Figure 5.10; notice the altered vertical axis for all species except TCE and lactate). As expected, the majority of the dechlorination for Run 2 occurred in the first 6 months of treatment due to direct interaction of TCE and lactate within the fractures. However, such a small fraction of the total TCE is present in the fractures (1%) that even very effective treatment in this region has negligible impact on total mass treated. A small amount of sustained dechlorination is observed in the Post-Treatment period due to back-diffusion of sorbed TCE and coincident back-diffusion of lactate into the fractures. Nevertheless, the total extent of dechlorination, as revealed through chloride production (Figure 5.15) demonstrates the significantly reduced effectiveness of EISB when microorganisms are not active in the rock matrix. These results are consistent with the concentration distributions of the various species (see Figure B1, Appendix B for Run 2, Figure 5.8 for Base Case), where only 1% of the initial total TCE mass present in the domain was demonstrated to be reduced (Table 5.5).

Figure 5.16 demonstrates that, in fact, the TCE mass discharge at the downgradient boundary was very similar for Run 1 and Run 2 during the initial lactate injection period. In both cases, a more rapid decrease than the 'No EISB' case in the first 6 months was observed associated with mass destruction in the fractures. However, in the Post-Treatment period the TCE mass discharged (as revealed in Table 5.5) in the 'fracture bioremediation only' simulation is only slightly lower than the 'No EISB' case, revealing the inability to effectively treat back-diffusing TCE mass. This is because during the Post-Treatment period, the rate of bioremediation is limited by the back-diffusion rate of lactate from the matrix. A similar conclusion is obtained by examining the downgradient concentration at each horizontal fracture (Figure 5.17).

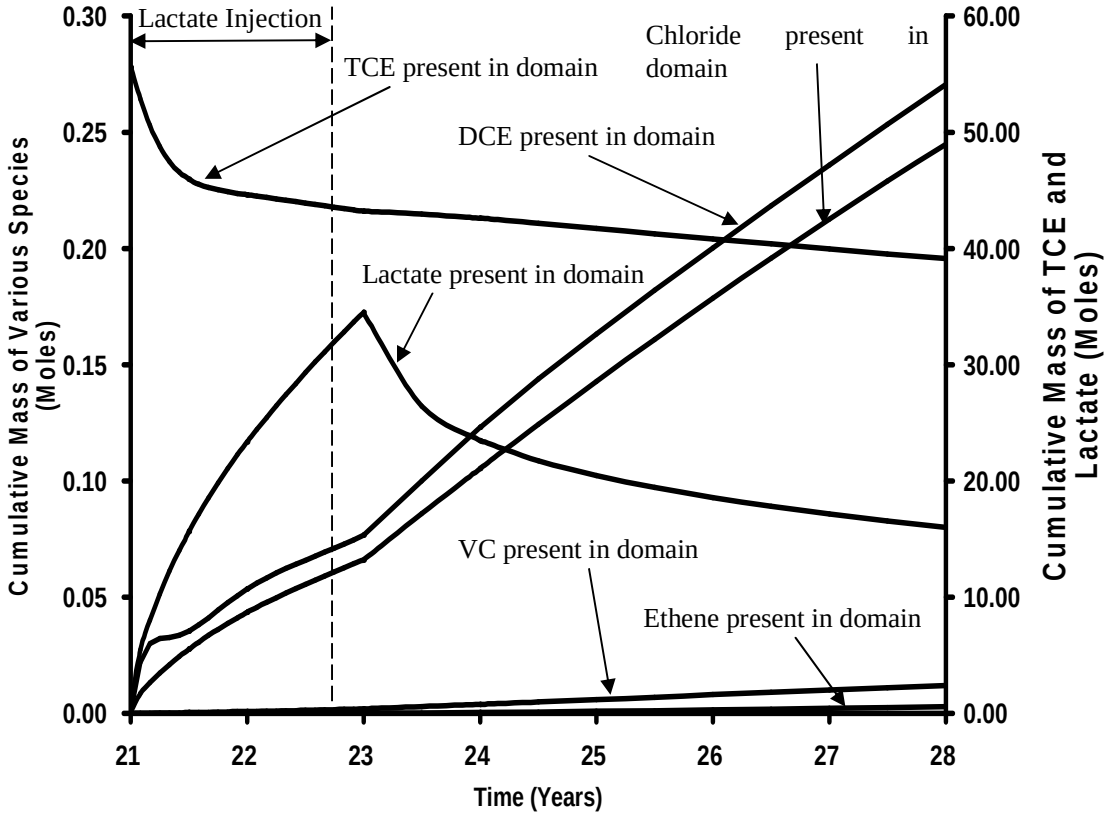

Figure 5.14: Cumulative mass of species involved in bioremediation for the case when indigenous bacteria is only present in fractures.

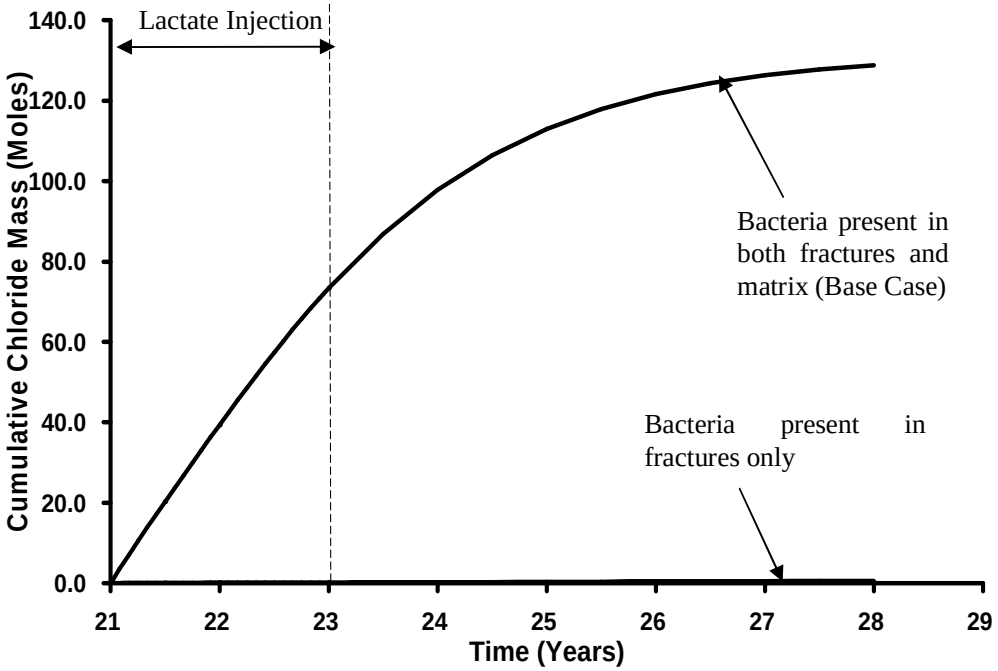

Figure 5.15: Cumulative mass of chloride produced for microorganisms active in the matrix and fractures (base case) versus in fractures only (Run 2).

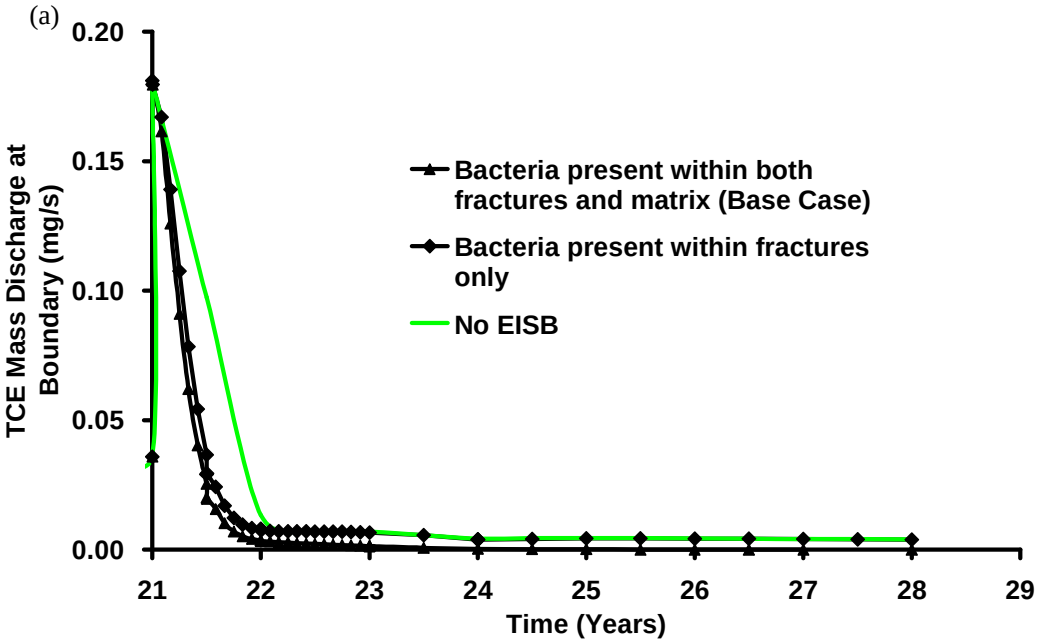

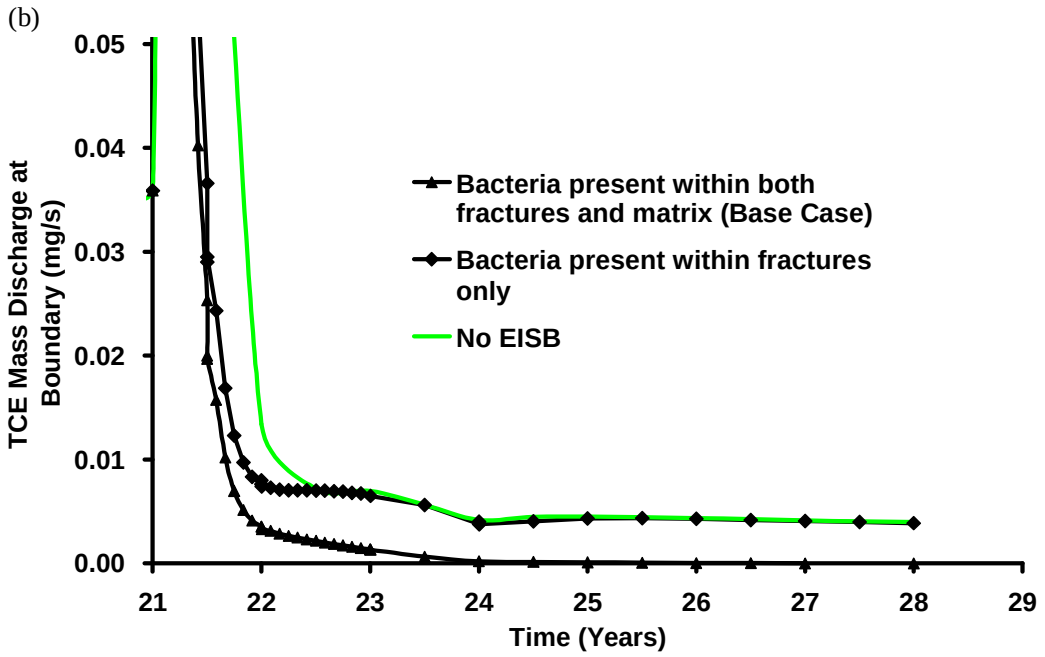

Figure 5.16: Comparison of total boundary mass discharge (TCE) for base case with (a) bioremediation within fractures only and (b) since the start of the Treatment Stage only (timescale expanded for clarity).

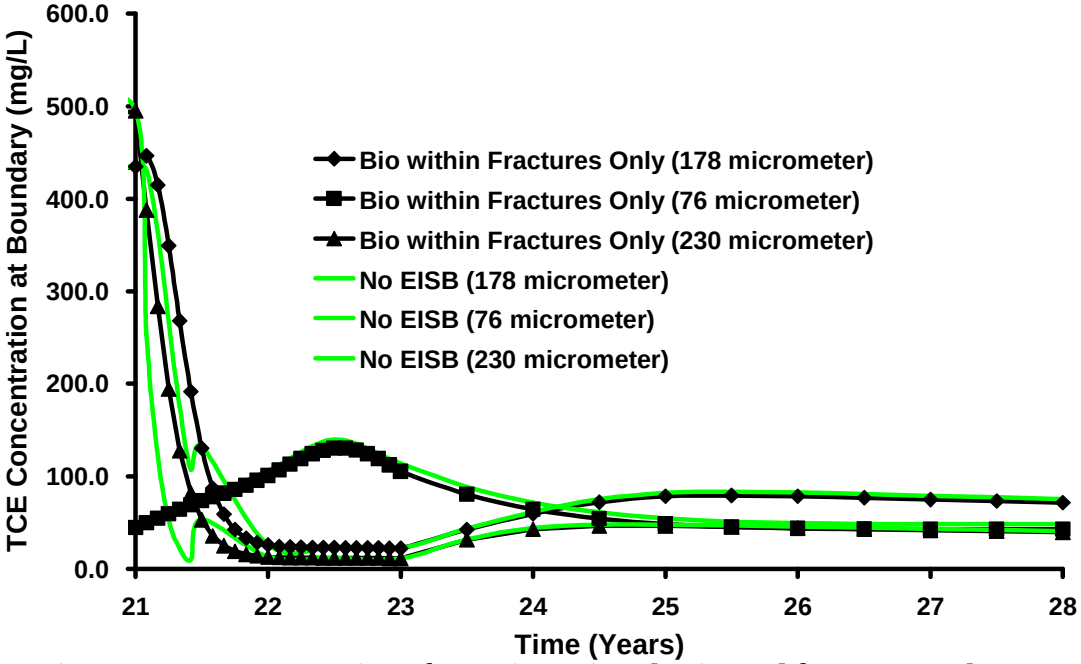

Figure 5.17: Concentration of TCE in various horizontal fractures at downgradient boundary for bioremediation within fractures only.

5.5.2.2 Sensitivity to Dechlorination Rate Parameters

As demonstrated in Figure 5.18, the total extent of dechlorination (as measured by the mass of chloride being produced) is highly sensitive to the first-order decay rate parameters. For example, when the decay rate parameters were increased by one order of magnitude (Run 3), all anaerobic dechlorination ceased approximately one year after lactate injection began. Figure 5.19a, plotting the cumulative mass of the key species in the domain for this simulation, illustrates that all the chlorinated products in the domain have been reduced to non-detect after one year. In contrast, when the decay rates were lowered by one order of magnitude, chloride production and ethene slowed dramatically (Figure 5.18 and Figure 5.19b). The total mass of chloride produced during the Treatment and Post-Treatment period was 150, 129 and 25 moles and the total mass of TCE reduced was 52.3, 45.9 and 18.7 moles for the high, median (Base Case) and low decay rates, respectively. This indicates that the overall bioremediation efficiency was more sensitive to decreases in decay rates than increases for this scenario; this is likely due to the fact that the Base Case already exhibited such a high degree of remediation. Concentration distribution images for the key species support these findings (Figure B2, Appendix B).

Figure 5.19b further reveals that the cumulative mass of the daughter-products of TCE is on the increase by the end of the simulation; indicating that dechlorination is still taking place within the domain at late times.

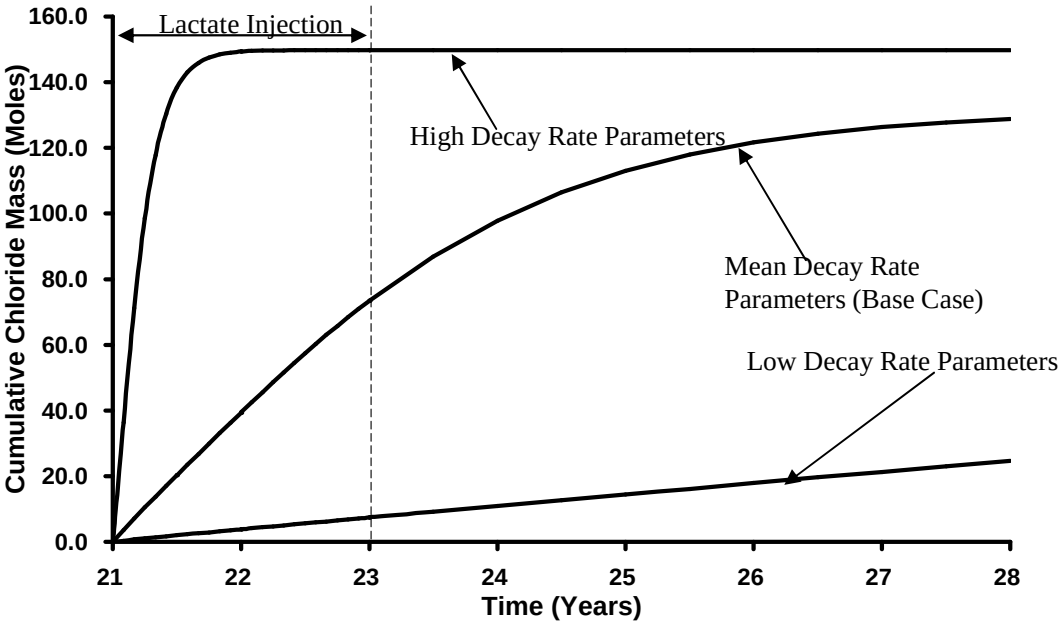

Figure 5.18: Cumulative mass of chloride being produced over time for different decay rate parameters.

Figure 5.20 reveals the TCE mass discharged for the high reaction rates simulation was reduced to non-detect by 6 months of treatment. In contrast, the mass discharged in the low reaction rates simulation is very similar to the 'No EISB' simulation after the first year of treatment. It is noted that there is sufficient amount and distribution of lactate through the subsurface (see Figure B2, Appendix B) but that the contact time – even in the diffusion limited matrix – is too low relative to the reduced dechlorination rates for effective treatment.

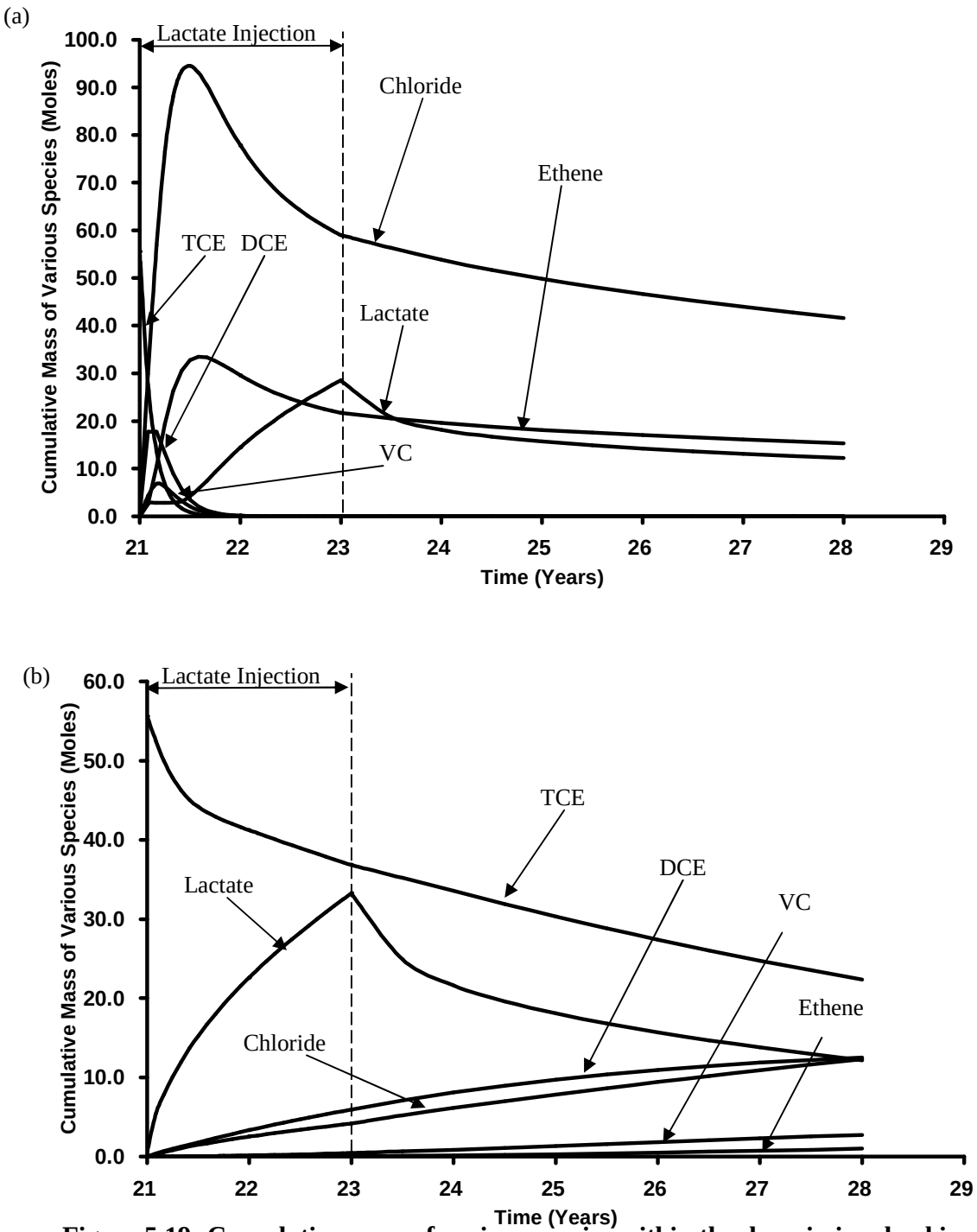

Figure 5.19: Cumulative mass of various species within the domain involved in (a) high decay rate and (b) low decay rate parameters over time.

(a)

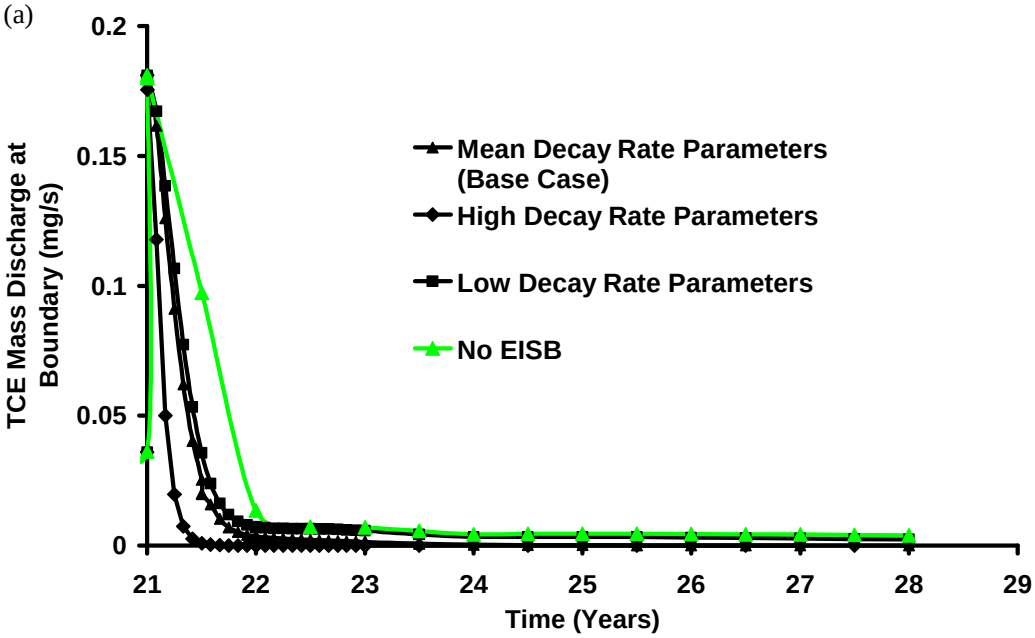

(b)

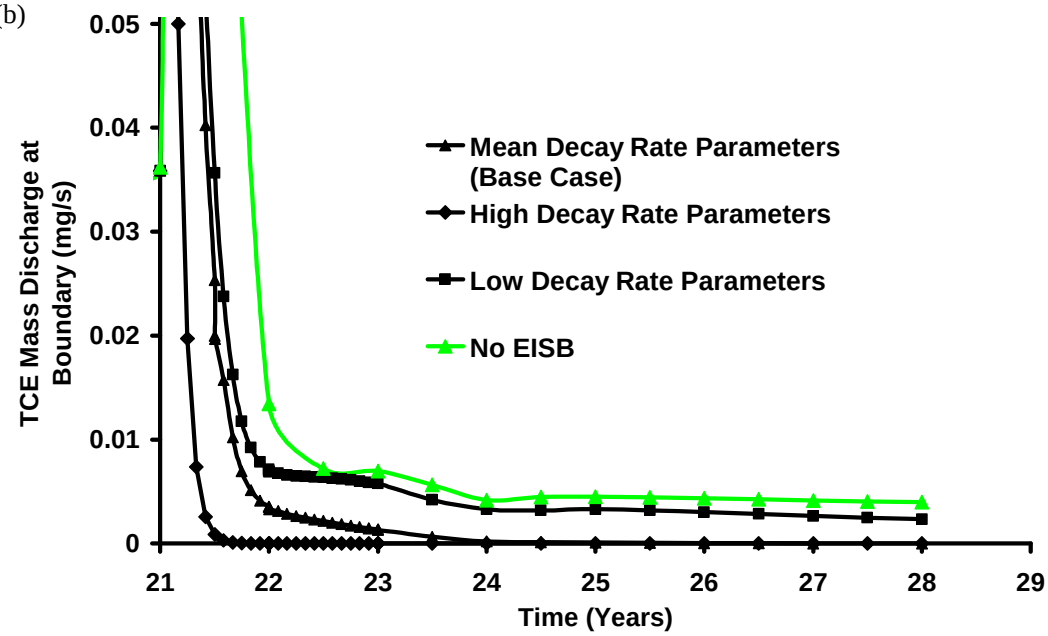

Figure 5.20: Comparison of total boundary mass discharge (TCE) for base case with (a) various decay rates (b) since the start of the Treatment Stage only (timescale expanded for clarity).

5.5.2.3 Sensitivity to Pulsed Injection of Organic Substrate

As demonstrated in Figure 5.21 and 5.22 the total masses of chloride and ethene produced at the end of the Post-Treatment period for these simulations and their spatial distribution (Figure 5.8 and Figures B5, B6 and B7 in Appendix B) were indistinguishable. Furthermore, Figure 5.23 illustrates no significant difference in TCE mass discharge was observed for the three cases. The distribution of lactate in this scenario (and thus the extent of dechlorination) is insensitive to pulsing since it remains in excess. It is recognized that, in reality, pulsing may have advantages not observed in this work such as allowing the dissipation of acids so as to recover near-neutral pH, reducing bioclogging, etc. However, with respect to effectively distributing the lactate in a biologically active fractured sandstone, these simulations suggest no significant influence.

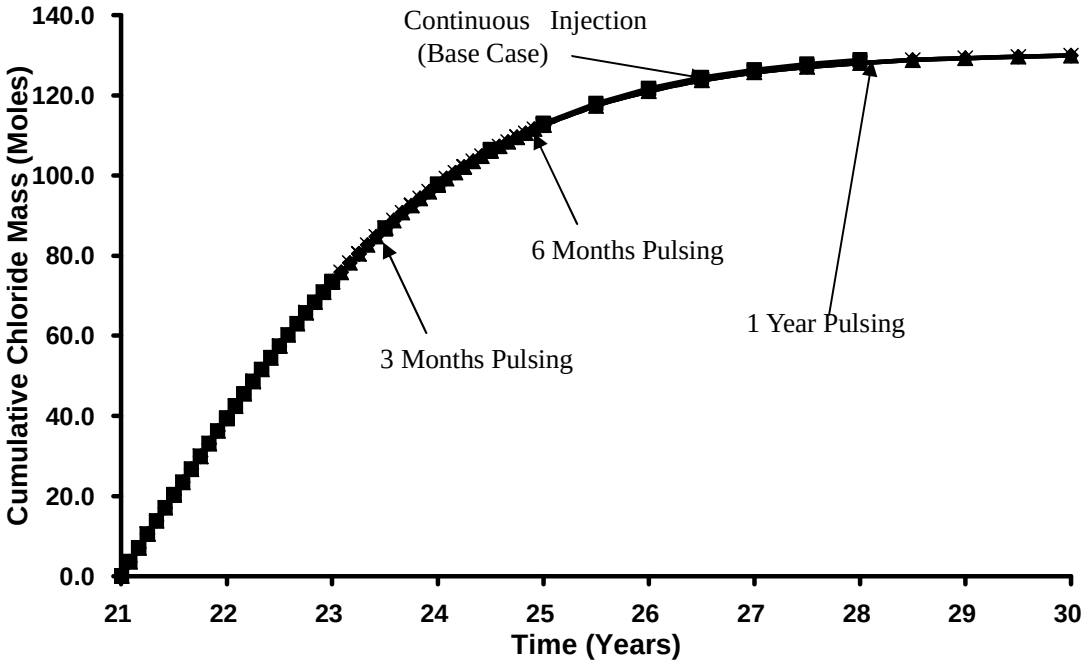

Figure 5.21: Cumulative mass of ethene being produced over time for different pulsing method.

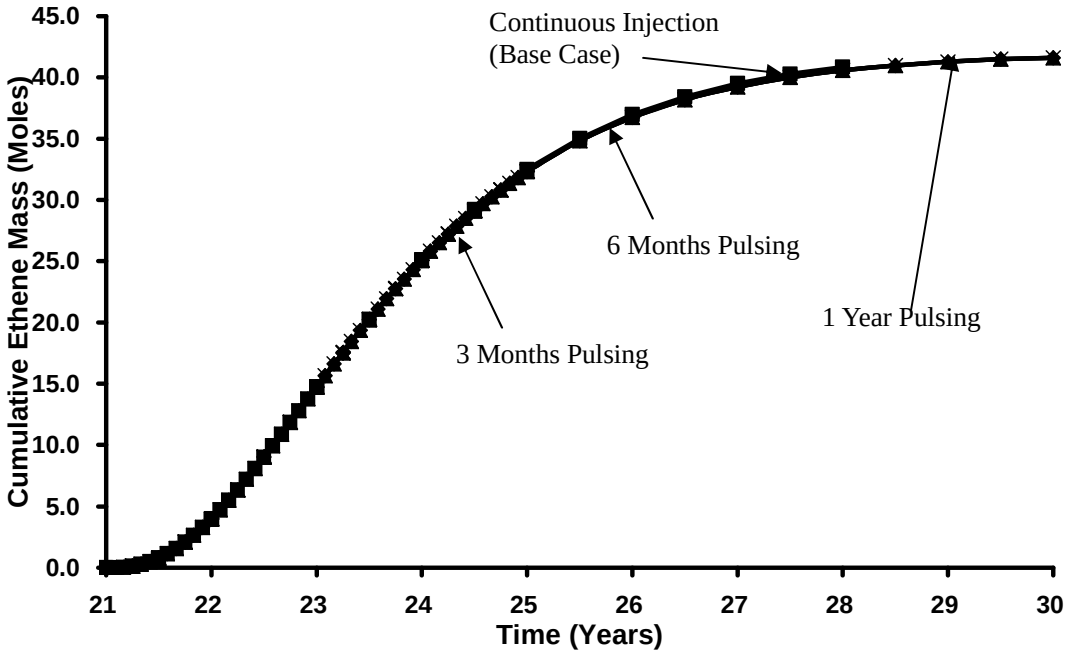

Figure 5.22: Cumulative mass of ethene being produced over time for different pulsing method.

(a)

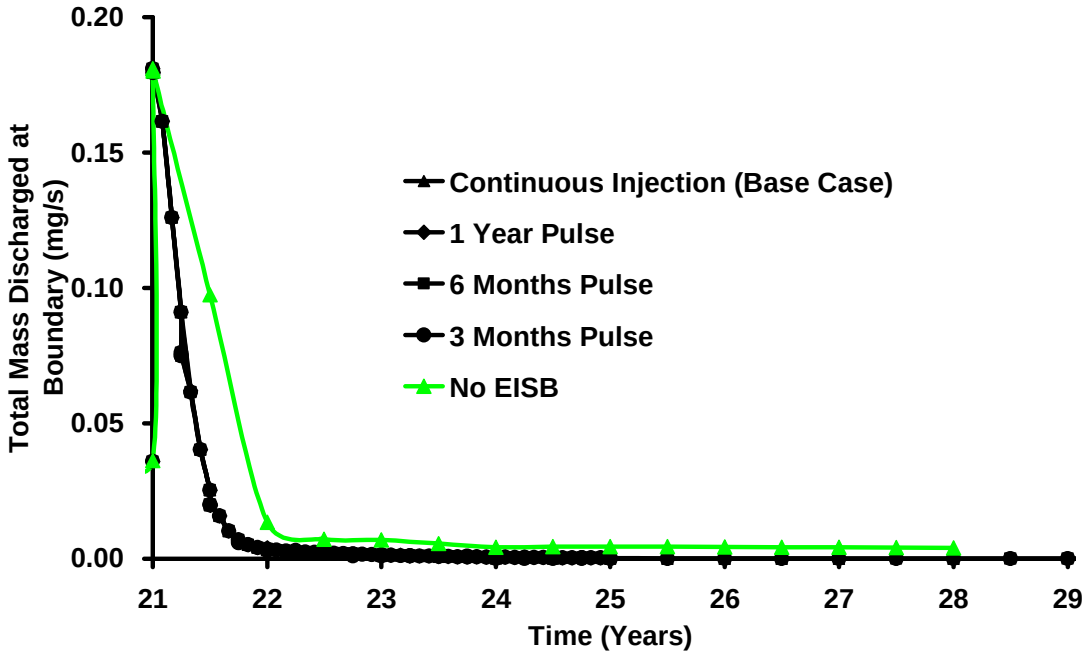

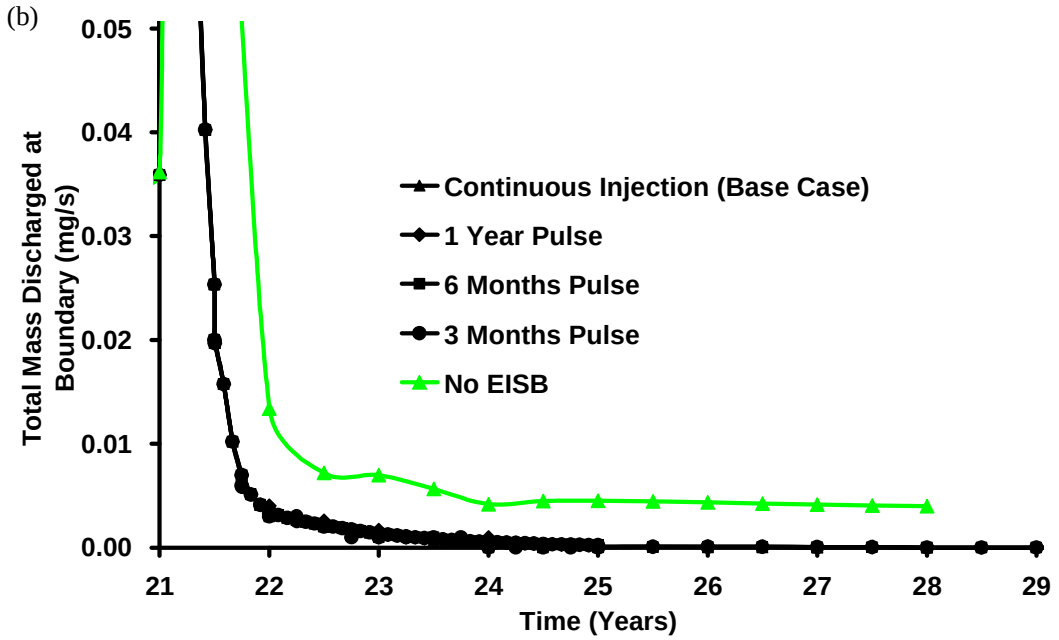

Figure 5.23: Comparison of total boundary mass discharge (TCE) for base case with (a) various pulsing methods (b) since the start of the Treatment Stage only (timescale expanded for clarity).

5.5.2.4 Sensitivity to Organic Substrate Concentration

Figure 5.24, plotting the cumulative mass of chloride produced for 4 g/L, 2 g/L, and 1 g/L (Runs 8, 1, and 9, respectively), reveals that the lactate concentration had virtually no effect on the remediation efficiency (give that the time of injection was adapted to ensure equal total mass injected in each case). Moreover, the amount of each chlorinated ethene transformed with time was essentially identical (Figures B8 and B9, Appendix B). Moreover, the distribution of the key species were essentially identical in all three cases at the end of the Post-Treatment stage (Figure 5.8, and Figures B8 and B9, Appendix B).

Figure 5.25, plotting the cumulative mass discharge of lactate at the downgradient boundary for the three simulations, reveals that, regardless of the concentration injected, an equivalent total mass exits the domain and, therefore, an equivalent mass penetrates

the matrix in all three cases. The fraction of the total moles of lactate that exited the domain relative to that injected is 91.5% in all three cases. Furthermore, no significant difference in the simulations was observed for TCE mass discharge (Figure 5.26) or TCE distribution (Figures B8 and B9, Appendix B). These plots illustrate that the ability of lactate to diffuse throughout the rock matrix was equivalent and substantial in all three cases; clearly the lack of matrix sorption for lactate was critical in this regard and as a result, sensitivity to the concentration gradient from the fractures to the matrix was low (at least at the relatively high concentrations injected here). The results further indicate that the lactate was always in excess, even in the lowest concentration case, and thus the first-order rate constants were likely the factors that limited complete clean-up in these cases.

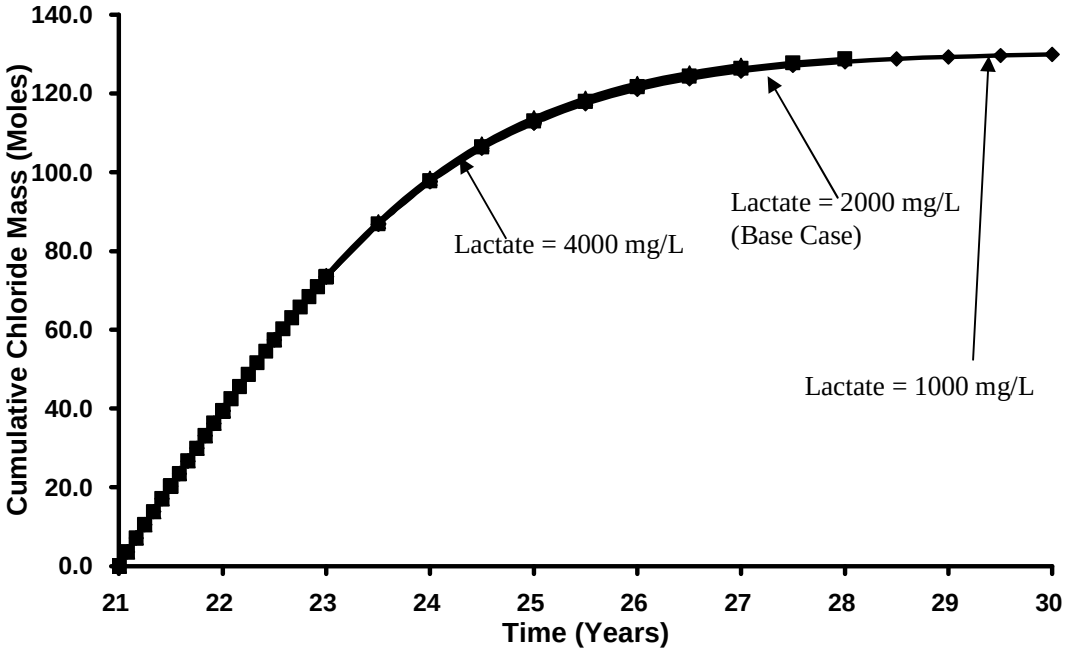

Figure 5.24: Cumulative mass of chloride being produced over time for different injected concentration.

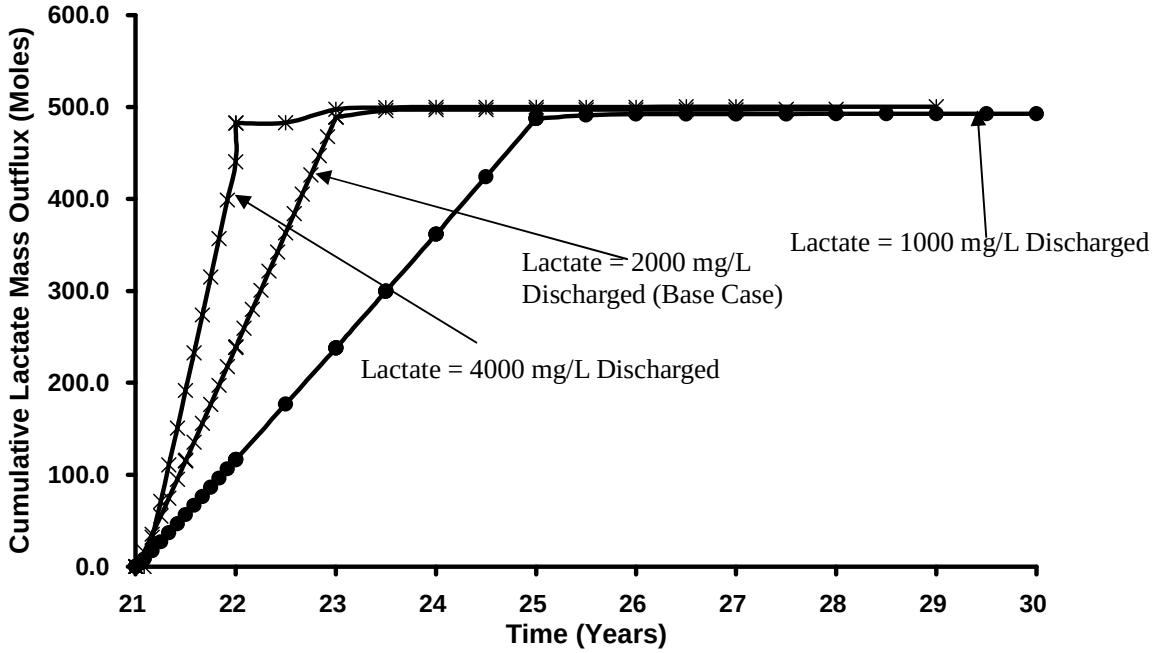

Figure 5.25: Cumulative mass of lactate discharged over time for different injected concentration.

(a)

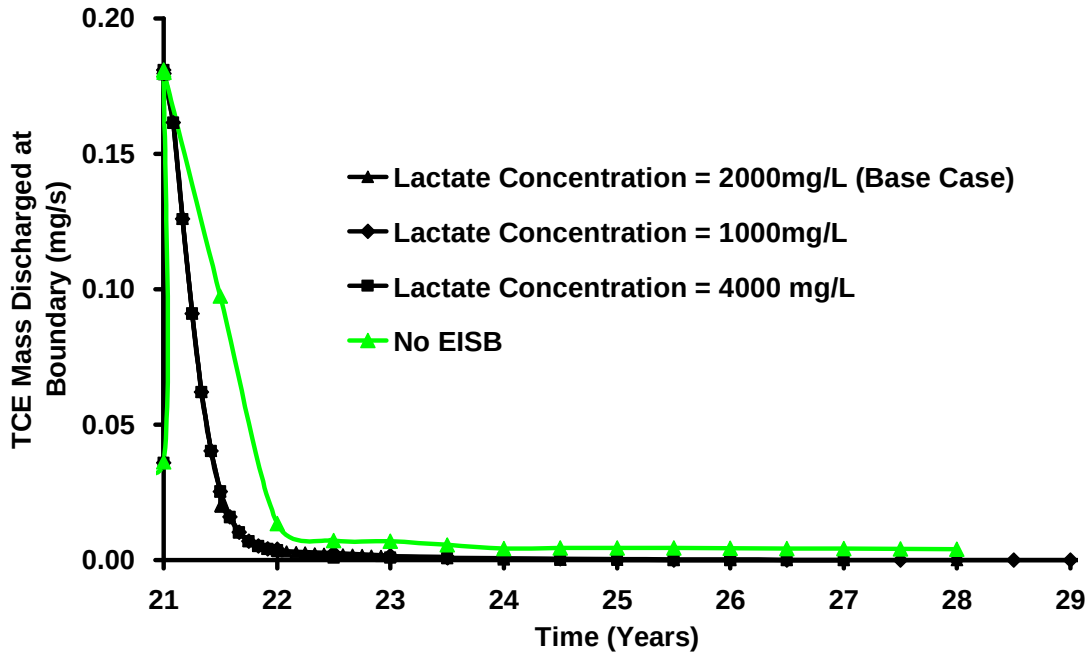

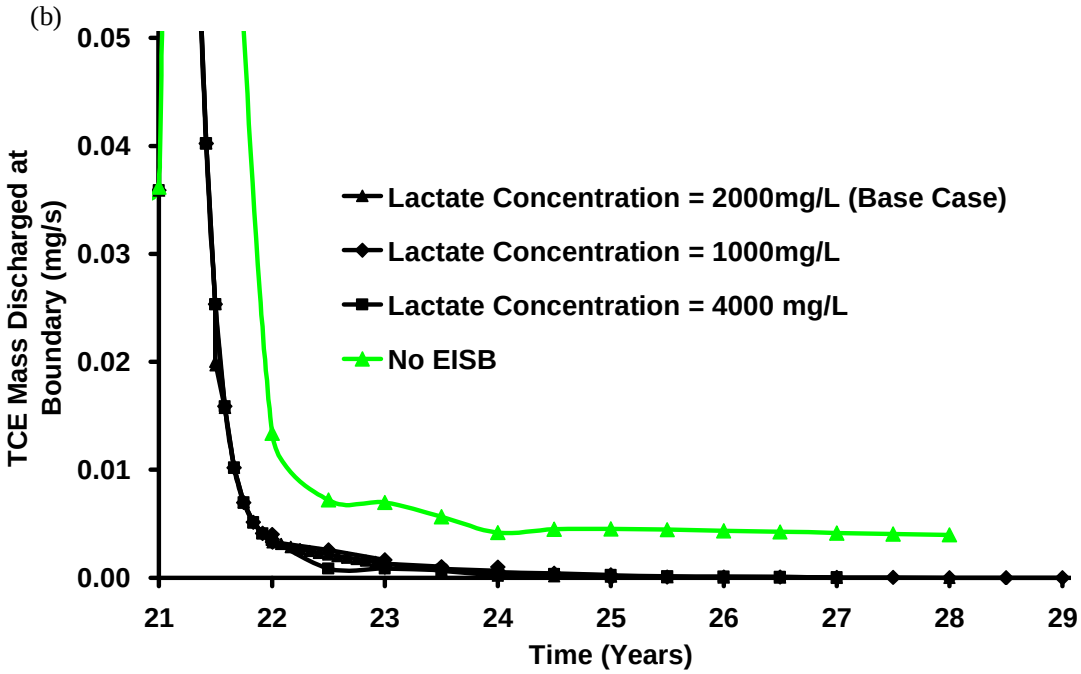

Figure 5.26: Comparison of total boundary mass discharge (TCE) for base case with (a) various lactate concentration (b) since the start of the Treatment Stage only (timescale expanded for clarity).

5.5.2.5 Sensitivity to Rock Type

At the end of the DNAPL Infiltration stage, the average DNAPL saturation was 0.75, the volume of DNAPL in the domain was 0.008 m^3, 0.01 m^3 and 0.018 m^3 for sandstone, shale and granite with 100% of the invaded nodes on drainage for all 3 rock types. At the end of the DNAPL redistribution stage, the average DNAPL saturation was 0.3 for all 3 rock types, the volume of DNAPL was 0.0036 m^3, 0.0047 m^3 and 0.0079 m^3 while the pool to residual ratio was 71:29%, 72:28% and 90:10% for sandstone, shale and granite respectively. The distributions of TCE DNAPL at the end of the redistribution stage for each rock type are illustrated in Figure 4.3 and Figure A6, Appendix A.

At the end of the 20 years Site Ageing stage (t_{TOTAL} = 21 years) the total mass of aqueous and sorbed TCE in the domain was 7.3 kg (55.6 moles), 6.8kg (50.8 moles) and 0.68 kg

(5.08 moles) for sandstone, shale and granite respectively. In each case, 97-99% of the total mass resided in the matrix, of which 97-98% was sorbed and only 1-2% remained in the aqueous phase. Although no DNAPL was left in the sandstone and shale domain at this time, 4.23 kg of DNAPL was found present in the granite domain. This observation is consistent with the findings in Parker e al. (1994) where it was suggested that due to the low porosity in granite, DNAPL could remain present in the fractures for decades. Figure 5.27 illustrates the distribution of aqueous phase TCE in sandstone, shale and granite at the end of the 20 year Site Ageing stage. In each case, the matrix immediately surrounding the fractures exhibits diffusion halos of TCE. However, given that the matrix is homogeneous, the depth and extent of TCE penetration of the matrix is observed to be highly dependent on properties of both the fractures and the matrix for each rock type. The combination of these impacts residence time of TCE in the source zone and it is the relative rates of TCE transport through fractures versus diffusion to the matrix that affects the final distribution of mass.

Figure 5.28 demonstrates that the mass flux of TCE out of the right boundary of the domain during the Site Ageing stage follows the order granite > shale > sandstone. The vertical axis of Figure 5.29 demonstrates that the percentage of initial TCE mass retained in the domain at the end of Site Ageing follows the order sandstone > shale > granite. These two results, mass lost to advection versus mass retained via sorption, reflect the overall balance of residence time versus matrix diffusion (See section 4.5.2.3 for calculations and further details). Peclet number (Pe) for fractured rock is defined as the ratio of advection to diffusion rates, $Pe = ve/(D^o\tau)$, where v is the advective velocity in

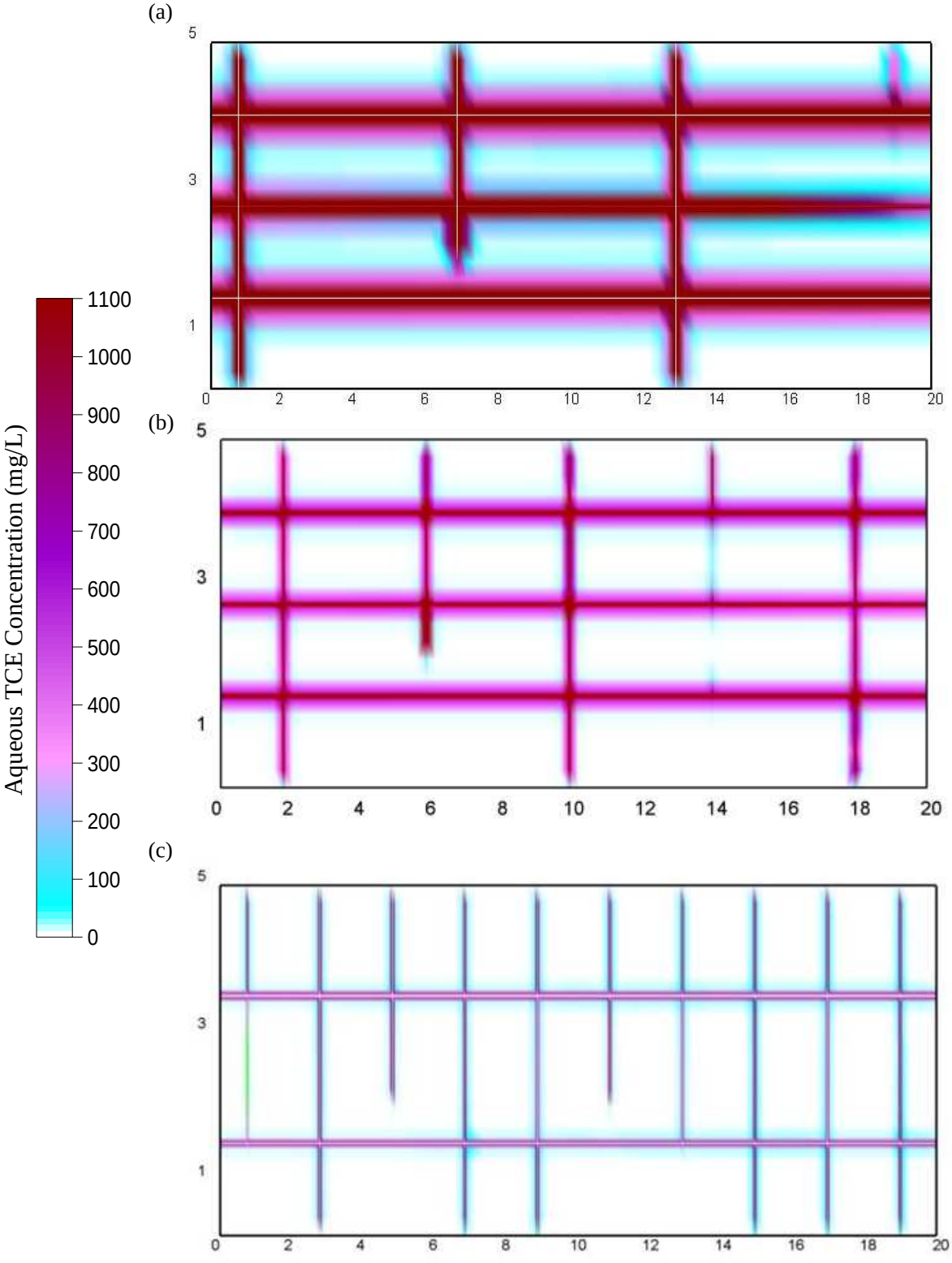

Figure 5.27: Distribution of aqueous TCE after 20 years (t_{TOTAL} = 21 years) of DNAPL dissolution (i.e., Site Ageing stage) in (a) Sandstone, (b) Shale and (c) Granite.

the fracture, e is the mean aperture, D^o is the free solute diffusion coefficient and τ is the matrix tortuosity (e.g., Fetter, 1993). Here v is taken as the mean horizontal advective velocity across each domain and e is the mean aperture of all horizontal fractures for each rock type. Figure 5.29 reveals that the percentage of TCE retained (in aqueous and sorbed forms) exhibits a linear dependence on the log(Pe) for the three rock types (R^2 = 0.9923) at the end of the Site Ageing stage (i.e., t_{TOTAL} = 21 years). This confirms expectations that lower Pe (i.e., lower advective velocity, smaller apertures, higher effective diffusion) corresponds to increased matrix diffusion (e.g., sandstone) while higher Pe corresponds to increased mass loss via advection (e.g., granite).

(a)

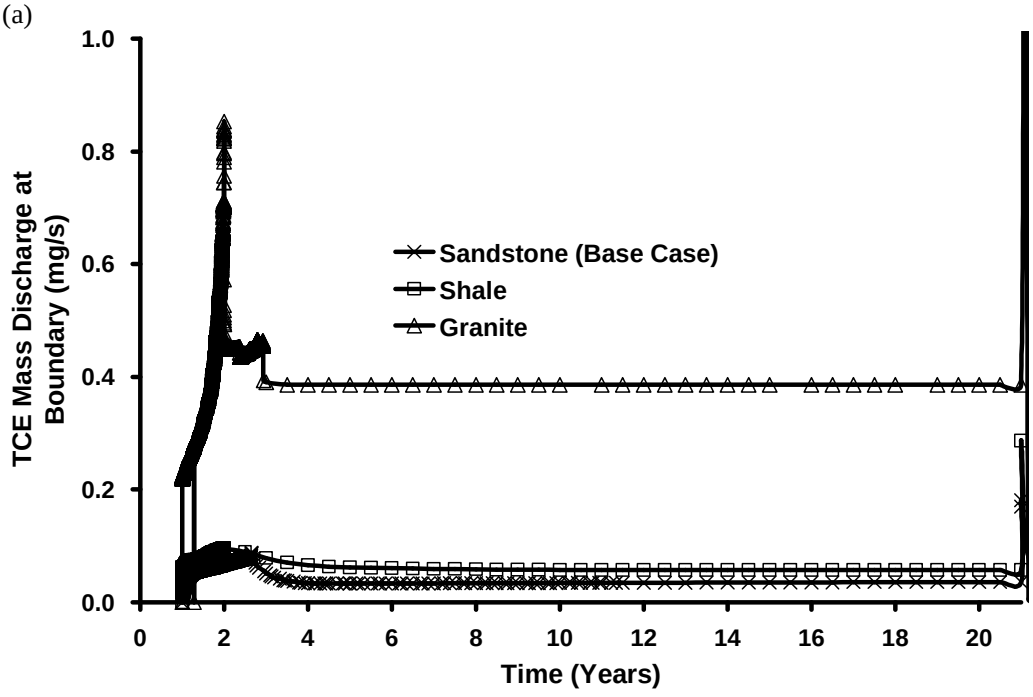

(b)

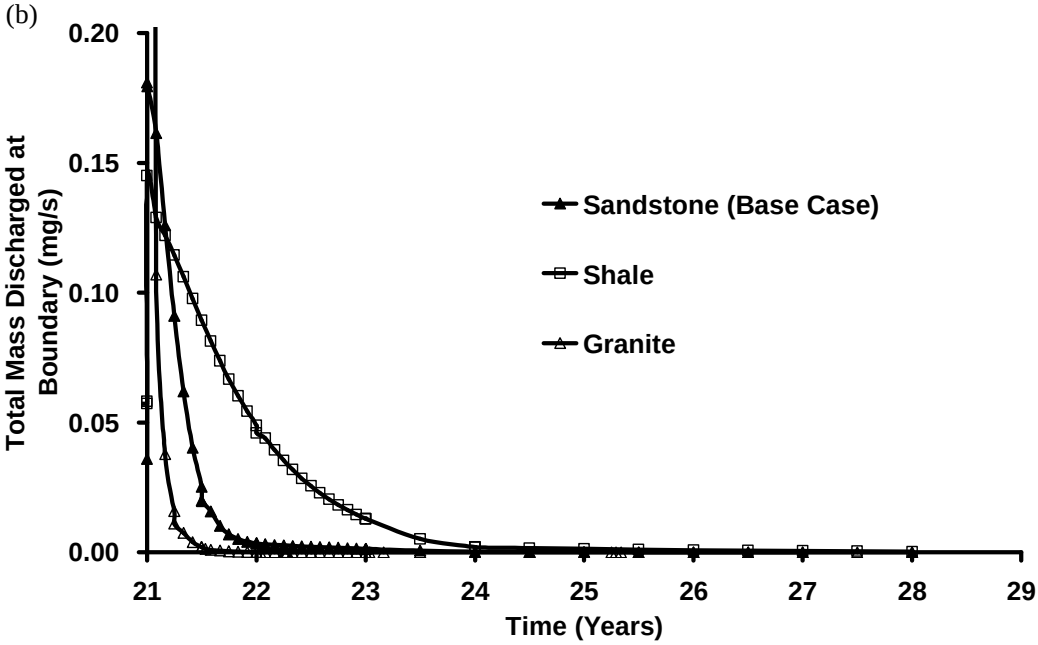

Figure 5.28: Comparison of total boundary mass discharge for different rock types; (a) from the beginning of the simulation to end of Site Ageing stage and (b) Treatment stage only (timescale expanded for clarity).

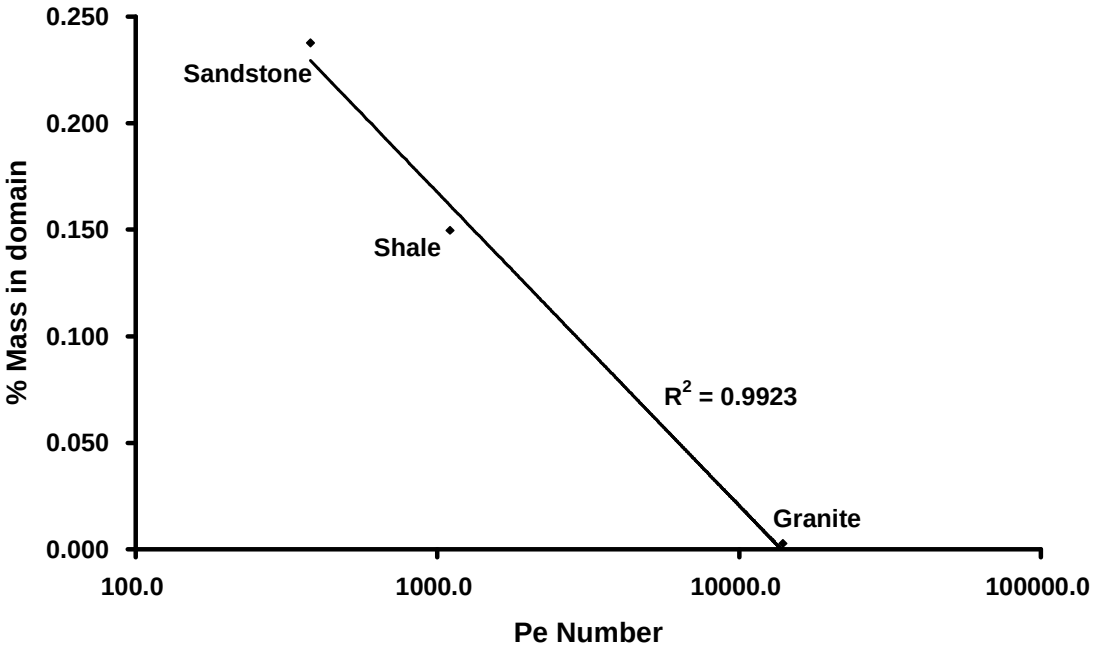

Figure 5.29: Mass of aqueous and sorbed TCE in various rock domains at end of Site Ageing stage (i.e., t_{TOTAL} = 21 years) vs. Peclet number (log scale) for each individual domain.

During the Treatment stage, 48.5 kg (545 moles), 35.1 kg (394 moles) and 436.3 kg (4900 moles) of lactate were injected into the domain for sandstone, shale and granite respectively (Table 5.5). The amount of lactate injected is equivalent to 9.8 times, 7.8 times and 964.6 times greater than the theoretical lactate mass required to dechlorinate all the TCE in the domain at the start of the Treatment stage. The differences in lactate mass injected are due the differences in bulk effective horizontal hydraulic conductivity while treatment period, injection concentration and hydraulic gradient were all held constant.

If all TCE present in the domain at the start of the Treatment stage was successfully reduced to ethene, the total mass of chloride produced would have been 166.8 moles, 152.4 moles and 15.24 for sandstone, shale and granite respectively. Figure 5.30 revealed the total moles of chloride produced were 128.8 moles, 36.8 moles and 0.06 moles for sandstone, shale and granite respectively. Thus, the efficiency of reductive dechlorination in the three rock types were 77.2%, 24.1% and 0.4% for sandstone, shale and granite respectively.

Figure 5.30 further revealed that the total moles of ethene produced were 40.8 moles, 5.67 moles and 0.0003 moles for sandstone, shale and granite respectively by the end of the simulations. These masses when compared to the TCE mass present in the domain at the start of the Treatment stage, revealed 73.5%, 11.2% and 0.006% of the initial mass has been successfully reduced to ethene.

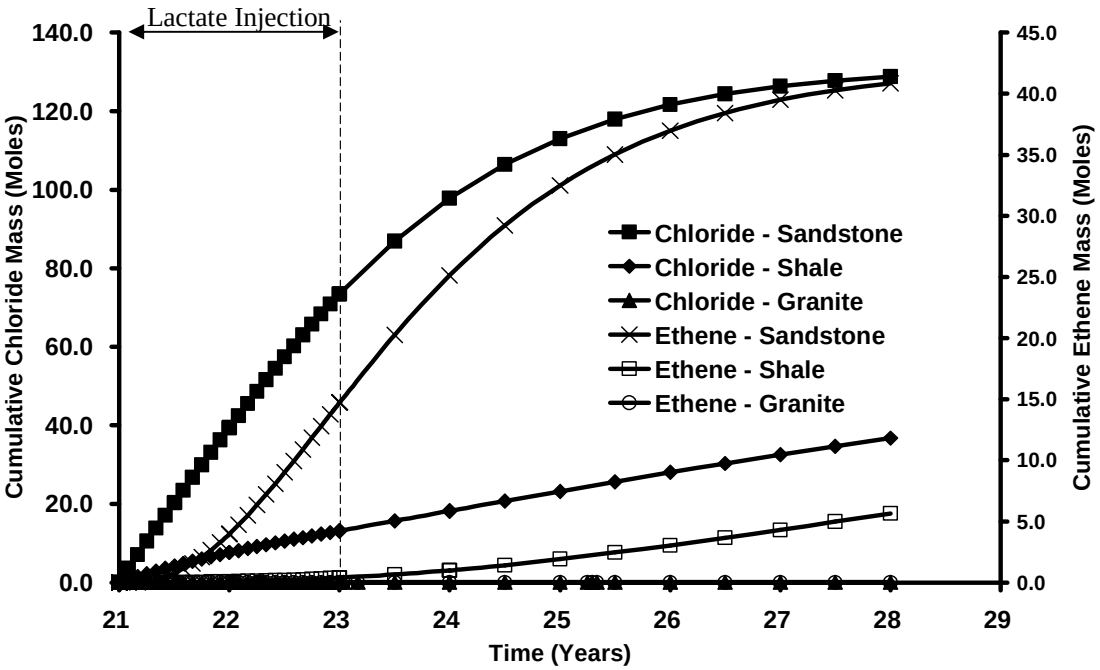

Figure 5.30: Cumulative mass of chloride and ethene produced over time for different rock types.

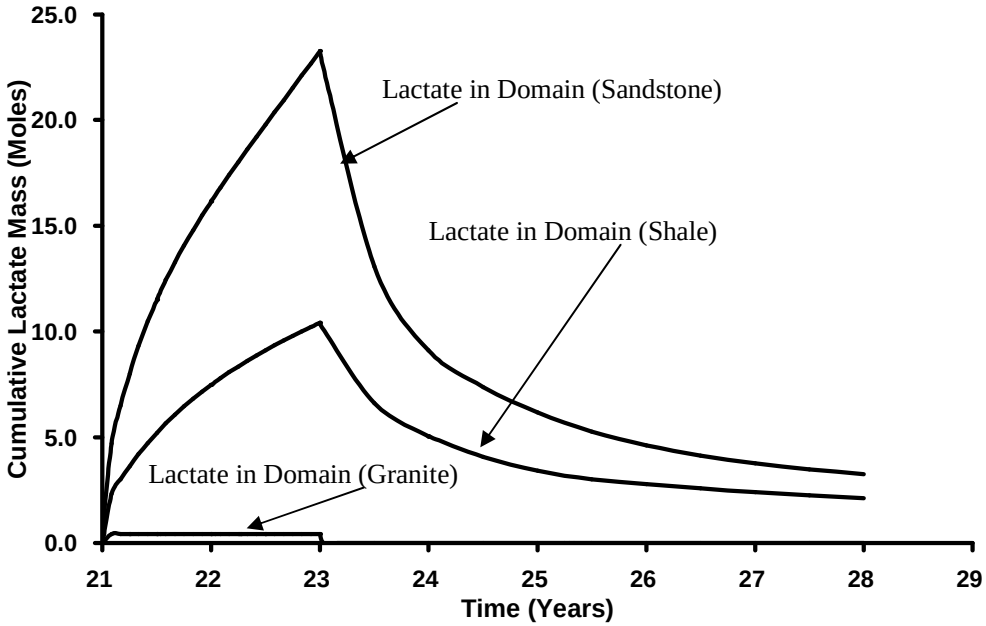

Figure 5.31: Cumulative mass of lactate present in the domains over time.

Figure 5.31 demonstrated that once the lactate injection ceased at t_{TOTAL} = 23 years, the cumulative mass of lactate present in the three rock domains began to decrease until the end of the simulation (i.e. t_{TOTAL} = 28 years). Correspondingly, the efficiency of EISB was found to be inversely related with the average Pe for each rock type. With higher Pe (i.e., higher advective velocity - granite), diffusion into the matrix is diminished relative to advection through the factures. Since TCE experienced forward diffusion for 20 years while lactate only has 2 years to penetrate the matrix, Pe has a significant impact on increasing the spatial distribution of lactate in the sandstone versus the granite domain.

5.5.2.6 Sensitivity to DNAPL Type

In this study, results were compared between PCE and TCE; in contrast to the previous simulations, the distribution of DNAPL at the start of the Site Ageing stage was not identical. At the end of the DNAPL Infiltration stage, the average DNAPL saturation was 0.75 while the volume of DNAPL in the domain was 0.008 m^3 (compared to a total fracture volume of 0.012 m^3) with 100% of the nodes in drainage in both simulations. At the end of the DNAPL redistribution stage, the average DNAPL saturation was 0.3 for both TCE and PCE , the volume of DNAPL present was 0.0036 m^3 (5.26 kg) and 0.0037 m^3 (6.03 kg), and the pool to residual ratio was 71:29% and 51:49% for TCE and PCE, respectively (Figures 5.5 and A14 of Appendix A respectively). The higher density of PCE, leading to higher mobility and more DNAPL migration out of the bottom of the domain, is most likely the cause of the reduced pool-to-residual ratio in that case.

At the end of the Site Ageing stage (t_{TOTAL} = 21 years) the total mass of TCE and PCE in the domain was 7.3 kg (55.6 moles) and 3.3kg (20.2 moles) respectively. As

demonstrated by Figure 5.33, the PCE DNAPL was almost completely dissolved after 16 years of Site Ageing (t_{TOTAL} = 17 years), as compared to only 2.5 years for TCE (Base Case, Figure 5.9). One reason for this is the lower solubility of PCE (Table 5.4). Another reason is that the PCE DNAPL in the fractures caused reduced relative permeability to water; in conjunction with a fixed gradient, this caused reduced water flux through the source zone. Figure 5.32 confirms that identical boundary conditions resulted in considerably different time series of water discharge (m^3/s) at the exit boundary. Both simulations experience increasing water discharge as DNAPL dissolves until the maximum is achieved when no DNAPL remains, but the rate of increase varies due to the difference in DNAPL dissolution rates. The reduced aqueous phase relative permeability in the fractures in the presence of PCE DNAPL resulted in reduced water velocities and, in turn, even further reduced aqueous PCE mass flux. Grant and Gerhard (2007b) comment upon this dynamic link between DNAPL saturation and water velocity and its impact on the evolution of source zones in unconsolidated porous media. Of the 3.3 kg (20.2 moles) PCE mass in the domain at the end of Site Ageing, more than 99.9% resided in the sandstone matrix, of which 98.7% was sorbed and only 1.3% remained in the aqueous phase.

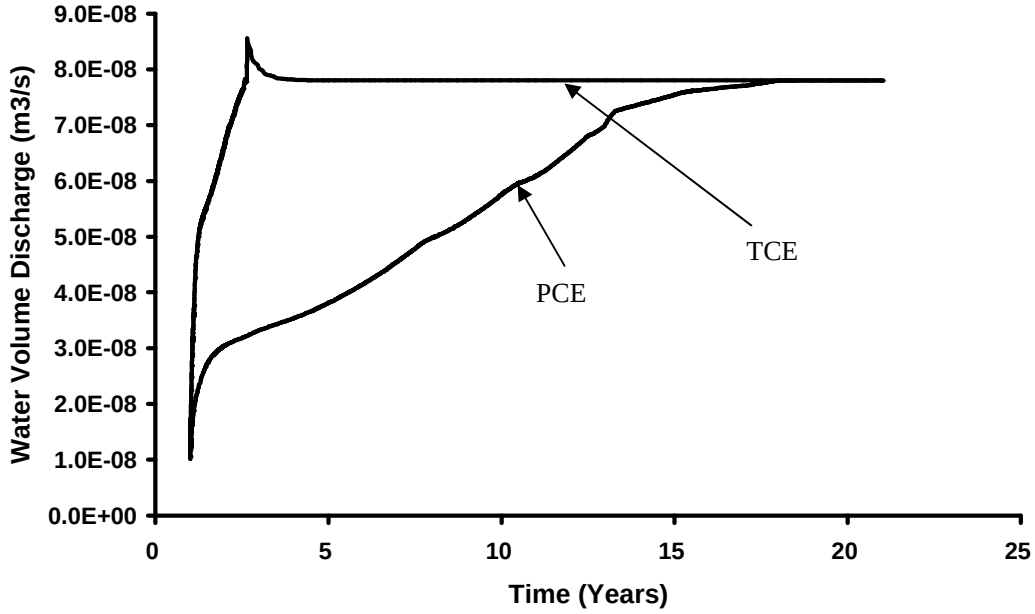

Figure 5.32: Downgradient water volume discharge for (i) TCE and (ii) PCE Simulations.

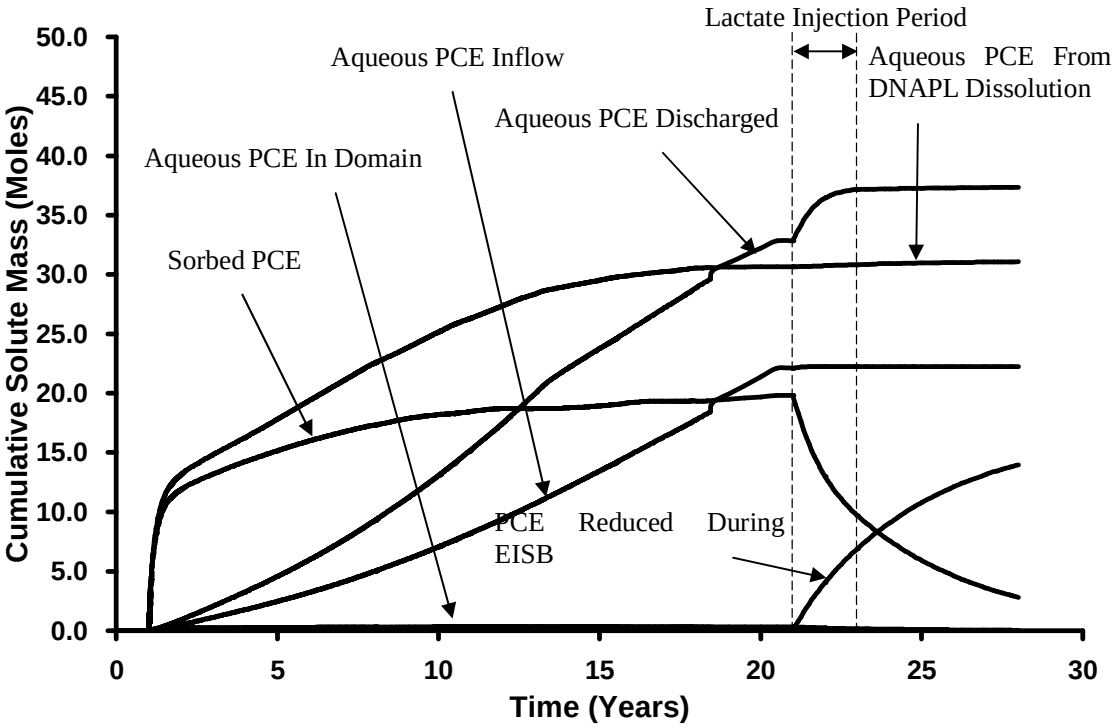

Figure 5.33: Cumulative aqueous and sorbed PCE from all sinks and sources for PCE Simulation.

The distribution of aqueous and sorbed PCE at the end of Site Ageing is shown in Figure A15, Appendix A, as compared to that for TCE at the same time (Figure 5.6). There are a number of reasons why the depth of matrix penetration for PCE is considerably less than TCE. First, the constant concentration of aqueous solvent provided at the upgradient boundary throughout the Site Ageing stage (50% solubility) was much lower for PCE (100mg/L) than TCE (550mg/L). In addition, the R and alpha value for PCE is 60 and 780, while for TCE is 21 and 270, this is because the Koc for PCE is approximately 3 times greater than TCE (i.e., KOC_{PCE} = 364 L/kg, KOC_{TCE} = 126 L/kg; Pankow and Cherry, 1996). The effective diffusion rate for PCE is 1.88 x 10^{-10} m^2/s while for TCE it is 2.02 x 10^{-10} m^2/s. Therefore, the diffusion rate divided by the rock capacity factor for PCE is 2.4 x 10^{-13}, while for TCE it is 7.4 x 10^{-13}. For these reasons, although the initial volume of DNAPL was similar in both simulations, the mass present in the PCE domain at the end of the Site Ageing stage (3.3 kg) is much lower than the TCE domain (7.3 kg) (Table 5.5).

As demonstrated in Figure 5.34, although the total mass of lactate injected into the domain was similar in both simulations, the total amount of lactate used for chlorinated ethenes reduction was 6.56% for TCE and 2.43% for PCE. This is found despite the fact that 25% more hydrogen (and therefore more lactate) is required to dechlorinate 1 mole of PCE than TCE (Equations 5.3 – 5.7). Figure 5.35 reveals that 73.5% of the initial TCE mass was successfully reduced to ethene as compared to 45% in the PCE simulation. However, Figures 5.9, and 5.34 – 5.36 all reveal that while TCE dechlorination had effectively run its course (see rates of TCE reduction and chloride

production diminishing substantially towards zero) PCE dechlorination rates had not yet started to diminish. The evidence suggests that the bioremediation process was substantially slower for PCE but it is possible that a similar degree of clean-up may have been achieved if a longer post-treatment period was simulated.

There are a number of reasons why PCE bioremediation was substantially slower in these simulations. One reason is due to the lower mass of PCE present at the start of the Treatment stage: with first-order reactions the rate of dechlorination of each chlorinated ethene is proportional to the amount present. A second reason is the higher Koc value for PCE, which implies that, for a given concentration, a higher proportion of PCE than TCE will be sorbed instead of in the aqueous phase (and only the aqueous phase is available to the microorganisms for dechlorination). A third reason is that the PCE dechlorination pathway requires one additional rate-limited step which necessarily slows down the overall conversion rate from parent solvent to ethene.

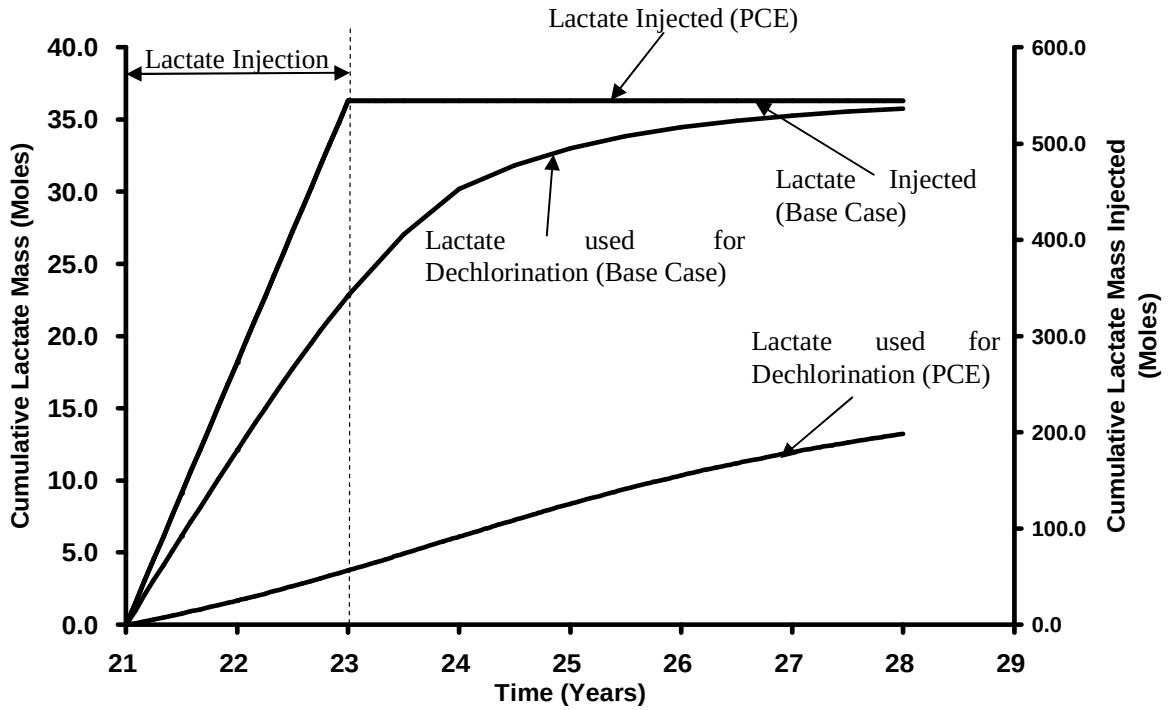

Figure 5.34: Cumulative mass of lactate over time for different DNAPL simulations.

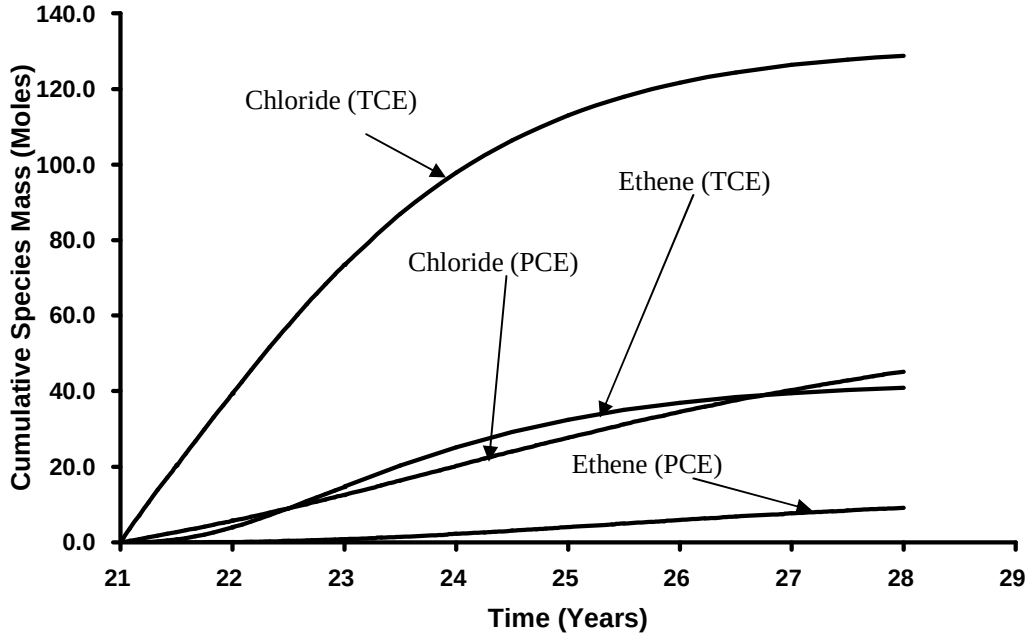

Figure 5.35: Cumulative mass of chloride and ethene produced over time for different DNAPL simulations.

(a)

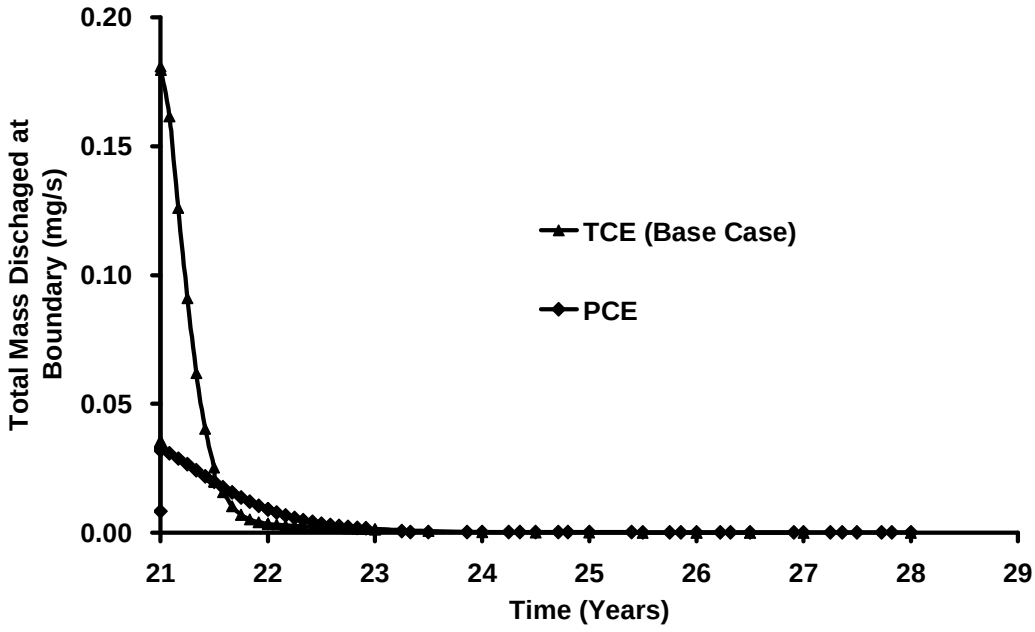

(b)

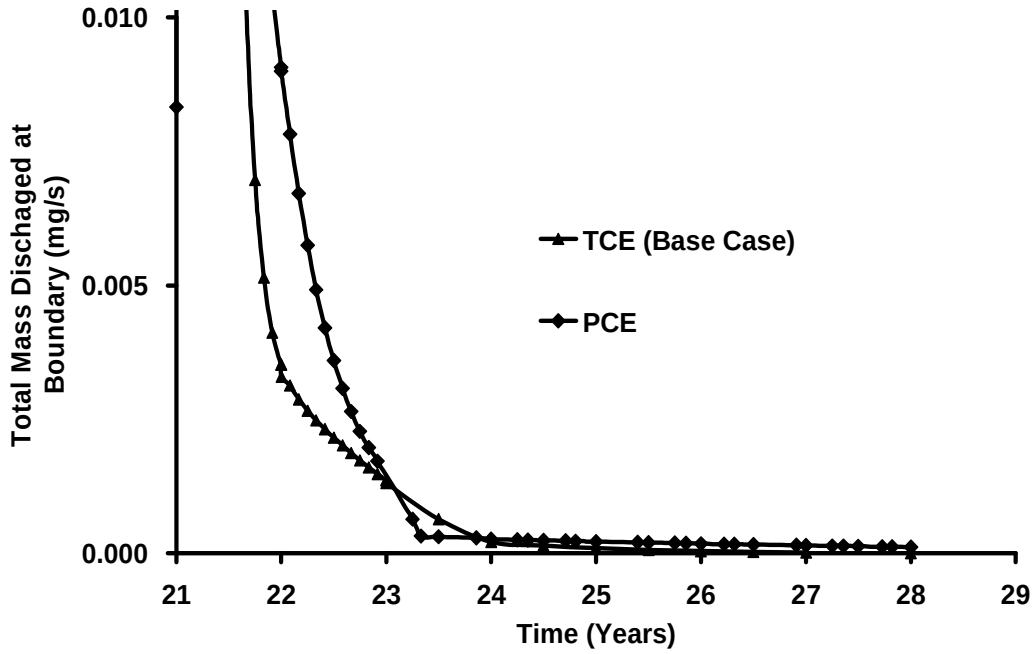

Figure 5.36: Comparison of total boundary mass discharge for (a) different DNAPL and (b) since the start of the Treatment Stage only (timescale expanded for clarity).

Figure 5.36 agrees with this analysis since the reduction in PCE mass flux at the downgradient boundary is slower than that for TCE. Figure 5.36b illustrates that in the case for PCE, downgradient mass discharge did not reduce to non-detect levels by the end of the simulation. Therefore, the untreated PCE mass in the domain acts as a long-term source of contamination to the downgradient boundary. Figure 5.36 further reveals a rapid change in PCE mass discharged at approximately t_{TOTAL} = 23.3 years, suggesting that dechlorination of PCE is more difficult than TCE.

5.6 CONCLUSION

In the Base Case, EISB was demonstrated to produce relatively positive results. Of the total initial mass present, 73.5% was demonstrated to have successfully been reduced to

ethene. It was further noted that the size of facture apertures directly affects the downgradient discharge where fractures with smaller apertures were noted to take a longer time before the discharged mass decreases below detection limits as compared to larger fractures. This represents an ideal case, with robust first-order decay rates, active microorganisms throughout the fractures and matrix, presence of TCE rather than PCE, and low peclet numbers that enhance diffusion of lactate to the matrix-bound contaminant.

However, when the bacterial consortium was assumed to be confined to within the sandstone fractures, it was found that the mass of chloride produced was 200 times less than the Base Case. Since the majority of the mass resided in the matrix, lack of bioremediation in the matrix significantly reduced effectiveness of treatment. It is noted that some treatment of back-diffusing TCE occurred in the fractures, but this was significant only for the smallest horizontal fractures, which contribute least to the downgradient mass flux, and thus the overall long-term effect on mass discharge was negligible.

These sensitivity studies suggest that the concentration and the rate at which lactate was injected – given that the total mass injected is identical - have little influence on EISB effectiveness during and after the treatment process. It is acknowledged that this may differ in scenarios where lactate is not in excess or where bioclogging, pH effects, and other complicating factors may plan an important role.

For scenarios in which diffusive flux is significant (e.g., sandstone/TCE simulations) substantial mass becomes stored in the matrix via forward diffusion. High diffusive flux is promoted by high matrix porosity, high diffusion coefficient, high aqueous solvent concentrations (i.e., high solubility), and low sorptive capacity (i.e., low Koc and/or low foc). The results revealed that both the mass of TCE reduced and the time required to reduce this mass can vary significantly in different rock types, with mean fracture Pe observed to be inversely related to the efficiency of EISB. Clearly the rock properties that influence matrix loading of contaminants and diffusive rate of electron donor during the treatment period dominate EISB performance, assuming that effective ESIB is able to occur in the matrix.

EISB was substantially slower for PCE than TCE but it is possible that a similar degree of clean-up may have been achieved if a longer post-treatment period was simulated.

The post-treatment TCE mass discharged was found to be able to achieve negligible levels when (i) bioremediation was assumed to take place throughout the matrix and (ii) first-order biodegradation rates exceeded a threshold. These results indicate that ideal conditions (i.e., inhibition is low, significant dechlorination occurs in the matrix) and favourable scenarios (e.g., low Pe number formations such as sandstone, rapidly degrading compounds such as TCE) may be required for successful application of EISB. This is because success appears to depend on effective penetration of electron donor into the matrix during the treatment period and the ongoing treatment that occurs after injection ceases.

It is acknowledged that numerous assumptions and simplifications were employed in this work. In the majority of circumstances, the assumptions were chosen to present a 'best case' scenario that favours effective treatment (e.g., constant injection concentration with elevated gradient, two-dimensional flow with little opportunity for bypassing, no Bioclogging, etc.). This approach underscores the challenges associated with effectively treating aged source zones in fractured rock with EISB. The limited number of simulations conducted using specific site templates on a small field scale implies that these results cannot be directly extended to a wide variety of complex real sites. Nevertheless, it is expected that the importance influence of key variables, including decay rate parameters, the spatial distribution of microorganisms, the rock type, and DNAPL type, will likely have similar impacts in field applications of EISB to chlorinated solvent-impacted fractured rock scenarios.

CHAPTER 6 – NUMERICAL SIMULATION OF DNAPL SOURCE ZONE REMEDIATION WITH SURFACTANT FLUSHING IN FRACTURED ROCK

6.1 ABSTRACT

Numerical simulations were conducted to investigate the benefits and challenges of *in situ* surfactant flushing for chlorinated solvent dense, nonaqueous phase liquid (DNAPL) in fractured rock aquifers at the field scale. Two-dimensional (cross-section) simulations were conducted with DNAPL3DRX-FRAC, a finite difference multiphase flow-aqueous transport-reaction numerical model developed specifically for fractured rock simulations and augmented with enhanced DNAPL and aqueous solvent solubility for surfactant flooding applications. The base case simulation employed a complex DNAPL distribution in the fracture network generated via a surface release of trichloroethylene (TCE) and site ageing via dissolution and diffusion achieved significant matrix contamination. 11 surfactant flushing simulations with Tween-80 were conducted to explore sensitivity of DNAPL recovery and downgradient mass flux to a number of site specific properties (rock type, DNAPL type, extent of site ageing), engineering parameters (surfactant concentration), and modelling assumptions (mass transfer expression).

Surfactant flushing was found to be effective for DNAPL residing within horizontal fractures; however DNAPL was not removed from dead-end vertical fractures even after 5 years of post-treatment. Furthermore, all simulations predicted limited treatment for

both aqueous and sorbed solvent within the matrix. Minimal difference was found in terms of the efficiency of surfactant flushing when the surfactant concentration was increased from 20g/L to 40g/L. Higher treatment efficiencies were observed in the shale and sandstone while granite, with the largest fraction of initial mass entrapped in vertical fractures, experiences the lowest fraction of mass being recovered among the three rock types. It was further revealed that the aging period of each site, which directly affects the mass of aqueous and sorbed TCE within the matrix surrounding the fractures; affects the amount of TCE molecules being solubilised by surfactant micelles and subsequently the amount of back-diffusion when treatment ceases. When surfactant was applied to different DNAPLs, due to the difference in molar solubilisation ratios (MSRs), it was found that a higher fraction of aqueous PCE mass was entrained into micelles than for TCE. Furthermore, different mass transfer models were found to lead to significant difference to the amount of DNAPL left in the domain by the end of the simulation

6.2 INTRODUCTION

Surfactants are surface acting agents that concentrate at interfacial regions between two fluid phases (e.g., oil and water). They are amphiphilic agents that exhibit dual behaviour (i.e., affinity for both water and oil). This behaviour is possible due to their molecular structure which is made up of one soluble and one insoluble moiety. Surfactants are classified according to the nature of the hydrophilic portion of the molecule. The head can be positively charged (cationic), negatively charged (anionic), both negatively and positively charged (zwitterionic) or not charged (nonionic) (West and Harwell, 1992). Individual surfactant molecules are single monomers. However, when the aqueous concentration of monomers exceeds a critical value - the critical micelle concentration (CMC) - and the solution is above the limiting Krafft temperature, T_k, the monomers form into spherical clusters called micelles. Micelles exhibit a hydrophilic surface around an lipophilic core.

Due to these properties, micelles are capable of encapsulating non-aqueous phase liquids (NAPLs) and forming microemulsions. As a result, surfactants can decrease the interfacial tension (IFT) between water and NAPL and can increase the effective aqueous solubility of NAPL components. The former allows NAPLs contacted with surfactants to be mobilized towards recovery wells due to a reduction in capillary resistance to flow, while the latter allows NAPL mass to be removed by enhanced dissolution. However, mobilization of DNAPL in particular may cause it to move deeper into former uncontaminated zones (Pankow and Cherry, 1996). For this reason, some researchers recommend using solubilisation rather than mobilization as the primary surfactant

treatment mechanism in DNAPL systems. However, solubilisation of contaminant by the surfactant creates a microemulsion phase that is denser than the surrounding groundwater and can travel downward before being captured by an extraction well (Ramsburg and Pennell, 2002).

Laboratory-scale experiments have demonstrated that DNAPLs can be efficiently recovered in unconsolidated porous media using two-phase (immiscible) displacement technologies (e.g., Lunn and Kueper, 1999; Ramsburg and Pennell, 2002; Miller et al., 2000; Kostarelos et al., 1998). Surfactant-enhanced aquifer remediation has been demonstrated to effectively recover contaminants (including chlorinated solvents) in a variety of subsurface environments, (Taylor et al., 2004; Zhong et al., 2003, Abriola et al., 2005; Suchomel et al., 2007). The use of surfactants for remediation of unconsolidated porous media at field sites contaminated by DNAPL has been investigated by numerous research groups (e.g., Ellis et al., 1986; Gannon et al., 1992; Pennell et al., 1994; Pope and Wade, 1995; Shiau et al., 1995; Fountain et al., 1996; Martel and Gelinas, 1996; Hirasaki et al., 1997).

However, the effectiveness of surfactants in fractured rock is not known. The author has found only one publication investigating the use of surfactants for DNAPL trapped in fractures. Yeo et al. (2003) conducted three bench scale experiments using an artificial two-dimensional fracture network that was made from a 20 cm by 15 cm acrylic plate with a thickness of 2 cm. The removal of DNAPL trapped in vertical dead-end fractures was examined in this study. It was found that a water-flushing method failed to remove DNAPL TCE from fractures, failing to overcome the vertical capillary and gravity forces

that trapped the DNAPL. Subsequently, a fluid denser than TCE (made up of a mixture of 50% water and 50% calcium bromide) was injected into the fracture network, but this too did not displace the TCE DNAPL. However, a mixture of calcium bromide and 0.8% sodium doceyl sulphate surfactant did effectively displace the trapped DNAPL, suggesting that surfactants could act similarly in fractured rock as in unconsolidated porous media.

The objective of this work is to examine the benefits and challenges of DNAPL source zone remediation in fractured bedrock aquifers by surfactants at the field scale. Numerical simulations are employed to evaluate the effectiveness of surfactant remediation via enhanced dissolution as a function of key site parameters (fractured rock type, degree of contamination, DNAPL type) as well as an engineering parameter (surfactant concentration), and a modelling assumption (rate of mass transfer).

6.3 MODEL DEVELOPMENT

A more detailed description on the development of the model DNAPL3DRX-FRAC is provided in Chapter 3. The processes described here are aimed to provide the reader with an understanding of the approach being adopted to develop the surfactant treatment package of the model.

6.3.1 Surfactant Flushing Kinetics

For the purpose of this study, the subsequent discussion is limited to surfactant flushing of DNAPLs by Tween-80 (polyoxyethylene (20) sorbitan monooleate). Although a number of surfactant types exist, Tween-80 was selected for these studies due to its

frequent use in DNAPL remediation research and field trials (e.g., Abriola et al., 1993; Jafvert et al., 1995; Ramsburg and Pennell, 2002; Ramsburg et al., 2005, Chu and So, 2001; Zhang et al., 2006). Nonionic surfactants such as Tween-80 tend to possess the most desirable characteristics for *in situ* subsurface remediation. For example, nonionic surfactants do not dissociate and do not produce ions in an aqueous solution, they are fairly insensitive to electrolytes, and can be utilized in aqueous solutions with high salinity or significant hardness. Additionally, nonionic surfactants tend to have low biotoxicity and may be biodegradable. Tween-80 is typically applied at concentrations in the range of 2.0 – 6.0% (Abriola et al., 1993; Jafvert et al., 1995; Ramsburg and Pennell, 2002; Ramsburg et al., 2005).

DNAPL solubilisation will be considered the dominant recovery mechanism in this work. DNAPL mobilization is not expected to be as significant a recover mechanism in DNAPL source zones which have undergone considerable redistribution (and loss) of DNAPL outside the treatment zone. This work considers scenarios in which, after termination of the source, DNAPL has been allowed to redistribute freely out of the sides and bottom of the domain prior to remediation commencing in the near-surface fractured rock source zone. Hence much of the DNAPL is at residual and the remaining horizontal DNAPL pools are limited and only present at high saturations in dead-end vertical fractures. Neglecting IFT reduction by Tween-80 in these situations is expected to not have a dominant effect on the conclusions.

6.3.1.1 Solubilisation

A measure of the effectiveness of a particular surfactant in solubilising a given DNAPL is

known as the molar solubilisation ratio (MSR). MSR is defined as the number of moles of organic compound solubilised per mole of surfactant added to solution (Attwood and Florence, 1983). The MSR may be calculated (Edwards et al., 1991):

$$MSR = \frac{C_{eq}^{CE} - C_{cmc}^{CE}}{\left(C^{Surf} - C_{cmc}^{Surf}\right)} \qquad (6.1)$$

Where C_{eq}^{CE} (mol/L) is the equilibrium chlorinated ethene solute concentration in the presence of a given surfactant concentration greater than the CMC; C_{cmc}^{CE} (mol/L) is the concentration of chlorinated ethene DNAPL at CMC (normally assumed to be the solubility of the DNAPL); C^{Surf} is the given surfactant concentration and C_{cmc}^{Surf} is the surfactant CMC. C_{cmc}^{Surf} is 13mg/L for Tween-80 (Taylor et al., 2001).

6.3.1.2 Micellear Partitioning Below DNAPL Solubility

Equation 6.1 is only valid in the presence of both DNAPL (i.e. $C_{eq}^{CE} > C_{cmc}^{CE}$) and surfactant concentrations greater than the CMC. Since most studies in unconsolidated porous media are particularly focused on the interactions of high surfactant concentrations with excess DNAPL, this equation is typically considered sufficient. However, in fractured rock, the matrix may prevent DNAPL penetration but nevertheless be a significant medium for diffusive transport of both aqueous chlorinated solvents and surfactant monomers/micelles. Thus, it is necessary here to consider surfactant concentrations above the CMC in the presence of chlorinated solvent concentrations that are less than their standard equilibrium solubility (C_{cmc}^{CE}).

Using batch partitioning experiments, Kim et al. (2007) demonstrated a linear correlation between the fraction of chlorinated ethene (TCE and PCE) that remained external to the micelles (extramicellar) as a function of aqueous chlorinated ethene concentration up to their standard aqueous solubilities (Figure 6.1). The figure further demonstrates that for a given concentration of aqueous PCE and TCE, as the concentration of Tween-80 increased from 0.2 to 1.0 wt%, the extramicellar mass fraction decreased approximately 50% (Figure 6.1).

Each curve in Figure 6.1 was averaged to obtain a single ratio of extramicellular chlorinated ethene to total chlorinated ethene concentration as a function of surfactant concentration (Figure 6.2, for TCE; Figure C1, Appendix C, for PCE). An exponential relationship was best-fit to the range of concentrations examined by Kim et al (2007), 0.2% < C^{Surf} < 1.0% (R^2 = 0.989). As shown in Figure 6.2, this function was extrapolated to obtain a relevant extramicellular ratio for Tween-80 at 4.0%. In the absence of data, a linear function was assumed to apply in the region C^{Surf} < 0.20%. Therefore, the model employs these relationships to determine the equilibrium extramicellular mass fraction of chlorinated ethene at a given surfactant concentration (C_{TCE}^{EX}) in the absence of DNAPL:

TCE:

$$\frac{C_{TCE}^{EX}}{C_0} = 1 - 3.515 C^{Surf}, \; 0.0\% \leq C^{Surf} \leq 0.2\% \qquad (6.2a)$$

$$\frac{C_{TCE}^{EX}}{C_0} = 0.37 e^{-C^{Surf}}, \; C^{Surf} \geq 0.2\% \qquad (6.2b)$$

PCE:

$$\frac{C_{PCE}^{EX}}{C_0} = 1 - 4.406 C^{Surf}, \quad 0.0\% \leq C^{Surf} \leq 0.2\% \qquad (6.3a)$$

$$\frac{C_{PCE}^{EX}}{C_0} = 0.12 e^{-C^{Surf}}, \quad C^{Surf} \geq 0.2\% \qquad (6.3b)$$

(a)

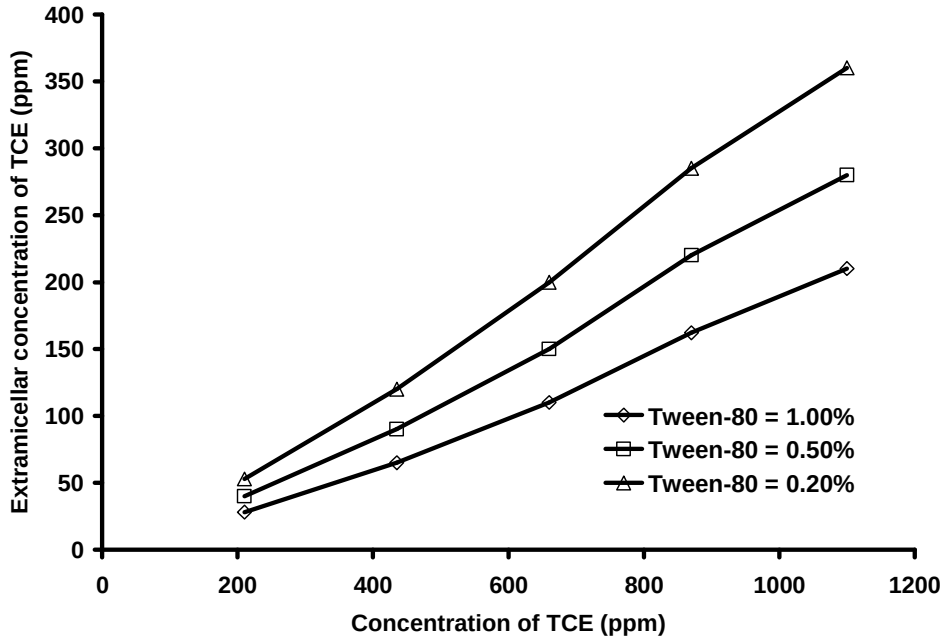

(b)

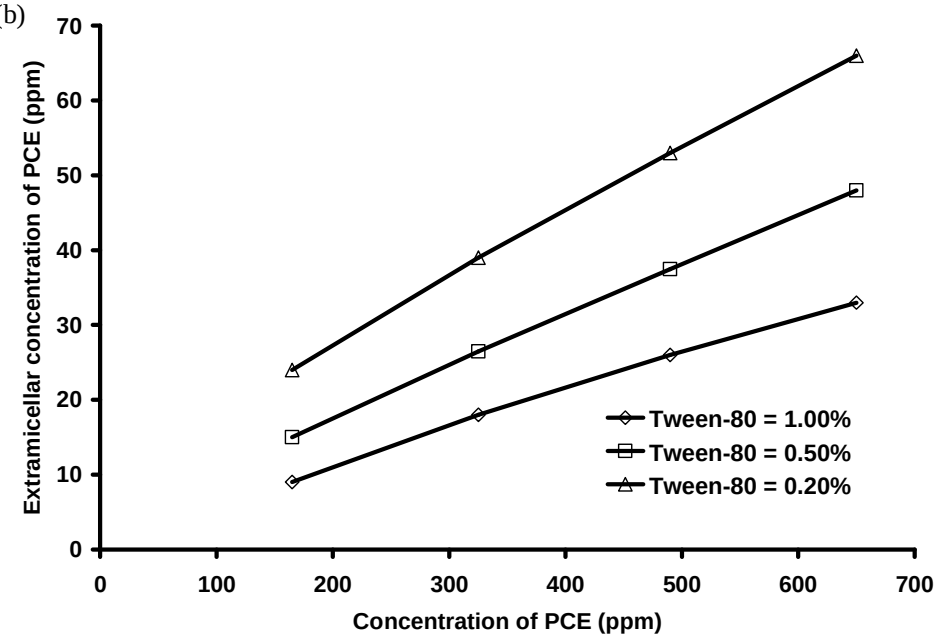

Figure 6.1: Extramicellar concentration of (a) TCE and (b) PCE in Tween-80 solution (Data extracted from Kim et al., 2007).

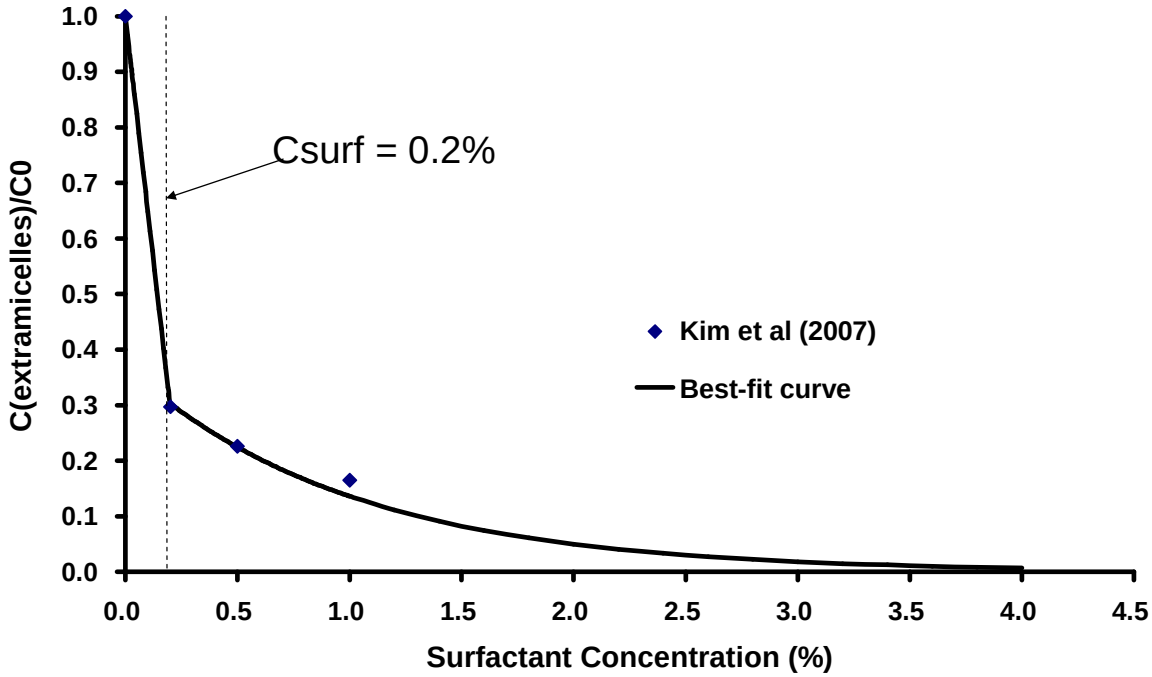

Figure 6.2: Extramicellar best fit curves for TCE based on results extrapolated from Kim et al., 2007.

6.3.1.3 Surfactant Reaction Module

The model simulates three separate, mobile aqueous species: (1) aqueous chlorinated ethene solute (2) 'surfactant' (monomers and micelles free of chlorinated ethene), and (3) 'micelles' (surfactant micelles containing chlorinated ethene).

Within each timestep, the model determines the distribution of surfactant and treats separately those nodes with DNAPL and those without. For nodes containing DNAPL and if the concentration of surfactant is above the CMC level, C_{eq}^{CE} (the equilibrium concentration of chlorinated ethene for a given surfactant concentration) is determined via Equation 6.1. Equilibrium mass transfer is assumed in reducing the DNAPL saturation and increasing the concentration of chlorinated ethene in the aqueous phase. If C_{eq}^{CE} exceeds the standard DNAPL aqueous solubility (i.e., 1100mg/L for TCE and

200 mg/L for PCE), all the mass that exceeds the standard solubility is then immediately moved from the aqueous solvent species into the micelle species (i.e., the former decreases in proportion the increase in the latter; no kinetics assumed). As micelles become occupied with solvent, the micelle species increases in concentration and the surfactant species concentration decreases correspondingly (i.e., total surfactant mass is conserved).

For nodes containing chlorinated ethene mass but no DNAPL, (e.g., a matrix node), if the concentration of surfactant is present and above the CMC level, Equations 6.2 or 6.3 is employed to determine the amount of mass that partitions into the micelles, and the concentration of all three species are updated accordingly. It is assumed that, once entrained, chlorinated ethene mass will not partition back out of the micelles.

After which, the model calculates the concentration of the micelles for each node by summing up the mass of chlorinated ethene partitioned into the micelles together with the surfactant mass used in this process and dividing it by the molecular weight of the micelle species as determined by the sum of molecular weight of chlorinated ethene and surfactant.

6.3.1.4 Sorption

Abriola et al. (2005) found that sorption of Tween-80 to sand conformed to a Langmuir isotherm. The retardation factor for a Langmuir sorption isotherm is (Fetter, 1993):

$$R = 1 + \frac{\rho}{\phi}\left(\frac{\alpha\beta}{(1+\alpha C)^2}\right) \qquad (6.4)$$

where α is an adsorption constant related to the binding energy (L^3M^{-1}), β is the maximum amount of solute that can be adsorbed by the solids (MM^{-1}), ρ is the dry bulk density (ML^{-3}), ϕ is the porosity of the matrix (-) and C is the concentration of the solute (ML^{-3}). Via the batch experiments, Abriola et al. (2005) yielded a maximum sorption capacity of 0.17 ± 0.02 mg/g and an adsorption constant of 0.12 ± 0.04 L/mg.

This finding was consistent with previous studies in which the maximum sorption of Tween-80 by sands having low organic carbon content ranged from 0.16 to 0.19 mg/g (Taylor et al., 2001). In the absence of literature on the sorption capacity of Tween-80 in fractured rocks, a Langmuir isotherm is assumed. In this work, an appropriate fraction of organic carbon is assigned to the matrix for each rock type and thus Equation 6.4 applies to all matrix nodes. However, the fractures are assumed to be free of organic carbon and thus sorption is negligible in the fractures. Lipson et al. (2005) studied a system of equally spaced fractures from the field and determined that when matrix diffusion effects are dominant, fracture retardation can be assumed equal to 1. Sensitivity to different Tween-80 sorption isotherms is likely small at the high surfactant concentrations (40000 – 60000 mg/l) employed in this work.

For the purpose of this study, the retardation factor for the aqueous chlorinated ethene is calculated as:

$$R_i = 1 + Koc \times foc_i \frac{\rho}{\theta} \qquad (6.5)$$

where ρ is the dry bulk density (ML^{-3}), θ is the porosity of the matrix (-), and *Koc* is the organic carbon partition coefficient (L^3M^{-1}). No sorption was assumed for the micelles

(Liu et al., 1992). The proper implementation of both retardation isotherms in the model was verified at both the scales of a single node and field scale simulation (see Chapter 3.3.4 for details),

6.3.1.5 Mass Transfer

DNAPL to water mass transfer is treated as an equilibrium process in the simulations presented in this work. It is acknowledged that non-equilibrium mass transfer has been observed in experimental fractured systems (e.g., Glass and Nicholl 1995; Dickson and Thomson 2003). Chapters 3 of this thesis, which examined DNAPL dissolution over substantial aging periods in fractured rock, suggested that the matrix provides such a substantial mass sink that chlorinated solvent DNAPL dissolves relatively rapidly (on the order of years, not decades). Therefore, it may be that DNAPL dissolution in these scenarios is relatively insensitive to mass transfer routine.

However, since surfactant flushing is a mass transfer-dependent technology, the prudent step was taken to incorporate an appropriate rate-limited dissolution model for fractures. Dickson and Thomson (2003) carried out eight long-term dissolution experiments using 1,1,1-trichloroethane (1,1,1-TCA) and trichloroethylene (TCE) in two laboratory-scale dolomitic limestone variable aperture fractures. The experimental data were used in conjunction with statistical techniques to develop a continuous empirical model describing the (initial) pseudosteady and transient stages of dissolution. The model was then used in that work to successfully replicate effluent concentration data from two separate dissolution experiments providing an indication of the expected dissolution behaviour of entrapped DNAPLs.

Sherwood number, proportional to kinetic mass transfer rate, was determined to be (Dickson and Thomson, 2003):

$$Sh = 7.718 R_e^{1.621} \delta^{2.439} Sn^*(t)^{8.826} \qquad Sn^*(t) \geq 1 \qquad (6.6a)$$

$$Sh = 7.718 R_e^{1.621} \delta^{2.439} Sn^*(t)^{4.338} \qquad Sn^*(t) \leq 1 \qquad (6.6b)$$

$$Sn^*(t) = \frac{Sn(t)}{Sn_{8\%}} \qquad (6.6c)$$

where $Sn(t)$ and $Sn_{8\%}$ are the DNAPL saturation and DNAPL saturation when 8% of initial mass is removed, respectively. *Re* is the Reynold's number and δ is the aperture ratio which takes into account of the range of extreme apertures (δ is taken equal to unity in this study, corresponding to parallel plate fracture geometries). The majority of mass removal was demonstrated to occur during the initial pseudosteady and early transient stages of dissolution (Dickson and Thomson, 2003; Miller et al., 1990). Dickson and Thomson (2003) demonstrated the initial pseudosteady stage to typically last until an average of 8% of the initial mass trapped was removed, or until the initial volumetric DNAPL saturation Sn(t = 0) was reduced by 8% as denoted by $Sn_{8\%}$.

6.3.2 Model Verification

A more detail description on the model verification process of DNAPL3DRX-FRAC is provided in Chapter 3. For the purpose of this study the subsequent discussion is limited to the verification of the surfactant treatment package of the model.

6.3.2.1 Surfactant Flushing Verification

Since no analytical solution is available for verifying the surfactant model in fractured rock, several steps were taken to build confidence in the developed model. First, a one-dimensional simulation of surfactant flushing of a DNAPL pool in a single horizontal fracture was carried out and compared with calculations via Equation 6.1. Fluid properties and reaction parameters for this simulation are listed in Table 6.1. It is noted that, in the absence of a published diffusion coefficient for micelles, this was taken as equal to the diffusion coefficient of Tween-80.

The simulation considers a representative sandstone formation at the scale of a single DNAPL pool via a two-dimensional domain 20 m wide × 2.25 m high with unit depth. The coarse, uniformly discretized domain employed DX = 0.25m and DY = 0.25m. A single, horizontal fracture was defined with an aperture of 128μm. Grid refinement was then conducted using N = 5 together with nodal dimensions increasing exponentially with distance from the fracture.

The initial condition was a stationary 5.0m pool of TCE DNAPL, located in the fracture 1.0 m from the left hand boundary, exhibiting an effective DNAPL saturation of 0.3 (Figure 6.3). DNAPL migration was not permitted in order to focus on the solubilisation process exclusively in this test. Surfactant solution (4.0% Tween-80) was then injected via the left hand boundary for 1 year. A series of calculations for all three species in the domain were then conducted to check mass balance of all species throughout the entire simulation.

Table 6.1 Fluid Properties and Reaction Parameters for Verification Simulation

Parameter	Notation	Value
TCE Density [a]	ρ_{NWtce}	1460 kg/m^3
TCE Viscosity [a]	μ_{NWtce}	0.0005 Pa s
TCE Solubility [a]	$Solub_{TCE}$	1100 mg/L
TCE Free Solute Diffusion Coefficient [b]	D^O_{TCE}	1.01 x10^{-9} m^2/s
Tween 80 Free Solute Diffusion Coefficient [c]	$D^O_{Tween\ 80}$	2.00 x10^{-6} m^2/s
Micelles Free Solute Diffusion Coefficient	D^O_{TCEMic}	2.00 x10^{-6} m^2/s

a – Pankow and Cherry (1996)
b –Wilke and Chang (1955) at 25^{o}C
c –Amidon et al. (1982)

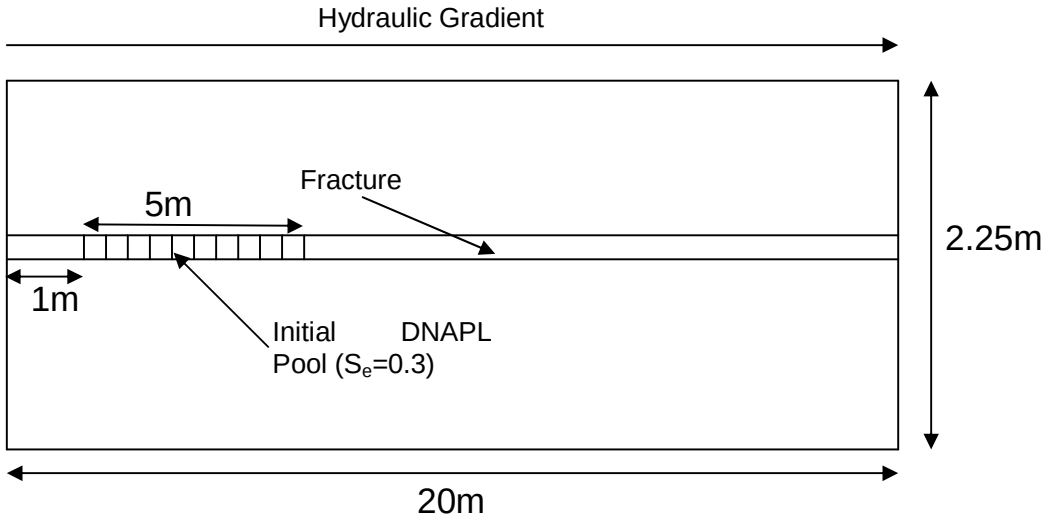

Figure 6.3: Sketch of domain layout for test simulation.

Figure 6.4 plots the cumulative concentration of TCE, surfactant and micelles within a node in the horizontal fracture, 1.5m from the left boundary (in the DNAPL pool) over time. Recall that 'surfactant' refers to monomers plus micelles that are TCE-free while 'micelles' refers to the TCE concentration occupying the micelles. It is demonstrated

that as surfactant was injected into the fracture, micelles began to form quickly as the DNAPL was solubilised by the surfactant. By the second month, Figure 6.4 reveals the TCE solute in the aqueous phase decreases quickly, indicating that DNAPL in this node has been completely solubilised (Figure 6.5). Figure 6.4 further demonstrates that prior to the disappearance of DNAPL from this node, the surfactant species concentration in this node was negligible; indicating that virtually all the Tween-80 in this node was used in solubilising the DNAPL in the node. These results are consistent with what one would expect to find with respect to DNAPL solubilisation, providing confidence that the model is working accurately. Additionally, excellent mass balance was observed throughout the entire simulation for all three species (Figure not shown).

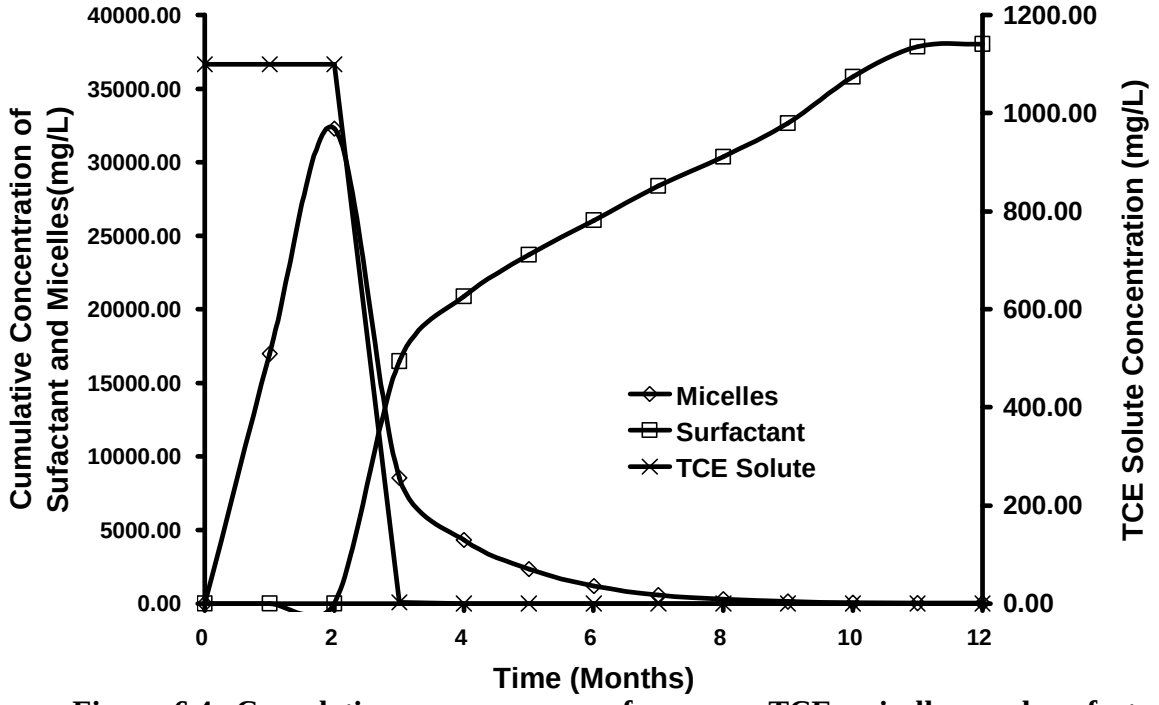

Figure 6.4: Cumulative aqueous mass of aqueous TCE, micelles, and surfactant species in a node over time for verification run.

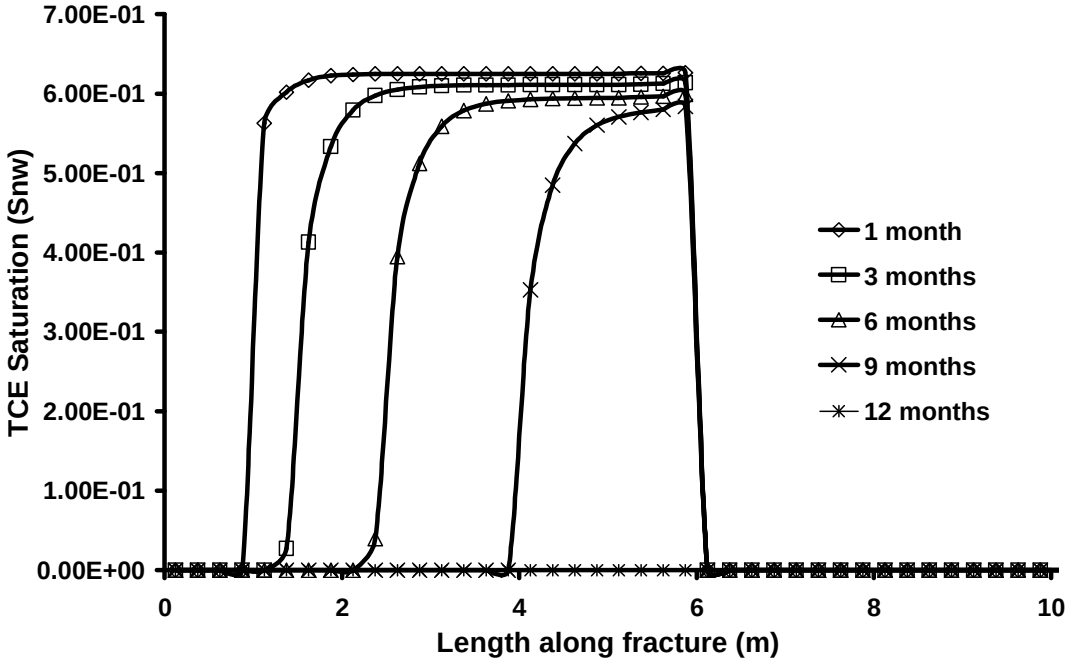

Figure 6.5: TCE saturation along the length of fracture over time.

The simulation also confirmed that, in addition to DNAPL solubilisation, micellularization of aqueous TCE in the absence of DNAPL is correctly modelled (Equations 6.2a and 6.2b) (calculations not shown).

In order to verify the accuracy of the rate-limited mass transfer model, one scenario from Dickson and Thomson (2003) was reproduced. Dickson and Thomson (2003) calibrated their predictions to their laboratory results for DNAPL dissolution in a single rough-walled fracture. As demonstrated by Figure 6.6, DNAPL3DRX-FRAC predicted similar behaviour to the published results of Dickson and Thomson (2003), providing confidence that the rate-limited mass transfer model is correctly implemented in the code. Altogether, these simulations provide confidence in the model to calculate both the surfactant treatment reaction kinetics equations 6.1 – 6.6 and the rate limited mass

transfer process accurately.

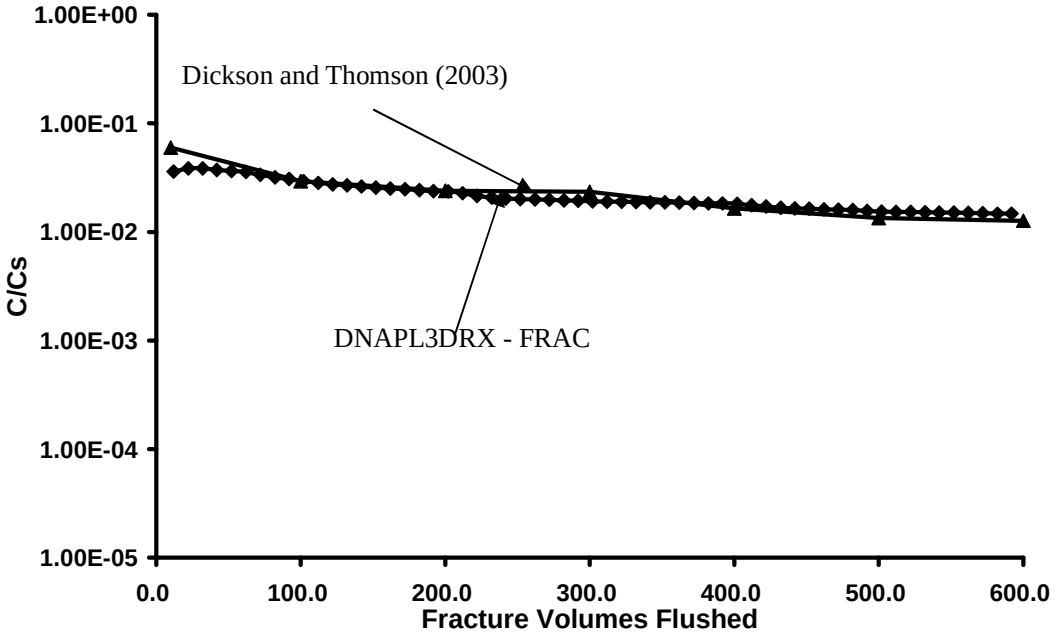

Figure 6.6: Verification of rate-limited model and compared against results from Dickson and Thomson, 2003.

6.4 NUMERICAL SIMULATIONS

6.4.1 Modelled Scenario

This section describes characteristics common to all of the simulations conducted for the surfactant treatment study (See Section 4.4.1 for the layout of the domain applicable to each simulation), while the next details the characteristics of the individual runs.

Each simulation in the surfactant treatment study evolved according to six distinct stages: (i) DNAPL Release, (ii) DNAPL Redistribution, (iii) Site Ageing, (iv) DNAPL Mapping, (v) Treatment Application, and (vi) Post-Treatment Ageing. For all stages, the water table was set to be coincident with the top boundary. During the DNAPL Release and

DNAPL Redistribution stages, constant head specified at the side boundaries during DNAPL migration established a zero hydraulic gradient across the domain. Also, the bottom boundary permitted the free exit of both water and DNAPL. At t = 0, the 'DNAPL Release' stage began by specifying a constant DNAPL saturation of 30% across the entire top boundary. Note that in this work, DNAPL is considered the nonwetting fluid. DNAPL was permitted to flow into the domain for 6 months, by which time it was established that saturations had achieved steady state values (i.e., DNAPL inflow at the top equaled DNAPL outflow at the bottom). The DNAPL source was then terminated, and DNAPL redistribution was simulated for 6 months, at which time it was established that DNAPL movement had effectively ceased. Thus, at the end of the 'DNAPL Redistribution' stage, at t_{TOTAL} = 1 yr, the fracture network exhibited a complex distribution of DNAPL pools and residual characteristic of the fracture network of the rock type under investigation.

For the 'Site Ageing' stage, the side boundaries were modified such that a groundwater hydraulic gradient of 0.005 from left to right across the domain was established. DNAPL dissolution, aqueous phase transport, diffusion, and sorption of aqueous phase chlorinated solvent were simulated for 20 years during this stage (i.e., from t_{TOTAL} = 1 yr to t_{TOTAL} = 21 yrs). During this stage, a constant aqueous phase concentration of 550 mg/L TCE was specified along the entire left boundary, representing the impact of additional upgradient DNAPL upon the domain. This recognized that only a subsection of a typical source zone was simulated and resulted in (i) increased longevity of the DNAPL by reducing the concentration gradient driving dissolution and (ii) substantial

mass loading to the matrix within the domain.

At the end of 20 years of ‘Site Ageing’, for the Base Case (sandstone) it was found that no DNAPL remained. In fact, DNAPL dissolution enhanced by loss of mass via diffusion into the matrix and subsequent sorption depleted the DNAPL in only 3 years. For the Base Case, of the 7.3 kg of aqueous TCE in the domain at the end of the Site Ageing stage, 99% is within the matrix and 98% is sorbed. Clearly, such a scenario would not benefit from surfactant flushing.

In order to pursue the objectives of this work, it was necessary to have a realistic DNAPL distribution as well as a realistic distribution of solvent mass in the matrix. Thus, the DNAPL saturation distribution at t_{TOTAL} = 1 year was overlaid onto the TCE solute concentration distribution from t_{TOTAL} = 21 yrs to generate a new, combined source zone scenario appropriate for surfactant flushing (hereafter referred to as ‘DNAPL Mapping’). For the Base Case, this new t_{TOTAL} = 21 yrs scenario exhibited 5.18 kg TCE DNAPL and 7.3 kg TCE solute. This represents a scenario in which a second DNAPL release occurred or long-term, continuous release to the subsurface took place, or one in which the DNAPL mass spilled is so substantial that despite 20 years of dissolution/diffusion/sorption, significant DNAPL remains at the time of treatment.

In the ‘Treatment Application’ stage, surfactant was initiated by injecting a constant aqueous phase concentration of 40.0 g/L surfactant for 2 years (i.e., 21 yrs $\leq t_{TOTAL} \leq$ 23 yrs) at the horizontal fractures along the left boundary. During surfactant application,

the upgradient TCE injection was terminated (i.e., assuming complete and instantaneous treatment of the upgradient source zone); while this is unrealistic, it provides the best opportunity for success within the domain and thus supports viewing these results as approximating a best case for the technology. In all cases, MSR calculations confirm that the total mass of surfactant injected is greater than the theoretical surfactant mass required to solubilise all the TCE in the domain at the start of the Treatment stage; for example, for the Base Case, 160 kg (122 moles) of surfactant was injected over the Treatment stage and 7.3 kg (55.6 moles) of aqueous TCE mass and 5.18 kg (39.4 moles) of TCE DNAPL was present; this represents an excess of 12.3 times, considering that 1 mole of surfactant is capable of solubilising 9.57 moles of TCE (Taylor et al., 2001) .

Following the Treatment stage, an additional five years were simulated (i.e., 23 yrs $\leq t_{TOTAL} \leq$ 28 yrs) to examine the impact of surfactants and potential rebound of chlorinated solvent concentrations in the post-treatment period. During this stage no upgradient concentration of any species (i.e., surfactant or chlorinated solvent) was applied.

Several assumptions were employed in this work to facilitate reasonable simulation times:

1. All fractured rock simulations presented are two-dimensional; this assumption likely benefits the technology since the reduced dimensionality is expected to reduce bypassing of the treatment fluid around DNAPL-occupied fractures;
2. The matrix is presumed to have a sufficient displacement pressure so as to exclude DNAPL entry; this assumption likely benefits the technology because

the highest fraction of DNAPL is retained in the fractures which are most accessible to the treatment fluid;

3. Advection of groundwater through the matrix is assumed to be negligible; this is reasonable given that the high permeability contrast between the fractures and matrix. For example, for the sandstone Base Case, the matrix permeability is approximately 6 orders of magnitude less than the average fracture permeability. The Peclet number for the matrix (Pe = vx/D where v is horizontal velocity in matrix) if advection were not neglected is 0.166; since Pe<1 it is reasonable to assume that the matrix is diffusion dominated and advection is negligible (Trivedi et al., 2008).

6.4.2 Base Case and Sensitivity Simulations

Table 6.2 presents the suite of 11 simulations conducted in this study. The Base Case considered a fractured sandstone template site. Table 6.3 presents the parameters employed to characterize the sandstone as well as the other two rock types (shale and granite). The sandstone domain, employed in all simulations except Run 5 and Run 6, is presented in Figure 6.7a. The sandstone parameters were chosen to be broadly representative of North American sandstone aquifers (e.g., Lipson et al., 2005). Table A1 (Appendix A) provides, for each rock type, the observed ranges for each parameter synthesized from the literature. Table 4.3 reveals that this sandstone exhibits - relative to the other template rock types - low fracture density, low mean aperture (125µm), high matrix porosity (7.7%), and intermediate foc (0.005).

The sandstone Base Case employed TCE as the DNAPL targeted by the surfactant treatment. Fluid properties and reaction parameters are listed in Table 6.4. The Base Case employed a continuous injection of surfactant at 40.0 g/L for 2 years during the Treatment stage (Table 6.2). This concentration is representative of values applied in typical treatment scenarios (e.g., Abriola et al. 1993; Rathfelder et al., 2001)

Table 6.2. Field Scale Surfactant Flushing in Fractured Rock Simulations

Run No.	DNAPL Type	Material	Surfactant Concentration (mg/L)	Degree of Matrix Loading	Mass Transfer
1 (Base Case)	TCE	Sandstone	40000	20 Years Aging	Equilibrium
2	TCE	Sandstone	20000	20 Years Aging	Equilibrium
3	TCE	Sandstone	60000	20 Years Aging	Equilibrium
4	PCE	Sandstone	40000	20 Years Aging	Equilibrium
5	TCE	Shale	40000	20 Years Aging	Equilibrium
6	TCE	Granite	40000	20 Years Aging	Equilibrium
7	TCE	Sandstone	40000	0 Years Aging	Equilibrium
8	TCE	Sandstone	40000	5 Years Aging	Equilibrium
9	TCE	Sandstone	40000	10 Years Aging	Equilibrium
10	TCE	Sandstone	40000	20 Years Aging	Rate Limited
11	TCE	Sandstone	0.0	20 Years Aging	Equilibrium

Table 6.3. Properties of Field Scale Fractured Rock Template Sites

Rock Type	Fracture Spacing (m)	Matrix Permeability (m^2)	Matrix Porosity	Foc	Bulk Density (g/cm^3)	Matrix Tortuosity	Fracture Aperture Range (μm)	Mean Aperture (μm)
Sandstone	6.0 (Ver) [*] 1.0 (Hor) [a]	1.05×10^{-15}	7.7% [a]	0.005 [a]	2.49 [a]	0.2 [a]	25 - 230 [a]	125
Shale	4.0 (Ver) [*] 1.0 (Hor) [*]	1.05×10^{-15}	3.0% [b]	0.009 [*]	2.619 [**]	0.1 [*]	50 - 250 [c]	150
Granite	2.0 (Ver) [d] 2.0 (Hor) [d]	1.05×10^{-15}	0.1% [*]	0.0005 [*]	2.697 [**]	0.05 [*]	100 - 500 [e]	300

[a] *Lipson et al., 2005*
[b] *Morris and Johnson, 1967*
[c] *Jardine et al., 1999*
[d] *Sousa 2007*
[e] *Sausse 2002*
**Data supplied by B.H Kueper (personal communication) based upon consulting experience on sites of all three rock types.*
*** Calculated using Bulk Density = Grain Density x (1-porosity), assuming a grain density of 2.7 for Shale and Granite.*
Ver – Vertical Fractures
Hor – Horizontal Fractures

Table 6.4. Fluid Properties and Reaction Parameters

Parameter	Notation	Value
TCE Density [a]	ρ_{NWtce}	1460 kg/m^3
TCE Viscosity [a]	μ_{NWtce}	0.0005 Pa s
TCE Solubility [a]	$Solub_{TCE}$	1100 mg/L
TCE MSR [b]	MSR_{TCE}	9.57 mol/mol
PCE Density [a]	ρ_{NWpce}	1630 kg/m^3
PCE Viscosity [a]	μ_{NWpce}	0.0009 Pa s
PCE Solubility [a]	$Solub_{PCE}$	200 mg/L
PCE MSR [c]	MSR_{PCE}	5.41 kg/kg

a – Pankow and Cherry (1996)
b – Taylor et al. (2004)
c – Zhong et al. (2003)

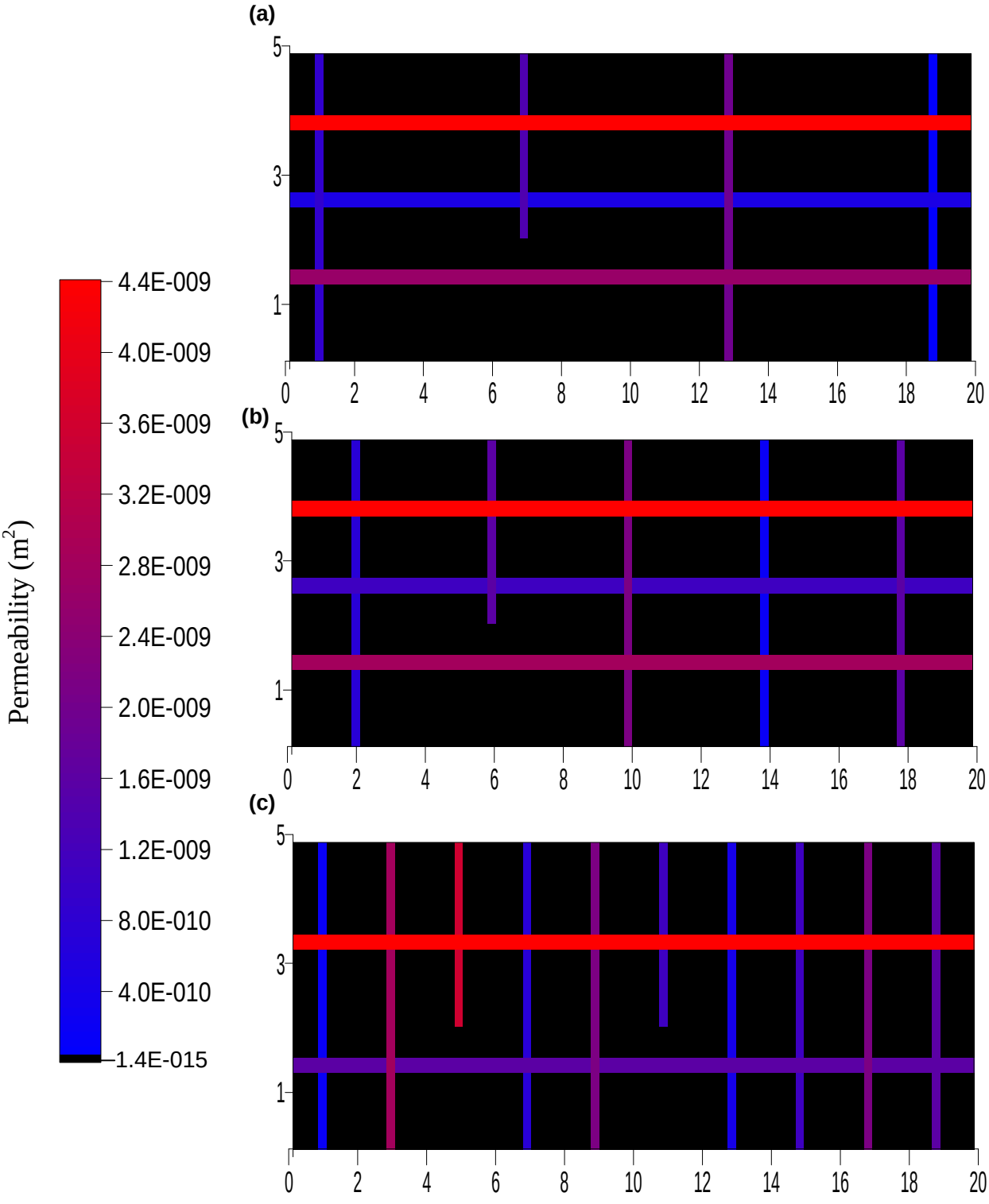

Figure 6.7 Distribution of permeability for the field scale fractured rock domains: (a) sandstone, (b) shale, and (c) granite. Colour corresponds to fracture permeability according to the scale bar provided; matrix permeability is uniform (black). Note that fracture apertures are exaggerated for visual purposes.

As illustrated in Table 6.2, Runs 2 - 3 examine variations in treatment strategy, while Runs 4 -10 explore the influence of site conditions. All parameters, boundary conditions, and source conditions were established identically to the Base Case for all simulations, except for changing the parameter(s) whose influence was being examined in each study.

It is noted that a 'No Surfactant' case was simulated for comparison purposes. In all respects but one, this simulation was identical to the Base Case. In this case, the Treatment stage employed identical boundary conditions as the Post-Treatment stage, and thus ambient conditions (in the absence of an updgradient TCE source) were simulated for 7 years following Site Ageing.

6.4.2.1 Surfactant Concentration

To examine the effects of surfactant concentration, the injected (i.e., boundary) concentration was increased by 50% and reduced by 50% relative to the Base Case in Runs 2 and 3, respectively. These range of concentrations investigated here are within the typical range of Twen-80 concentrations applied at field sites (Abriola et al., 1993; Jafvert et al., 1995; Ramsburg and Pennell, 2002; Ramsburg et al., 2005). In order to ensure the total volume of surfactant injected by the end of the Treatment stage was kept constant, the injection period was changed accordingly to 1.3 years and 4 years when concentration was increased by 50% and reduced by 50% respectively. This sensitivity study comprises of three simulations.

6.4.2.2 DNAPL

Run 4 utilized PCE DNAPL in the Base Case domain. PCE fluid and reaction parameters are provided in Table 6.4. For both the TCE and PCE simulations, all boundary conditions and stage parameters were identical. This sensitivity study comprises of two simulations.

6.4.2.3 Rock Type

Runs 1, 5, and 6 compare surfactant treatment performance in three different types of fractured rock at the field scale, each exhibiting a characteristic set or range of hydrogeological parameters (Table 6.3). Figure 6.7 presents the distribution of intrinsic permeability for the three domains, illustrating the distribution of fractures. In each case, the mean aperture is at the midpoint of the range specified in the table. It is noted that, characteristic of these rock types in natural environments, the shale template site exhibits (relatively) intermediate fracture density, low mean aperture (150μm), intermediate matrix porosity (3%), and high *foc* (0.009) while the granite exhibits high fracture density, high mean aperture (300μm), low matrix porosity (0.1%), and low *foc* (0.0009).

6.4.2.4 Aging Time

To examine the effects of the extent of contaminant penetration into the matrix on surfactant flushing success, Runs 7-9 varied the length of the Site Ageing stage: 0 years, 5 years, and 10 years (the Base Case was 20 years). In each case, before the Treatment stage, the T_{total}=1 year DNAPL distribution in the fractures was overlaid on the simulated distribution of aqueous and sorbed phases present in the matrix. It is acknowledged that by doing so, the total amount of DNAPL mass present was identical but the aqueous and

sorbed mass in the domain differed in each simulation. The (aqueous + sorbed) TCE present at the start of the Treatment stage for Runs 7, 8, 9 and 1 (Base Case) were 0.0 kg, 4.13 kg, 5.33 kg, and 7.3 kg, respectively, while the mass of TCE DNAPL for all of those runs were 5.18 kg. The effectiveness of surfactant flushing will be examined in these cases by considering the percentage of mass removed due to surfactant flushing.

6.4.2.5 Mass Transfer Model

Since the effectiveness of surfactant flushing is expected to be dependent on the rate of DNAPL mass transfer within the fractures, it is deemed important to examine the effect a rate-limited mass transfer model has on surfactant flushing of fractured rock source zones. The rate-limited model adopted from Dickson and Thomson (2003) was employed to compare with the equilibrium mass transfer relationship (Base Case).

6.5 RESULTS AND DISCUSSIONS

Table 6.5 summaries a selection of key numerical results for all 11 simulations conducted in this study. These data will be discussed as each set of simulations is presented.

Table 6.5: Summary of Results for All Surfactant Flushing Simulations

Run No.	DNAPL St 2 (kg)	DNAPL St 3 (kg)	Aq + Sorb St 3 (kg)	Surf Inject (kg)	DNAPL St 5 (kg)	Aq + Sorb St 5 (kg)	Mass Discharge St 5 (10^{-3} mg/s)	Surf React (kg)	CS React (kg)
1	5.26	5.26	7.30	160.0	0.020	4.32	2.69	4.33	4.16
2	5.26	5.26	7.30	160.0	0.016	4.11	2.42	4.15	3.98
3	5.26	5.26	7.30	160.0	0.021	4.40	2.81	4.39	4.21
4	6.03	6.03	3.30	165.0	0.452	0.92	0.0001	6.50	4.45
5	6.86	6.86	6.80	263.0	0.175	3.34	0.0001	5.03	4.83
6	11.53	11.53	0.68	1730.0	4.075	0.34	0.010	7.47	7.17
7	5.26	5.26	0.00	160.0	0.012	0.40	0.000	3.17	3.04
8	5.26	5.26	4.13	160.0	0.014	1.04	0.019	3.64	3.49
9	5.26	5.26	5.33	160.0	0.019	2.11	0.715	4.08	3.92
10	5.26	5.26	7.30	162.0	0.527	4.11	2.70	3.43	3.25
11	5.26	5.26	7.30	0.0	0.020	7.23	5.62	0.00	0.00

St 2 = mass present at the end of Stage 2 (DNAPL redistribution)
St 3 = mass present at the end of Stage 3 (Site Ageing)
St 5 = mass present at end of Stage 5 (Post-Treatment)
DNAPL = mass of DNAPL present
Aq + Sorb = combined mass of aqueous and sorbed chlorinated solvent present
Surf Inject = mass of surfactant injected during the treatment period
Mass Discharge = mass per time of chlorinated solvent leaving the domain at the end of Post-Treatment stage
Surf React = total mass of surfactant that reacted (with chlorinated solvent in all phases)
CS React = total mass of chlorinated solvent (in all phases) solubilised by surfactant

6.5.1. Base Case Results

Figures 6.8(a) and 6.8(b) illustrate the distribution of the TCE DNAPL at the end of the infiltration and redistribution phases, respectively (relevant to all simulations except Runs 5 and 6). Figures 6.8(a) and 6.8(b) reveal a heterogeneous distribution of DNAPL pools (i.e., connected phase) and residual (i.e., trapped) due to the influence of capillary forces (and, specifically, fracture entry pressures), the order of encounter of fractures, and the permeability contrasts between fractures. At the end of the DNAPL infiltration stage, the average DNAPL saturation was 0.75, the mass of DNAPL in the domain equaled 11.68 kg, the DNAPL volume was 0.008 m^3 (compared to a total fracture volume of 0.012 m^3) with 100% of the nodes in drainage. At the end of DNAPL redistribution

stage, the average DNAPL saturation was 0.3, the volume of DNAPL was 0.0036 m^3 (equal to a mass of 5.18 kg) and the pool to residual ratio was 71:29%. Note in Figure 6.8(b) that, as expected, the lone remaining pool exhibiting a high DNAPL saturation resides in a vertical dead-end fracture and other pools of various lengths occur in horizontal fractures, separated by areas of residual DNAPL.

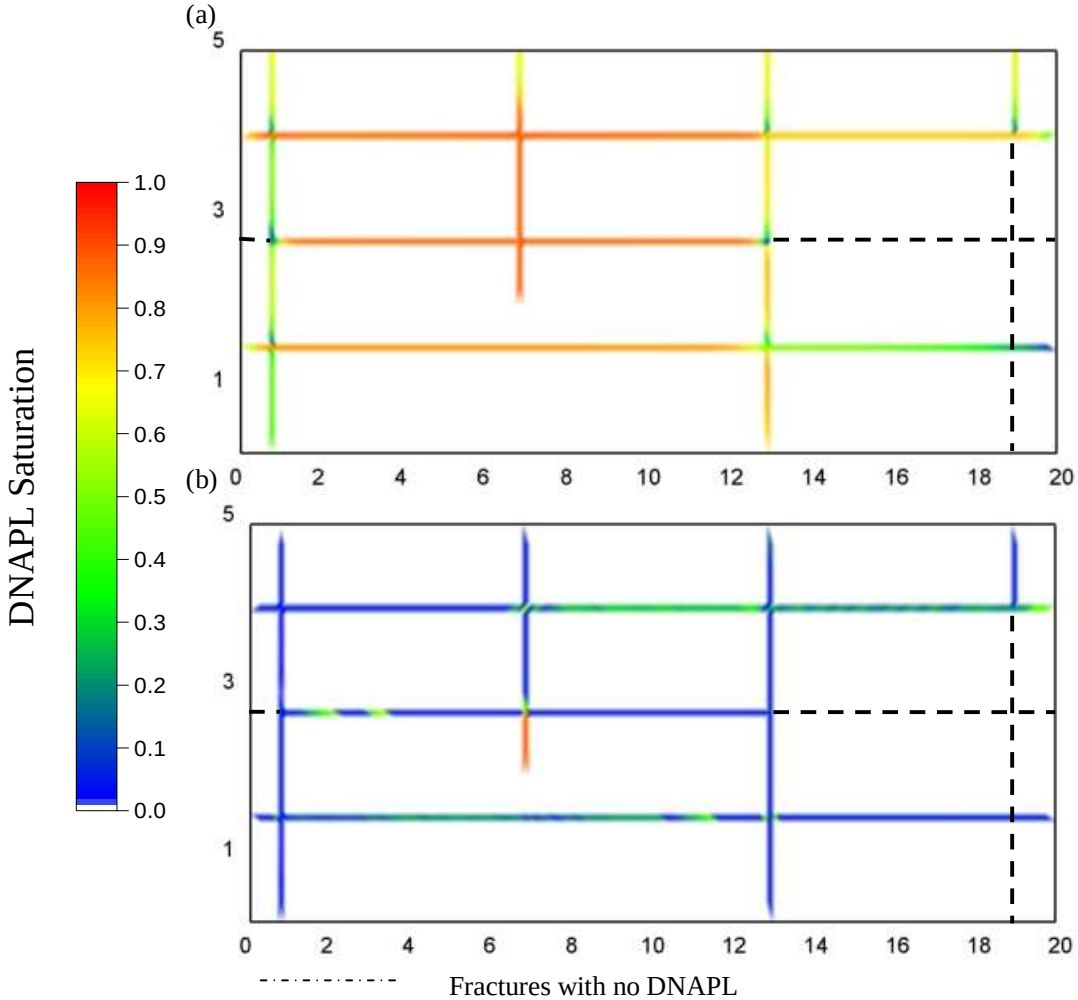

Figure 6.8: DNAPL distribution for Base Case at (a) t_{TOTAL} = 0.5 years when DNAPL inflow and outflow are equal, and (b) t_{TOTAL} = 1 year when all DNAPL migration has ceased.

Figure 6.9 illustrates the distribution of aqueous phase TCE at the end of the 20 year Site Ageing stage (t_{TOTAL} = 21 years). Evident are the expected diffusion halos in the

sandstone matrix blocks adjacent to fractures containing DNAPL as well as those horizontal fractures without DNAPL but subject to significant aqueous mass flux (Figure 6.8b). At this time, no DNAPL remained in the domain. This occurred despite the constant influent concentration equal to 50% of TCE solubility. The reason is the substantial TCE sink provided by matrix diffusion and sorption. At this time, the total mass of TCE in the domain was 7.3 kg, of which 99% resided in the matrix; of the mass in the matrix, 98% was sorbed and only 2% remained in the aqueous phase. It appears that the matrix acts as a substantial sink for TCE, rapidly promoting DNAPL dissolution.

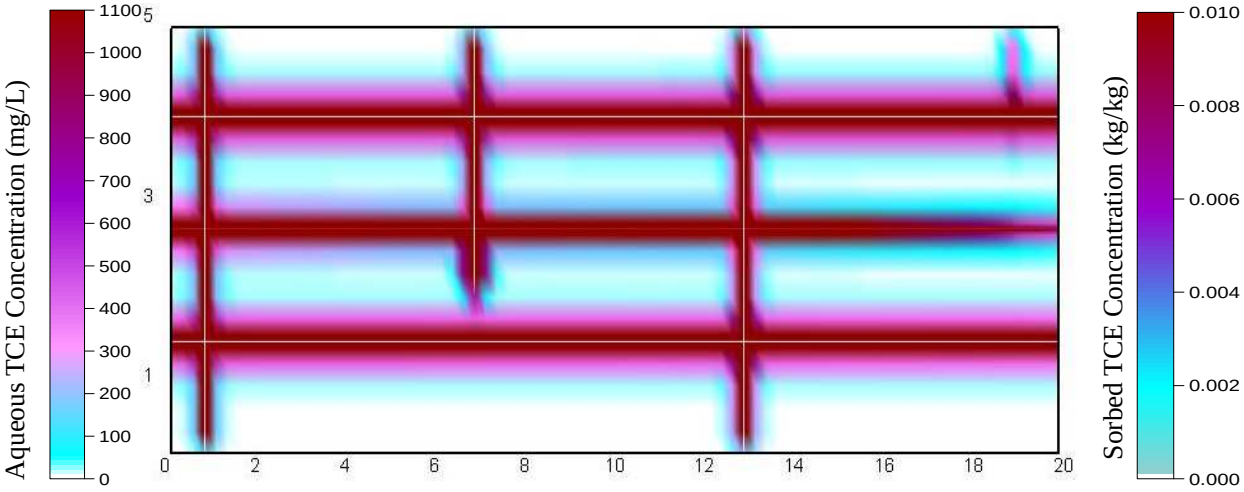

Figure 6.9: Distribution of aqueous and sorbed TCE after 20 years (t_{TOTAL} = 21 years) of DNAPL dissolution.

Figure 6.10 provides the concentration plots of aqueous TCE, surfactant, micelles and DNAPL saturation throughout the domain after the Treatment stage (i.e., 2 years of surfactant injection, t_{TOTAL} = 23 years). It is noted by this time, the injected surfactant has traversed the full extent of all three horizontal fractures present in the domain. Figure 6.10c further demonstrates that micelles in the top and bottom horizontal factures (largest apertures) have been flushed out, while the middle horizontal fracture still

contains micelles as the solubilisation process continues. In addition, Figure 6.10c demonstrates substantial TCE-occupied micelle mass present in the matrix close to most of the fractures within the domain.

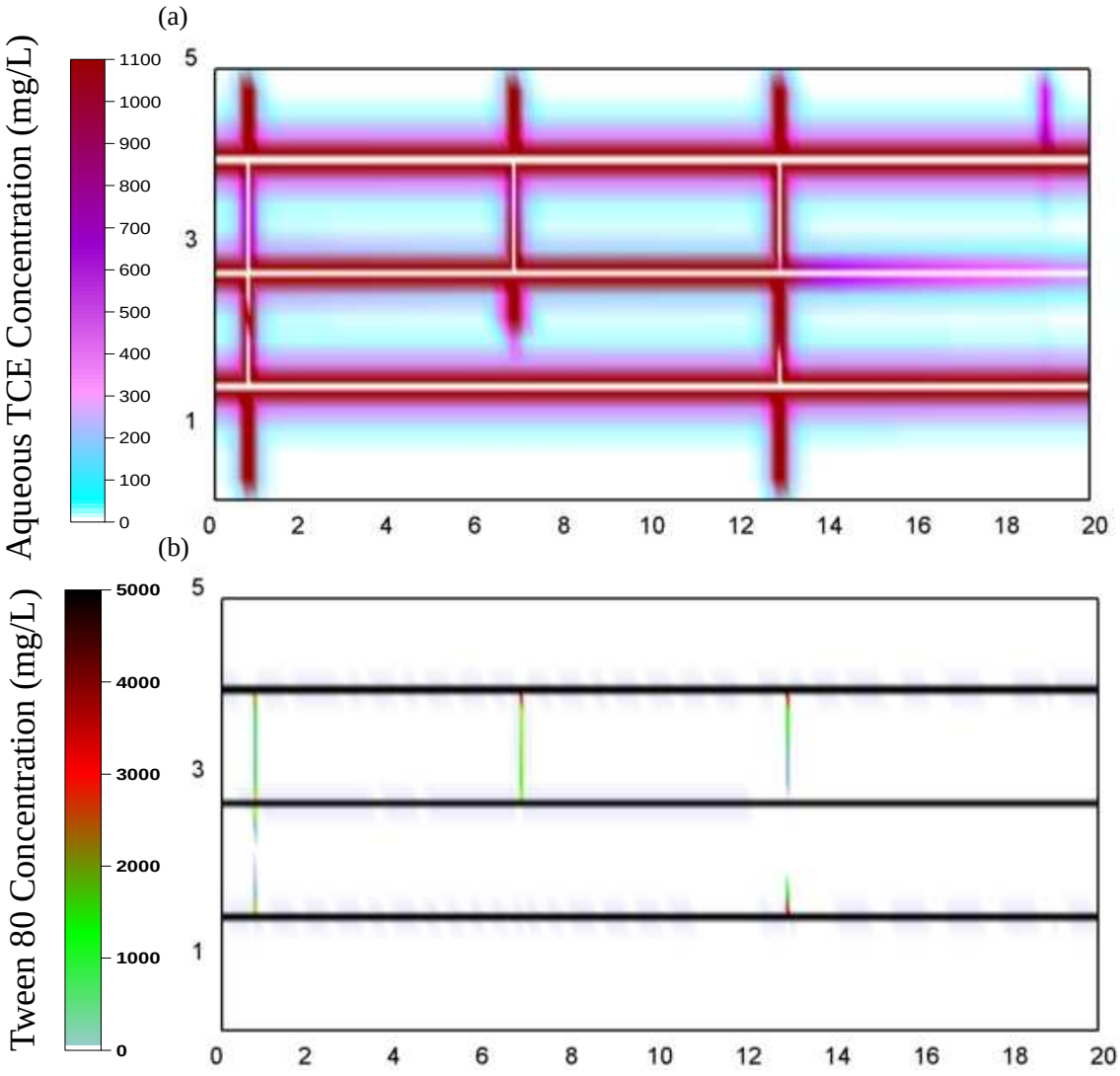

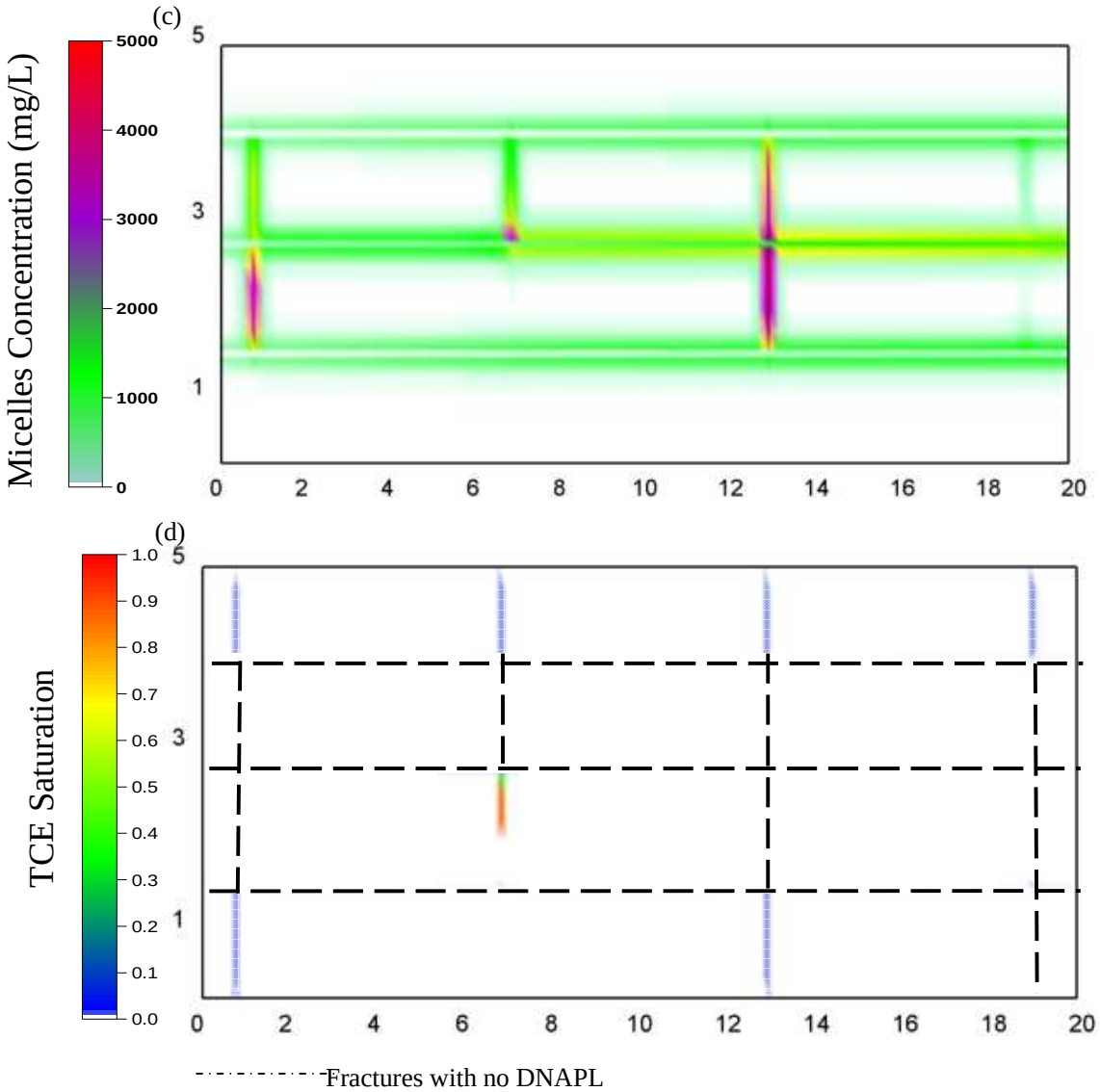

Figure 6.10: Distribution of (a) Aqueous TCE; (b) Surfactant; (c) Micelles; (d) TCE Saturation, 2 years after surfactant injection.

Figure 6.11 presents the concentration of aqueous TCE and various species throughout the domain at the end of the post-treatment stage (i.e. 5 years post-surfactant injection, t_{TOTAL} = 28 years). Figure 6.11d reveals that some DNAPL remains in one of the vertical dead-end fractures; as expected, this is not readily accessed by the surfactant flush. Moreover, the figure illustrates that minimal surfactant remains while forward

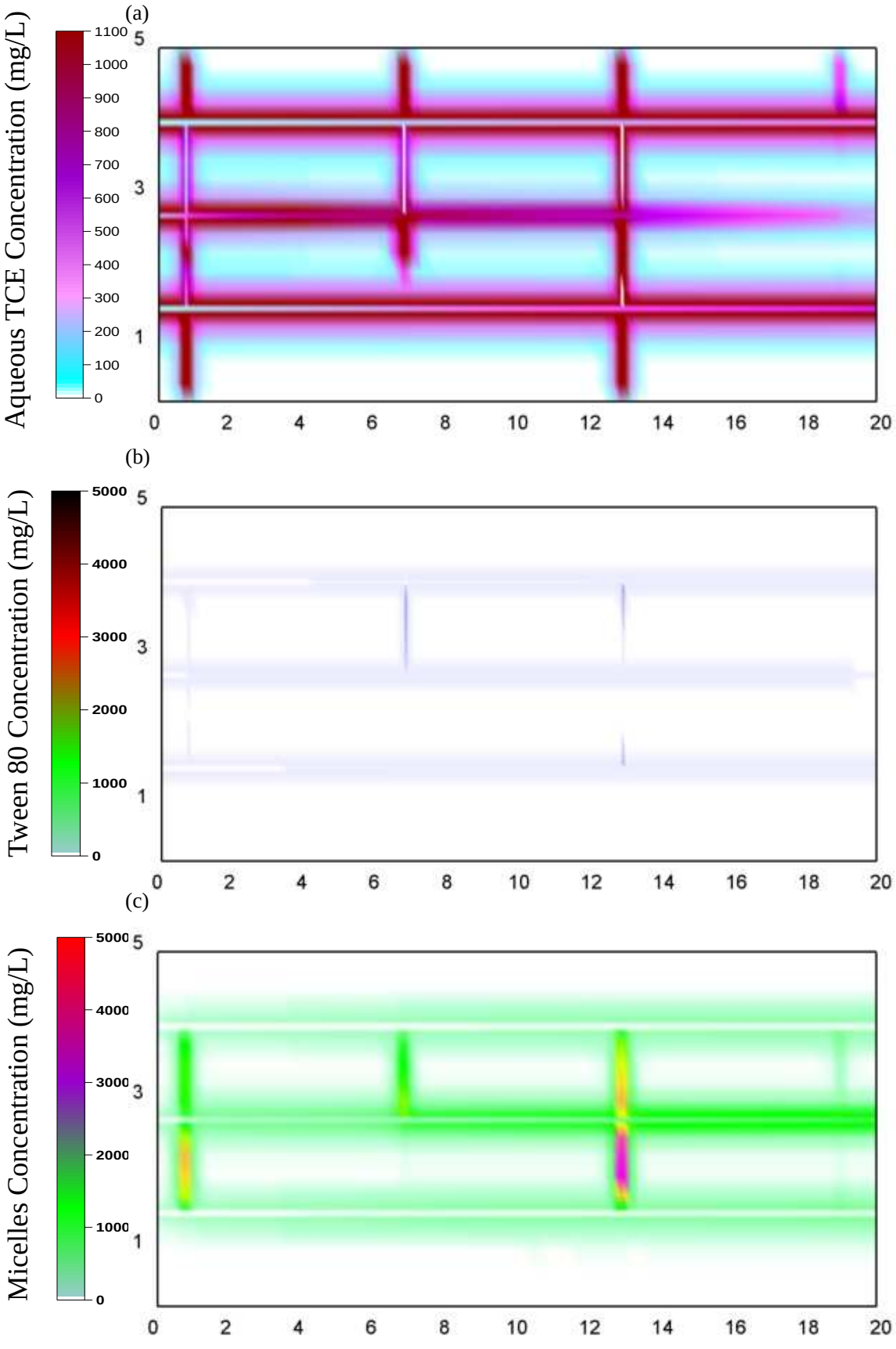
(a)
Aqueous TCE Concentration (mg/L)
1100
1000
900
800
700
600
500
400
300
200
100
0
5
3
1
0
2
4
6
8
10
12
14
16
18
20
(b)
Tween 80 Concentration (mg/L)
5000
4000
3000
2000
1000
0
5
3
1
0
2
4
6
8
10
12
14
16
18
20
(c)
Micelles Concentration (mg/L)
5000
4000
3000
2000
1000
0
5
3
1
0
2
4
6
8
10
12
14
16
18
20

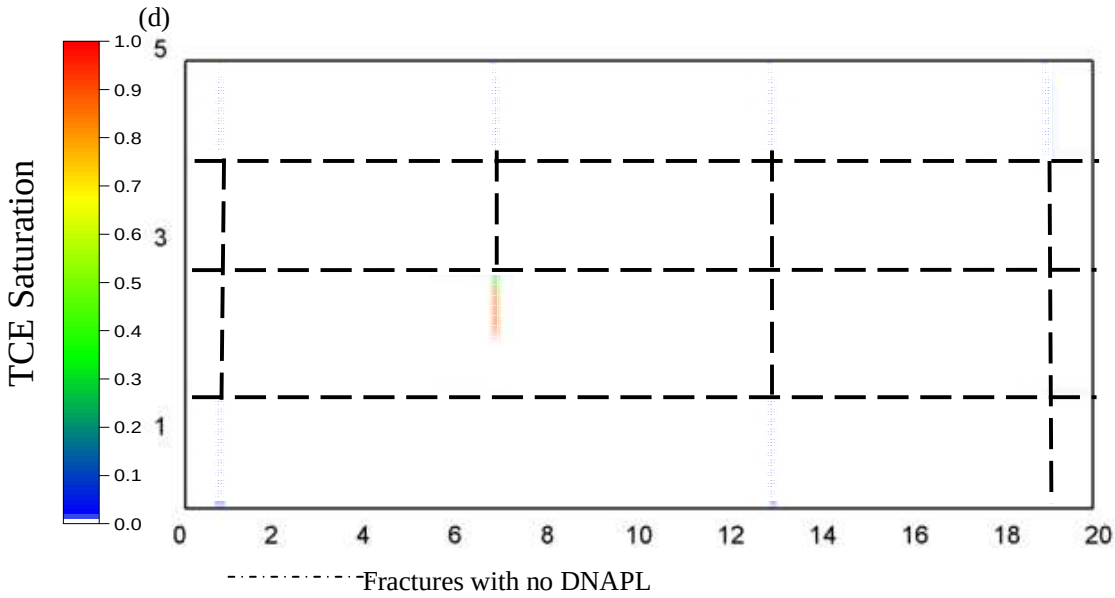

Figure 6.11: Distribution of (a) Aqueous TCE; (b) Aqueous surfactant; (c) Micelles; (d) TCE saturation, 5 years after surfactant injection.

and backward diffusion are smearing the distribution of TCE and TCE-occupied micelles in the matrix adjacent to the two 'clean' horizontal fractures.

Figure 6.12 presents cumulative mass plots of all sinks and sources of TCE during the Base Case simulation. Summed totals of these plots, in which:

Mass Dissolute In + Mass Influx = Mass Destroyed + Mass Outflux + Mass Sorbed + Mass In Domain (6.7)

revealed that the model has excellent mass balance (plots not shown to improve clarity of the figure) and this was confirmed by excellent computed mass balance on all species. The figure reveals that majority of DNAPL dissolution occurred rapidly at the beginning of the simulation due to DNAPL dissolution and diffusion into the matrix, corresponding

to a rapid increase in sorbed TCE in the matrix. Until t_{TOTAL} = 3 years, TCE flux out of the domain was greater than the flux into the domain due to a proportion of the dissolved TCE exiting via fracture flow. However, beyond this time, with dissolution virtually completed, TCE influx exceeded outflux as the incoming background TCE contributed to a steady rise in mass retained via sorption. It was also noted the cumulative mass of aqueous TCE in the domain (sum of that in the fractures and matrix) was a small fraction of the amount sorbed.

At t_{TOTAL}=21 years, as mentioned above, DNAPL distribution at t_{TOTAL} = 1 year, (equivalent to a mass of 5.18 kg) was mapped onto the domain. Figure 6.12 reveals that as surfactant was injected into the domain, DNAPL solubilisation increases dramatically before reaching a constant level at t_{TOTAL} = 22.3 years. It reveals at this time approximately 96.5% (i.e., 5.0 kg) of initial DNAPL mass present in the fractures has been solubilised by surfactant.

Following the Treatment stage, Figure 6.12 revealed that although the mass of TCE removed by surfactant continued to increase, this increase throughout the 5 years of Post-Treatment stage only accounts of 0.35% of the total mass removed.

Figure 6.13 reveals that of the 160 kg of surfactant injected, approximately 94.4% of the total mass was flushed out of the domain, while only 2.71% (Table 6.5) was used for the solubilisation of TCE while the rest of the surfactant was sorbed onto the matrix of the fractured rock.

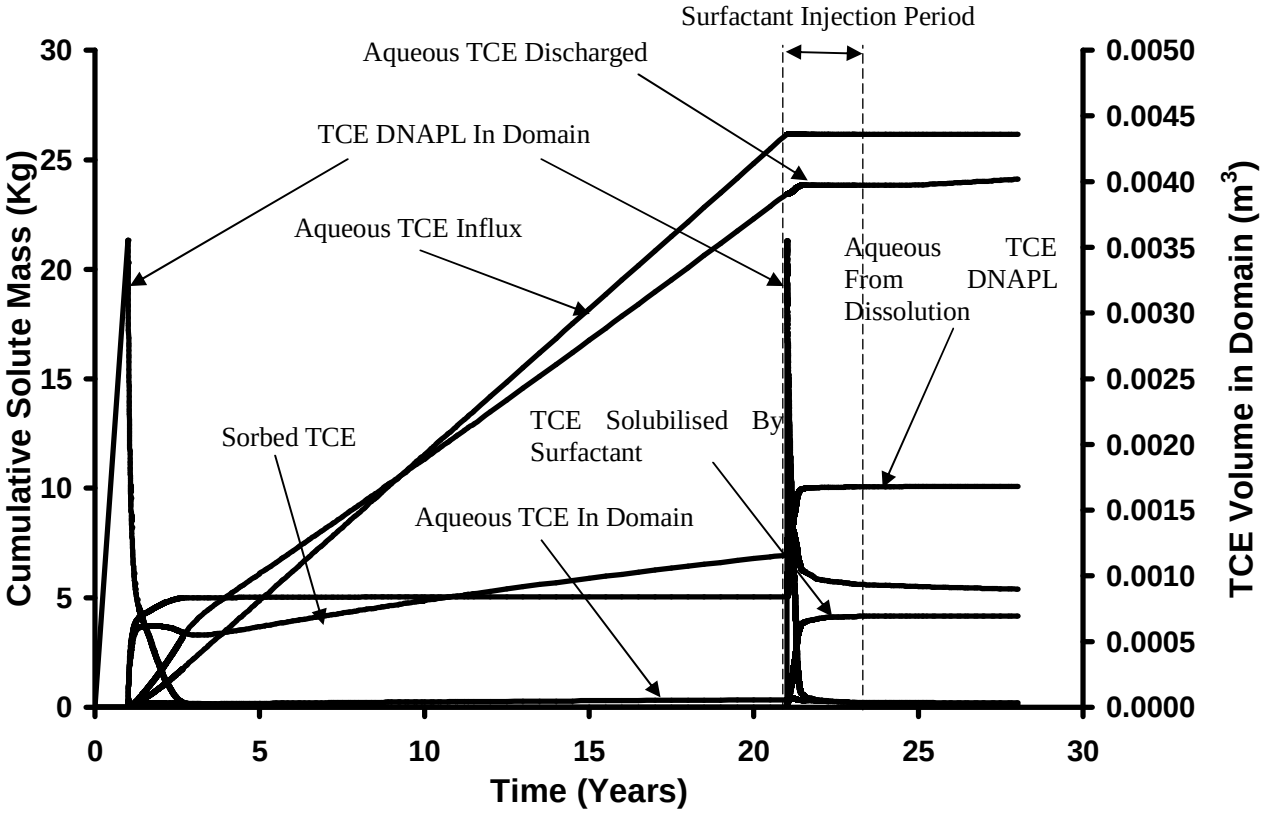

Figure 6.12: Cumulative aqueous and sorbed TCE from all sinks and sources for Base Case Simulation.

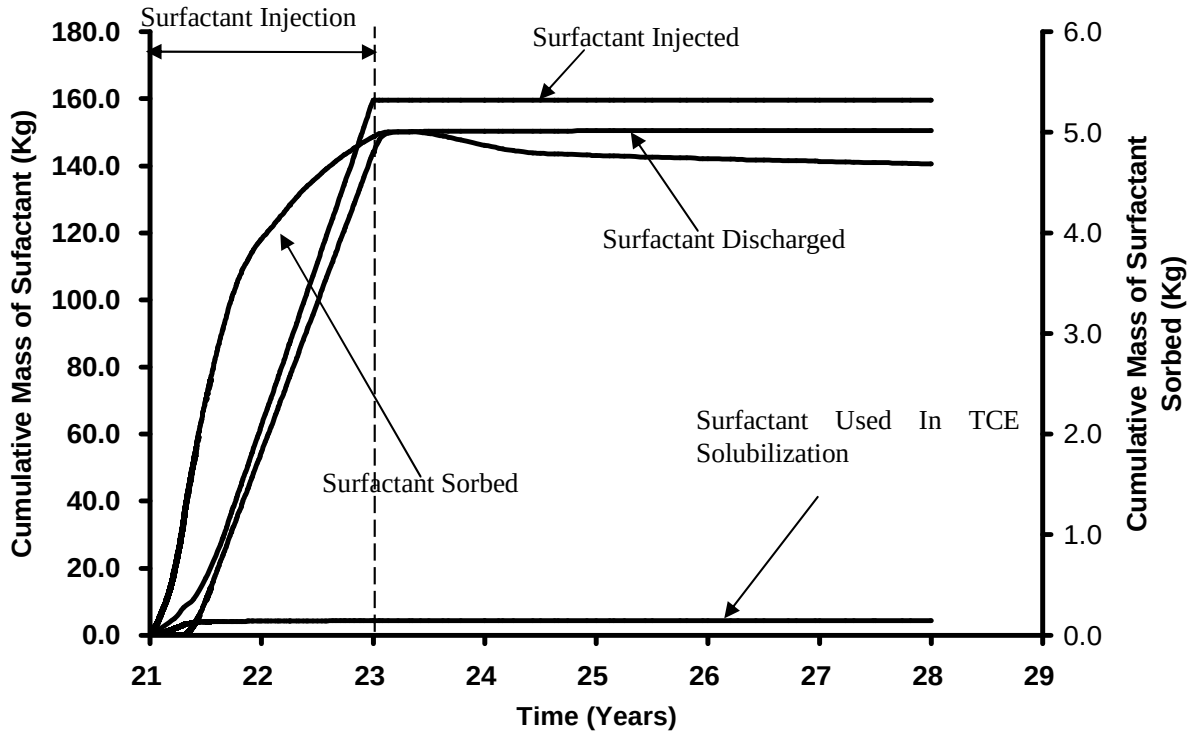

Figure 6.13: Cumulative aqueous and sorbed surfactant from all sinks and sources for Base Case Simulation.

Figure 6.14 reveals that, as expected, at the start of the Treatment stage the DNAPL dissolution rate increases dramatically and the amount of TCE encapsulated by micelles rises correspondingly. These rapid increases only last for approximately 6 months while the remaining 78 months of the treatment period show very little additional solublization. This is because most of the DNAPL that could be accessed by the surfactant has been solubilised in the first 6 months of the treatment. It is noted that the amount of sorbed mass decreases equally quickly during the first 6 months of treatment, indicating that desorption was occurring (Figure 6.12). And as the cumulative mass of micelles stops increasing; the rate of decrease of sorbed mass declines. Throughout the Post-treatment stage, the amount of TCE solubilised is insignificant.

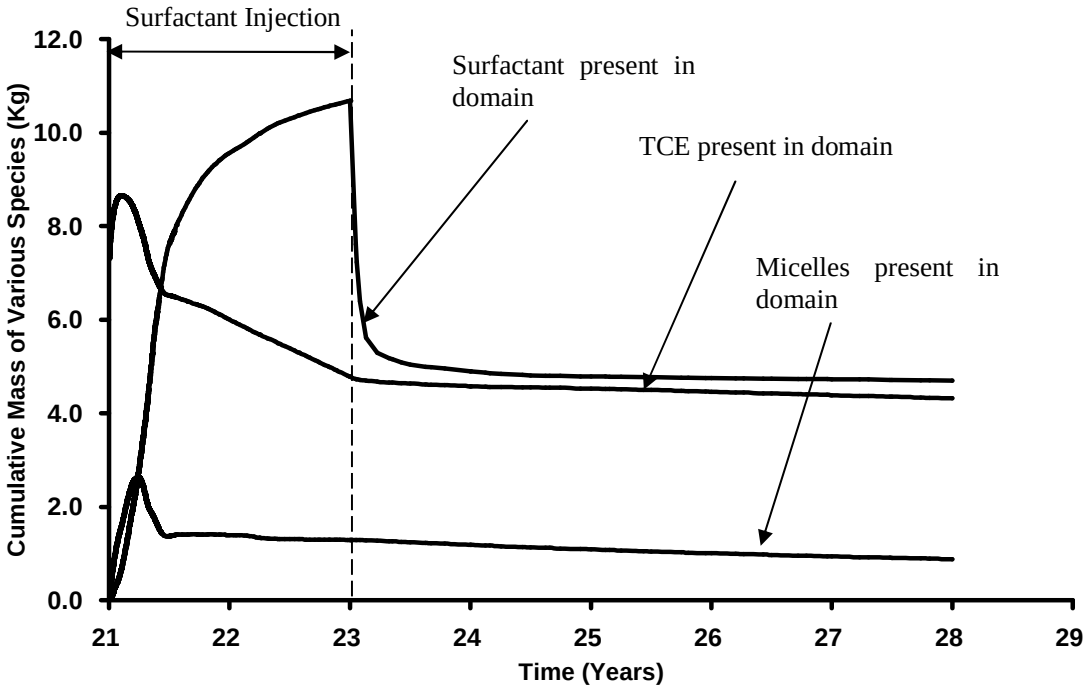

Figure 6.14: Cumulative mass of TCE, surfactant and micelles for Base Case Simulation.

Figure 6.15 compares the total TCE solute mass discharged at the right-hand boundary of the domain for the Base Case and the 'No Surfactant' simulation. During the Treatment stage (i.e., t_{TOTAL} = 21 to 23 years), the difference in mass discharged between the 2 simulations were observed to vary significantly. In the 'No Surfactant' simulation, the boundary mass discharge is observed to increase exponentially until t_{TOTAL} = 23.5 years, before decreasing at a relatively steady state to a relatively constant level at t_{TOTAL} = 25.75 years. On the other hand, when surfactant was injected in the Base Case simulation, Figure 6.15 demonstrates the boundary TCE mass discharge to increase rapidly during the initial Treatment stage before decreasing to negligible level by t_{TOTAL} = 21.4 years. Figure 6.15 further reveals the mass discharged in the Base Case at t_{TOTAL} = 24.5 years to increase from negligible level to a constant level of 0.002mg/s (Table 6.5), until the end of the simulation. This trend in the Base Case simulation can be broken down to 3 stages:

1. Due to the mapping of DNAPL into the Base Case, the mass outflux experiences a sudden drop at the beginning of the Treatment stage before steadily increasing due to the DNAPL solubilisation by the injected surfactant.
2. As majority of the DNAPL within the domain was solubilised by the injected surfactant (i.e., t_{TOTAL} = 21.5 years), the mass discharged decreases to a negligible value. This observation is supported by the corresponding increase in concentration of the micelle species within the domain (Figure 6.14).

3. In the final stage, after the injection of surfactant has ceased for 1.5 years (i.e. t_{TOTAL} = 24.5 years), the TCE mass outflux is observed to rebound again due to back-diffusion of previously sorbed TCE from the matrix.

It is further observed that the post-treatment mass outflux in the 'No Surfactant' case is approximately 2.8 times more (i.e. 0.0056 mg/s vs. 0.0027 mg/s) than the Base Case (refer to Table 6.5). This is because of the long-term, back-diffusion of stored TCE mass in the matrix (aqueous + sorbed) and slow dissolution of TCE DNAPL in the fractures (low groundwater velocity pathways). The total TCE mass in the domain at the end of the Post-Treatment stage (aqueous + sorbed + DNAPL) in the source zone is 4.34 kg for the Base Case and 7.25 kg for the No Surfactant case.

Figure 6.16, which is the same data as 6.15 but expands the time axis to focus on the first year during treatment, reveals three areas of 'abrupt slope changes' (circled areas) on the TCE mass discharge curve. It is believed these 'abrupt slope changes' are associated with the mass flux through each horizontal fracture in the domain. As demonstrated in Figure 6.18, depending on the size of the aperture, the downgradient discharge varies for each fracture. The discharge in Figure 6.16 was dominated at first by the largest aperture fracture (circle 1), followed by the middle aperture fracture (circle 2), and then after both were flushed out, the mass from the smallest aperture fracture finally arrived at the boundary (circle 3).

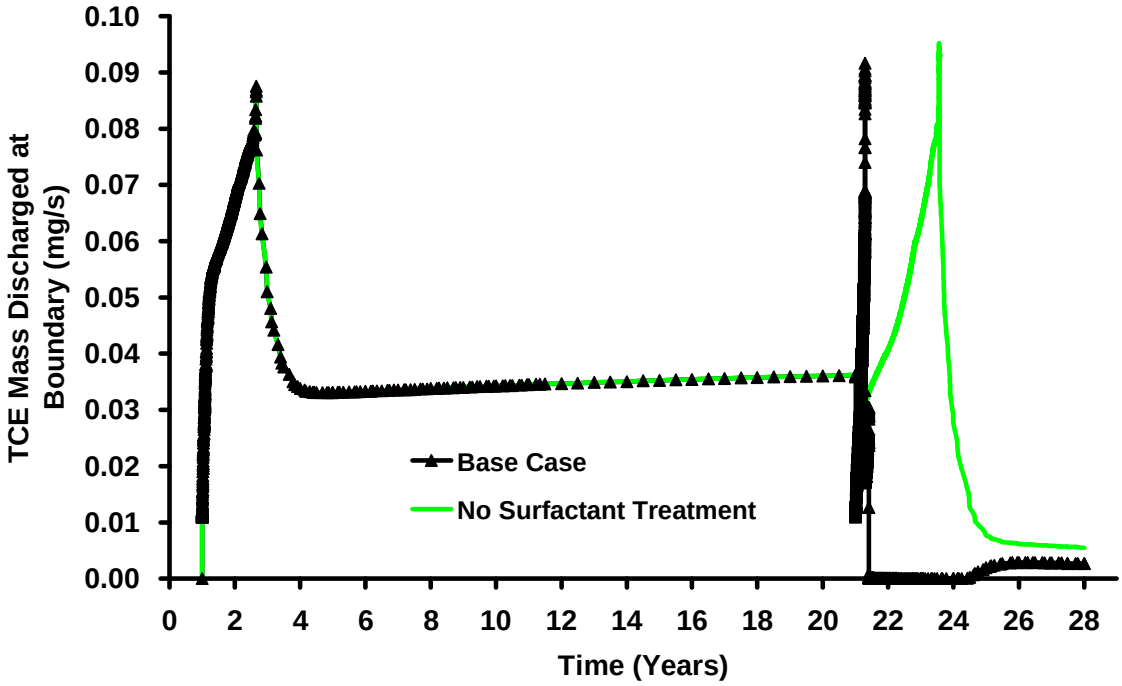

Figure 6.15: Comparison of total boundary mass discharge (TCE) for (a) base case with a simulation where no surfactant was injected (b) since the start of the Treatment Stage for 1 year only (timescale expanded for clarity).

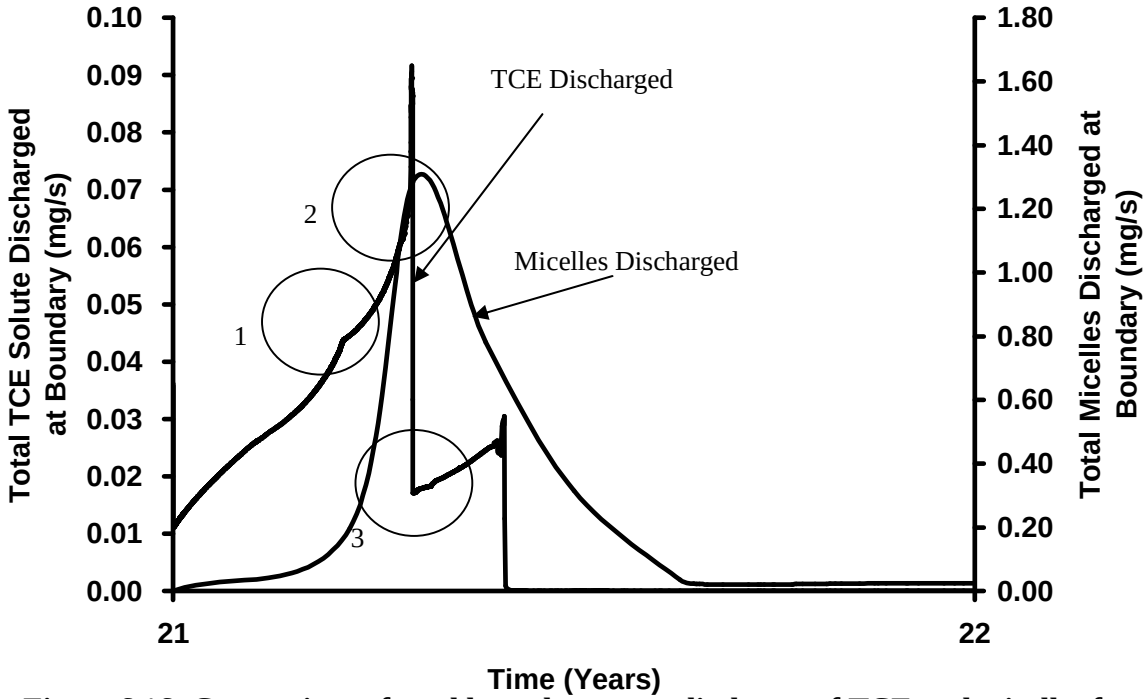

Figure 6.16: Comparison of total boundary mass discharge of TCE and micelles for base case simulation since the start of the Treatment Stage for 1 year only (timescale expanded for clarity).

Figure 6.16 further demonstrates that the concentration of micelles discharged at the boundary increased rapidly during the first quarter of the Treatment stage before decreasing to a low, constant concentration at t_{TOTAL} = 21.65 years. Although boundary TCE mass discharge was observed to decrease to negligible level by this time, It is recognised that in every simulation conducted in this study, micelles containing TCE will be discharged downgradient even though the mass discharge for TCE has reached a negligible level.

Figure 6.17 plots the cumulative downgradient mass discharge of aqueous and entrained TCE in micelles for the base case. During the first 6 months of the Treatment stage, the discharge of TCE mass contained in micelles is observed to increase significantly. It is further noted that the mass of TCE in micelles being discharged is 5.5 times more than the mass of aqueous TCE being flushed out, indicating that surfactant is efficient in solubilising and removing TCE from the domain.

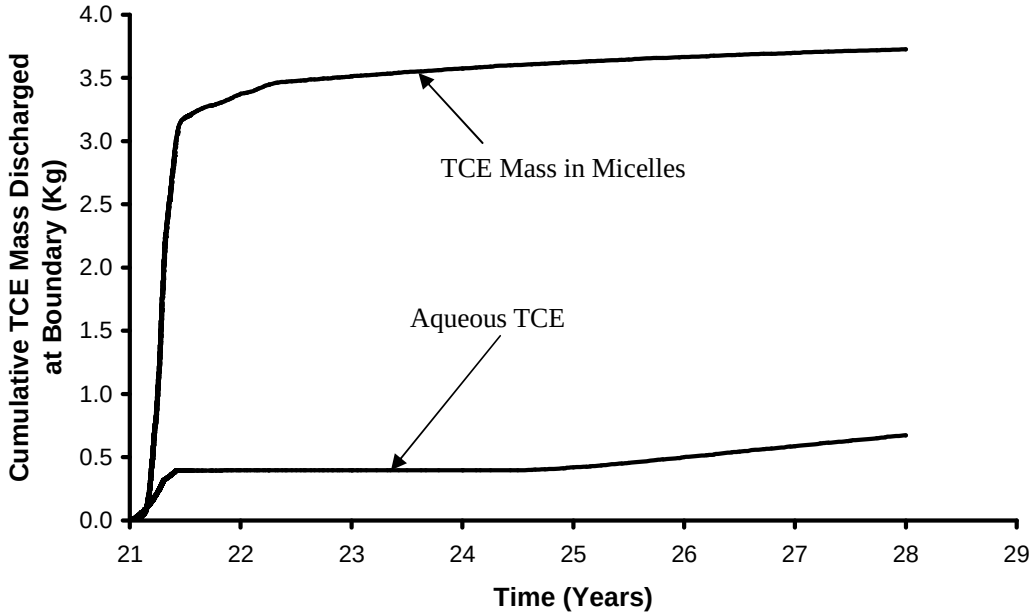

Figure 6.17: Cumulative TCE mass discharged at downgradient boundary.

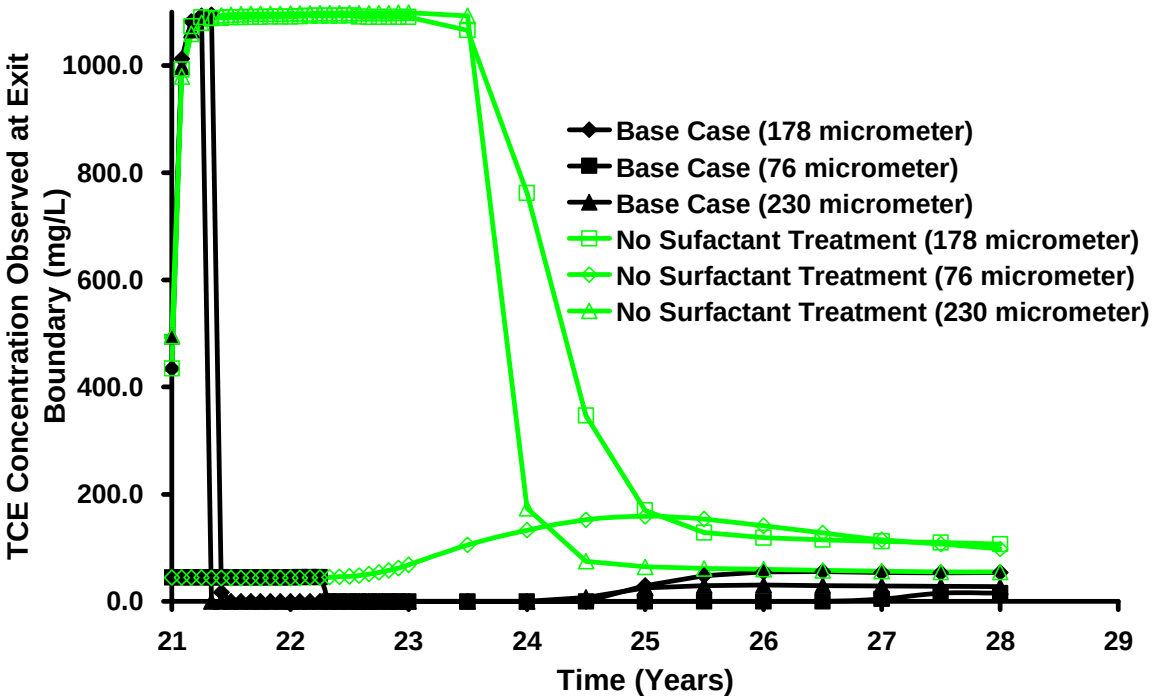

Figure 6.18: Concentration of TCE in various horizontal fractures at downgradient boundary.

Figure 6.18 reveals the average discharge of TCE solute concentration within the horizontal fractures at the downgradient boundary can vary significantly over time. This figure demonstrates that in bigger fractures (e.g., 178μm ~ 230μm), the solute concentration decreased significantly during the initial few months of surfactant injection. On the other hand, it was noted that if the fracture aperture was small (i.e., 76 μm), although the initial concentration outflux in this fracture was much lower than the other two larger factures, it took a much longer time before the downgradient outflux was reduced to undetectable limits; probably due to the difficulty in gaining access to both the DNAPL and contaminant solute in these area by the injected surfactant.

Of the 5.18 kg of TCE DNAPL and 7.3 kg aqueous and sorbed TCE present in the domain at the end of the 20 year Site Ageing stage (t_{TOTAL} = 21 years), 0.02 kg and 4.32

kg, respectively (Table 6.5), remained at the end of the Treatment stage in the Base Case. For the 'No Surfactant' case, 0.02 kg of DNAPL and 7.23 kg of aqueous plus sorbed TCE remained at the end of the Treatment stage. However, the Base Case achieved this DNAPL amount in 7.5 months (Figure 6.12) versus 31.2 months in the 'No Surfactant' case (Figure C2, Appendix C). The difference noted in the matrix-bound TCE is the cause of the observed difference in long-term mass discharge during the Post-Treatment stage.

6.5.2 Sensitivity Simulations

6.5.2.1 Sensitivity to Surfactant Concentration

Figure 6.19 presents the volume of DNAPL in the domain over time. Recall that, in order to conserve total surfactant mass injected, the 60 g/L, 40 g/L, and 20 g/L surfactant solutions were injected for 1.3, 2.0 and 4.0 years, respectively. It is revealed that at any time, the higher the concentration of surfactant injected, the lower the volume of DNAPL is present in the domain. Figure 6.19 further reveals after 6 months of surfactant treatment, more than 90% of the initial DNAPL mass in the domain has been solubilised before reaching a constant level. Mass solubilisation, while highest at early time for the most accessible TCE, accounts for the quick decrease in DNAPL volume during the first 6 months of surfactant treatment. The constant low volume at late time is mainly contributed by the entrapped DNAPL in the dead-end fracture (Figure 6.11).

Figure 6.20 plots the cumulative mass of total TCE present in the domain (i.e., sorbed + aqueous + DNAPL) solubilised by surfactant for Runs 1, 2 and 3. It reveals that an

increase from 20 g/L to 40 g/L causes a total improvement of 1.45% of the total TCE recovered (from 3.98 kg to 4.16 kg (Table 6.5), recalling that the total DNAPL mass in the domain was 5.26 kg). Moreover, the 40 g/L completes solublization in 4.8 months versus 7.8 months for the 20 g/L simulation (Figure 6.18). However, a further increase from 40 g/L to 60 g/L causes small further improvement in rate or in total amount; the latter because all readily-accessed DNAPL is solubilised. Overall, the sensitivity of the results is minor within the range of concentrations examined. It is expected that more significant deterioration of results would occur if injected concentrations were further reduced.

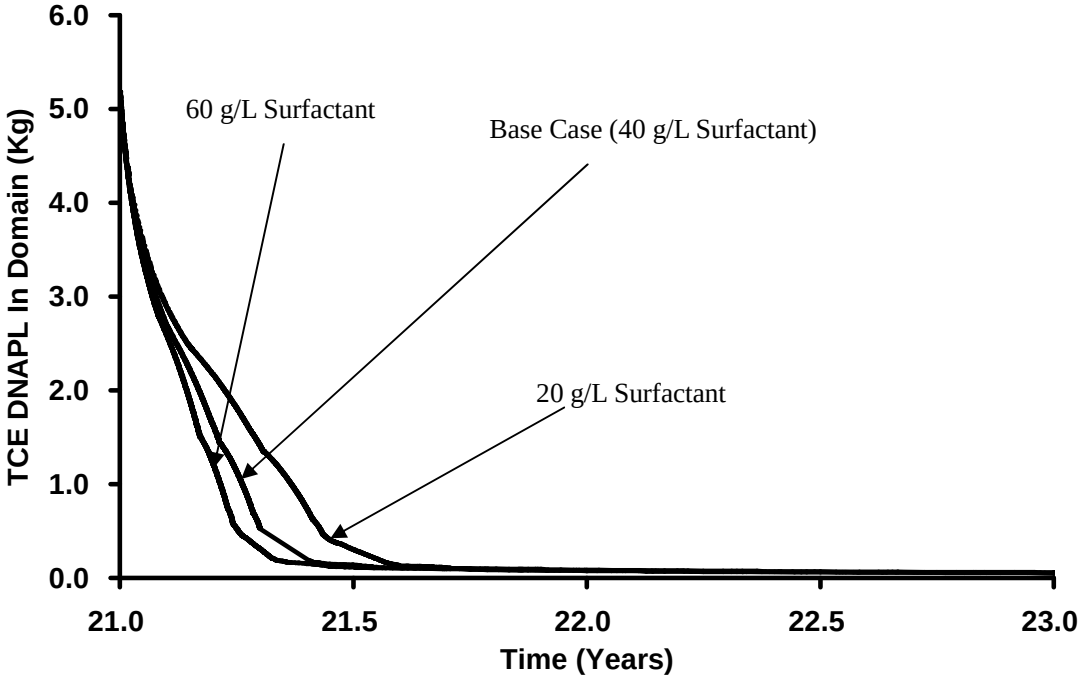

Figure 6.19: Total TCE DNAPL present in domain over time for (a) Base Case, (b) 20000mg/L and (c) 60000 mg/L of surfactant injected.

Figure 6.21 plots the cumulative surfactant mass (i.e., TCE-free) discharged at the downgradient boundary for the three simulations. It reveals that higher concentrations of surfactant resulted in a smaller portion of the injected mass leaving the domain without TCE. As demonstrated by Figure 6.22, a higher proportion of surfactant was used to solubilise the chlorinated ethene present in the domain when a higher concentration of surfactant was injected.

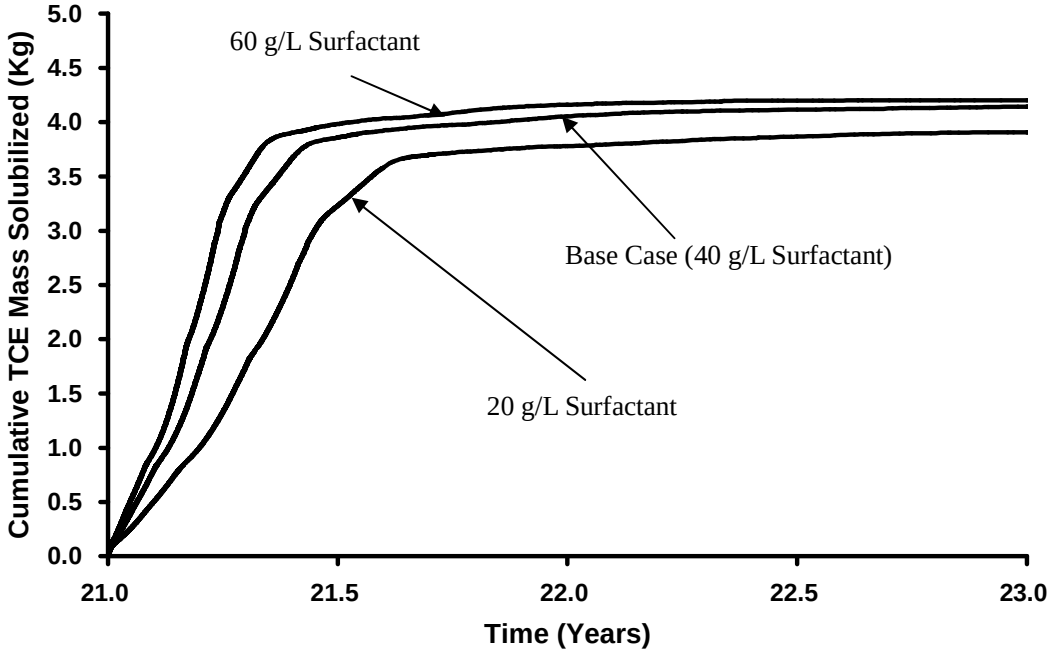

Figure 6.20: Cumulative mass of TCE solubilised by micelles over time for different injected concentration.

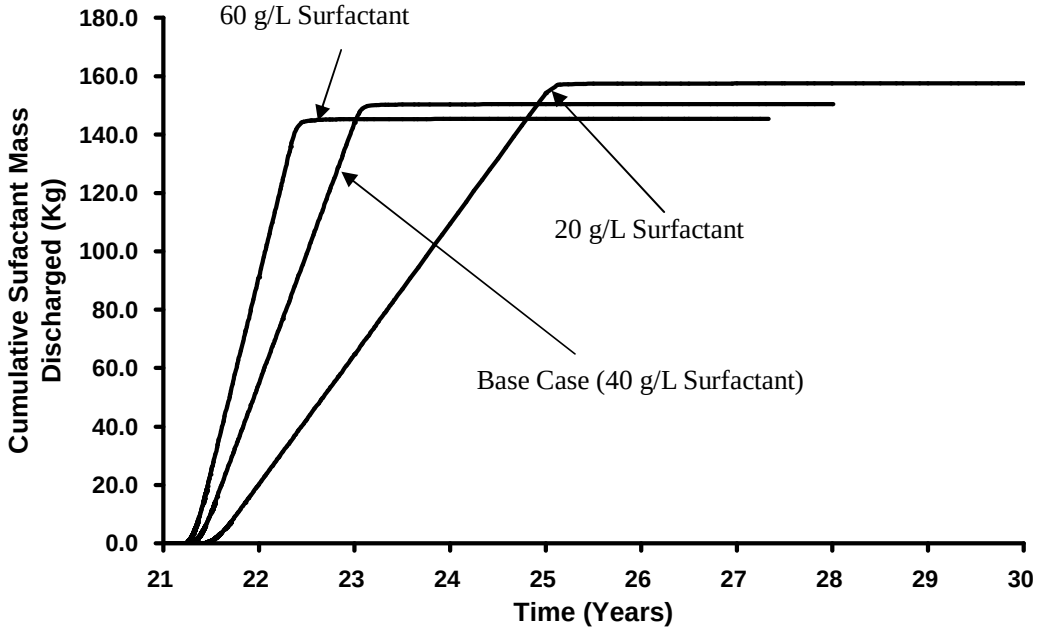

Figure 6.21: Cumulative mass of surfactant discharged over time for different injected concentration.

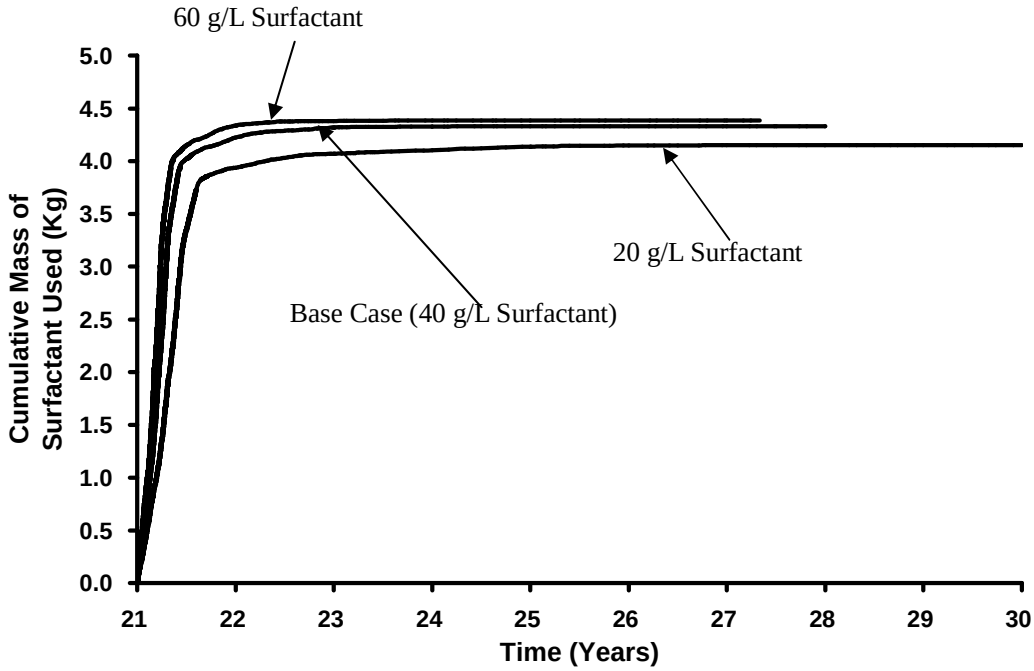

Figure 6.22: Cumulative mass of surfactant used for solubilising DNAPL over time for different injected concentration.

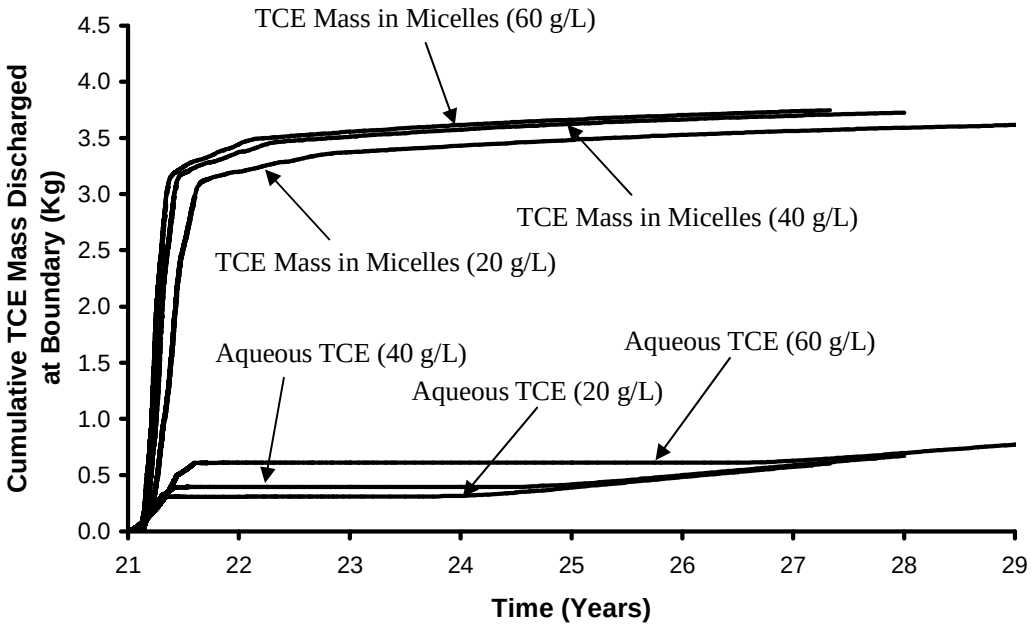

Figure 6.23: Cumulative TCE mass discharged at downgradient boundary for various concentrations.

Figure 6.23 plots the cumulative downgradient mass discharge of aqueous and entrained TCE in micelles for all 3 different concentration simulations. During the first 6 months of Treatment stage, the discharge of TCE mass contained in micelles is observed to increase significantly. It is further noted in all 3 simulations, the mass of TCE entrained in micelles being discharged is at least 5.5 times more than the mass of aqueous TCE being flushed out.

No significant difference between the 3 cases is observed during the Post-Treatment stage with respect to mass discharge (Figure C3, Appendix C) or exit concentrations of surfactant (figure not shown). Moreover, the distribution of TCE, surfactant, and micelles are observed to be essentially identical after the Treatment stage (compare Figure 6.11 and Figures C4 and C5 in Appendix C).

6.5.2.2 Sensitivity to DNAPL

In this study, results were compared between PCE and TCE. At the end of the DNAPL Infiltration stage, the average DNAPL saturation was 0.5 while the volume of DNAPL in the domain was 0.008 m^3 (compared to a total fracture volume of 0.012 m^3) with 100% of the nodes in drainage in both simulations. At the end of DNAPL redistribution stage, the average DNAPL saturation was 0.3 for both TCE and PCE while the volume of DNAPLs present was 0.0036 m^3 (5.18 kg) and 0.0037 m^3 (6.03 kg) while the pool to residual ratio was 71:29% and 51:49% for TCE and PCE, respectively.

At the end of the Site Ageing stage (t_{TOTAL} = 21 years) the total mass of aqueous and sorbed TCE and PCE in the domain was 7.3 kg (55.6 moles) and 3.3kg (20.2 moles) respectively. Of the PCE mass in the domain, more than 99.9% resided in the matrix, of which 98.7% was sorbed and only 1.3% remained in the aqueous phase.

Although the initial volume of DNAPL injected into the domain was similar in both simulations, it is important to note that the concentration of continuous influx throughout the Site Ageing stage was considerably lower for PCE (100mg/L) than TCE (550mg/L). As a result, the mass present in the PCE-contaminated domain at the end of the Site Ageing stage was much lower than the Base Case. Prior to the Treatment stage, the TCE and PCE DNAPL masses mapped into the domain were 5.18 kg and 6.03 kg, respectively.

As demonstrated in Figure 6.24, the total mass of surfactant injected into the domain was similar for both the Base Case and the PCE simulation. Despite this, Figure 6.24 reveals

that the total mass of TCE (i.e., sorbed + aqueous + DNAPL) solubilised by surfactant was slightly lower than that for PCE (4.16 kg versus 4.45 kg). Closer inspection of Figure 6.24 revealed that initially the rate of TCE solubilisation exceeded PCE solubilisation. This could be explained by (1) higher MSR for TCE (9.57 mol/mol) than PCE (5.41 mol/mol), and (2) larger initial total TCE mass (12.48 kg) than total PCE mass (9.33 kg) (Refer to Table 6.5). However, after approximately 6 months of treatment, the total mass of PCE being solubilised surpassed the total mass of TCE; this coincides with the time when TCE DNAPL solubilisation was effectively complete (Figure 6.12; note that PCE DNAPL solubilisation was effectively complete 8 months after the start of the Treatment stage). After the easily accessed DNAPL was removed, increased amount of solubilised TCE was dominated by the partitioning of aqueous solute into micelles. Recall that, at chlorinated ethene concentrations less than solubility (i.e., in absence of DNAPL), the extramicellular fraction of PCE solute is about one-third that of TCE solute (Figure 6.1, Kim et al., 2007). In other words, under similar conditions, a higher fraction of aqueous PCE mass was entrained into micelles than for TCE, thus leading to the higher PCE recovery at late time observed in Figure 6.24. This finding is backed by evidence (Figure C6, Appendix C) demonstrating that the remediated volume of matrix surrounding the horizontal fractures is larger for the PCE case than the Base Case (Figure 6.24).

Figure 6.25 reveals that by the end of the Treatment stage, the chlorinated ethene mass discharge at the downgradient boundary was reduced to nondetectable in both simulations. However, while the mass discharge in for TCE rebounded slightly at t_{TOTAL} = 24.5 years,

no such rebound was observed in the PCE simulation.

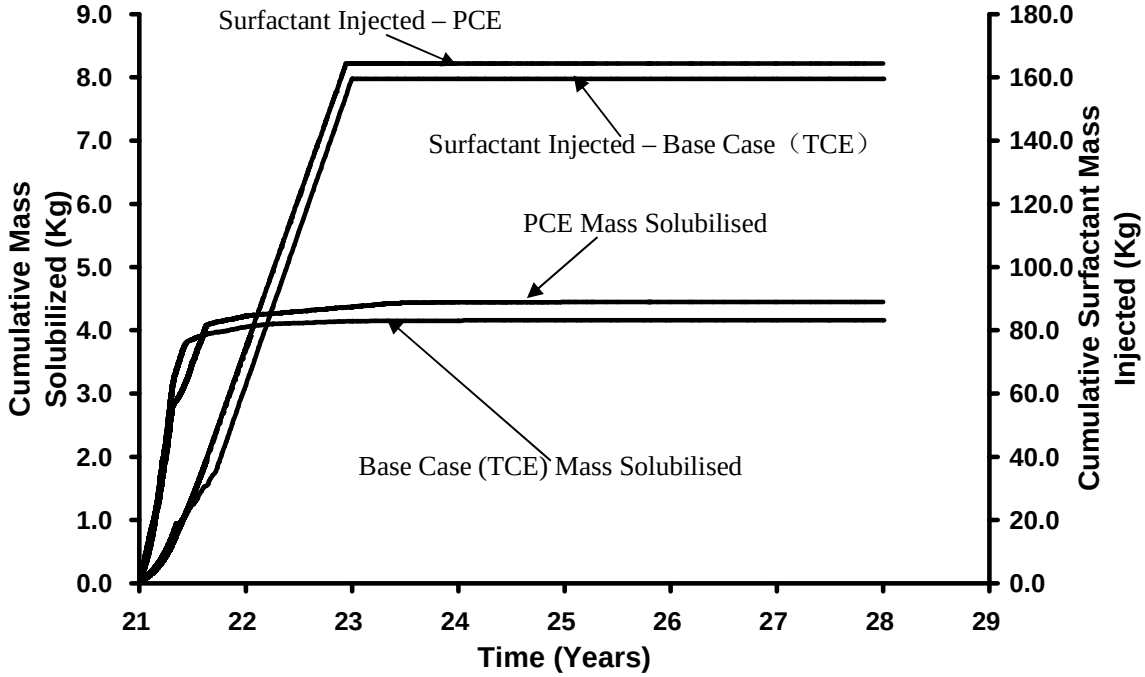

Figure 6.24: Comparison of cumulative mass solubilised by micelles and surfactant injected for period between 21 to 28 years.

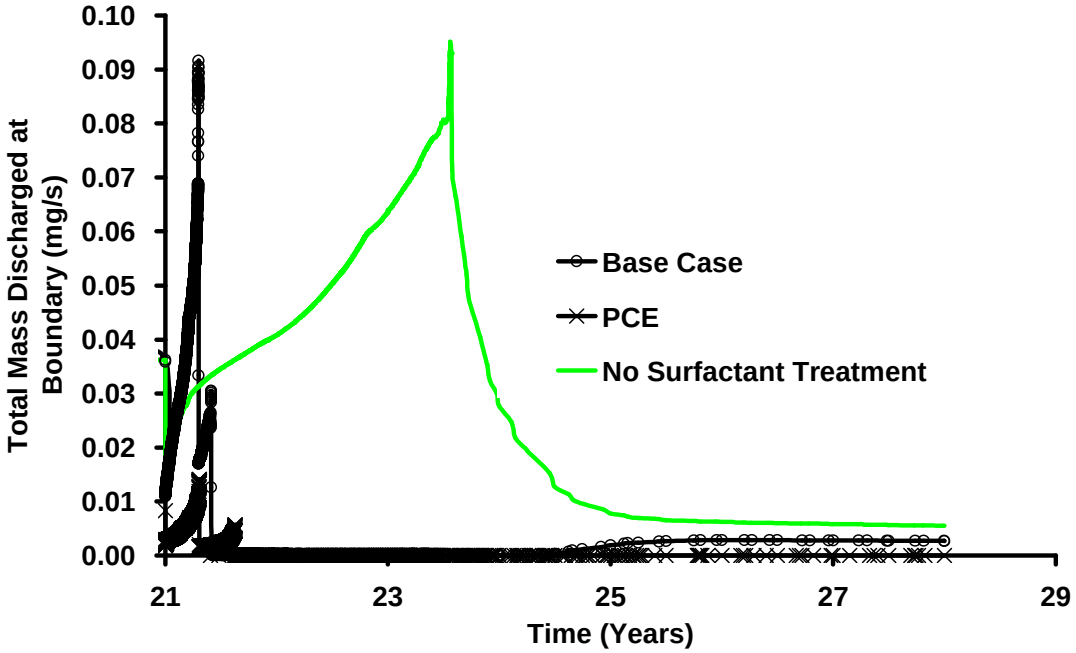

Figure 6.25: Comparison of total boundary mass discharge for different DNAPL with a simulation where no surfactant treatment (sandstone) was carried out for period between 21 to 28 years.

Figure 6.26 plots the cumulative discharged mass of aqueous and DNAPL mass entrained in micelles for both PCE and TCE. It is observed in both cases, the discharge for solubilised chlorinated solvent is significantly higher than that exiting the domain in the aqueous phase external to the micelles. Additionally, the discharge of entrained PCE mass is observed to be approximately 8% higher than the entrained TCE mass discharged.

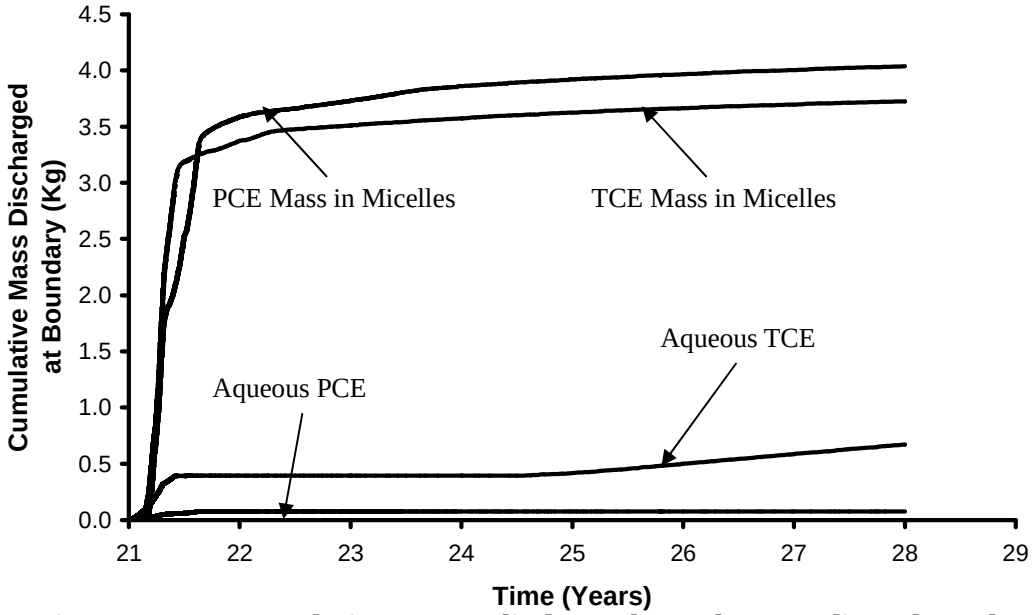

Figure 6.26: Cumulative mass discharged at downgradient boundary for various DNAPL simulations.

This further corroborates the observation described above that the extramicellar fraction of PCE entrained into micelles is higher than the extramicellar fraction of TCE in the absence of DNAPL, with significant impacts on long term mass discharge.

6.5.2.3 Sensitivity to Rock Type

At the end of the DNAPL Infiltration stage, the average DNAPL saturation was 0.75, the volume of DNAPL in the domain was 0.008 m^3, 0.010 m^3 and 0.0181 m^3 for sandstone,

shale and granite with 100% of the invaded nodes on drainage for all 3 rock types. At the end of DNAPL redistribution stage, the average DNAPL saturation was 0.3 for all 3 rock types, the volume of DNAPL was 0.0036 m^3, 0.0047 m^3 and 0.0079 m^3 while the pool to residual ratio was 71:29%, 72:28% and 90:10% for sandstone, shale and granite, respectively. The distribution of TCE DNAPL at the end of the Redistribution stage for all three is illustrated in Figure A6, Appendix A.

At the end of the 20 years Site Ageing stage (t_{TOTAL} = 21 years) the total mass of aqueous and sorbed TCE in the domain was 7.3 kg, 6.8 kg and 0.68 kg for sandstone, shale and granite respectively (Table 6.5). In each case, 97-99% of the total mass resided in the matrix, of which 97-98% was sorbed and only 1-2% remained in the aqueous phase. Although no DNAPL was left in the sandstone and shale domain at this time, 4.23 kg of DNAPL was present in the granite domain. This observation is consistent with the findings in Parker e al. (1994) where it was demonstrated that due to the low porosity in granite, DNAPL could remain present in the fractures for decades. Figure 6.27 illustrates the distribution of aqueous phase TCE in sandstone, shale and granite at the end of the 20-year Site Ageing stage. In each case, the matrix immediately surrounding the fractures exhibits diffusion halos of TCE. However, the depth and extent of TCE penetration of the matrix is observed to be highly dependent on properties of both the fractures and the matrix for each rock type. The combination of these impacts residence time of TCE in the source zone and it is the relative rates of TCE transport through fractures versus diffusion to the matrix that affects the final distribution of mass diffusion (See section 4.5.2.3 for calculations and further details).

The vertical axis of Figure 6.28 demonstrates that the percentage of initial TCE mass retained in the domain at the end of Site Ageing follows the order sandstone > shale > granite. Peclet number (Pe) for fractured rock is defined as the ratio of advection to diffusion rates, $Pe = ve/(D^o\tau)$, where v is the advective velocity in the fracture, e is the mean aperture, D^o is the free solute diffusion coefficient and τ is the matrix tortuosity (e.g., Fetter, 1993). Here v is taken as the mean horizontal advective velocity across each domain and e is the mean aperture of all horizontal fractures for each rock type. Figure 6.28 reveals that the percentage of TCE retained (in aqueous and sorbed forms) exhibits a linear dependence on the log(Pe) for the three rock types ($R^2 = 0.9923$) at the end of the Site Ageing stage (i.e., t_{TOTAL} = 21 years). This confirms expectations that lower Pe (i.e., lower advective velocity, smaller apertures, higher effective diffusion) corresponds to increased matrix diffusion (e.g., sandstone) while higher Pe corresponds to increased mass loss via advection (e.g., granite).

At t_{TOTAL}=21 years, as mentioned above, DNAPL distribution at t_{TOTAL} = 1 year was mapped onto the domain. As a result, the total TCE DNAPL mass (and total aqueous + sorbed TCE mass) present in sandstone, shale and granite were 5.18 kg (7.30 kg), 6.88 kg (6.67 kg) and 11.53 kg (0.68 kg), respectively, at the beginning of the Treatment stage.

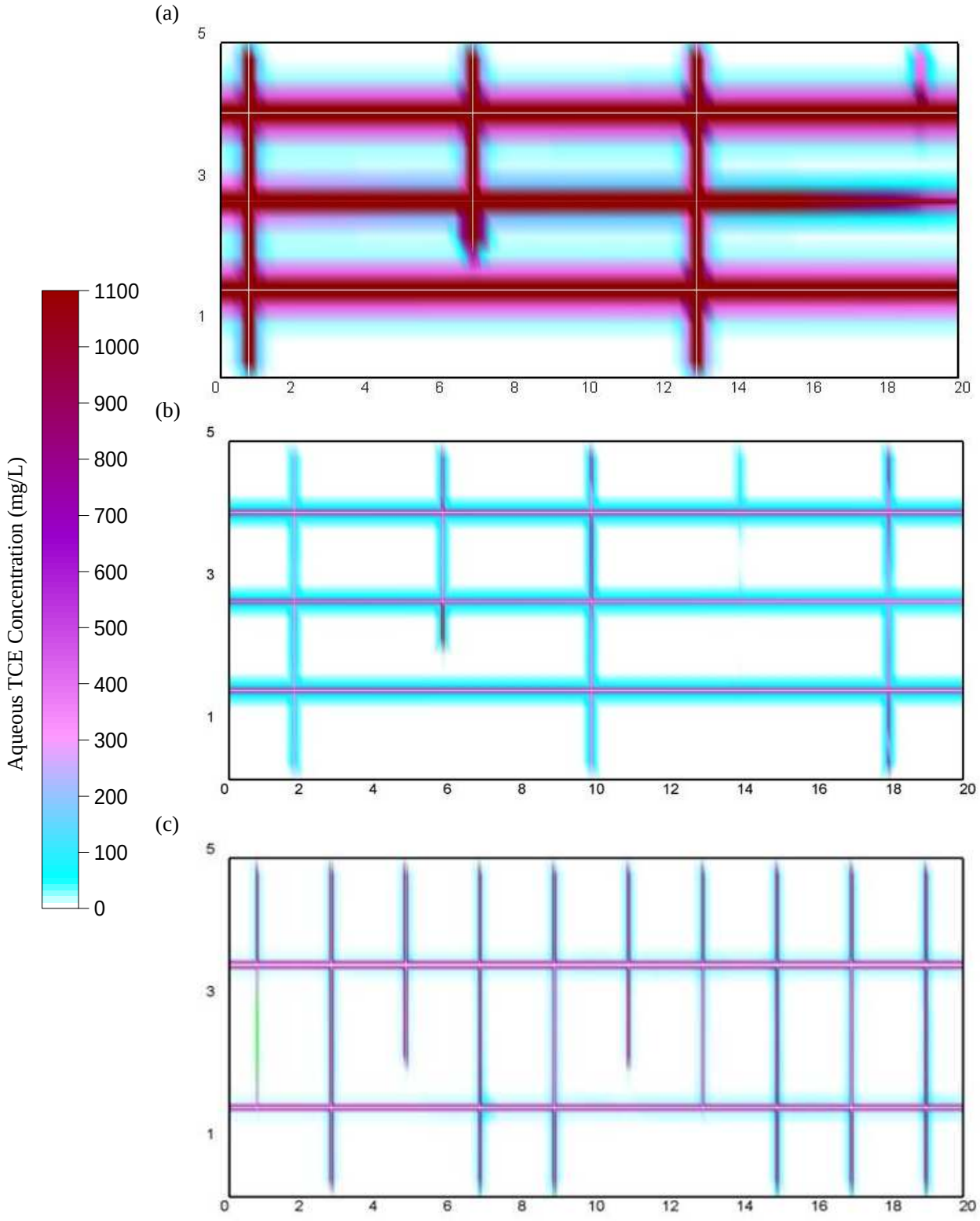

Figure 6.27: Distribution of aqueous TCE after 20 years (t_{TOTAL} = 21 years) of DNAPL dissolution in (a) Sandstone, (b) Shale and (c) Granite.

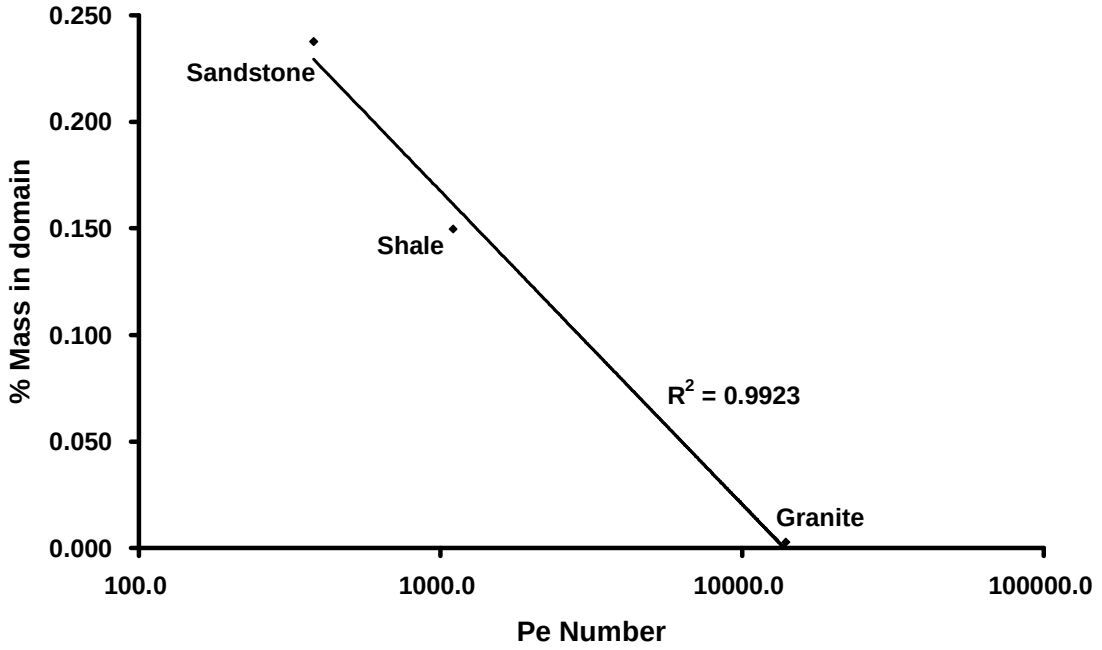

Figure 6.28: Mass of aqueous and sorbed TCE in various rock domains at end of Site Ageing stage (i.e., t_{TOTAL} = 21 years) vs. Peclet number (log scale) for each individual domain.

Figure 6.29, presenting the mass of TCE (i.e., sorbed + aqueous + DNAPL) solubilised, reveals that granite (which exhibits the largest mean fracture aperture of the three rock types) exhibits the highest solubilised TCE mass while sandstone (i.e., Base Case) exhibits the lowest. These observations are mainly due to the presence of more DNAPL within the fractures at the start of the Treatment stage. Although granite exhibits the highest solubilised mass among the three rock types investigated, the fraction of mass recovered is only equivalent to 62.1% of the initial DNAPL mass present in the domain at the start of the Treatment stage. Interestingly, this is lower than the 70.2% and 80.2% of chlorinated ethene mass recovered in shale and sandstone respectively. Figure 6.11 and Figures C7 and C8 of Appendix C revealed that vertical fractures, contaminated by the downward vertical movement of DNAPL appear to be relatively unaffected by

horizontally driven surfactant. This is confirmed by the lack of micelles being formed in the vicinity of the vertical fractures, especially near the top and bottom areas of the vertical fractures in the respective domains. Given the largest vertical fracture volume in granite (hence the largest fraction of initial mass entrapped in vertical fractures), it could be understood why granite experienced the lowest fraction of mass being recovered among the three rock types.

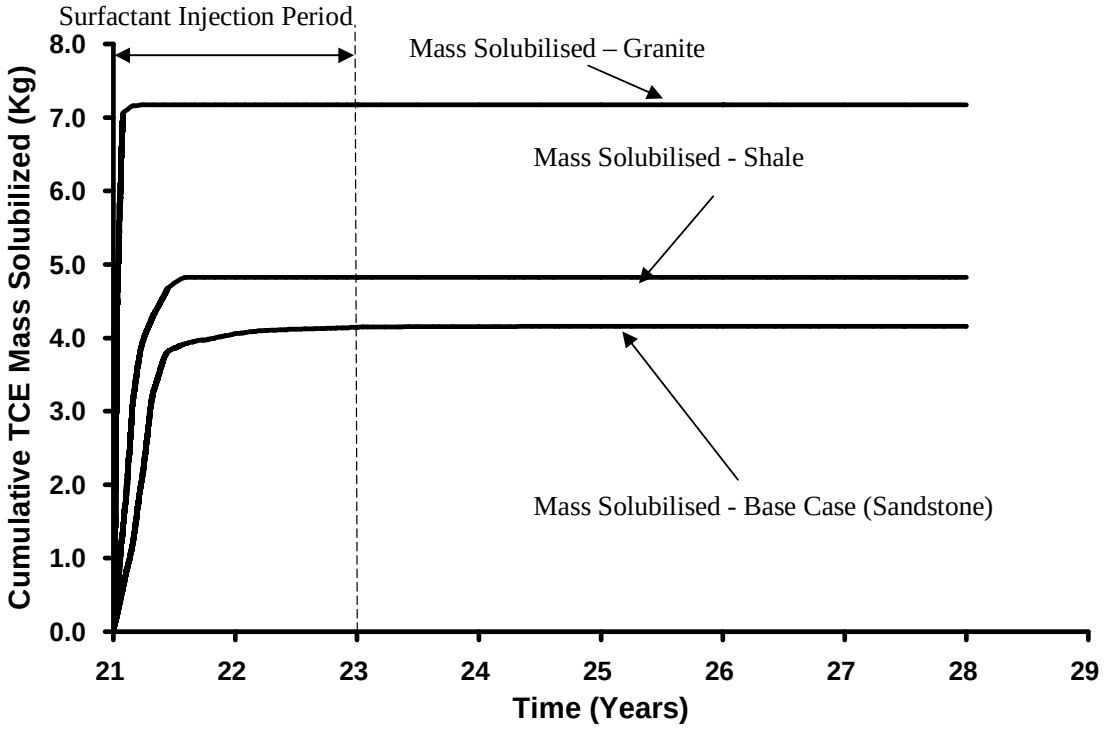

Figure 6.29: Cumulative TCE mass solubilised by surfactant over time for various rock types.

Figure 6.30 reveals a total of 160kg, 263kg and 1730kg of surfactant being injected over 2 years for sandstone, shale and granite respectively (Table 6.5). The amount of surfactant injected is equivalent to 12.3 times, 18.5 times and 136.0 times greater than the theoretical mass required to solubilise and entrain all the TCE in the domain at the start of the Treatment stage. The differences in surfactant mass injected are due the differences

in bulk effective horizontal hydraulic conductivity while treatment period, injection concentration and hydraulic gradient were all held constant. This figure further reveals that of the surfactant injected, only 4.33kg, 5.03kg and 7.47kg (Table 6.5) were used in the solubilisation and capturing of TCE into micelles in the sandstone, shale and granite, respectively.

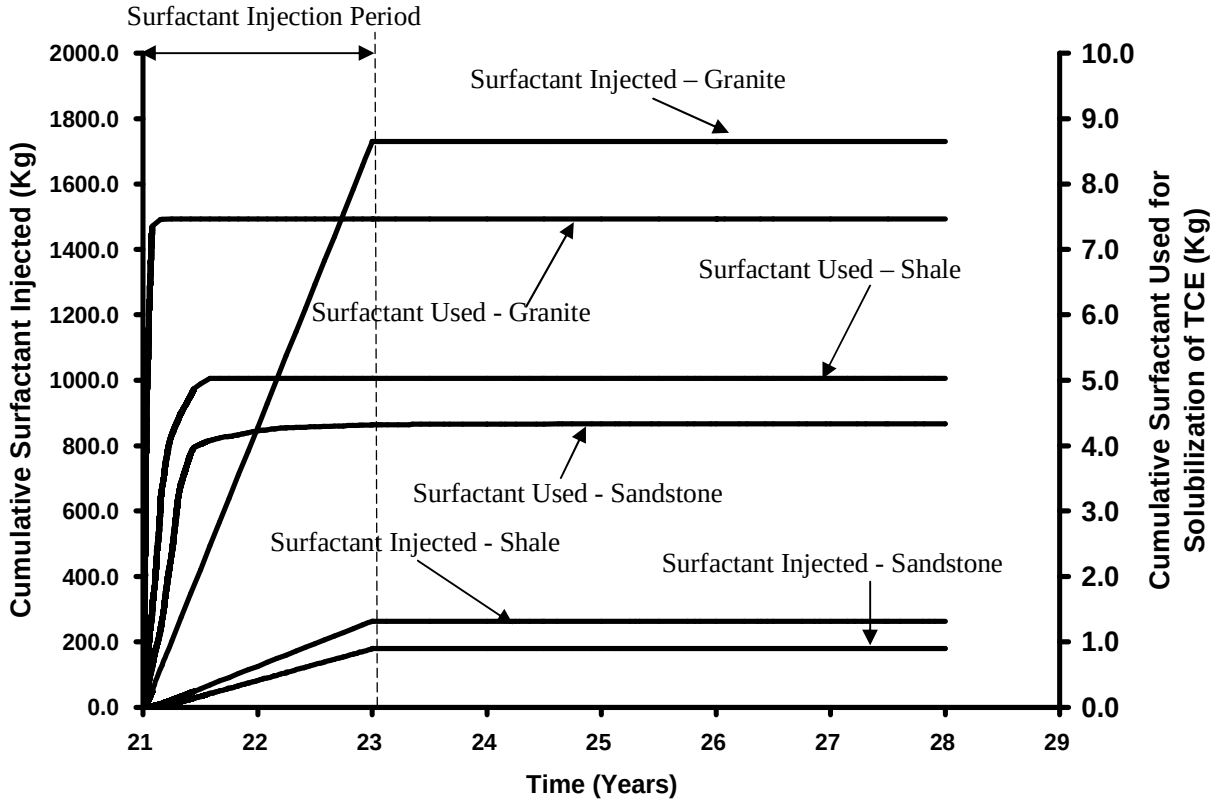

Figure 6.30: Cumulative surfactant injected and used for TCE solubilization for various rock types simulations.

Figure 6.31 presents the total boundary mass discharge for the three rock types. As revealed in this figure, the mass discharges for all three simulations were quickly reduced to negligible level in less than half a year after treatment began. Figure 6.31b further reveals that the mass discharge for granite diminishes at the fastest rate among the three rock types. This confirms expectations that granite with a higher peclet number (i.e., a

more advective dominated domain) allows the injected surfactant to travel through the fractures at a quicker rate, thus in turn solubilises and partitions TCE molecules within the fractures into the surfactant micelles at a faster rate than sandstone and shale (i.e., less advective dominated domains). During the Post-Treatment stage, the 'No surfactant treatment' simulation exhibited a low but relatively constant mass discharge associated with reverse diffusion. Meanwhile, only sandstone (which possesses the highest diffusive flux scenario among the three rock types) exhibited a re-bound in mass discharged while shale and granite both reveal negligible mass discharge level throughout this period.

Figure 6.32 plots the cumulative discharged mass of aqueous and entrained TCE mass in micelles for sandstone, shale and granite respectively. Although the aqueous mass discharged is similar in all three rock types during the Treatment stage, the sandstone simulation revealed an increase in mass discharge during late times; reaffirming the observation of reverse diffusion in this particular domain. Figure 6.32 further reveals the mass of entrained TCE being discharged as granite > shale > sandstone. This observation is consistent with the previous findings where granite exhibits the highest solubilised TCE mass while sandstone (i.e., Base Case) exhibits the lowest. Together with the high peclet number (therefore a more advective domain) in granite, it can be understood why granite exhibits the largest amount of entrained TCE mass being discharged out of the domain.

Refer Figure C7 and C8, Appendix C for the concentration profiles of all three aqueous

species at t_{TOTAL}=28 years.

(a)

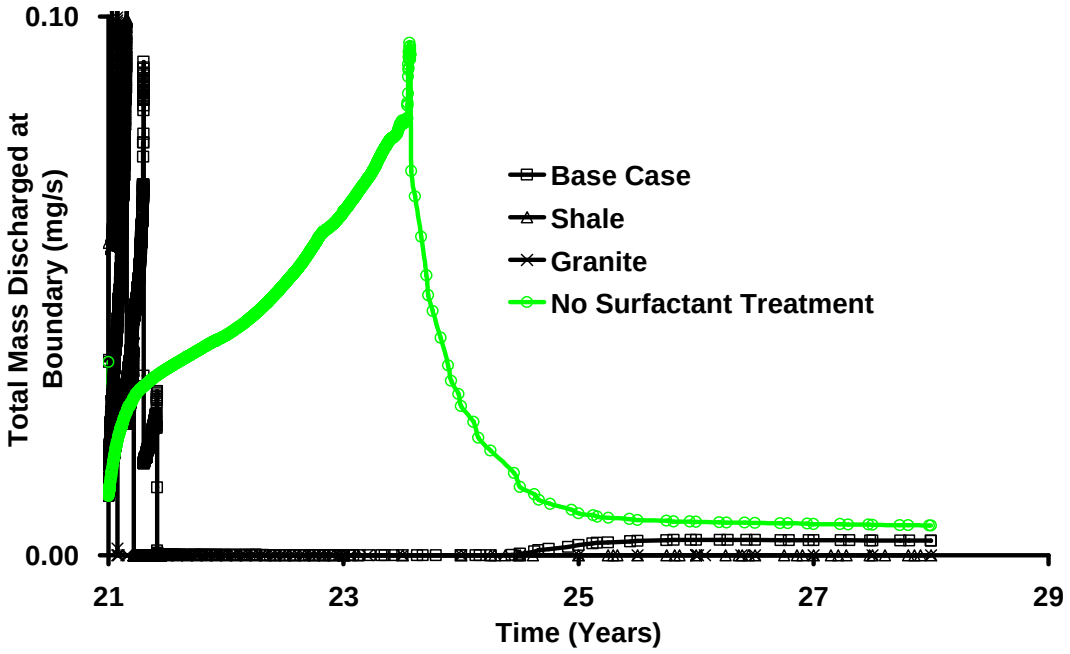

(b)

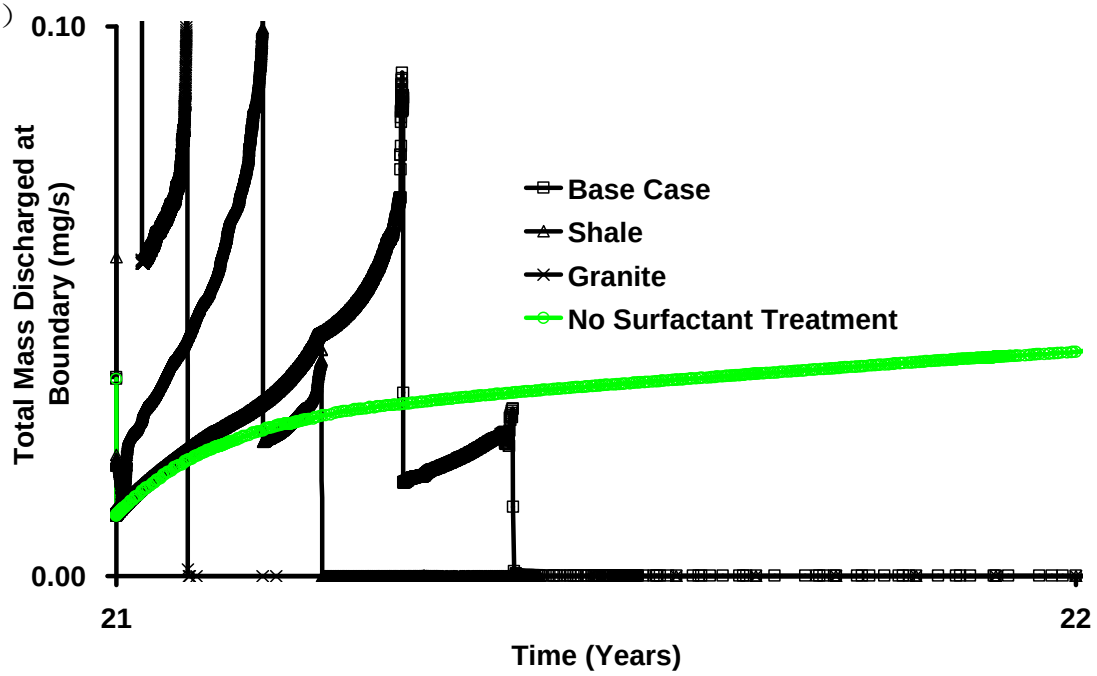

Figure 6.31: Comparison of total boundary mass discharge for (a) different rock type with a simulation where No surfactant treatment (sandstone) was carried out for period between 21 to 28 years (b) since the start of the Treatment Stage for 1 year only (timescale expanded for clarity).

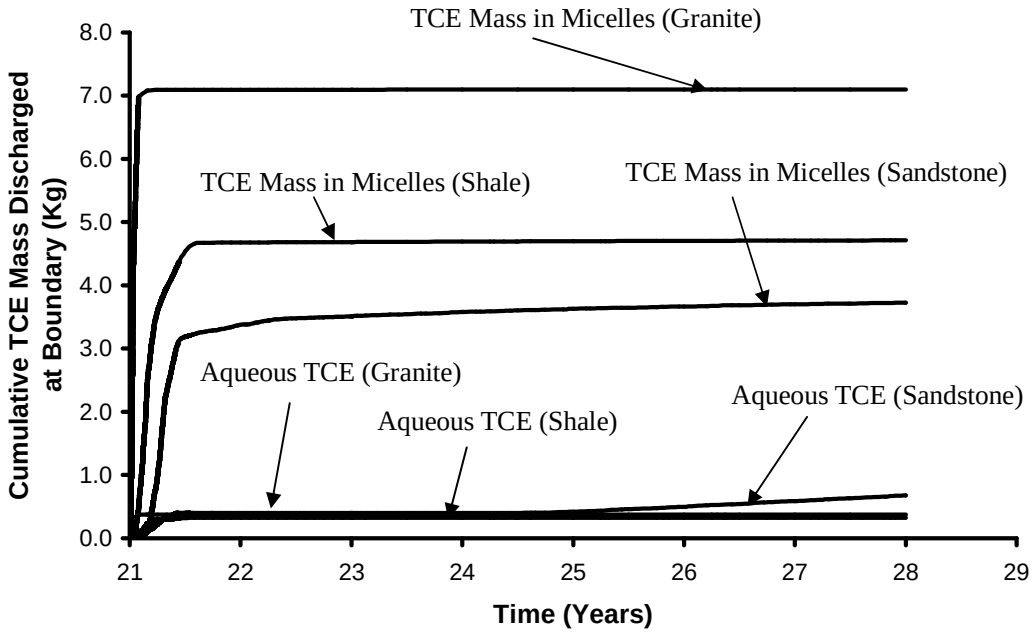

Figure 6.32: Cumulative mass discharged at downgradient boundary for (a) sandstone; (b) shale and (c) granite.

6.5.2.4 Sensitivity to Aging Time

In this sensitivity study, the effects of the duration of 'aging' process on surfactant flushing were investigated. In each case, the DNAPL volume and distribution is the same but the aqueous and sorbed TCE mass contaminates the matrix to different extents at the start of treatment. Prior to the Treatment stage, the total aqueous and sorbed TCE present in the domain was 0.00 kg, 4.13 kg, 5.33 kg and 7.30 kg for 0 years, 5 years, 10 years and 20 years aging (Base Case), respectively, while the DNAPL mass in each case was 5.18 kg.

Figure 6.33 reveals that the total TCE mass (DNAPL solubilised and solute entrained) removed by surfactant is directly related to the extent of TCE loading of the matrix (i.e., aging period). Therefore, some recovery of the matrix-bound TCE is observed.

However, the fraction of initial TCE + aqueous and sorbed mass recovered was 59%, 38%, 37% and 33% for ageing periods of 0 years, 5 years, 10 years and 20 years, respectively. These results underscore that while surfactant flushing of fractures is effective, recovering diffused and sorbed mass in the matrix is relatively inefficient with this inefficiency increasing as the timescale of the site ageing increases relative to the timescale of the treatment.

Figure 6.34 plots the cumulative TCE (aqueous + sorbed) mass discharged for these 4 simulations. For the purpose of clarity, only the mass discharged for the Treatment and Post-Treatment stages were plotted. This figure reveals that in all cases the downgradient mass discharge was reduced to zero in a short time during the treatment period. It is further noted that only the cases with significant matrix contamination – namely, Site Ageing for 5 years, 10 years and 20 years - exhibited rebound of mass flux

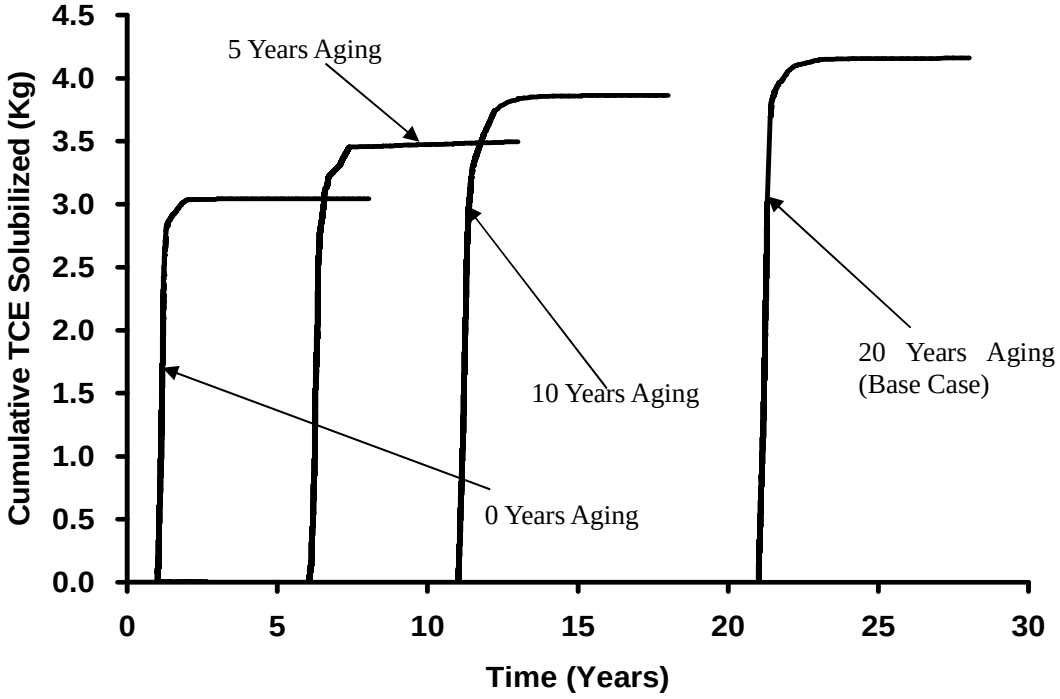

Figure 6.33: Cumulative mass of TCE solubilised over time for different aging period.

within a 2-year period after terminating treatment. Although only 59% of the initial TCE mass was recovered in the '0 years' Ageing simulation, it is believed the high concentration of surfactant that remained in the vicinity of the factures (Figure C9, Appendix C) has prevented a rebound of mass flux after Treatment has ceased. It is revealed that the mass discharge for '5 years', '10 years' and '20 years' aging were 1.91 x 10^{-5} mg/s, 7.15 x 10^{-4} mg/s and 2.69 x 10^{-3} mg/s respectively (Table 6.5), indicating that the magnitude of rebound is more significant as the length of site ageing increases. As expected, when the extent of rock matrix that was contaminated with aqueous and sorbed TCE increases beyond a threshold amount, a constant volume of surfactant cannot access it all in the limited Treatment period.

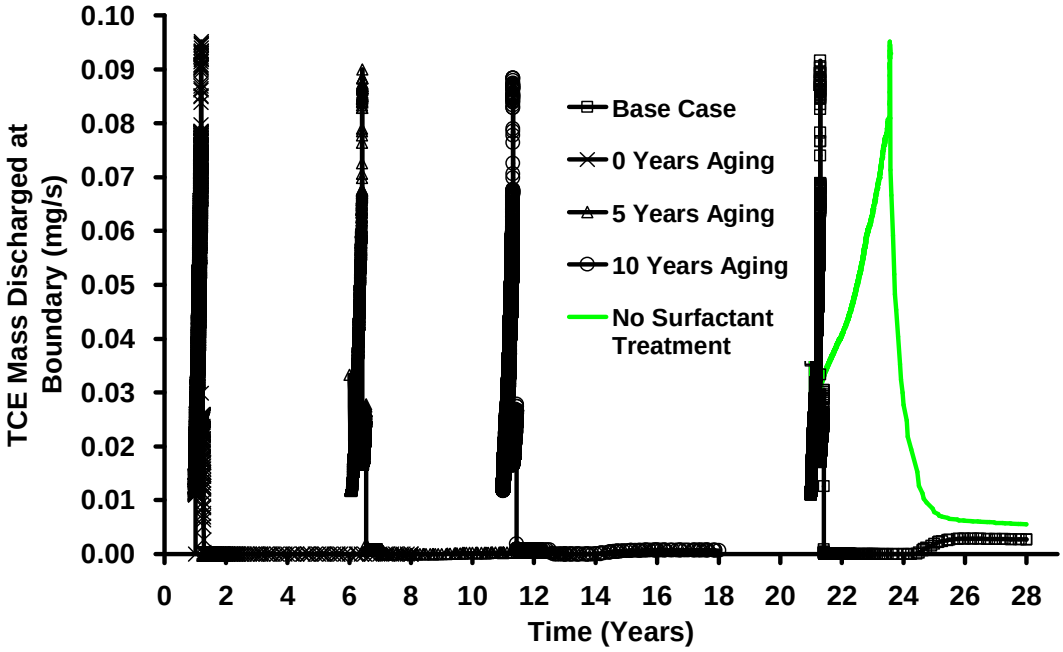

Figure 6.34: Comparison of total boundary mass discharge for different aging period with a simulation where no surfactant treatment was carried out for period from 2 years of Treatment and 5 years of Post-Treatment.

Figure 6.35 plots the cumulative downgradient mass discharge of aqueous and entrained TCE in micelles for '0 years', '5 years', '10 years' and '20 years' aging simulation. As per all other simulations, this figure reveals higher entrained TCE mass being discharged than aqueous TCE. It is further revealed that as the years of aging increases, the amount of mass of TCE entrained in micelles being discharged increases accordingly. This reaffirms with the previous observation where the extent of the total TCE mass (DNAPL solubilised and solute entrained) removed by surfactant is directly related to the extent of TCE loading of the matrix (i.e., aging period).

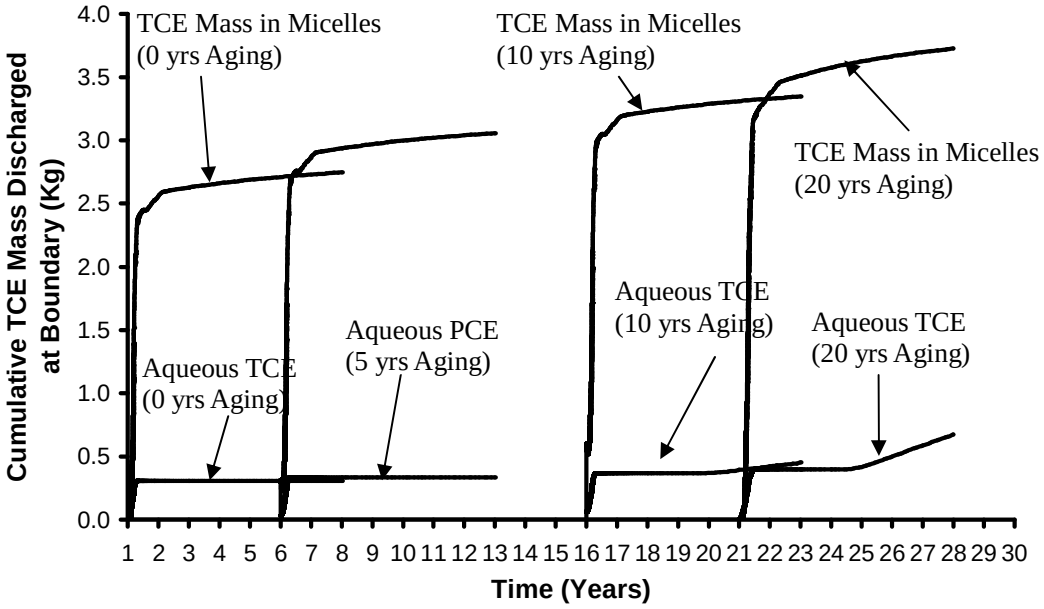

Figure 6.35: Cumulative mass discharged at downgradient boundary for (a) 0 years aging; (b) 5 years aging (c) 10 years aging and (d) 20 year aging.

6.5.2.5 Sensitivity to Mass Transfer Model

This sensitivity study compared the influence of the rate-limited mass transfer model of Dickson and Thomson (2003) to that from the equilibrium dissolution model. Figure 6.36 reveals that although the total mass of surfactant injected into the domain is similar

in each simulation, the total cumulative mass of TCE (i.e., sorbed + aqueous + DNAPL) solubilised in the Base Case was approximately 21% higher than the rate-limited case. Figure 6.37 reveals the result of a predicted stall in DNAPL mass transfer in the rate-limited case before all the DNAPL was depleted. In this case, a rapid slowdown in mass transfer rate is observed at t_{TOTAL} = 21.5 years. It is believed this slowdown is due to an end of the initial pseudosteady and early transient stages of dissolution, where majority of mass transfer is to take place (Dickson and Thomson, 2003). This is backed-up by Figure 6.38 where DNAPL saturations in the domain are generally observed to be at 0.1 or less (except for the immediate vicinity of the dead-end vertical fracture), indicating more than 8% of the initial mass has been removed from virtually all locations – a criteria which marked the end of the initial pseudosteady and early transient stages of dissolution (refer to Section 6.3.2.4 for more details).

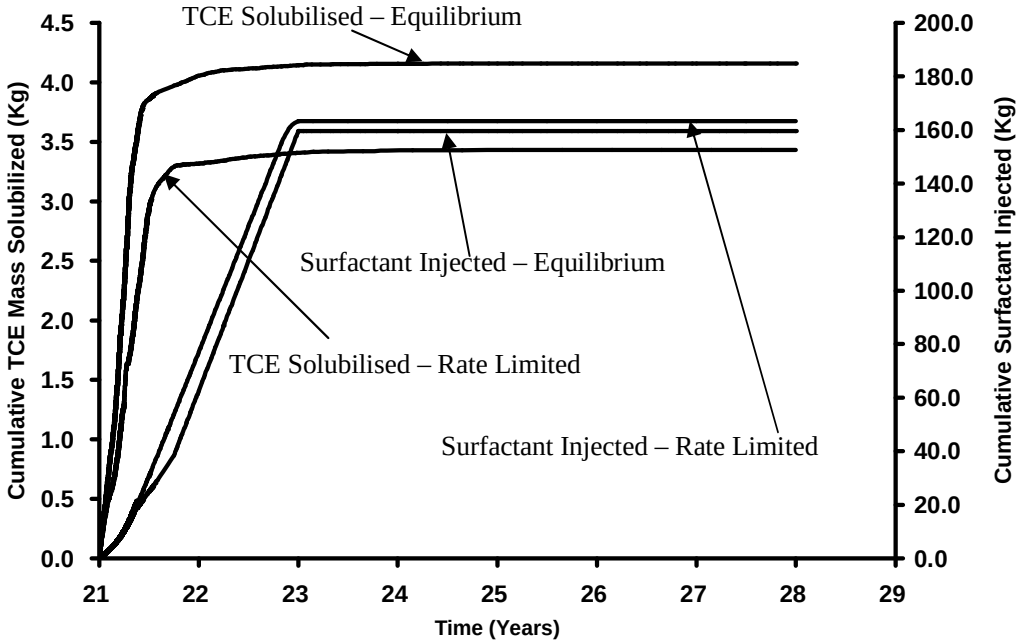

Figure 6.36: Cumulative TCE captured and Tween-80 injected over time for rate-limited mass transfer simulation.

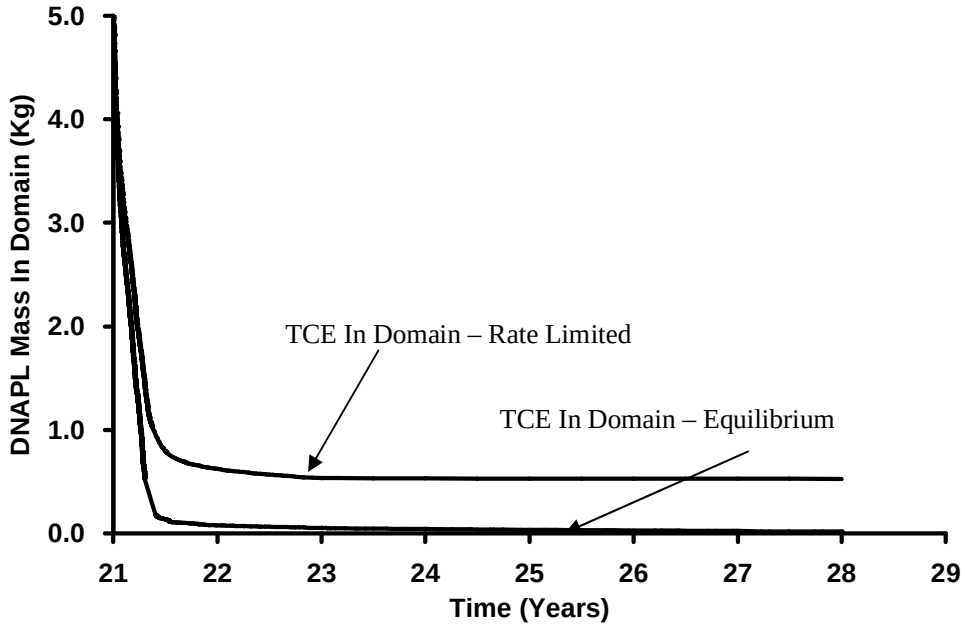

Figure 6.37: Cumulative TCE mass in domain for (a) rate-limited mass transfer simulation (b) Base Case, over time.

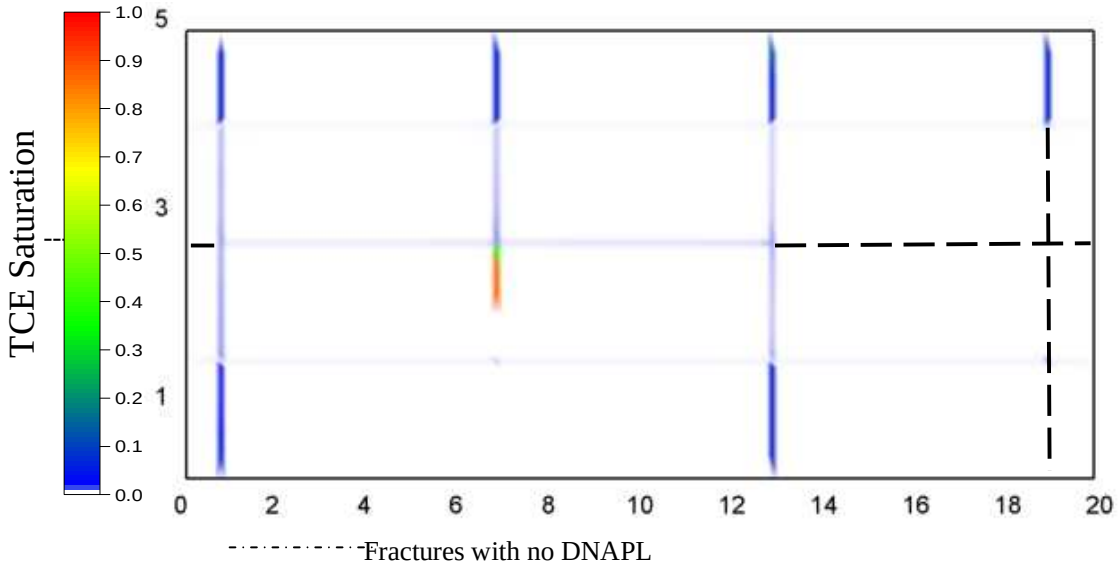

Figure 6.38: Distribution of TCE saturation, at the end of Treatment stage (i.e., t_{TOTAL} = 23 years).

Figure 6.39, presenting the total TCE mass discharge from both runs, reveals that during the Treatment stage, the mass discharge in both simulations are reduced to negligible

level in less than one year. However, it is further noted that during the first year of treatment, the mass discharge curve is significantly different in the two simulations. In the rate-limited mass transfer simulation, the decrease in mass discharge is more gradual than the equilibrium mass transfer model simulation with no sharp downturn in the downgradient discharge rate. This is most possibly due to longer presence of DNAPL within the fractures in the rate limited simulation, thus leading to overlapping of the three distinct stages of mass flux through each horizontal fracture in the domain (Refer to 6.5.1 for more details). Figure 6.39 further reveals that in both simulations a rebound of similar magnitude of boundary mass discharge is observed at late times.

Figure 6.40 plots the cumulative downgradient mass discharge of aqueous and entrained TCE in micelles for both the equilibrium (i.e. Base Case) and rate-limited mass transfer model. This figure revealed that although the equilibrium model has a higher mass discharge for entrained TCE - a finding consistent with a previous observation where more TCE mass was solubilised in the Base Case; the rate-limited simulation has a higher aqueous TCE mass discharge. Indicating surfactant flushing is less efficient in a rate-limited scenario.

Refer to Figure C12, Appendix C for the concentration profiles of all three species at t_{TOTAL}=28 years.

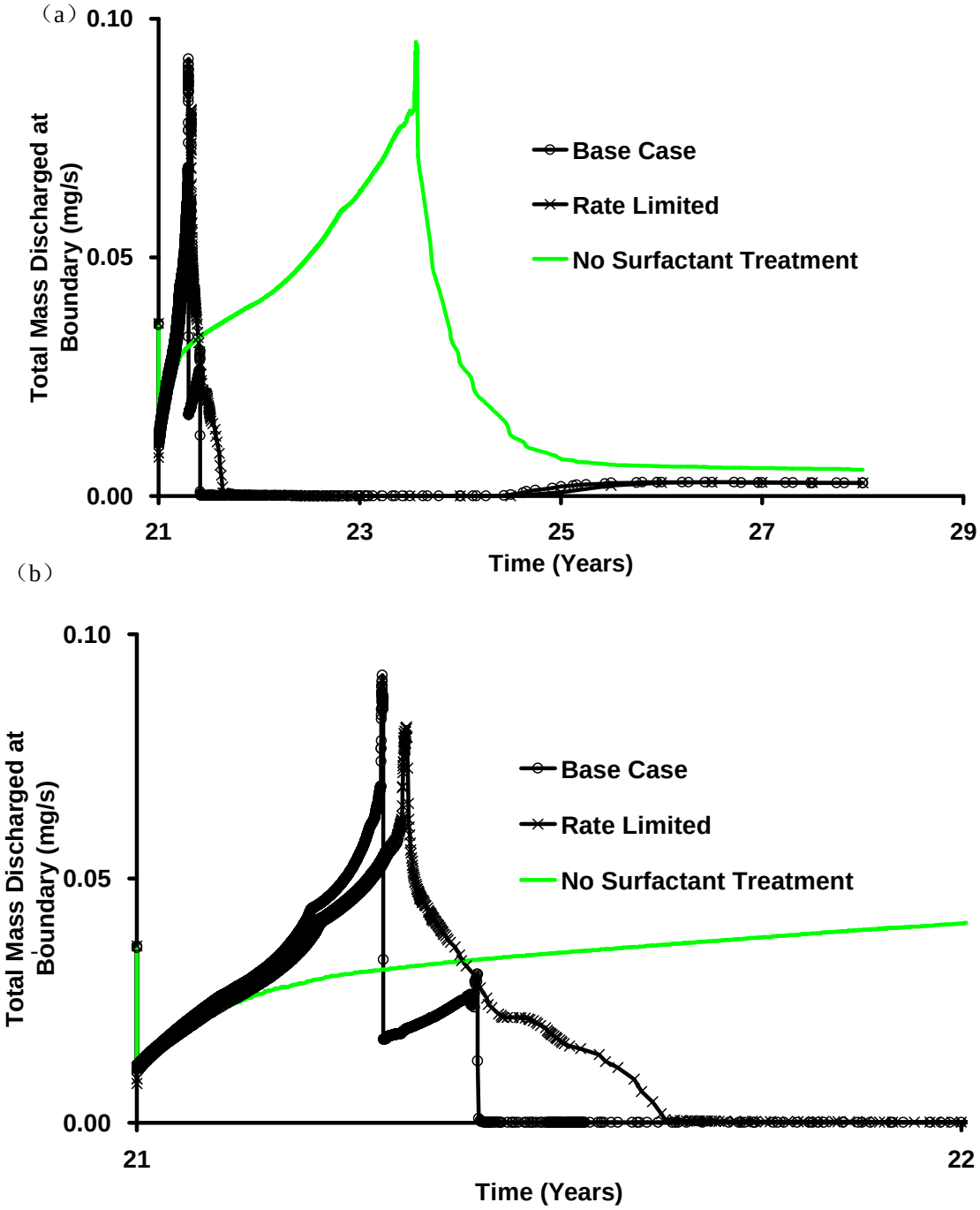

Figure 6.39: Comparison of total boundary mass discharge for (a) different mass transfer model with a simulation where No surfactant treatment (equilibrium mass transfer) was carried out for period between 21 to 28 years (b) since the start of the Treatment Stage for 1 year only (timescale expanded for clarity).

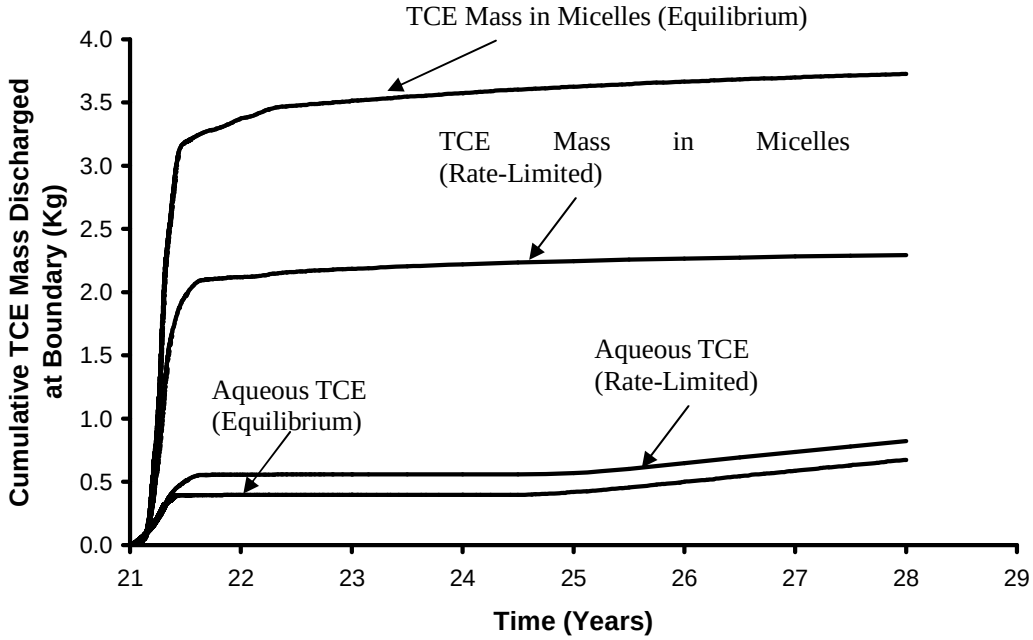

Figure 6.40: Cumulative mass discharged at downgradient boundary for (a) equilibrium and (b) rate limited mass transfer model.

6.6 CONCLUSION

Surfactant treatment with Tween-80 was proven to be a relatively effective technique in solubilising and removing DNAPL from the horizontal fractures within the domain. However, by comparing the aqueous and sorbed mass at the start and end of the Treatment stage, it is revealed that surfactant treatment is relatively ineffective in removing the mass that resides within the matrix.

Higher treatment efficiencies were observed in the shale and sandstone, with TCE mass reduced during treatment 70.2% and 80.2% of the initial DNAPL mass, respectively. Results revealed that vertical fractures, contaminated by the downward vertical movement of DNAPL appear to be relatively unaffected by horizontally driven surfactant. Granite with the largest fraction of initial mass entrapped in vertical fractures experiences

the lowest fraction of mass being recovered among the three rock types. Furthermore, granite with the lowest diffusive flux is able to achieve negligible mass discharge at a faster rate than sandstone and shale. This confirms expectations that granite with a higher peclet number (i.e., a more advective dominated domain) allows the injected surfactant to travel through the fractures at a quicker rate, thus in turn solubilises and partitions TCE molecules within the fractures into the surfactant micelles at a faster rate than sandstone and shale (i.e., less advective dominated domains). DNAPLs were identified to exist in dead end vertical fractures within all three rock types by the end of all simulations. This indicates that although surfactant treatment may be efficient in solubilising DNAPL in fractures, the injected surfactant experiences difficulty in accessing DNAPL entrapped in dead-end fractures.

When different concentration of surfactant was injected into the domain, it was found that as the concentration was increased from 20g/L to 40g/L, a small improvement in the total mass solubilised was noted. However, a further increase from 40 g/L to 60 g/L causes negligible further improvement in rate or in total amount; the latter because all readily accessed DNAPL is solubilised. On the other hand, it was revealed that as the aging period of each site increases; therefore an increase in the mass within the matrix, the mass being recovered from the matrix by surfactant increases as well. However, the overall percent recovery of chlorinated solvent mass from the source zone decreased with increasing ageing time due to similar volumes of DNAPL being solubilised but decreasing fractions of the matrix-bound mass was removed.

When surfactant was applied to different DNAPLs, due to the difference in MSRs, it was found that a higher fraction of aqueous PCE mass was entrained into micelles than for TCE. It was further noted that unlike the TCE simulation, no rebound in the chlorinated ethene mass discharge was observed in the PCE simulation. This further corroborates the observation that PCE is better solubilised than TCE, with potential impacts on long term mass discharge.

Different mass transfer models were found to lead to significant difference to the amount of DNAPL left in the domain by the end of the simulation. By employing a rate-limited mass transfer model, it was found that the amount of DNAPL present in the domain never decreases to negligible level (as compared to most DNAPL being solubilised by 4.8 months in the Base Case). The rate-limited model was also found to contribute significant differences to the boundary mass discharge curve during the first year of surfactant treatment. No sharp downturn in the downgradient discharge rate was observed when rate-limited mass transfer model was employed, indicating longer presence of DNAPL within the fractures in the rate limited simulation, thus leading to overlapping of the three distinct stages of mass flux through each horizontal fracture in the domain.

It is acknowledged that numerous assumptions and simplifications were employed in this work. In the majority of circumstances, the assumptions were chosen to present a 'best case' scenario that favours effective treatment (e.g., no sorption of micelles, TCE molecules do not partition back out from the micelles, two-dimensional flow with little opportunity for bypassing, equilibrium mass transfer). This approach underscores the

challenges associated with effectively treating aged source zones in fractured rock with surfactant. The limited number of simulations conducted using specific site templates on a small field scale implies that these results cannot be directly extended to a wide variety of complex real sites. For these reasons, these results are not intended to be predictive; rather they speak to the overall effectiveness of the technique in fractures versus matrix and focus on the relative performance between scenarios.

CHAPTER 7 - SUMMARY

7.1 OVERALL CONCLUSIONS

The goal of this research was to develop a better understanding of the effectiveness of various remediation technologies in remediating DNAPL contaminated fractured rock environments. This was pursued with numerical simulations using a gridding routine (GR) that was demonstrated to sufficiently discretize fracture elements within the domain to accurately capture diffusion into the matrix, but yet require relatively low computing power.

The work conducted examining the fate of DNAPL in fractured rock source zones prior to treatment revealed the dominant influence of matrix diffusion and sorption to matrix organic carbon. Sorbed chlorinated solvent in the rock matrix was responsible for, on average, greater than 38% of the initial DNAPL mass released and a key factor in DNAPL disappearance in approximately 1- 2 years in sandstone and shale formations. Matrix diffusion and corresponding DNAPL disappearance was less dominant in granite environments. Overall, the extent of matrix contamination was observed to correspond to the large scale peclet number of the domain. Diffusion dominated domains were promoted by high matrix porosity, high diffusion coefficient, high aqueous solvent concentrations (i.e., high solubility), and low sorptive capacity (i.e., low Koc and/or low foc). The influence of the large scale Pe number on the fate of chlorinated solvents in the source zone during the site ageing phase, as well as on the forwards and back diffusion of the injected fluids and contaminants during treatment, was critical to performance for all technologies investigated.

The work suggests that in situ chemical oxidation (ISCO) with permanganate in fractured rock aquifers would be relatively ineffective and inefficient across a wide range of scenarios. The fraction of permanganate consumed by natural oxidant demand in the matrix exceeded 90% in all cases. For scenarios in which diffusive flux is significant - high matrix porosity, high diffusion coefficient, high aqueous solvent concentrations (i.e., high solubility), and low sorptive capacity (i.e., low Koc and/or low foc) (e.g., sandstone/TCE) - substantial TCE mass becomes stored in the matrix via forward diffusion. Vertical fractures, while contaminated by the downward vertical movement of DNAPL and its subsequent dissolution and diffusion, appear to be relatively unaffected by horizontally driven chemical oxidation. Oxidant demand and rate of destruction exceeded supply in such cases, causing virtually no treatment to occur when injection was not active. Moreover, reverse diffusion was significant in these scenarios after treatment ceased causing rebound of the TCE mass discharged and TCE concentrations at the downgradient boundary. Higher treatment efficiencies were observed in the shale and granite, however, these scenarios did not exhibit more efficient use of the injected oxidant; rather, higher large scale peclet numbers significantly reduced depth of matrix diffusion, thereby increasing access of oxidant to the TCE that was concentrated near the fractures. While PCE also experienced less matrix diffusion than TCE, it experience lower treatment efficiency because, in part, of reduced reaction rates with MnO_4. For the sandstone base case investigated, all of the metrics examined for ISCO proved insensitive to the injection strategy (varied concentration or pulsed injection) and TCE mass destroyed increased only with increased total mass of MnO_4 injected. Since numerous assumptions were included in this work that favours ISCO success (e.g.,

ignoring permeability reduction due to MnO_2 rind formation), it is expected that these conclusions are not unfairly pessimistic.

In addition, the work suggests that enhanced in situ bioremediation (EISB) may only be highly successful under ideal conditions – in particular, when active dechlorination occurs throughout the contaminated rock matrix. In the sandstone/TCE scenario, approximately 74% of the initial mass underwent dechlorination to ethene; however, this represents the most favourable case, with robust first-order decay rates and active microorganisms throughout the fractures and matrix. When fermentation and dechlorination were assumed to exist only within the fractures, only 0.006% of the initial mass was reduced to ethene. As with ISCO, performance was insensitive to the rate at which lactate was injected and only influenced by the total mass injected. It is acknowledged that this may differ in scenarios where lactate is not in excess or where bioclogging, pH effects, and other complicating factors may plan an important role. In contrast to ISCO, EISB exhibited the advantage of effective penetration of electron donor into the matrix during the treatment period and ongoing treatment occurring after injection ceased. However, the effectiveness of EISB was found to decrease as the mean large scale peclet number for the rock type increased, assuming that bioremediation was active in the matrix. Downgradient TCE mass discharged and TCE concentration in horizontal fractures were sensitive to first-order biodegradation rates, indicating that the presence of inhibiting factors (e.g., toxicity from solvents, pH variations, fermentation spatially separated from dechlorination, etc.) may significantly reduce EISB performance. Sensitivity studies for different treatment strategies were found to be able to achieve

negligible concentration levels (apart from the simulations where (i) bioremediation was assumed to take place only within the fractures and (ii) low biodegradation rates) by the end of the simulations. These results indicate that under ideal conditions (i.e., inhibition is low, significant dechlorination occurs in the matrix) and particularly in sandstone formations, EISB may be a potential remediation strategy in fractured rock.

Surfactant flushing with Tween-80 was proven to be a relatively effective technique in removing DNAPL from the horizontal fractures but relatively inefficient in removing the aqueous and sorbed chlorinated solvent residing within the matrix and DNAPL in vertical, dead-end fractures. As with ISCO and EISB, the fraction of contaminant mass treated increased with scenarios with lower large scale peclet numbers (e.g., sandstone and shale). However, higher peclet numbers (e.g., granite) resulted in the most rapid reduction in TCE mass discharge. When different concentration of surfactant was injected into the domain, it was found that as the concentration was increased from 20g/L to 40g/L, a small improvement in the total solubilised mass was noted. However, a further increase from 40 g/L to 60 g/L causes negligible further improvement in rate or in total amount; the latter because all readily accessed DNAPL is solubilised. An increase in the aging period, which increases the mass of TCE within the matrix and the depth of penetration surrounding the fractures (here, independently of DNAPL mass in fractures), leads to an overall decrease in efficiency in recovering the initial contaminant mass within the domain. These results underscore that while surfactant flushing of fractures is effective, recovering diffused and sorbed mass in the matrix is relatively inefficient with this inefficiency increasing as the timescale of the site ageing increases relative to the

timescale of the treatment.

When surfactant was applied to different DNAPLs, due to the difference in MSRs, it was found that a higher fraction of initial PCE mass was entrained into micelles than TCE. It was further noted that unlike the TCE simulation, no rebound in the chlorinated ethene mass discharge was observed in the PCE simulation. PCE was found to be overall better solubilised than TCE, with significant impacts on long term mass discharge. Employing a rate-limited mass transfer model specific for DNAPL dissolution in variably aperture fractures resulted in the inability of surfactant to completely remove the DNAPL in the fractures during the 2 year treatment period.

It is acknowledged that numerous assumptions and simplifications were employed in this work. In the majority of circumstances, the assumptions were chosen to present a 'best case' scenario that favours effective treatment. This approach underscores the challenges associated with effectively treating aged source zones in fractured rock with various treatments. The limited number of simulations conducted using specific site templates on a small field scale implies that these results cannot be directly extended to a wide variety of complex real sites. For these reasons, these results are not intended to be predictive; rather they speak to the overall effectiveness of the various techniques on contaminants in fractures versus in the matrix and focus on the relative performance between scenarios.

The use of numerical model to investigate the efficiency and drawbacks of various

treatment techniques has been shown to be a powerful tool, allowing insights into the controlling factors within different types of fractured rocks. Further works can be carried out including the investigation of different remediation techniques (e.g., thermal desorption, pump and treat) with different rock types (e.g. limestone, chalk, basalt). Additionally, this model can be used for future studies of the same remediation techniques but employing different ranges of rock properties or looking at the efficiency by combining different remediation techniques. Three-dimensional simulations would be advantageous if coupled with increased processing power or incorporation of multi-processor modelling to reduce computational demand. The presented Gridding Routine could be adapted to three-dimensional orthogonal fracture networks in a relatively straightforward manner. Alternatively, significant modification would be required to adapt the gridding routine to a network of randomly distributed non-orthogonal fractures.

CHAPTER 8 - REFERENCES

Abdul, A.S., Gibson, T.L., Rai, D.N. 1990, Selection of surfactants for the removal of petroleum products from shallow sandy aquifers, *Ground Water* 28 (6), 920.

Abriola, L. M., Dekker, T. J., and Pennell, K. D. 1993, Surfactant-enhanced solubilisation of residual dodecane in soil columns. 2. Mathematical modelling, *Environmental Science & Technology*, 27 (12), 2341-2351.

Abriola, L. M., Drummond, C. D., Hahn, E. J., Hayes, K. F., Kibbey, T. C. G., Lemke, L.D., Pennell, K. D., Petrovskis, E. A., Ramsburg, C. A., and Rathfelder, K. M. 2005, Pilot-Scale Demonstration of Surfactant-Enhanced PCE Solubilization at the Bachman Road Site. 1. Site Characterization and Test Design, *Environmental Science & Technology*, 39 (6), 1778-1790.

Abriola. L. and Pinder, G. 1985a, A multiphase approach to the modelling of porous media contamination by organic compounds. 1. Equation development. *Water Resour. Res.* 21(1): 11-18.

Abriola. L. and Pinder, G. 1985b, A multiphase approach to the modelling of porous media contamination by organic liquids. 2. Numerical simulation. *Water Resour. Res.*, 21(1): 19-26.

Adamson D.T, McDade J.M, Hughes JB. 2003, Inoculation of a DNAPL source zone to initiate reductive dechlorination of PCE. *Environ Sci Technol* 37(11):2525-33.

Adamson D.A, Lyon D.Y, Hughes J.B. 2004, Flux and product distribution during biological treatment of tetrachloroethene dense non-aqueous-phase liquid. *Environ Sci Technol* 38(7):2021-8.

Allen, D.J., Bloomfield, J.P., Gibbs, B.R. and Wagstaff, S.J., 1998. Fracturing and the hydrogeology of the Permo-Triassic Sandstones in England and Wales. Technical Report of the British Geological Survey WD/98/1.

Amidon, G. E., Higuchi, W. I., and Ho, N. F. H. 1982, Theoretical and experimental studies of transport of micelle-solubilised solutes. *J. Pharm. Sci.*, 71(1), 77–84.

Amos B.K, Christ J.A, Abriola L.M, Pennell K.D, Loeffler F.E. 2007, Experimental evaluation and mathematical modelling of microbially enhanced tetrachloroethene (PCE) dissolution. *Environ Sci Technol* 41(3):963-70

Anderson. M.R.. Johnson, R.L. and Pankow. J.F. 1992a, Dissolution of dense chlorinated solvent into ground water. 1. Dissolution from a well-defined source. *Ground Water.* 30(2): 250-256.

Anderson. M.R.. Johnson, R.L. and Pankow. J.F. 1992b, Dissolution of dense chlorinated solvent into ground water. 2. Modelling contaminant plumes from fingers and pools of solvents. *Environ. Sci. Technol.,* 26(5): 901-908.

Anderson, S.E., Thomson, N.R. 1999, Two-phase flow in a variable aperture fracture: laboratory validation of a two-dimensional numerical model. *Proceedings from Dynamics of Fluids in Fractured Rocks*: Concepts and Recent Advances, Berkeley, CA, 30–34.

Andrews S.D., Mahaffey W, Barlock, V., and Santangelo-Dreiling, T. 2002, Methane-Enhanced In Situ Biological Degradation Of Chlorinated Hydrocarbons – A Case Study, *Proceedings of the Third International Conference on Remediation of Chlorinated and Recalcitrant Compounds Part B,* Paper 2B-55.

Amarante, D. 2000, *Applying In Situ Chemical Oxidation*, Pollution Engineering, February.

Attwood D. and Florence A. T. 1983, In Surfactant Systems: Their Chemistry, Pharmacy and Biology.Chapman & Hall, New York.

Babadagli, T. 2003, Selection of proper enhanced oil recovery fluid for efficient matrix recovery in fractured oil reservoirs, *Colloids and surfaces A-Physicochemical and Engineering aspects*, 223 (1-3): 157-175, AUG 21.

Baehr, A.L. and Corapcioglu, M.Y. 1987, A compositional multiphase model for groundwater contamination by petroleum products, 2. Numerical simulation. *Water Resour. Res.,* 23(l): 201-203.

Bailey J.E, Ollis D.F. 1986, Biochemical engineering fundamentals. 2nd edition. McGraw-Hill, New-York.

Baraka-Lokmane, S. 2002, Hydraulic versus pneumatic measurements of fractured sandstone permeability, *Journal of Petroleum Science and Engineering*, 36, pp.183– 192.

Battelle. 2001, Chemical Oxidation of a DNAPL Source Zone at Launch Complex 34 in Cape Canaveral Air Station, Draft Final Technology Evaluation Report, 101 pp.

Baveye, P., P. Vandevivere, B. L. Hoyle, P. C. DeLeo, and D. Sanchez de Lozada. 1998, Environmental Impact and Mechanisms of the Biological Clogging of Saturated Soils and Aquifer Materials, *Critical Reviews in Environmental Science and Technology*. 28(2): 123-191.

Bear. J. 1972, Dynamics of Fluids in Porous Media. 764 pp., Dover, Mineola, N.Y.

Bear, J., C. F. Tsang, and G. de Marsily, (Eds.) 1993, Flow and Contaminated Transport in Fractured Rock, *Academic,* San Diego, Calif.

Becker, M.W., Metge, D.W., Collins, S.A., Shapiro, A.M., and Harvey, R.W., 2003 Bacterial transport experiments in fractured crystalline Bedrock. *Ground Water*, 41(5), 682-689.

Becker, M.W., Shapiro, A.M. 2000, Tracer transport in fractured crystalline rock: evidence of nondiffusive breakthrough tailing. *Water Resour.* 36, 1677–1686.

Bekins, B. A., Godsy, E. M., and Warren, E. 1999, Distribution of Microbial Physiologic Types in an Aquifer Contaminated by Crude Oil, *Microbial Ecology*, 37 (4), 263-275.

Birkhölzer, J., Rubin, H., Daniels, H., and Rouvè, G.. 1993a, Contaminant transport in fractured permeable formation. 1. Parametric evaluation and analytical solution, *J. Hydrol.*, 144, 1–33.

Bloomfield, J.P., Gooddy, D.C., Bright, M.I., Williams, P.J., 2001. Pore-throat size distributions in sandstones and some implications for contaminant hydrogeology. *Hydrogeology Journal*, 9 (3), 219–230.

Brandon, B., Marajh-Whittemore, P., McTigue, D., Chaffin, D. 2002, Regulatory perspective: In situ chemical oxidation pilot test in fractured granite, *Proceedings of the Third International Conference on Remediation of Chlorinated and Recalcitrant Compounds* , 1447-1458.

Brooks R H and A.T. Corey 1966, Properties of porous media affecting fluid flow. *Journal of the Irrigation and Drainage Division, Proceedings of the American Society of Civil Engineers*, pages 61-88, 1966.

Brusseau, M.L. 1992, Rate-limited mass transfer and transport of organic solutes in porous media that contain immobile immiscible organic liquid. *Water Resour. Res.*, 28(l): 33-45.

Busch, A., Alles, S., Gensterblum, Y., Prinz, D., Dewhurst, D.N., Raven, M.D., Stanjek, H., B.M., Krooss. 2008, Carbon dioxide potential of shale, *International Journal of Greenhouse Gas Control*, pp. 297 – 308.

Carr, C.S., and Hughes, J.B. 1998, Enrichment of High-Rate PCE Dechlorination and Comparative Study of Lactate, Methanol, and Hydrogen as Electron Donors To Sustain Activity, *Environmental Science & Technology*, 32 (12), 1817-1824.

Carr C.S., Garg S., Hughes J.B. 2000, Effect of dechlorinating bacteria on the longevity and composition of PCE-containing nonaqueous phase liquids under equilibrium dissolution conditions. *Environ Sci Technol* 34(6):1088-94.

Castellanos, M.R., Peel, T.A., McMaster M.L., Adkisson, J., Dworatzek. S. 2002, Laboratory Evaluation of Enhanced Bioremediation of Chlorinated Ethenes in Groundwater at the MLP/VAB Area, *Proceedings of the Third International Conference on Remediation of Chlorinated and Recalcitrant Compounds* , 1405-1411, Paper 2B-30.

Chaki, S., Takarli, M., Agbodjan, W.P. 2008, Influence of thermal damage on physical properties of a granite rock: Porosity, permeability and ultrasonic wave evolutions, *Construction and Building Materials*, 22, pp. 1456–1461.

Chapelle FH. 1996, Identifying redox conditions that favor natural attenuation of chlorinated solvents in contaminated ground-water systems. *In: Proceedings of the Symposium on Natural Attenuation of Chlorinated Organics in Ground Water, Dallas, Texas.*

Charbonneau, A., Novakowski, K., and Ross, N. 2006, The effect of a biofilm on solute diffusion in fractured porous media, *Journal of Contaminant Hydrology*, 85 (3-4), 212-228.

Chen, Z. 1995, Large Scale Averaging Analysis of Multiphase Flow in Fractured Reservoirs, *Tran. Por. Media*, 21, pp 269- 295.

Cherry, J.A. 1989, Hydrogeologic contaminant behaviour in fractured and unfractured clayey deposits in Canada. In: H.E. Kobus and W. Kinzelbach (Editors), *Contaminant Transport in Groundwater.* A.A. Balkema, Rotterdam, pp. 11-20.

Christ J.A., Ramsburg C.A., Abriola L.M., Pennell K.D., Löffler F.E. 2005, Coupling aggressive mass removal with microbial reductive chlorination for remediation of DNAPL source zones: A review and assessment. *Environ Health Perspect* 113(4):465-74.

Christ, J. A., and Abriola, L. M. 2007, Modelling metabolic reductive dechlorination in dense non-aqueous phase liquid source-zones, *Advances in Water Resources*, 30 (6-7), 1547-1561.

Cho, H. J., Fiacco, R. J. and M. H. Daly. 2002, Soil vapor extraction and chemical oxidation to remediate chlorinated solvents in fractured crystalline rock. *Remediation Journal*, in press.

Chown, J.C., Kueper, B.H., McWhorter, D.B. 1997, The use of upward hydraulic gradients to arrest downward DNAPL migration in rock fractures, *Ground Water* Volume 35, Issue 3, Pages 483-491.

Chu M., Kitanidis P.K., McCarty P.L. 2003, Effects of biomass accumulation on microbially enhanced dissolution of a PCE pool: A numerical simulation. *J Contam Hydrol* 65(1-2):79-100.

Chu M, Kitanidis P.K., McCarty P.L. 2004, Possible factors controlling the effectiveness of bioenhanced dissolution of non-aqueous phase tetrachloroethene. *Adv Water Resour* 27(6):601-615.

Clement, T. P. 1997, RT3D - A Modular Computer Code for Simulating Reactive Multispecies Transport in 3-Dimensional Groundwater Systems (Version 1.0), 59 pp, Pacific Northwest National Laboratory, Richland, Washington 99352.

Clement, T. P., Sun, Y., Hooker, B. S., and Petersen, J. N. 1998, Modelling Multispecies Reactive Transport in Ground Water, *Ground Water Monitoring & Remediation*, 18 (2), 79-92.

Colwell, F.S., Stormberg, G.J., Phelps, T.J., Birnbaum, S.A., McKinley, J., Rawson, S.A., Veverka, C., Goodwin, S., Long, P.E., Russell, B.F., Garland, T., Thompson, D., Skinner,

Conrad, M.E., DePaolo, D.J., Kennedy, B.M., Miller, E.C. 1997b, Carbon isotope evidence for degradation of mixed contaminants in the vadose zone, *Geol. Soc. Am.*, Abstr. Prog. 26 (6), A186.

Conrad, S.H., Glass, R.J., Peplinski, W.J. 2002, Bench-scale visualization of DNAPL remediation processes in analog heterogeneous aquifers: surfactant floods and in situ oxidation using permanganate. *J. Contam. Hydrol.* 58, 13– 49.

Cornuet, T. S., Sandefur, C., Eliason, W. M., Johnson, S. E., and Serna, C. 2000, Aerobic and Anaerobic Bioremediation of cis-1,2-Dichloroetene and Vinyl Chloride, In Accelerated Bioremediation of Chlorinated compounds in Groundwater. Editors: Koenigsberg, S. S. and Ward, C. H., *Regenesis Bioremediation Products*, pp. 41-49.

Cope N, Hughes J.B. 2001, Biologically-enhanced removal of PCE from NAPL source zone. *Environ Sci Technol*;35(10):2014-21.

Crow C.W, 1968. New Treating Technique to Remove Bacterial Residues From Water-Injection Wells, Journal of Petroleum Technology, Vol 20, No.5, pp 475-478.

Cumbie, D.H. and MacKay, L.D. 1999. Influence of diameter on particle transport in a fractured shale saprolite. *Journal of Contaminant Hydrology*, 37, 139-157.

Cupples A.M., Spormann A.M., McCarty P.L. 2004a, Vinyl chloride and cis-dichloroethene dechlorination kinetics and microorganism growth under substrate limiting conditions. *Environ Sci Technol*, 38(6):1102-7.

Cupples A.M., Spormann A.M., McCarty P.L. 2004b Comparative evaluation of chloroethene dechlorination to ethene by *dehalococcoides*-like microorganisms. *Environ Sci Technol*, 38(18):4768-74.

Dana, E. and Skoczylas, F. 2002, Experimental study of two-phase flow in three sandstones. II. Capillary pressure curve measurement and relative permeability pore space capillary models, *International Journal of Multiphase Flow*, 28, 1965–1981.

Dayan, H., Abrajano, T., Sturchio, N.C. and Winsor, L. 1999, Carbon isotopic fractionation during reductive dehalogenation of chlorinated ethenes by metallic iron, *Org. Geochem.*, 30: 755-763.

de Beer, D., Stoodley, P., and Lewandowski, Z. 1997, Measurement of local diffusion coefficients in biofilms by microinjection and confocal microscopy, *Biotechnology and Bioengineering*, 53 (2), 151-158.

de Lima, O.A.L. and Niwas S. 2000, Estimation of hydraulic parameters of shaly sandstone aquifers from geoelectrical measurements, *Journal of Hydrology*, 235, pp.12–26.

Dennis, F., Andrews, N.J., Parker, A., Poole, J., Wolf, M. 1997, Isotopic and noble gas study of Chalk groundwater in the London Basin, England, *Applied Geochemistry*, Vol. 12, pp. 763-773.

Dickson, S.E., Thomson, N.R. 2003, Dissolution of entrapped DNAPLs in variable aperture fractures: experimental data and empirical model, *Environ. Sci. Technol.* 37, 4128-4137, Paper 1D-01.

Domenico, P.A and Schwartz F.W. Physical and chemical hydrogeology. John Wiley & Sons, Inc, 1990.

Driese, S.G., and MacKay, L.D., 2004. Epi-fluorescence micromorphology of saprolite reveals evidence for colloid retention in microscale pore systems. *Geoderma* 121, 143-152.

Dullien, F.A.L. 1992, Porous Media: Fluid Transport and Pore Structure, *2nd ed. Academic Press*, Inc., San Diego, CA. 574 pp.

Dutton S.P. and Loucks R.G. 2010, Diagenetic controls on evolution of porosity and permeability in lower Tertiary Wilcox sandstones from shallow to ultradeep (200–6700 m) burial, Gulf of Mexico Basin, U.S.A., *Marine and Petroleum Geology,* 27, 69–81.

Edwards, D. A., Luthy, R. G., and Liu, Z. 1991, Solubilization of polycyclic aromatic hydrocarbons in micellar nonionic surfactant solutions, *Environmental Science & Technology*, 25 (1), 127-133.

Eikemo B., Lie K., Eigestad G.T.,Dahle H.K., 2009, Discontinuous Galerkin methods for advective transport in single-continuum models of fractured media. *Advances in Water Resources*, 32 (2009) 493–506.

Ellis D.E., Lutz E.J., Odom J.M., Buchanan Jr R.J., Bartlett C.L., Lee M.D., Harkness M.R., Deweerd K.A. 2000, Bioaugmentation for accelerated in situ anaerobic bioremediation. *Environ Sci Technol*,34(11):2254-60.

Ellis, W.D., Morgan, D.R., Ranjithan, S.R. 1986, Treatment of contaminated soils with aqueous surfactants, EPA/600/2-85/129, *Hazardous Waste Engineering Research Laboratory*.

Environmental Protection Agency (EPA). 2001, The State-of-the Practice of Characterization and Remediation of Contaminated Ground Water at Fractured Rock Sites. EPA542-R-01-010.

Esposito S. J. and Thomson N. R. 1999, Two-phase flow and transport in a single fracture-porous medium system, *Journal of Contaminant Hydrology* Volume 37, Issues 3-4 , Pages 319-341.

Feenstra, S. 1992, Geochemical evaluation of polychlorinated biphenyls (PCBs) in groundwater. In: S. Lesage and R.E. Jackson (Editors), Groundwater Contamination and Analysis at Hazardous Waste Sites. Marcel Dekker, New York, NY, 545 pp.

Feenstra, S., Mackay, D.M., Cherry, J.A. 1991, Presence of residual NAPL based on organic chemical concentrations in soil samples. *Ground Water Monit.* Rev. 11 (2), 128–136.

Fennell, D. E., Gossett, J. M., and Zinder, S. H. 1997, Comparison of Butyric Acid, Ethanol, Lactic Acid, and Propionic Acid as Hydrogen Donors for the Reductive Dechlorination of Tetrachloroethene, *Environmental Science & Technology*, 31 (3), 918-926.

Fennell D.E., Gossett J.M. 1998, Modelling the production of and competition for hydrogen in a dechlorinating culture. *Environ Sci Technol,* 32(16):2450-60.

Fetter, C.W. 1993, Contaminant Hydrogeology, *Macmillan Publishing Company,* New York. pp. 458

Forsyth, P.A. 1991, A control volume finite element approach to NAPL groundwater contamination. SIAM (Sot. Ind. Appl. Math.) *J. Sci. Stat. Comput.*, 12(5): 1029-1057.

Forsyth, P.A., Shao, B.Y. 1991, Numerical Simulation of Gas Venting for NAPL Site Remediation; *University of Waterloo,* Ontario, Res. Rep. CS-91-06.

Fountain, J.C., Starr, R.C., Middleton, T., Beikirch, M., Taylor, C., Hodge, D. 1996, A controlled field test of surfactant-enhanced aquifer remediation, *Ground Water* 35 (5), 910–916.

Freeze, R.A., Cherry, J.A. 1979, *Groundwater*, Prentice-Hall, Englewood Cliffs, NJ.

Freeze, R.A., McWhorter, D.B. 1997, A framework for assessing risk reduction due to DNAPL mass removal from low-permeability soils, *Ground Water* Volume 35, Issue 1, Pages 111-123.

Fried, J.J., Muntzer, P. and Zilloix, L. 1979, Groundwater pollution by transfer of oil hydrocarbons. *Ground Water,* 17(6): 586-594.

Frind, E.O., J.W. Molsen, and M. Schirmer. 1999, Dissolution and mass transfer of multiple organics under field conditions: The Borden emplaced source, *Water Resources Research,* 35(3), 683-694.

Gabrovsek, F. , Romanov, D. , Dreybrodt, W. 2004, Early karstification in a dual-fracture aquifer: The role of exchange flow between prominent fractures and a dense net of fissures, Journal of Hydrology Volume 299, Issue 1-2, Pages 45-66.

Gandhi, R.K., G.D. Hopkins, M.N. Goltz, S.M. Gorelick, and P.L. McCarty, 2002, Fullscale demonstration of in situ cometabolic biodegradation of trichloroethylene in groundwater, 1: Dynamics of a recirculating well system, *Water Resources Research*, awaiting print.

Gandhi, S., Oh, B., Schnoor J.L., Alvarez P. J. 2002, Degradation of TCE, Cr(VI), sulfate, and nitrate mixtures by granular iron in flow-through columns under different microbial conditions. *Water Research* 36(8), 1973-1982

Gannon, O.K., Bribing, P., Raney, K., Ward, A., Wilson, J., Underwood, J.L., Deblak, K.A. 1992, Soil clean up by in situ surfactant flushing: III. Laboratory results, *Journal of Science Technology*, September, pp.1073–1094.

Garavito, A.M., Kooi, H., Neuzil, C.E. 2006, Numerical modeling of a long-term in situ chemical osmosis experiment in the Pierre Shale, South Dakota, *Advances in Water Resources*, 29, pp. 481–492.

Geller, J.T. and Hunt, J.R. 1993, Mass transfer from non aqueous-phase organic liquids in water saturated porous media, *Water Resour. Res.*, 29(4): 833-845.

Geosyntec Consultants. 2004, Accessing the feasibility of DNAPL source zone remediation: Review of case studies, April.

Geosyntec Consultants. – Private communications with Geosyntec Consultants 2007

Gerhard, J. I., Kueper, B. H., and Hecox, G. R. 1998, The Influence of Waterflood Design on the Recovery of Mobile DNAPLs, *Ground Water,* 36 (2), 283-292.

Gerhard, J. I., Kueper, B. H., Hecox, G. R., and Schwarz, E. J. 2001, Site-Specific Design for Dual Phase Recovery and Stabilization of Pooled DNAPL, *Ground Water Monitoring & Remediation*, 21 (2), 71-88.

Gerhard, J. I., and Kueper, B. H. 2003a, Capillary pressure characteristics necessary for simulating DNAPL infiltration, redistribution, and immobilization in saturated porous media, *Water Resources Research*, 39 (8).

Gerhard, J. I., and Kueper, B. H. 2003b, Influence of constitutive model parameters on the predicted migration of DNAPL in heterogeneous porous media, *Water Resources Research*, 39 (10), 1279.

Gerhard, J. I., and Kueper, B. H. 2003c, Relative permeability characteristics necessary for simulating DNAPL infiltration, redistribution, and immobilization in saturated porous media, *Water Resources Research*, 39 (8), 1213.

Gerhard, J. I., Pang, T.W. and Kueper, B. H. 2007, Time scales of DNAPL migration in sandy aquifers examined via numerical simulation, *Ground Water* Vol. 45 (2) pp 147–157.

Glass R.J. and M.J. Nicholl, 1995, Quantitative visualization of entrapped phase dissolution within a horizontal flowing fracture. *Geophysical Research Letters*, 22:1413-1416.

Godsy, E. M., Goerlitz, D. F., and Grbic-Galic, D. 1992, Methanogenic Biodégradation of Creosote Contaminants in Natural and Simulated Ground-Water Ecosystems, *Ground Water*, 30 (2), 232-242.

Gonullu, T., Farquhar, G.J. 1989, Oxidation to Remove TCE from Soil, Internal Report Department of Civil Engineering, Univ. of Waterloo. Available at http://www.civil.uwaterloo.ca/groundwater/oxlitrev.html.

Gooddy, D.C., Bloomfield, J.P., Harrold, G., Leharne, S.A. 2002, Towards a better understanding of tetrachloroethene entry pressure in the matrix of Permo-Triassic sandstones, *Journal of Contaminant Hydrology*, 59, pp. 247– 265.

Grant, G. P. 2005, The Evolution of Complex DNAPL Releases: Rates of Migration and Dissolution, Ph.D. thesis, 431 pp, The University of Edinburgh, Edinburgh, Scotland, United Kingdom.

Grant, G. P., and Gerhard, J. I. 2004, Sensitivity of Predicted DNAPL Source Zone Longevity to Mass Transfer Correlation Model, Geoenvironmental Engineering: Integrated Management of Groundwater and Contaminated Land, *Telford Publishing, London*, 59-67.

Grant, G. P., and Gerhard, J. I. 2007a, Simulating the dissolution of a complex dense nonaqueous phase liquid source zone: 1. Model to predict interfacial area, *Water Resources Research*, 43 (12).

Grant, G. P., and Gerhard, J. I. 2007b, Simulating the dissolution of a complex dense nonaqueous phase liquid source zone: 2. Experimental validation of an interfacial areabased mass transfer model, *Water Resources Research*, 43 (12).

Grant, G. P., Gerhard, J. I., and Kueper, B. H. 2007，Multidimensional validation of a numerical model for simulating a DNAPL release in heterogeneous porous media Journal of Contaminant Hydrology 92 109–128

Grant, G. P., Gerhard, J. I., and Kueper, B. H. 2007a, Field scale impacts of spatially correlated relative permeability in heterogeneous multiphase systems, *Advances in WaterResources*, 30 (5), 1144-1159.

Grisak, G.E., Pickens, J.F. 1981, An analytical solution for solute transport through fractured media with matrix diffusion, *J. Hydrol.* 52, 47–57.

Gutierrez, M., Øino, L.E., Nygard, R. 2000, Stress-dependent permeability of a de-mineralised fracture in shale, *Marine and Petroleum Geology,* 17, pp. 895–907.

Gwo, J.P., Jardine, P.M., Sanford, W.E. 2005, Modelling field-scale multiple tracer injection at a low-level waste disposal site in fractured rocks: Effect of multiscale heterogeneity and source term uncertainty on conceptual understanding of mass transfer processes, Journal of Contaminant Hydrology Volume 77, Issue 1-2, Pages 91-118.

Gwo, J.P., Mayes, M.A., Jardine, P.M. 2007, Quantifying the physical and chemical mass transfer processes for the fate and transport of Co(II)EDTA in a partially-weathered limestone–shale saprolite, *Journal of Contaminant Hydrology*, 90, pp. 184–202.

Haghighi, M., Xu, B, and Y.C. Yortsos. 1994, Visualization and Simulation of Immiscible Displacement in Fractured Systems Using Micromodels: 1. Drainage, *J. Coll. Int. Sci.,* 166, pp 168-179.

Harrison, B., E.A. Sudicky, and J.A. Cherry 1992, Numerical analysis of solute migration through fractured clayey deposits into underlying aquifers. *Water Resources Research*, 28:515-526.

Hanson, J.R., C.R. Ackerman, and K.M. Scow. 1999, Biodegradation of Methyl tertbutyl ether by a bacterial pure culture, *Appl. Environ. Microbiol.* 65:4788-4792.

Haston Z.C., McCarty P.L.1999, Chlorinated ethene half-velocity coefficients (Ks) for reductive dehalogenation. *Environ Sci Technol*, 33(2):223-6.

Hazen, T., Jiménez, L., López de Victoria, G., and Fliermans, C. 1991, Comparison of bacteria from deep subsurface sediment and adjacent groundwater, *Microbial Ecology*, 22 (1), 293-304.

Hirasaki, G.J., Miller, C.A., Szafranski, R., Lawson, J.B., Akiya, N. 1997, Surfactant foam process for aquifer remediation. SPE paper 37257. *SPE International Symposium on Oil Field Chemistry*, Houston, TX.

Hitchmough, A.M., Riley, M.S., Herbert, A.W., Tellam, J.H. 2007, Estimating the hydraulic properties of the fracture network in a sandstone aquifer, *Journal of Contaminant Hydrology*, 93, pp. 38–57.

Hood, E., Major, D., Driedger, G. 2007, The effect of concentrated electron donors on the solubility of Trichloroethene, *Ground Water Monitoring & Remediation*, 27(4) 93-98.

Hood, E.D., and Thomson, N.R. 2000, Numerical simulation of in situ chemical oxidation, In *Chemical Oxidation and Reactive Barriers; International Conference on Remediation of Chlorinated and Recalcitrant Compounds*. Battelle Press.

Hood, E.D., Thomson, N.R., Grosse, D. and Farquhar, G.J. 2002. Experimental determination of the kinetic rate law for the oxidationd of perchloroethylene by potassium permanganate. *Chemosphere*, 40:1383-1388.

Hu, Q.H. and Mori, A. 2008, Radionuclide transport in fractured granite interface zones, *Physics and Chemistry of the Earth*, 33, pp.1042–1049.

Hunt, J.R., Sitar, N. and Udell, K.S. 1988a, Non aqueous-phase liquid transport and cleanup, 1. Analysis of mechanisms. *Water Resour. Res.*, 24(8): 1247- 1258.

Hunt, J.R., Sitar. N. and Udell, K.S. 1988b, Non-aqueous-phase liquid transport and cleanup, 2. Experimental studies. *Water Resour. Res*., 24(8): 1259- 1269.

Hunter, K.S., Wang, Y., Van Cappellen, P. 1998, Kinetic modelling of microbially-driven redox chemistry of subsurface environments: coupling transport, microbial metabolism and geochemistry, *Journal of Hydrology,* 209, pp. 53-80.

Interstate Technology and Regulatory Cooperation Work Group (ITRC). 2001, Technical and Regulatory Guidance for In Situ Chemical Oxidation of Contaminated Soil and Groundwater. *Prepared by the In Situ Chemical Oxidation Work Group.*

Imhoff, P.T., P.R. Jaffé and G.F. Pinder. 1993, An experimental study of complete dissolution of a nonaqueous phase liquid in saturated porous media, *Water Resour. Res.*, 30(2): 307-320.

Imhoff, P.T., S.N. Gleyzer, J.F. McBride, L.A. Vancho, I. Okuda, and C.T. Miller, 1995, Cosolvent-enhanced remediation of residual dense nonaqueous phase liquids: experimental investigation, *Environmental Science and Technology* 29(8): 1966-1976.

Jafvert, C.T., Van Hoof, P.L., and Chu, W. 1995, The Phase Distribution of Polychlorobiphenyl Congeners in Surfactant-Amended Sediment Slurries, *War. Res.* Vol. 29, No. 10, pp. 2387-2397.

James, G. and R. Hiebert. 2001, Biofilm barriers for groundwater containment, *The Sixth International In Situ and On-Site Bioremediation Symposium*, pp. 79-85, San Diego, CA, 2001.

Jardine, P.M., Brooks, S.C., Wilson, G.V. and W.E. Sanford. 2000, Basic research strategies for resolving remediation needs in contaminated fractured media, In B. Faybishenko, P.A. Witherspoon, and S.M. Benson (Eds.), Dynamics of Fluids in Fracture Rock, pp. 389-400. American Geophysical Union, Washington, DC.

Jardine, P.M., Mehlhorn, T.L., Larsen, I.L., Bailey, W.B., Brooks, S.C., Roh, Y., Gwo, J.P. 2002, Influence of hydrological and geochemical processes on the transport of chelated metals and chromate in fractured shale bedrock, *Journal of Contaminant Hydrology*, 55, pp.137– 159.

Jardine, P.M., Sanford, W.E., Gwo, J.P., Reedy, O.C., Hicks, D.S., Riggs, J.S., Bailey, W.B. 1999, Quantifying diffusive mass transfer in fractured shale bedrock. *Water Resour. Res.* 35 (7), 2015–2030.

Jardine, P.M., Weber, N., McCarthy, J., 1989. Mechanisms of dissolved organic carbon adsorption on soil. Soil Sci. Soc. Am. 53, pp.1378– 1385.

Johnson, R.L. and Pankow, J.F. 1992, Dissolution of dense chlorinated solvents into groundwater, 2. Source functions for pools of solvent. *Environ. Sci. Technol.,* 26(5): 896-901.

Kalish, P. J., Stewart, J. E., Rogers, W. F., and Bennett., E. O. 1964, The Effect of Bacteria on Sandstone Permeability, *Journal of Petroleum Technology*, 805- 814.

Kaluarachchi. J.J. and Parker, J.C. 1990, Modelling multicomponent organic chemical transport in three-fluid phase porous media. *J. Contam. Hydrol.,* 5(4): 349-374.

Kalyuzhnyi S, de Leon Fragaso C, Rodriguez Martinez J. 1997, Biological sulphate reduction in an UASB reactor fed with ethanol as electron donor. Mikrobiologiya 66(5):562-7.

Karickhoff, S.W., Brown, D.S., and Scott, T.A. 1979, Sorption of Hydrophobic Pollutants on Natural Sediments, *Water Research* v.13, pp. 241-248.

Karickhoff, S.W. 1981, Semi-empirical Estimation of Sorption of Hydrophobic Pollutants on Natural Sediments and Soils, *Chemosphere*. v. 10, pp. 833-846.

Karickhoff, S.W. 1984, Organic Pollutants Sorption in Aquatic Systems, *Journal of Hydraulic Engineering*, v. 110, pp. 707-735.

Kauffman, M.D., LaChance, J.C., Traviglia, A.M., Krivansky, M.E., Leipert, M.W. 2002, In situ chemical oxidation of CVOCs in fractured bedrock, *Proceedings of the Third International Conference on Remediation of Chlorinated and Recalcitrant Compounds* , 1405-1411, Paper 2C-40.

Kean, J.A., Graves, D., Bishop K., Mott-Smith, E. and Lodato, M. 2002, Obstacles to Complete PCE Degradation During Reductive Dechlorination, *Proceedings of the Third International Conference on Remediation of Chlorinated and Recalcitrant Compounds*, Part C, Paper 2B-48.

Keller, A.A. 1998, Steam injection to displace DNAPLs from fractured media, *IAHS-AISH Publication* Issue 250, Pages 105-110.

Kim, K.S., Kwon, T.S., Yang, J.S., and Yang, J.W. 2007, Simultaneous removal of chlorinated contaminants by pervaporation for the reuse of a surfactant, *Desalination*, 205, 87–96.

Klutz. Tony, Andrew Baird, George Maalouf, and Daniel McDonnell, Craig Sandefur. 2002, Accelerated Bioremediation of Trichloroethylene: A comparison between saprolite and crystalline bedrock aquifers, *Proceedings of the Third International Conference on Remediation of Chlorinated and Recalcitrant Compounds,* Part C, Paper 2C-46.

Koenigsberg, S.S., Farone, W. The Use of Hydrogen Release Compound (HRCTM) for CAH Bioremediation, In: Leeson, A., Alleman, B.C. (eds.). 1999, Engineered Approaches for In Situ Bioremediation of Chlorinated Solvent Contamination, pp. 67-72, *Battelle Press*, Columbus, OH.

Koenigsberg, S.S., C. Sandefur and K. Lapus. 2001, Time-Release Electron Donor Technology: Results of Forty-Two Field Applications, In: Magar, V.S., Fennell, D.E., Morse, J. J., B.C. Alleman and A. Leeson (Eds.), Anaerobic Degradation of Chlorinated Solvents, pp. 257-264. *Battelle Press,* Columbus, OH.

Kölbel-Boelke, J., Anders, E. M., and Nehrkorn, A. 1988, Microbial communities in the saturated groundwater environment II: Diversity of bacterial communities in a Pleistocene sand aquifer and their in vitro activities, *Microbial Ecology*, 16 (1), 31-48.

Konzuk, J.S., Kueper, B.H. 2004, Evaluation of cubic law based models describing single-phase flow through a rough-walled fracture, Water Resources Research Volume 40, Issue 2, December 2004, W024021-W02402117.

Kostarelos K., Pope G. A., Rouse B. A. and Shook G. M. 1998, A new concept: the use of neutrally-buoyant microemulsions for DNAPL remediation, *Journal of Contaminant Hydrology* Volume 34, Issue 4 , Pages 383-397.

Kozar, M. S., McIlvaine, C.L., Duffy, B.E., Street, W.M. 2002, Enhanced degradation of chlorinated solvents in fractured rock ground water using subsurface injection of HRC, *Proceedings of the Third International Conference on Remediation of Chlorinated and Recalcitrant Compounds*, Pages 2441-2447, Paper 2C-42.

Kueper, B.H. and E.O. Frind. 1991a, Two-phase flow in heterogeneous porous media: 2. Model development. *Water Res. Res.* 27 (6), 1049–1057.

Kueper, B.H., and E.O. Frind. 1991b, Two phase flow in heterogeneous porous media: 2. Model application, *Water Resources Research*, 27(6), 1059-1070.

Kueper, B.H., and E.O. Frind 1992, Numerical modelling of multiphase / multicomponent flow and transport in porous media: An overview, in: *Proceedings of the International Conference on Subsurface Contamination by Immiscible Fluids*, Calgary, Canada, April 18-20.

Kueper, B.H., Haase, C.S., King, H.L. 1992, Leakage of dense, nonaqueous phase liquids from waste impoundments constructed in fractured rock and clay—theory and case-history. *Canadian Geotechnical Journal*, 29, 234–244.

Kueper, B.H., McWhorter, David B. 1991, Behavior of dense, nonaqueous phase liquids in fractured clay and rock, *Ground Water* Volume 29, Issue 5, Pages 716-728.

Kueper, B.H.; McWhorter, D. B. 1996, In Dense Chlorinated Solvents and Other DNAPLs in Groundwater; Pankow, J. K., Cherry, J. A., Eds.; Waterloo Press: Portland, OR, pp 337-353.

Kueper, B.H., Mcwhorter, D.B. 1998, DNAPL pool mobilization in fractured rock, *IAHS-AISH Publication* Issue 250, Pages 149-155.

Kueper, B.H., Wealthall G.P., Smith, J.W.N., Leharne, S.A. and Lerner, D.N. 2003, An illustrated handbook of DNAPL transport and fate in the subsurface. ISBN: 1844320669, Environment Agency, UK.

Le Thiez, P.A., Ducreux, J., 1994. A 3-D numerical model for analyzing hydrocarbon migration into soils and aquifers. In: Siriwardane, Zaman (Eds.), Computer Methods and Advances in Geomechanics. Balkema, Rotterdam, pp. 1165–1170.

Lee I.S., Bae J-H, Yang Y., McCarty P.L. 2004, Simulated and experimental evaluation of factors affecting the rate and extent of reductive dehalogenation of chloroethenes with glucose. *J Contam Hydrol* 74(1-4):313-31.

Lee Y.J., Miyahara T., Noike T. 2002, Effect of pH on microbial hydrogen fermentation. *J Chem Technol Biotechnol*, 77(6):694-8.

Lee, M.D., J.M. Odom, and R.J. Buchanan Jr. 1998, New Perspectives on Microbial Dehalogenation of Chlorinated Solvents: Insights from the Field, *Annual Review of Microbiology* 52: 423-452.

Leech, Kennedy, Gevaert, 1984. Sondierbohrung Böttstein: hydrological testing of cristaline rocks. National Cooperative for the Disposal of Radioactive Waste (NAGRA), Baden, Switzerland.

Lerman, A. 1979, Geochemical Processes: Water and Sediment Environments, John Wiley and Sons, Inc., New York, 481 pp.

Lerner D.N., Wealthall, G.P., Steele, A. 2002, Assessing risk from DNAPLs in fractured aquifers. *Agricultural Sciences*, 7(2):47-52

Lever, D.A. and Bradbury, M.H. 1985, Rock-matrix diffusion and its implications for radionuclide migration, *Mineral Mag.* 49, 245-254.

Lide, D. R. 2004, *CRC Handbook of Chemistry and Physics*, 85th ed., Chemical Rubber Company, Cleveland, Ohio, USA

Lipson, D.S., Kueper, B.H. and Gefell, M.J. 2005, Matrix Diffusion-Derived Plume Attenuation in Fractured Bedrock, *Ground Water*, 43 (1), 30-39.

Liu, Z., Edwards, D.A., Luthy, R.G., 1992. Sorption of non-ionic surfactants onto soil. *Water Res.* 26 (10), 1337–1345.
Lomize, G. M. 1951, Flow in Fractured Rocks (in Russian), 127 pp., *Gosenergoizdat*, Moscow.

Long C.M. and Border R.C. 2006, Enhanced Reductive Dehlorination in Columns Treated with Edible Oil Emulsion, *Journal of Contaminant Hydrology*, 87, 54-72.

Longino, B.L., Kueper, B.H. 1999, Nonwetting phase retention and mobilization in rock fractures, *Water Resources Research*, Volume 35, Issue 7, Pages 2085-2093.

Longino, B.L., Kueper, B.H. 1999, Effects of capillary pressure and use of polymer solutions on dense, non-aqueous-phase liquid retention and mobilization in a rough-walled fracture, *Environ. Sci. Technol.* Vol. 33, 2447-2455.

Louis, C., A study of groundwater flow in jointed rock and its influence on the stability of rock masses, *Rock Mech. Res. Rep.* 10, 90 pp., Imp. Coll. London, 1969.

Lowe SE, Jain MK, Zeikus JG. 1993, Biology, ecology, and biotechnical applications of anaerobic bacteria adapted to environmental stresses in temperature, pH, salinity, or substrates. Microbiol Rev 57:451-509.

Lunati, I., Kinzelbach, W. 2004, Water-soluble gases as partitioning tracers to investigate the pore volume-transmissivity correlation in a fracture, Journal of Contaminant Hydrology Volume 75, Issue 1-2, Pages 31-54.

Lunn, S.R.D. and B.H. Kueper. 1997, Removal of Pooled Dense, Nonaqueous Phase Liquid from Saturated Porous Media Using Upward Gradient Alcohol Floods, *Water Resour. Res*. 33(10):2207-2219.

Lunn, S.R.D., Kueper, B.H. 1999, Risk reduction during chemical flooding: Preconditioning DNAPL density in situ prior to recovery by miscible displacement, *Environmental Science and Technology* Volume 33, Issue 10, Pages 1703-1708.

Macbeth, T.W., Cummings, D.E., Spring, S., Petzke, L.M., Sorenson, K.S. Jr, 2004, Molecular Characterization of a Dechlorinating Community Resulting from In Situ Biostimulation in a Trichloroethene-Contaminated Deep, Fractured Basalt Aquifer and Comparison to a Derivative Laboratory Culture, *Applied and Environmental Microbiology*, 70 (12) p. 7329–7341.

Mackay, D.M., Cherry, J.A. 1989, Groundwater Contamination: Pump-and-treat remediation, *Environ. Sci. Technol.* Vol.23, No. 6, Pages 630-636.

Mackay, D.M., Shiu, W.Y., Maijanen, A. and Feenstra, S.1991, Dissolution of non-aqueous phase fluids in groundwater, *J. Contam. Hydrol.*, 8(l): 23-42.

MacKinnon, L.K., Cox, E.E., Hood, E.D., Mumford, K.G., Thomson, N.R. 2002, Evaluation of oxidation and bioremediation for CVOCs in fractured bedrock, *Proceedings of the Third International Conference on Remediation of Chlorinated and Recalcitrant Compounds* , 2467-2474, Paper 2H-58.

MacKinnon, L.K., Thomson, N.R. 2002, Laboratory-scale in situ chemical oxidation of a perchloroethylene pool using permanganate, *J. Contam. Hydrol.* 56 (1– 2), 49–74.

Mahani, H., 2005. Upscaling and Optimal coarse grid Generation for the Numerical Simulation of Two-Phase Flow in Porous Media. PhD thesis, Department of Earth Science and Engineering. London, Imperial College London.

Major D.W., McMaster M.L., Cox E.E., Edwards E.A., Dworatzek S.M., Hendrickson E.R., Starr M.G., Payne J.A., Buonamici L.W. 2002, Field demonstration of successful bioaugmentation to achieve dechlorination of tetrachloroethene to ethene. *Environ Sci Technol*, 36(23):5106-16.

Maloszewski, P., Zuber. 1991, A, Influence of matrix diffusion and exchange reactions on radiocarbon ages in fissured carbonate aquifers. *Water Resour. Res.* 27, 1937– 1945.

Maloszewski, P., Zuber, A. 1993, Tracer experiments in fractured rocks: matrix diffusion and the validity of models. *Water Resour. Res.* 29, 2723–2735.

Manger, G.E. 1963, Porosity and bulk density of sedimentary rocks, U.S. Geological Survey Bull. 1144-E.

Martel, R., Gelinas, P.J. 1996, Surfactant solutions developed for NAPL recovery in contaminated aquifers. *Ground Water* 34 (1), 143–154.

Mason, A. R., and Kueper, B. H. 1996, Numerical Simulation of Surfactant-Enhanced Solubilization of Pooled DNAPL, Environmental Science & Technology, 30 (11), 3205-3215.

Mayes, M.A., Jardine, P.M., Mehlhorn, T.L., Bjornstad, B.N., Ladd, J.L., Zachara, J.M., 2003. Transport of multiple tracers in variably saturated humid region structured soils and semi-arid region laminated sediments. *J. Hydrol.* 275, 141–161.

Maymó-Gatell, X., Chien, Y., Gossett, J. M., Zinder, S. H. (1997). Isolation of a Bacterium That Reductively Dechlorinates Tetrachloroethene to Ethene. *Science* 276: 1568-1571.

McCarty, P.L., Goltz, M.N., Hopkins, G.D., Dolan, M.W., Allan, J.P., Kawakami, B.T., Carrothers, T.J. 1998, Full scale evaluation of in situ cometabolic degradation of trichloroethylene in groundwater through toluene injection. *Environ. Sci. Technol.* 32, 88–100.

McWhorter, D. B., and D. K. Sunada 1990, Exact intergral solutions for two-phase flow, *Water Resour. Res.*, 26, 399-413.

Mejías, M., Renard, P., Glenz, D. *2009*, Hydraulic testing of low-permeability formations: A case study in the granite of Cadalso de los Vidrios, Spain, *Engineering Geology*, 107, pp.88–97.

Mendoza, C.A. 1992, Capillary Pressure and Relative Transmissivity Relationships Describing Two-phase Flow through Rough-walled Fractures in Geologic Materials, PhD thesis, University of Waterloo, Waterloo, Ontario.

Mercer, J. W., and R. M. Cohen. 1990, A review of immiscible fluids in the subsurface: Properties, models, characterization and remediation, *J. Contam. Hydrol.*, 6, 107–163.

Mercer, J.W., and R.M. Cohen. 1993, DNAPL Site Evaluation, 6, pp. 107-163, C.K.Smoley. CRC Press, Inc. 200 Corporate Boulevard, NW., Boca Raton, Florida 33431., Boca Raton.

Michael Basel, Leo Lehmicke. 2002, Natural attenuation of Freons and TCE in fractured rock, *Proceedings of the Third International Conference on Remediation of Chlorinated and Recalcitrant Compounds*, Part D, Paper 2D-15.

Miller, C.T., M.M. Poirier-McNeill and A.S. Mayer. 1990, Dissolution of trapped nonaqueous phase liquids: mass transfer characteristics, *Water Resour. Res.*, 26(11): 2783-2796, 1990.

Miller, C.T., Christakos, G., Imhoff, P.T., McBride, J.F., Pedit, J.A. 1998, Multiphase flow and transport modelling in heterogeneous porous media: challenges and approaches, *Adv. Water Resour.* 21 (2), 77– 120.

Miller, C.T., E.H. Hill III, and M. Moutier. 2000, Remediation of DNAPL-Contaminated Subsurface Systems Using Density Motivated Mobilization, *Environ. Sci. Technol.* 34(4):719-724.

Millington, R.J. and J.P. 1961, Quirk, Permeability of Porous Solids. *Trans. Faraday Society.* v.57, pp. 1200-1207.

Mohamedzein, Y.E-A., Al-Rawas, A.A., Al-Aghbari, M.Y., Qatan, A., Al-Rawas, A.H. 2005, Assessment of crushed shales for use as compacted landfill liners, *Engineering Geology*, 80, pp. 271–281.

Mohnke, O. and Yaramanci, U. 2008, Pore size distributions and hydraulic conductivities of rocks derived from Magnetic Resonance Sounding relaxation data using multi-exponential decay time inversion, *Journal of Applied Geophysics,* 66, pp.73–81.

Moreno, L., Y. W. Tsang, C. F. Tsang, F. V. Hale, and I. Neretnieks. 1988, Flow and tracer transport in a single fracture: A stochastic model and its relation to some field observations, *Water Resour. Res.*, 24(12), 2033–2048.

Morris, D.A. and A.I. Johnson, 1967. Summary of hydrologic and physical properties of rock and soil materials as analyzed by the Hydrologic Laboratory of the U.S. Geological Survey, U.S. *Geol. Surv. Water-Supply* Paper 1839-1842p.

Mumford, K. G., Thomson, N. R., and Allen-King, R. M. 2005, Bench-Scale Investigation of Permanganate Natural Oxidant Demand Kinetics, *Environmental Science & Technology*, 39 (8), 2835-2840.

Mundle, K., Reynolds, D. A., West, M. R., and Kueper, B. H. 2007, Concentration Rebound Following In Situ Chemical Oxidation in Fractured Clay, *Ground Water*, 45 (6), 692-702.

Murphy, J.R., Thomson, N.R. 1993, Two-phase flow in a variable aperture fracture, *Water Res. Res.* 29 (10), 3453–3476.

Mutch, R. D., Scott, J. I., and Wilson, D. J. 1993, Cleanup of fractured rock aquifers: Implications of matrix diffusion, Environmental Monitoring and Assessment, 24 (1), 45-70.

Nakashima M, Wu X, Okada, R. and Nishigaki M. 2002, Enhanced Bioremediation of a Site in Japan Contaminated with Chlorinated Solvents using HRC Injection, *Proceedings of the Third International Conference on Remediation of Chlorinated and Recalcitrant Compounds*, Paper 2B-42.

Nambi, I.M., and S.E. Powers. 2003, Mass transfer correlations for nonaqueous phase liquid dissolution from regions with high initial saturations, *Water Resources Research*, 39(2), SBH41-SBH411.

National Research Council, 1984 . Groundwater Contamination, National Academy Press, pp 61.

National Research Council (NRC). 1994, Alternatives for groundwater cleanup. National Academy Press, Washington, DC.

National research Council. 1996, Rock Fractures and Fluid Flow, Natl. Acad. Press, Washington, D.C.

Newell, C. J., Cowie, I., McGuire, T. M., and Walt W. McNab, J. 2006, Multiyear Temporal Changes in Chlorinated Solvent Concentrations at 23 Monitored Natural Attenuation Sites, *Journal of Environmental Engineering*, 132 (6), 653-663.

Novakowski, K.S. 1992, The analysis of tracer experiments conducted in divergent radial flow fields. *Water Resour. Res.* 28(12), 3215–3225.

Nyer, E., Lenzo, F.L., Burdick, J. S. 1998, In Situ Reactive Zones: Dehalogenation of Chlorinated Hydrocarbons, *Groundwater Monitoring Review*, Spring.

Ogata, A., and Banks, R. B. 1961, A Solution of the Differential Equation of Longitudinal Dispersion in Porous Media, USGS, Reston, Virginia, USGS Prof. Paper No. 411-A

Pakdel, H., Couture, G., Roy, C., Masson, A., Locat, .I., Gelinas, P. and Lesage, S. 1992, Developing methods for the analysis of toxic chemicals in soil and groundwater: The case of Ville Mercier, Quebec, Canada. In: S. Lesage and R.E. Jackson (Editors), *Groundwater Contamination and Analysis at Hazardous Waste Sites.* Marcel Dekker, New York, NY, 545 pp.

Palumbo, A.V., McCarthy, J.F., Parker, A., Pfiffner, S., Colwell, F.S., Phelps, T.J. 1994, Potential for microbial growth in arid subsurface sediments, *Appl. Biochem. Biotechnol.* 45-46, 823–834.

Pankow, J. F. and Cherry, J. A. 1996, Dense Chlorinated Solvents and Other DNAPLs in Groundwater: *History, Behaviour, and Remediation, Waterloo Press* pp.1-46, pp129-143, pp508, pp522.

Pape, H., Tillich, J.E., Holz, M. 2006, Pore geometry of sandstone derived from pulsed field gradient NMR, *Journal of Applied Geophysics*, 58, pp. 232–252.

Parker, B.L. 1996, Effects of molecular diffusion on the persistence of dense, immiscible phase organic liquids in fractured porous geologic media. PhD Thesis, Univ. of Waterloo.

Parker, B L., Gillham, Robert W., Cherry, John A. 1994, Diffusive disappearance of immiscible-phase organic liquids in fractured geologic media, *Ground Water,* Volume 32, Issue 5, Pages 805-819.

Parker, B.L., McWhorter, D.B., Cherry, J.A. 1997, Diffusive loss of non-aqueous phase organic solvents from idealized fracture networks in geologic media, *Ground Water*, Volume 35, Issue 6, Pages 1077-1088.

Parker, J. C., and Park, E. 2004, Modelling field-scale dense nonaqueous phase liquid dissolution kinetics in heterogeneous aquifers, *Water Resources Research*, 40 (W05109), 1-12.

Pedersen, K., and S. Ekendahl. 1990. Distribution and activity of bacteria in deep granitic groundwaters of southeastern Sweden. *Microb. Ecol.* 20:37–52.

Pennell, K.D., Jin, M., Abriola, L.M., Pope, G.A. 1994, Surfactant enhanced remediation of soil columns contaminated by residual tetrachloroethylene. *J. Contaminant Hydrology* 16 (1), 35.

Pennell, K. D., Pope, G. A., and Abriola, L. M. 1996, Influence of Viscous and Buoyancy Forces on the Mobilization of Residual Tetrachloroethylene during Surfactant Flushing, *Environmental Science & Technology*, 30 (4), 1328-1335.

Persoff, P. and K. Pruess. 1995, Two Phase flow Visualization and relative Permeability Measurement in Natural Rough-Walled Rock Fractures, *Water Res. Res.*, 31(5), pp 1175-1186.

Pettijohn, F. J., Potter, P. E., and Siever, R. 1987, Sand and sandstone, Springer, New York.

Pitkänen, Snellman, Leino-Forsman, Front, 1992. Groundwater chemistry and water–rock interaction at Olkiluoto: Report YJT-92-02. *Nuclear Waste Commission of Finnish Power Companies*, Helsinki, Finland, pp. 321.

Pope, G.A., Wade, W.H. 1995, Lessons from enhanced oil recovery research for surfactant enhanced aquifer remediation. In: Sabatini, D.A., Knox, R.C., Harwell, J.H.Eds, Surfacant-enhanced subsurface remediation: emerging technologies, ACS symposium series No. 594. *American Chemical Society,* Washington, DC, pp. 142–160.

Powers, S.E., Loureiro, C.O., Abriola, L.M. and Weber, Jr., W.J. 1991, Theoretical study of the significance of non equilibrium dissolution of non-aqueous-phase liquids in subsurface systems, *Water Resour. Res.*, 27(4): 463-477.

Powers, S. E., Abriola, L. M., and Weber Jr., W. J. 1992, An experimental investigation of nonaqueous phase liquid dissolution in saturated subsurface systems: Steady state mass transfer rates, *Water Resour. Res.*, 28(10), 2691–2706.

Pruess, K., Tsang, Y.W. 1990, On two-phase relative permeability and capillary pressure of rough-walled rock fractures. *Water Resour. Res*. 26 (9), 1915–1926.

Pyrak-Nolte, L.J. 1991, Multiphase flow in a fracture. *Proceedings of the 1991 Coalbed Methane Symposium*, University of AlabamarTuscaloosa, pp. 433–442.

Ramsburg, C. A., and K. D. Pennell. 2002, Density-modified displacement for DNAPL source zone remediation: Density conversion and recovery in heterogeneous aquifer cells, *Environ. Sci. Technol.*, 36, 3176 – 3187.

Ramsburg, C. A., Pennell, K. D., Abriola, L. M., Daniels, G., Drummond, C. D., Gamache, M., Hsu, H. L., Petrovskis, E. A., Rathfelder, K. M., Ryder, J. L., and Yavaraski, T. P. 2005, Pilot-Scale Demonstration of Surfactant-Enhanced PCE Solubilization at the Bachman Road Site. 2. System Operation and Evaluation, *Environmental Science & Technology*, 39 (6), 1791-1801.

Rangel-German, E., Akin, S., Castanier, L., 2006, Multiphase-flow properties of fractured porous media, *Journal of Petroleum Science and Engineering*, 51(3-4), pp 197-213.

Rathfelder, K. M., Abriola, L. M., Taylor, T. P., and Pennell, K. D. 2001, Surfactant enhanced recovery of tetrachloroethylene from a porous medium containing low permeability lenses: 2. Numerical simulation, *Journal of Contaminant Hydrology*, 48 (3-4), 351-374.

Reitsma, S. 1992, Laboratory measurement of capillary pressure – saturation relationships in natural rock fractures, M.Sc. Thesis, University of Waterloo, Waterloo, Ontariom Canada, 152pgs.

Reitsma, S., Kueper, B.H. 1994, Laboratory measurement of capillary pressure – saturation relationships in a rock fracture. *Water Resour. Res*. 30(4), 865-878.

Reynolds, D.A. 2001, Multiphase Flow and Transport in Fractured Geologic Environments, PhD thesis, University of Kingston, Ontario, Canada.

Reynolds, D.A., Kueper, B.H. 2001, Multiphase flow and transport in fractured clay/sand sequences, *J. Contam. Hydrol.* 51 (1–2), 41– 62.

Reynolds, D.A., Kueper, B.H. 2004, Multiphase flow and transport through fractured heterogeneous porous medium, *J. Contam. Hydrol*. 71, 89– 110.

Robinson, C., Barry, D.A., McCarty, P.L., Gerhard, J.I. and Kouznetsova I. 2009, pH Control for Enhanced Reductive Bioremediation of Chlorinated Solvent Source Zones. *Science of the Total Environment,* 407, 4560-4573.

Ross, B., Lu, N. 1999, Dynamics of DNAPL penetration into fractured porous media, *Ground Water* Volume 37, Issue 1, Pages 140-147.

Ross, N., Kennedy, C., Voralek, J., Lesage, S., Novakowski K., Samson, R. 2002, Biofilm development in a large-scale planar fracture, *Proceedings of the Third International Conference on Remediation of Chlorinated and Recalcitrant Compounds,* Pages 2441-2447, Paper 2C-41.

Saba, T., and T.H. Illangasekare. 2000, Effect of groundwater flow dimensionality on mass transfer from entrapped nonaqueous phase liquid contaminants, *Water Resources Research*, 36(4), 971-979.

Sardin, M., Dridl-Dhaouadi, S., Maunier, C. and Simonnot, M.O. 1998, Transient Transport of Surfactant in a Calcaeous and Clayey Sand, *Physics and Chemistry of the Earth*, 23(2) , pp. 221-227.

Sausse, J. 2002, Hydromechanical properties and alteration of natural fracture surfaces in the Soultz granite (Bas-Rhin, France), *Tectonophysics*, 348, pp.169– 185.

Sausse, J., Fourar, M., Genter, A. 2006, Permeability and alteration within the Soultz granite inferred from geophysical and flow log analysis, *Geothermics,* 35, pp. 544–560.

Schnarr, M., Truax, C., Farquhar, G., Hood, E., Gonullu, T., Stickney, B. 1998, Laboratory and controlled field experiments using potassium permanganate to remediate trichloroethylene and perchloroethylene DNAPLs in porous media, *J. Contam. Hydrol.* 29 (3), 205– 224.

Schroth, M.H., Oostrom, M., Wietsma, T.W., Istok, J.D. 2001, In-situ oxidation of trichloroethene by permanganate: effects on porous medium hydraulic properties, *J. Contam. Hydrol.* 50, 79–98.

Schwartz, F.W., Cherry. J.A. and Roberts, J.A. 1982, A case study of chemical spill polychlorinated biphenyls, 2: Hydrogeological conditions and contaminant migration, *Water Resour. Res,* 18(3): 535-545.

Schwarzenbach, R.P. and Westhall J. 1981, Transport of nonpolar organic compounds from surface water to groundwater: Laboratory Studies, *Environmental Science and Technology,* v. 15, pp. 1360-1367.

Schwarzenbach, R.P., Gschwend, P. M., and Imboden, D.M. 1993, *Environmental Organic Chemistry*, John Wiley and Sons, Toronto, pp. 681.

Schwille, F. 1988, Dense chlorinated solvents in porous and fractured media; Model experiments. Translated by J.F. Pankow. Lewis Publishers.

Seagren E.A., Rittmann B.E., Valocchi A.J. 1994, Quantitative evaluation of the enhancement of NAPL-pool dissolution by flushing and biodegradation. *Environ Sci Technol*, 28(5):833-9.

Sehayek, L., Vandell, T.D., Sleep, B.E., Lee, M.D., Chien, C. 1999, Investigation and remediation of a 1,2-dichloroethane spill: Part I: Short and long-term remediation strategies, *Ground Water Monitoring and Remediation Volume* 19, Issue 3, Pages 71-81.

Seol, Y., Zhang, H., and Schwartz, F.W. 2003, A review of In Situ Chemical Oxidation and Heterogeneity, *Environment & Engineering Geoscience*, 9(1), February, pp. 37-49.
Shapiro, A.M. 2001, Effective matrix diffusion in kilometer-scale transport in fractured crystalline rock. *Water Resour.* 37, 37507–37522.

SERDP. 2001, SERDP/ESTCP Expert Panel Workshop on Research and Development Needs for Cleanup of Chlorinated Solvent Sites.

Shiau, B., Rouse, J.D., Sabatini, D.A., Harwell, J.H. 1995, Surfactant selection for optimizing surfactant-enhanced subsurface remediation. In: Sabatini, D.A., Knox, R.C., Harwell, J.H.(Eds), Surfacant-enhanced subsurface remediation: emerging technologies, ACS symposium series No. 594. American Chemical Society, Washington, DC, pp. 65–79.

Siegrist, R. L., Urynowicz, M. A., West, O. R., Crimi, M. L., and Lowe, K. S. 2001, Principles and Practices of in Situ Chemical Oxidation Using Permanganate, 348 pp., *Battelle Press*, Columbus, Ohio, USA

Sleep B.E., Sykes J.F. 1993, Compositional simulation of groundwater contamination by organic compounds. 1, Model development and verification. *Water Resour Res*, 29(6):1697-1708.

Slough, K.J., Sudicky, E.A., Forsyth, E.A. 1999a, Numerical Simulation of Multiphase Flow and Phase Partitioning in Discretely Fractured Geologic Media, *J. Cont. Hyd.*, 40, p 107-136.

Slough, K.J., Sudicky, E.A., Forsyth, E.A. 1999b, Grid refinement for modelling multiphase flow discretely fractured porous media, *Advances in Water Resources* 23, pp 261-269.

Smith, L. and F.W. Schwartz. 1984, An Analysis of the Influence of Fracture Geometry on Mass Transport in Fractured Media. *Water Resour. Res.* 20, 1241-1252.

Sorenson, K. S. 2002. Enhanced bioremediation for treatment of chlorinated solvent residual source areas. *ACS Symp.* Ser. 837:119–131.

Sousa, L.M.O. 2007, Granite fracture index to check suitability of granite outcrops for quarrying, *Engineering Geology*, 92, pp.146–159.

Streltsova, T.D. 1976a, Advances and uncertainties in the study of groundwater flow in fissyred rocks, *Adv. Groundwater Hydrol*., pp. 48-56.

Steele A. and Lerner D.N. 2001, Predictive modelling of NAPL injection tests in variable aperture spatially correlated fractures, *Journal of Conyaminant Hydrology*, 49 (3-4): 287-310.

Suarez, M.P., and Rifai, H.S., 1999. Biodegradation rates for fuel hydrocarbons and chlorinated solvents in groundwater, CRC Press LLC, 337-362.

Suchomel, E. J., Ramsburg, C. A., and Pennell, K. D. 2007, Evaluation of trichloroethene recovery processes in heterogeneous aquifer cells flushed with biodegradable surfactants, *Journal of Contaminant Hydrology*, 94 (3-4), 195-214.

Sudicky, E.A., Frind, E.O. 1982, Contaminant transport in fractured porous media: analytical solutions for a system of parallel fractures. *Water Resour. Res.* 18, 1634–1642.

Sudicky, E.A., Slough, K.J. 1998, Forsyth, P.A., DNAPL migration in fractured porous rock media: Parameter sensitivity, prediction uncertainty and implications for remediation, IAHS-AISH Publication Issue 250, Pages 157-165.

Sung, Y., K. M. Ritalahti, R. A. Sanford, J. W. Urbance, S. J. Flynn, J. M. Tiedje, and F. E. Lo¨ffler. 2003. Characterization of two tetrachloroethene-reducing, acetate-oxidizing anaerobic bacteria and their description as *Desulfuromonas michiganensis* sp. nov. Appl. Environ. Microbiol. 69:2964–2974.

Suthersan, S and F. Payne. 2005. *In Situ* Remediation Engineering. Boca Raton: CRC Press.

Swanson, S.K., Bahr, J.M., Bradbury, K.R., Anderson, K.M. 2006, Evidence for preferential flow through sandstone aquifers in Southern Wisconsin, *Sedimentary Geology*, 184, pp. 331–342.

Tang, D.H., Frind, E.O., and Sudicky, E.A. 1981, Contaminant Transport in Fractured Porous Media: Analytical Solution for a Single Fracture, *Water Resources Research*, 17 (3), 555-564.

Taylor, T. P., Pennell, K. D., Abriola, L. M., and Dane, J. H. 2001, Surfactant enhanced recovery of tetrachloroethylene from a porous medium containing low permeability lenses 1. Experimental studies, *Journal of Contaminant Hydrology*, 48 (3-4), 325-350.

Taylor, T. P., Rathfelder, K. M., Pennell, K. D., and Abriola, L. M. 2004, Effects of ethanol addition on micellar solubilization and plume migration during surfactant enhanced recovery of tetrachloroethene, *Journal of Contaminant Hydrology*, 69 (1-2), 73-99.

Thomson, N.R., Fraser, M.J., Lamarche, C., Barker, J.F.,Forsey S.P., 2008, Rebound of a coal tar creosote plume following partial source zone treatment with permanganate, *Journal of Contaminant Hydrology,* 102, 154–171.

Tomlin, A., Berzins, M., Ware, J., Smith, J. and Pilling M.J., 1997, On the use of adaptive gridding methods for modelling chemical transport from multi-scale sources, *Atmospheric Environment*, 31(18), Pages 2945-2959.

Trivedi, J.J., Babadli, T. 2008, Experimental and numerical modelling of the mass transfer between rock matrix and fracture, Chemical Engineering Journal, In-Press.

Tsang, Y.W., Tsang, C.F. 1987, Channel model of flow through fractured media, *Water Resour. Res.* 23, 467– 479.

Tsang, Y.W. 1992, Usage of "equivalent apertures" for rock fractures as derived from hydraulic and tracer tests, *Water Resours. Res.*, 28(5): 1451-1455.

Tunnicliffe B. S. and Thomson N. R. 2004, Mass removal of chlorinated ethenes from rough-walled fractures using permanganate, *Journal of Contaminant Hydrology* Volume 75, Issues 1-2 , Pages 91-114.

Uhlman, K, Barner, W. 1998, Contaminant transport mechanisms in karst terranes, *IAHS-AISH Publication Issue* 253, Pages 327-335.

Unger, A.J.A., Sudicky, E.A. and Forsyth, P.A. 1995, Mechanisms controlling vacuum extraction coupled with air sparging for remediation of heterogeneous formations contaminated with dense non-aqueous-phase liquids, *Water Resour. Res.,* 31(8): 1913-1925.

USEPA, 2001. The State-of-the Practice of Characterization and Remediation of Contaminated Ground Water at Fractured Rock Sites EPA 542-R-01-010.

USEPA, 2003b. Chemical Oxidation Site Profiles. Available at http://www.clu-in.org/products/chemox/search/chem_search.cfm

Urynowicz, M.A., and Siegrist, R.L. 2005. Interphase mass transfer during chemical oxidation of tce dnapl in an aqueous system. *Journal of Contaminant Hydrology*, 80:93-106.

VanderKwaak, J.E., Sudicky, E.A.1996, Dissolution of non-aqueous-phase liquids and aqueous-phase contaminant transport in discretely-fractured porous media, *Journal of Contaminant Hydrology* 23, Pages 45-68.

Vasconcelos, G., Lourenco, P.B., Alves, C.A.S., Pamplona, J. 2008, Ultrasonic evaluation of the physical and mechanical properties of granites, *Ultrasonics*, 48, pp. 453–466.

Vella, P.A., and Veronda, B. 1992, Oxidation of trichloroethylene: Comparison of potassium permanganate and fenton's reagent, chemical oxidation technologies for the nineties. *Technical report*, Technomin, Lancaster, PA, USA.

Vella, P.A. and B. Veronda. 1994, Oxidation of Trichloroethylene: A comparison of potassium permanganate and Fenton's reagent. *3rd Intern. Symposium on Chemical Oxidation. In: In Situ Chemical Oxidation for the Nineties.* Vol. 3. Technomic Publishing Co., Inc. Lancaster, PA. pp.62-73.

Vilks P., Cramer, J.J., Jensen, M., Miller, N.H., Miller, H.G., Stanchell, F.W. 2003, In situ diffusion experiment in granite: Phase I, *Journal of Contaminant Hydrology*, 61, 191– 202.

Villaume, J.F. 1985, Investigations at sites contaminated with dense, non-aqueous-phase liquids (NAPLs), *Ground Water Monit. Rev.*, 5(2): 60-75.

Walker, Rhén, Gurban, 1997. Summary of hydrogeological conditions at Aberg, Beberg and Ceberg. *Technical Report*, TR 97-23, SKB SKB Stockholm, Sweden.

Walter, G.R., G.M. Thompson. 1982, A repeated pulse technique for determining the hydraulic properties of tight formations, *Ground Water* 20, 186-193.

Water Science and Technology Board (WSTB). 2004, Contaminants in the Subsurface: Source Zone Assessment and Remediation, National Research Council of the National Academies, *The National Academies Press*, Washington D.C.

Watkins, 2003. Determining a representative hydraulic conductivity of the Carnmenellis granite of Cornwall, UK, based on a range of sources of information. *Paper presented at the IHP International Hydrological Program*, Bratislava, Slovak Rep.

Wealthall, G.P., Lerner, D.N. 2002, Fractured rock mass characterisation to predict DNAPL source zones, *Proceedings of the Third International Conference on Remediation of Chlorinated and Recalcitrant Compounds*, Pages 239-246, Paper 1D-07.

Wealthall, G.P., Steele, A., Bloomfield, J.P., Moss, R.H. and Lerner, D.N. 2001, Sediment filled fractures in the Permo-Triassic sandstones of the Cheshire Basin: observations and implications for pollutant transport, *Journal of Contaminant Hydrology* 50, 41-51.

Wealthall, G.P., S.F. Thornton, and D.N. Lerner. 2001. Assessing the trasport and fate of MTBE-amended petroleum hydrocarbones in the UK Chalk aquifer. Paper presented at Groundwater Quality 2001, Third International Conference on Groundwater Quality, June 18-21, 2001, in University of Sheffield, United Kingdom.

Werner, P.G.. 2002, Chemical oxidation of Tetrachloroethene (PCE) contamination in a fractured saprolitic bedrock aquifer, *Proceedings of the Third International Conference on Remediation of Chlorinated and Recalcitrant Compounds*, Part C, Paper 2C-44.

West M.R. 2009, Mathematical Modelling of DNAPL Source Zone Remediation, PhD Thesis, Queens University, Kingston, Ontario.

West, M. R., Grant, G. P., Gerhard, J. I., and Kueper, B. H. 2008, The influence of precipitate formation on the chemical oxidation of TCE DNAPL with potassium permanganate, *Advances in Water Resources*, 31 (2), 324-338.

West, C.C. and Harwell, J.H. 1992, Surfactants and Subsurface Remediation, *Environ. Sci. Technol.*, Vol. 26, No. 12.

Wice, R.B., Vogeding, J.R., Walters, G., Ficklen, H.D. 2002, Enhanced DNAPL recovery from fractured limestone AFP4, Fort Worth, Texas, *Proceedings of the Third International Conference on Remediation of Chlorinated and Recalcitrant Compounds*, Pages 2441-2447, Paper 2H-55.

Widdowson M.A. 2004, Modelling natural attenuation of chlorinated ethenes under spatially varying redox conditions. *Biodegradation*, 15(6):435-51.

Williams, C.L., Spiers C.A. 2002, Degradation of Trichloroethene (TCE) in a fractured bedrock aquifer using Sodium Permanganate, *Proceedings of the Third International Conference on Remediation of Chlorinated and Recalcitrant Compounds*, Pages 2441-2447, Paper 2C-43.

Wilke, C. R., and Chang, P. 1955, Correlation of diffusion coefficients in dilute solutions, *AIChE Journal*, 1 (2), 264-270.

Witherspoon, P. A., J. S. Y. Wang, K. Iwai, and J. E., Gale. 1980, Validity of cubic law for fluid flow in a deformable rock fracture, *Water Resour. Res.*, 16(6), 1016– 1024.

Wood, B.D., Ginn, T.R., and Dawson, C.N. 1995, Effects of Microbial Metabolic Lag in Contaminant Transport and Biodegradation Modelling, *Water Resources Research*, 31 (3), pp. 553-563.

Wu, W.-M., Nye, J., Jain, M. K., and Hickey, R. F. 1998, Anaerobic dechlorination of trichloroethylene (TCE) to ethylene using complex organic materials, *Water Research*, 32 (5), 1445-1454.

Wu, X., Alshawabkeh, A.N., Gent, D.B., Larson, S. L. and Davis J. L., 2007, Lactate transport in soil by DC Fields, *J. Geotech and Geoenvir. Eng.*, 133(12), 1587-1596.

Wulff, A.M., Raab, S., Huenges, E. 2000, Alteration of Seismic Wave Properties and Fluid Permeability in Sandstones due to Microfracturing, *Phys. Chem. Earth (A)*, Vol. 25, No. 2, pp. 141-147.

Yager, R. M., S. E. Bilotta, C. L. Mann, and E. L. Madsen. 1997. Metabolic adaptation and in situ attenuation of chlorinated ethenes by naturally occurring microorganisms in a fractured dolomite aquifer near Niagara Falls, New York. Environ. Sci. Technol. 31:3138–3147.

Yang, Y., and McCarty, P.L. 1998, Competition for Hydrogen Within a Chlorinated Solvent Dehalogenating Anaerobic Mixed Culture, *Environmental Science and Technology*. 32(22):3591-3597.

Yang, Y., and McCarty, P. L. 2000a, Biomass, Oleate, and Other Possible Substrates for Chloroethene Reductive Dehalogenation, *Bioremediation Journal*, 4 (2), 125 - 133.

Yang Y., McCarty .PL. 2002, Comparison between donor substrates for biologically enhanced tetrachloroethene DNAPL dissolution. *Environ Sci Technol*,36(15):3400-4.

Yan, Y.E. and Schwartz, F.W. 1996, Oxidation of chlorinated solvents by permanganate. Proc. Intern. Conf. On Remediation of Chlorinated and Recalcitrant Compounds, Ohio: *Battelle Press.* pp. 403-408.

Yan, Y.E., and Schwartz, F.W. 1999, Oxidative degradation and kinetics of chlorinated ethylenes by potassium permanganate, *Journal of Contaminant Hydrology*, 37 (3-4), 343-365.

Yan, Y.E., and Schwartz, F.W. 2000, Kinetics and Mechanisms for TCE Oxidation by Permanganate, *Environmental Science & Technology*, 34 (12), 2535-2541.

Yeo, I.W., Ji, S.-H., Lee, K.-K. 2003, Density-surfactant-motivated removal of DNAPL trapped in dead-end fractures, *Geophysical Research Letters* Volume 30, Issue 9, Pages 24-1.

Yu, J., and Pinder, K. L. 1994, Effective diffusivities of volatile fatty acids in methanogenic biofilms, *Bioresource Technology*, 48 (2), 155-161.

Yu S., Semprini L. 2004, Kinetics and modelling of reductive dechlorination at high PCE and TCE concentrations. *Biotechnol Bioeng*, 88(4):451-64.

Zekri, AY; Almehaideb, R. 2003 Microbial and waterflooding of fractured carbonate rocks: An experimental approach, *Petroleum Science and Technology*, 21 (1-2): 315-331.

Zhang, X., Sanderson, D.J., Harkness, R.M., and N.C. Last. 1996, Evaluation of the 2-D Permeability Tensor of Fractured Rock, *Int. J. Rock Mech. Min. Sci.*, 33, p 17-37.

Zhang, X., Sanderson, D.J. 1999, Scale up of Two-dimensional Conductivity Tensor for Heterogeneous Fracture Networks, Eng. Geol., 53, p 83-99.

Zhang, H., and Schwartz, F. W. 2000, Simulating the in Situ Oxidative Treatment of Chlorinated Ethylenes by Potassium Permanganate, *Water Resources Research,* 36 (10), 3031-3042.

Zhong, LR; Mayer, A; Glass, RJ. 2001, Visualization of surfactant-enhanced nonaqueous phase liquid mobilization and solubilization in a two-dimensional micromodel, *Water resources research,* 37 (3): 523-537.

Zhong, L., Mayer, A. S., and Pope, G. A. 2003, The effects of surfactant formulation on nonequilibrium NAPL solubilization, *Journal of Contaminant Hydrology*, 60 (1-2), 55-75.

Zhuang P., Pavlostathis S.G. 1995, Effect of temperature, pH and electron donor on the microbial reductive dechlorination of chloroalkes. *Chemosphere,* 31(6):3537-48.

APPENDIX A

Table A1: Summary of Different Rock Properties for Sandstone, Shale and Granite

Parameters	Sandstone	Shale	Granite
Porosity (%)	2.2 – 49.0 [a]	1.0 – 47.0 [h]	0.5 – 7.2 [o]
Matrix Permeability (m^2)	$2 \times 10^{-13} – 9 \times 10^{-15}$ [b]	$1 \times 10^{-17} – 1 \times 10^{-21}$ [i]	$9 \times 10^{-16} – 2 \times 10^{-21}$ [p]
Foc (-)	0.0002 – 0.01 [c]	0.005 – 0.006 [j]	-
Bulk Density (g/cm^3)	2.06 – 2.64 [d]	1.34 – 2.33 [k]	2.63 – 2.69 [q]
Fracture Apertures (µm)	10 – 100000 [e]	30 – 102 [l]	448 – 748 [r]
Fracture Spacing (m)	0.01 – 10.0 [f]	2.0 – 200.0 [m]	0.98 – 2.80 [s]
Matrix Tortuosity (-)	0.2 – 1.6 [g]	0.37 – 0.45 [n]	1.29 – 1.43 [t]

[a] *Lipson et al., 2005; Morris and Johnson, 1967; Baraka-Lokmane, 2002; Hitchmough et al., 2007; Lima and Niwas 2000; Mohnke and Yaramanci, 2008; Dutton and Loucks, 2010; Gooddy et al., 2002; Bloomfield et al., 2001; Pape et al., 2006.*
[b] *Dana and Skoczylas, 2002; Wulff et al., 2000.*
[c] *Lipson et al., 2005; Gooddy, unplublished data.*
[d] *Lipson et al., 2005; Dana and Skoczylas, 2002.*
[e] *Hitchmough et al., 2007; Lipson et al., 2005; Allen et al., 1998.*
[f] *Hitchmough et al., 2007; Lipson et al., 2005; Allen et al., 1998.*
[g] *Hitchmough et al., 2007; Lipson et al., 2005.*
[h] *Gutierrez et al. 2000; Morris and Johnson, 1967; Busch et al., 2008; Cumbie and McKay, 1999; Gwo et al., 2007; Jardine et al., 1999; Silva et al., 2008.*
[i] *Gutierrez et al. 2000; Garavito et al. 2006.*
[j] *Busch et al., 2008; Jardine et al., 1989.*
[k] *Busch et al., 2008; Cumbie and McKay, 1999; Gwo et al., 2007.*
[l] *Jardine et al., 2002; Jardine et al., 1999; Cumbie and McKay, 1999.*
[m] *Jardine et al., 1999; Jardine et al., 2002.*
[n] *Busch et al., 2008; Gwo et al., 2007; Jardine et al., 2002.*
[o] *Chaki et al., 2008; Hu and Mori, 2008; Vasconcelos et al., 2008; Schild et al., 2001.*
[p] *Chaki et al., 2008; Sausse et al., 2006; Vilks et al., 2003.*
[q] *Sausse et al., 2006; Chaki et al., 2008.*
[r] *Sausse 2002.*
[s] *Sousa 2007.*
[t] *Vilks et al., 2003.*

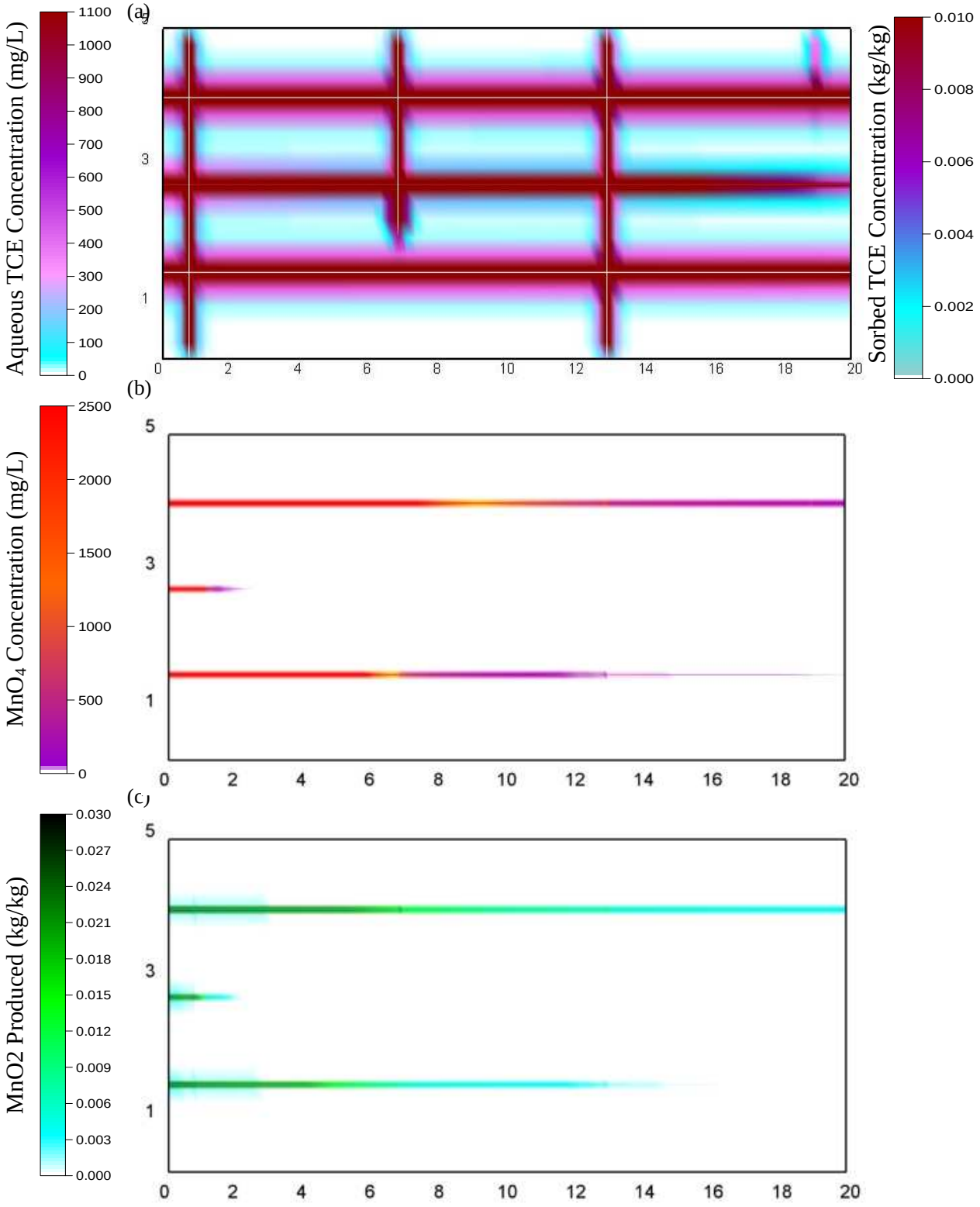

Figure A1: Distribution of aqueous species concentrations at t_{TOTAL} =23 years for 5000 mg/L of MnO4 Simulation, after 2 years of chemical oxidation (i.e., Treatment stage): (a) TCE, (b) MnO_4, (c) MnO_2

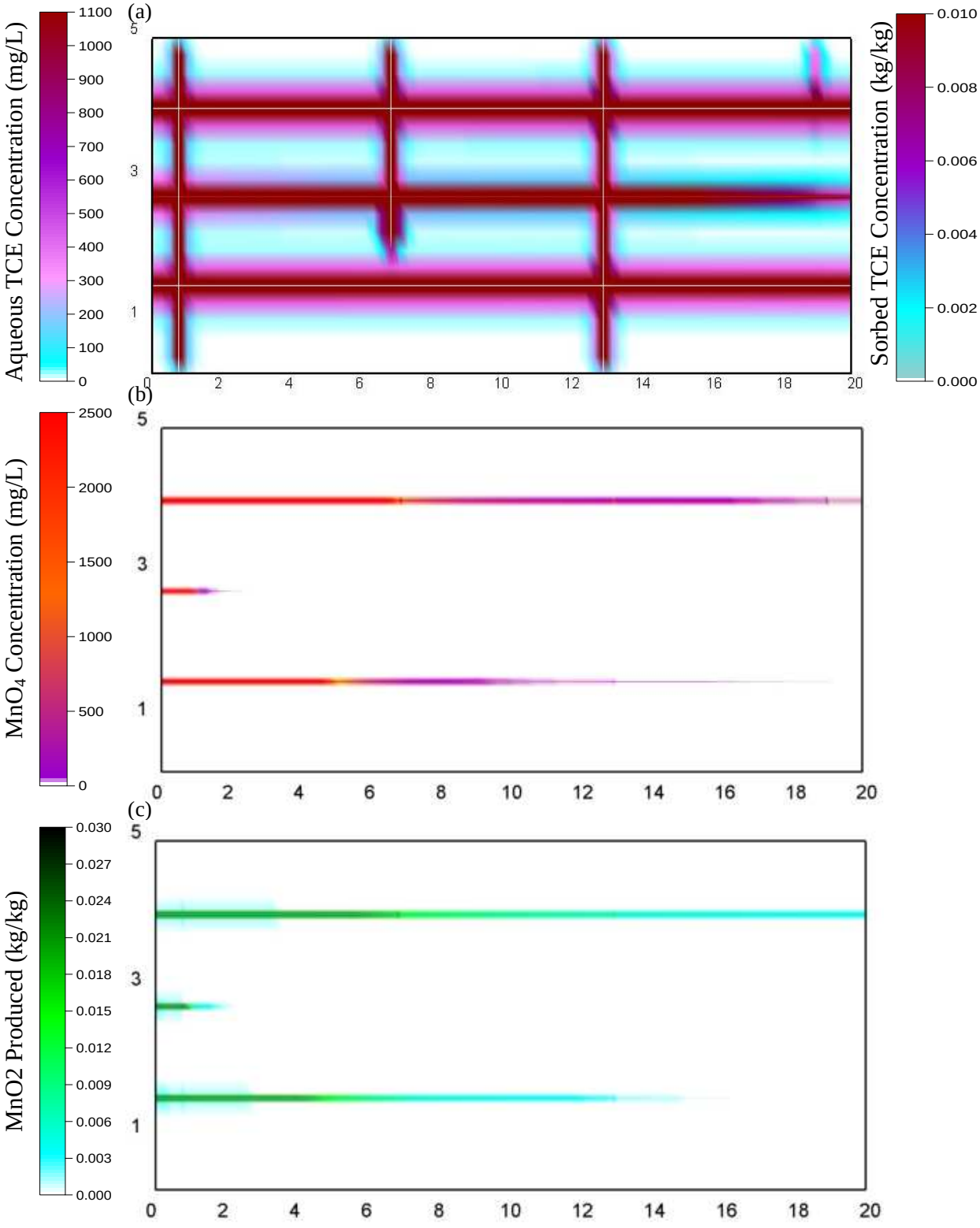

Figure A2: Distribution of aqueous species concentrations at t_{TOTAL} =23 years for 1250 mg/L of MnO4 Simulation, after 2 years of chemical oxidation (i.e., Treatment stage): (a) TCE, (b) MnO_4, (c) MnO_2

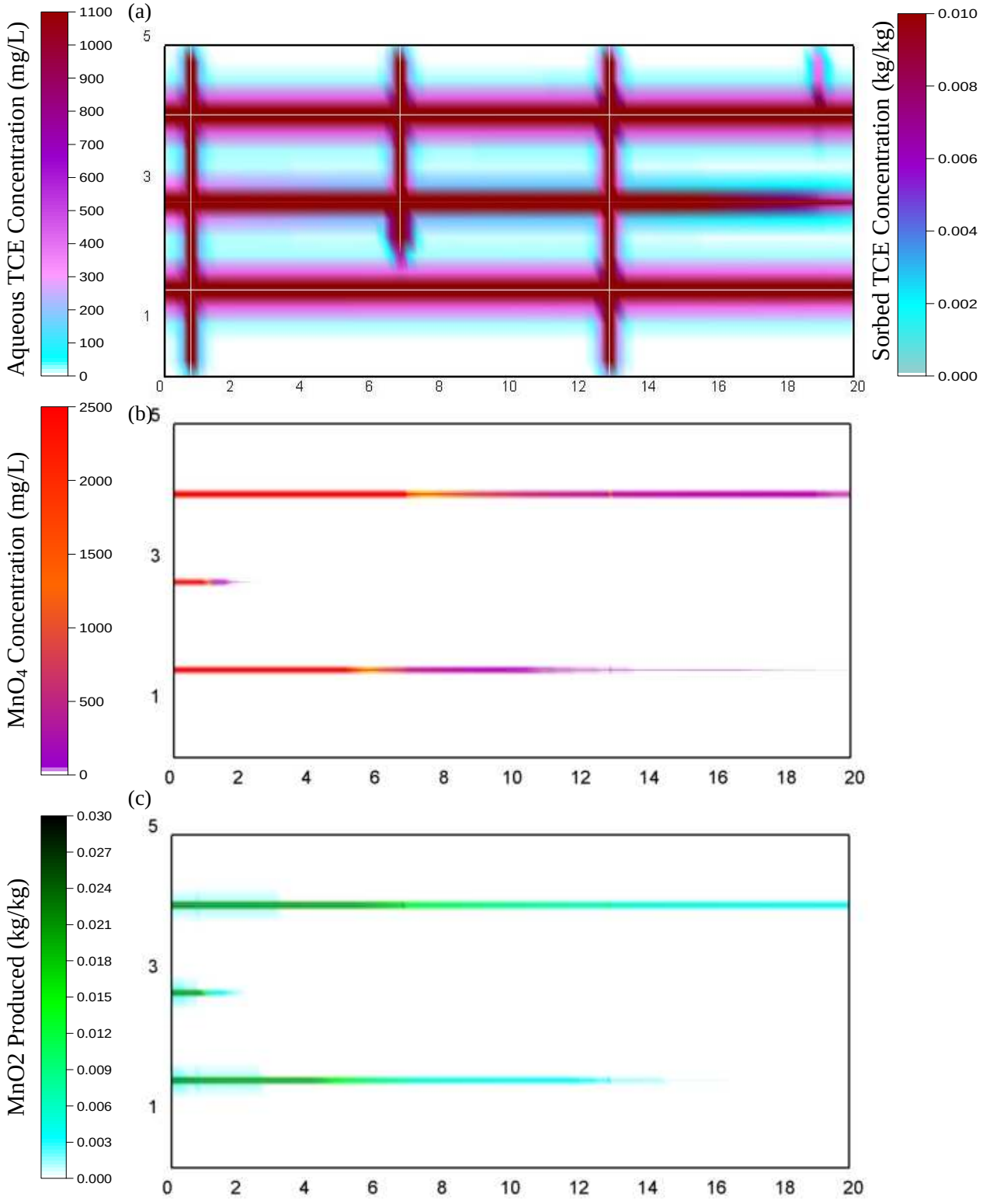

Figure A3: Distribution of aqueous species concentrations at t_{TOTAL} =23 years for 3 Months Pulsing Simulation, after 2 years of chemical oxidation, aging period: (a) TCE, (b) MnO_4, (c) MnO_2

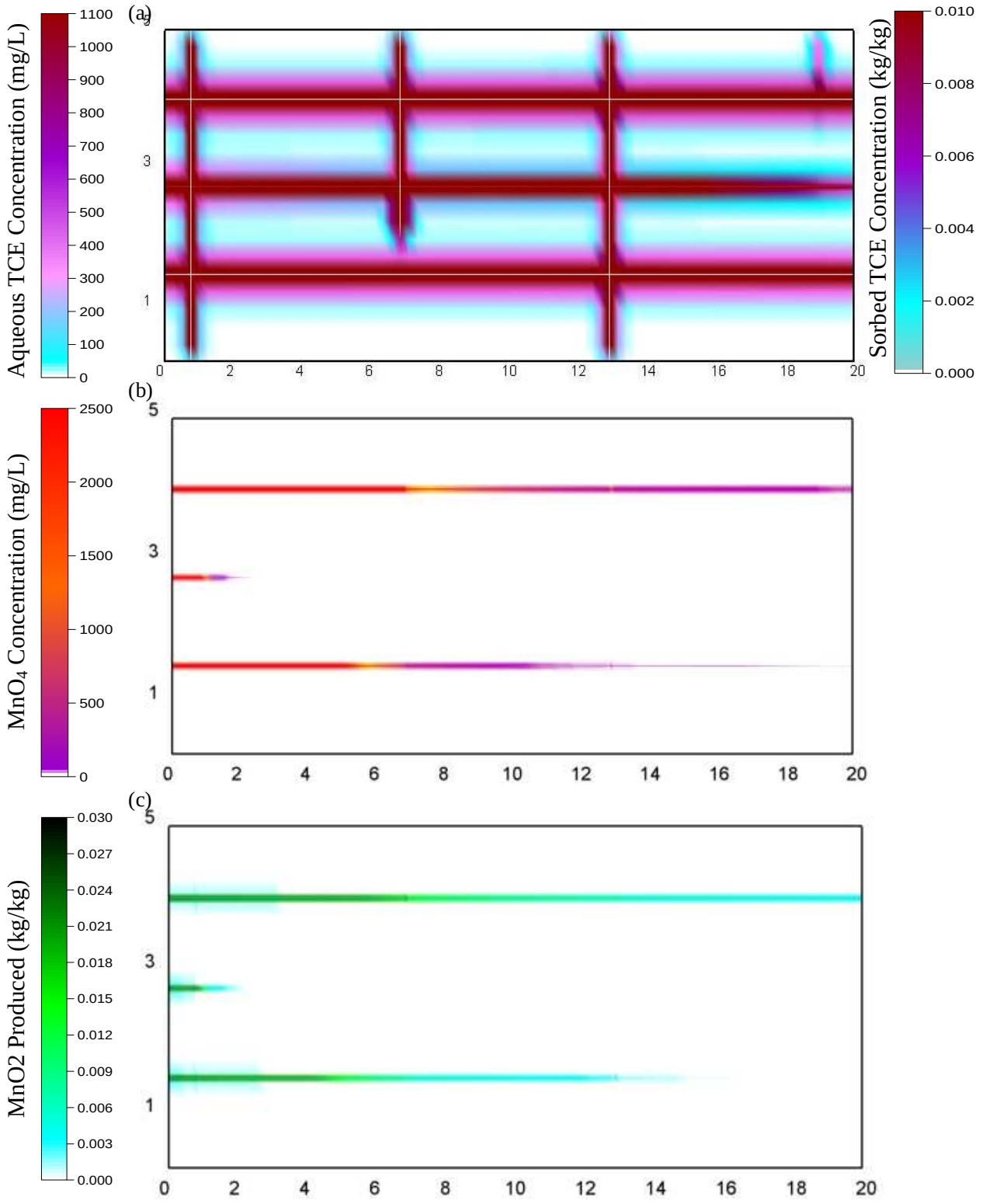

Figure A4: Distribution of aqueous species concentrations at t_{TOTAL} =23 years for 6 Months Pulsing Simulation, after 2 years of chemical oxidation, aging period: (a) TCE, (b) MnO_4, (c) MnO_2

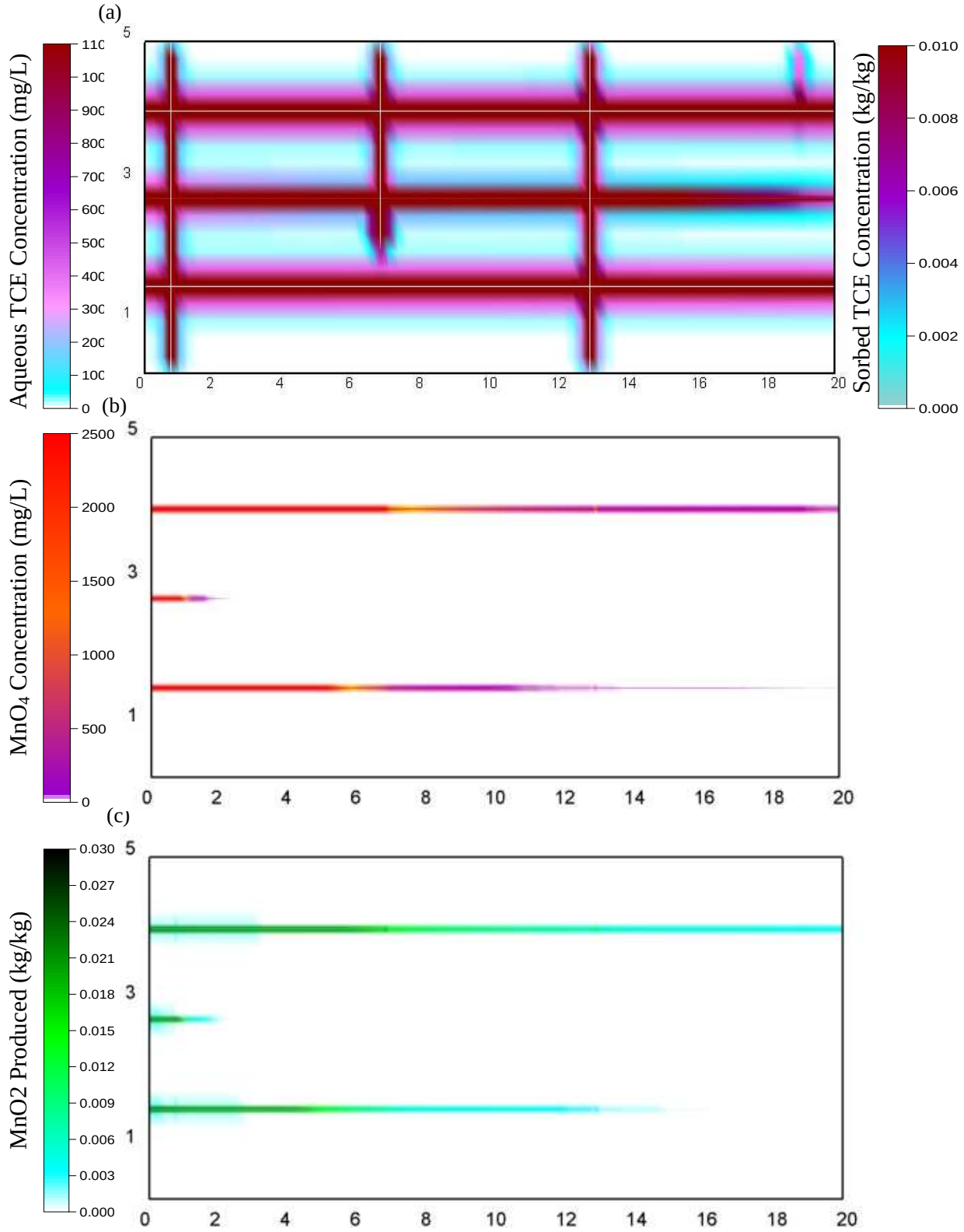

Figure A5: Distribution of aqueous species concentrations at t_{TOTAL} =23 years for 1 Year Pulsing Simulation, after 2 years of chemical oxidation, aging period: (a) TCE, (b) MnO_4, (c) MnO_2

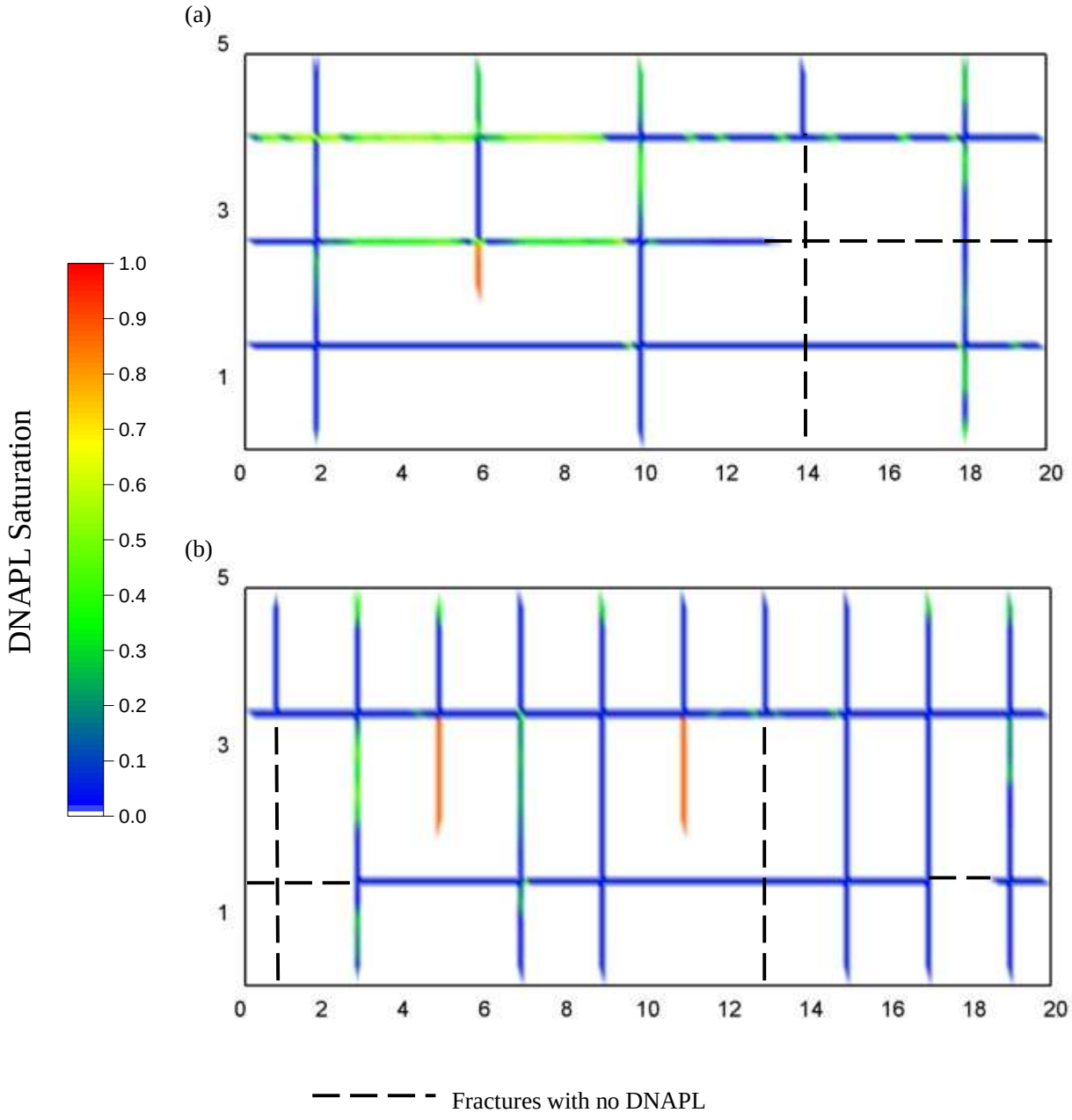

Figure A6: DNAPL distribution for (a) Shale and (b) Granite at t_{TOTAL} = 1 year when all DNAPL migration has ceased.

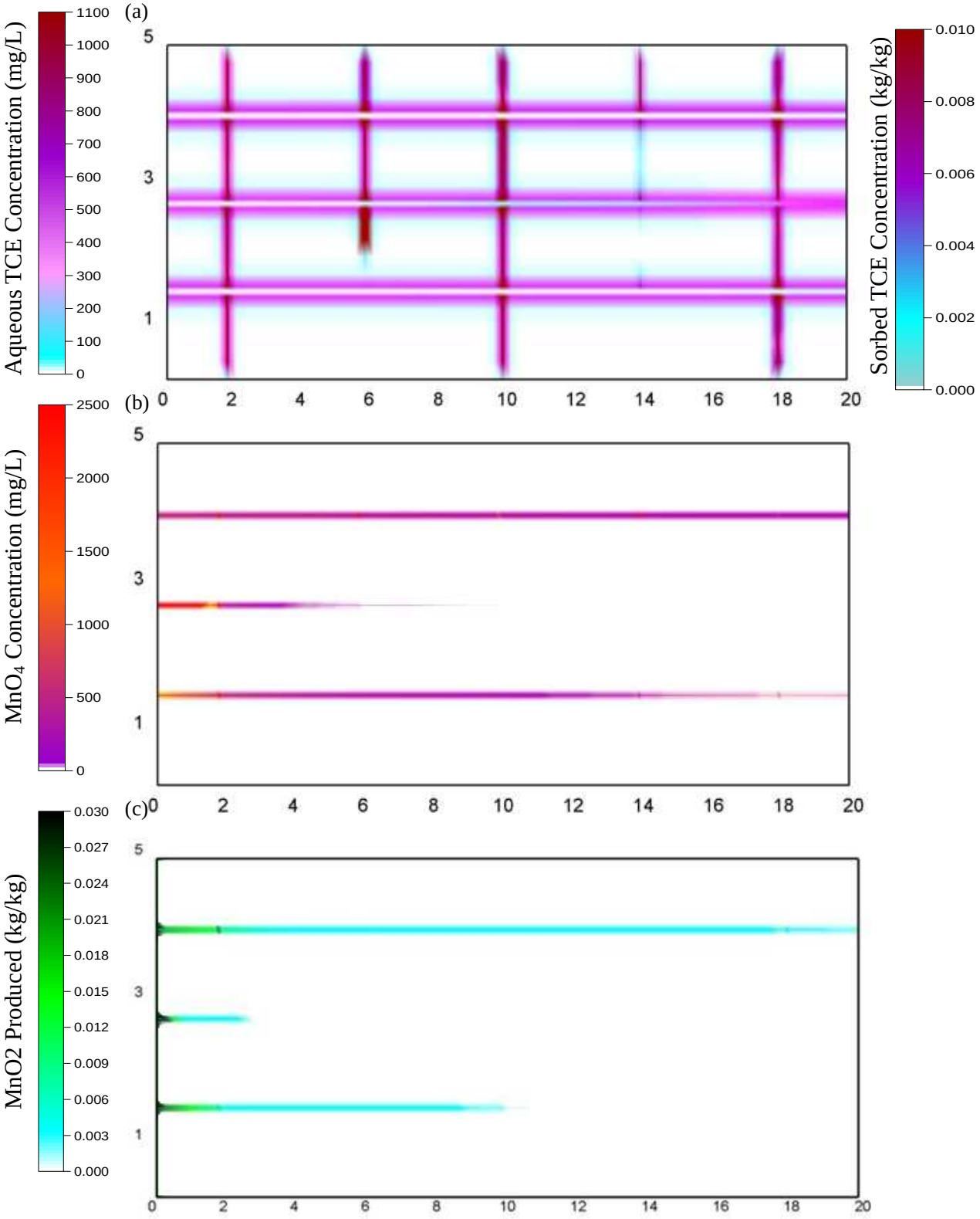

Figure A7: Distribution of aqueous species concentrations at t_{TOTAL} =23 years for Shale, after 2 years of chemical oxidation, aging period: (a) TCE, (b) MnO_4, (c) MnO_2

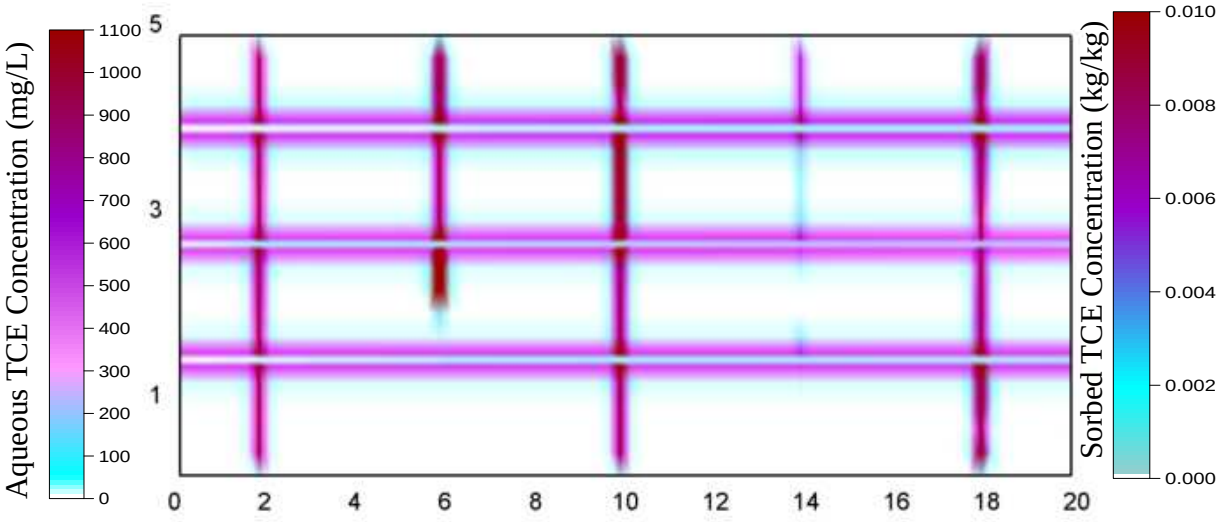

Figure A8: Distribution of aqueous TCE concentrations at t_{TOTAL} =28 years for Shale, 5 years after chemical oxidation

(a)

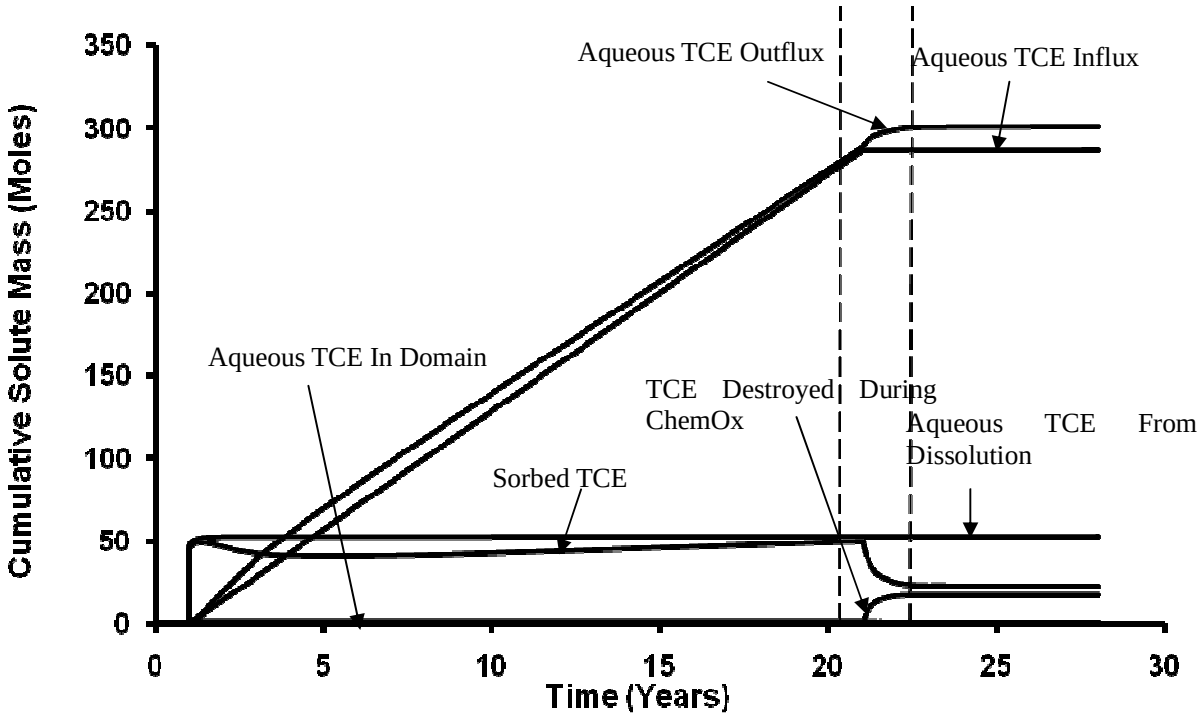

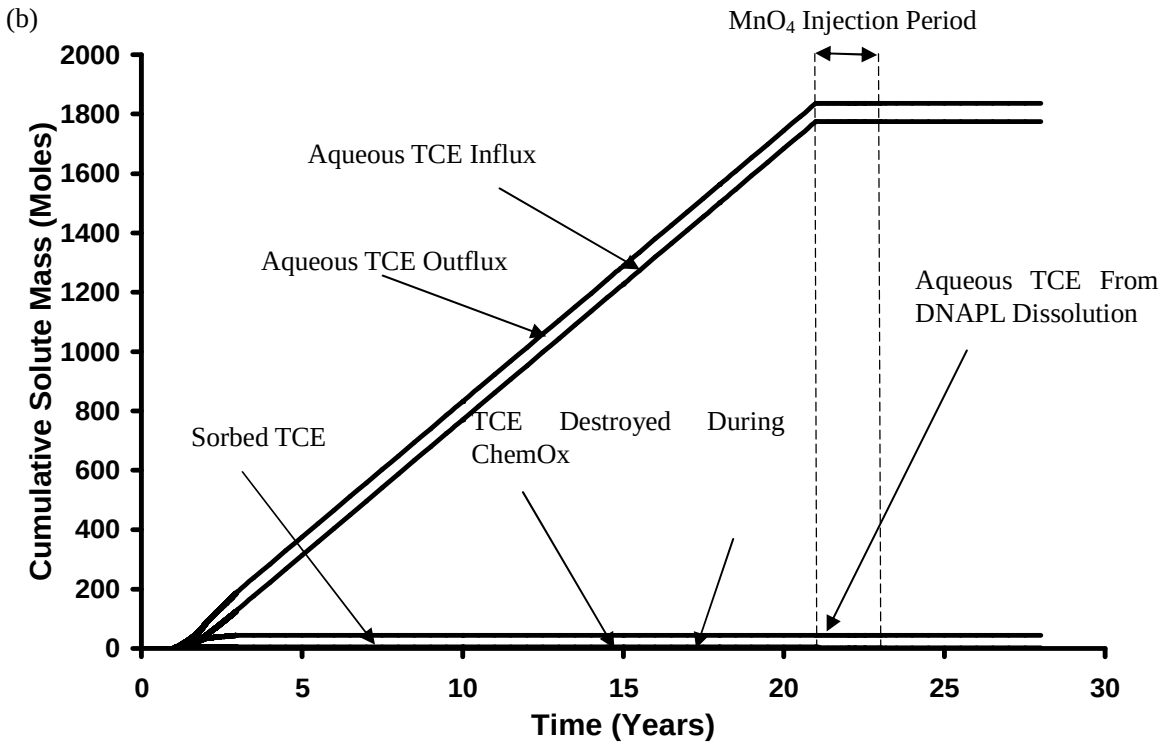

Figure A9: Cumulative aqueous and sorbed TCE from all sinks and sources for (a) Shale Simulation and (b) Granite Simulation.

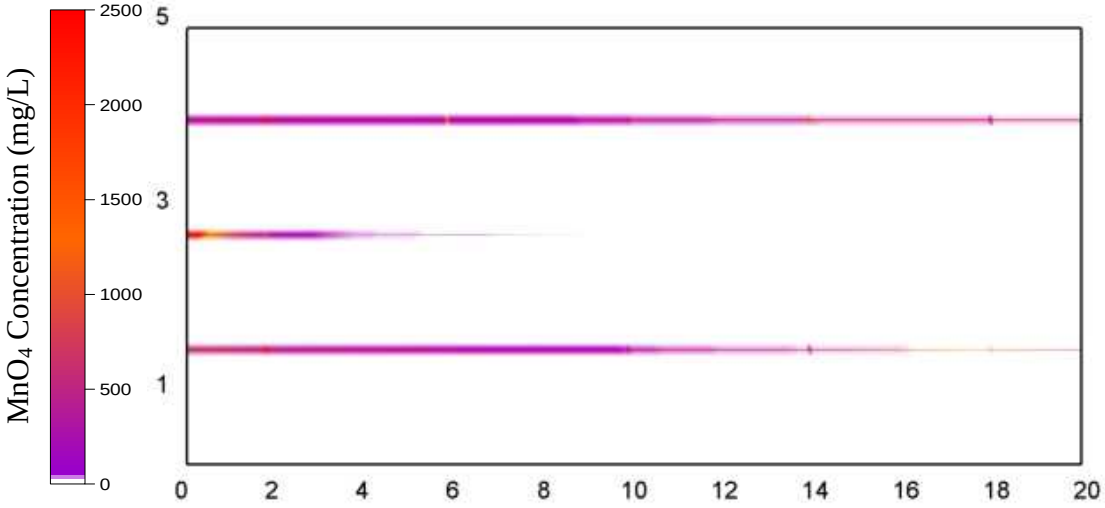

Figure A10: Distribution of MnO4 concentrations at t_{TOTAL} =22 years for Shale, 1 years after chemical oxidation

(a)

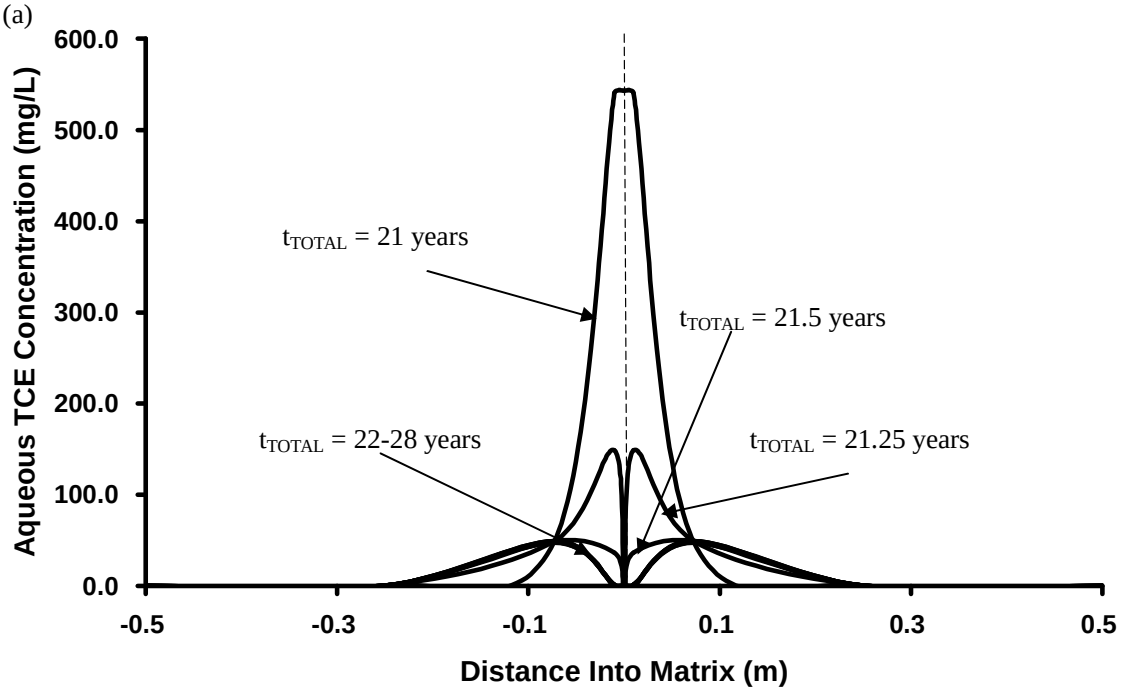
600.0
500.0
400.0
300.0
200.0
100.0
0.0
Aqueous TCE Concentration (mg/L)
-0.5
-0.3
-0.1
0.1
0.3
0.5
Distance Into Matrix (m)
t_TOTAL = 21 years
t_TOTAL = 21.5 years
t_TOTAL = 22-28 years
t_TOTAL = 21.25 years

(b)

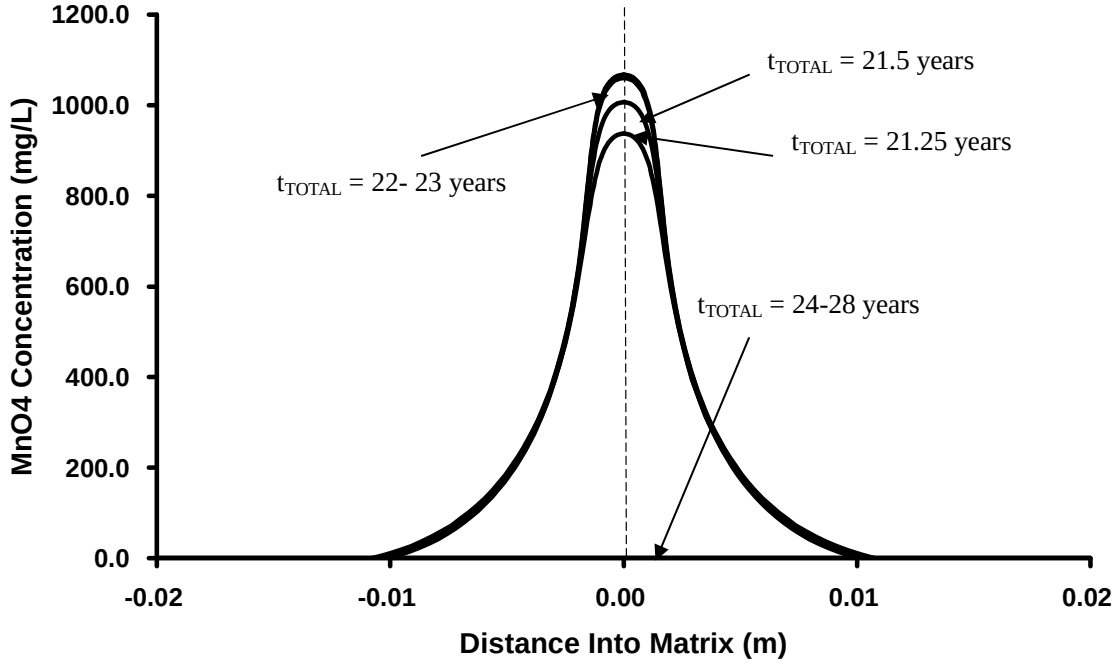
1200.0
1000.0
800.0
600.0
400.0
200.0
0.0
MnO4 Concentration (mg/L)
-0.02
-0.01
0.00
0.01
0.02
Distance Into Matrix (m)
t_TOTAL = 21.5 years
t_TOTAL = 21.25 years
t_TOTAL = 22- 23 years
t_TOTAL = 24-28 years

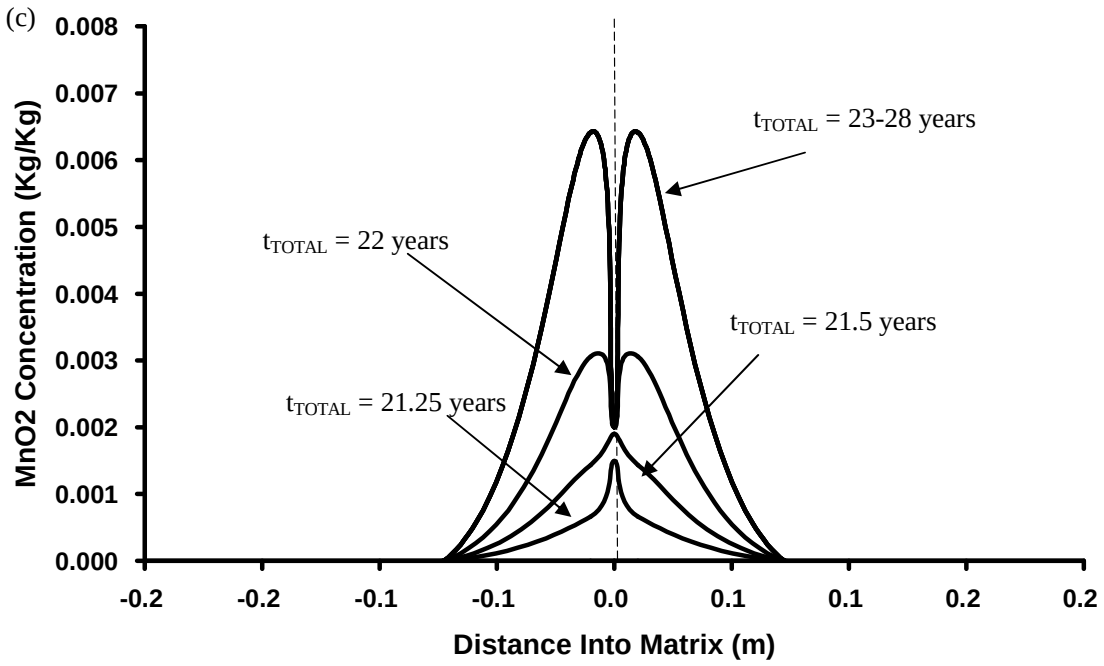

Figure A11: Concentration profile of (a) aqueous TCE; (b) MnO_4 and (c) MnO_2across a single fracture for the Base Case. Shown is a 1.0 m cross-section across a horizontal fracture (dotted line denotes location of the facture).

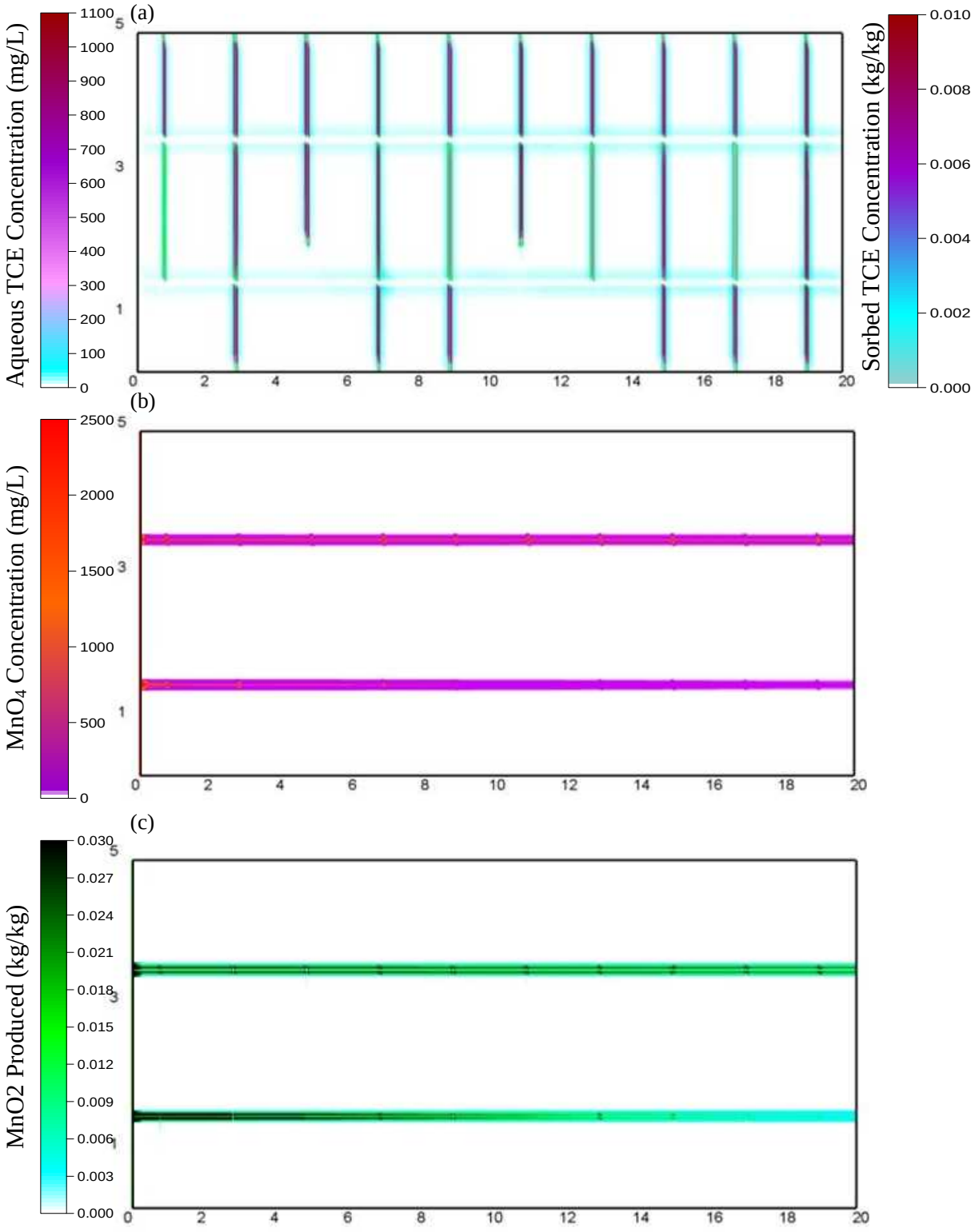

Figure A12: Distribution of aqueous species concentrations at t_{TOTAL} =23 years for Granite, after 2 years of chemical oxidation, aging period: (a) TCE, (b) MnO_4, (c) MnO_2

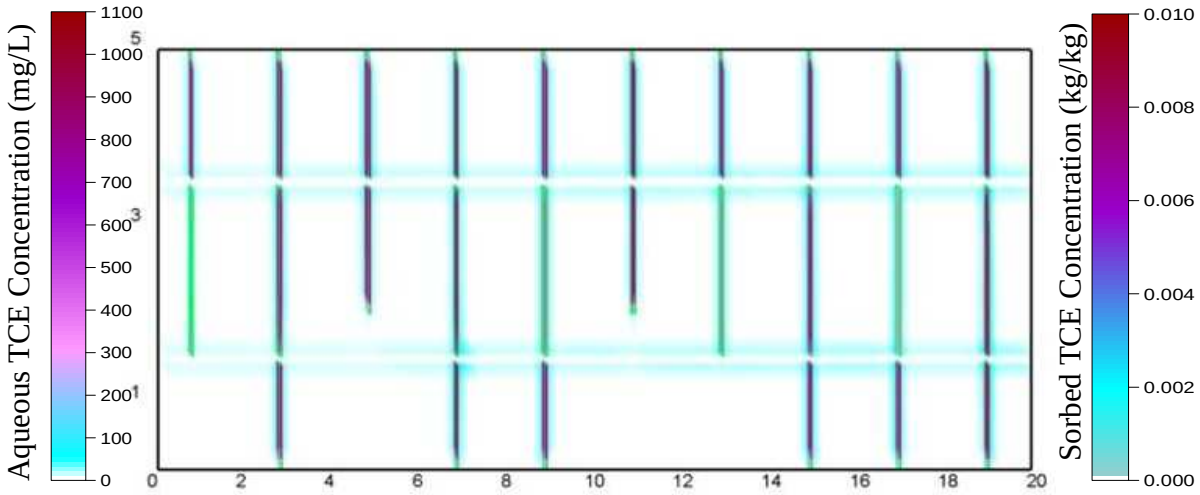

Figure A13: Distribution of aqueous TCE concentrations at t_{TOTAL} =28 years for Granite, 5 years after chemical oxidation

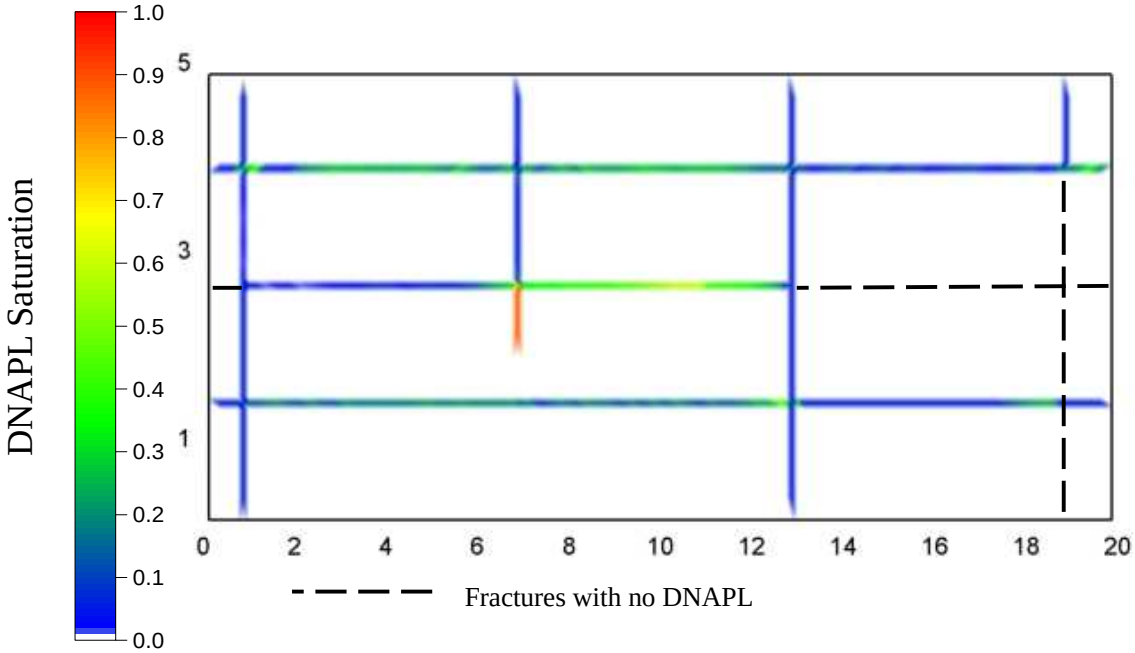

Figure A14: DNAPL distribution for PCE Simulation at t_{TOTAL} = 1 year when all DNAPL migration has ceased.

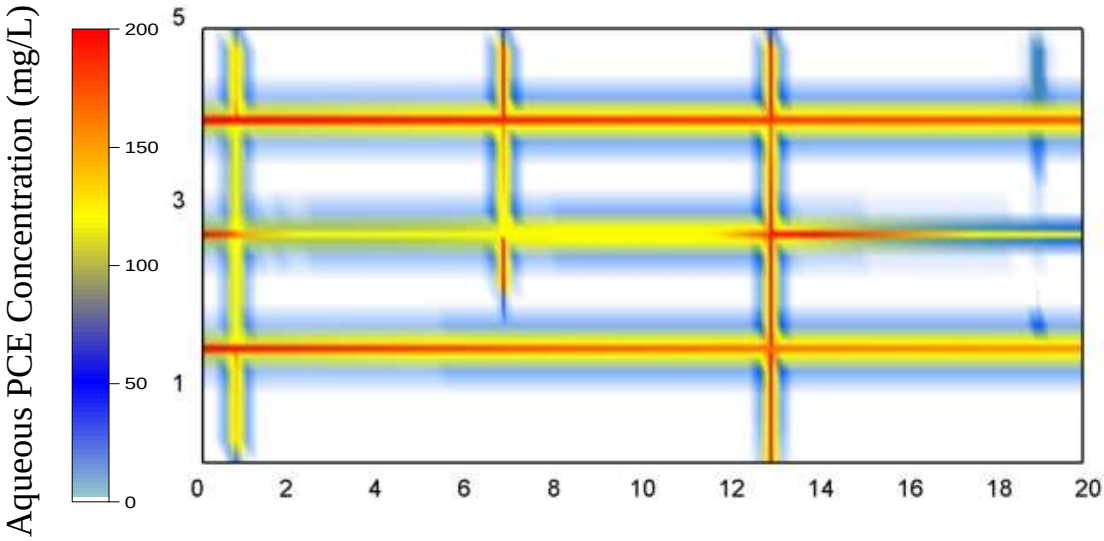

Figure A15: Distribution of aqueous PCE after 20 years of site aging (i.e., t_{TOTAL} = 21 years) for PCE simulation.

APPENDIX B

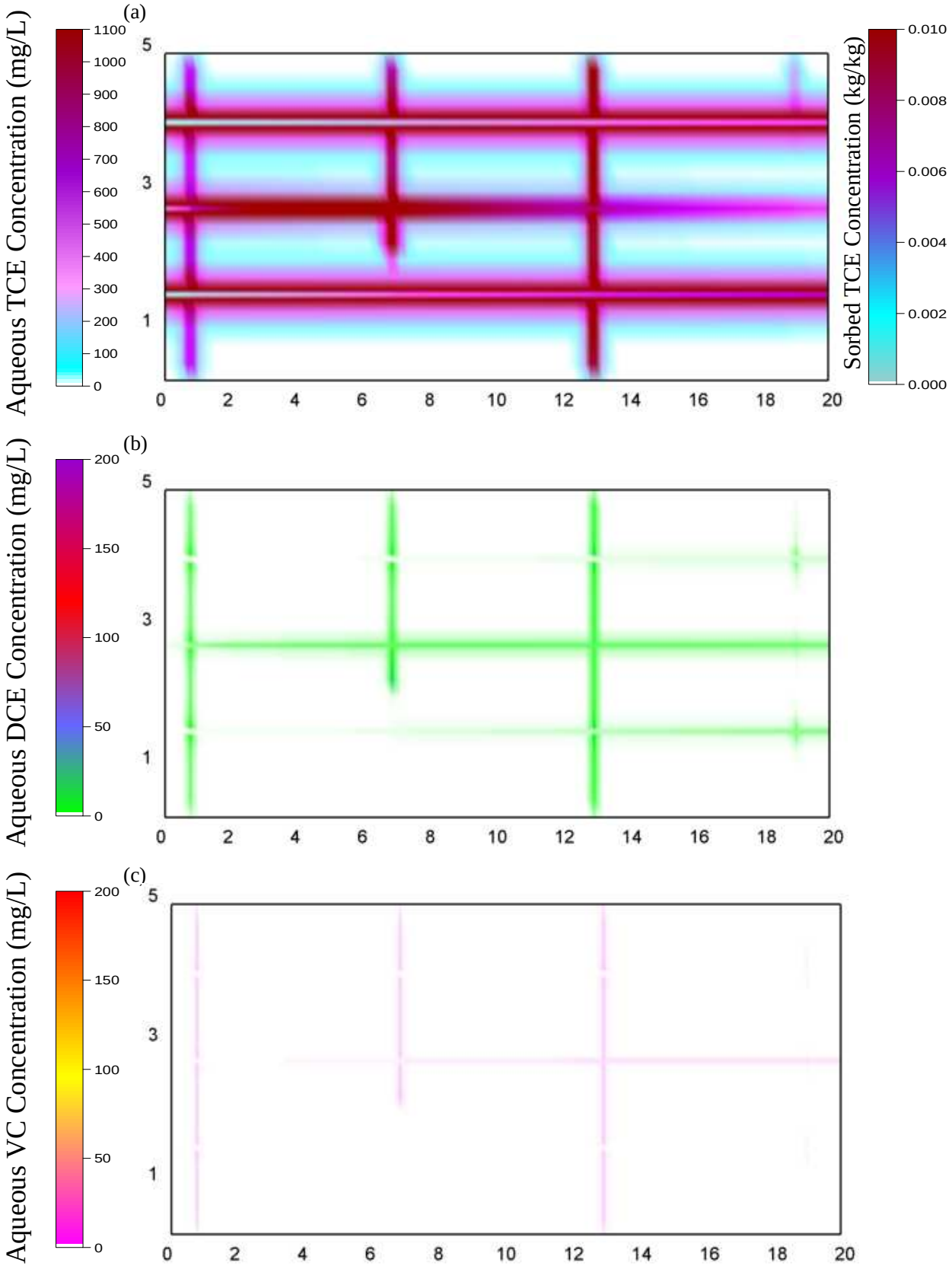
(a)
Aqueous TCE Concentration (mg/L)
1100
1000
900
800
700
600
500
400
300
200
100
0
Sorbed TCE Concentration (kg/kg)
0.010
0.008
0.006
0.004
0.002
0.000
5
3
1
0
2
4
6
8
10
12
14
16
18
20
(b)
Aqueous DCE Concentration (mg/L)
200
150
100
50
0
(c)
Aqueous VC Concentration (mg/L)

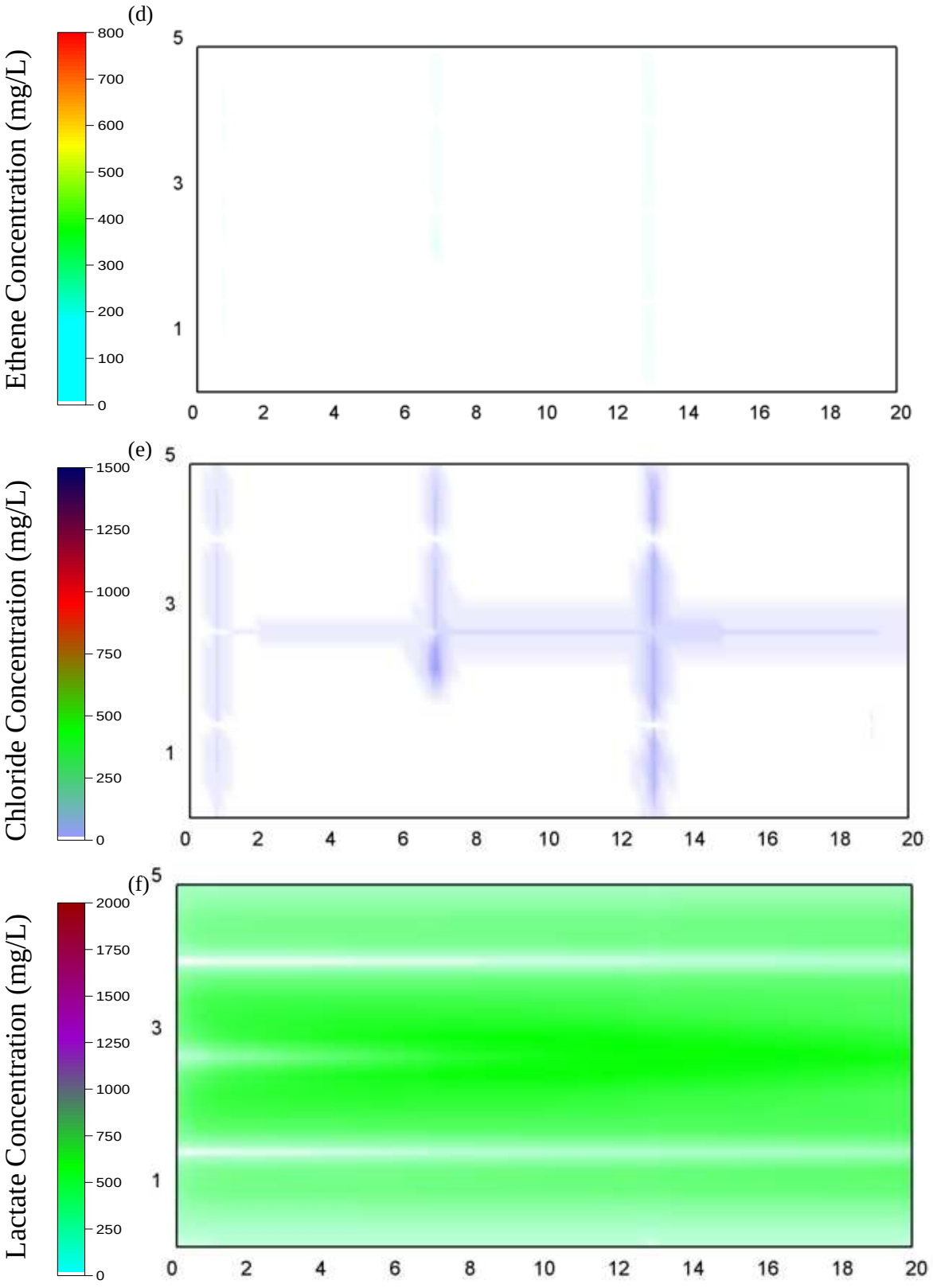

Figure B1: Distribution of (a) Aqueous TCE; (b) Aqueous DCE; (c) Aqueous VC; (d) Ethene; (e) Chloride; (f) Lactate, 5 years after lactate injection for indigenous bacteria present in facture only.

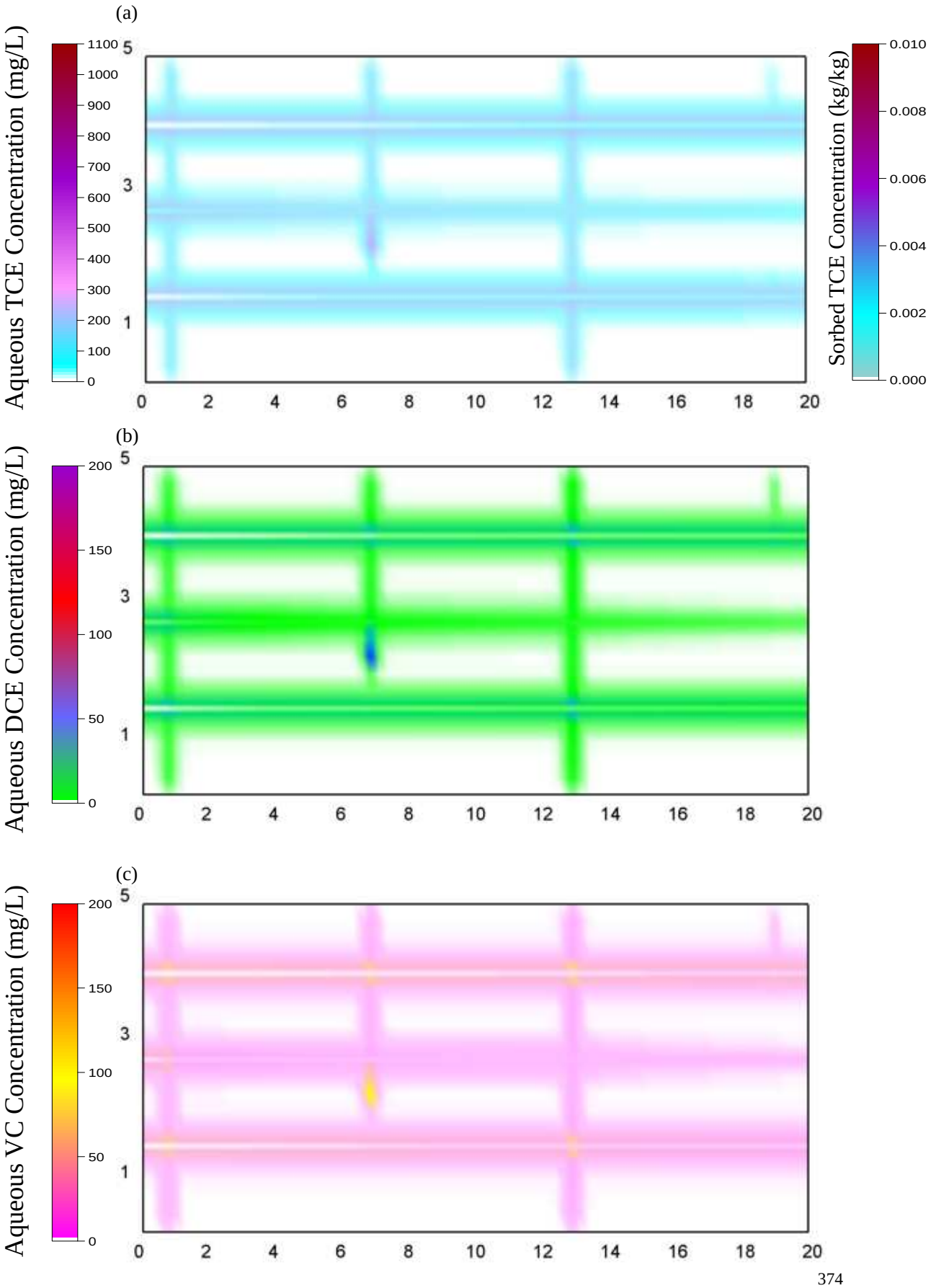
(a)
Aqueous TCE Concentration (mg/L)
1100
1000
900
800
700
600
500
400
300
200
100
0
Sorbed TCE Concentration (kg/kg)
0.010
0.008
0.006
0.004
0.002
0.000
5
3
1
0
2
4
6
8
10
12
14
16
18
20
(b)
Aqueous DCE Concentration (mg/L)
200
150
100
50
0
(c)
Aqueous VC Concentration (mg/L)

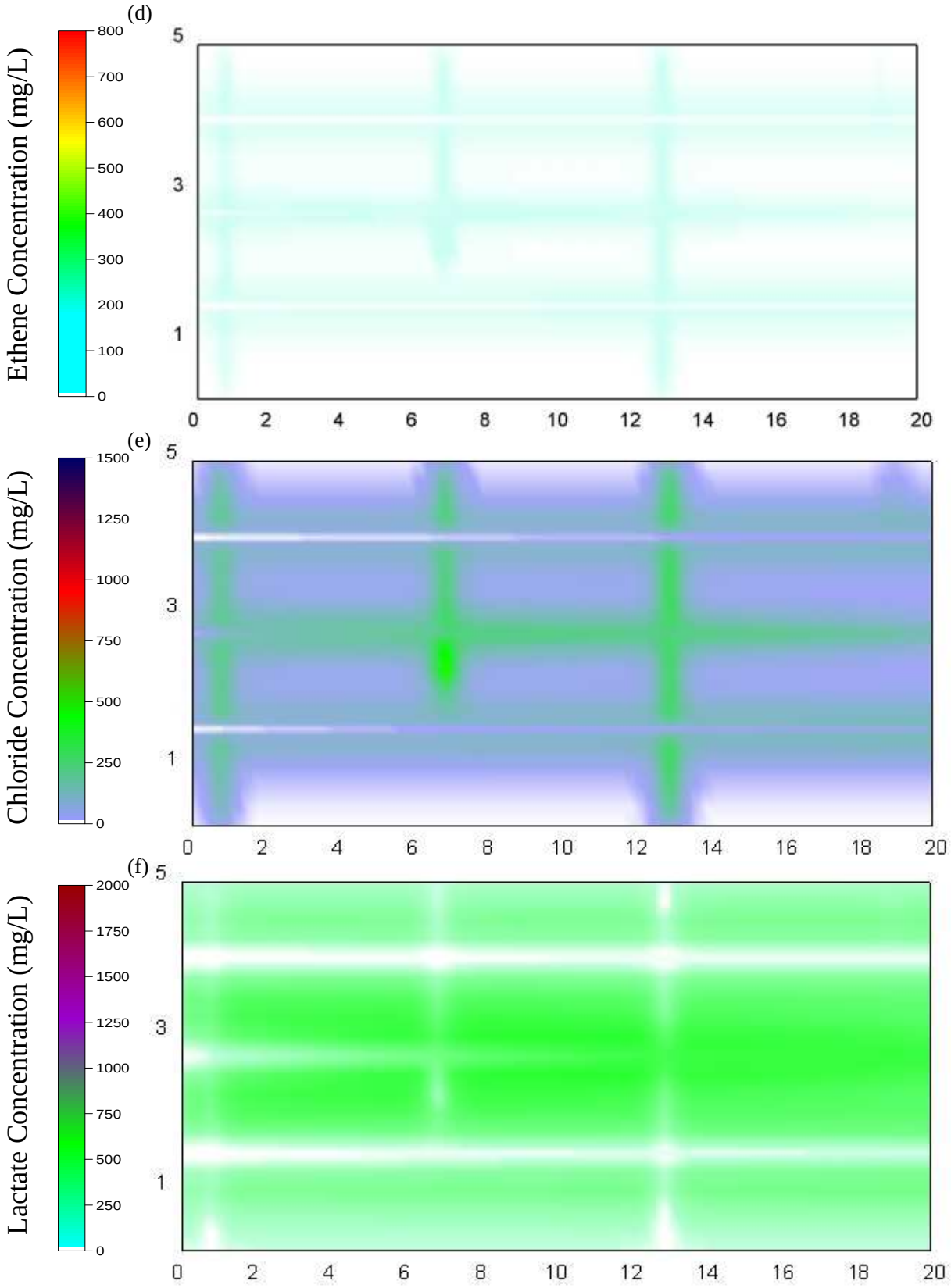

Figure B2: Distribution of (a) Aqueous TCE; (b) Aqueous DCE; (c) Aqueous VC; (d) Ethene; (e) Chloride; (f) Lactate, 5 years after lactate injection for low decay rate.

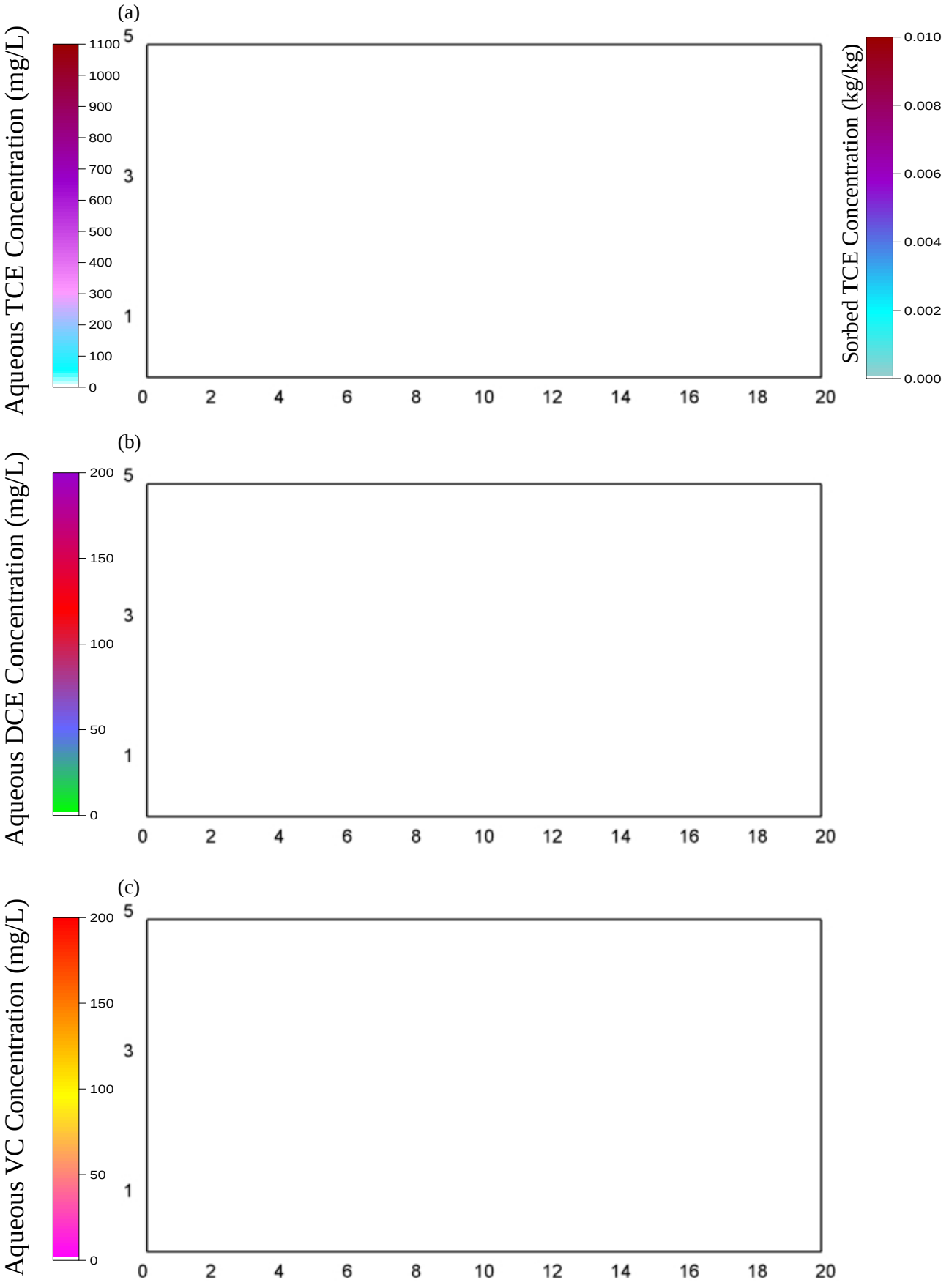
(a)
Aqueous TCE Concentration (mg/L)
1100
1000
900
800
700
600
500
400
300
200
100
0
Sorbed TCE Concentration (kg/kg)
0.010
0.008
0.006
0.004
0.002
0.000
5
3
1
0
2
4
6
8
10
12
14
16
18
20
(b)
Aqueous DCE Concentration (mg/L)
200
150
100
50
0
(c)
Aqueous VC Concentration (mg/L)

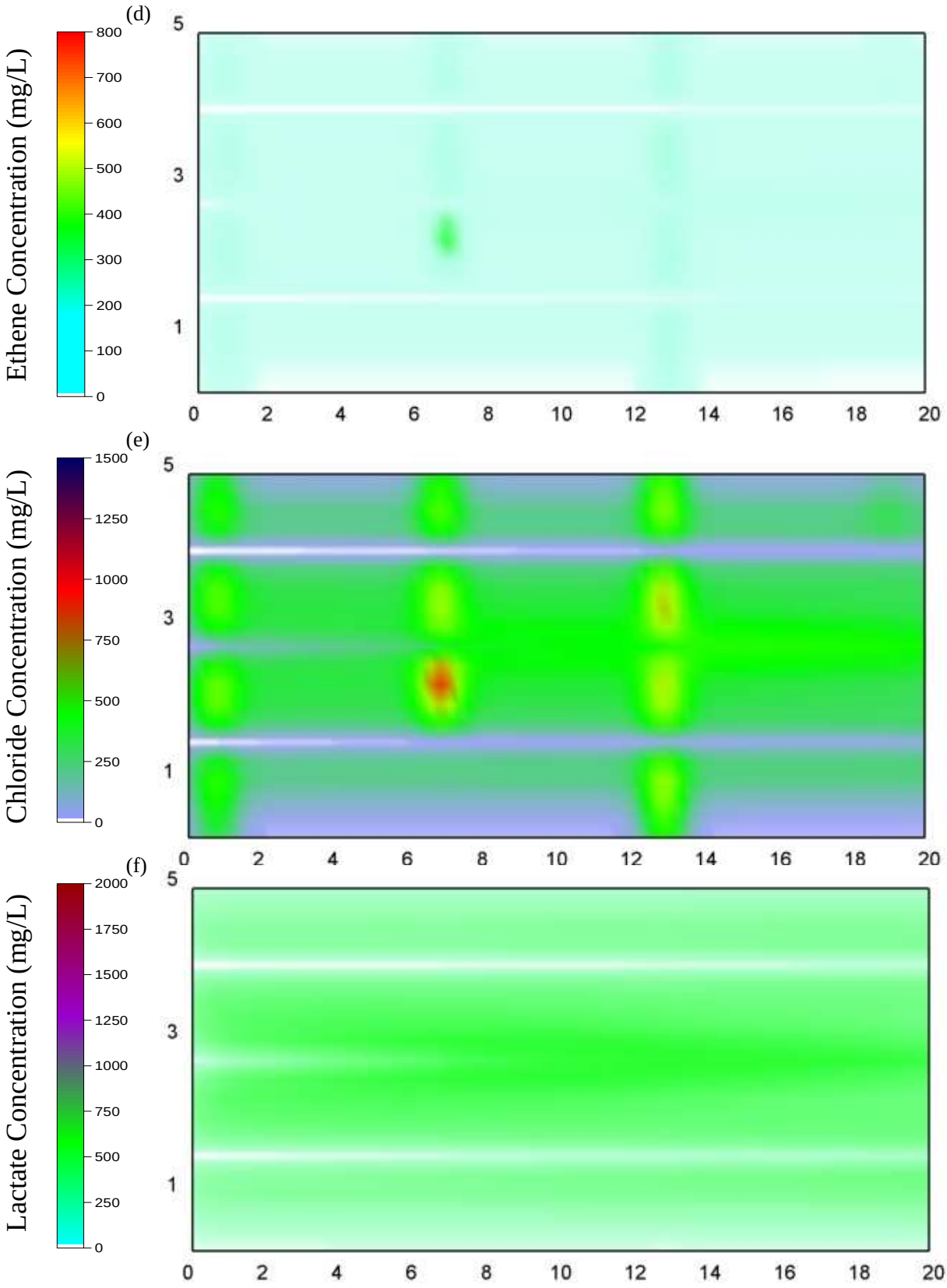

Figure B3: Distribution of (a) Aqueous TCE; (b) Aqueous DCE; (c) Aqueous VC; (d) Ethene; (e) Chloride; (f) Lactate, 5 years after lactate injection for high decay rate.

(a)

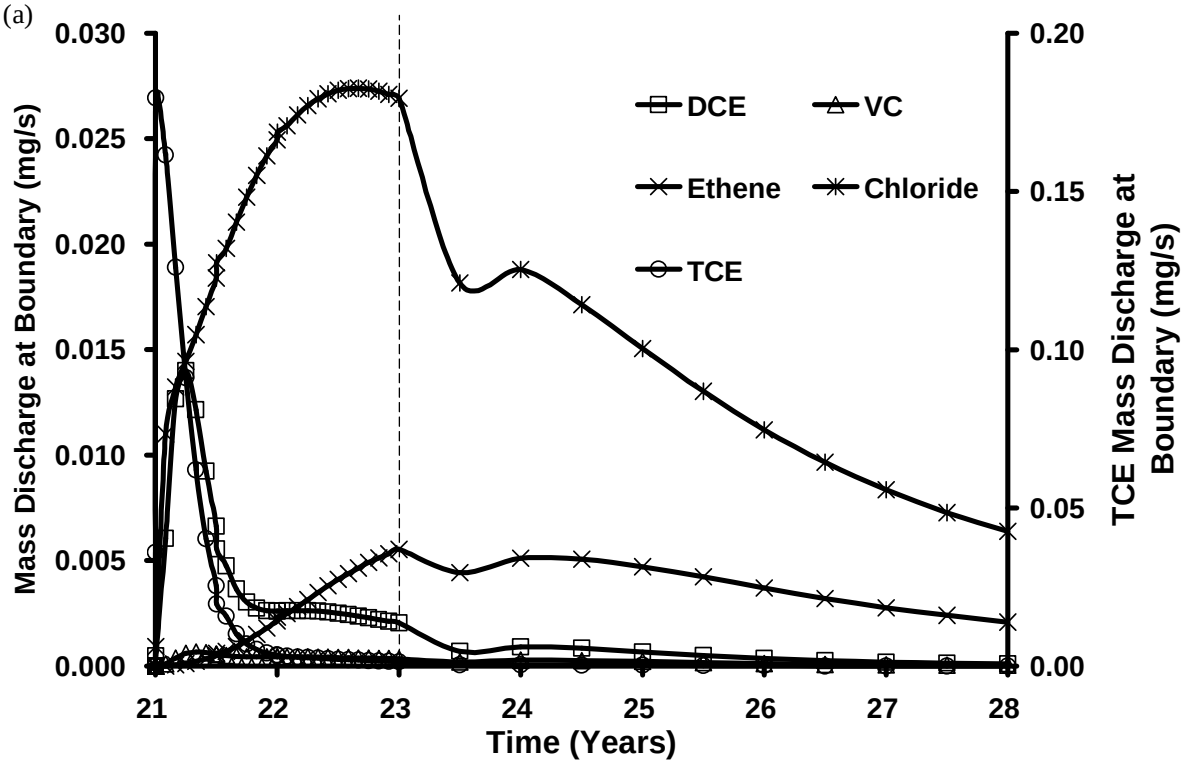
Mass Discharge at Boundary (mg/s)
TCE Mass Discharge at Boundary (mg/s)
Time (Years)
DCE
VC
Ethene
Chloride
TCE
0.030
0.025
0.020
0.015
0.010
0.005
0.000
0.20
0.15
0.10
0.05
0.00
21
22
23
24
25
26
27
28

(b)

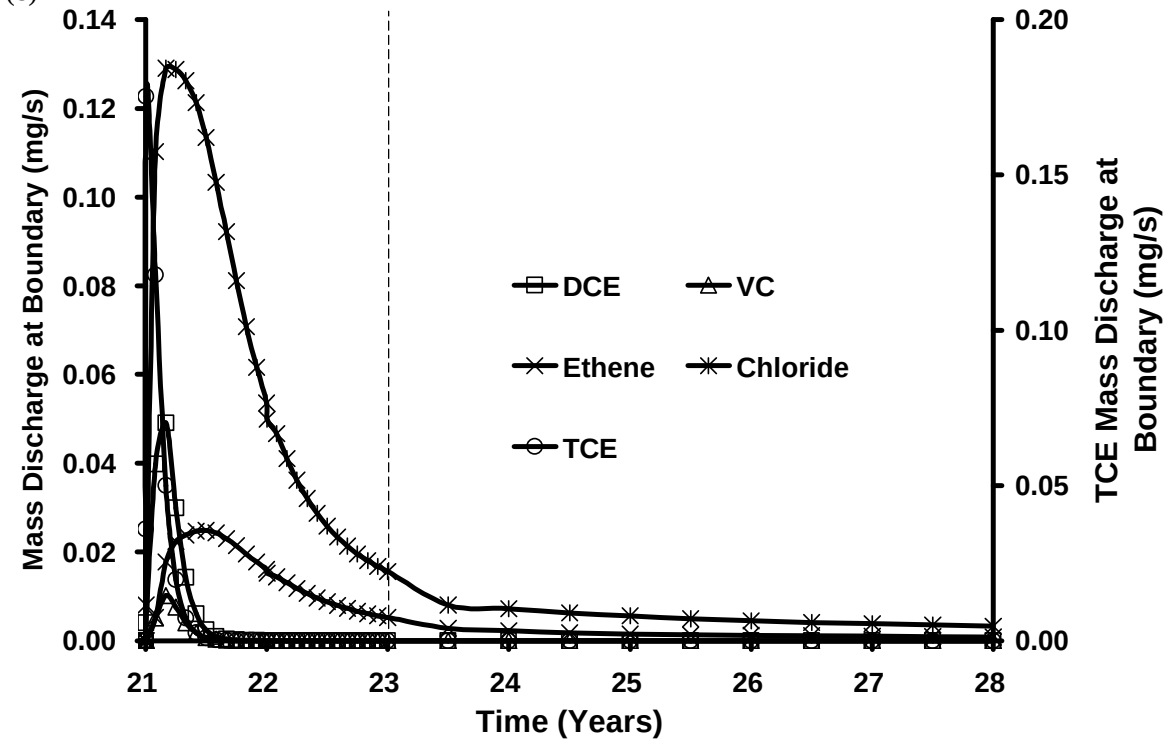
Mass Discharge at Boundary (mg/s)
TCE Mass Discharge at Boundary (mg/s)
Time (Years)
DCE
VC
Ethene
Chloride
TCE
0.14
0.12
0.10
0.08
0.06
0.04
0.02
0.00
0.20
0.15
0.10
0.05
0.00
21
22
23
24
25
26
27
28

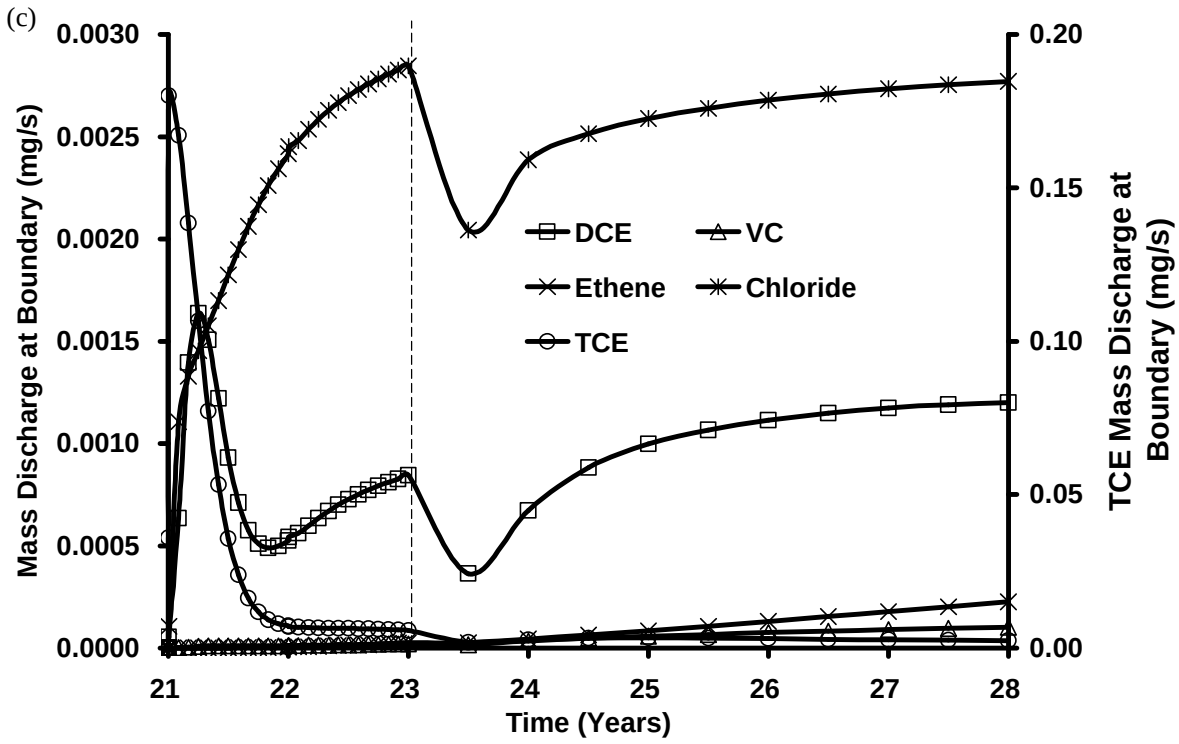

Figure B4: Total boundary mass discharge for various species in (a) Base Case; (b) High Decay Rate Parameter; (c) Low Decay Rate Parameter over time.

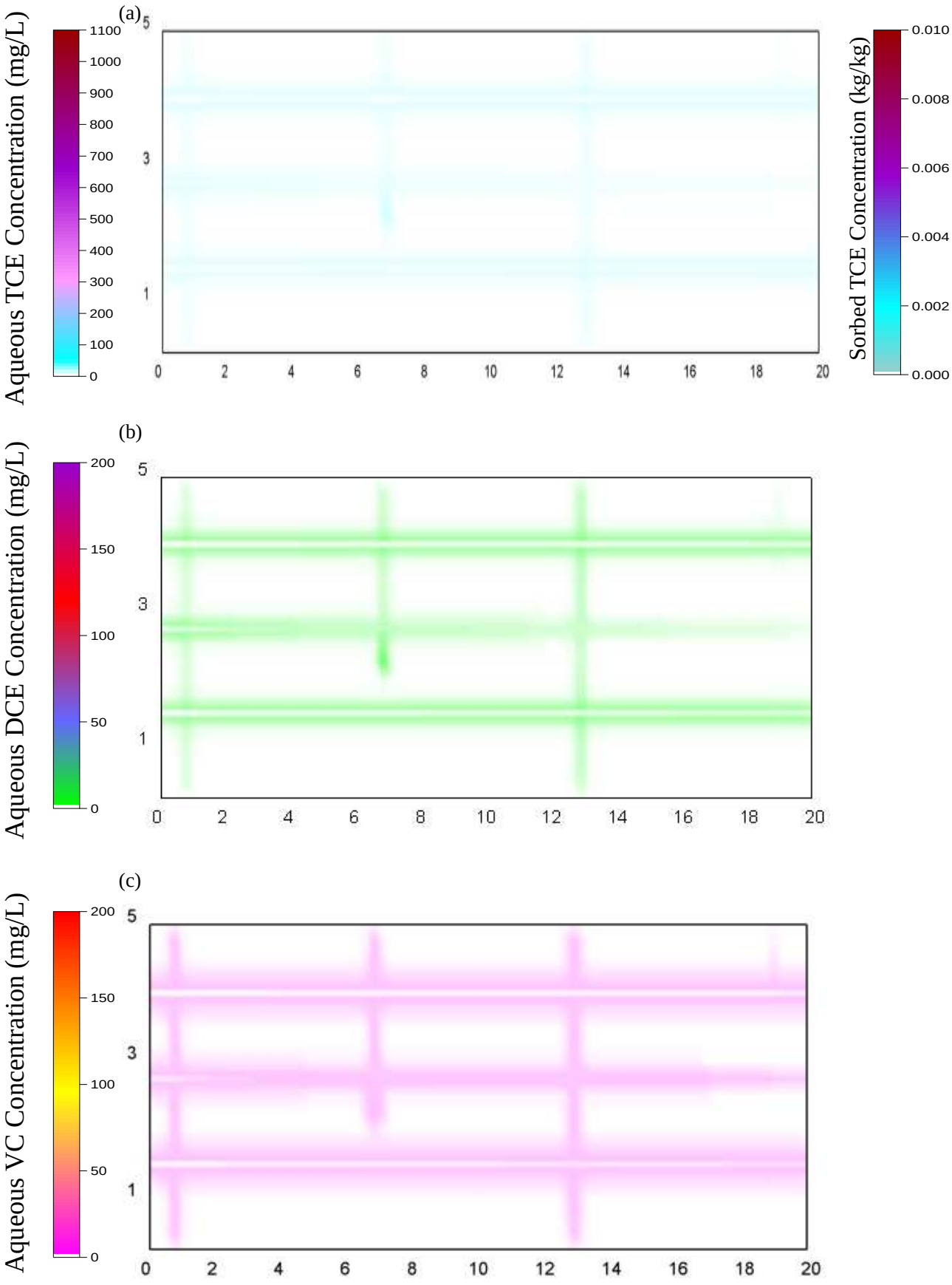
(a)
Aqueous TCE Concentration (mg/L)
1100
1000
900
800
700
600
500
400
300
200
100
0
5
3
1
0
2
4
6
8
10
12
14
16
18
20
Sorbed TCE Concentration (kg/kg)
0.010
0.008
0.006
0.004
0.002
0.000
(b)
Aqueous DCE Concentration (mg/L)
200
150
100
50
0
5
3
1
0
2
4
6
8
10
12
14
16
18
20
(c)
Aqueous VC Concentration (mg/L)
200
150
100
50
0
5
3
1
0
2
4
6
8
10
12
14
16
18
20

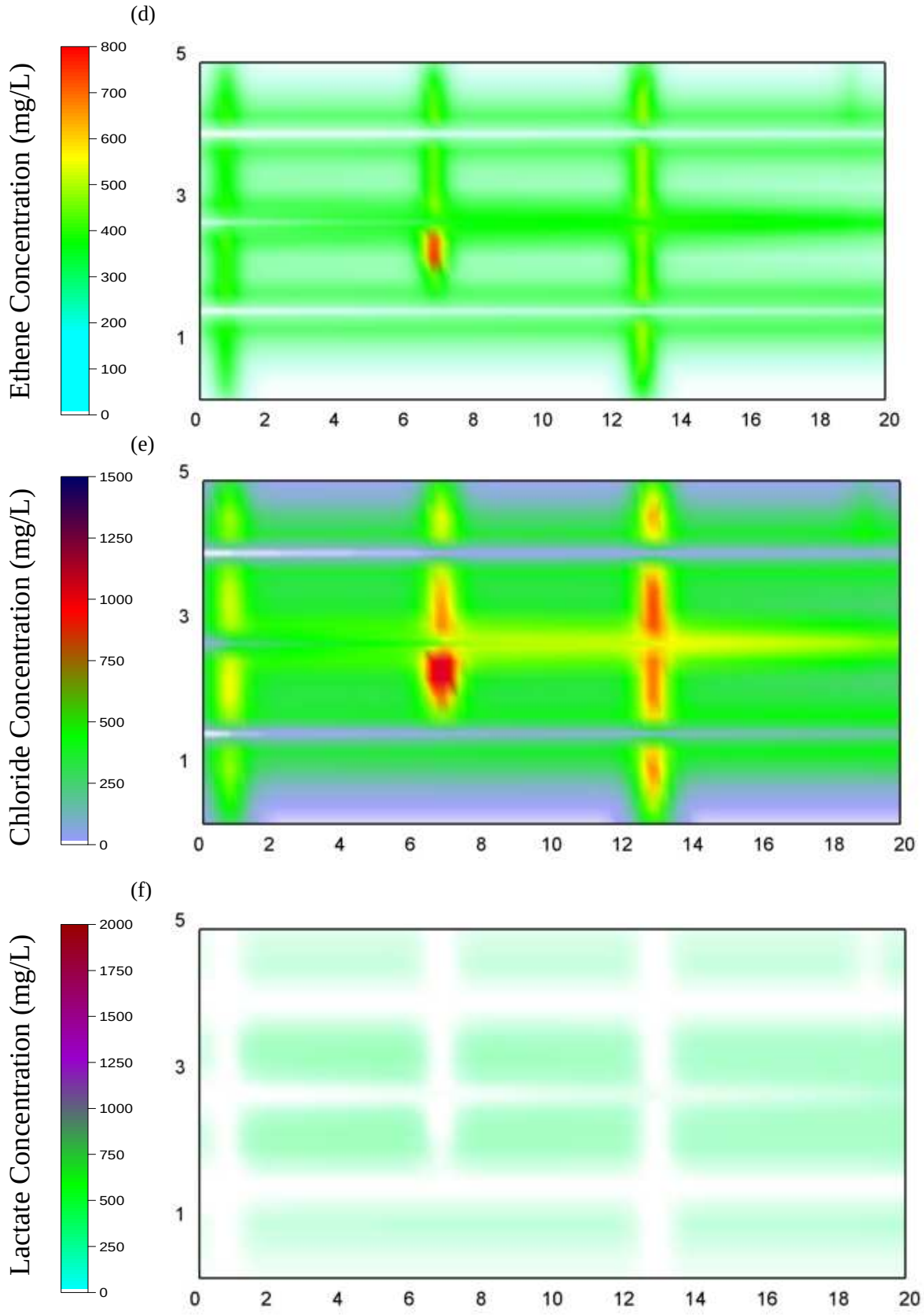

Figure B5: Distribution of (a) Aqueous TCE; (b) Aqueous DCE; (c) Aqueous VC; (d) Ethene; (e) Chloride; (f) Lactate, 5 years after lactate injection for 3 Months pulse injection simulation.

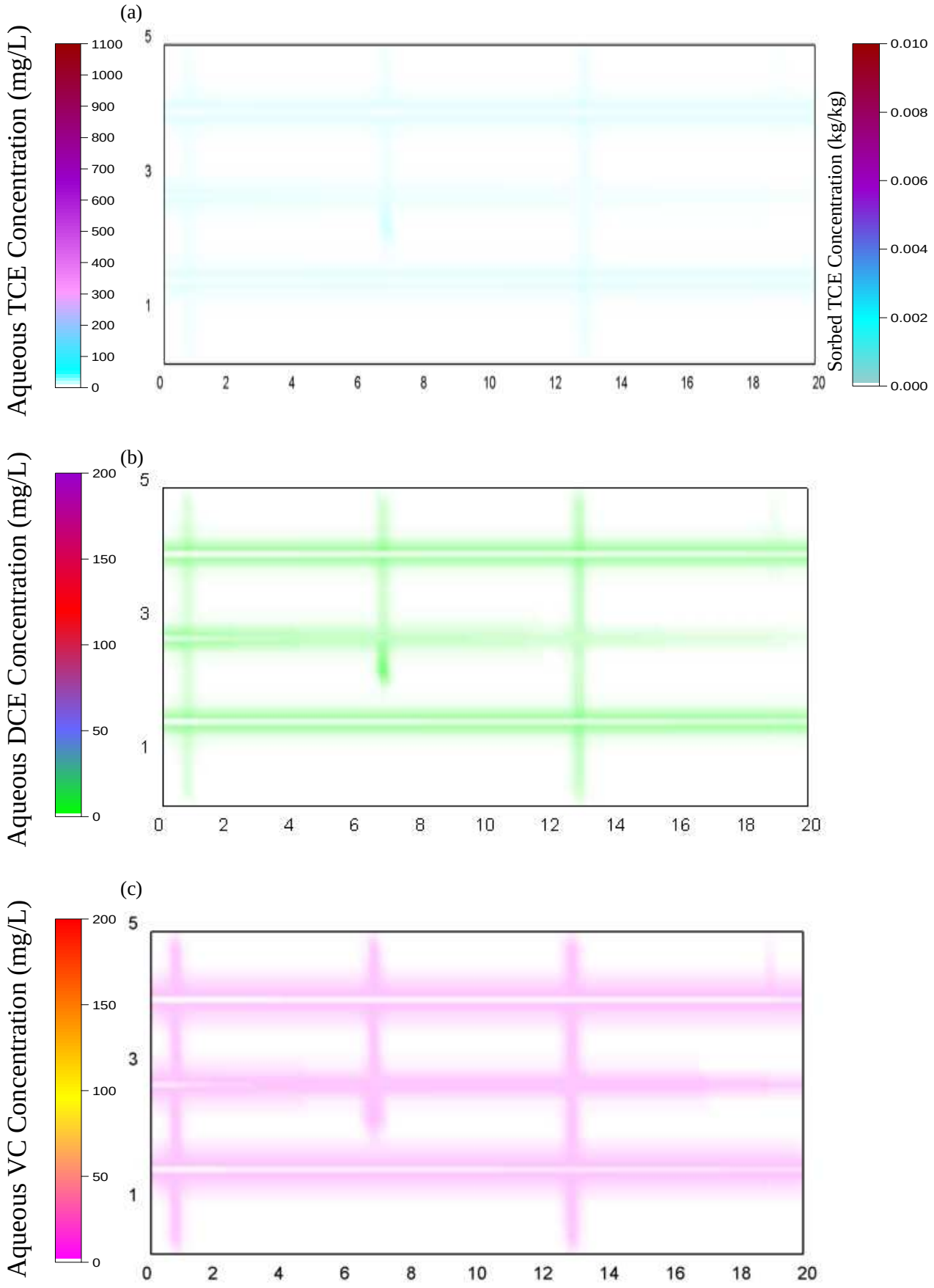
(a)
Aqueous TCE Concentration (mg/L)
1100
1000
900
800
700
600
500
400
300
200
100
0
5
3
1
0
2
4
6
8
10
12
14
16
18
20
Sorbed TCE Concentration (kg/kg)
0.010
0.008
0.006
0.004
0.002
0.000
(b)
Aqueous DCE Concentration (mg/L)
200
150
100
50
0
5
3
1
0
2
4
6
8
10
12
14
16
18
20
(c)
Aqueous VC Concentration (mg/L)
200
150
100
50
0
5
3
1
0
2
4
6
8
10
12
14
16
18
20

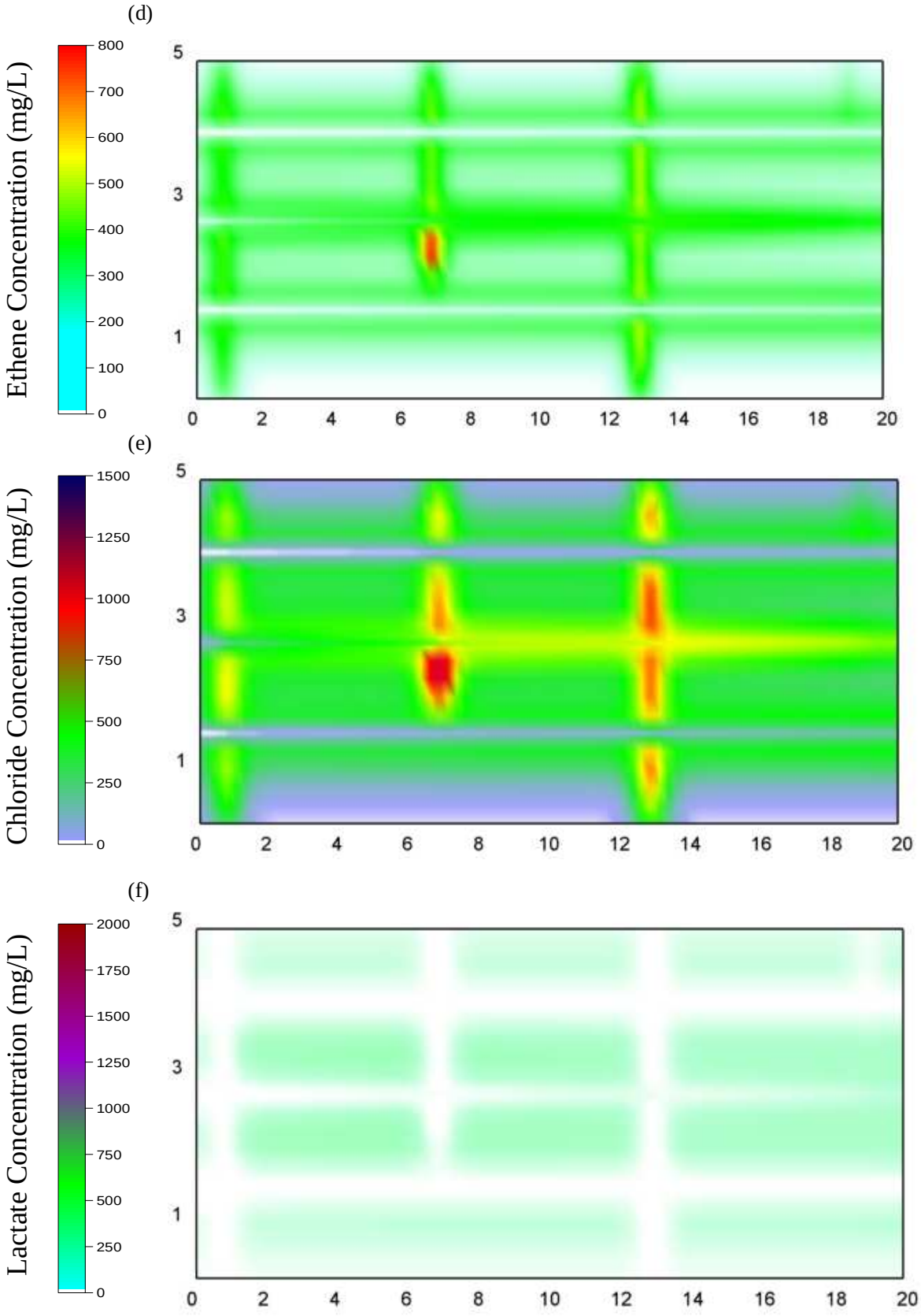

Figure B6: Distribution of (a) Aqueous TCE; (b) Aqueous DCE; (c) Aqueous VC; (d) Ethene; (e) Chloride; (f) Lactate, 5 years after lactate injection for 6 Months pulse injection simulation.

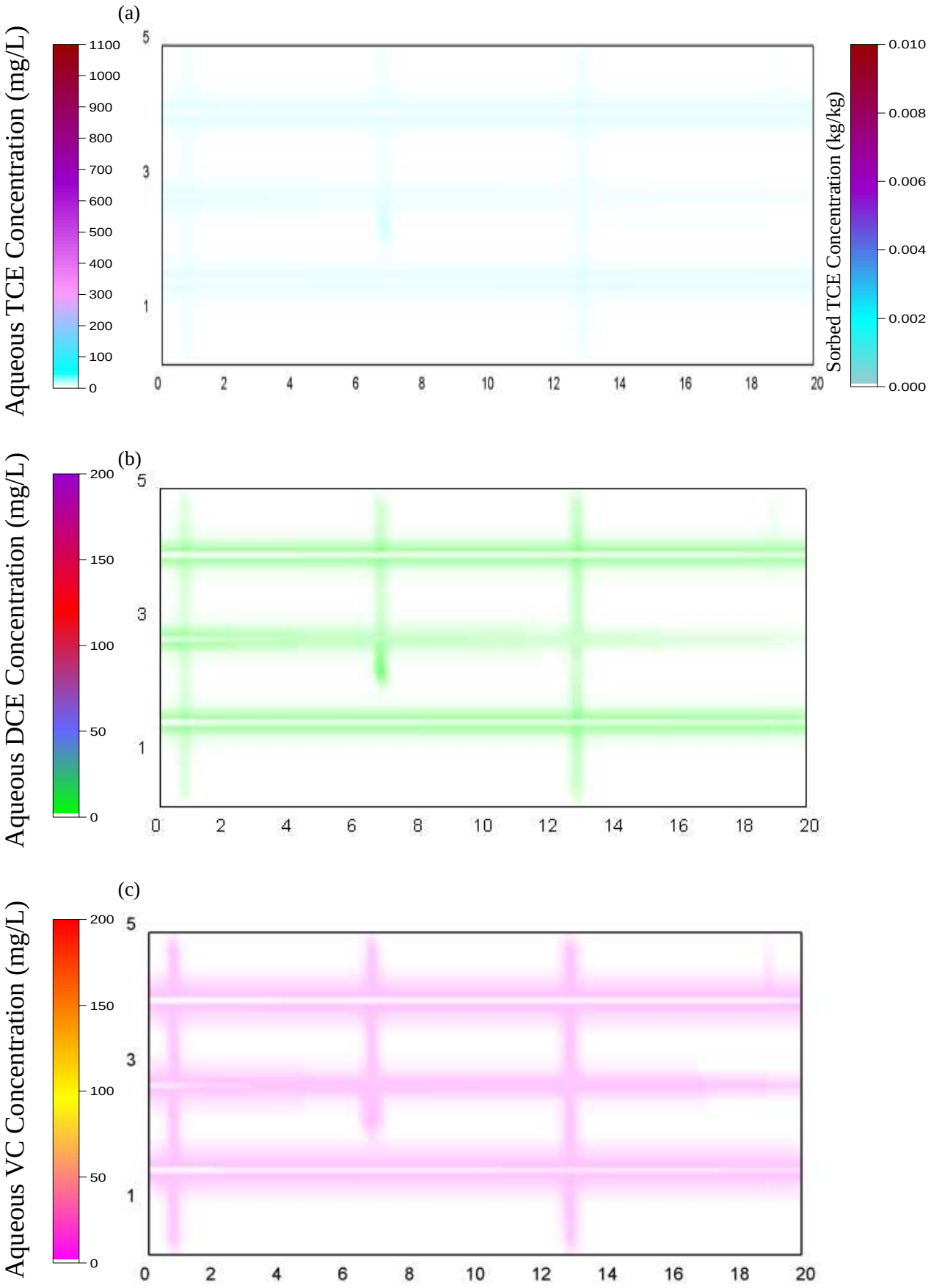
(a)
Aqueous TCE Concentration (mg/L)
1100
1000
900
800
700
600
500
400
300
200
100
0
5
3
1
0
2
4
6
8
10
12
14
16
18
20
Sorbed TCE Concentration (kg/kg)
0.010
0.008
0.006
0.004
0.002
0.000
(b)
Aqueous DCE Concentration (mg/L)
200
150
100
50
0
5
3
1
0
2
4
6
8
10
12
14
16
18
20
(c)
Aqueous VC Concentration (mg/L)
200
150
100
50
0
5
3
1
0
2
4
6
8
10
12
14
16
18
20

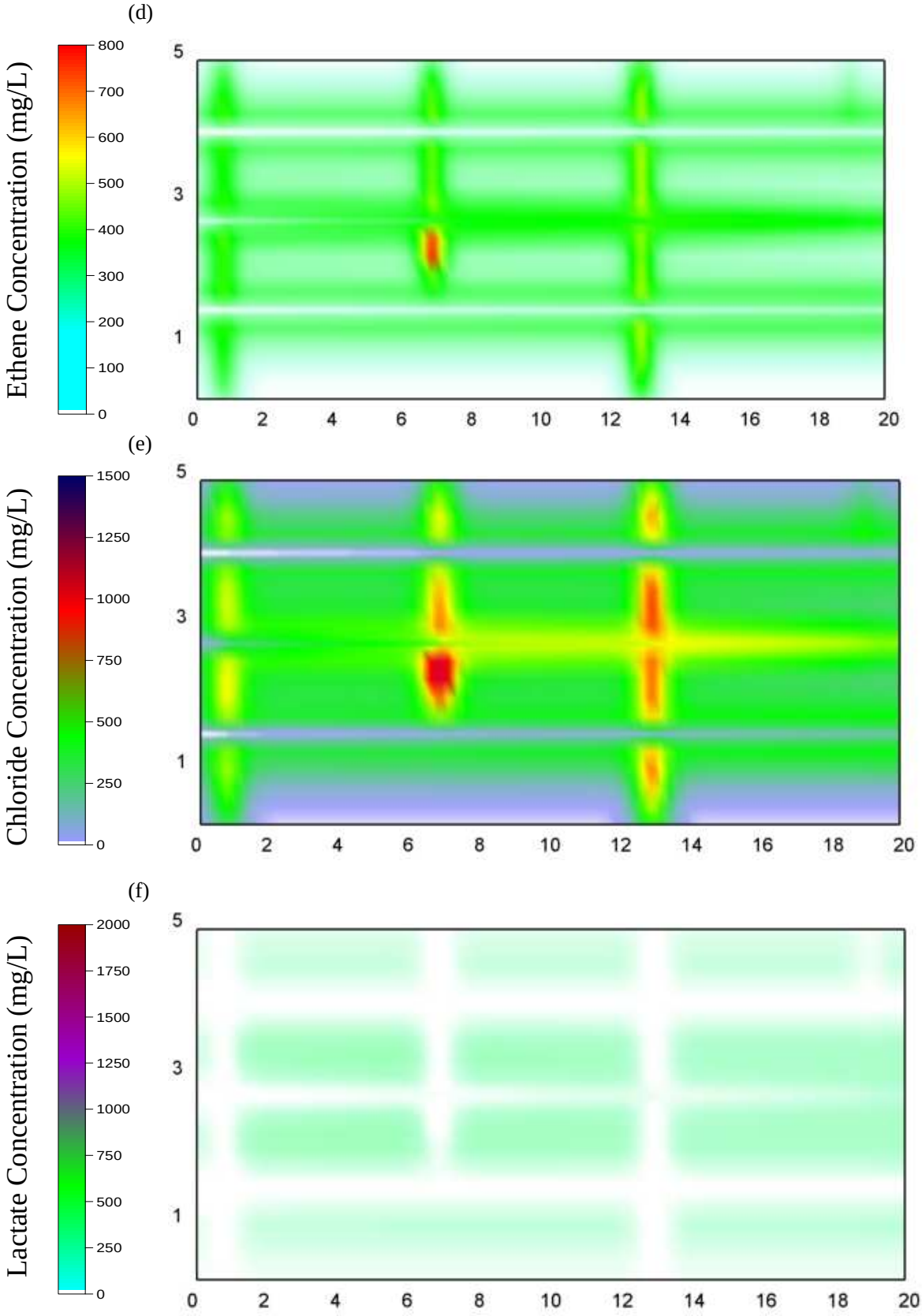

Figure B7: Distribution of (a) Aqueous TCE; (b) Aqueous DCE; (c) Aqueous VC; (d) Ethene; (e) Chloride; (f) Lactate, 5 years after lactate injection for 12 Months pulse injection simulation.

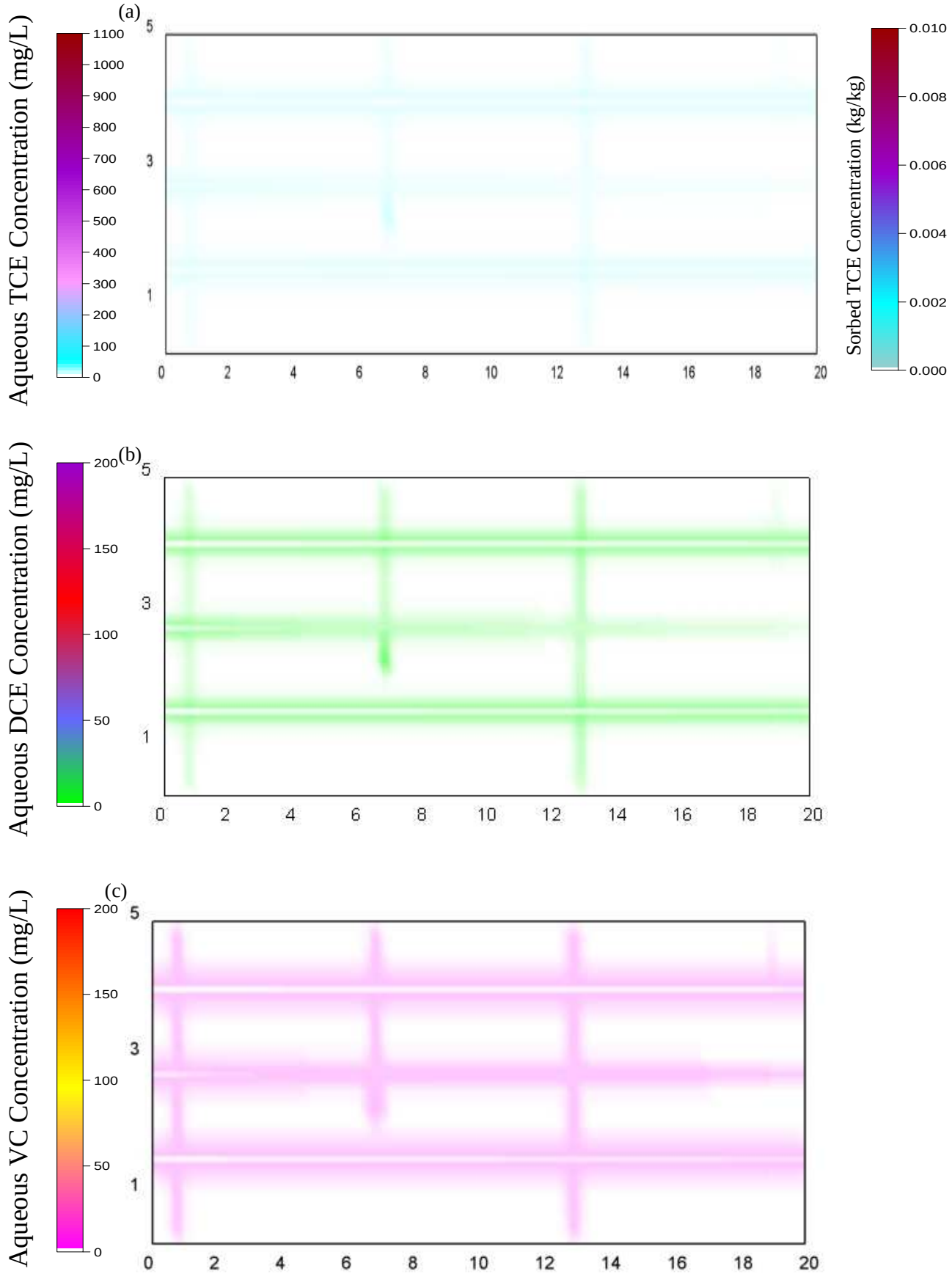
(a)
Aqueous TCE Concentration (mg/L)
1100
1000
900
800
700
600
500
400
300
200
100
0
5
3
1
0
2
4
6
8
10
12
14
16
18
20
Sorbed TCE Concentration (kg/kg)
0.010
0.008
0.006
0.004
0.002
0.000
(b)
Aqueous DCE Concentration (mg/L)
200
150
100
50
0
5
3
1
0
2
4
6
8
10
12
14
16
18
20
(c)
Aqueous VC Concentration (mg/L)
200
150
100
50
0
5
3
1
0
2
4
6
8
10
12
14
16
18
20

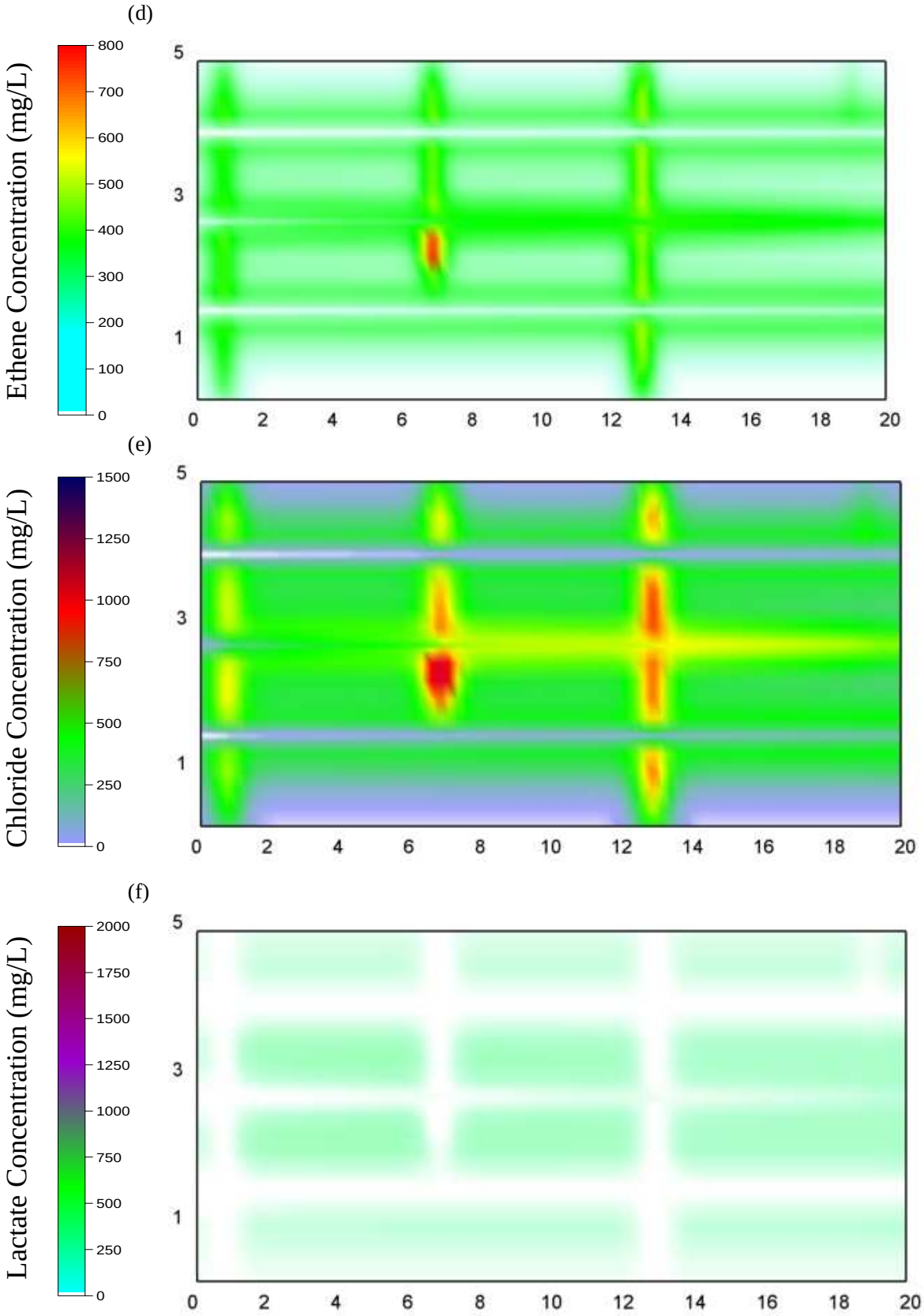

Figure B8: Distribution of (a) Aqueous TCE; (b) Aqueous DCE; (c) Aqueous VC; (d) Ethene; (e) Chloride; (f) Lactate, 5 years after lactate injection for 1000mg/L of lactate injection simulation.

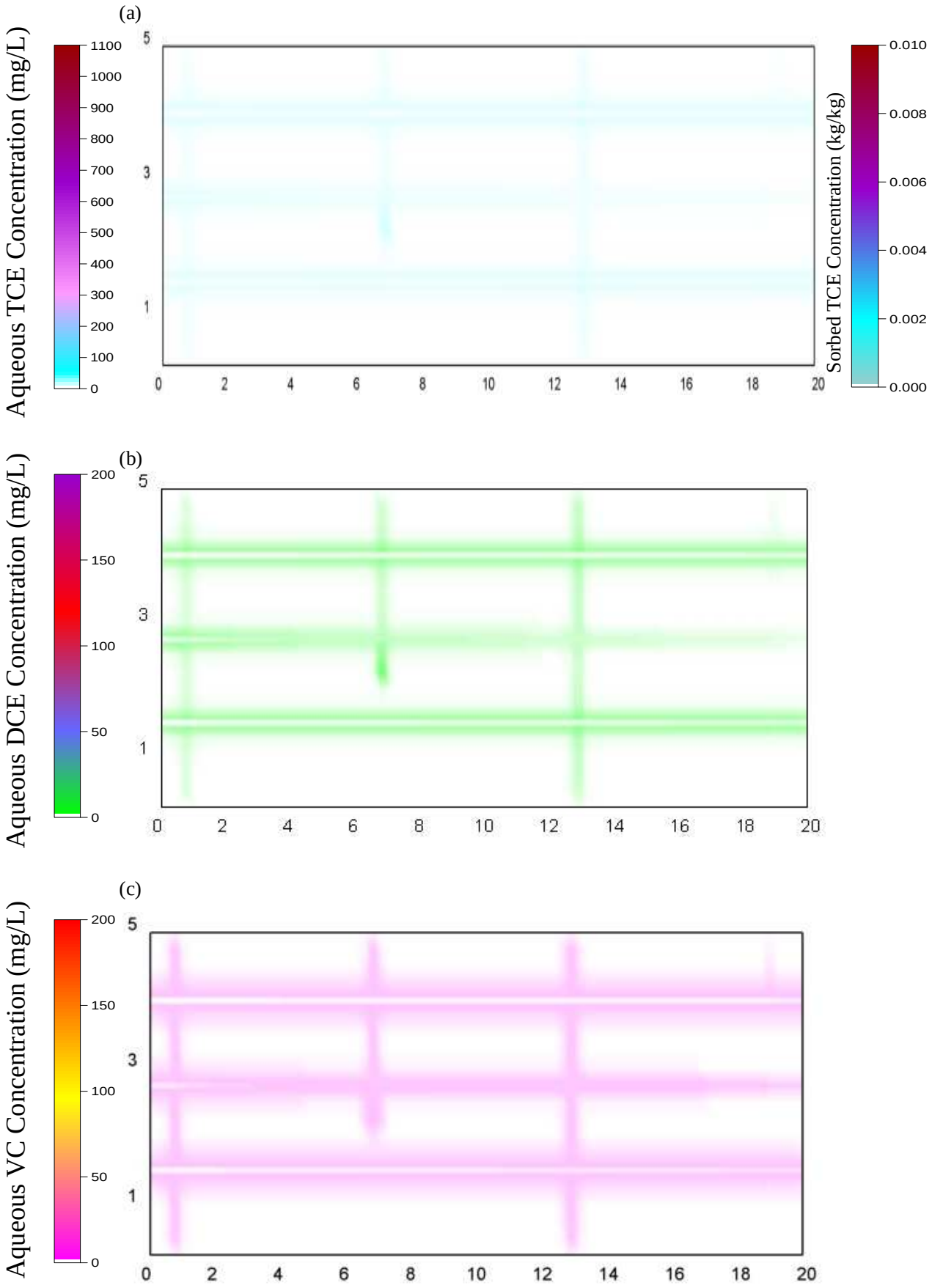
(a)
Aqueous TCE Concentration (mg/L)
1100
1000
900
800
700
600
500
400
300
200
100
0
5
3
1
0
2
4
6
8
10
12
14
16
18
20
Sorbed TCE Concentration (kg/kg)
0.010
0.008
0.006
0.004
0.002
0.000
(b)
Aqueous DCE Concentration (mg/L)
200
150
100
50
0
5
3
1
0
2
4
6
8
10
12
14
16
18
20
(c)
Aqueous VC Concentration (mg/L)
200
150
100
50
0
5
3
1
0
2
4
6
8
10
12
14
16
18
20

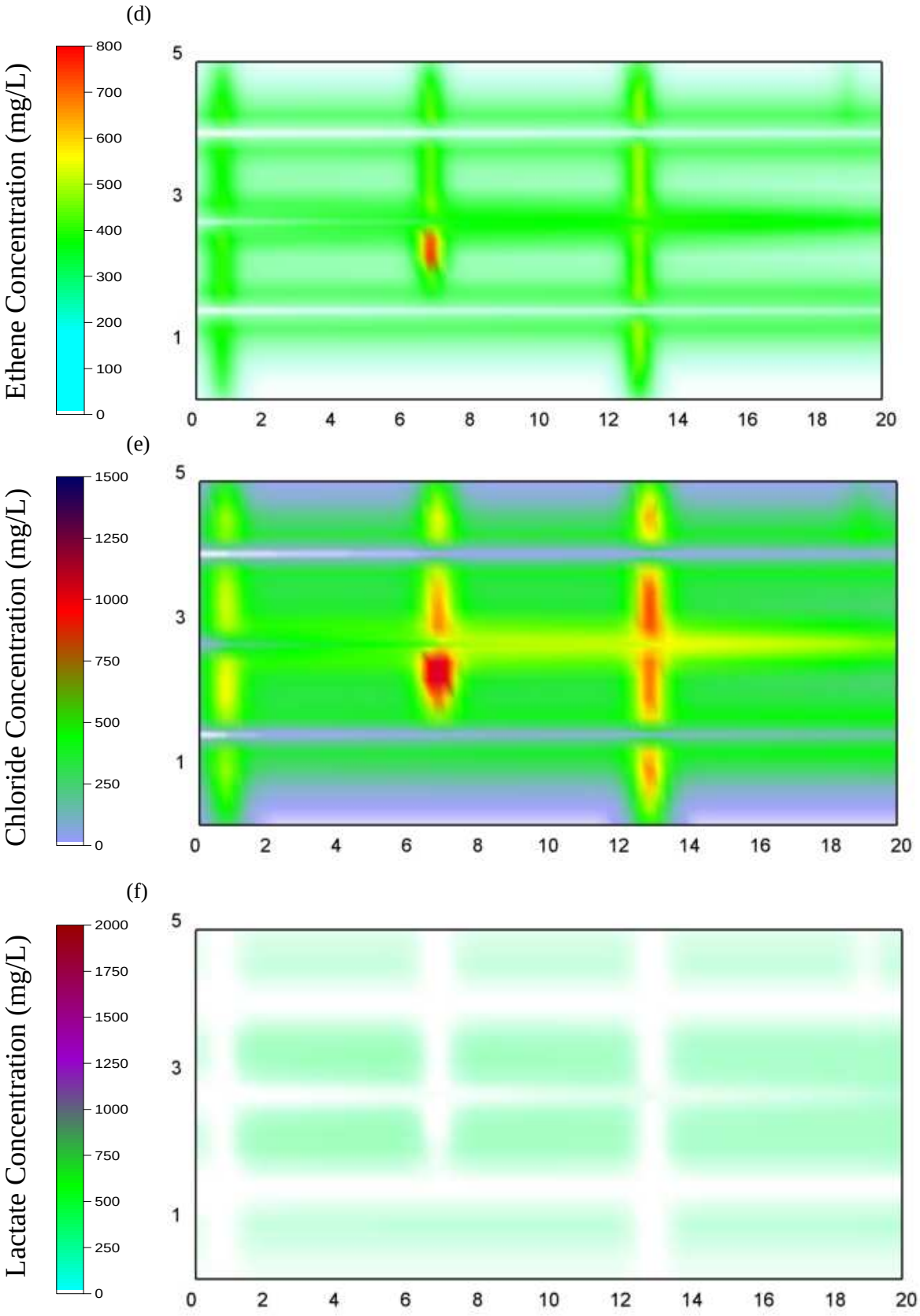

Figure B9: Distribution of (a) Aqueous TCE; (b) Aqueous DCE; (c) Aqueous VC; (d) Ethene; (e) Chloride; (f) Lactate, 5 years after lactate injection for 4000mg/L of lactate injection simulation.

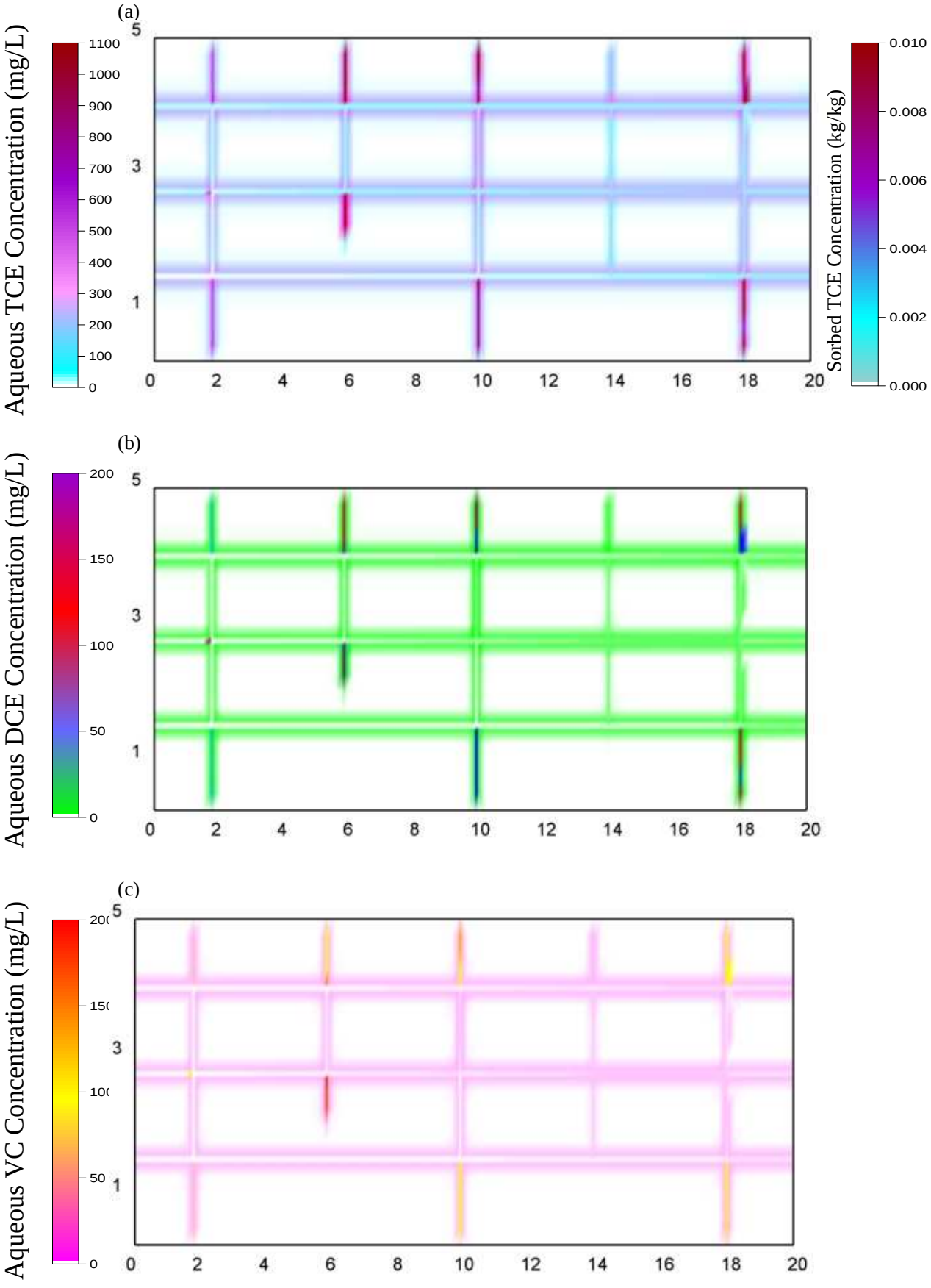
(a)
Aqueous TCE Concentration (mg/L)
1100
1000
900
800
700
600
500
400
300
200
100
0
Sorbed TCE Concentration (kg/kg)
0.010
0.008
0.006
0.004
0.002
0.000
5
3
1
0 2 4 6 8 10 12 14 16 18 20
(b)
Aqueous DCE Concentration (mg/L)
200
150
100
50
0
5
3
1
0 2 4 6 8 10 12 14 16 18 20
(c)
Aqueous VC Concentration (mg/L)
5
3
1
0 2 4 6 8 10 12 14 16 18 20

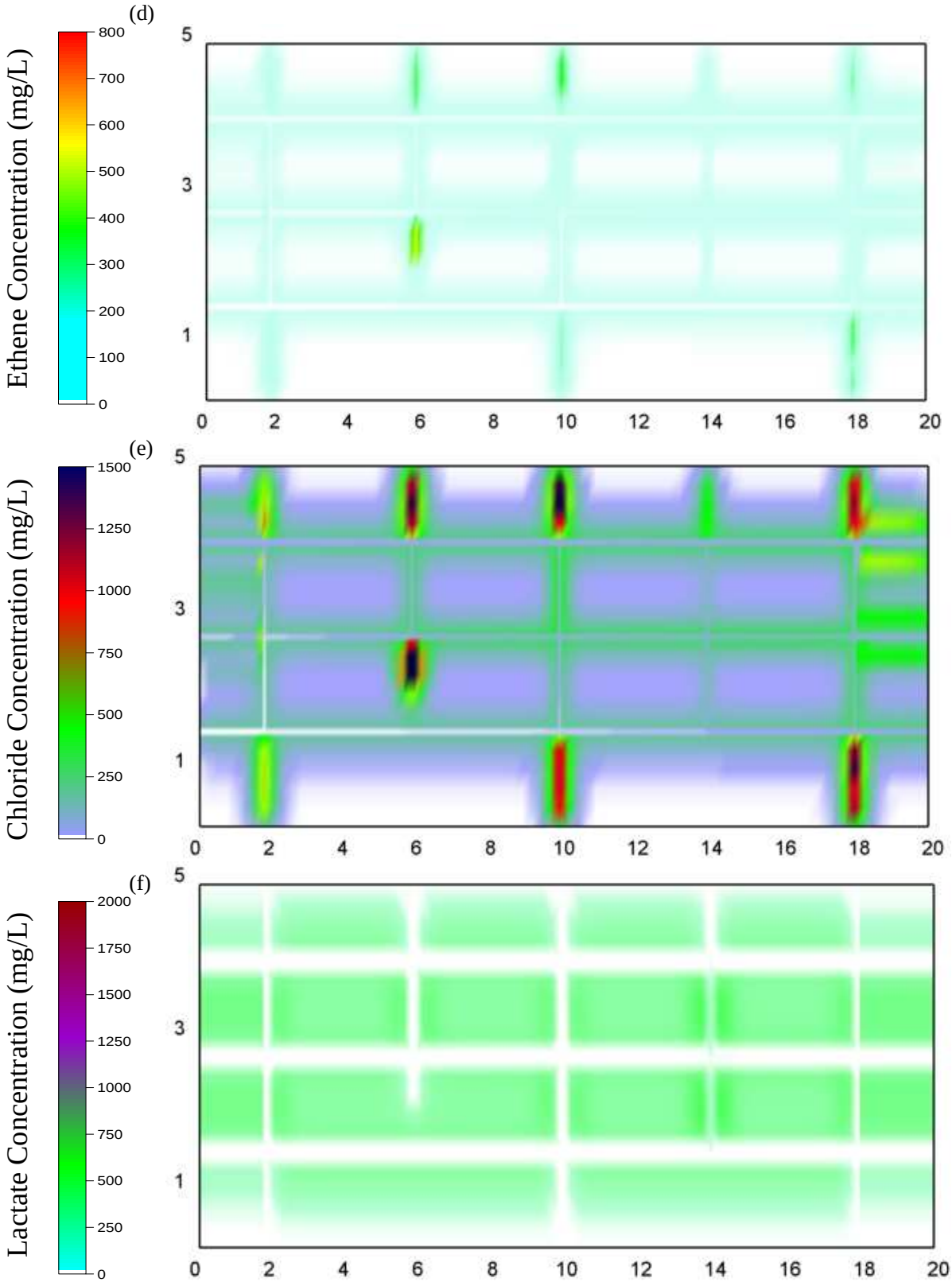

Figure B10: Distribution of (a) Aqueous TCE; (b) Aqueous DCE; (c) Aqueous VC; (d) Ethene; (e) Chloride; (f) Lactate, 5 years after lactate injection for Shale simulation.

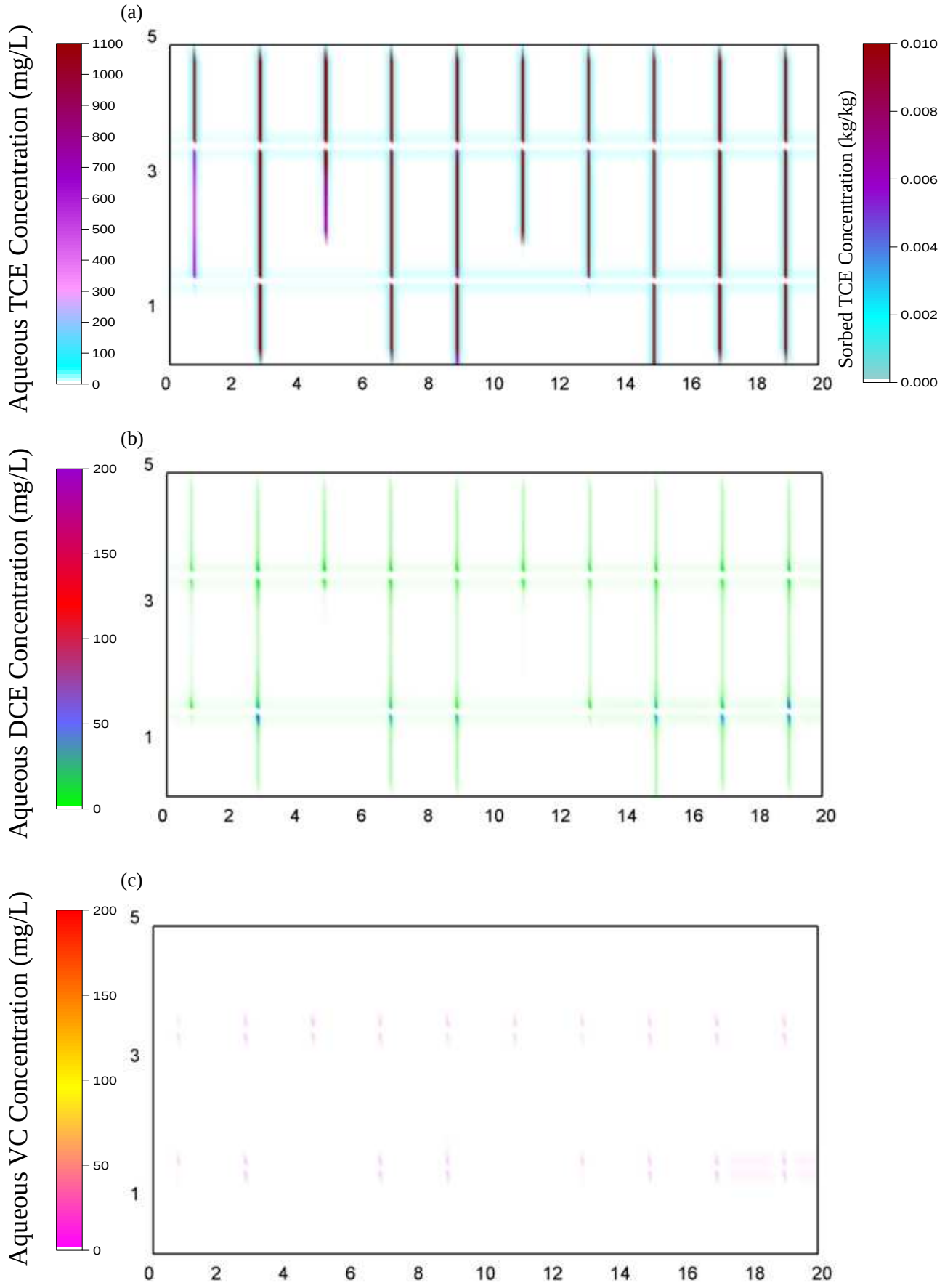
(a)
Aqueous TCE Concentration (mg/L)
1100
1000
900
800
700
600
500
400
300
200
100
0
5
3
1
0
2
4
6
8
10
12
14
16
18
20
Sorbed TCE Concentration (kg/kg)
0.010
0.008
0.006
0.004
0.002
0.000
(b)
Aqueous DCE Concentration (mg/L)
200
150
100
50
0
5
3
1
0
2
4
6
8
10
12
14
16
18
20
(c)
Aqueous VC Concentration (mg/L)
200
150
100
50
0
5
3
1
0
2
4
6
8
10
12
14
16
18
20

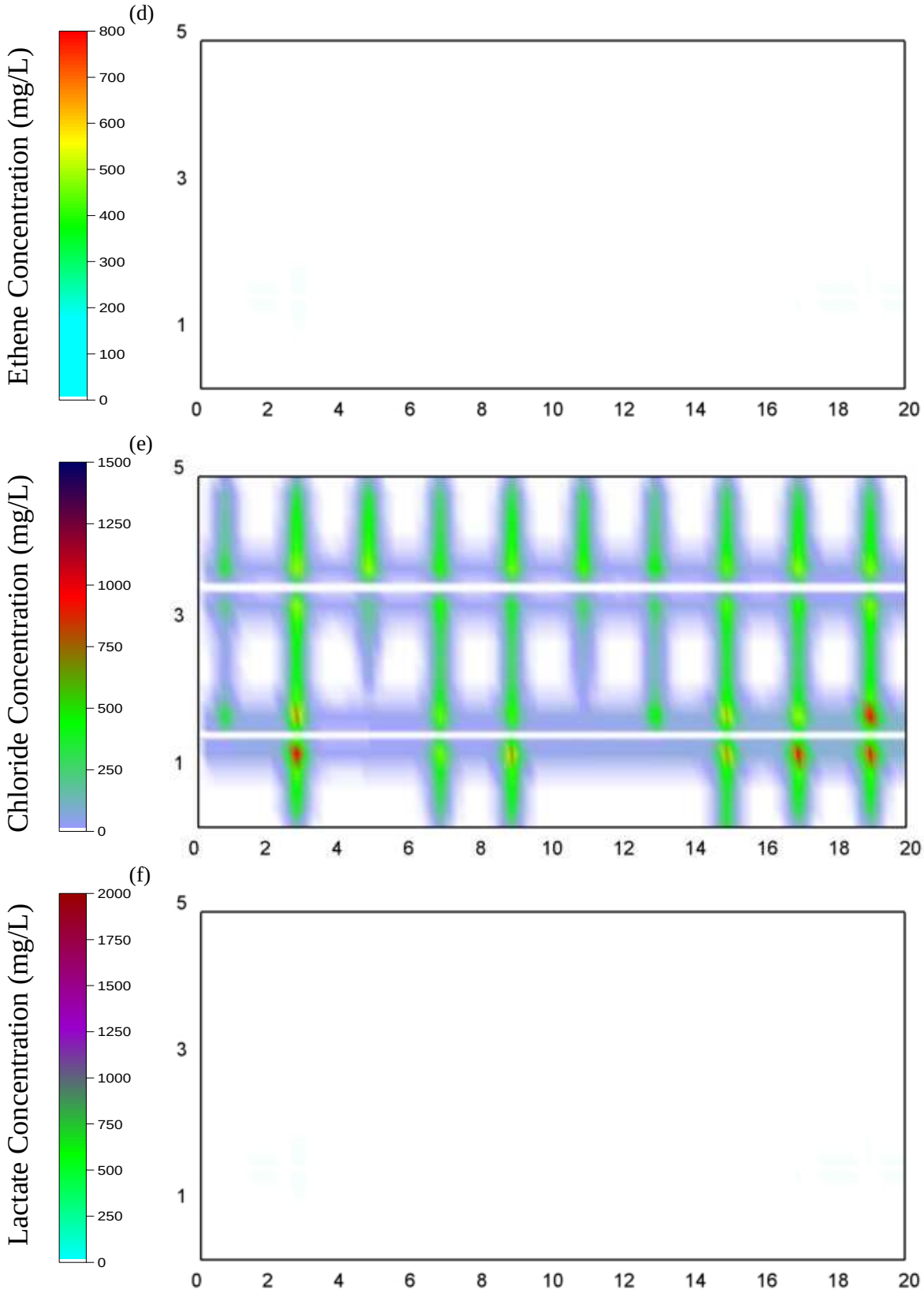

Figure B11: Distribution of (a) Aqueous TCE; (b) Aqueous DCE; (c) Aqueous VC; (d) Ethene; (e) Chloride; (f) Lactate, 5 years after lactate injection for Granite simulation.

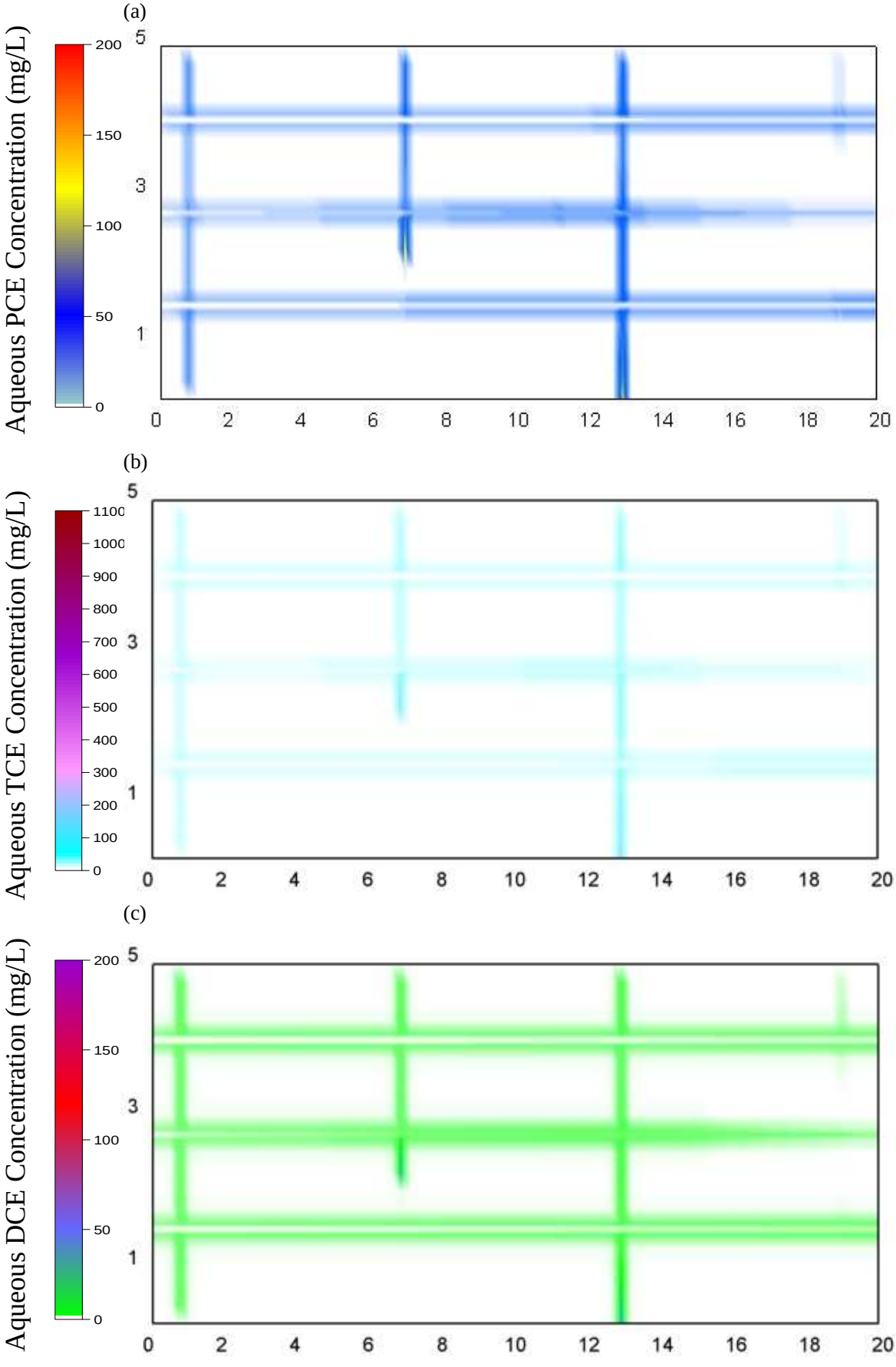
(a)
Aqueous PCE Concentration (mg/L)
200
150
100
50
0
5
3
1
0
2
4
6
8
10
12
14
16
18
20
(b)
Aqueous TCE Concentration (mg/L)
1100
1000
900
800
700
600
500
400
300
200
100
0
5
3
1
0
2
4
6
8
10
12
14
16
18
20
(c)
Aqueous DCE Concentration (mg/L)
200
150
100
50
0
5
3
1
0
2
4
6
8
10
12
14
16
18
20

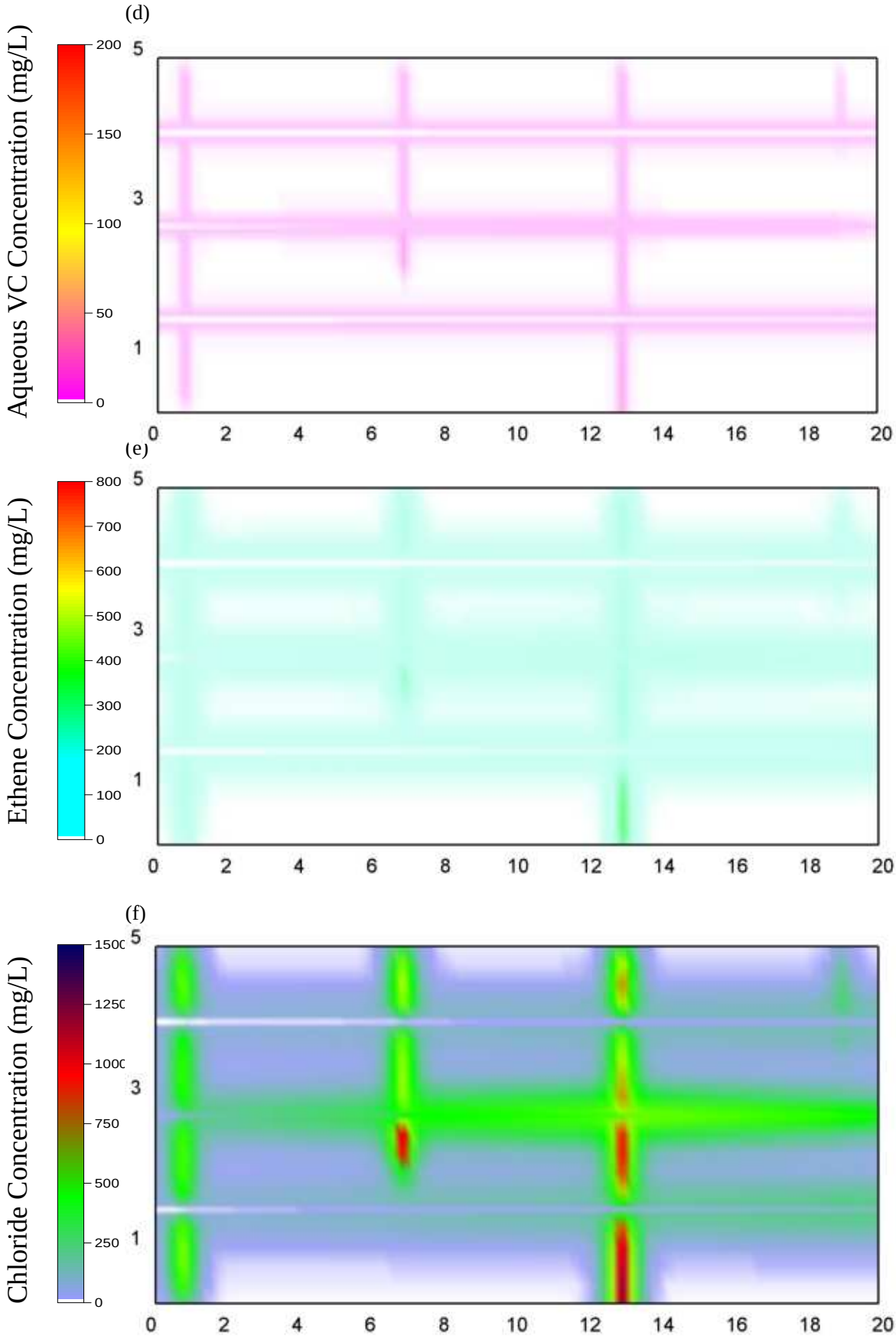
(d)
Aqueous VC Concentration (mg/L)
200
150
100
50
0
5
3
1
0
2
4
6
8
10
12
14
16
18
20
(e)
Ethene Concentration (mg/L)
800
700
600
500
400
300
200
100
0
5
3
1
0
2
4
6
8
10
12
14
16
18
20
(f)
Chloride Concentration (mg/L)
1500
1250
1000
750
500
250
0
5
3
1
0
2
4
6
8
10
12
14
16
18
20

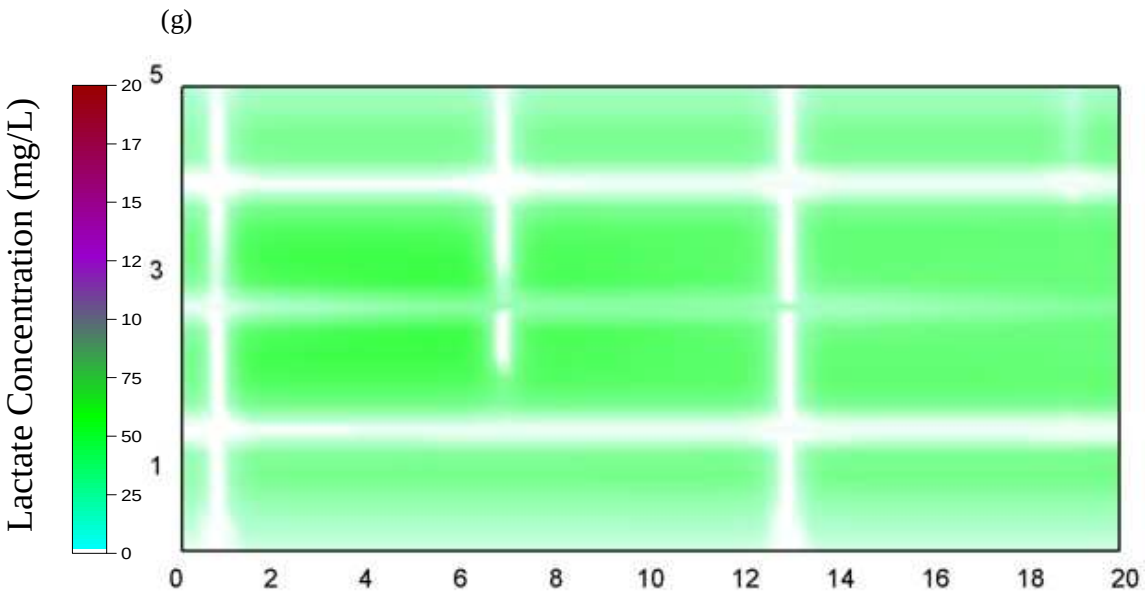

Figure B12: Distribution of (a) Aqueous PCE (b) Aqueous TCE; (c) Aqueous DCE; (d) Aqueous VC; (e) Ethene; (f) Chloride; (g) Lactate, 5 years after lactate injection for PCE simulation.

APPENDIX C

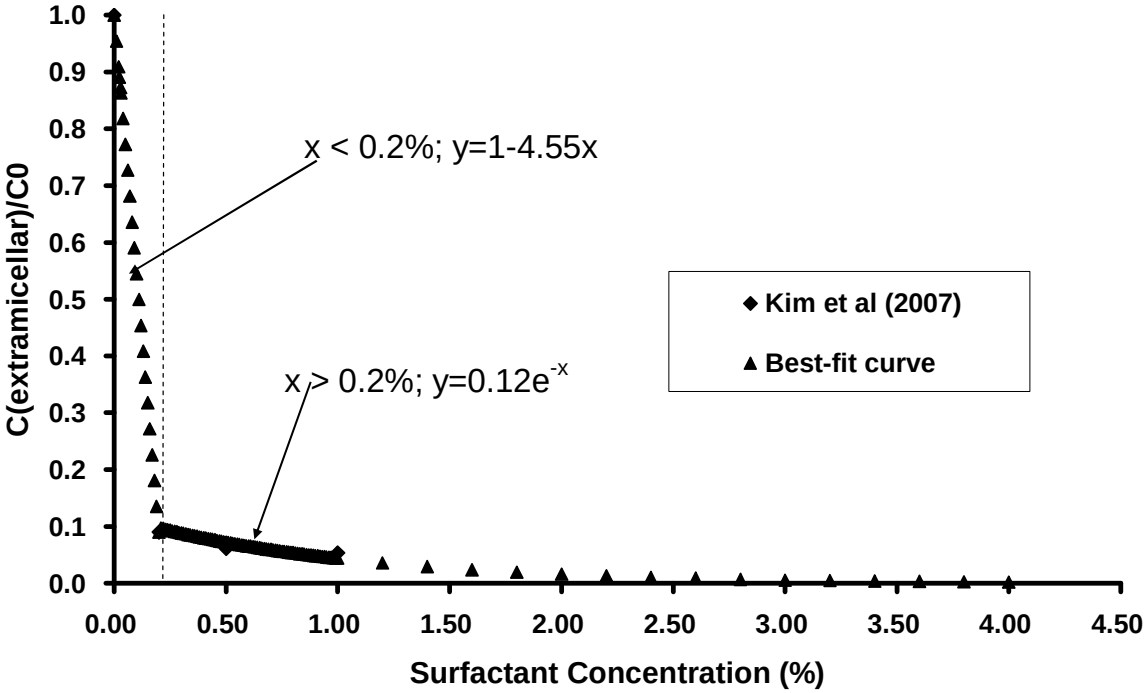

Figure C1: Extramicellar best fit curves for PCE based on results interpolated from Kim et al., 2007.

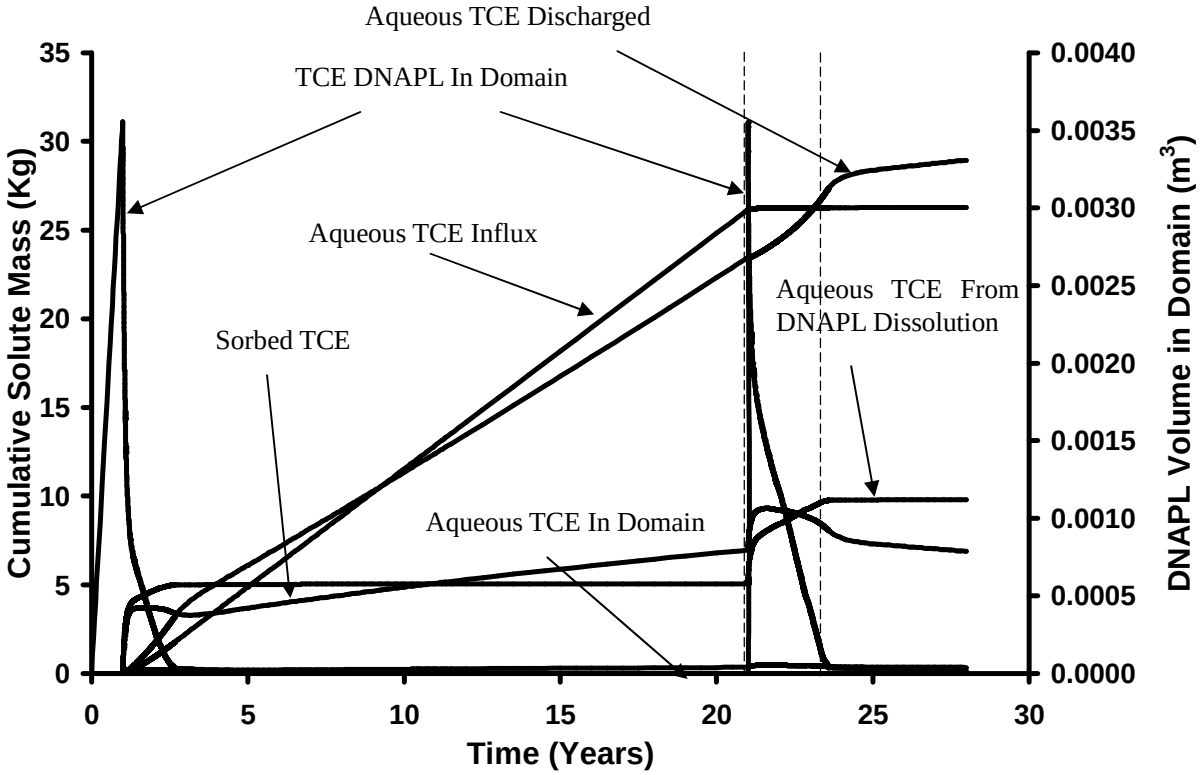

Figure C2: Cumulative aqueous and sorbed TCE from all sinks and sources for No Surfactant Simulation.

(a)

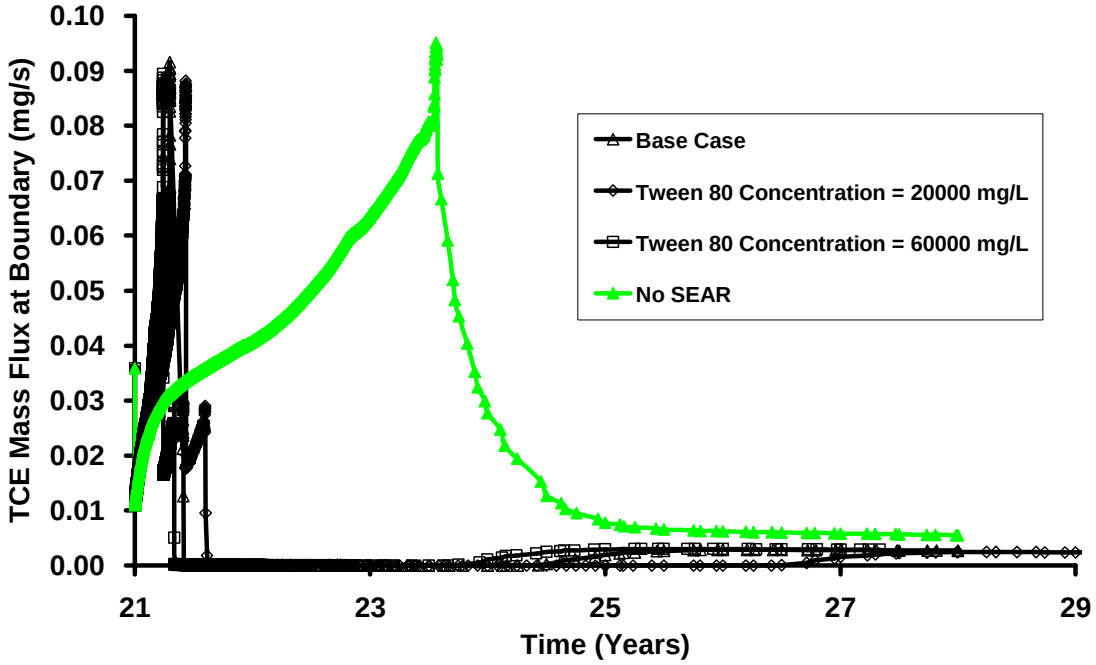

(b)

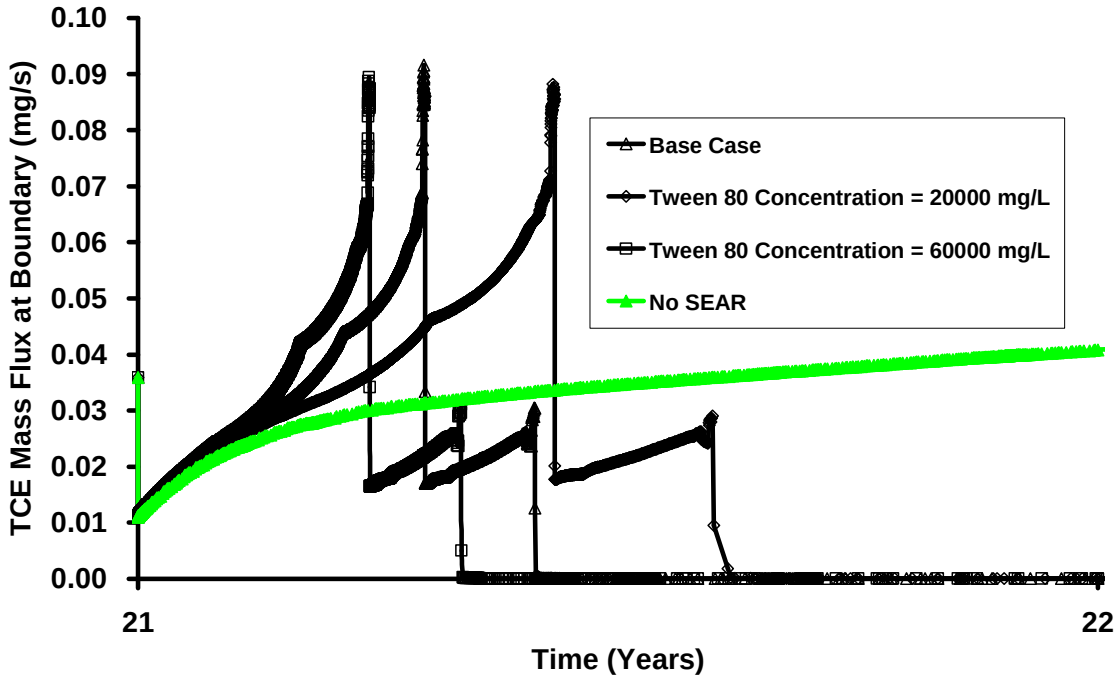

Figure C3: Comparison of total boundary mass discharge (TCE) for base case with (a) various Tween-80 concentration (b) zoom in of results.

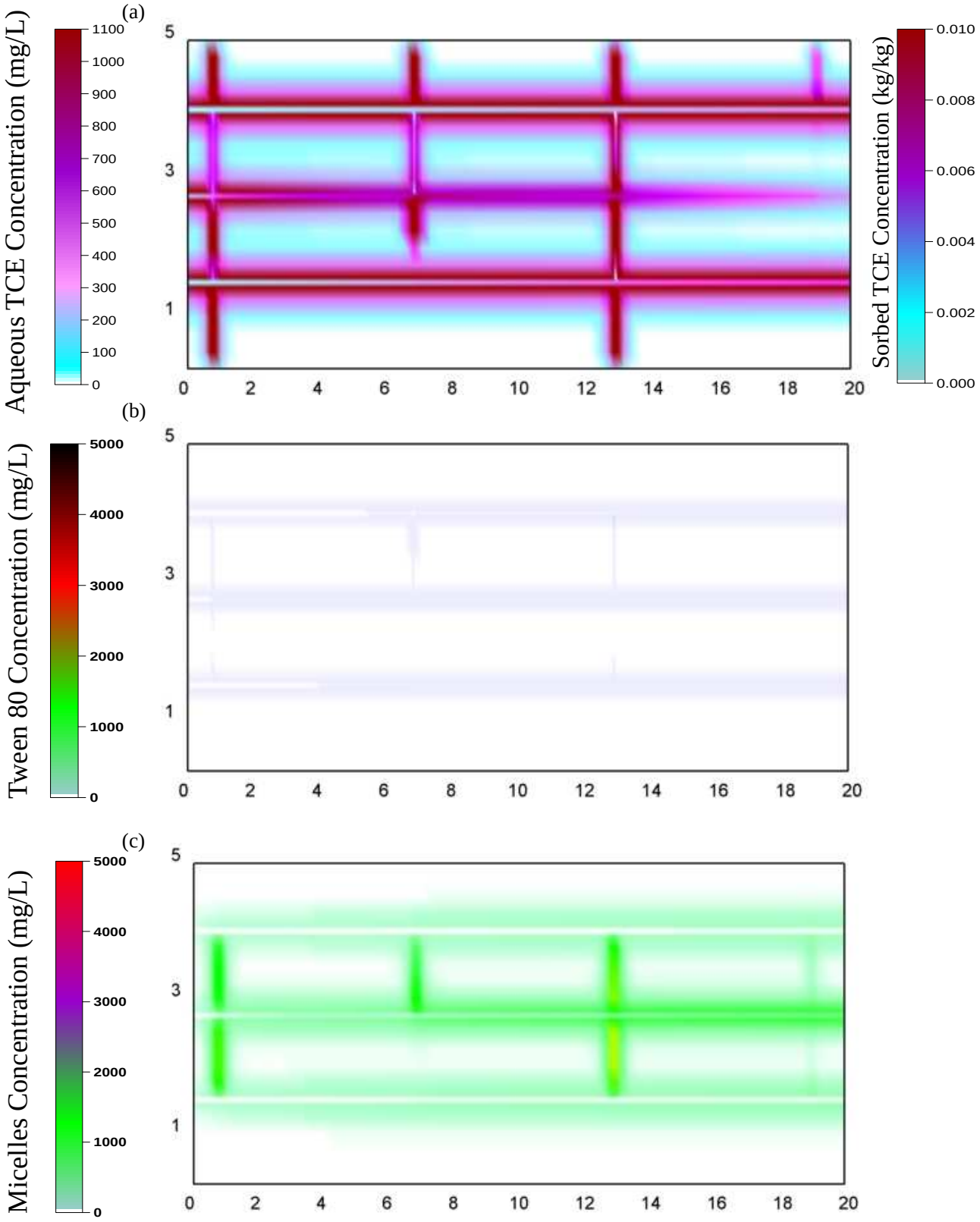

Figure C4: Distribution of (a) Aqueous TCE; (b) Tween-80; (c) TCE occupied micelles, 5 years after injecting 20000mg/L of Tween-80.

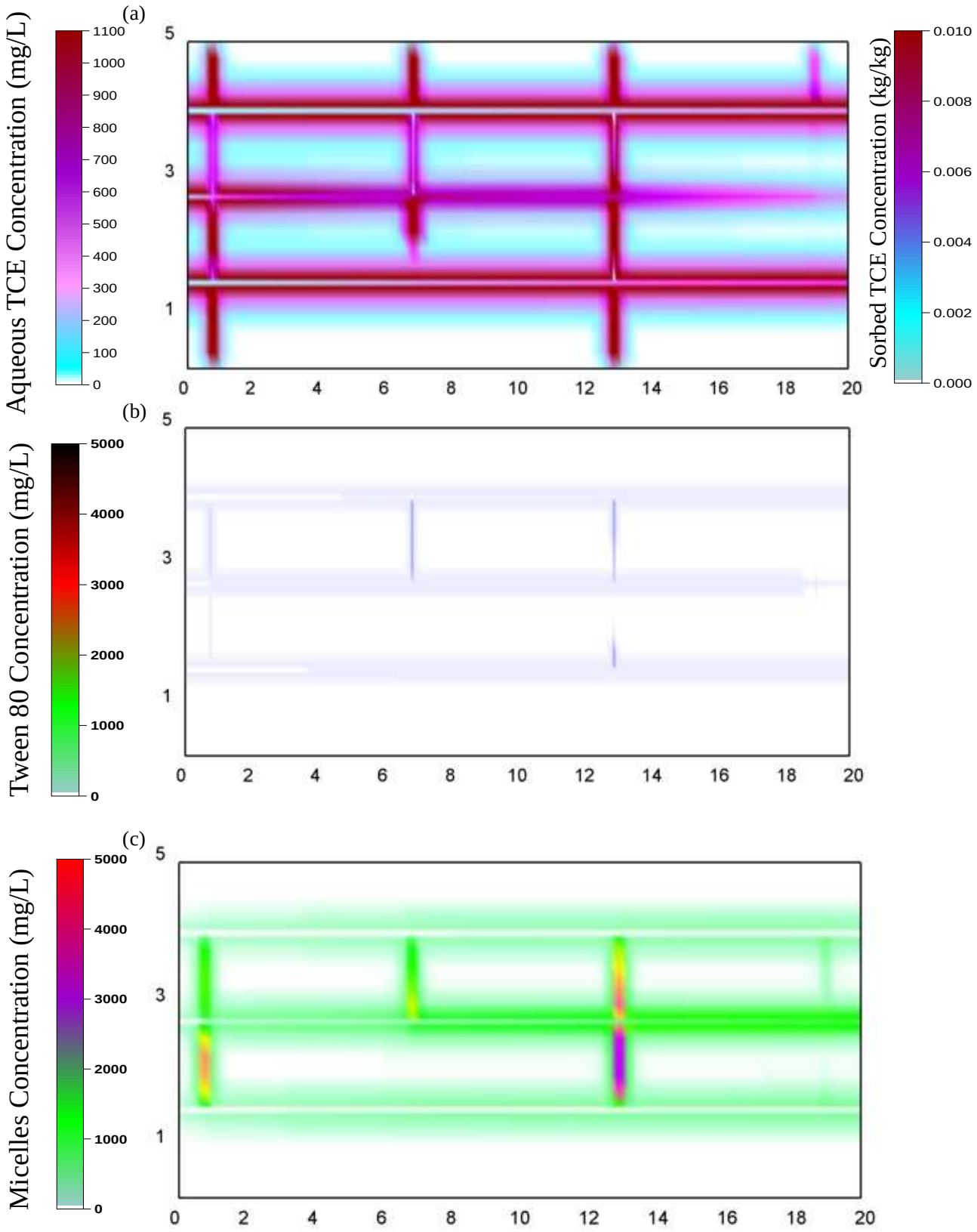

Figure C5: Distribution of (a) Aqueous TCE; (b) Tween-80; (c) TCE occupied micelles, 5 years after injecting 60000mg/L of Tween-80.

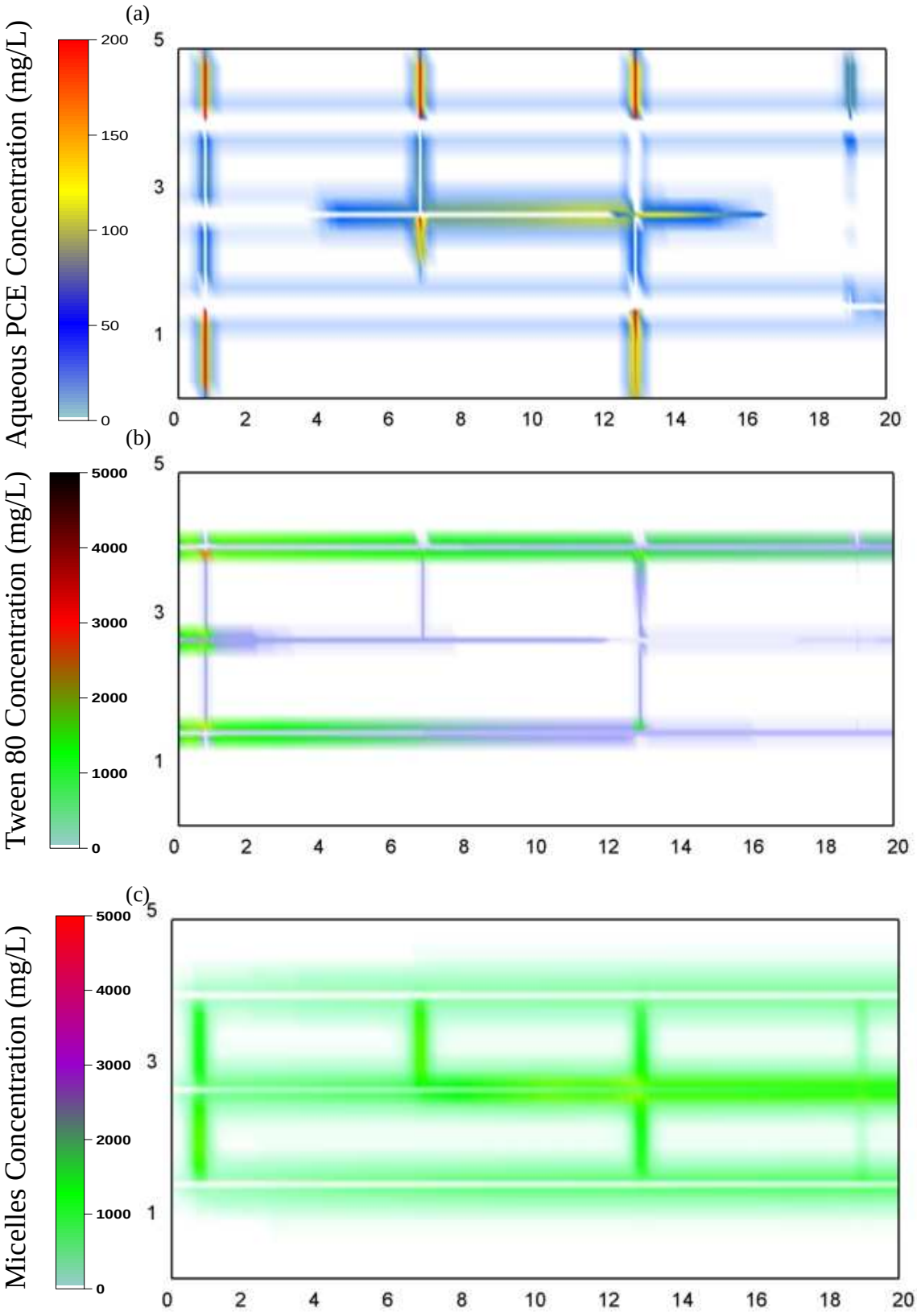

Figure C6: Distribution of (a) Aqueous PCE; (b) Tween-80; (c) PCE occupied micelles, 5 years after surfactant injection for a domain inhibited with PCE.

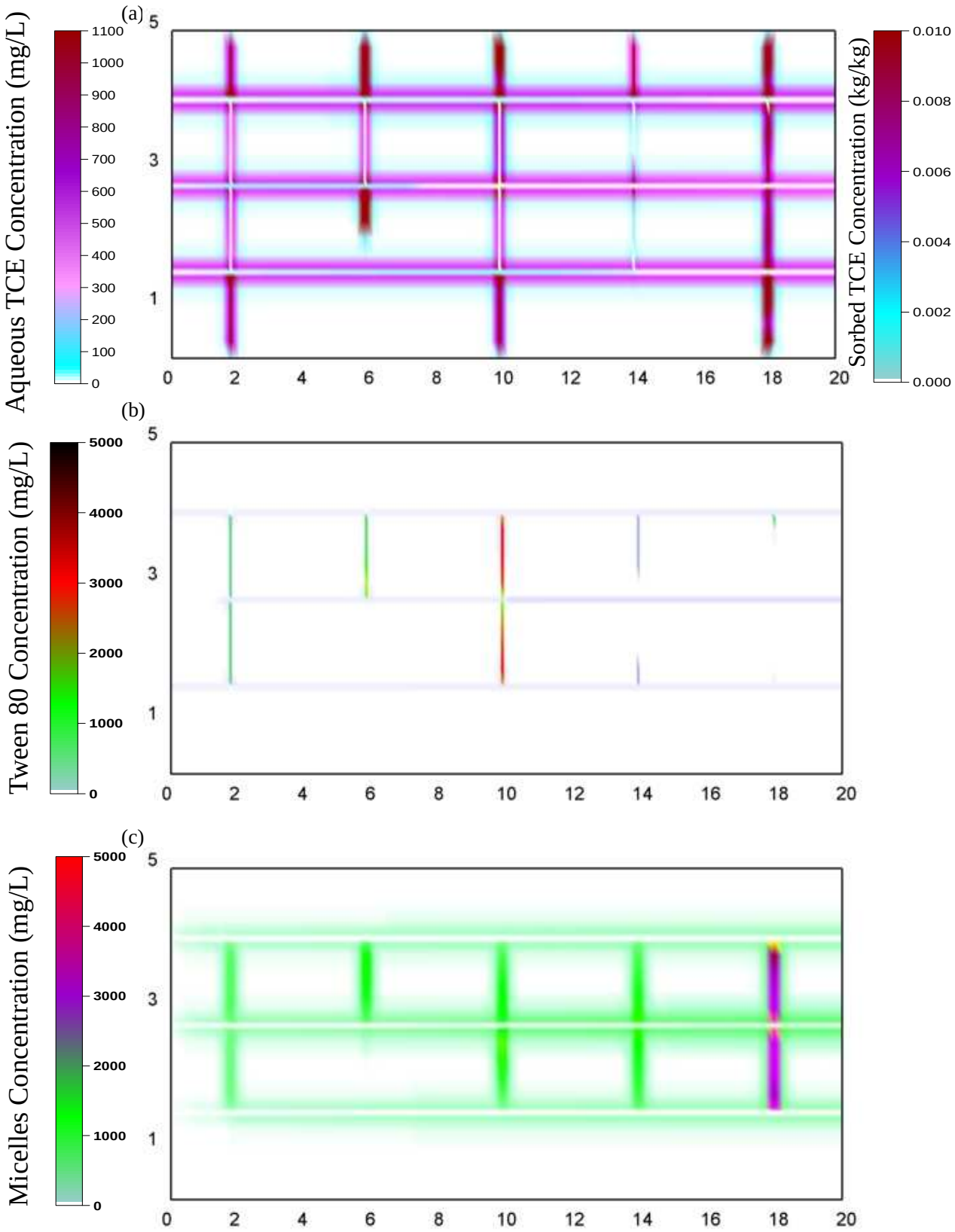

Figure C7: Distribution of (a) Aqueous TCE; (b) Tween-80; (c) TCE occupied micelles, 5 years after surfactant injection for Shale.

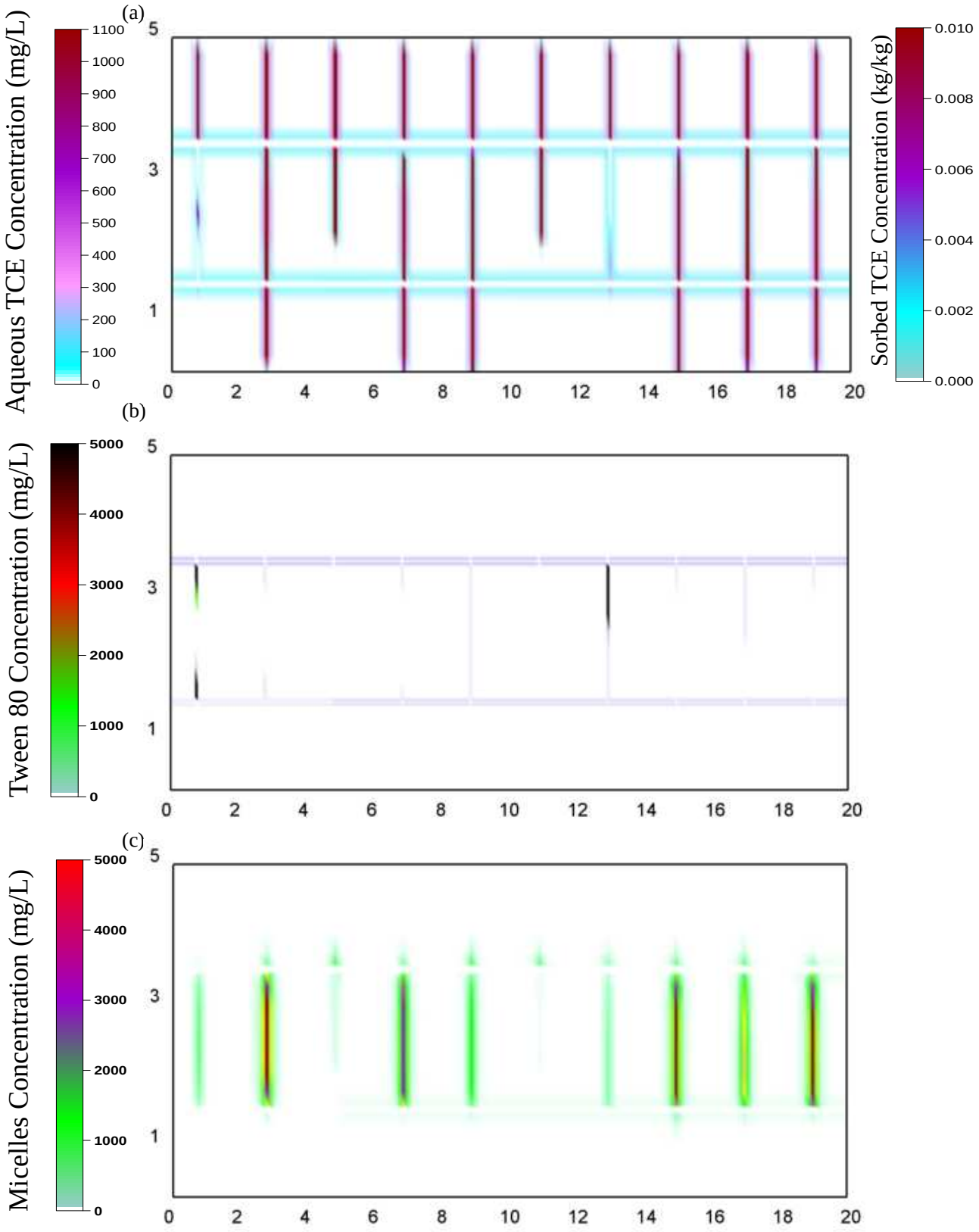

Figure C8: Distribution of (a) Aqueous TCE; (b) Tween-80; (c) TCE occupied micelles, 5 years after surfactant injection for Granite.

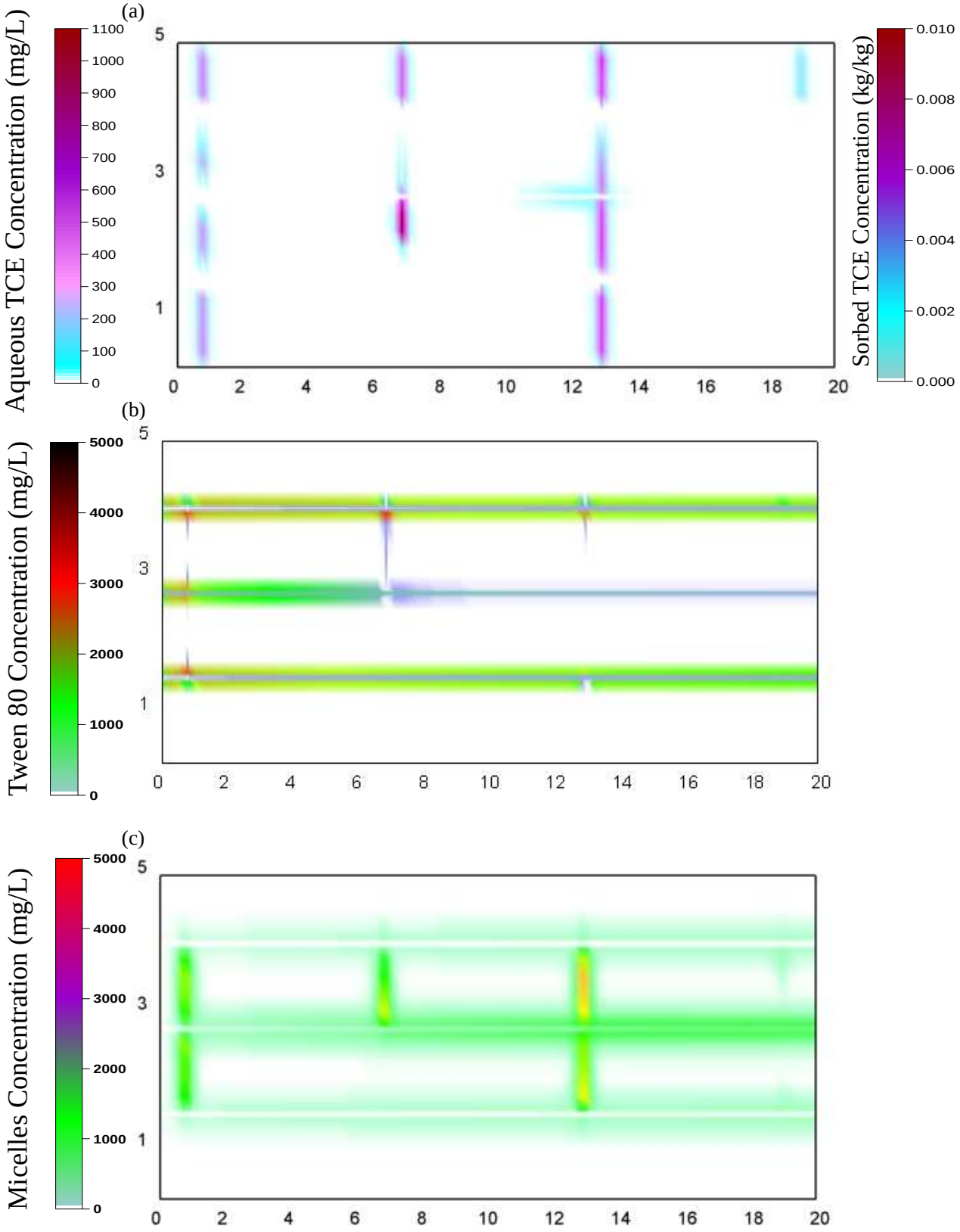

Figure C9: Distribution of (a) Aqueous TCE; (b) Tween-80; (c) TCE occupied micelles, 5 years after Tween-80 injection for a 0-year 'aged' site.

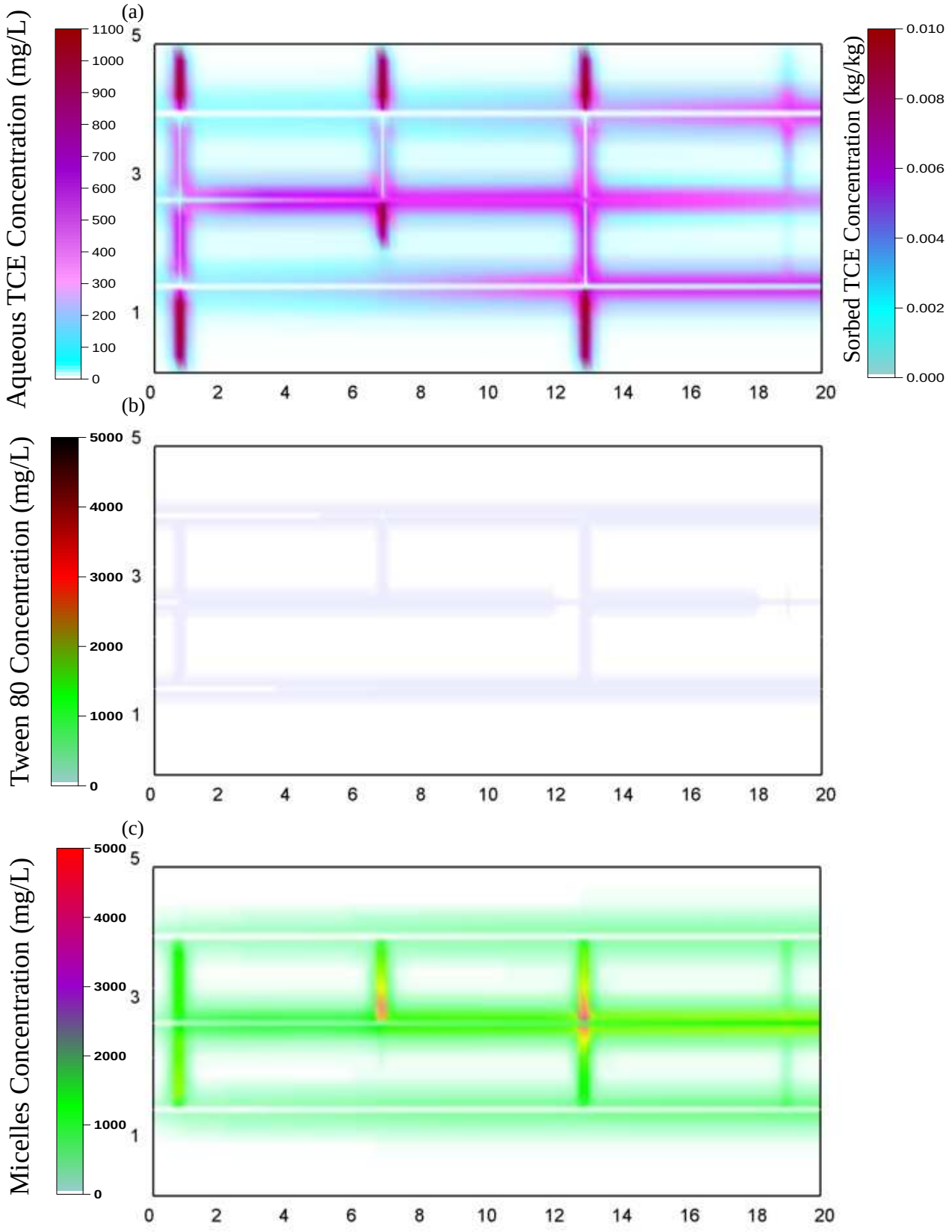

Figure C10: Distribution of (a) Aqueous TCE; (b) Tween-80; (c) TCE occupied micelles, 5 years after Tween-80 injection for a 5-years 'aged' site.

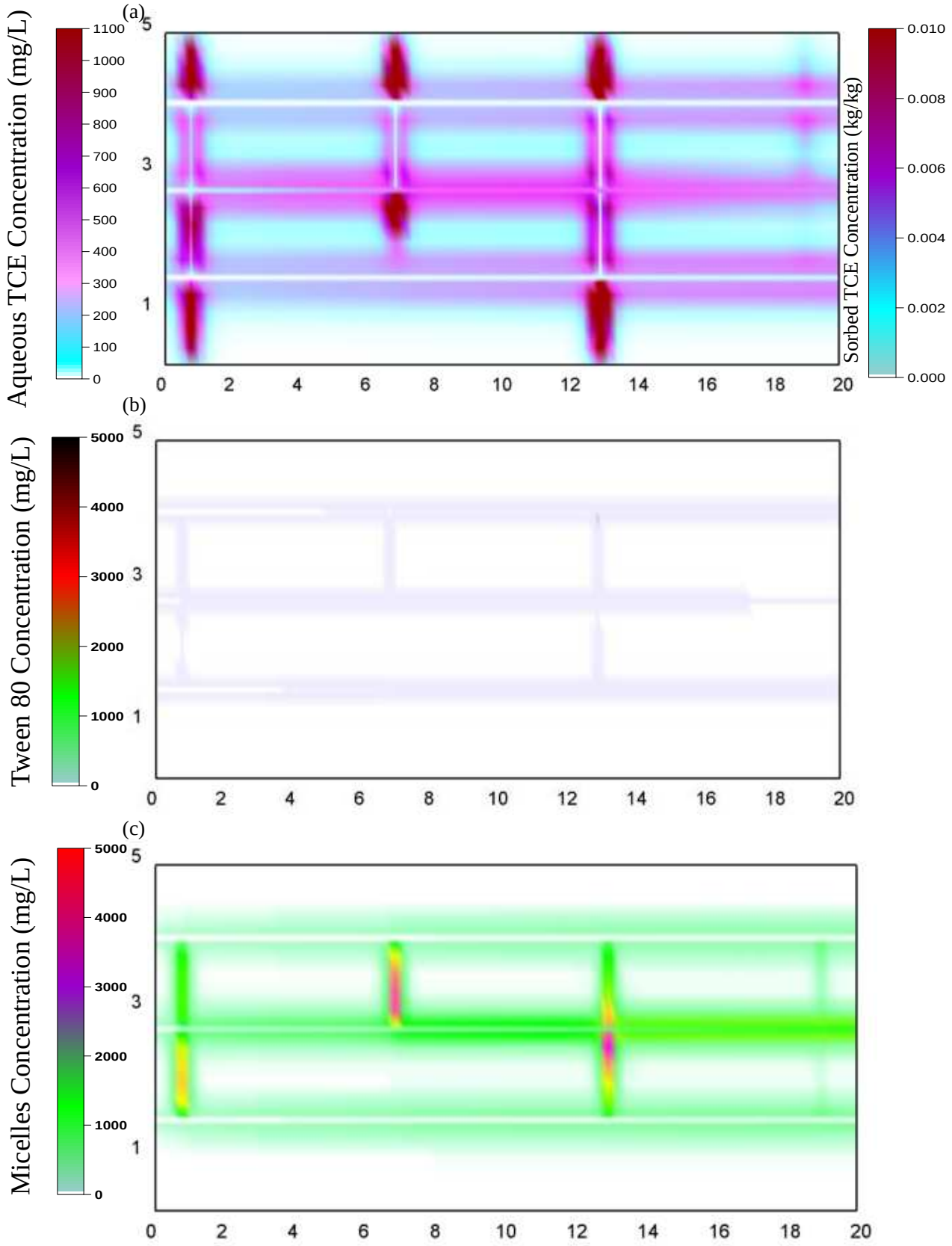

Figure C11: Distribution of (a) Aqueous TCE; (b) Tween-80; (c) TCE occupied micelles, 5 years after Tween-80 injection for a 10-years 'aged' site.

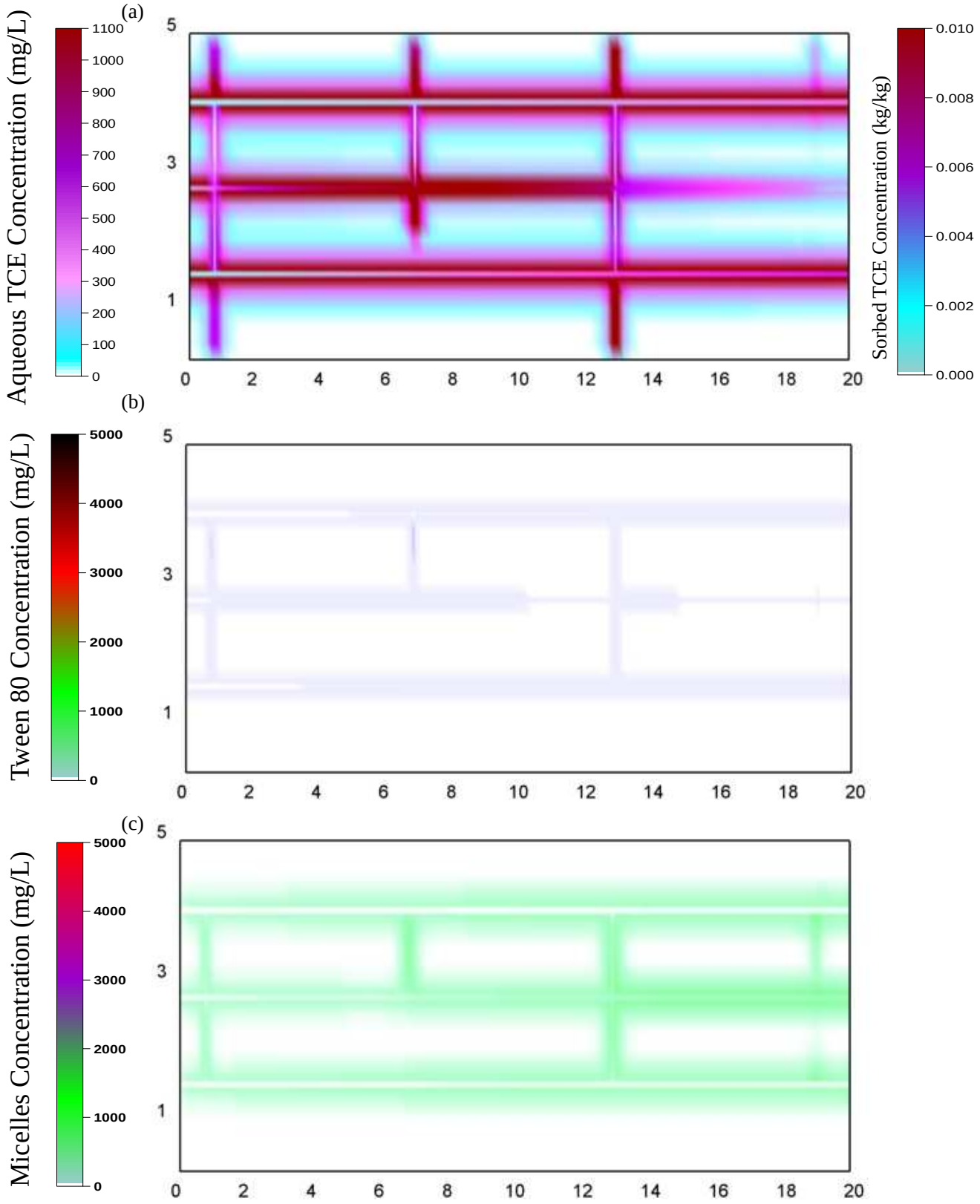

Figure C12: Distribution of (a) Aqueous TCE; (b) Tween-80; (c) TCE occupied micelles, 5 years after surfactant injection for rate-limited mass transfer model.